

INTERSTELLAR PROBE

Humanity's Journey to Interstellar Space

NASA Solar and Space Physics Mission Concept Study
for the Solar and Space Physics 2023–2032 Decadal Survey

December 13, 2021

Ralph L. McNutt Jr.
Principal Investigator
Ralph.McNutt@jhuapl.edu

Michael V. Paul
Project Manager
Michael.Paul@jhuapl.edu

Pontus C. Brandt
Project Scientist
Pontus.Brandt@jhuapl.edu

Jim D. Kinnison
Mission Systems Engineer
Jim.Kinnison@jhuapl.edu

List of Authors

Primary Team

Name	Position	Affiliation
Ralph L. McNutt Jr.	Principal Investigator	Johns Hopkins Applied Physics Laboratory
Michael V. Paul	Project Manager	Johns Hopkins Applied Physics Laboratory
Glen Fountain	Deputy Project Manager/Senior Advisor and Mission Lifetime Analysis	Johns Hopkins Applied Physics Laboratory
James P. Mastandrea	Assistant Project Manager	Johns Hopkins Applied Physics Laboratory
Pontus C. Brandt	Project Scientist	Johns Hopkins Applied Physics Laboratory
Kathleen E. Mandt	Deputy Project Scientist	Johns Hopkins Applied Physics Laboratory
Jim Kinnison	Mission Architecture and Acting Radioisotope Power Systems	Johns Hopkins Applied Physics Laboratory
Alice A. Cocoros	Payload System Engineer	Johns Hopkins Applied Physics Laboratory
Reza Ashtari	Deep Space Communications	Johns Hopkins Applied Physics Laboratory
Stuart Bale	Heliophysics – Fields	University of California, Berkeley
David J. Copeland	Deep Space Communications	Johns Hopkins Applied Physics Laboratory
Bob DeMajistre	Heliophysics – ENA	Johns Hopkins Applied Physics Laboratory
André Galli	Heliophysics – Neutrals	University of Bern
Andrea Harman	Program Communications	—
Matthew E. Hill	Heliophysics – Particles	Johns Hopkins Applied Physics Laboratory
Bryan Holler	Planetary Deputy Lead	Space Telescope Science Institute
Stephen Jaskulek	Mission Lifetime Analysis	Johns Hopkins Applied Physics Laboratory
Kathy Kha	Costing and Financial Planning	Johns Hopkins Applied Physics Laboratory
Peter Kollmann	Heliophysics – Particles	Johns Hopkins Applied Physics Laboratory
Bill Kurth	Heliophysics – Fields	University of Iowa
Carey M. Lisse	Astrophysics Lead	Johns Hopkins Applied Physics Laboratory
Douglas Mehoke	Solar Shield Analysis and Testing	Johns Hopkins Applied Physics Laboratory
Parisa Mostafavi	Deputy Heliophysics Lead	Johns Hopkins Applied Physics Laboratory
David Napolillo	Spacecraft Configuration Studies	Johns Hopkins Applied Physics Laboratory
Romina Nikoukar	Space Physicist	Johns Hopkins Applied Physics Laboratory
Kimberly J. Ord	Concept of Operations	Johns Hopkins Applied Physics Laboratory
Elena A. Provornikova	Heliophysics Lead	Johns Hopkins Applied Physics Laboratory
Gabe Rogers	Spacecraft Control Analysis	Johns Hopkins Applied Physics Laboratory
Christopher M. Rose	Avionics	Johns Hopkins Applied Physics Laboratory
Kirby D. Runyon	Planetary Lead	Johns Hopkins Applied Physics Laboratory
Abigail M. Rymer	Exoplanet Lead	Johns Hopkins Applied Physics Laboratory
Wayne R. Schlei	Trajectory Analyses	Johns Hopkins Applied Physics Laboratory
Fazle Siddique	Trajectory Analyses	Johns Hopkins Applied Physics Laboratory
Clayton Smith	Mission Lifetime Analysis	Johns Hopkins Applied Physics Laboratory
Robert Stough	SLS Coordination	NASA Marshall Space Flight Center
Justyna Sokol	Heliophysics Community Coordinator	Southwest Research Institute

Name	Position	Affiliation
Jamey Szalay	Heliophysics – Dust	Princeton University
Drew L. Turner	Heliophysics – Particles	Johns Hopkins Applied Physics Laboratory
Vikas Vepachedu	Payload System Engineer	Johns Hopkins Applied Physics Laboratory
Steven R. Vernon	Launch Vehicles Options and Alternatives	Johns Hopkins Applied Physics Laboratory
Janet Vertesi	Social Science	Princeton University
Sally Whitley	Mission Lifetime Analysis	Johns Hopkins Applied Physics Laboratory
Lawrence S. Wolfarth	Costing and Financial Planning	Johns Hopkins Applied Physics Laboratory
Michael Zemcov	Astrophysics Deputy Lead	Center for Detectors, Rochester Institute of Technology

Collaborators

Name	Affiliation
Caitlin Ahrens	NASA Goddard Space Flight Center
Frederic Allegrini	Southwest Research Institute
Ben Alterman	Southwest Research Institute
Nicolas Altobelli	European Space Agency
Erika Alvarez	NASA
Brian Anderson	Johns Hopkins Applied Physics Laboratory
Andrew Annex	Johns Hopkins University
Fran Bagenal	Laboratory for Atmospheric and Space Physics, University of Colorado
Elizabeth Bailey	Caltech
Dan Baker	Laboratory for Atmospheric and Space Physics, University of Colorado Boulder
Igor Baliukin	Space Research Institute, Russian Academy of Sciences
Michele Bannister	Queen’s University Belfast
Stas Barabash	Institutet för Rymdfysik, Swedish Institute of Space Physics
Vladimir Baranov	Ishlinsky Institute for Problems in Mechanics of the Russian Academy of Sciences
Konstantin Batygin	Caltech
Chas Beichman	NASA Jet Propulsion Laboratory
Susan Benecchi	Planetary Science Institute
Jean-Loup Bertaux	Institut de Recherche en Sciences de l’Environnement
Gary Blackwood	NASA Jet Propulsion Laboratory
Michel Blanc	Institut de Recherche en Astrophysique et Planétologie
Maciej Bzowski	Space Research Centre, Polish Academy of Sciences
Joshua Cahill	Johns Hopkins Applied Physics Laboratory
Richard Cartwright	SETI Institute
Andy Cheng	Johns Hopkins Applied Physics Laboratory
Eric Christian	NASA Goddard Space Flight Center
John Clarke	Boston University
William Cochran	The University of Texas at Austin
Christina Cohen	Caltech
John Cooper	NASA Goddard Space Flight Center
Asantha Cooray	University of California, Irvine

Name	Affiliation
Athena Coustenis	l'Observatoire de Paris
Andrzej Czechowski	Centrum Badań Kosmicznych PAN
Diganta Das	University of Maryland, Center for Advanced Life Cycle Engineering (CALCE)
Rob Decker	Johns Hopkins Applied Physics Laboratory
Mihir Desai	Southwest Research Institute
Kostas Dialynas	Department of Physics, National and Kapodistrian University of Athens
Bruce Draine	Princeton University
Heather Elliott	Southwest Research Institute
Stefan Eriksson	Laboratory for Atmospheric and Space Physics, University of Colorado Boulder
Hans Fahr	Argelander-Institut für Astronomie
Brian Fields	University of Illinois at Urbana-Champaign
Len Fisk	University of Michigan
Vladimir Florinski	University of Alabama
Robert Forsyth	Imperial College London
Federico Fraternali	University of Alabama in Huntsville
Louis Friedman	Planetary Society
Priscilla Frisch	University of Chicago
Herb Funsten	Los Alamos National Laboratory
Steve Fuselier	Southwest Research Institute
Yoshifumi Futaana	Swedish Institute of Space
Matina Gkioulidou	Johns Hopkins Applied Physics Laboratory
Randy Gladstone	Southwest Research Institute
George Gloeckler	University of Michigan
Arnie Goldberg	Johns Hopkins Applied Physics Laboratory
Mike Gruntman	University of Southern California
Don Gurnett	University of Iowa
Sonny Harman	NASA Ames Research Center
George Ho	Johns Hopkins Applied Physics Laboratory
Mihály Horányi	Laboratory for Atmospheric and Space Physics, University of Colorado Boulder
Timothy Horbury	Imperial College London
Sona Hosseini	NASA Jet Propulsion Laboratory
Silvan Hunziker	ETH Zurich
Noam Izenberg	Johns Hopkins Applied Physics Laboratory
Vlad Izmodenov	Space Research Institute, Russian Academy of Sciences
Steve Jaskulek	Johns Hopkins Applied Physics Laboratory
Olga Katushkina	Space Research Institute, Russian Academy of Sciences
James Keane	NASA Jet Propulsion Laboratory
Sascha Kempf	Laboratory for Atmospheric and Space Physics, University of Colorado Boulder
Roman Kezerashvili	New York City College of Technology
Tae Kim	University of Alabama in Huntsville
Kelly Korreck	Harvard University
Haje Korth	Johns Hopkins Applied Physics Laboratory
Dimitra Koutroumpa	Laboratory for Atmospheres, Environments, Space Observations (LATMOS)
Izabela Kowalska-Leszczynska	Space Research Centre, Polish Academy of Sciences

Name	Affiliation
Tom Krimigis	Johns Hopkins Applied Physics Laboratory
Marzena Kubiak	Space Research Centre, Polish Academy of Sciences
Harald Kucharek	University of New Hampshire
Rosine Lallement	l'Observatoire de Paris
Lou Lanzerotti	New Jersey Institute of Technology
Benoit Lavraud	Institut de Recherche en Astrophysique et Planétologie
Joseph Lazio	NASA Jet Propulsion Laboratory
Anny-Chantal Levasseur-Regourd	Sorbonne Université
Hui Li	State Key Laboratory of Space Weather
Paulett Liewer	NASA Jet Propulsion Laboratory
Jeffrey Linsky	JILA, University of Colorado
Stefano Livi	Southwest Research Institute
Kelvin Long	Initiative for Interstellar Studies
Philip Lubin	University of California, Santa Barbara
Bennett Maruca	University of Delaware
John Mather	NASA Goddard Space Flight Center
Gregory Matloff	New York City College of Technology
Erin May	Johns Hopkins Applied Physics Laboratory
Laura Mayorga	Johns Hopkins Applied Physics Laboratory
Majd Mayyasi	Boston University
David McComas	Princeton University
Bill McKinnon	Washington University in St. Louis
Dick Mewaldt	Space Radiation Lab at California Institute of Technology
Adam Michael	Johns Hopkins Applied Physics Laboratory
Jesse Miller	University of Illinois at Urbana-Champaign
Don Mitchell	Johns Hopkins Applied Physics Laboratory
Eberhard Moebius	University of New Hampshire
Hans Mueller	Dartmouth College
Hari Nair	Johns Hopkins Applied Physics Laboratory
Stella Ocker	Cornell University
Merav Opher	Boston University
Colleen O'Shea	Johns Hopkins Applied Physics Laboratory
Jeewoo Park	NASA Goddard Space Flight Center
Nick Paschalidis	NASA Goddard Space Flight Center
Larry Paxton	Johns Hopkins Applied Physics Laboratory
Nick Pogorelov	University of Alabama in Huntsville
Andrew Poppe	University of California, Berkeley
Frank Postberg	Freie Universität Berlin
Eric Quemerais	Laboratory for Atmospheres, Environments, Space Observations (LATMOS)
Ashique Rahman	Johns Hopkins Applied Physics Laboratory
Jamie Rankin	Princeton University
Nour Raouafi	Johns Hopkins Applied Physics Laboratory
Romana Ratkiewicz	Centrum Badań Kosmicznych PAN

Name	Affiliation
Seth Redfield	Wesleyan University
Kurt Retherford	Southwest Research Institute
John Richardson	Massachusetts Institute of Technology
Ed Roelof	Johns Hopkins Applied Physics Laboratory
Kyle Ryan	Johns Hopkins Applied Physics Laboratory
Nathan Schwadron	University of New Hampshire
Bishwas Shrestha	University of Alabama in Huntsville
Steinn Sigurdsson	Penn State University
Jon Slavin	Harvard and Smithsonian Center for Astrophysics
David Smith	NASA Marshall Space Flight Center
Linda Spilker	NASA Jet Propulsion Laboratory
Ralf Srama	Universität Stuttgart
Veerle Sterken	ETH Zürich
Alan Stern	Southwest Research Institute
Ted Stryk	Roane State Community College
Pawel Swaczyna	Princeton University
Adam Szabo	NASA Goddard Space Flight Center
Sarah Vines	Johns Hopkins Applied Physics Laboratory
Jan-Erik Wahlund	Swedish Institute of Space Physics
Joe Westlake	Johns Hopkins Applied Physics Laboratory
Robert Wicks	Northumbria University Newcastle
Phil Willems	NASA Jet Propulsion Laboratory
Bob Wimmer	Christian-Albrechts-Universität zu Kiel
Brian Wood	U.S. Naval Research Laboratory
Peter Wurz	Space Research & Planetary Sciences, Universität Bern
June Zakrajsek	NASA
Gary Zank	University of Alabama
Philippe Zarka	l'Observatoire de Paris
Lingling Zhuo	University of Alabama in Huntsville
Qiugang Zong	Institute of Space Physics and Applied Technology and Center for Planetary and Space Science, Peking University

Data Release, Distribution, and Cost Interpretation Statements

This document is intended to support the 2023–2032 Solar and Space Physics Decadal Survey.

The data contained in this document may not be modified in any way.

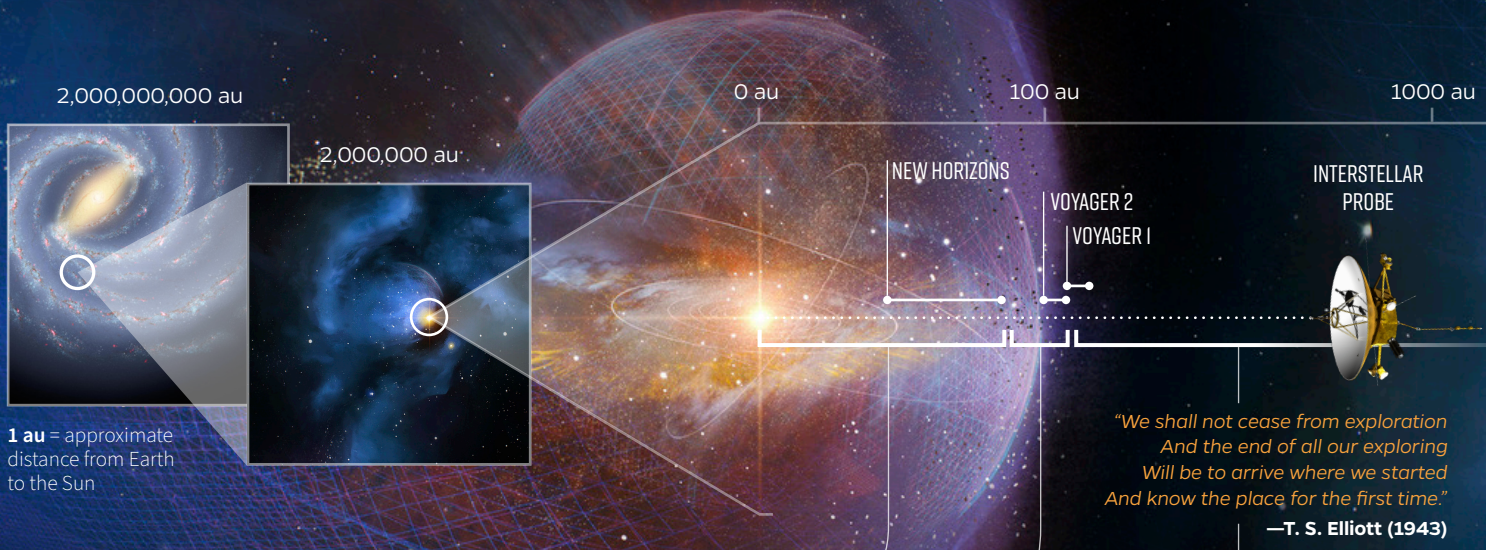
Cost estimates described or summarized in this document were generated as part of a preliminary concept study, are model-based, assume an APL in-house build, and do not constitute a commitment on the part of APL.

Cost reserves for development and operations were included as prescribed by the NASA ground rules for the Planetary Mission Concept Studies program. Unadjusted estimate totals and cost reserve allocations would be revised as needed in future more-detailed studies as appropriate for the specific cost risks for a given mission concept.

INTERSTELLAR PROBE

Humanity's Journey to Interstellar Space

Traveling far beyond the Sun's sphere of influence, Interstellar Probe would be the boldest move in space exploration to date. This pragmatic near-term mission concept would enable groundbreaking science using technology that is near-launch-ready now. Flying the farthest and the fastest, it would venture into the space between us and neighboring stars, discovering uncharted territory. It would provide the first real vantage point of our life-bearing system from the outside, allowing us to better understand our own evolution. In an epic 50-plus-year journey, Interstellar Probe will explore questions about our place in the universe, enabled by multiple generations of engineers, scientists, and visionaries.



1 au = approximate distance from Earth to the Sun

*"We shall not cease from exploration
And the end of all our exploring
Will be to arrive where we started
And know the place for the first time."
—T. S. Elliott (1943)*

Baseline Goal

Understand our habitable astrosphere and its home in the galaxy

HELIOSPHERE PHASE

HELIOSHEATH PHASE

INTERSTELLAR PHASE

SCIENCE QUESTIONS

- 1 How is our heliosphere upheld by the physical processes from the Sun to the very local interstellar medium?
- 2 How do the Sun's activity as well as the interstellar medium and its possible inhomogeneity influence the dynamics and evolution of the global heliosphere?

- 3 How do the current interstellar medium properties inform our understanding of the evolutionary path of the heliosphere?

OBJECTIVES

Pickup ion evolution/acceleration	
Interstellar neutrals	
Ribbon/belt remote	Ribbon/belt in situ
Heliospheric dynamics	
Galactic cosmic ray modulation and shielding	
Termination shock	
Heliosheath dynamics	
Heliopause	
Anomalous cosmic ray acceleration	
	Extent of solar disturbances
	Bow wave
	Hydrogen wall
	Interstellar medium
	Galactic cosmic ray origin

Optional Cross-Divisional Science Goals:

Planetary flybys, dust studies, astrophysical observations

BASELINE MISSION CHARACTERISTICS

Launch 2036 **Mass** 860 KG **Trajectory** Passive Jupiter Gravity Assist To (~22°S, 180°E) **Peak Exit Speed** 7.0 au/year

Telecommunication

X-band with 5-m fixed antenna capable of sufficient downlink (~10 Mbit/week) at 1000 au using Next Generation Very Large Array or equivalent resource

Power

Two Next Generation Radioisotope Thermoelectric Generators for 300 W (electric) at end of mission

Mechanical

Spin-stabilized, 50-m PWS wire antennas

Launch Vehicle

Super Heavy-Lift Launch Vehicle with additional third and fourth stages

Lifetime

50-year lifetime drives reliability and longevity, requiring a multigenerational approach to staffing be built in from the beginning

Launch Opportunities

Every 13 months, from 2036 to 2042, exiting forward hemisphere of heliosphere at similar speed to baseline trajectory

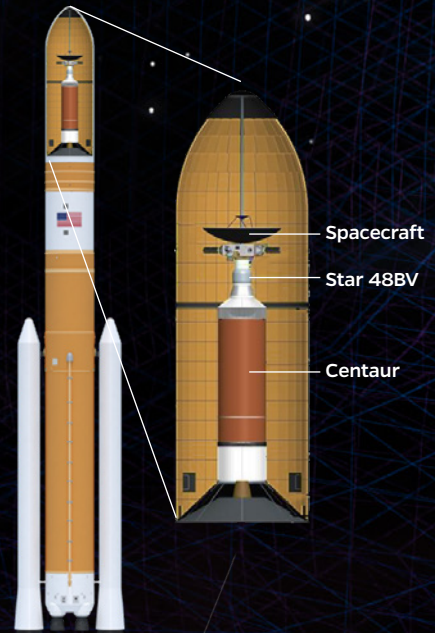
Technology Horizon

Could be ready to launch by 1 January 2030 (independent of funding and policy constraints)

SPACECRAFT MASTER EQUIPMENT LIST SUMMARY

Equipment	Mass (kg) (includes contingency)
Payload (including accommodation hardware)	100.5
Telecommunications	83.4
Guidance and Control (G&C)	16.8
Power	169
Thermal Control	70.8
Avionics	12.8
Propulsion	37.2
Mechanical/Structure	150
Harness	29.3
Propellant	106
Total	776
Margin	84
Launch Mass	860

Example Stack Configuration



ESTIMATED COSTS (FY25\$)

Phases A-D without launch costs \$1689M*
Phase E ~\$230M/decade*

*without reserves

BASELINE EXAMPLE PAYLOAD

87.4 KG | 86.7 W

INSTRUMENTS

30% CHARGED PARTICLES
 Plasma Subsystem (PLS)
 Pickup Ions (PUI)
 Energetic Particles (EPS)
 Cosmic Rays (CRS)

19% FIELDS AND WAVES
 Magnetometer (MAG)
 Plasma Waves (PWS)

14% ENERGETIC NEUTRAL ATOM IMAGING
 ENA Imager (ENA)

12% DUST
 Interstellar Dust Analyzer (IDA)

11% NEUTRALS
 Neutral Mass Spectrometer (NMS)

14% LYMAN-ALPHA
 Lyman-Alpha Spectrograph (LYA)

PERCENTAGE OF PAYLOAD MASS

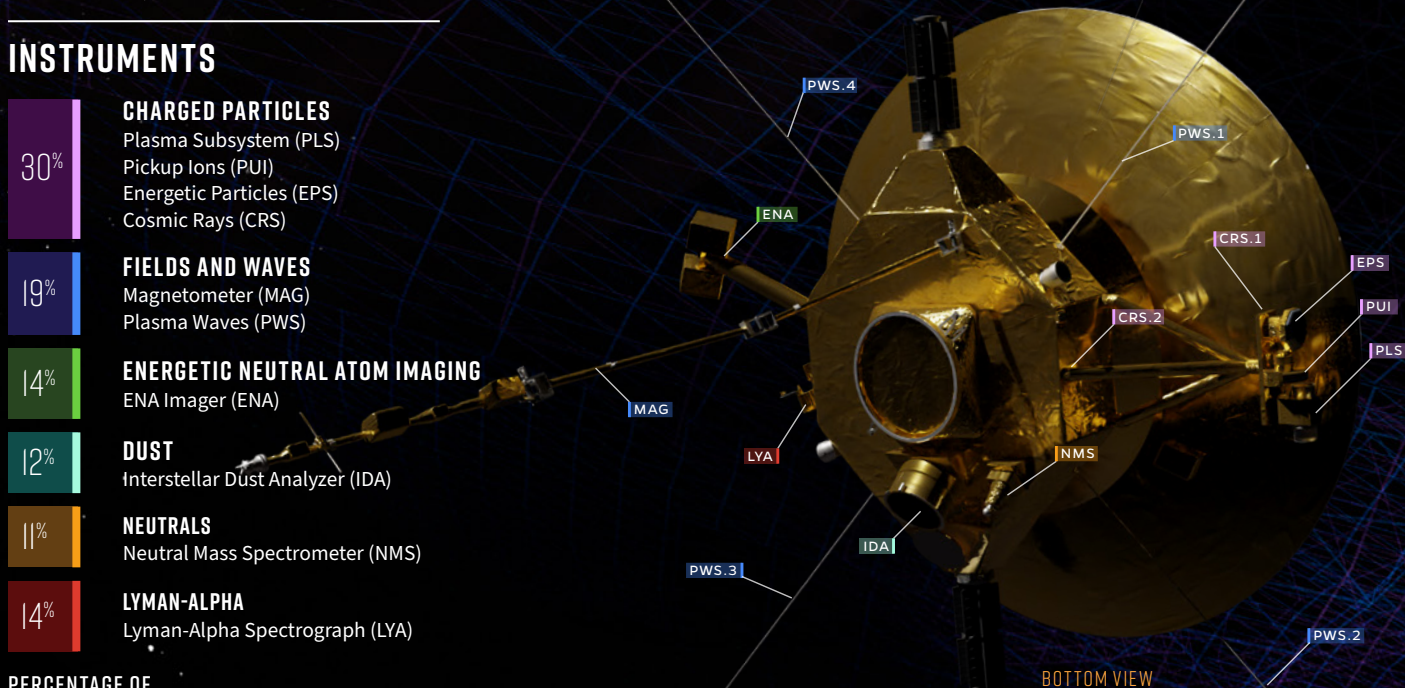


Table of Contents

List of Authors.....	i
Primary Team.....	i
Collaborators	ii
Data Release, Distribution, and Cost Interpretation Statements.....	vi
Fact Sheet.....	vii
Table of Contents.....	ix
List of Figures.....	xx
List of Tables	xxxv
1. Executive Summary.....	1-1
2. Science Goals and Questions	2-1
2.1 Science Rationale.....	2-1
2.2 Science Questions.....	2-2
2.2.1 Question 1: How is our heliosphere upheld by the physical processes from the Sun to the VLISM?	2-2
2.2.2 Question 2: How do the Sun’s activity as well as the interstellar medium and its possible inhomogeneity influence the dynamics and evolution of the global heliosphere?	2-9
2.2.3 Question 3: How do the current VLISM properties inform our understanding of the evolutionary path of the heliosphere?	2-12
2.3 Science Traceability to Closure	2-17
2.4 Mission Success Criteria	2-20
2.5 Mission Rationale	2-20
2.6 Science Investigations	2-21
2.6.1 Heliosphere Investigation.....	2-22
2.6.2 Heliosheath Investigation.....	2-25
2.6.3 Heliospheric Dynamics Investigation	2-27
2.6.4 VLISM Investigation	2-27
2.7 Science Closure.....	2-29
2.8 Cross-Divisional Opportunities.....	2-31
2.9 Section 2 References	2-33

3.	High-Level Mission Concept	3-1
3.1	Mission Design Summary	3-1
3.1.1	Mission Design	3-1
3.1.1.1	Overview	3-1
3.1.1.2	Trajectory Trade Space	3-2
3.1.1.3	Baseline Trajectory	3-3
3.1.1.4	Alternative Launch Opportunities.....	3-4
3.2	Concept of Operations	3-4
3.2.1	Mission Timeline	3-4
3.2.1.1	Launch and Checkout Phase.....	3-5
3.2.1.2	Cruise to Jupiter Phase	3-5
3.2.1.3	Wire Antenna Deployment/Final Commissioning	3-5
3.2.1.4	Jupiter Gravity Assist Phase.....	3-5
3.2.1.5	Heliosphere Phase (Jupiter to 90 au).....	3-6
3.2.1.6	Heliosheath Phase (90–120 au)	3-6
3.2.1.7	Interstellar Phase to 50 Years.....	3-6
3.2.1.8	Interstellar Phase to 1000 au	3-9
3.2.2	Telecommunications	3-9
3.2.2.1	Downlink	3-9
3.2.2.2	Uplink.....	3-10
3.2.3	Data Management	3-10
3.2.4	Concept Maturity Level	3-11
3.2.5	Technology Readiness Level.....	3-11
3.3	Launch Vehicle.....	3-12
3.4	Section 3 References	3-14
4.	Science Implementation	4-1
4.1	Measurements.....	4-1
4.1.1	Magnetic Fields	4-1
4.1.1.1	Magnetometer (MAG) Investigation	4-2
4.1.1.2	Measurement Requirements	4-2
4.1.1.3	Example Instrumentation	4-3
4.1.1.4	Instrument Trades.....	4-3
4.1.1.5	Enhancing Technology Development.....	4-5

4.1.2	Charged Particles	4-5
4.1.2.1	Plasma Subsystem (PLS).....	4-7
4.1.2.2	Pickup Ion Subsystem (PUI)	4-12
4.1.2.3	Energetic Particle Subsystem (EPS)	4-17
4.1.2.4	Cosmic Ray Subsystem (CRS).....	4-21
4.1.3	Plasma Wave Measurements.....	4-25
4.1.3.1	Plasma Wave Subsystem (PWS) Investigation.....	4-26
4.1.3.2	Measurement Requirements	4-28
4.1.3.3	Instrumentation.....	4-29
4.1.3.4	Instrument Trades.....	4-30
4.1.3.5	Enhancing Technology Development.....	4-30
4.1.4	Energetic Neutral Atom (ENA) Imaging	4-30
4.1.4.1	ENA Investigation	4-31
4.1.4.2	Measurement Requirements	4-32
4.1.4.3	Instrumentation.....	4-34
4.1.4.4	Instrument Trades.....	4-34
4.1.4.5	Enhancing Technology Development.....	4-35
4.1.5	In Situ Interplanetary and Interstellar Dust Detection and Compositional Analysis.....	4-36
4.1.5.1	In Situ Dust Investigation	4-37
4.1.5.2	Measurement Requirements	4-40
4.1.5.3	Instrumentation.....	4-40
4.1.5.4	Instrument Trades.....	4-40
4.1.5.5	Enhancing Technology Development.....	4-41
4.1.6	Neutral Gas.....	4-43
4.1.6.1	Neutral Mass Spectrometer (NMS) Investigation	4-43
4.1.6.2	Measurement Requirements	4-44
4.1.6.3	Instrumentation.....	4-45
4.1.6.4	Instrument Trades.....	4-46
4.1.6.5	Enhancing Technology Developments	4-47
4.1.7	Lyman-Alpha	4-48
4.1.7.1	Lyman-Alpha (LYA) Investigation	4-48
4.1.7.2	Measurement Requirements	4-50

4.1.7.3	Instrumentation.....	4-50
4.1.7.4	Instrument Trades.....	4-52
4.1.7.5	Enhancing Technology Development.....	4-53
4.2	Trajectory Science Trades	4-53
4.3	Example Model Payload	4-55
4.4	Science Operations.....	4-60
4.4.1	Heliosphere Phase	4-63
4.4.2	Heliosheath Phase	4-64
4.4.3	Interstellar Phase	4-64
4.5	Data Volume	4-65
4.6	Section 4 References	4-72
5.	Technical Implementation	5-1
5.1	Critical Subsystems.....	5-3
5.1.1	Guidance and Control.....	5-3
5.1.2	Avionics.....	5-4
5.1.3	Telecommunications	5-5
5.1.4	Power.....	5-7
5.1.5	Propulsion	5-8
5.1.6	Thermal	5-8
5.2	Ground System	5-9
5.2.1	Automation and Unattended Contact Operations.....	5-10
5.3	Section 5 References	5-10
6.	Programmatic/Mission Management.....	6-1
6.1	High-Level Mission Schedule.....	6-1
6.2	Mission Life-Cycle Cost.....	6-1
6.3	Mission Ground Rules and Assumptions.....	6-2
6.4	Cost Benchmarking.....	6-3
6.5	Costing Methodology and Basis of Estimate.....	6-4
6.5.1	Phases A–D.....	6-4
6.5.2	Phase E	6-9
6.5.3	Cost Risk and Cost Reserves	6-10
6.5.4	Cost Validation	6-14
6.5.5	Conclusion	6-14

6.5.6	Development Cost by WBS and Fiscal Year	6-15
6.6	Risks of Implementing	6-15
6.7	Risks	6-16
6.8	Section 6 References	6-18
Appendix A. Augmented Science Mission		A-1
A.1	Science Goals and Objectives.....	A-1
A.1.1	Science Rationale of an Augmented Mission	A-1
A.1.2	Goal 2: Understand the Origin and Evolution of Planetary Systems	A-2
A.1.2.1	Science Question 2.1: How did the solar system form and evolve compared to other planetary systems?	A-2
A.1.2.2	Science Question 2.2: What dynamical and chemical processes produced the structure and composition of the circumsolar dust disk?	A-2
A.1.3	Goal 3: Explore the Universe beyond Our Circumsolar Dust Cloud.....	A-5
A.1.3.1	Science Question 3.1: What role do the composition, evolution, and thermodynamics of the nearby and distant interstellar medium (ISM) play in determining the habitability of planetary bodies?	A-5
A.1.3.2	Science Question 3.2: What is the total diffuse red-shifted light emitted by all the stars and galaxies in the universe since the beginning of cosmic time?	A-5
A.1.4	Science Traceability for Augmentation.....	A-6
A.1.5	Technical Implementation of the Augmented Mission	A-9
A.1.6	Science Investigations.....	A-9
A.1.6.1	Dwarf Planet Investigation	A-9
A.1.6.2	Small Bodies Investigation	A-15
A.1.6.3	Exoplanet Analogs Investigation	A-16
A.1.6.4	Space Physics Investigation during Flyby	A-16
A.1.6.5	Dust Disk Investigation.....	A-17
A.1.6.6	Near and Far ISM Investigation	A-19
A.1.6.7	Extragalactic Background Light Investigation	A-20
A.1.6.8	Giant Planet Flyby Investigation.....	A-24
A.1.7	Space Physics Measurements during Flyby.....	A-25
A.2	Science Implementation of Augmentation	A-26
A.2.1	Changes to the Flight System	A-26

A.2.2	Science Implementation	A-27
A.2.2.1	VISNIR Flyby Imaging.....	A-27
A.2.2.2	IRM Imaging	A-30
A.2.2.3	Instrument Trades	A-34
A.2.2.4	Other Instrument Options	A-35
A.3	Augmented Example Payload and Trades.....	A-41
A.3.1	Example Payload and Accommodation Trades	A-41
A.3.2	Science Trades against Baseline Mission	A-43
A.3.2.1	Plasma Wave Subsystem	A-43
A.3.2.2	Lyman- α Science	A-44
A.4	Science Operations.....	A-45
A.4.1	Mission Timeline	A-45
A.4.1.1	Launch and Checkout Phase.....	A-46
A.4.1.2	Cruise to Jupiter Phase	A-46
A.4.1.3	Jupiter Gravity Assist Phase	A-46
A.4.1.4	Heliosphere Phase (Jupiter to 90 au).....	A-47
A.4.1.5	Heliosheath Phase (90–120 au)	A-48
A.4.1.6	Interstellar Phase to 50 Years.....	A-49
A.4.1.7	Interstellar Phase to 1000 au	A-49
A.4.2	Telecommunications	A-49
A.4.3	Operations.....	A-49
A.4.3.1	Coupled versus Decoupled Operations	A-50
A.4.4	Data Management	A-50
A.4.5	Flyby Imaging	A-50
A.4.5.1	Dwarf Planet Approach.....	A-51
A.4.5.2	Dwarf Planet Flyby	A-51
A.4.5.3	Looking Back	A-51
A.4.6	Dust Disk Imaging and EBL Observations	A-51
A.4.6.1	Despun Three-Axis Operations	A-53
A.4.6.2	Accommodations for Pure-Spinner Operations	A-54
A.5	Data Volume	A-54
A.6	Appendix 6 References.....	A-59

Appendix B. Heritage Tables	B-1
B.1 Appendix B References	B-14
Appendix C. Powered Jupiter Gravity Assist	C-1
Appendix D. Solar Oberth Maneuver	D-1
D.1 Description of the Solar Oberth Maneuver.....	D-1
D.2 Flight System Description.....	D-2
D.2.1 Solid Rocket Motor	D-3
D.2.2 Thermal Protection Shield.....	D-3
D.2.3 Ballast	D-4
D.2.4 Interstage Module	D-4
D.2.5 Observatory.....	D-4
D.3 Mission Design.....	D-5
D.3.1 Launch to Jupiter Gravity Assist	D-5
D.3.2 Jupiter Gravity Assist.....	D-5
D.3.3 Solar Oberth Maneuver	D-6
D.3.4 Observatory Separation.....	D-6
D.3.5 Primary Science Mission.....	D-7
D.4 SOM Performance and Escape Trade	D-7
D.4.1 Initial Trade Study	D-7
D.4.1.1 “Baseline” Spacecraft.....	D-13
D.4.2 Point Design Case Study	D-15
D.4.2.1 Optimal Solutions	D-16
D.4.2.2 Comparison with Non-SOM Performance	D-16
D.4.2.3 Determining “Break-Even” Mass for SOM versus Non-SOM Architectures	D-18
D.5 Constraints and Risks.....	D-19
D.5.1 System Constraints	D-19
D.5.2 Additional Technical Risks	D-20
D.6 Programmatic Issues	D-21
D.7 Appendix D References	D-24
Appendix E. Radiation Work.....	E-1
E.1 Environments Overview	E-1
E.2 Description of Ballistic Jupiter Gravity Assist Jovian Flyby Environments	E-2

E.3	Heliosphere, Heliosheath, and Interstellar Radiation Environments	E-3
E.4	Interstellar and Local Interstellar Medium Environments	E-4
E.5	Spacecraft Charging.....	E-4
E.6	Appendix E References.....	E-7
Appendix F. Longevity Analysis for Interstellar Probe.....		F-1
F.1	Introduction	F-1
F.2	Long-Duration Mission Reliability	F-3
F.2.1	Introduction	F-3
F.2.1.1	Scope	F-4
F.2.1.2	Interstellar Probe Mission Lifetime Goal.....	F-4
F.2.1.3	Interstellar Probe Reliability Design Philosophy	F-4
F.2.2	Literature Survey.....	F-4
F.2.2.1	Space System Reliability.....	F-4
F.2.2.2	Failure Mechanisms for Long Durations	F-6
F.2.3	Industry Communications and Panel Discussions.....	F-9
F.2.3.1	Panels for Reliability of Long-Duration Missions	F-10
F.2.3.2	Other Discussions with NASA	F-11
F.2.4	Data Analysis of Interplanetary Missions	F-11
F.2.4.1	Probability of Success of Interplanetary Missions.....	F-14
F.2.4.2	Reasons Long Missions End.....	F-15
F.2.4.3	Mission time versus Design Life	F-16
F.2.4.4	Lifetime Assessment	F-17
F.2.5	Reliability Engineering	F-19
F.2.5.1	Invalidity of Constant Failure Rate Models	F-20
F.2.5.2	Reliability Framework for Interstellar Probe.....	F-25
F.2.6	Defining Mission Success.....	F-27
F.2.6.1	Science Traceability Matrix.....	F-27
F.2.6.2	Fault Tree Analysis.....	F-28
F.2.6.3	Science Requirement Assessments	F-29
F.2.7	Reliability Prediction	F-51
F.2.7.1	Interstellar Probe Reliability Model	F-51
F.2.7.2	Spacecraft Bus Model	F-51
F.2.7.3	Instrument Suite Model.....	F-53

F.2.7.4	Data Sources and Analysis	F-54
F.2.7.5	Dust Impact Probabilities.....	F-55
F.2.7.6	Mission Reliability Results.....	F-55
F.2.7.7	Augmented Mission Architecture.....	F-58
F.2.8	Probabilistic Physics of Failure	F-58
F.2.8.1	Physics of Failure Modeling.....	F-58
F.2.8.2	Ensuring Confidence in Parts.....	F-65
F.2.9	Material Longevity	F-70
F.2.9.1	Interstellar Environment.....	F-70
F.2.9.2	Material Degradation Mechanisms	F-71
F.2.9.3	Implications of Materials for System Failure	F-71
F.2.9.4	System Test Requirements.....	F-71
F.2.9.5	Conclusions	F-73
F.2.10	Radioisotope Thermoelectric Generator Longevity.....	F-74
F.2.10.1	Historical Lifetime Data Analysis	F-74
F.2.10.2	Radioisotope Thermoelectric Generator Reliability	F-78
F.2.10.3	Time-Dependent Performance Analysis.....	F-78
F.2.10.4	Conclusion.....	F-79
F.3	Ground Longevity	F-79
F.3.1	Introduction	F-79
F.3.2	Mission Operations Center (Srama et al.), Science Operations Center (SOC), and Ground Data System (GDS) Infrastructure.....	F-81
F.3.2.1	Upgrades	F-81
F.3.2.2	Platforms.....	F-81
F.3.2.3	Simulators and Ground Support Equipment	F-81
F.3.2.4	Data Storage Systems	F-82
F.3.2.5	Ground Software	F-82
F.3.3	Navigation, Mission Design, and Ground Communications Infrastructure	F-84
F.3.3.1	Communications and Navigation Longevity Challenges	F-84
F.3.3.2	Network Security	F-85
F.3.4	Archiving and Records Retention.....	F-86
F.3.5	Science.....	F-86

F.3.6	Long-Term Ground Segment Planning	F-88
F.4	Organizing for the Long Term	F-89
F.4.1	A Bureaucratic Structure	F-89
F.4.2	Instrumentation and Leadership.....	F-91
F.4.3	Ritualized Role Turnover	F-92
F.4.4	Funding Management	F-94
F.5	Summary and Work Going Forward	F-95
F.5.1	Summary of Spacecraft Reliability	F-95
F.5.2	Summary of Ground System	F-96
F.5.3	Summary of Teams and Organization.....	F-97
F.5.4	Work Going Forward	F-97
F.6	Appendix F References.....	F-98
Appendix G. Cost Trades		G-1
G.1	Augmented Mission.....	G-1
G.1.1	Augmented Payload.....	G-2
G.1.2	Augmented Phase E.....	G-3
G.2	Solar Oberth Maneuver (SOM)	G-4
G.2.1	SOM Spacecraft.....	G-4
G.2.2	SOM Phase E	G-5
G.3	Comparisons to Baseline	G-6
Appendix H. Mission Architecture.....		H-1
H.1	Background	H-1
H.2	Trade-Space Methodology.....	H-1
H.2.1	Staging Selections	H-1
H.2.2	Parametric Injected Mass Inversion	H-3
H.2.3	Additional SLS and Non-SLS Cases	H-3
H.2.4	Implementation of the SOM Cases.....	H-4
H.2.4.1	Input Conditions	H-5
H.2.4.2	Option 3 Study Approach	H-6
H.2.4.3	Option 3 Solution Methodology	H-8
H.2.5	“Best” Trajectories.....	H-10
H.2.5.1	Guidelines	H-10
H.2.5.2	Trajectory Results.....	H-11

H.2.5.3	Trajectory Overview	H-12
H.3	Available Performance versus Implementation “Requirements”	H-16
H.3.1	Past Studies	H-16
H.3.1.1	High-Speed “Solutions”	H-17
H.3.2	State-of-the-Art Ballistic Opportunities	H-20
H.4	Appendix H References	H-21
Appendix I. Acronyms and Abbreviations.....		I-1

List of Figures

Figure 2-1. During the evolution of our solar system, its protective heliosphere has plowed through dramatically different interstellar environments that have shaped our home through incoming interstellar gas, dust, plasma, and galactic cosmic rays. Interstellar Probe on a fast trajectory to the very local interstellar medium (VLISM) would represent a snapshot to understand the current state of our habitable astrosphere in the VLISM, to ultimately be able to understand where our home came from and where it is going. (Image credit: Johns Hopkins Applied Physics Laboratory.)..... 2-2

Figure 2-2. PUIs and suprathermal particles dominate the total pressure in the heliosheath; however, lack of in situ measurements of these populations represents a critical gap. A combination of ~ 10 -eV to ~ 344 -MeV in situ ion measurements from the Voyager 2/Plasma Science (PLS)/Low-Energy Charged Particle (LECP)/Cosmic Ray Subsystem (CRS) experiments and remotely sensed ~ 110 -eV to ~ 55 -keV energetic neutral atom (ENA) measurements from the Interstellar Boundary Explorer (IBEX) and Cassini missions over 2009–2016 along Voyager 2’s trajectory through the heliosheath is shown (from Dialynas et al. (2020))...... 2-3

Figure 2-3. (Top) Analysis of IBEX-Hi ENA data (0.71–4.29 keV) during a full solar cycle shows that the HP is compressed southward of the nose and has a distinct tail extending to at least 380 au (from Reisenfeld et al. (2021)). (Bottom) Cassini/INCA ENA data (5–55 keV) suggest a bubble-like heliosphere with the HP extending toward the tail to 200 au as an upper limit (from Dialynas et al. (2017))..... 2-6

Figure 2-4. State-of-the-art global models of the heliosphere predict different shapes: a comet-like shape (left model by Izmodenov & Alexashov (2020) and right model by Zhang et al. (2020)) and the “croissant” model (by Opher et al. (2015)). 2-7

Figure 2-5. Global dynamic interaction as seen in IBEX-Hi ENA images. ENA fluxes on the sky respond to changes of the solar wind dynamic pressure from solar minimum to solar maximum (McComas et al., 2020). SC, spacecraft; SW, solar wind. 2-9

Figure 2-6. The TS shock responds to the solar wind dynamic pressure pulses moving to several astronomical units outward and inward. Solar wind shocks and waves create highly dynamic flows in the heliosheath. The HP also responds to the disturbances but with smaller amplitude (simulations by Washimi et al. (2011)). 2-10

Figure 2-7. VLISM hydrogen density controls the size of the heliosphere. (Left) The HP is ~ 25 au from the Sun when the heliosphere moves through the dense cool interstellar cloud. (Right) The HP is at 300 au when the heliosphere moves in the fully ionized interstellar plasma. Distances on axes are in astronomical units (simulations by Müller et al. (2008)). 2-12

Figure 2-8. Recent studies suggest that the Sun is on the path to leave the LIC and may be already in contact with four interstellar clouds with different properties (Linsky et al., 2019). (Left: Image credit to Adler Planetarium, Frisch, Redfield, Linsky.)..... 2-13

Figure 2-9. (Top panel) Direct knowledge of interstellar dust composition and size distribution brings new understanding of the chemical evolution of the galaxy. The second panel is for the defocusing solar wind magnetic field, and the bottom panel is for the focusing polarity. The inner white curve indicates the location of the termination shock, while the outer white curve shows the heliopause location (simulations by Slavin et al. (2012)). The color scale indicates the density relative to the ambient interstellar dust density. (Image credit: NASA, NOAO, ESA and The Hubble Heritage Team (STScI/AURA) and Donald E. Brownlee, University of Washington, Seattle, and Elmar Jessberger, Institut für Planetologie, Münster, Germany.) 2-16

Figure 2-10. Understanding the heliospheric boundary and the VLISM requires a dedicated set of measurements of particles over a wide energy range, from the inner heliosphere to well beyond the HP. Voyager and New Horizons are the only missions exploring the outer heliosphere, but their limited instrumentation represents only a sliver of the required measurements. Interstellar Probe will carry the first dedicated set of instruments to span the wide range of particle composition and energies to fully investigate the new regime of space physics that governs the formation of our heliosphere in the VLISM. CRS, Cosmic Ray Subsystem; LECP, Low-Energy Charged Particle; PEPSSI, Pluto Energetic Particle Spectrometer Science Investigation; PLS, Plasma Science; STs, suprathermals; W, solar wind; SWAP, Solar Wind Around Pluto. (Image credit: Johns Hopkins Applied Physics Laboratory.)..... 2-23

Figure 2-11. (a) The TS is believed to reflect and preferentially heat PUIs (Zank et al., 1996). (b) While Voyager magnetic field measurements revealed features indicative of these processes, it did not measure the detailed plasma and PUI distributions required to fully understand this new type of shock (Burlaga et al., 2008). 2-24

Figure 2-12. (Left) Simulated H ENA image at 80 keV assuming the flows as modeled by Opher et al. (2018) (right)..... 2-26

Figure 2-13. Scientific disciplines inevitably become blurred together as our exploration of space pushes outward. The baseline concept of an Interstellar Probe is a pragmatic pathfinder for such a necessary cross-divisional approach, and with only modest augmentations to payload and architecture, it will return science on the level of large individual planetary and astrophysics missions (Appendix A). (Image credit: Johns Hopkins Applied Physics Laboratory.) 2-31

Figure 3-1. Sky map (ECLIPJ2000) for ballistic JGA cases with $m = 860$ kg ($C3 = 304.07$ km²/s²) over 2030–2042. (Image credit: Johns Hopkins Applied Physics Laboratory.) 3-3

Figure 3-2. Interstellar Probe heliocentric trajectory going to (−22°S, 180°E). (Image credit: Johns Hopkins Applied Physics Laboratory.) 3-3

Figure 3-3. Solar system exit speed variation throughout launch period. (Image credit: Johns Hopkins Applied Physics Laboratory.)..... 3-4

Figure 3-4. SLS Block 2 high-range launch curves expected for a likely Interstellar Probe mission (Creech et al., 2019; Creech et al., 2020). (Reprinted from Kinnison et al. (2021) with permission; © IEEE.) 3-13

Figure 3-5. SLS stack configurations including possible third and fourth stages. (Reprinted from Kinnison et al. (2021) with permission; © IEEE.) 3-13

Figure 4-1. Voyager 1 magnetic field measurements from 2009 to 2018 covering both the inner and outer heliosheath. (Image courtesy of A. Szabo.) 4-3

Figure 4-2. (Top) MMS fluxgate sensor with harness, as shown in Figure 3 of Russell et al. (2016). (Bottom) MESSENGER spacecraft with the magnetometer boom deployed, along with other labeled payload instruments, as shown in Figure 7 in Gold et al. (2001) (reprinted with permission from Elsevier). GRS, Gamma-Ray Spectrometer; MAG, Magnetometer; MASCS, Mercury Atmospheric and Surface Composition Spectrometer; MDIS, Mercury Dual Imaging System; MLA, Mercury Laser Altimeter; XRS, X-Ray Spectrometer. 4-4

Figure 4-3. Voyager observations of plasma radial velocity, density, and temperature from Earth to the heliopause. (Figure courtesy of John Richardson, MIT.) 4-6

Figure 4-4. The Voyager Faraday cups obtained the only existing plasma measurement in the heliosheath and VLISM, but their pointing made it difficult to accurately determine the required plasma moments of electrons and major ions. Although generally less sensitive, an optimized ESA instrument for electrons and ions can also obtain plasma moments. Although designed for the solar wind, the Solar Wind Electrons Alphas and Protons (SWEAP)/Solar Probe Analyzers (Ocker et al., 2021) dual-head ESA has sufficient resolution and range for this task, as seen from the example data from this first pass of Parker Solar Probe (Whittlesey et al., 2020). 4-9

Figure 4-5. (Top) Cross-sectional view of an example ESA measuring plasma electrons and ions with electrostatically sweeping entrance aperture (Kasper et al., 2016). (Bottom) The SPAN-A heads on board Parker Solar Probe (image credit: Parker Solar Probe SWEAP website). 4-11

Figure 4-6. (Top) PUI measurements halfway to the termination shock by New Horizons (McComas et al., 2021). (Bottom) PUI measurements by Ulysses/Solar Wind Ion Composition Spectrometer (SWICS) (reprinted from Geiss & Gloeckler (2001) with permission; © 2001 Springer Nature Limited)..... 4-14

Figure 4-7. Although small, Ulysses/SWICS provides a functional example of a PUI instrument. (Top) Functional overview. (Bottom) Photo of SWICS. (Both images reprinted from Gloeckler et al. (1992) with permission; © ESO.)..... 4-16

Figure 4-8. Major ions of the heliosheath as measured by Voyager/Low-Energy Charged Particle (LECP) (reprinted from Krimigis et al. (2019) with permission; © 2019 Springer Nature Limited). 4-19

Figure 4-9. (Top) Functional overview of the EPI-Lo sensor as an example of heritage instrumentation, although an LECP-type instrument can also be considered (McComas et al., 2016). PWB, printed wiring board. (Bottom) EPI-Lo sensor as part of the ISOIS suite (image credit: Johns Hopkins Applied Physics Laboratory). 4-20

Figure 4-10. Voyager 1 provided only a few points over a relatively narrow range of energies of the important Li, Be, and B (top panel; reproduced from Cummings et al. (2016) with permission; © AAS). This has left an important gap in the spectrum for constraining the production of light elements in stars and the role of spallation on heavy ions in the VLISM. Note: The intensities of Li, Be, and B are comparable to those of C, N, and O. Cosmic ray proton (hydrogen) and helium spectra in the VLISM from Voyager 1 are shown in the bottom two panels for comparison. (Reproduced from Cummings et al. (2016) with permission; © AAS.)..... 4-23

Figure 4-11. (Top) EPI-Hi instrument on Parker Solar Probe (Figure 28 from McComas et al. (2016)). (Bottom) Details of the EPI-Hi LET1, LET2, and HET telescope configurations (Figure 29 from McComas et al. (2016))..... 4-25

Figure 4-12. Low-frequency radio emissions generated at and beyond the heliopause via mode conversion from electron plasma oscillations in the foreshock of shocks and pressure pulses moving through the ISM. (Image courtesy of W. Kurth.)..... 4-26

Figure 4-13. Electron plasma oscillations observed beyond the HP showing the increase in interstellar plasma density in the LISM. (Reproduced from Pogorelov et al. (2017) with permission; © AAS.)..... 4-27

Figure 4-14. The recent discovery of the “hum” showing up as a quasi-continuous line at the plasma frequency, implying a significant and unexpected suprathermal electron population of the VLISM (Burlaga et al., 2021; Gurnett et al., 2021; Ocker et al., 2021). (Top panel courtesy of W. Kurth. Bottom panel taken from Burlaga et al. (2021).) 4-28

Figure 4-15. (a) PWS functional block diagram. (b) PWS deployment mechanism. (c) Parker Solar Probe/FIELDS radio/thermal noise board. (All images courtesy of S. Bale.)..... 4-29

Figure 4-16. Reference ion (solid) and ENA (dotted) intensity spectra in the heliosheath (Dialynas et al., 2020). The green box in each panel shows the required energy range of the ENA measurements. (Reproduced from Dialynas et al. (2020) with permission; © AAS.)..... 4-33

Figure 4-17. ENA maps from IBEX of the tail and lobe regions. (Reproduced from Schwadron et al. (2014) with permission; © AAS.) 4-34

Figure 4-18. (Top) The example IMAP-Ultra camera with triple coincidences including a tight 4-ns timing window (Mitchell et al., 2016). (Bottom) The JUpiter ICy Moons Explorer (JUICE)/Jovian Energetic Neutrals and Ions (JENI) flight model without thermal blankets (image credit: Johns Hopkins Applied Physics Laboratory). 4-35

Figure 4-19. Predicted ISM dust population distribution that Interstellar Probe should encounter (solid black curve from Draine (2009)). The dust consists of both silicate and carbonaceous dust grains formed from the thick stellar winds of asymptotic giant branch

(AGB) stars and supernovae outflows (Draine, 2011). These predictions, based on the best Earth-based remote-sensing measurements of the VLISM, are in strong conflict with the inflowing ISM particles measured in situ by Ulysses and Galileo in the inner heliosphere (Landgraf, 2000, blue squares), which resemble much more the 0.3- to 100- μm dust grains found from interplanetary sources. (Reprinted from Draine (2009) with permission; © 2009 Springer Nature Limited.) 4-38

Figure 4-20. (Left) IDA cutaway diagram of the Interstellar Dust Experiment (IDEX) on the IMAP mission (McComas et al., 2018). IDEX detects dust impacts via impact-ionization-produced charge (left) and concurrently produces high-mass-resolution compositional spectra. (Right) Dust counter for detection of the largest (and thus, rarest) particles impinging on the spacecraft (image credit: NASA/Johns Hopkins Applied Physics Laboratory/Southwest Research Institute). The detector relies on the impact-generated removal of polarized material, creating an electrical signal proportional to the amount of plastic removed (and thus the particle's mass). A heritage instrument, the Student Dust Counter, has most recently been flown on the New Horizons spacecraft out beyond 50 au (Piquette et al., 2019; Poppe et al., 2019). HRD, High Rate Detector..... 4-40

Figure 4-21. An example mass spectrum of a pyroxene particle (radius ~ 30 nm, speed ~ 18 km/s) as recorded in the IDA lab model at the CU/LASP dust accelerator facility. The mass resolution of $m/\Delta m > 100$ clearly resolves several isotopes of Mg and Si, for example. (Image courtesy of M. Horanyi.) 4-42

Figure 4-22. Mass spectrum recorded with JUPITER ICy Moons Explorer's (JUICE) Neutral gas and Ion Mass spectrometer (NIM) with FC5311 as calibration gas. (Reprinted from Föhn et al. (2021) with permission; © 2021 IEEE.) 4-44

Figure 4-24. Schematics (left) and photograph (right) of the NIM TOF mass spectrometer designed for the JUPITER ICy Moons Explorer (JUICE) mission. (Both images reprinted from Föhn et al. (2021) with permission; © 2021 IEEE.) 4-47

Figure 4-25. Observed falloff in brightness of interplanetary Lyman- α emission viewed in the upwind direction as measured by the UVS on Voyager 1 (red crosses) and Voyager 2 (blue crosses) scaled downward by 2.4x, and by Alice on New Horizons (black asterisks, with 3- σ error bars). Additional distant upstream brightness of 40 R to the expected 1/r dependence is needed to explain Alice data. (Figure from Gladstone et al. (2018).)..... 4-50

Figure 4-26. Spectrum of interplanetary hydrogen Lyman- α emission observed by IUVS echelle on MAVEN in December 2013 during the cruise to Mars. The black line is a coadded spectrum from the total 3 hours of integration. Instrument line spread function (green) and best fit to the data (red) are shown. (Figure from Mayyasi et al. (2017).)..... 4-51

Figure 4-27. (Left) MAVEN Imaging Ultraviolet Spectrograph (IUVS) instrument image taken during instrument testing at the Laboratory for Atmospheric and Space Physics (Bale et al., 2016) at the University of Colorado (reprinted from McClintock et al. (2015) with permission; © 2015 Springer Nature Limited). (Right) IUVS optical schematic showing the light path through a prism-echelle grating combination (P-E) in the echelle mode enabling resolution of H and D Lyman- α emission lines (Clarke et al., 2017). FUV, far ultraviolet;

MUV, middle ultraviolet; note that other labels indicate different optical components of the instrument. 4-52

Figure 4-28. Optical layout of an all-reflective spatial heterodyne spectrometer. (Reprinted from Harris et al. (2004) with permission; © 2004 SPIE.) 4-52

Figure 4-29. Colored contours of spacecraft speed at 100 au across the sky achieved by an SLS Block 2 using Centaur III (Atlas V second stage) and Star 48BV additional upper stages. Launch date runs with ecliptic longitude, and resulting speed depends on the relative position of Jupiter and Earth and details of their orbits about the Sun. The heliosphere nose and tail are marked on the figure. Additionally, the region of highest fluxes of ENAs in the IBEX ribbon is shown with contours and labeled as “IBEX Ribbon” in the figure. (Image credit: Johns Hopkins Applied Physics Laboratory.) 4-54

Figure 4-30. Artistic rendering of the spacecraft, showing a clear view of the magnetometer boom. (Image credit: Johns Hopkins Applied Physics Laboratory.) 4-59

Figure 4-31. A view of the spacecraft showing the full length of the plasma wave antennas. (Image credit: Johns Hopkins Applied Physics Laboratory.) 4-59

Figure 4-32. A close-up of the particle suite boom. From left to right and top to bottom, EPS, one of the CRS telescopes, PUI, and PLS. The other CRS telescope is to the left of the base of the boom. (Image credit: Johns Hopkins Applied Physics Laboratory.) 4-60

Figure 4-33. ENA out on a boom, with LYA to the left. (Image credit: Johns Hopkins Applied Physics Laboratory.) 4-60

Figure 4-34. NMS and IDA located on the bottom of the spacecraft. (Image credit: Johns Hopkins Applied Physics Laboratory.) 4-61

Figure 4-35. Science starts soon after launch with investigations of how the heliospheric boundary is formed by processes deep in the heliosphere and continues throughout the heliospheric boundary (heliosheath) and into the VLISM. (Image credit: Johns Hopkins Applied Physics Laboratory.) 4-62

Figure 4-36. Data rates for each instrument as a function of time. These rates are not allocations. Rates in the early mission are based on what has been used within the solar system, while rates in and beyond the outer heliosphere are representative of what is required to address the science. Summing up these rates (orange) demonstrates that the available downlink capacity (red) is sufficient to perform the required science. Note the increase in available downlink capacity around 2050 is concurrent with the switch to the Next Generation Very Large Array (ngVLA) (see Section 3.2.4 for more details). (Image credit: Johns Hopkins Applied Physics Laboratory.) 4-67

Figure 5-1. Conceptual Interstellar Probe spacecraft in science configuration. (Image credit: Johns Hopkins Applied Physics Laboratory.) 5-2

Figure 5-2. Conceptual block diagram of baseline spacecraft. Note: Batteries are included as an optional element and are not required for the mission. (Image credit: Johns Hopkins Applied Physics Laboratory.) 5-3

Figure 5-3. Baseline telecommunications subsystem. (Image credit: Johns Hopkins Applied Physics Laboratory.)5-6

Figure 5-4. Downlink performance for ground stations. DSN, Deep Space Network; GBT, Green Bank Telescope; ngVLA, Next Generation Very Large Array. (Reprinted from Kinnison et al. (2021) with permission; © IEEE.).....5-7

Figure 5-5. Expected data volume per week through the mission. JGA, Jupiter gravity assist. (Reprinted from Kinnison et al. (2021) with permission; © IEEE.).....5-7

Figure 5-6. Interstellar Probe example ground system. (Reprinted from Kinnison et al. (2021) with permission; © IEEE.) 5-10

Figure 6-1. Interstellar Probe Phase A–D cost benchmarking. Mission names are listed only for APL-managed missions; missions managed by other organizations are indicated by number. Source: NASA’s Cost Analysis Data Requirement Database (CADRe). EAC, estimate at completion.....6-4

Figure 6-2. Interstellar Probe Phase E cost benchmarking. Source: The Planetary Society Planetary Exploration Budget Dataset, Johns Hopkins Applied Physics Laboratory.6-5

Figure 6-3. Interstellar Probe cost risk cumulative distribution function/S-curve. (Image credit: Johns Hopkins Applied Physics Laboratory.)..... 6-12

Figure 6-4. Twenty-five percent reserves on the estimated cost of Phase E covers cost risk sufficiently during operations. (Image credit: Johns Hopkins Applied Physics Laboratory.) 6-14

Figure A-1. A wide range of unique, transformational science can be done from the Interstellar Probe spacecraft heading out of the solar system with modern purpose-built instrumentation, including close flybys of outer-solar-system planetesimals and dwarf planets, imaging of our solar system’s entire circumstellar debris disk and planets as exoplanets, and accurate measurement of the cosmic background light. Note: IR, infrared; KBO, Kuiper Belt object. (Image credit: Johns Hopkins Applied Physics Laboratory.) A-1

Figure A-2. Trajectory “heat map” showing solar system exit velocities (color bar) as a function of year (2030–2042), illustrating which dwarf planets and Kuiper Belt objects are in which part of the sky during 2030–2042 (paths move left to right). The heliosphere nose and tail are marked on the figure. Additionally, the region of highest fluxes of energetic neutral atoms in the IBEX ribbon are shown with contours and labeled as “IBEX Ribbon” in the figure. A flyby of Orcus or Quaoar in particular balances exit direction and energetic neutral atom ribbon science with compelling planetary science. (Image credit: Johns Hopkins Applied Physics Laboratory.)..... A-3

Figure A-3. Predicted dust cloud morphologies arising from solar system Jupiter-family comet (JFC), Oort cloud comet (OCC), and Edgeworth-Kuiper Belt (EKB) sources. (Top) Looking down on the solar system. (Bottom) Looking through the plane of the solar system. (Reproduced from Poppe et al. (2019) with permission; © AAS.) A-4

Figure A-4. Pluto’s southern encounter hemisphere from New Horizons, shown at slightly coarser than 1 km/pixel. This level of detail or finer is necessary for interpreting geologic features on planets’ surfaces. For instance, a flowing nitrogen ice glacier fills in the low-

lying areas around towering water-ice mountains. (Image credit: NASA/Johns Hopkins Applied Physics Laboratory/Southwest Research Institute [http://pluto.jhuapl.edu/Galleries/Featured-Images/image.php?page=1&gallery_id=2&image_id=543&keyword=42&search_cat=].) A-10

Figure A-5. In situ measurements (black data points) and predicted dust flux contributions (colored curves) for the solar system’s debris disks (Poppe et al., 2019; Greaves & Wyatt, 2010). The overall relative shapes of the inner and outer disks scale well, and the predicted crossover at ~10 au from JFC-dominated to EKB-dominated is seen. Interstellar Probe will help determine whether another crossover from EKB-dominated to OCC-dominated occurs at ~100 au and whether the EKB dust is rich in ice, rock, and organics like KBOs and comets. Note: NH SDC, New Horizons Student Dust Counter. (Reproduced from Poppe et al. (2019) with permission; © AAS.)..... A-19

Figure A-6. Disconnect between the nearby ISM dust size distribution predicted from remote-sensing measurements (black) and ISM dust counts measured inside the solar system (blue) (Weingartner & Draine, 2001; Draine & Hensley, 2016). Further, only evidence for siliceous ISM-derived dust has been found to date inside the heliosphere, suggesting some process has preferentially removed carbonaceous solids from dust instreaming from the VLISM. (Reprinted from Draine (2009) with permission; © 2001 Springer Nature Limited.) A-20

Figure A-7. Our current understanding of the thermal history of the universe, beginning at the Big Bang and running through 13.8 Gyr to today. Measurements of the EBL integrate the emission from all sources whose rest-frame emission falls into a given region of the spectrum. At optical and near-IR wavelengths, direct emission from stars sources most of the light, while at mid- and far-IR wavelengths, star formation in cold nebulae is the source. Together, both trace the history of stars and nucleosynthesis since the very first generation of stellar objects. (Image credit: C. Carreau, European Space Agency.) A-21

Figure A-8. The cosmic EBL over all wavelengths (bottom; adapted from Hill et al., 2018) and at wavelengths falling between the UV and far-IR (top; adapted from Cooray, 2016). The cosmic radio, microwave, X-ray, and gamma-ray backgrounds (CRB, CMB, CXB, and CGB, respectively) are well measured and understood. On the other hand, the cosmic IR, optical, and UV backgrounds (CIB, COB, CUB, respectively) have large uncertainties due to the interplanetary dust that is 100–1000× brighter than the astrophysical backgrounds. The has led to a wide range of constraints, as highlighted in the bottom panel, which only data taken in the outer solar system will be able to discriminate. A-22

Figure A-9. The VIR and IRM are circled to show their inclusion on the augmented payload. Note the shorter Plasma Wave Subsystem (PWS) antenna to the left. (Image credit: Johns Hopkins Applied Physics Laboratory.)..... A-27

Figure A-10. Top, Ralph camera integrated on the New Horizons spacecraft (image credit: Johns Hopkins Applied Physics Laboratory). Bottom, Ray-trace schematic for Ralph (image credit: Reuter et al., 2008). Note: LEISA, Lisa Hardaway Infrared Mapping Spectrometer (formerly Linear Etalon Imaging Spectral Array); MVIC, Multispectral Visible Imaging Camera..... A-29

Figure A-11. The focal plane conceptual schematic for the Europa Imaging System camera showing its panchromatic framing area and multispectral pushbroom area. The pushbroom section enables non-smearred images at high speed across multiple color channels, allowing for compositional information and single-track stereo. The framing area is useful for optical navigation, panchromatic, and certain stereophotogrammatic observations. Conceptually, this design is ideal for flyby dwarf planet VISNIR reconnaissance. WAC refers to the EIS Wide Angle Camera. (Image credit: Johns Hopkins Applied Physics Laboratory, <https://www.hou.usra.edu/meetings/lpsc2019/eposter/3065.pdf>.) A-30

Figure A-12. Observed distributions on the sky of 25- μm thermal emission from the galaxy (bright yellow/red structure spanning left to right) and the circumsolar dust disk (light-blue sideways S-shaped structure going from bottom left to upper right). Note how bright the galaxy appears, even though it contains mainly very cold ($T = 15\text{--}30\text{ K}$) dust; this is because it contains a massive amount of this dust. By contrast, the circumsolar (or “zodiacal”) emission is much fainter, even though it is dominated by emission from $T \sim 260\text{ K}$ dust near the Earth. It is these two “foreground” components that Interstellar Probe will be mapping using the IRM in order to also accurately measure the much fainter EBL flux in the sky created by the light of all the stars in all the galaxies since the beginning of the universe (dark black regions). (Image credit: NASA/Cosmic Background Explorer [COBE] Science Team.) A-31

Figure A-13. Top, Schematic representation of our strawman IRM mapper instrument design. The telescope uses an off-axis three-element design and couples to a standard VISNIR HgCdTe detector patterned with a linear variable filter (LVF) for spectroscopic mapping, with the option for broadband far-IR channels through the use of a beamsplitter. Nested thermal shields efficiently reject radiant heat and help passively cool the FPA to $<10\text{ K}$. The instrument would weigh $<5\text{ kg}$ and require $\sim 5\text{ W}$ to power. The current technology readiness level (TRL) of the instrument’s components would support a 2030 launch. Bottom, A schematic representation of the Interstellar Probe IRM mapper optical chain. Low spectral resolution is achieved with an LVF that will be flipped into or out of the optical path as needed. The shutter in the filter mechanism could be used to verify the dark current of the system, and (space permitting) broadband filters for calibration purposes. Note: FIR, far-infrared; NIR, near-infrared. (Images courtesy of M. Zemcov.) A-33

Figure A-14. The basic concept of operations for a camera on a spinning spacecraft, staring ahead and approximately aligned with the spin axis. This illustration uses a fictional instrument on a digital model of New Horizons. Top row: sunward of the spacecraft looking outward with the SpinCam rotating on the disc of a dwarf planet. Bottom row: anti-sunward of the spacecraft looking back to the inner solar system. Each subsequent frame shows the spacecraft and SpinCam rotated in a different direction. A-38

Figure A-15. The ring-field geometry. Note that although an image sensor (or set of image sensors) can be placed anywhere within the ring, the field angle is always the same. (Image credit: Johns Hopkins Applied Physics Laboratory.) A-39

Figure A-16. The CIS125 visible imaging sensor chip as designed for the Centre for Earth Observation Instrumentation (CEOI) program of the UK Space Agency. Note the use of stitching (a method to create semiconductors of arbitrary size by patterning a mask across the wafer), allowing the number of channels and size of the array to be customized. Pixels on the CMOS are read out at the column level. (Image credit: Johns Hopkins Applied Physics Laboratory.) A-40

Figure A-17. VIR and IRM shown above the particle suite boom, respectively. They are pointed 90° to the spacecraft ram direction. (Image credit: Johns Hopkins Applied Physics Laboratory.) A-41

Figure A-18. A view of the bottom of the spacecraft, showing the shorter, rigid PWS antennas. (Image credit: Johns Hopkins Applied Physics Laboratory.) A-43

Figure A-19. Using New Horizons’ flyby of Charon (comparable in size to many dwarf planets), we have modeled the type of images that Interstellar Probe could acquire of a dwarf planet. This modeling uses the Europa Imaging System – Narrow Angle Camera (EIS-NAC) boresight with an FOV of 2.3° in the cross-track direction. For ~1 minute around closest approach, the boresight slews off the planet to allow for a high-resolution, multiphase-angle strip or noodle. The slew would be ~1500 $\mu\text{rad/s}$. Top, Approach to a dwarf planet with the imager’s FOV superimposed as a cyan box. Middle, Imaging footprint on the planet during approach. The color ranges from 500 to 80 m/pixel from red to blue. Bottom, View of the New Horizons spacecraft scanning Charon with three of its imagers (LORRI, Ralph, and Alice). This is comparable to what Interstellar Probe could do at a dwarf planet. (Image credit: Johns Hopkins Applied Physics Laboratory.) A-52

Figure A-20. Comparison of the available data rates (red) with the sum of minimum data rates of all instruments (orange). Table A-5 provides a brief rationale for the assumed data rates. More details are provided below. A-55

Figure C-1. Sky map (ECLIPJ2000) for powered JGA cases with $m = 930 \text{ kg}$ ($C_3 = 203.91 \text{ km}^2/\text{s}^2$) over 2030–2042. (Image credit: Johns Hopkins Applied Physics Laboratory.) C-1

Figure C-2. Escape speed variation across the launch period for the powered JGA option. C-2

Figure C-3. Heliocentric mission geometry for notional powered JGA to (12°S, 284°E) with associated timeline. Planetary positions in panel (a) correspond to the powered JGA on 6 December 2040. C-2

Figure D-1. Views of the SOM flight system for the 2 R_s , Star 48BV case. (a) Sun-facing view showing the thermal protection system. (b) Anti-sunward view. (c) Side view with identification of flight system components. (Image credit: Johns Hopkins Applied Physics Laboratory.) D-2

Figure D-2. Example SOM mission scenario. (Image credit: Johns Hopkins Applied Physics Laboratory.) D-6

Figure D-3. The full space of solutions computed via a broad search is plotted in terms of optimality metrics launch C_3 , TOF, and post-SOM energy (here translated into $v_{100 \text{ au}}$). The

optimal subset of solutions is identified via black circles. As expected, the best-performing solutions in terms of TOF and energy are found at the highest C_3 values (2030 launch). (Image credit: Johns Hopkins Applied Physics Laboratory.) D-16

Figure D-4. Optimal SOM solution subsets across all launch years are plotted as the dark blue regions near the ecliptic plane, with launch year labeled beneath in white. Background surface sky maps depicting the analogous non-SOM ballistic JGA (a) and powered JGA (b) solutions are included for comparison, with launch years labeled in gray. Clearly, the non-SOM cases significantly outcompete the SOM case study. (Image credit: Johns Hopkins Applied Physics Laboratory.)..... D-17

Figure D-5. Fastest single trajectory is shown for a range of lift mass values (case study appears as a 7-ton point solution; launch in 2030 is assumed for all cases). Each point is colored by associated SRM ΔV and labeled with corresponding maximum launch C_3 . The best ballistic and powered JGA performance ranges across 2030–2042 are included as the purple and orange bands, respectively. (Image credit: Johns Hopkins Applied Physics Laboratory.) D-18

Figure E-1. Spherical shell cumulative dose [rad(Si)] versus depth (millimeter equivalent aluminum) illustrating contributions from the inner heliosphere mission phase, JGA, LISM, and background RTG. (Image credit: Johns Hopkins Applied Physics Laboratory.)E-1

Figure E-2. Spherical shell dose [rad(Si)] versus depth (millimeter equivalent aluminum for Interstellar Probe’s JGA; no margins are reflected). Dose at 100 mil (2.54 mm) aluminum is at least 10× less than predicted Europa Clipper mission doses. (Image credit: Johns Hopkins Applied Physics Laboratory.)E-3

Figure E-3. LET spectrum for GCR ions of $Z = 1$ to $Z = 28$ at a shielding depth of 2.54 mm. GCR fluxes at most LETs are two to four times higher in the LISM. (Image credit: Johns Hopkins Applied Physics Laboratory.)E-5

Figure E-4. Interstellar Probe’s JGA results in short-duration internal charging fluxes (top panel) and fluences (bottom panel) comparable with recent Jovian missions. (Image credit: Johns Hopkins Applied Physics Laboratory.)E-6

Figure F-1. Electromigration process in a given electronic package (Khan, 2012). (Image credit: Johns Hopkins Applied Physics Laboratory.) F-7

Figure F-2. Stress migration on a device. (Reprinted from Heryanto et al. (2010) with permission; © 2010 IEEE.) F-8

Figure F-3. A snapshot of the electron motion that leads to time-dependent dielectric breakdown (Wong, 2012)..... F-8

Figure F-4. The processes by which negative-bias temperature instability may occur. (a) The net charge at the dielectric interface may have positive ion drift occurring, leading to a decrease in the net charge. (b) If there is a charge imbalance on either side of the dielectric interface, then there may be an exchange of an electron for a proton (or hydrogen ion), causing a net-positive increase in the charge in the dielectric interface. (Reprinted from Stathis & Zafar (2006), with permission from Elsevier.)..... F-9

Figure F-5. The hot carrier injection process (Noda, 2008). (Image credit: Johns Hopkins Applied Physics Laboratory.) F-9

Figure F-6. Demonstration of the effects of solder fatigue on the package assembly (Serebreni, 2021). (Image credit: Johns Hopkins Applied Physics Laboratory.) F-10

Figure F-7. Probability of success for interplanetary missions as measured against design life is high (Edwards et al., 2021). (Image credit: Johns Hopkins Applied Physics Laboratory.) F-14

Figure F-8. Majority of interplanetary spacecraft retire without failure (Edwards et al., 2021). (Image credit: Johns Hopkins Applied Physics Laboratory.) F-16

Figure F-9. Design life versus actual life illustrates the margin that an interplanetary spacecraft possesses (Edwards et al., 2021). DL, design life; MD, mission duration. (Image credit: Johns Hopkins Applied Physics Laboratory.) F-17

Figure F-10. Lifetime distribution indicates a high confidence of an interplanetary spacecraft lasting for longer than 50 years. F-18

Figure F-11. An example of a failure rate bathtub curve for a given product. (Reprinted from Lu et al. (2016) with permission; © 2016 Springer Nature Limited.) F-21

Figure F-12. Framework to assess potential 50-year mission. EOL, end of life; PoF, physics of failure. (Image credit: Johns Hopkins Applied Physics Laboratory.) F-26

Figure F-13. Fault tree symbols. F-29

Figure F-14. Top level of science fault tree based on the science traceability matrix. Each box labeled Q1.x.x represents a science question fault tree found in this section. (Image credit: Johns Hopkins Applied Physics Laboratory.) F-30

Figure F-15. Example science question instrument mapping from the science traceability matrix. (Image credit: Johns Hopkins Applied Physics Laboratory.) F-31

Figure F-16. Legend for fault trees. (Image credit: Johns Hopkins Applied Physics Laboratory.) F-32

Figure F-17. STM fault tree for Question 1.1.1. (Image credit: Johns Hopkins Applied Physics Laboratory.) F-33

Figure F-18. STM fault tree for Question 1.1.2. (Image credit: Johns Hopkins Applied Physics Laboratory.) F-34

Figure F-19. STM fault tree for Question 1.1.3. (Image credit: Johns Hopkins Applied Physics Laboratory.) F-35

Figure F-20. STM fault tree for Question 1.1.4. (Image credit: Johns Hopkins Applied Physics Laboratory.) F-36

Figure F-21. STM fault tree for Question 1.1.5. (Image credit: Johns Hopkins Applied Physics Laboratory.) F-37

Figure F-22. STM fault tree for Question 1.1.6. (Image credit: Johns Hopkins Applied Physics Laboratory.) F-38

Figure F-23. STM fault tree for Question 1.1.7. (Image credit: Johns Hopkins Applied Physics Laboratory.)F-39

Figure F-24. STM fault tree for Question 1.1.8. (Image credit: Johns Hopkins Applied Physics Laboratory.)F-40

Figure F-25. STM fault tree for Question 1.2.1. (Image credit: Johns Hopkins Applied Physics Laboratory.)F-41

Figure F-26. STM fault tree for Question 1.2.2. (Image credit: Johns Hopkins Applied Physics Laboratory.)F-42

Figure F-27. STM fault tree for Question 1.2.3. (Image credit: Johns Hopkins Applied Physics Laboratory.)F-43

Figure F-28. STM fault tree for Question 1.3.1. (Image credit: Johns Hopkins Applied Physics Laboratory.)F-44

Figure F-29. STM fault tree for Question 1.3.2. (Image credit: Johns Hopkins Applied Physics Laboratory.)F-45

Figure F-30. STM fault tree for Question 1.3.3. (Image credit: Johns Hopkins Applied Physics Laboratory.)F-46

Figure F-31. STM fault tree for Question 1.3.4. (Image credit: Johns Hopkins Applied Physics Laboratory.)F-47

Figure F-32. STM fault tree for Question 1.3.5. (Image credit: Johns Hopkins Applied Physics Laboratory.)F-48

Figure F-33. STM fault tree for Question 1.3.6. (Image credit: Johns Hopkins Applied Physics Laboratory.)F-49

Figure F-34. Top-level Interstellar Probe mission RBD. Each box is further decomposed with the bus and payload RBDs. (Image credit: Johns Hopkins Applied Physics Laboratory.).....F-51

Figure F-35. Spacecraft bus RBD. Each system box is decomposed into its own RBD. (Image credit: Johns Hopkins Applied Physics Laboratory.)F-52

Figure F-36. Avionics system RBD. (Image credit: Johns Hopkins Applied Physics Laboratory.)F-52

Figure F-37. Power system RBD. (Image credit: Johns Hopkins Applied Physics Laboratory.)F-52

Figure F-38. Guidance, navigation, and control sensors RBD. (Image credit: Johns Hopkins Applied Physics Laboratory.)F-52

Figure F-39. Telecom RBD. (Image credit: Johns Hopkins Applied Physics Laboratory.)F-53

Figure F-40. Propulsion system RBD. (Image credit: Johns Hopkins Applied Physics Laboratory.)F-53

Figure F-41. Structure and mechanisms RBD. (Image credit: Johns Hopkins Applied Physics Laboratory.)F-53

Figure F-42. Top-level reliability estimates with uncertainty. (Image credit: Johns Hopkins Applied Physics Laboratory.)F-56

Figure F-43. System-level reliability estimates with uncertainty. (Image credit: Johns Hopkins Applied Physics Laboratory.)F-56

Figure F-44. Workflow for identifying the most reliable part for application. (Image credit: Johns Hopkins Applied Physics Laboratory.).....F-66

Figure F-45. Process for completing stress and damage modeling for reliability prediction. (From Smith et al. (2021); reprinted with permission from AIAA.)F-67

Figure F-46. Using Moore's Law scaling to estimate node size and, in due course, estimate the effective gate length for the transistor. (Image credit: Johns Hopkins Applied Physics Laboratory.)F-69

Figure F-47. RPS systems last longer than their intended design lives. (Image credit: Johns Hopkins Applied Physics Laboratory.)F-78

Figure F-48. Bayesian assessment shows uncertainty of both Weibull distribution parameters. (Image credit: Johns Hopkins Applied Physics Laboratory.)F-79

Figure F-49. GPHS-RTG power prediction for Interstellar Probe through 100 years with 16 GPHS units. (Image credit: Johns Hopkins Applied Physics Laboratory.)F-80

Figure H-1. MEL basis for option 3. The spacecraft adds 40 kg to the 860-kg option 1 observatory to accommodate the twin RTG booms that must be deployed after the SOM (in practice after passing Venus' orbit outbound). This provides a better view of deep space and, hence, a lower cold-side temperature to allow the RTGs to come up to full power. Given all of the uncertainties, an unallocated margin of 30% is added to the spacecraft, interstage, and thermal shield assembly and all of those masses. CBE, current best estimate. (Image credit: Johns Hopkins Applied Physics Laboratory.)..... H-6

Figure H-2. Thermal shield assembly component masses for a Star 48BV, Star 48GXV, and Orion 50XL motor as a function of perihelion distance (2–6 solar radii from the center of the Sun). (Image credit: Johns Hopkins Applied Physics Laboratory.) H-7

Figure H-3. Point-design matrix for option 3 baseline spacecraft. Decreasing kick-stage engine size is to the right, and decreasing perihelion design distance is toward the bottom. The number of shields required to “step down” the external temperatures on the shield exposed directly to sunlight increases with decreasing distance, as does the length and width of the shield because of the increasing solid angle filled by the solar disk. The Orion 50XL and Star 48GXV have comparable lengths, with the latter having a smaller diameter (and less propellant load). (Image credit: Johns Hopkins Applied Physics Laboratory.) H-9

Figure H-4. Time versus distance for the 860-kg observatory case across all three options. Flyout times to 200 years versus heliocentric flyout distances to 1000 au are plotted for 112 valid trajectories (another 69 trial trajectories did not work). (Image credit: Johns Hopkins Applied Physics Laboratory.) H-14

Figure H-5. Expansion of the lower left-hand corner of Figure H-4 by a factor of 5. Options 1 and 2 are clearly separated from option 3 trajectories. Option 3 trajectories also show different performances for Parker Solar Probe versus new UHT material thermal shields. Only a few option 3 trajectories overtake option 1 and 2 trajectories within 50 au. (Image credit: Johns Hopkins Applied Physics Laboratory.)..... H-15

Figure H-6. Baseline spacecraft for option 3 with “interstage” (yellow), ballast (top), Orion 50XL kick stage, undeployed RTGs (one visible at center), and TSA designed for $2R_s$ perihelion. (Image credit: Johns Hopkins Applied Physics Laboratory.) H-16

Figure H-7. SLS Block 1B+ Cargo, now referred to as SLS Block 2 Cargo, high-energy performance with upper stages for 18 of the configurations used in this study. (Image credit: Johns Hopkins Applied Physics Laboratory.)..... H-21

List of Tables

Table 3-1. Event timeline.....	3-4
Table 3-2. Alternative launch options for the Interstellar Probe mission.....	3-4
Table 3-3. Interstellar Probe mission phases.....	3-5
Table 3-4. Interstellar Probe telecommunications coverage.	3-9
Table 3-5. Interstellar Probe uplink plan.....	3-10
Table 3-6. Interstellar Probe downlink volume.	3-11
Table 4-1. Four flyout directions across the sky have been identified, each with its own benefits and trades. Flyout time estimates to 100 au of the Interstellar Probe are given.....	4-55
Table 4-2. Interstellar Probe science operations.....	4-63
Table 4-3. Scientific events along the trajectory.	4-65
Table 4-4. Columns group nominal instruments, range of reasonable data rates, and representative rates during different mission phases. Values are in bits per second. Each instrument line includes a data rate and, where applicable, a justification. More details on the justification are in the main text. Green cells are fixed values, and gray cells are calculated from scaling as described in the text.	4-69
Table 5-1. Baseline concept spacecraft MEL summary.....	5-3
Table 5-2. Assumed RTG characteristics.....	5-4
Table 5-3. End-of-life power mode.	5-4
Table 5-4. Communications specifications compared to notable deep-space missions.	5-6
Table 5-5. Ground station alternatives for Interstellar Probe.	5-6
Table 6-1. Interstellar Probe project phase durations.	6-1
Table 6-2. Interstellar Probe project schedule with key milestones.....	6-1
Table 6-3. Interstellar Probe life-cycle cost estimate (FY25\$M).	6-2
Table 6-4. Interstellar Probe payload cost summary (FY25\$M).	6-7
Table 6-5. Interstellar Probe spacecraft estimate by subsystem (FY25\$M).	6-7
Table 6-6. Interstellar Probe parametric cross-check results (FY25\$M).....	6-8
Table 6-7. Interstellar Probe MOCET results (FY25\$M).	6-9
Table 6-8. Interstellar Probe Phase E: first decade (FY25\$M).....	6-10
Table 6-10. Development cost summary results.....	6-11
Table 6-11. Interstellar Probe reserves (FY25\$M).	6-12
Table 6-12. Development costs by work breakdown structure and fiscal year.....	6-15

Table 6-13. Risk consequence definitions.....	6-15
Table 6-14. Risk likelihood definitions.	6-16
Table 6-15. Risk matrix.....	6-16
Table 6-16. Risk list.....	6-17
Table A-1. Measurement requirements for the Visible-Near Infrared Imager (VIR).....	A-28
Table A-2. Measurement requirements for the Infrared Spectral Mapper (IRM).....	A-30
Table A-3. Estimated camera performance at 90 au, with 64 stages of TDI and a spacecraft-to-target distance of 45,000 km.....	A-40
Table A-4. Interstellar Probe mission phases.	A-45
Table A-5. Formatting is equivalent to Table 4-4. The augmented mission has the same instruments as discussed in Table 4-4 except LYA, and includes the IRM and VIR.	A-56
Table B-1. Flown magnetometer resources and capabilities.	B-1
Table B-2. Examples of current charged particle instruments that have flown, are in operation, or are in development.....	B-2
Table B-3. Examples of current energetic neutral atom (ENA) instruments that have flown, are in operation, or are in development.	B-4
Table B-4. Examples of current neutral mass spectrometers that have flown, are in operation, or are in development.....	B-7
Table B-5. Examples of current ultraviolet (UV) instruments that have flown, are in operation, or are in development.....	B-8
Table B-6. Examples of current plasma wave instruments that have flown, are in operation, or are in development.....	B-9
Table B-7. Examples of current dust instruments that have flown, are in operation, or are in development.	B-10
Table B-8. Examples of current infrared (IR) instruments that have flown, are in operation, or are in development.....	B-11
Table B-9. Examples of current visible/near infrared (VISNIR) imagers that have flown, are in operation, or are in development.....	B-12
Table D-1. Mass breakdown of flight system components for a solar Oberth trajectory with perihelion at $3 R_s$	D-3
Table D-1. Mass breakdown of flight system components for a solar Oberth trajectory with perihelion at $3 R_s$	D-3
Table D-2. Shield and support masses for a range of SOM trajectory perihelia.....	D-4
Table D-3. Perihelia as a function of C_3 for direct-to-Jupiter trajectories.....	D-9
Table D-4. SOM performance versus kick stage for 250-kg observatory mass.	D-12
Table D-5. SOM performance versus kick stage for 478.3-kg observatory mass.	D-13

Table D-6. Point design studied for SOM architecture. D-15

Table D-7. Launch date ranges for optimal solutions, with $\max(v_{100 \text{ au}})$ given (launch years highlighted in yellow correspond to departure toward the nose of the heliopause. D-16

Table F-1. Constituent mission phases create the mission lifetime goal of 50 years..... F-4

Table F-2. Interplanetary spacecraft listing for longevity analysis. F-12

Table F-3. Weibull parameters using Bayesian updating..... F-17

Table F-4. Studies showing that the hazard rate of electronics is dominated only by wearout mechanisms..... F-19

Table F-6. Instrument cut sets..... F-50

Table F-7. COTS device reliability data..... F-54

Table F-8. Electronic board reliability data..... F-55

Table F-9. Limited-life items. F-57

Table F-10. List of parameters needed to solve for time to failure in Equation 1, with the source information and estimated range of values of the parameter..... F-69

Table F-11. Materials reliability factors for materials on an interstellar probe..... F-72

Table F-12. Listing of radioisotope system that have flown. F-75

Table F-13. Probability of success metrics..... F-77

Table H-1. Parametric C_3 versus injected mass. H-4

Table H-2. Thermal control kick-stage mass..... H-6

Table H-3. Nominal minimum C_3 s for indicated perihelia (ideal circular planetary orbits; R. L. McNutt, Jr. (2021)). H-10

Table H-4. Option results for 860-kg observatory..... H-11

Table H-5. “Best” trajectories for 860-kg observatory..... H-12

Table H-6. Interstellar Probe mission requirements and concepts, 1960–2019..... H-16

1. Executive Summary

Interstellar Probe is a scientific mission to capture a unified view of our heliosphere and its surroundings in interstellar space. It will capture that view using an optimized set of modern, state-of-the-art scientific instruments beginning with its launch from Earth. Throughout its journey into nearby interstellar space, Interstellar Probe will carry out investigations of (1) the processes within the heliosphere responsible for the formation of the heliospheric boundary, (2) the detailed physical processes at work in the heliosheath, (3) the global dynamics of the heliosphere, and (4) conditions in, and characteristics of, the very local interstellar medium (VLISM), including the Sun’s influence therein. Understanding the dynamics and structure of our heliosphere is fundamental to understanding the dynamics and structure of other astrospheres (“heliospheres” that surround other stellar systems) as well as how astrospheres interact with the galaxy and how the galaxy interacts back in response. The primary goal for such a mission can be summarized as: “Understand Our Habitable Astrosphere and Its Home in the Galaxy.”

Practically, Interstellar Probe is a ≥ 50 -year-long mission to reach several hundreds of astronomical units past the heliopause (HP) and into the nearby interstellar medium (ISM). It will be providing new, unified measurements along the way of the conditions throughout the heliosphere and the heliosheath. Temporally, these measurements will also stretch across almost five solar cycles and, as a result, will help ascertain and quantify how solar activity maps throughout the solar system, past the planets, into the Kuiper Belt, and into the ISM itself. This farthest reach of the mission will build upon the more familiar, closer-by regions explored serendipitously by the extended missions of Pioneer 10 and 11, Voyager 1 and 2, and New Horizons. Interstellar Probe can benefit enormously from the preliminary discoveries and learned limitations of the payloads on those missions when combined with modern technologies. By taking a purpose-built, well-focused payload into the nearby galaxy, it will not only push further our knowledge of the nearby ISM but also determine how far the activity of our own Sun propagates into interstellar space and how the conditions there feed back to affect the structure and dynamics of the heliosphere itself. Interstellar Probe will provide the first transect through the heliosphere covering all charged particle energies with no energy gaps, especially in the critical suprathermal range, which can be compared with observations of corresponding populations closer to Earth obtained by other components of NASA’s Heliophysics System Observatory (HSO). A launch in the second half of the 2030s would enable a heliospheric exit near the interstellar-wind-facing (“ram”) direction but also sufficiently far “to the side” to observe the global structure remotely via energetic neutral atoms (ENAs) detected at the spacecraft.

A principal goal of interstellar probe mission concepts, now stretching back 60 years since the report to the Space Science Board by the “Simpson Committee”¹ in March 1960, has been to gain new insight into both the current state and past history of the interaction of our Sun and solar system

¹ Formally *Committee 8 – Physics of Fields and Particles in Space* of the Space Science Board (now the Space Studies Board) of the National Academies

with the ISM through which they continue to travel. Such insight will inform the conditions for habitability within both our heliosphere and other astrospheres, the latter of which can only be studied remotely.

To study and select a menu of “appropriate” science drivers, required measurements, and example payload instruments for such a mission, both an internal Johns Hopkins Applied Physics Laboratory (APL) team and a large number of external and unpaid volunteers were assembled via a set of four workshops (9–12 October 2018 – by invitation; 15–18 October 2019 – open; 16–20 November 2020 – open/virtual; and 27 September to 1 October 2021 – open/virtual). A corresponding support community was self-selected, divided into eight Topical Science Groups comprising over 80 active members. A website was established to summarize the work, communicate with 532 people from 181 institutions in over 30 countries, and archive the recordings of 16 webinars held from 28 May 2020 through 24 June 2021. The webinars were attended by 1044 people at 131 organizations in 24 countries. The website also contains links to 11 white papers submitted to the Heliophysics 2050 Workshop and references 199 presentations given at 70 conferences and meetings from 2017 through November 2021.

This mission concept has also been discussed at various times over the past four years via 20 news articles in the popular press as well as the technical venues discussed already. In addition, early-career community members include 73 graduate students and 97 undergraduate students from 13 countries who have participated in activities.

The “support community” assembled a consensus science traceability matrix in which three key science questions were identified:

1. How is our heliosphere upheld by the physical processes from the Sun to the VLISM?
2. How do the Sun’s activity as well as the interstellar medium and its possible inhomogeneity influence the dynamics and evolution of the global heliosphere?
3. How do the current VLISM properties inform our understanding of the evolutionary path of the heliosphere?

All these science questions support the goal of “Understand Our Habitable Astrosphere and Its Home in the Galaxy.”

These questions are mapped to the four overarching investigations of (1) the heliosphere, (2) the heliosheath, (3) the dynamics of the overall system, and (4) the VLISM. These, in turn, have been mapped to 15 objectives. Twelve of those objectives have been mapped to 12 corresponding detailed investigations; the other three objectives have been mapped back to a total of seven other detailed investigations. Hence, for this Heliospheric Baseline Mission, there is a hierarchy of one goal, three science questions, four overarching investigations, 15 objectives, and 19 detailed investigations (Section 2).

The set of underlying measurement requirements demands a spacecraft making a rapid escape from the Sun’s gravity well, but not so rapid that the termination shock and HP structure cannot

be resolved. Also to be resolved are the temporal variations in the heliosheath, presumably set at least partially by solar-cycle variations, and known from the Voyagers (Section 3).

The Working Groups crafted a notional set of remote-sensing and in situ instruments to address the three notional objectives via the 19 detailed investigations (Section 4). Six of the Working Groups map to six instrument types from which 10 notional instruments have been put forward. The notional instruments have relatively high technical maturities (high technology readiness levels [TRLs]) for the purpose of meeting the measurement requirements while providing a low risk to meeting an engineering target of 85–90 kg and 85–90 W for the suite mass and power, respectively. These divide into (1) fields and waves (two instruments), (2) charged particles (four instruments), (3) dust (one instrument), (4) neutral particles (one instrument), (5) ENA imaging (one instrument), and (6) ultraviolet imaging (one instrument). These, in turn, provide 19 sets of analysis products to the 19 detailed investigations, and those provide science closure to the 15 objectives.

In addition to this baseline heliophysics mission, an augmented mission encompassing potential, easily added planetary science and astrophysics goals was also studied using input from two other Topical Science Groups (Appendix A). In addition to the previous heliophysics goal, the augmented mission added two more important goals achievable only far from the Sun, namely: “Goal 2. Understand the Origin and Evolution of Planetary Systems” and “Goal 3. Explore the Universe Beyond Our Circumsolar Dust Cloud.” The augmented science mission includes a New Horizons–style flyby of a Kuiper Belt object and measurement of all the visible light ever produced in the universe, the extragalactic background light (EBL), which is obscured from view at Earth by the zodiacal cloud of dust in the inner solar system. These goals provided two additional science questions each:

1. What dynamical and chemical processes produced the current structure and composition of the interplanetary dust disk?
2. How did the solar system form and evolve compared to other planetary systems?

And

1. What role do the composition, evolution, and thermodynamics of the nearby and distant ISM play in determining the habitability of planetary bodies?
2. What is the total diffuse red-shifted light emitted by all the stars and galaxies in the universe since the beginning of cosmic time?

These two goals were each accompanied by eight and five new additional objectives, respectively, mapping to two overarching investigations for each of the two goals. Together these added 13 new objectives mapped across 17 detailed investigations. To accomplish this augmented mission, one instrument was removed from the “baseline” heliophysics payload, two new instruments were added, and one (the Plasma Wave Subsystem instrument) was degraded in capability in order to support periods of three-axis stabilization of the spacecraft. Although the detailed notional mass and power numbers changed slightly, the trades were made such that the basic supporting spacecraft (the “Observatory”) could be agnostic with respect to payload mass, power, and downlink requirements of the “baseline” and “augmented” cases. Hence, the augmented mission would

require periods of three-axis stabilization within longer periods of spin stabilization, similar to the operating scheme of New Horizons.

In both cases, the payload instrumentation has been selected to provide functional redundancy across the objectives and to give complementarity of observations in case of problems. Such redundancy also provides for important consistency checks via results obtained with more than one instrument. While actual payload instruments would be designed explicitly for this mission, developed instruments with similar measurement requirements were used to provide mass and power requirements for the nominal baseline and augmented payloads (Appendix B).

The detailed engineering (Section 5) and trade-off studies (Appendices D and H) presented in this report have shown that an interstellar probe mission supporting the aforementioned science investigations can be designed, built, and launched in the near term of the 2030s. The nominal “best” concept uses a super heavy-lift launch vehicle (SHLLV)² with one or two additional stages and a passive Jupiter gravity assist (JGA) to leave the Sun’s gravity field with an asymptotic escape speed about twice that of Voyager 1 (“Option 1”). The example design uses a Voyager-sized, 860-kg (wet mass) spacecraft (the “Observatory”) carrying ~90 kg of “appropriate” scientific instruments (as discussed above). Detailed study trades have focused on the Space Launch System Block 2 Cargo configuration (driven by the public availability of performance data for multiple staging concepts using that system). This configuration is planned for an initial operational capability in the late 2020s as part of the Artemis program. After a study of well over a hundred different launch configurations and launch modes, the “best” system design for Interstellar Probe incorporates generous margins, appropriate technologies, and the lowest risk posture for a 50-year, by design, mission. The approach allows for a mission best able to address all the identified key science questions at minimal cost and low risk.

Other options studied included “holding back” the final stage for a prograde-powered JGA (Option 2) (Appendix C) or a prograde-powered maneuver near a very close perihelion (less than 6 solar radii from the Sun’s center) (Option 3: a “solar Oberth maneuver” or SOM) (Appendix D). The Option 2 approach appears to offer some minimal increase in performance (~0.5 au/year extra asymptotic speed) but also carries a significant new risk in keeping such a large solid rocket motor (SRM) within thermal and thermal gradient specifications for an ~1-year flight time to Jupiter (such a maneuver at Jupiter with a detachable stage has never been done before). Significant effort was applied in studying Option 3, the SOM, because of its oft-cited potential for enabling rapid solar system escape (beginning with Oberth in 1929). After funding an investigation into new promising ultrahigh temperature materials that postdate Parker Solar Probe thermal shield development, the materials were used to scope out thermal shield designs in concert with existing SRMs. It has become clear that all the potential advantages of the SOM are outweighed by the thermal shield mass required for existing and even low-TRL kick stages. These negative aspects are exacerbated by the sizable risks of such an approach. The most notable is that the time-critical propulsive burn must be done under extreme thermal conditions for which even coupon-scale testing may not be possible before the actual flight. Even with potentially larger asymptotic speeds (and totally ignoring the

² Although definitions vary, an SHLLV is generally taken to be a launch vehicle capable of lifting more than ~100 metric tons into low Earth orbit (cf. https://en.wikipedia.org/wiki/Super_heavy-lift_launch_vehicle).

risks), the additional time spent in getting from the Earth close to the Sun adds ~ 3 years to the de facto “start time,” leading to a longer travel time to several hundred astronomical units compared with the less risky and more technologically mature Option 1.

All mission options include a close flyby of Jupiter near its rotational plane (but skirting Jupiter’s ring system). The flybys are very fast, but there is still a non-negligible radiation dose from Jupiter’s radiation belts, as well as from galactic cosmic rays in the interstellar phase of the mission. Both radiation sources are taken into account in the engineering study (Appendix E). Similarly, an extensive study of requirements to enable a successful 50-year mission lifetime was undertaken (Appendix F).

Low-thrust, in-space propulsion (e.g., nuclear electric propulsion and solar sails) was considered but not studied in detail because of the current low TRL of such approaches coupled with the current low investment levels for advancing the required TRLs for using these approaches on Voyager-sized spacecraft.

The use of a JGA ties the flyout direction to the position of Jupiter at launch. However, such a flyby of Jupiter adds ~ 3 au/year to the flyout speed, almost doubling that which can be achieved with a totally unconstrained launch window. The details of the spacecraft engineering design and instrumentation are agnostic with respect to launch date. To maximize the flyout speed, and hence distance traveled, the only requirement is to place the launch window near optimal Earth-to-Jupiter transfer orbits, which occur close to the 13-month synodic period of Jupiter. For the notional mission example studied here, we have pointed to a 21-day launch window opening 28 August 2036. While the self-imposed mission readiness requirement is to be able to support a launch anytime after 1 January 2030, the 2036 window is the first opportunity after 2030 to pass through the “IBEX (Interstellar Boundary Explorer) ribbon” and exit the heliosphere within 90° of the incoming interstellar wind. The escape speed varies from 6.8 to 7.0 au/year across the window, and the spacecraft would reach well over 300 au in 50 years of travel time. Launch opportunities, with varying escape speeds, and passing through the ribbon occur at ~ 13 -month intervals through December 2041. In any case, an exact target on the sky would be a future NASA decision likely informed by a Science and Technology Definition Team (STDT) given that task along with NASA scheduling and policy considerations.

With the complement of instruments and the need to immediately begin collecting a baseline near 1 au, significant scientific results will begin to accrue as soon as checkout after launch is complete (i.e., at the very beginning of Phase E). In addition to the in situ measurements, the initial “frames” in grand “movies” of the Lyman- α background and ENA sky view will begin to be collected. The EBL can be fully characterized by 10 au from the Sun, once Interstellar Probe passes Saturn’s orbit. These measurements can begin in synchronization with Earth orbital assets of the HSO and continue to provide a “moving viewpoint” for comparison with the view from Earth over the course of the Interstellar Probe mission.

The long mission lifetime by design dictates a workable, robust apprenticeship and rolling management and science team plan. This is currently envisioned as taking place over a decade or so timescale, which is also adequately funded to support the approach. Data products would regularly be available to be made public via all appropriate NASA channels, including scientific confer-

ences and publications and appropriate interactions through public channels. Plans for the notional mission have been costed to provide for a robust and ongoing analysis and release of data. Although it will be a NASA choice, the challenge of multiple decades of data archiving is best served by adhering to stringent metadata requirements, such as those currently employed by NASA's Planetary Data System.

In addition, a discrete-element cost estimate for the entire mission has been generated for the baseline mission for Phases A–D as well as for Phases E and F (Section 6). The same methodology has also been applied to the augmented mission, as well as separately to a spacecraft design tailored to accomplish a SOM (Appendix G). Cost estimates and schedules are informed by applying appropriate cost models to the notional baseline spacecraft, based, in turn, on experience gleaned from the development of other APL missions, notably Parker Solar Probe and New Horizons, as well as from interrogation of other cost databases. Instrumentation cost estimates are based on the model payloads and assumed TRLs of 4 or 5 for those instrument types discussed. Phase E cost estimates are based on a phased approach of science team initiation, turnover, and retirement to maximize the scientific return across three to five generations of scientists and engineering staff while providing for appropriate knowledge retention and training resources to implement such a multigenerational plan. This mission can be the realization of the beginning of the diversity and longevity of a real “Star Trek.”

As a large strategic mission, it is envisioned that a future STDT as well as members of the upcoming Solar and Space Physics Decadal Survey could draw upon this document as a “menu” from which to select and/or reject science goals, solar-system-flyout direction, and potential instruments for a scientific payload.

There are no “showstoppers”; it is “time for the stars.” An interstellar probe can be made ready for launch in the 2030s. The choice is ours; we write the history of future generations. The road to the stars awaits.

2. Science Goals and Questions

2.1 Science Rationale

During the evolution of the solar system, the Sun and its protective heliosphere have completed nearly 20 revolutions around the galactic core. During this “solar journey” around the galaxy, the heliosphere has plowed through widely different interstellar environments that have all shaped the system we live in today. The orders-of-magnitude differences in interstellar properties have had dramatic consequences for the penetration of interstellar gas, dust, and galactic cosmic rays (GCRs) that have affected elemental and isotopic abundances, chemical atmospheric evolution, and perhaps even biological evolution. Along the evolutionary path, high interstellar cloud densities and ionization fractions have likely compressed the heliosphere down to below 25 au (Müller et al., 2009). Evidence is emerging for supernovae explosions as recent as 3 million years ago at only 20–50 pc from the Sun that probably compressed the heliosphere even below the orbit of Saturn and perhaps more, exposing the terrestrial planets to almost the full force of interstellar material and GCRs (Wallner et al., 2020).

As far as we know, only some 60,000 years ago, the Sun entered what we call the Local Interstellar Cloud (LIC) and is now either at the very edge of it or already in contact with four of the surrounding clouds (Figure 2-1). Estimates place the heliosphere in a completely different interstellar environment in less than 2000 years, which will continue to shape the evolution of the heliosphere.

With its limited planetary payload, Voyager discovered that the heliospheric boundary represents a whole new regime of space physics that is decisive not only for our own heliosphere but also for understanding other astrospheres that potentially host habitable exoplanetary systems, whose atmospheric and surface habitability is controlled by the stellar and interstellar environment. The exploration of the outer heliosphere provides a unique way to understand the critical mechanisms by which inflowing interstellar plasma, including its magnetic field and its neutral, ionized, and nonthermal particles, controls the shape and properties of astrospheres. In situ measurements of the pristine interstellar medium (Clarke et al., 2017) and the modifications produced by the solar wind and magnetic field are needed to provide realistic predictions of the properties of astrospheres and the exoplanets that reside within them.

Primary Goal: Understand Our Heliosphere as a Habitable Astrosphere and Its Home in the Galaxy

An interstellar probe on a fast, escaping trajectory through the outer heliosphere and into the very local interstellar medium (VLISM) would therefore represent a snapshot of our place along the solar journey through the galaxy, to determine the current state of the heliosphere and its surrounding VLISM, to ultimately understand where our home came from, and where we are going.

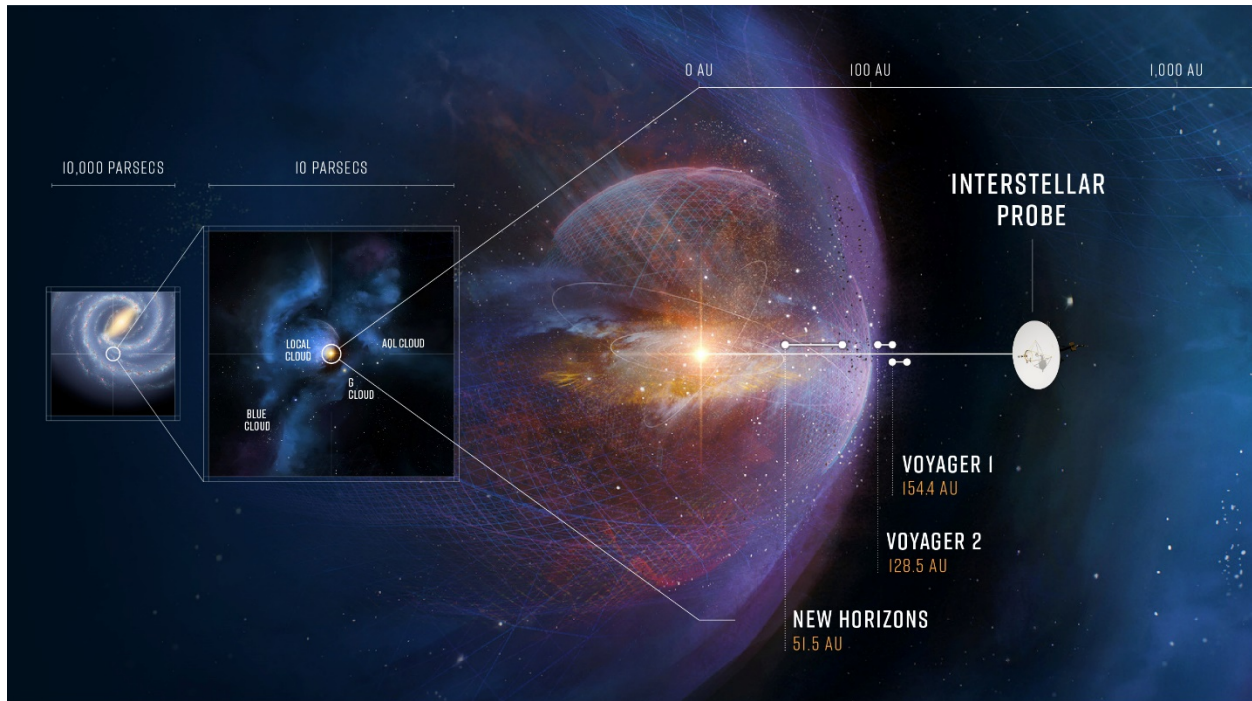


Figure 2-1. During the evolution of our solar system, its protective heliosphere has plowed through dramatically different interstellar environments that have shaped our home through incoming interstellar gas, dust, plasma, and galactic cosmic rays. Interstellar Probe on a fast trajectory to the very local interstellar medium (VLISM) would represent a snapshot to understand the current state of our habitable astrosphere in the VLISM, to ultimately be able to understand where our home came from and where it is going. (Image credit: Johns Hopkins Applied Physics Laboratory.)

2.2 Science Questions

2.2.1 Question 1: How is our heliosphere upheld by the physical processes from the Sun to the VLISM?

The solar wind, expanding from the Sun, flows beyond the orbits of the solar system planets until it interacts with the VLISM and forms the heliosphere, a plasma bubble around the Sun. Both the Sun and VLISM shape a unique plasma environment in the heliosphere through complex dynamic processes between charged and neutral particles and magnetic fields of solar and galactic origin. The heliosphere hosts planets with their magnetospheres and atmospheres and controls their structure, dynamics, and radiation level. The heliosphere protects Earth and other planets, shielding them from high-energy GCRs coming from distant space. *Determining the physical processes upholding the boundary to the VLISM is critical for understanding the current state of the entire heliosphere and how it protects our habitable solar system. Exploration of the heliospheric boundary is also the only way to gain understanding of other astrospheres and their stellar environments in which exoplanetary systems live and evolve.*

The formation of the heliospheric boundary already starts deep inside the inner heliosphere near the Sun. Here, the neutral interstellar gas that permeates the heliosphere is ionized by photo- and electron-impact ionization as well as charge-exchange processes creating suprathermal interstellar

pickup ions (PUIs). Once ionized, PUIs are “picked up” by the solar wind convection electric field and rapidly accelerated up to twice the solar wind speed. PUIs are also formed from interaction with an “inner source” of interplanetary dust grains and the solar wind. Beyond Neptune’s orbit, PUIs strongly mediate the solar wind speed and temperature, and once they interact with and flow across the termination shock (TS), the PUI population dominates the force balance in the heliosheath and at the heliopause (HP) against the apparent ENA flow of the VLISM (Rankin, et al., 2019a).

PUIs are mostly singly charged and have unique velocity distribution functions, with a sharp cutoff at twice the bulk speed of the local plasma. PUIs play a dominant role in the dynamics of the outer heliosphere and VLISM because they carry most of the particle pressure in the increasingly tenuous solar wind at such large heliocentric distances (Gloeckler & Fisk, 2015). Their crucial role in the dynamics of the outer heliosphere and the VLISM could not be studied with Voyager 1 and 2 because PUIs were and are not measured by those spacecraft (Figure 2-2). While the physics of PUIs within the inner heliosphere has been previously addressed with Ulysses/Solar Wind Ion Composition Spectrometer (SWICS) and Advanced Composition Explorer (ACE)/Solar Wind Ion Composition Spectrometer (SWICS) observations (Allegrini et al., 2005; Geiss et al., 1995; Gloeckler et al., 1992; Gloeckler & Geiss, 1996; Schwadron et al., 2000), the lack of full 3D velocity distribution function measurements (i.e., arrival directions of ions) and the small geometric factor of SWICS inhibited progress in understanding the particle processes in the heliosphere. For example, neither the origin nor the production mechanism for “inner-source” PUIs has been established (Allegrini et al., 2005; Gloeckler & Geiss, 1996), and although the cosmologically important density of pickup $^3\text{He}^+$ was measured for the first time with Ulysses/SWICS (Gloeckler et al., 1992), this value had a large uncertainty. It is now becoming likely that New Horizons may have sufficient power to be able to observe light PUIs (Elliott et al., 2019; Kollmann et al., 2019) out through the TS and perhaps

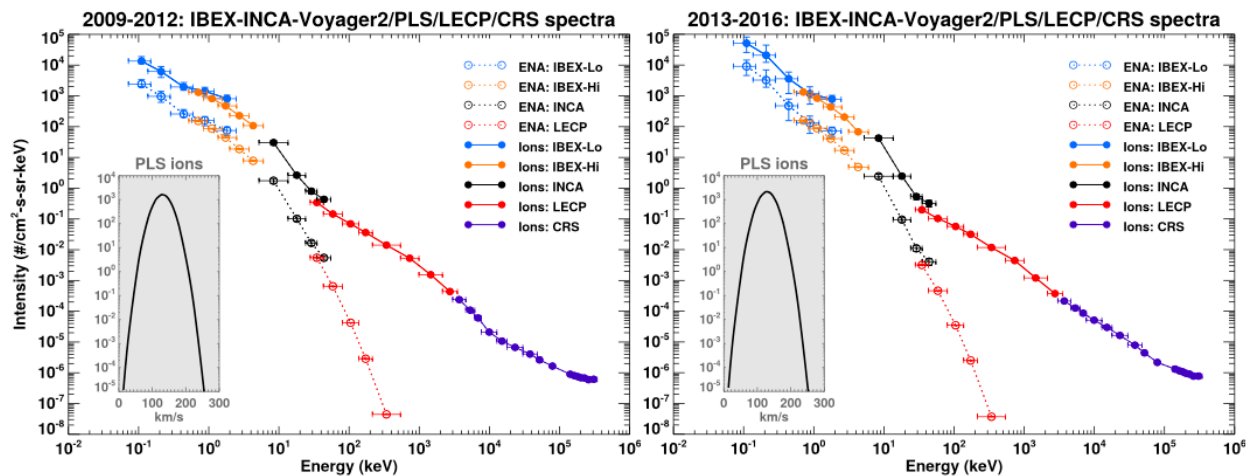


Figure 2-2. PUIs and suprathermal particles dominate the total pressure in the heliosheath; however, lack of in situ measurements of these populations represents a critical gap. A combination of ~10-eV to ~344-MeV in situ ion measurements from the Voyager 2/Plasma Science (PLS)/Low-Energy Charged Particle (LECP)/Cosmic Ray Subsystem (CRS) experiments and remotely sensed ~110-eV to ~55-keV energetic neutral atom (ENA) measurements from the Interstellar Boundary Explorer (IBEX) and Cassini missions over 2009–2016 along Voyager 2’s trajectory through the heliosheath is shown (from Dialynas et al. (2020)).

some distance into the heliosheath. However, the New Horizons instrumentation was not designed to measure multiple and heavier species of PUIs. It is essential for the Interstellar Probe to determine the relative roles between the thermal plasma, PUIs, and the energetic particles in driving forces governing the balance between the solar wind and plasma in the outer heliosphere and local interstellar medium (LISM) as well as identify any other thermal populations over the energy range of electronvolts to hundreds of kiloelectronvolts, considering also that Voyager left a gap at 5–30 keV. Hence, the first Interstellar Probe objective (1.1.1) is to ***“Resolve the birth and evolution of interstellar and inner-source pickup ions.”***

The evolution, acceleration, and transport processes occurring in the solar wind and interplanetary shocks are important for understanding how they affect the heliosheath. Following the previous discovery by Voyager 2 of solar wind heating and deceleration in the outer heliosphere (Richardson & Smith, 2003), New Horizons has confirmed a noticeable slowdown of the solar wind at ~30 au due to the mass-loading of PUIs (Elliott et al., 2019). The temperature profile was also found to be well above what is expected for an adiabatic profile, which is consistent with turbulent heating caused by the initially unstable ring-beam distributions of newly born PUIs that indirectly heat the solar wind as they are scattered by low-frequency turbulence (Zank et al., 2018). Many open questions exist because of the lack of complete measurements, including particle distributions and primarily magnetic fields and coordinated observations of wave-particle interactions. The general problem is to determine the dissipation processes in a plasma that comprises a suprathermal PUI distribution embedded in a cold Maxwellian plasma. Understanding these processes is the core of Interstellar Probe Objective 1.1.2, ***“Characterize acceleration and transport mechanisms in the solar wind.”***

While interstellar electrons and ions flow around the HP, the interstellar neutral gas propagates inside the heliosphere and dramatically affects the solar wind energetics in the outer heliosphere and governs the size of the heliosphere. The neutral gas mainly consists of H atoms (~90%) with a range of minor species (e.g., He, O, N, Ne, Ar, and other elements) (Geiss & Gloeckler, 2003; Gloeckler et al., 2009). The effectiveness of the passage of elements through the heliosphere boundary and the depth to which they can advance into the heliosphere depends on atomic properties. Because of coupling of neutral atoms with plasma, atoms are filtered at the heliosphere boundary (Izmodenov et al., 1999). The resulting relative abundances and velocity distributions of different neutral atoms in the heliosphere are different from original interstellar abundances and velocity distributions. H atoms effectively charge-exchange with plasma protons everywhere from the VLISM to the inner heliosphere, creating different H atom populations with different properties (e.g., warmer and slower than in VLISM H atoms created beyond the HP in the hydrogen wall, $V = 22$ km/s, $T = 12,000$ K; hot H atoms created in the heliosheath, $T = 200,000$ K; fast H atoms created in the supersonic solar wind region, $V = 400$ km/s, $T = 100,000$ K; Quémerais & Izmodenov, 2002). The charge-exchange process leads to the solar wind deceleration especially beyond 30 au, which was confirmed by Voyager 2 Plasma Science (PLS) and New Horizons Solar Wind Around Pluto (SWAP) measurements (Elliott et al., 2019; Richardson et al., 1995; Wang et al., 2000). H atoms have a mean free path comparable to the size of the heliosphere, leading to an essentially non-Maxwellian nature of H distribution function. The properties of H atoms in the heliosphere are controlled by the charge-exchange coupling with plasma, variations of the solar radiation pressure, and ionization due to

extreme ultraviolet (EUV) photons and electron impact. These ionization processes create a cavity void of neutral hydrogen atoms close to the Sun, with a cavity size of ~ 1 au in the solar minimum and increasing toward the solar maximum (Qu  merais et al., 2006). Physical processes shaping the distribution of hydrogen atoms in the heliosphere as well as their dependence on the solar cycle and VLISM conditions are fundamental to the formation of the entire heliosphere but are currently very poorly known. Therefore, Interstellar Probe Objective 1.1.3 probe is to ***“Determine the properties of interstellar neutral hydrogen beyond the solar ionization cavity.”***

Voyager 1 and 2 crossed the heliospheric boundary (i.e., HP) in the nose hemisphere in 2012 and 2018, respectively, revealing surprisingly similar distances from the Sun to the HP, 121 au for Voyager 1 and 119 au for Voyager 2. This is despite the fact that the two Voyager spacecraft were separated 60° in latitude and 170 au in distance and the crossings occurred in different solar-cycle conditions. Imaging of the global interaction in energetic neutral atoms (ENAs) from the Interstellar Boundary Explorer (IBEX) (0.01–6 keV) and Cassini/Ion and Neutral Camera (INCA) (5–55 keV) missions provided a unique opportunity to gain insights into the global heliosphere shape and size. ENA observations on IBEX and Cassini in different energy ranges revealed completely unexpected emission features in the sky: the IBEX ENA ribbon (McComas et al., 2009) and the Cassini ENA belt (Krimigis et al., 2009). The physical processes behind these global features still remain inconclusive.

Later, IBEX-Hi data show that the heliosphere has a distinct tail extending to at least 380 au (Reisenfeld et al., 2021) (Figure 2-3, top). Cassini/INCA data suggest a different scenario, with a heliosphere having a bubble-like shape (Dialynas et al., 2017) (Figure 2-3, bottom). Imaging from vantage points inside the heliosphere hinders unambiguous determination of the global shape. State-of-the-art models of the global interaction of the solar wind with the VLISM also do not agree about the shape of the heliosphere (Figure 2-4), showing a comet-like shape (left, right) or a “croissant” shape (middle). The complex interactions of the plasma, magnetic field, and neutral interstellar gas taking place throughout the heliosphere, through the heliosheath, and out to the pristine ISM remain one of the most outstanding questions of space physics today, and therefore also form Interstellar Probe Objective 1.1.4, ***“Determine the processes and particle origin across the heliosheath that uphold the force balance and their global manifestation.”***

The outward trajectory to the VLISM offers a unique platform for remote ENA observations and in situ measurements within the emission source region, and therefore Interstellar Probe Objective 1.1.5 is to ***“Determine the physical processes that control the extent and shape of the ribbon and belt.”*** Measurements of in situ particle distributions and fields in the source regions of the IBEX ribbon and the Cassini/INCA belt ENAs will enable understanding of the mechanisms behind these ENA features and provide a direct link to the global heliosphere structure and interaction with the VLISM. In addition to critical in situ plasma and neutral observations from the source region of the heliospheric “ribbon” and “belt,” Interstellar Probe would enable ENA observations of the “ribbon” and “belt” from various different vantage points along the spacecraft trajectory, including looking back on the heliosphere from outside it in the VLISM. NASA’s upcoming Interstellar Mapping and Acceleration Probe (IMAP) mission (McComas et al., 2018) will provide a leap in imaging resolution and understanding of these features and will thus guide the mission planning of Interstellar Probe. The additional changing vantage point offered by Interstellar Probe would drastically increase the impact and understanding of these observations.

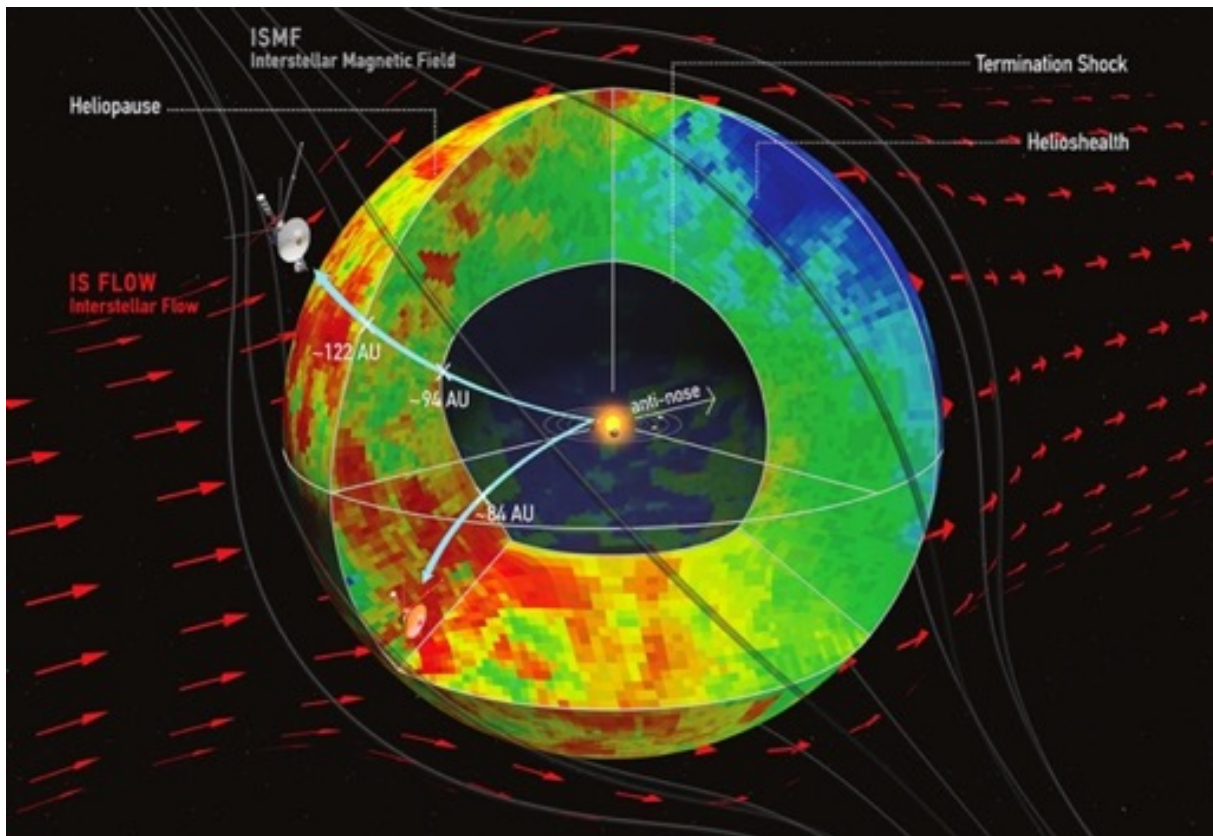
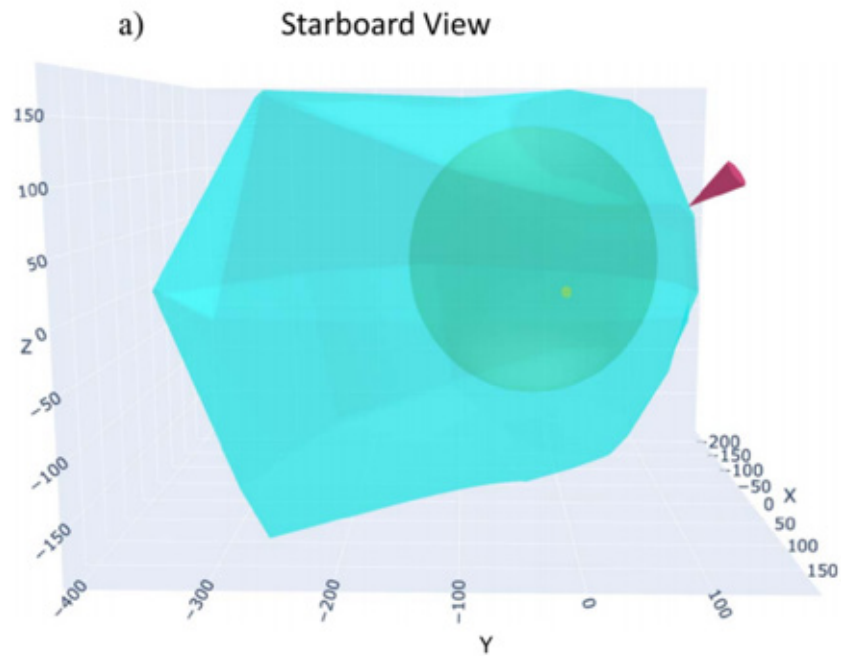


Figure 2-3. (Top) Analysis of IBEX-Hi ENA data (0.71–4.29 keV) during a full solar cycle shows that the HP is compressed southward of the nose and has a distinct tail extending to at least 380 au (from Reisenfeld et al. (2021)). (Bottom) Cassini/INCA ENA data (5–55 keV) suggest a bubble-like heliosphere with the HP extending toward the tail to 200 au as an upper limit (from Dialynas et al. (2017)).

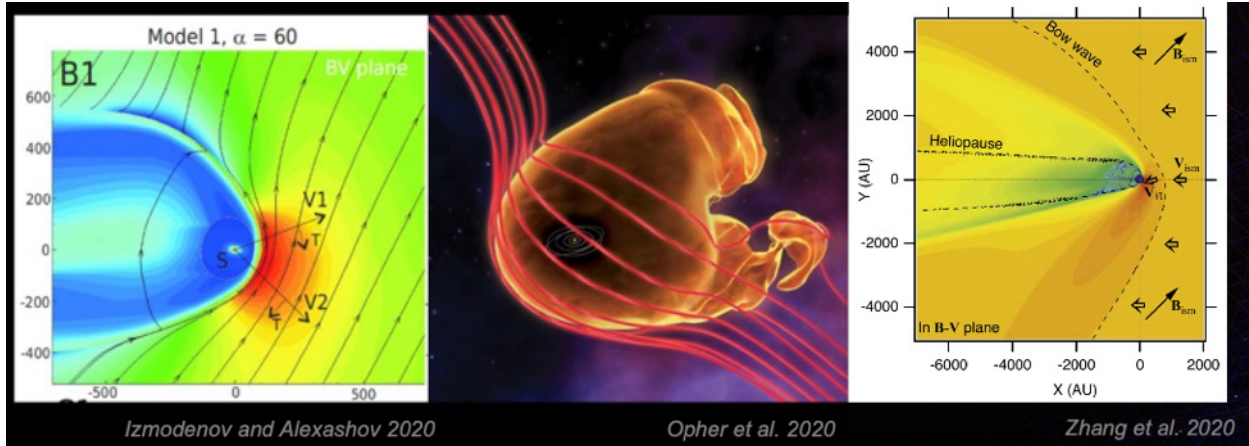


Figure 2-4. State-of-the-art global models of the heliosphere predict different shapes: a comet-like shape (left model by Izmodenov & Alexashov (2020) and right model by Zhang et al. (2020)) and the “croissant” model (by Opher et al. (2015)).

The Voyager mission discovered anomalous cosmic rays (ACRs), which are produced from interstellar PUIs (Fisk et al., 1974) that are accelerated to energies of tens to hundreds of MeV/nuc (Geiss et al., 2006). Contrary to the expectation that the largest shock in the heliosphere, the TS, is an efficient accelerator, ACR intensities did not peak at the TS but continued to increase as the Voyagers traversed deeper into the heliosheath, indicating the importance of other, possibly remote, acceleration mechanisms. While several explanations emerged (e.g., acceleration at the flanks of the TS (McComas & Schwadron, 2006), by compressive turbulence in the heliosheath (Fisk & Gloeckler, 2009), by magnetic reconnection near the HP (Drake et al., 2010), by small-scale flux ropes in the heliosheath (Zhao et al., 2019)), the sources of ACRs remain elusive and, thus, form the important Interstellar Probe Objective 1.1.6, “**Determine the sources and dominant acceleration mechanisms of anomalous cosmic rays.**” To determine the energization pathway of ACRs and determine their elusive source and relation to singly charged PUIs, measurements of protons, He, Li-Be-B, C, N, O, Ne, and other heavy ions from 100s of keV to ~100 MeV/nuc as well as their anisotropies are required. It must be stressed that composition is key for next-generation discoveries pertaining to ACR science because potential acceleration mechanisms like diffusive shock acceleration, first order Fermi acceleration, and reconnection- and turbulence-driven acceleration are all mass dependent (e.g., Decker et al., 2005; Drake et al., 2006; Ergun et al., 2020; Turner et al., 2018). Understanding ACR acceleration is critical to a wide range of topics considering that ACRs contribute ~20% of the thermal pressure in the heliosheath and LISM (e.g., Rankin et al., 2019a) and may be an important contribution to the seed population of higher-energy GCRs accelerated elsewhere in the galaxy. Better understanding of ACR sources and acceleration is also important to exoplanetary physics and the search for life in the universe because exoplanetary researchers typically only consider GCRs in energy input for atmospheric chemistry, but in some stellar systems with particularly efficient ACR acceleration, ACRs might dominate and contribute significantly to atmospheric chemistry in other astrospheres.

The TS transition by Voyager 1 (at 94 au from the Sun in 2004; Stone et al., 2005) and Voyager 2 (at 84 au in 2007; Stone et al., 2008) marked the first signature of the edges of the outer heliosphere. While the TS was anticipated to be observed as a strong shock, the observed changes in plasma

showed a weak shock (Richardson et al., 2008) with almost absent heating of the solar wind plasma. It came as a complete surprise that the solar wind flow downstream of the TS remained supersonic with respect to thermal ions. Unlike interplanetary shocks and planetary bow shocks, the TS is mediated not by thermal plasma populations but instead by suprathermal PUIs. Therefore, the TS represents a completely new regime of space plasma physics. As the solar wind crosses from upstream (closer to the Sun) to downstream (farther from the Sun) across the TS, the magnetic field strength and temperature suddenly increase with a corresponding sudden decrease in the flow speed (Li et al., 2008) by the factor of ~ 4 predicted by the Rankine–Hugoniot jump conditions. Interestingly, because of the nature of this shock, the plasma density observed by Voyager 2 increases only by a factor of ~ 2 (Li et al., 2008). With its baseline instrumentation for thermal and suprathermal plasma, PUIs, and energetic particles extending up to ACR energies, Interstellar Probe offers the comprehensive set of observations required to study the true nature of the heliospheric TS, its evolution and structure, and its role in particle acceleration either directly or via shock–shock interactions with interplanetary shocks; those questions and unknowns have direct relevance to astrophysics and improving our understanding of other astrospheres. These studies address Interstellar Probe Objective 1.1.7, *“Determine particle acceleration mechanisms occurring at the termination shock in the context of other shocks.”*

When the Voyager mission finally crossed the HP (Burlaga et al., 2019; Krimigis et al., 2019), it did not encounter the theoretically expected sharp discontinuity separating the solar wind plasma and the VLISM plasma. Instead, Voyager discovered a region with complex interactions between heliospheric energetic particles and particles coming from interstellar space and magnetic fields of different origin. The two crossings of the HP share many similarities but also show some striking differences (Krimigis et al., 2019). For both crossings, inside the heliosphere there is a region of increased intensities of GCRs of similar spatial scale around 1 au. However, Voyager 1 observed several episodes of enhanced GCR intensities right before HP crossing that were absent with Voyager 2. The situation with the heliospheric ions appears to be similar. The most noticeable difference is the extent of the upstream region before disappearance of solar material, 0.25 au for Voyager 1 and 0.6 au for Voyager 2. Also, there is a substantial structure in ions at Voyager 2 and none at Voyager 1. There is apparent leakage of solar particles out of the heliosheath that extends 0.6 au beyond the HP at Voyager 2. Confoundingly, neither of the Voyagers observed any significant rotation of the magnetic field across the HP, despite their drastic separation. While ideas started to form to understand magnetic topology and particle interaction at the HP, the physical processes near this boundary remain an open question. It is unknown whether magnetic reconnection, turbulence, or viscous boundary interactions are important along the HP and to what extent they are enabling the interaction between the heliosphere and VLISM. Critical observations of the full particle distributions (including PUIs) and fields on both sides of the HP are required to answer the outstanding questions remaining from the Voyagers’ crossings. The practically unknown nature of the HP therefore lies at the heart of Interstellar Probe Objective 1.1.8, *“Characterize the nature and structure of the heliopause.”*

2.2.2 Question 2: How do the Sun’s activity as well as the interstellar medium and its possible inhomogeneity influence the dynamics and evolution of the global heliosphere?

The Sun’s activity causes various types of evolving multi-scale structures in the solar wind, from long-lived corotating interaction regions (CIRs) to more transient but more extreme events such as coronal mass ejections (CMEs). The solar wind dynamic pressure changes roughly by a factor of 2 from solar minimum to solar maximum and can vary by over two orders of magnitude from average conditions to those in transient phenomena such as CMEs. As structures in the solar wind propagate outward from the Sun, they evolve, merge, and interact with each other and the ambient solar wind. Voyager 1 and Voyager 2 provided the first unique in situ measurements of these structures in the outer heliosphere. In particular, Voyager observations in the heliosheath showed highly variable plasma flows indicating effects of solar variations extending from the Sun to the heliosphere boundaries. The Cassini (Krimigis et al., 2004) and IBEX missions mapped the ENA intensities across the sky for the entire solar cycle (Figure 2-5). ENA images show substantial variations from solar minimum to maximum demonstrating that the Sun’s activity drives the global response of the entire heliosphere and its interaction with the VLISM.

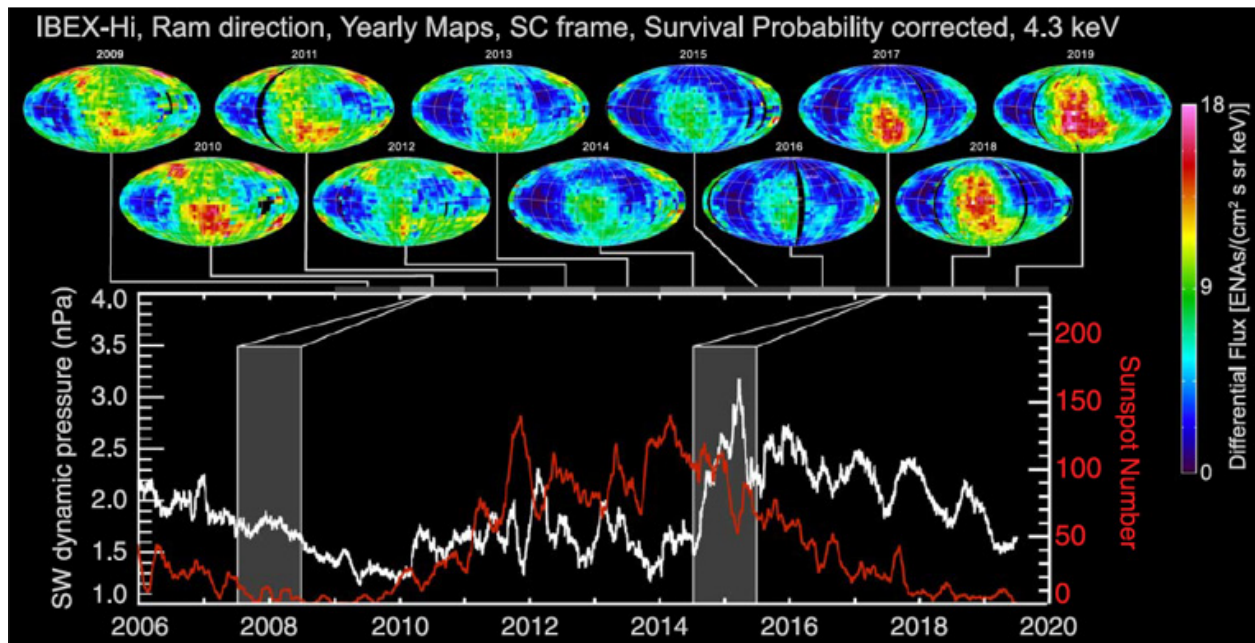


Figure 2-5. Global dynamic interaction as seen in IBEX-Hi ENA images. ENA fluxes on the sky respond to changes of the solar wind dynamic pressure from solar minimum to solar maximum (McComas et al., 2020). SC, spacecraft; SW, solar wind.

Determining the dynamical response of the physical processes upholding the heliosphere not only provides deeper insight into the variations of the current-day heliosphere but also represents the means by which the Interstellar Probe investigations can enable extrapolations of the past state of the heliosphere and the evolutionary path that it has taken on its journey around the galactic core.

State-of-the-art simulations have demonstrated that effects of the solar cycle strongly influence the TS and HP locations and flows in the heliosheath (Baranov & Zaitsev, 1998; Izmodenov et al., 2005; Izmodenov et al., 2008; Pogorelov et al., 2009; Scherer & Fahr, 2003; Zank, 1999; Zank & Müller, 2003). Models suggest that the TS reflects variations in the solar wind dynamic pressure observed at 1 au in about 1 year and that the TS position in the nose direction can fluctuate by 7 au. The boundaries of the heliosphere are constantly in motion (Figure 2-6). Despite the fact that Voyagers 1 and 2 crossed the HP under very different solar-cycle conditions and in different locations, the crossing distances are very similar, raising a question about the HP response to solar wind dynamic pressure changes. Models suggest that the HP may vary by 2 au. How multi-scale solar wind structures propagate and evolve in the outer heliosphere; what plasma flows they cause in the heliosheath; and how locations of boundaries change because of pressure pulses, shocks, and waves in the solar wind are open questions. These open questions lead to Interstellar Probe Objective 1.2.1, *“Determine how the heliospheric boundary is modified by solar dynamics.”*

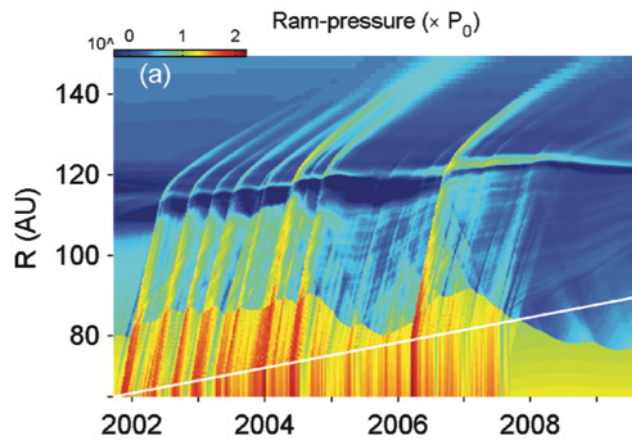


Figure 2-6. The TS shock responds to the solar wind dynamic pressure pulses moving to several astronomical units outward and inward. Solar wind shocks and waves create highly dynamic flows in the heliosheath. The HP also responds to the disturbances but with smaller amplitude (simulations by Washimi et al. (2011)).

Voyager 1 data revealed an unexpected discovery detecting shocks and pressure waves beyond the heliosphere in the VLISM (Burlaga et al., 2013; Gurnett & Kurth, 2019). Voyager 1 magnetic field data beyond the HP show an interval (2014.6–2015.4) with 28-day oscillations in the magnetic field (Burlaga & Ness, 2016) indicating a possible relationship with CIRs in the solar wind having periodicity of the solar rotation. This suggests that the Sun influences this region; however, the origin of these oscillations is not fully understood. The properties of the broad and weak VLISM shocks observed by Voyager are surprisingly different from shocks in the heliosphere. The VLISM is a much colder and denser plasma than the heliosphere, which we have extensively explored with different missions. Thus, the very different physics of the VLISM affects the properties of shocks and turbulence in this region. Our understanding of the VLISM dynamics, drivers for shocks and waves, as well as their properties and evolution in the VLISM is very limited. This leads to the second Interstellar Probe Objective, 1.2.2, under Science Question 2, *“Determine the extent and impact of solar disturbances in the VLISM.”*

The heliospheric bubble acts as a radiation shield of sorts, deflecting lower-energy ($< \sim 1$ GeV/nuc) GCRs from penetrating into the heliosphere. This shielding is evident throughout the 11-year solar cycle, where the variability of the solar magnetic field (interplanetary magnetic field [IMF]) and the occurrences of solar wind transient events (CIRs, CMEs) during the cycle are reflected in the intensity of GCRs observed at Earth (e.g., McCracken & Beer, 2007). Depletions of GCR intensities are also observed at shorter timescales associated with the passage of individual solar wind transient events (CIRs, CMEs) throughout the heliosphere, an effect known as Forbush decreases (Forbush, 1938), which can extend into the heliosheath and beyond into the VLISM (Hill et al., 2020). All combined, this shielding represents an important aspect of the interaction between the heliosphere and the ISM, because those shielded GCRs would otherwise present a non-negligible source of radiation throughout the inner heliosphere, including where life was known to develop and gain a foothold on Earth. GCRs are also an important aspect of space weather because they result in a radiation hazard to human systems and are the source of Earth's very intense inner radiation belt ions (Dachev et al., 2012; Li & Hudson, 2019).

GCR anisotropies are sensitive to remote field variations and are therefore used as an effective remote diagnostic of the field configuration of the heliosphere, and once beyond the heliopause, they provide insight into how the solar disturbances can propagate deep into the VLISM (Gurnett et al., 2015; Hill et al., 2020; Krimigis et al., 2013; Rankin, et al., 2019b). The Voyagers' cosmic ray instrument had limited look directions, and (Rankin, et al., 2019b, 2020) reported confounding, species-dependent anisotropies in GCR angular distributions. There is no current consensus on what causes those anisotropies, in which the GCRs at 90° local pitch angle are depleted significantly while the more field aligned GCRs show no variation at all. Rankin et al. (2019b) speculated that pitch-angle-dependent variability in GCR intensities may reflect effects of solar transient (e.g., interplanetary coronal mass ejections [ICMEs], CIRs/stream interaction regions [SIRs]) and/or compressed magnetic fields near the heliopause. Interstellar Probe would offer a new opportunity to study the nature of GCR anisotropies, GCR shielding by the heliosphere, and the properties of the unshielded GCR spectra in the ISM, including rare species and isotopes, that were not observed by the Voyager mission. Thus, those studies are encapsulated in Interstellar Probe Objective 1.2.3, *“Characterize how GCR intensities are modulated by heliocentric shielding, solar cycle, and solar dynamics.”*

On its galactic journey, the heliosphere has likely entered interstellar regions with very different properties (Frisch et al., 2011; e.g., cold dense neutral interstellar clouds, warm partially ionized clouds, and hot tenuous fully ionized plasma). Simulations have shown that, depending on the hydrogen density in the Sun's interstellar neighborhood, the heliosphere may look dramatically different (Figure 2-7; Müller et al. (2008)). Passing through a dense neutral cloud, the heliosphere would shrink with resulting HP location at ~ 25 au from the Sun. In contrast, moving through the fully ionized plasma, the heliosphere size would be an order of magnitude larger with HP distance in the nose direction ~ 300 au. Understanding the dynamical interaction between the Sun and the present conditions in the LIC is therefore critical for predicting a response of the heliospheric global structure to possible regions with different properties in the ISM.

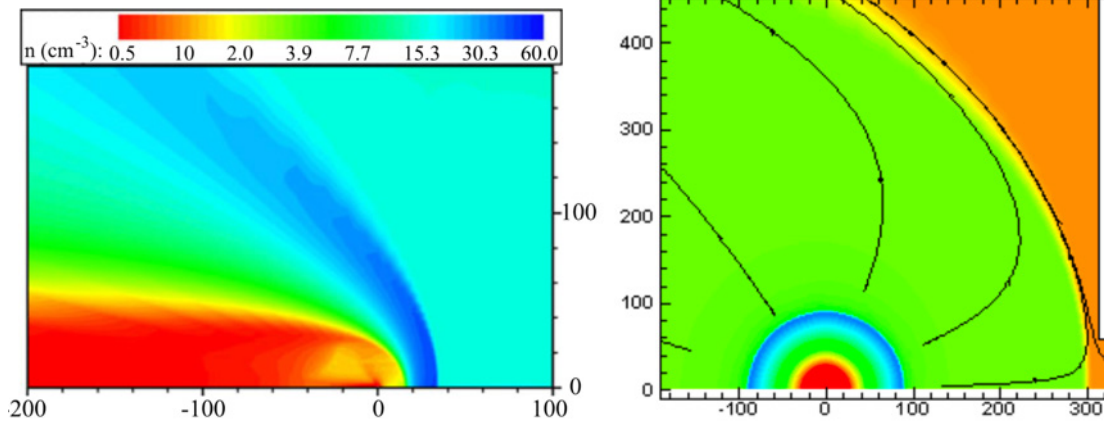


Figure 2-7. VLISM hydrogen density controls the size of the heliosphere. (Left) The HP is ~ 25 au from the Sun when the heliosphere moves through the dense cool interstellar cloud. (Right) The HP is at 300 au when the heliosphere moves in the fully ionized interstellar plasma. Distances on axes are in astronomical units (simulations by Müller et al. (2008)).

2.2.3 Question 3: How do the current VLISM properties inform our understanding of the evolutionary path of the heliosphere?

Our heliosphere is now exiting the LIC at a speed of 26 km/s in the direction of the neighboring G cloud (Linsky et al., 2019). Upper limits on the amount of interstellar Mg II absorption in this direction predict that the heliosphere will leave the outer shell of the LIC in less than 1900 years and therefore constitute a major event. Will the heliosphere directly enter the G cloud, or will it enter into a photoionized boundary layer with little neutral hydrogen? Figure 2-8 shows the four clouds in contact with the heliosphere and the direction of the inflowing VLISM plasma and where the Sun's motion will take the heliosphere. The size of the heliosphere, the properties of the solar wind, and the composition of gas in the heliosphere will change for either scenario. The size of the heliosphere controls the number of cosmic rays hitting Earth and other solar system bodies, which may play an important role in atmospheric chemistry and perhaps even in biological evolution.

Depending on a star's speed of motion in the ISM and properties of the interstellar gas itself, a bow shock may form ahead of the astrosphere. State-of-the-art physics-based multicomponent models of the solar wind interaction with the VLISM predicted an existence of the bow shock ahead of the heliosphere, a sharp transition where interstellar plasma flow becomes subsonic (Izmodenov, 2009; Zank et al., 2009). The VLISM flow relative to the Sun is supersonic, but it can be below the propagation speed of fast magnetosonic modes depending on the unknown magnetic field in the VLISM. In the case of the strong interstellar magnetic field, formation of the fast-mode bow shock is not possible. If the angle between magnetic field direction and velocity is small, then a formation of a slow mode bow shock remains possible (Chalov et al., 2010; Florinski et al., 2004; Pogorelov et al., 2011; Zieger et al., 2013). Heating of the VLISM plasma induced by charge exchange of incoming ENAs from the heliosphere may result in increased fast magnetosonic speed in the VLISM and weakening or even elimination of the bow shock structure (Pogorelov et al., 2017). In this case, the broad region of slowed down and piled up VLISM plasma forms what is called a bow wave. Only in situ measurements will solve the puzzle of whether the

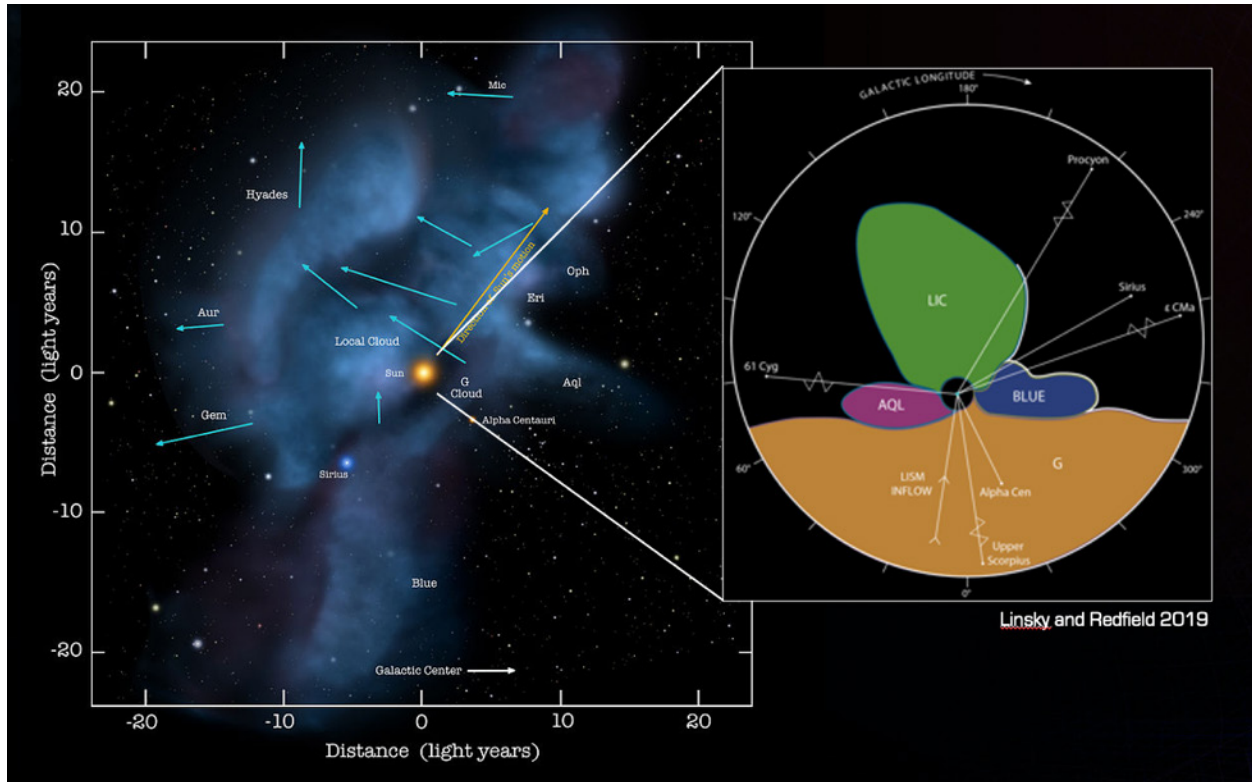


Figure 2-8. Recent studies suggest that the Sun is on the path to leave the LIC and may be already in contact with four interstellar clouds with different properties (Linsky et al., 2019). (Left: Image credit to Adler Planetarium, Frisch, Redfield, Linsky.)

heliosphere creates a bow shock or bow wave in the VLISM and how this structure may depend on potentially changing VLISM conditions. This leads us to Interstellar Probe Objective 1.3.1, *“Discover the nature of the bow shock or wave.”*

The hydrogen wall (H-wall) is a pileup of interstellar hydrogen beyond the heliosphere boundary. Simulations predict that the peak H-wall density occurs near 300 au and may extend outward to 400–600 au. The H-wall is created by H atoms that originated in a charge exchange between “pristine” interstellar H and slowed down and heated interstellar plasma flowing around the heliosphere. The H-wall was predicted by models of the outer heliosphere (Baranov & Malama, 1993; Gruntman et al., 2001; Zank et al., 2013). Analogous to the H-wall, there may also exist an oxygen wall (O-wall) of secondary interstellar oxygen atoms that originated in a charge exchange between oxygen ions and hydrogen (Izmodenov et al., 2004). Heliosphere H-wall absorption was discovered for the first time by Linsky & Wood (1996) in the Lyman- α spectra toward alpha-Centauri measured by Hubble Space Telescope/Goddard High Resolution Spectrograph (GHRS). The presence of a hydrogen layer near the heliosphere boundary is also suggested by Voyager/Ultraviolet Spectrometer (UVS) Lyman- α data (Katushkina et al., 2017; Quémerais et al., 2000). The Hubble Space Telescope found evidence of an H-wall presence around other stars, indicating that an H-wall is a common phenomenon for astrospheres. The most relevant example is the H-wall detected by Wood et al. (2004) around alpha-Centauri A and B. The heliospheric H-wall was never observed in situ. Understanding of H-wall properties—such as location of peak

density, spatial extension, shape, and enhancement of hydrogen (and oxygen) in the H-wall (O-wall) compared to the pristine ISM—and their impacts on the global interaction between the solar wind and VLISM are unknown, and lies in the heart of Interstellar Probe Objective 1.3.2, *“Discover and characterize the properties of the hydrogen wall.”*

The VLISM is a completely new region for exploration and discovery. We have a crude understanding of the VLISM environment inferred from in situ measurements inside the heliosphere of interstellar helium, PUIs, ENAs, remote observations of solar backscattered Lyman- α emission, and absorption line spectroscopy in the lines of sight of stars. We have no in situ measurements of most VLISM properties (e.g., ionization, plasma and neutral gas, magnetic field, composition, dust, and scales of possible inhomogeneities). Both Voyagers with their limited instrument capabilities have explored 30 au beyond the heliosphere boundary, providing for the first time direct measurements of the magnetic field magnitude (Burlaga et al., 2019) and direction and plasma density determined from plasma oscillation measurements (Gurnett & Kurth, 2019; Ocker et al., 2021). Observed VLISM properties suggest that this region is significantly influenced by the heliosphere. Advances in the understanding of these interactions have astrophysical ramifications for understanding the interaction of the astrospheres of stars with their LISM. The direct detection of interstellar dust (ISD) grains would provide new information about the chemical evolution of the galaxy and the location of our heliosphere. Moreover, making measurements in the ISM for a long time would help us ultimately discover any inhomogeneities in the LISM on scales of tens of astronomical units or even hundreds of astronomical units.

There is no reason to believe that the very-low-density plasma in the VLISM is in thermal or ionization equilibrium or that nonthermal particles do not dominate the ionization and total pressure. Chassefiere et al. (1986) showed that the timescales for ionization and recombination are on the order of 10^7 years, but supernovae in the nearby Scorpio–Centaurus Association have occurred as recently as a few million years ago, and their shock waves could have produced high ionization in the VLISM that is still recombining. New models of the velocity distribution of plasma in the outer heliosphere are beginning to include nonthermal components through the use of kappa functions (Vasyliunas, 1968) that differ from Maxwell–Boltzmann velocity distributions by including high-velocity tails (Swaczyna et al., 2019). The relative importance of these and potentially other sources of ionization and morphology in the VLISM needs to be understood. Only direct measurement of plasma (thermal and nonthermal) and magnetic fields in the VLISM can accomplish this.

Magnetic fields will be important in shaping the morphology of partially ionized clouds if the magnetic pressure exceeds the gas pressure in the VLISM clouds. Zirnstein et al. (2016) estimated the local interstellar magnetic field strength to be $2.93 \pm 0.08 \mu\text{G}$ on the basis of ENA emission from the “ribbon” feature observed by the IBEX mission. This magnetic field strength is close to equipartition with the gas pressure in the LIC, $P_{\text{gas}}/k \approx 2500 \text{ cm}^{-3}\text{K}$. More recently, Dialynas et al. (2019) estimated the interstellar magnetic field strength to be $\sim 5 \mu\text{G}$ from Voyager 2 charged-particle measurements in the HP and from Cassini data. A field strength this large would dominate the gas pressure and thereby shape the partially ionized VLISM clouds.

The VLISM consists of material in multiple hot, warm, and cold phases, each of which is characterized by different temperatures, densities, and stages of ionization—both atomic and molecular—as well as ISD grains. These are the condensed phases of the ISM, transporting the heavy elements produced by stellar nucleosynthesis through the different ISM phases (Draine, 2009). Although representing only ~1% of the mass of the ISM, ISD grains contribute significantly to the different evolutionary processes of the galaxy and are the building blocks of new stellar/planetary systems forming upon collapses of cold molecular clouds. Dust condensation from gaseous heavy elements occurs both in certain circumstellar environments as well as in protostellar nebulae. ISD grains ensure the transport and mixing of heavy elements across the different phases of the ISM, where they undergo multiple cycles of formation and destruction (Zhukovska et al., 2008). Any modern model describing galactic chemical evolution must therefore take their life cycles through the ISM into consideration. A direct in situ characterization of the ISD grains in the warm gas and dust phase surrounding the solar system, the LISM, and their interaction with the gas phase therefore enables an understanding of the true nature of the current building blocks of planetary systems in our galaxy.

Properties of ISD in the heliosphere are affected by deflection and filtration processes at the heliosphere boundary and effects near the Sun, such as gravity and radiation pressure. Alexashov et al. (2016) simulates the deflection of dust particles of various sizes in the heliospheric interface region and characterizes the dust flow at the entrance to the heliosphere. Simulations predict that dust particles of small size do not penetrate into the heliosphere flowing around the HP affected by the interstellar magnetic field. Large particles penetrate almost freely. Distribution of ISD particles of any size inside the heliosphere is very inhomogeneous in space (Godenko & Izmodenov, 2021). There are regions called peculiarities, where particles are concentrated. Sterken et al. (2012) explored effects on the ISD in the heliosphere of the time-dependent heliospheric magnetic field with the 22-year periodical changes of the heliospheric current sheet inclination and the 25-day rotation of the Sun and showed focusing and defocusing of dust over a solar cycle (Slavin et al. (2012); Figure 2-9). We are just beginning to explore the effects of ISD and synergies with heliosphere science. Dust and plasma go hand in hand because of the coupling of the dust with magnetic fields and charging by flying through different plasma regions. Properties of the ISD inside and outside the heliosphere, deflection and filtration processes, and possible effects of the dust on PUI production in the heliosphere remain open questions.

Lack of the “ground truth” of the VLISM properties in the Sun’s neighborhood is therefore the main driver for Interstellar Probe Objective 1.3.3, ***“Determine the properties, heliospheric filtration, and inhomogeneities of the VLISM.”***

Lithium, beryllium, and boron (Li, Be, and B) have very low nuclear binding energies and are not produced in any significant abundance by our Sun (and stars like it). In the ISM, however, Li, Be, and B are produced by cosmic ray spallation, and Li has an additional source in the deaths of certain low-mass stars. At cosmic ray energies, the abundance of Li, Be, and B is comparable (same order of magnitude) to that of C, N, and O, which is entirely different than the relative abundances within the heliosphere (e.g., Wiedenbeck et al., 2007). The relative abundances of Li, Be, and B are more than four to six orders of magnitude lower compared to their relative abundances in the ISM. Their spectra at lower energies (~50 MeV/nuc) in the VLISM provide important information on their sources (spallation versus stellar) and remain unknown due to the lack of measurements.

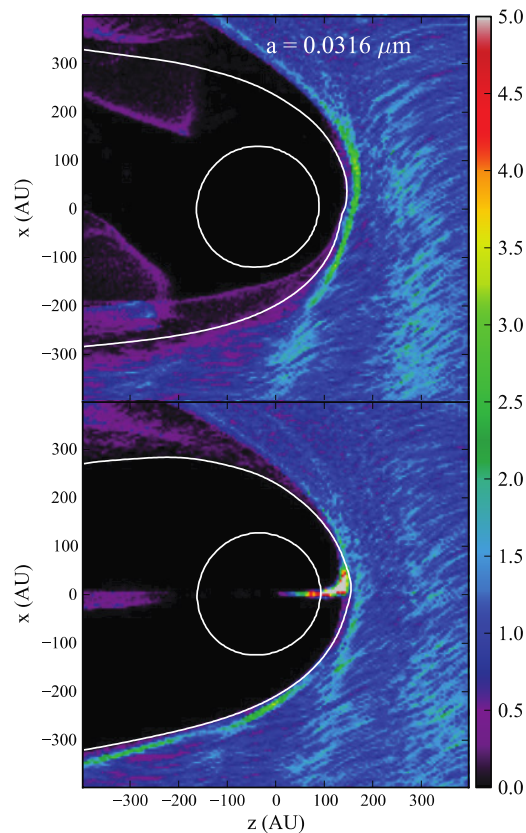


Figure 2-9. (Top panel) Direct knowledge of interstellar dust composition and size distribution brings new understanding of the chemical evolution of the galaxy. The second panel is for the defocusing solar wind magnetic field, and the bottom panel is for the focusing polarity. The inner white curve indicates the location of the termination shock, while the outer white curve shows the heliopause location (simulations by Slavin et al. (2012)). The color scale indicates the density relative to the ambient interstellar dust density. (Image credit: [NASA, NOAO, ESA and The Hubble Heritage Team \(STScI/AURA\)](#) and [Donald E. Brownlee, University of Washington, Seattle, and Elmar Jessberger, Institut für Planetologie, Münster, Germany.](#))

Consider as an analogy how we differentiate magnetosheath plasma from magnetospheric plasma from boundary layer and flux transfer event plasma (mixed) in observations near Earth's

magnetopause; Li-Be-B might offer that same capability for distinguishing solar from interstellar from mixed plasmas in the heliosheath, HP and boundary layer(s), and VLISM. This could prove to be of high importance to Interstellar Probe observations, particularly considering the extent of the solar system's influence on the VLISM and fundamental processes such as turbulence, reconnection, and boundary layer physics (e.g., Kelvin–Helmholz instability) along the HP and in the heliosheath, which will be important for determining the requirements for mass resolution for particle instrumentation.

GCRs in the 1 MeV/nuc to 1 GeV/nuc range are deflected by the heliosphere, and thus >75% of GCRs never reach the inner solar system where they otherwise could affect the chemical evolution of atmospheres. Therefore, it is important for general habitability to understand how an astrosphere shields its planetary system from GCRs. Well into the pristine ISM, where our Sun no longer has direct influence, the vantage point of an interstellar probe would allow spectra of GCRs that are unperturbed by the heliosphere to be obtained and therefore would provide further insight into their source and interaction with the galaxy. Despite the Voyagers having now measured the GCR spectra of primary elemental species in the ISM, new discoveries and outstanding questions in GCR physics still remain; the Voyagers left major open questions about and gaps in understanding of the full spectrum of cosmic rays in the LISM. Critically, the Voyager cosmic ray instruments could not resolve isotopic mass resolution of measured cosmic rays, yet as outlined (Mewaldt, 2013; Wiedenbeck et al., 2007, and references therein; Wiedenbeck, 2013), measurements of rare and unstable cosmic ray isotopes can be used to answer questions pertaining to cosmic ray source regions via spallation and direct acceleration, galactic escape rates, and solar modulation. These open questions and unobserved species of GCRs in the LISM are of importance not only to heliophysics and the nature of particle acceleration and consequences of GCRs in the heliosphere, but also to astrophysics and the nature of the universe itself. Observations of particularly rare GCR isotopes, GCR electrons, and antimatter in the LISM can even shed light on and further constrain models of the nature of the Big Bang and dark energy. However, because of heliospheric shielding of lower-energy GCRs, the critical observations required to answer such open questions rely on observations of these GCR species in the unperturbed LISM. These investigations are in the core of the final Interstellar Probe Objective 1.3.4, *“Constrain the origin of GCRs and implications on nearby ISM properties.”*

2.3 Science Traceability to Closure

To meet the science goal of Interstellar Probe, one must first understand the current nature of the heliosphere and VLISM to be able to then extrapolate to the past and the future possible conditions of the heliosphere. This approach is embodied in the three science questions above, where the first science question is focused on understanding the physical processes of the current state of the heliosphere and the second is focused on understanding how these physical processes act under the dynamics imposed by the active Sun. The third question determines the VLISM properties necessary to understand the interaction with the heliosphere and also the physics of the VLISM necessary to better understand the past and future environment along the evolutionary path of the solar system.

SCIENCE QUESTIONS	OBJECTIVES	INVESTIGATIONS	
1.1 How is our heliosphere upheld by the physical processes from the Sun to the VLISM?	1.1.1 Resolve the birth and evolution of interstellar and inner-source PUIs	Heliosphere Investigation Composition, charge states, and distributions of PUIs	
	1.1.2 Characterize acceleration and transport mechanisms in the solar wind		Heliosphere Investigation In-situ ion and electron distributions and magnetic field Sampling of turbulent wave spectra
	1.1.3 Determine the properties of interstellar neutral hydrogen beyond the solar ionization cavity		
	1.1.4 Determine the processes and particle origin across the heliosheath that uphold the force balance and their global manifestation	Heliosheath Investigation Particle distribution, composition, and charge states across the heliosheath ENA imaging from external vantage point Remote radio wave observations Lyman-alpha Doppler imaging	
	1.1.5 Determine the physical processes that control the extent and shape of the ribbon and belt		Heliosheath Investigation ENA imaging from changing vantage point In-situ ion distributions, flows, and fields between 90 and 300 au
	1.1.6 Determine the sources and dominant acceleration mechanisms of anomalous cosmic rays (ACRs)		
	1.1.7 Determine particle acceleration mechanisms occurring at the termination shock in the context of other shocks		Heliosheath Investigation In-situ thermal to ACR ion distributions and composition In-situ thermal to suprathermal electrons Magnetic fields and waves across the termination shock (±2 au)
	1.1.8 Characterize the nature and structure of the heliopause		
1.2 How do the Sun's activity as well as the interstellar medium and its possible inhomogeneity influence the dynamics and evolution of the global heliosphere?	1.2.1 Determine how the heliospheric boundary is modified by solar dynamics	Dynamics Investigation ENA imaging, plasma wave observations inside and outside heliosphere Solar wind magnetic fields, plasma, energetic particles	
	1.2.2 Determine the extent and impact of solar disturbances in the VLISM		
	1.2.3 Characterize how GCR intensities are modulated by heliocentric shielding, solar cycle, and solar dynamics		
1.3 How do the current VLISM properties inform our understanding of the evolutionary path of the heliosphere?	1.3.1 Discover the nature of the bow shock or wave	VLISM Investigation In-situ plasma to non-thermal populations and magnetic field at ion-inertial scales	
	1.3.2 Discover and characterize the properties of the Hydrogen Wall		
	1.3.3 Determine the properties, heliospheric filtration, processes and inhomogeneities of the VLISM		
	In-situ sampling of interstellar dust		
	In-situ sampling of magnetic fields, plasma to non-thermal populations		
1.3.4 Constrain the origin of GCRs and implications on nearby ISM properties	In-situ GCR elemental, isotopic composition and spectra beyond HP		

MEASUREMENT REQUIREMENTS	SPACECRAFT REQUIREMENTS
Magnetometer (MAG) 0.01–100 nT; 0.01 nT sensitivity, ≤60 s Two fluxgate magnetometers spaced 1/3 of boom	10-m boom, spinning, cleanliness program
Plasma Subsystem (PLS) e, H ⁺ ; He ⁺ , He ⁺⁺ ; C ⁺ , N-O ⁺ ; <3 eV/e – 20 keV/e; E/E ≤ 10%, ≤60 s iFOV ≥ 180° x 20°, GF ≥ 1e-3 cm ² sr, ESA+Postacceleration+TOF Analysis or Faraday Cups	Spinning for full sky coverage
Pick-Up Ions (PUI) 0.5–78 keV/e, E/E ≤ 10%, H, ² H, ³ He, ⁴ He, ⁶ Li, ¹² C, ¹⁴ N, ¹⁶ O, ²⁰ Ne, ²² Ne, Mg, Si, Ar, Fe, charge states iFOV ≥ 90° x 15°, GF ≥ 1e-3 cm ² sr, ESA+Postacceleration and TOF Analysis	Spinning to maximize angular coverage Accommodation to cover PUIs in heliosphere and interstellar ram direction
Energetic Particle Subsystem (EPS) 20 keV – 20 MeV, H, ³ He, ⁴ He, Li, C, O, Ne, Mg, Si, Ar, Fe, ΔE/E ≤ 30%, ≤60 s iFOV ≥ 180°, GF ≥ 0.1 cm ² sr, TOFxE or SSD stack	Spinning for full sky coverage
Cosmic Ray Subsystem (CRS) 1–10 MeV/e, 10 MeV/nuc – 1 GeV/nuc H-Sn, isotopes, m/Δm ≥ 10; ΔE/E ≤ 30%, hours GF ≥ 2 cm ² sr, two directions, 15°, SSD telescopes	Perpendicular mounting and spinning to cover anisotropies in the VLISM
Plasma Wave Subsystem (PWS) ~1 Hz – 5 MHz, ≤0.7 μV/m at 3 kHz, Δf/f ≤ 4%, ≤60 s full spectrum 4x50 m spin-plane antennas, sounder	4x50 m spin-plane deployed antennas
Energetic Neutral Atom Camera (ENA) ~1–100 keV H, ΔE/E ≤ 50%, ≤5°, ~weeks iFOV ≥ 170°, ultra-thin foils and TOF	Spinning to maximize angular coverage Accommodation to cover full sky except Sun exclusion zone
Interstellar Dust Analyzer (IDA) 1e-19 to 1e-14 g, 1–500 amu, m/Δm ≥ 200 iFOV ≥ 90°, impact based TOF with reflectron	Mount at angle to spin axis to cover interstellar dust ram direction Coboresighted with NMS
Neutral Mass Spectrometer (NMS) H, ³ He, ⁴ He, ¹⁴ N, ¹⁶ O, ²⁰ Ne, ²² Ne, ³⁶ Ar, ³⁸ Ar, m/Δm ≥ 100, 1e-3 cm ⁻³ sensitivity, weekly iFOV ≥ 10°, 120° antechamber, ionization source+TOF+reflectron	Mount at angle to spin axis to cover interstellar gas ram direction Coboresighted with IDA
Lyman-Alpha Spectrograph (LYA) ±100 km/s Doppler range, <10 km/s resolution, ≤5°, months, up- and downwind directions iFOV ≤ 5°, Echelle or Heterodyne spectrograph, scan mirror	Mount at angle to spin axis to cover noseward and tailward directions while maintaining Sun exclusion zone

HELIOSPHERE <TS														HELIOSHEATH TS THROUGH HP						INTERSTELLAR MEDIUM >HP						MISSION REQUIREMENT	ANALYSIS PRODUCT	CLOSURE	
MAG	PLS	EPS	CRS	PWS	ENA	IDA	NMS	LYA	MAG	PLS	EPS	CRS	PWS	ENA	IDA	NMS	LYA	MAG	PLS	EPS	CRS	PWS	ENA	IDA	NMS				LYA
●	●																										Operations out to TS	PUI mass spectra and angular/velocity distribution as a function of distance	Relative abundances of interstellar vs inner source Radial evolution of PUI distributions
●	●	●	●	●	●																							Average solar wind properties as a function of distance. Radial evolution of PUI distributions and turbulent spectra	Correlation of solar wind heating, slow-down, turbulence and PUI distributions
							●	●																				Neutral abundances as a function of distance	Interstellar gas distribution in heliosphere
							●	●																			Operations out through HP to ≥300 au Trajectory ≥45° off nose direction for external imaging and through ribbon for in-situ investigation	Boundary locations, flows, differential pressure and composition, relative abundances of solar vs interstellar, heliosheath structure, electron gradients, H temperatures	Heliosheath pressure New physical processes missing in current models 3D shape of the heliosphere
										●	○									○								Source location, flow velocities, pitch-angle distributions	ENA source location and mechanism
																												Spectral evolution across the heliosheath	ACR source distributions to differentiate acceleration hypotheses
●	●	●	●	●	●					●	●	●	●	●														Particle and wave spectra and distributions across shocks	Dominant acceleration mechanisms at different shocks
										●	●	●	●	●														Field vectors, plasma flows, particle spectra, temperatures, GCR anisotropies at ion inertial scales	Nature of instabilities and interaction with VLISM magnetic fields
●	●	●	●	●	●					●	●	●	●	●													Operations out to ≥350 au Trajectory in the noseward hemisphere of the heliosphere to reach VLISM within mission lifetime	Long-term ENA image sequences and solar wind dynamics pressure	Dynamics and drivers of heliospheric boundaries
										●	○																	Particle spectral evolution, plasma wave spectra	
●	●	●	●	●	●					●	●	●	●	●														Particle/wave spectra GCR anisotropies	Evolution of collisionless to collisional shocks Extent of Sun's influence
●																												Long-term variability of GCR spectra and anisotropies out to VLISM	GCR/ACR interaction with shocks and heliospheric magnetic field
																											Operations out to ≥350 au Trajectory in the noseward hemisphere of the heliosphere to sample 100's au in the VLISM within mission lifetime	Plasma distribution function, fields	Bow shock/wave existence, location and properties
																												H LOS temperature, density, flow	Spatial scales, peak density, structure, composition of the wall
																												H, He, O density and plasma moments	
																												Elemental/isotopic spectra, - from heliosphere to VLISM	Filtration by the heliosphere VLISM structure and processes
																												Dust composition, size, density distribution and flow from heliosphere to VLISM	
																												Plasma, densities, elemental/isotopic composition, temperatures, flows, charge fractions	Solar effects on VLISM LIC particle pressures and processes
																												GCR spectra and composition	GCR sources and test "leaky box" model for GCRs

As illustrated on the baseline science traceability matrix (STM) foldout, each science question is answered by a set of objectives, which, in turn, flow directly to four overarching science investigations, discussed below, that define the important bridge between the science and implementation with measurement and mission requirements (Section 4). The overarching investigations start with investigations of the inner heliosphere in the first decade of the mission, followed by an investigation of the heliosheath for the next 4–9 years depending on direction. The third investigation addresses the dynamics of the system, and, lastly, the fourth investigation focuses on the VLISM. The overarching science investigations are detailed in a set of fifteen more specific investigations as outlined in the “Investigations” column of the STM. These each drive measurement and mission requirements. Although many investigations map to unique measurement requirements, the most stringent measurement requirements that would drive instrument design are listed in a stand-alone column with color coding referring to the applicable investigation. This column also contains the next-level instrument requirements with specific requirements toward the spacecraft in the next column over. The specific derivations of measurement requirements are laid out in Section 4.

The applicability of specific measurements in different phases is laid out across the heliosphere phase from launch to the TS, the heliosheath phase including the TS crossing through the HP, and, lastly, the interstellar phase beyond the HP. Filled circles denote the primary measurements. Any supporting measurements that could be done as backup, or on a complementary basis, appear as open circles in the bottom row of the investigation row, with their respective primary measurement appearing in the corresponding upper row.

The right-hand side of the STM traces the investigations into mission requirements. The last two columns describe the analysis products of each investigation, and closure, or science results, refers to the higher-order results that allow one to meet the objectives and therefore also address the science question.

2.4 Mission Success Criteria

An interstellar probe offers an extraordinarily broad and rich science investigation. Therefore, mission success is not a preselected, limited set of objectives but rather constitutes multiple sets of combinations of objectives, where each set would constitute a success. To formulate this quantitatively, the success criteria of an interstellar probe are to *meet at least two science objectives under each science question*. This logical approach has been successfully taken on other missions, such as Parker Solar Probe. As will be seen in Section 3.4 (Reliability), this results in multiple “cut-sets” of measurements, each containing about six to eight instruments whose measurements in certain regions would constitute mission success. This, in turn, guides the requirements on redundancy of instruments and their subsystems and informs how the science drives the prioritization of instrumentation.

2.5 Mission Rationale

A spacecraft on a fast trajectory radially outward through the heliosphere and out into the VLISM provides the necessary snapshot of the current state of the heliosphere and VLISM. The uniqueness in such a mission is the dedicated in situ particles and fields measurements along the way of the new

physical processes governing the heliospheric interaction—measurements that neither the Voyager Interstellar Mission (VIM) nor New Horizons will be able to obtain with their limited payload. Armed with a balanced complement of remote imaging as well, an interstellar probe becomes a powerful large strategic mission for understanding the global manifestation of those physical processes that ultimately is required for determining the current state of the global heliospheric nature.

The journey into the unexplored VLISM, beyond the 170 au where VIM is expected to reach, is not only a pinnacle in humanity’s reach into space but very likely where the biggest discoveries will begin. The unknown structures of the bow shock and the hydrogen wall are likely at several hundreds of astronomical units, and possible inhomogeneities of the LIC material may be on the same scales. The constant “breathing” of the global heliosphere over solar cycles extends far beyond the HP and is important for our ability to extrapolate its current state to conditions in the past and in the future.

The outward flight direction spans the noseward (Frisch et al., 2013) hemisphere of the heliosphere, with launch windows opening up in 2036 and extending well into the 2040s (see Sections 3 and 4). These provide opportunities to explore features that have been remotely observed from 1 au by the IBEX and Cassini missions and will soon be explored by the IMAP mission. In addition, the noseward directions enable some level of certainty in arriving in the VLISM within a realistic time frame that tailward directions would not be able to offer.

A 50-year design lifetime is achievable with today’s reliability standards (see Appendix F) and would bring a probe to ~400 au with today’s propulsion technology (see Section 3). This distance would encompass hundreds of astronomical units of the unexplored VLISM in the interstellar phase, including the bow shock or wave, if any (McComas et al., 2012), and hydrogen wall, where Interstellar Probe would spend the majority of its nominal design life and up to three solar cycles. Given that Voyager has outlived its design lifetime by a factor of 10 and New Horizons is now well beyond its primary mission of 9.5 years (and expected to survive three times its primary mission life), it is plausible that an Interstellar Probe could survive up to 1000 au and in the end be limited only by the power supply. Exploration out to such distances not only would signify an order-of-magnitude increase of the explored space around our star but also means Interstellar Probe would likely encounter “pristine” interstellar space, where the Sun would no longer have any influence.

2.6 Science Investigations

The Interstellar Probe science investigation revolves around four fundamental investigations:

1. The investigation of the processes within the heliosphere that ultimately are responsible for the formation of the heliospheric boundary, including the birth and evolution of PUIs, TS physics and particle acceleration, and remote and in situ measurements of interstellar neutral hydrogen interaction with the heliosphere
2. The investigation of the detailed physical processes of the heliosheath responsible for the force balance, structure, and particle acceleration, including the nature and physics of the unique TS and the HP

3. The investigation of the global dynamics of the heliosphere that focuses on understanding the dynamical range of the physical processes and how those manifest themselves globally, including boundary motions, evolution of structures in the solar wind throughout the heliosphere, interactions with interstellar plasma and neutrals, dynamic responses of the heliosheath, and the extent of solar disturbances into the VLISM
4. The investigation of the VLISM seeking to discover and characterize the unexplored properties, including the interstellar composition, charge fractions, densities and flows, and plasma physics of the ISM, as well as undiscovered details of the properties and sources of the unshielded, low-energy GCRs, including rare isotopes

2.6.1 Heliosphere Investigation

Interstellar neutrals penetrate deep inside the heliosphere, where they are ionized to form interstellar PUIs and become part of the dynamical acceleration processes of the solar wind. Therefore, the investigation of the nature and global structure of the heliosphere begins in the inner heliosphere with measurements of interstellar neutrals and the subsequent birth and evolution of interstellar PUIs out to the TS.

Voyager 1 and Voyager 2 did not carry instrumentation to measure either PUIs or interstellar neutrals (Figure 2-10). However, a few studies have shed light on these processes, including Ulysses/SWICS observations of interstellar PUIs up to ^{22}Ne (Gloeckler & Geiss, 1998) at very low counting levels. New Horizons/SWAP continues to follow the evolution of interstellar H^+ and He^+ PUIs and associated solar wind slowdown and shock acceleration out to more than 50 au (Elliott et al., 2019; McComas et al., 2021).

Beginning shortly after commissioning, Interstellar Probe will address the open questions on the creation and role of inner-source PUIs (H^+ , He^+ , C^+ , N^+ , O^+ , and Ne^+) (Gloeckler & Fisk, 2007; Schwadron & Gloeckler, 2007) versus those of interstellar origin by measuring the full 3D velocity distribution functions of $^3\text{He}^+$ and of *singly charged* and *low-charge-state* He, C, N, O, Ne, Mg, Si, S, Ar, and Fe for bulk speeds from ~ 0 to 1000 km/s.

Although Interstellar Probe will directly sample cosmologically important species in the VLISM, the outward trajectory will provide an opportunity to measure the cosmologically important density of pickup $^3\text{He}^+$ (Steigman & Tosi, 1992) and its ratio to $^4\text{He}^+$ already inside the heliosphere. The $^3\text{He}^+$ density was measured for the first time with Ulysses/SWICS (Gloeckler et al., 1992), but the estimates were associated with large uncertainties. The ionization processes affect both of these isotopes identically, so their ratios in the inner heliosphere should be an accurate representation of the $^3\text{He}/^4\text{He}$ ratio in the interstellar cloud.

To understand the particle acceleration and transport mechanisms acting on the solar wind and its PUIs, Interstellar Probe will conduct particle measurements from thermal to cosmic ray energies along its entire trajectory of the inner heliosphere along with magnetic field and wave measurements. For the decade-long journey toward the TS, the mission will offer multiple encounters with interplanetary shocks, including the formation and effects of global merged interaction regions (GMIRs) and corotating merged interaction regions (CMIRs). This will be the

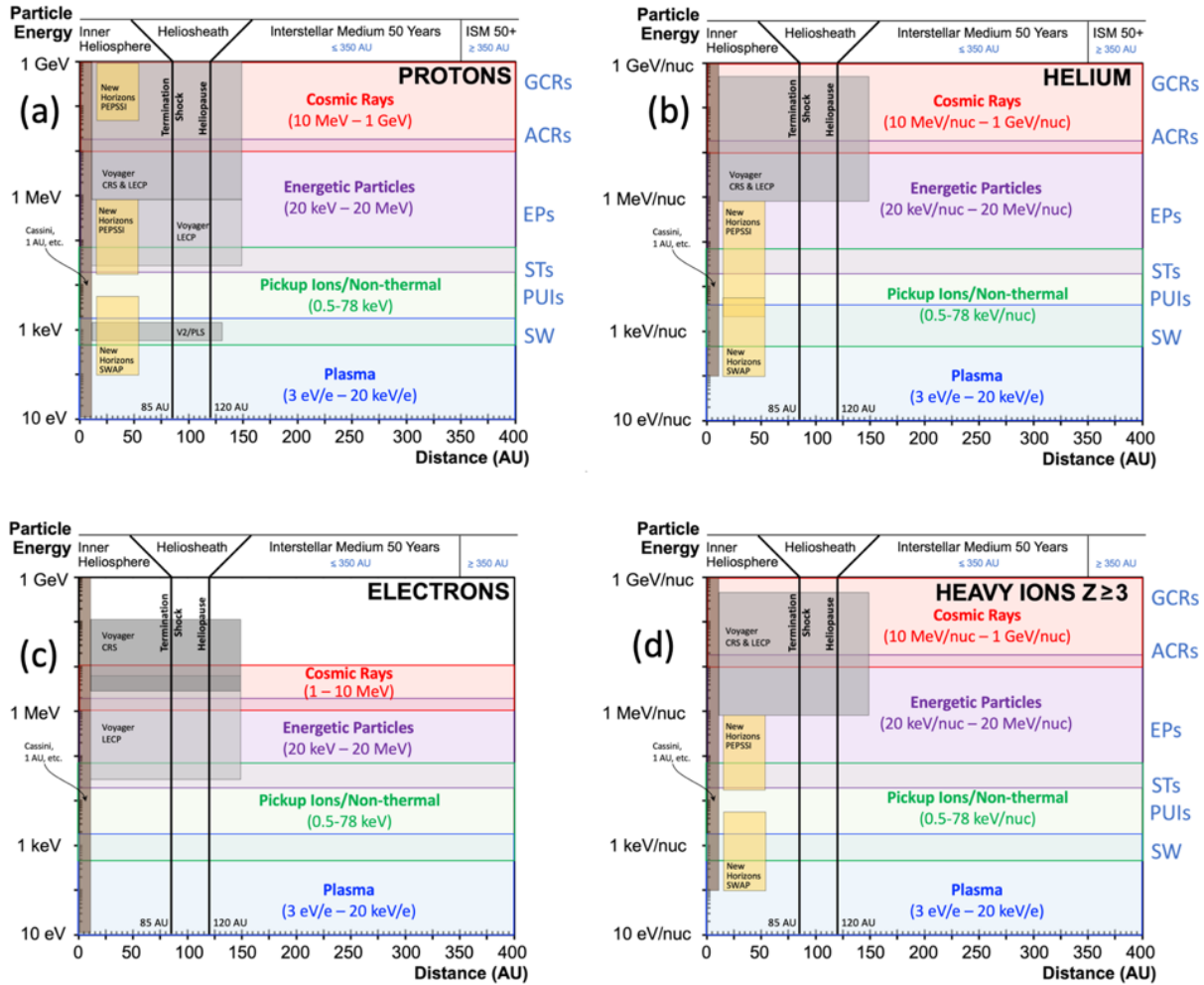


Figure 2-10. Understanding the heliospheric boundary and the VLISM requires a dedicated set of measurements of particles over a wide energy range, from the inner heliosphere to well beyond the HP. Voyager and New Horizons are the only missions exploring the outer heliosphere, but their limited instrumentation represents only a sliver of the required measurements. Interstellar Probe will carry the first dedicated set of instruments to span the wide range of particle composition and energies to fully investigate the new regime of space physics that governs the formation of our heliosphere in the VLISM. CRS, Cosmic Ray Subsystem; LECP, Low-Energy Charged Particle; PEPSSI, Pluto Energetic Particle Spectrometer Science Investigation; PLS, Plasma Science; STs, suprathermals; W, solar wind; SWAP, Solar Wind Around Pluto. (Image credit: Johns Hopkins Applied Physics Laboratory.)

first opportunity to study the physical interaction mechanisms by measuring the thermal and suprathermal particle populations of H^+ , He^{++} , and He^+ , as well as the dominant charge states (both low and high) of C, N, O, Ne, Mg, Si, S, Ar, and Fe from 15 to 500 keV per charge, together with fields and wave measurements. The role of turbulence on the particle populations, and in particular on PUIs, can be addressed by regularly sampling high-frequency spectra of fields and waves (Fraternal et al., 2016; Zank et al., 2018).

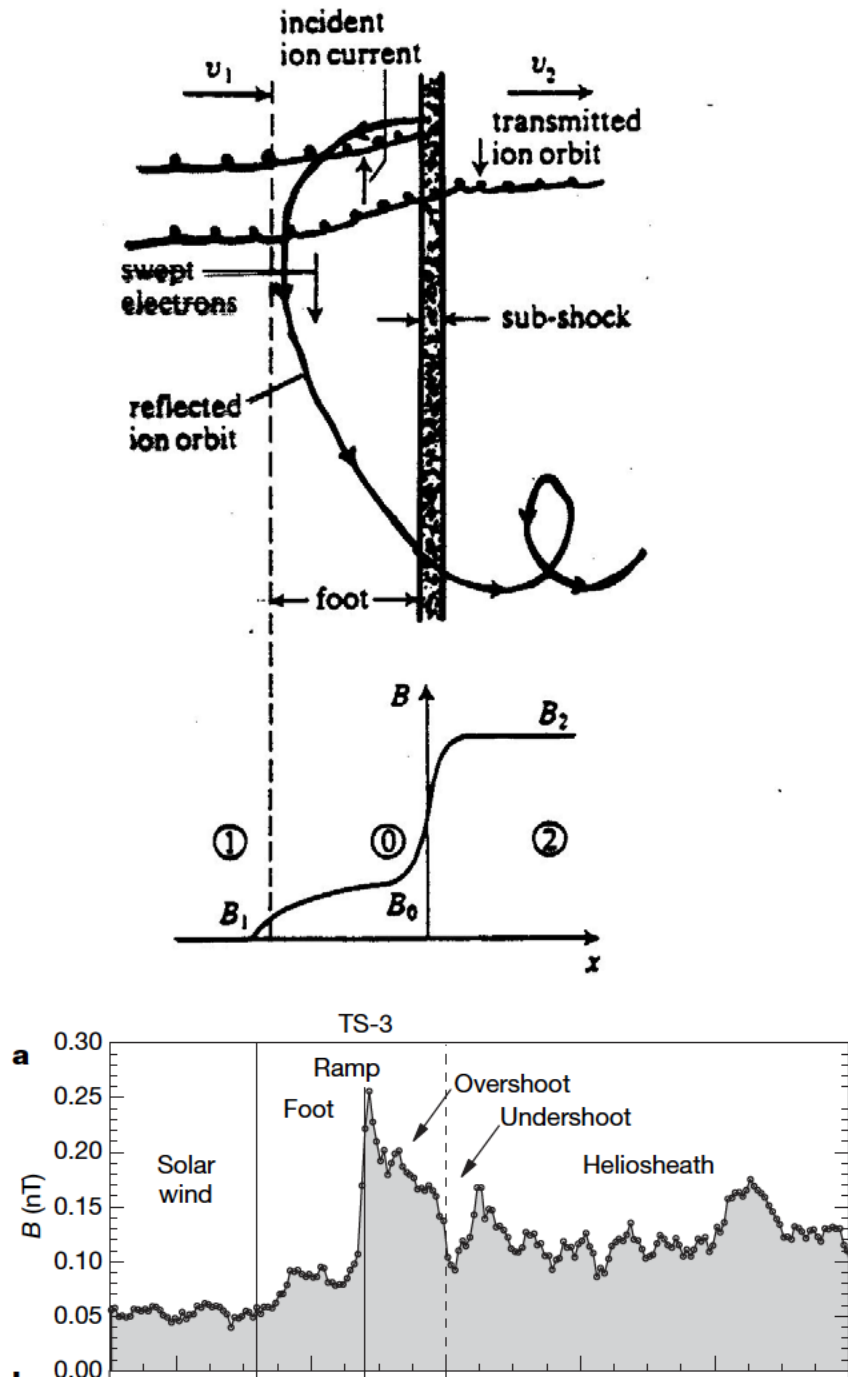


Figure 2-11. (a) The TS is believed to reflect and preferentially heat PUIs (Zank et al., 1996). (b) While Voyager magnetic field measurements revealed features indicative of these processes, it did not measure the detailed plasma and PUI distributions required to fully understand this new type of shock (Burlaga et al., 2008).

To fully understand the heliospheric penetration of interstellar neutral gas, Interstellar Probe will obtain remote Lyman- α line-of-sight (LOS) measurements of velocities, temperatures, and densities of the hydrogen gas and their variations with distance from the Sun. Together with in

situ measurements of interstellar neutrals such as H, ^3He , ^4He , ^{14}N , ^{16}O , ^{20}Ne , and ^{22}Ne , these measurements will provide insight into the radial variation of abundances, hydrogen flows, and temperatures. While IMAP will make the most detailed diagnosis of interstellar neutral gas flow directions and temperatures from 1 au, there are opportunities to make such an investigation from Interstellar Probe as well. However, this continues to be an important science trade that would require a significant mass allocation or optimizations of current neutral mass spectrometry to also resolve the direction (see Section 4.1.6, Neutral Gas Measurements).

Measurements of ISDs are important in this phase but are covered in the VLISM investigation below.

2.6.2 Heliosheath Investigation

The heliosheath holds many of the answers to the global nature and structure of the heliosphere and is therefore a central piece of the entire Interstellar Probe investigation. Once Interstellar Probe nears the expected distance of the TS, increased attention will be paid to observing high-resolution distributions of PUIs, thermal and suprathermal ions, and thermal and suprathermal electrons that are key to understanding the nature of the TS (Zank et al., 1996). These measurements will become critical at the so-called “foot,” “ramp,” and “overshoot” ion-kinetic-scale regions of the TS, but in general, dedicated investigation will begin even a couple of astronomical units before the TS crossing. Because the distance to the TS will not be known in advance, the detailed investigations will be facilitated by the use of the Selective Data Downlink system, where high-resolution data will be stored on the onboard memory. Specific periods of interesting high-resolution data can then later be selected for downlink by analyzing lower-resolution data that are regularly sent to the ground.

Once in the heliosheath, Interstellar Probe will continue to measure the full distribution of ions ranging from thermals and suprathermals to ACR energies, and some of their charge states, to determine the detailed force balance, plasma flows, and elusive acceleration sources of ACRs (Pesses et al., 1981). Observations of thermal and suprathermal electrons will also be made to determine their relative importance in the energy density of the heliosheath. To achieve full closure and understanding of the force balance, these results will be contrasted with direct measurements of the magnetic field and the thermal and nonthermal particles in the VLISM (see Section 2.6.4, VLISM Investigation). Throughout the heliosheath, regular sampling of high-resolution fields as well as wave and particle spectra will occur to understand the role of turbulent heating and the possible occurrence of reconnection in the heliosheath (Drake et al., 2010).

On the way out through the inner heliosphere, remote observations in ENAs provide an early constraint on the force balance in the heliosheath by obtaining ENA spectra across the sky of the proton populations in the heliosheath over the heated PUI energy range. These will offer additional data similar in nature to those obtained by Cassini (Dialynas et al., 2019) and those planned by IMAP. However, the strength of ENA imaging from Interstellar Probe lies in its ability to image the heliosheath from an external vantage point that will provide a unique way of discerning its structure. At energies above ~ 40 keV (H), the charge-exchange lifetime of ions convecting through the heliosheath becomes significant. Therefore, increasingly more of the global heliosheath structure is expected to be revealed at increasingly higher energies. Although

this high-energy imaging puts challenging requirements on the signal-to-noise ratio (SNR) and geometrical factor, it will return one of the strongest constraints on global models and is therefore a critical element in understanding the global nature of the interaction. Figure 2-12 shows a simulated H ENA image at 80 keV assuming the ion flows modeled by Opher et al. (2018). The image was simulated at 250-au distance at a vantage point 90° off the nose direction. The so-called horns or jets of the croissant model start appearing at ~40 keV. Other features at lower energies have also been simulated by, for example, Galli et al. (2019).

The changing vantage point will also be a unique method to further constrain the location and nature of the ribbon and the belt. With a relatively moderate resolution at a few kiloelectronvolts of H, it should be possible to discern a source location inside versus outside the HP. However, Interstellar Probe flying directly through the ribbon region would provide the ultimate in situ measurement to determine its generation mechanism and relation to the global heliospheric nature. There are multiple hypotheses on the generation of the ribbon (McComas et al., 2017). Of these, two different hypotheses have risen to the top of the scientific discussions. The first is the hypothesis that relies on the trapping of charge-exchanged solar wind neutrals beyond the HP (McComas et al., 2009), and the second relies on the so-called Compton–Getting effect caused by flows within the heliosheath (Roelof, 2012). From its changing vantage point, Interstellar Probe would be able to distinguish these two different source locations and resolve the mechanism uniquely by flying through the source region, confirming either the highly perpendicular pitch-angle distributions beyond the HP or the different plasma flow velocities in the heliosheath. New Horizons is on its way toward the ribbon and will likely have sufficient power through the TS crossing and therefore could conceivably address any ribbon mechanisms within the heliosheath, but it may not have sufficient power to make measurements beyond the HP.

Lastly, during the HP encounter, magnetic field directions and magnitudes will be measured with high fidelity together with the wide range of particle distributions to determine the nature of the

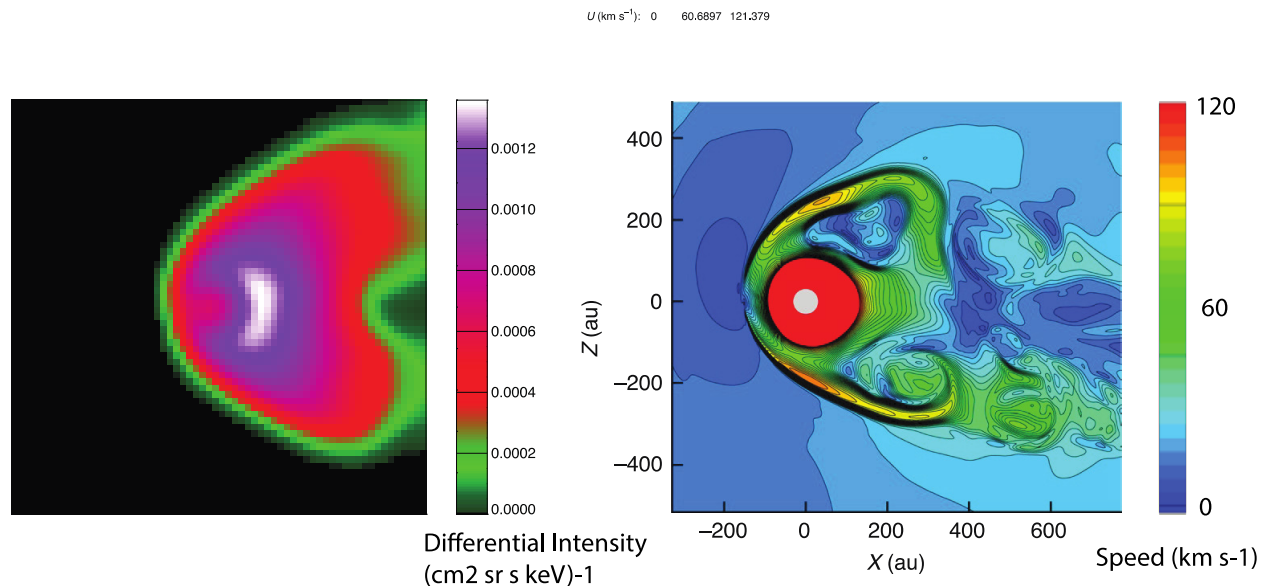


Figure 2-12. (Left) Simulated H ENA image at 80 keV assuming the flows as modeled by Opher et al. (2018) (right).

HP. Of particular interest is the possible interchange-type instability that manifests itself in inward flows of cold dense plasma and outward flows of hot tenuous plasma that extends several tens of astronomical units beyond the HP (Dialynas et al., 2021; Krimigis et al., 2019). The new instrumentation on Interstellar Probe will also enable determination of whether or not the upstream (with respect to the interstellar flow) HP is an open boundary, with solar wind magnetic fields actively reconnecting to those in the VLISM. Whether or not the HP is an open boundary is a critical open question that has implications for the interpretation of Voyager data and the effects of the VLISM on the heliosphere and vice versa.

2.6.3 *Heliospheric Dynamics Investigation*

This investigation flows from the three objectives that address the dynamics of the heliospheric boundaries, the extent of solar disturbances into the VLISM, and the modulation and anisotropies of GCRs throughout the heliosphere and beyond the HP.

From the inner heliosphere, ENA imaging will be used to diagnose the temporal and spatial evolution of the ENA emission pattern over a significant fraction of the solar cycle together with in situ measurements of the solar wind dynamic pressure. Once Interstellar Probe crosses over to the heliosheath, it will have opportunities to measure the dynamics of the TS in situ and study dynamics over a significant solar-cycle fraction of heliosheath particle populations.

It is well known that GCR and ACR intensities are modulated by the solar cycle and by solar transients. However, the exact physics of the modulation is not well understood, particularly in relation to the radial dependence and the GCR shielding. Although investigations into the shock propagation and associated effects on GCRs have been performed, many outstanding questions remain (Hill et al., 2020).

Once Interstellar Probe is beyond the HP, it will use GCR anisotropies as a tool to further understand and determine the extent of shock propagation into the VLISM. A tool unique to Interstellar Probe will be its ability to image the large-scale and long-term dynamics of the heliosheath in higher-energy ENAs. Although the very low ENA count rates likely prohibit capturing any short-term dynamics, month-long image accumulations would capture effects from GMIRs, or at least accumulative solar-cycle effects. This remote imaging, in combination with the diagnostic that the GCR anisotropies provide, may prove to be very powerful to understand the solar disturbances and their effects on the global dynamics of the heliosphere.

2.6.4 *VLISM Investigation*

The biggest discoveries likely lie beyond the HP in the unexplored VLISM. Here, Interstellar Probe will investigate the existence and nature of a heliospheric bow shock or bow wave, by measuring the magnetic field structure and the plasma densities and flows of major ion species and electrons. Measurements of the possible heated PUIs in the VLISM will be important because they may play a decisive role in the pressure balance in the VLISM and in the nature of the bow wave (Gurnett et al., 2015).

Up to ~ 300 au, remote Lyman- α measurements will continue to shed light on the nature of the H-wall. However, the detailed nature of this universally important feature will be investigated by determining the neutral gas densities and charge fractions of the major species, including H, He, and O, which will inform the existence of corresponding structures in these species.

Determining the difference in elemental and isotopic abundances from the heliosphere to the VLISM is critical for understanding how the heliosphere regulates the inflow of interstellar matter, and thus is also important for ultimately understanding how the heliosphere and the solar system evolved together along their evolutionary path around the galactic core. Interstellar Probe will measure the neutral gas elemental and isotopic composition of interstellar species from H, He isotopes, and up through the isotopes of Ne and Ar, starting in the inner heliosphere and continuing well out into the VLISM. Likewise, the size and compositional distribution of ISDs will be sampled along the outward trajectory to determine how the heliosphere acts to filter out the lighter dust grains (Slavin et al., 2012) and also to determine the elemental and isotopic composition locked up inside of ISDs that are believed to be an important window into the heavy ions created during stellar processes (Draine, 2009).

The in situ characterization of the VLISM will provide the first direct insight into the physical processes responsible for the LIC and the Local Bubble (Linsky & Redfield, 2021). To understand how the LIC and the Local Bubble were formed, Interstellar Probe will measure charge fractions and densities of interstellar gas up through at least ^{22}Ne (Slavin & Frisch, 2008), together with plasma temperatures of major ion species and electrons.

The role of nonthermal ions continues to be a complete unknown in the VLISM, but they may play a decisive role in the structure of the LIC (and others like it) and in the entire force balance with the heliosphere (Linsky et al., 2019). The source of such nonthermal ions has been hypothesized to be the ionized component of the neutral solar wind that is transported across the HP into the VLISM, where it is ionized through charge exchange and possibly by electron impact (Izmodenov et al., 2001; a PUI per definition).

Therefore, it is important to measure the PUI energies of at least the major species in the VLISM, which is an energy range that was not covered by the Voyager observations. Possible heating mechanisms will be investigated, including turbulent heating in the VLISM.

Although it is tempting to assume that at least the LIC is homogeneous, one has to remember that all large-scale information about its structure has been obtained by average LOS spectra toward the nearest stars and thus is far from accepted. An interstellar probe will be uniquely positioned to make potentially groundbreaking discoveries in this regard and will therefore sample all properties, including neutral densities, plasma densities, flows, and also ISD densities and flows along hundreds of astronomical units to discern any spatial or temporal inhomogeneities that have been hypothesized (Draine, 2009)

Beyond the HP, Interstellar Probe will measure the unshielded elemental and isotopic composition of GCRs that will provide a window into their origins. These include species up to Sn and the important Li, Be, and B and radioactive isotopes, whose low-energy spectral shape is crucial to understanding spallation from GCRs in the ISM and the nature of fusion of lithium nuclei in special

stellar processes (Bildsten et al., 1997). Although Voyager measures GCRs, only a few points along the wide spectrum exist for the lighter species, and no data points exist for atomic isotopes (Cummings et al., 2016); therefore, many interesting outstanding questions remain concerning GCRs and their implications on astrophysics and the fundamental nature of the universe (Wiedenbeck et al., 2007).

2.7 Science Closure

The inner heliosphere investigation closes when the relative abundances of interstellar versus inner-source PUIs and their radial evolution are determined. By also having determined (Objective 1.1.1) the evolution of the solar wind (including slowdown due to mass loading) with sampling of turbulent spectra and the evolution of the ring distributions of PUIs to isotropic, one will be able to confirm the unique role PUIs have in mediating and heating the solar wind (Objective 1.1.2). Lastly, the neutral abundance as a function of distance will enable closure on how interstellar neutral matter affects the inner heliosphere that ultimately controls the force balance of the heliosheath (Objective 1.1.3).

Closure will be achieved regarding the heliosheath processes and their global manifestation (Objective 1.1.4) of the heliosheath investigation by having the dominating differential pressures for major species, by having charge states to resolve origin, and by obtaining the plasma flows at a third point through the heliosheath. The detailed spectra of particles and fields and their evolution across the heliosheath will enable understanding of the new physical processes currently missing in the global model. Lastly, remote ENA imaging will provide the global context necessary to link the processes to their global manifestation, aided by the global models including the missing physics.

The source location and mechanism of the ribbon and belt (Objective 1.1.5) will be closed by having ENA images from changing vantage points. The primary closure, however, will be achieved by having measurements inside the source region. It is noted that depending how far New Horizons will operate, this objective could already be closed by that mission.

Determining the elusive source of ACR acceleration (Objective 1.1.6) can be closed by having detailed but currently missing measurements of the particle spectral evolution and distributions, in particular from PUIs to ACR energies, and plasma fluctuations together with complete field vector measurements to identify flux ropes that the Voyager mission was not able to do. This will allow one to differentiate hypotheses such as, for example, acceleration at the flanks of the TS (McComas & Schwadron, 2006), by compressive turbulence in the heliosheath (Fisk & Gloeckler, 2009), by magnetic reconnection near the HP (Drake et al., 2010), or by small-scale flux ropes in the heliosheath (Zhao et al., 2019).

Understanding the nature of, and acceleration at, the TS (Objective 1.1.7) will be achieved by having the detailed electron and ion distributions across the shock. Results including PUI distributions, their possible reflection, and predicted electron distributions would be particularly important for verifying theories such as PUI reflection and mediation (Zank et al., 1996).

To achieve closure in understanding the nature of the HP (Objective 1.1.8) that may potentially be important for also explaining the thickness of the heliosheath, it is important to obtain the

necessary analysis products to resolve the type of instability acting in this region. This includes identification of cold dense plasma flux tubes versus outward hot, tenuous flux tubes, and resolving GCR distributions at spatial scales shorter than their gyroradius. In addition, plasma moments and detailed magnetic field measurements on either side of the HP are needed to verify the decisive role of charge exchange on the formation of the HP (Pogorelov et al., 2017).

Under the dynamics investigation, the dynamics of the heliospheric boundary (Objective 1.2.1) is closed by first obtaining long-term sequences of ENA images along the outward trajectory during the heliospheric phase, with simultaneous measurements of solar wind properties. It is to be noted that such investigations have been performed by both IBEX and Cassini and will continue with IMAP. Once in the heliosheath, in situ particle spectra with the possible support of solar wind measurements from other missions inside the heliosphere will provide the details necessary to understand the processes acting on longer terms that correspond to the ENA intensifications. Once beyond the heliosphere, ENA imaging would uniquely provide dynamics of how the heliosheath morphology and spectra vary over solar cycles. All these observations taken together would provide necessary data to determine how and why the heliosheath responds to solar variability. This closure is also related to obtaining information about the extent and impact of solar disturbances (Objective 1.2.2), which will be accomplished by using the particle and wave spectra to understand the evolution from collisionless shocks to collisional shocks, while monitoring GCR anisotropies hundreds of astronomical units from the HP during solar cycles. Lastly, by having the long- and short-term variability of GCR and ACR spectra, anisotropies, and composition across the inner heliosphere out to the VLISM, one will be able to characterize and understand the interaction with interplanetary shocks and the heliospheric magnetic field (Objective 1.2.3).

In the final interstellar investigation, the nature of a bow wave or shock (Objective 1.3.1) will be understood by deriving plasma moments and measuring magnetic field magnitude and direction for calculating the Mach number, which is essential for discriminating between a wave and a shock structure. Jumps in plasma and field parameters will be used to determine the location and extent of the structure.

The hydrogen wall (Objective 1.3.2) can be understood by deriving spatial scales, peak densities, and composition from H LOS temperatures and velocities and, more importantly, the in situ neutral gas density distribution. Its formation processes through charge exchange can be determined by also having the estimates of charge fractions across the wall derived from in situ plasma measurements.

The central objective of the interstellar investigation is to determine VLISM properties, heliospheric filtration processes, and possible inhomogeneities (Objective 1.3.3). Understanding filtration processes will be closed by having elemental and isotopic neutral and dust spectra from the heliosphere to the VLISM. To understand the processes, one will use the derived charge fractions and elemental and isotopic abundances to determine the relative roles of various ionization processes. Results on nonthermal ions together with the distribution of neutrals will be used to achieve closure on the role of nonthermal pressures in the LIC and their possible generation mechanisms. All properties will be measured across several hundreds of astronomical units to determine any inhomogeneities of the LIC.

Finally, beyond the HP, having the composition and spectrum of, in particular, the elemental and isotopic abundances of unshielded, low-energy GCRs will provide the spectral shapes necessary to verify theories of GCR production, in particular the under-resolved Li, Be, and B spectra and completely unobserved spectra of critically telltale GCR isotopes (Wiedenbeck et al., 2007) (Objective 1.3.4).

2.8 Cross-Divisional Opportunities

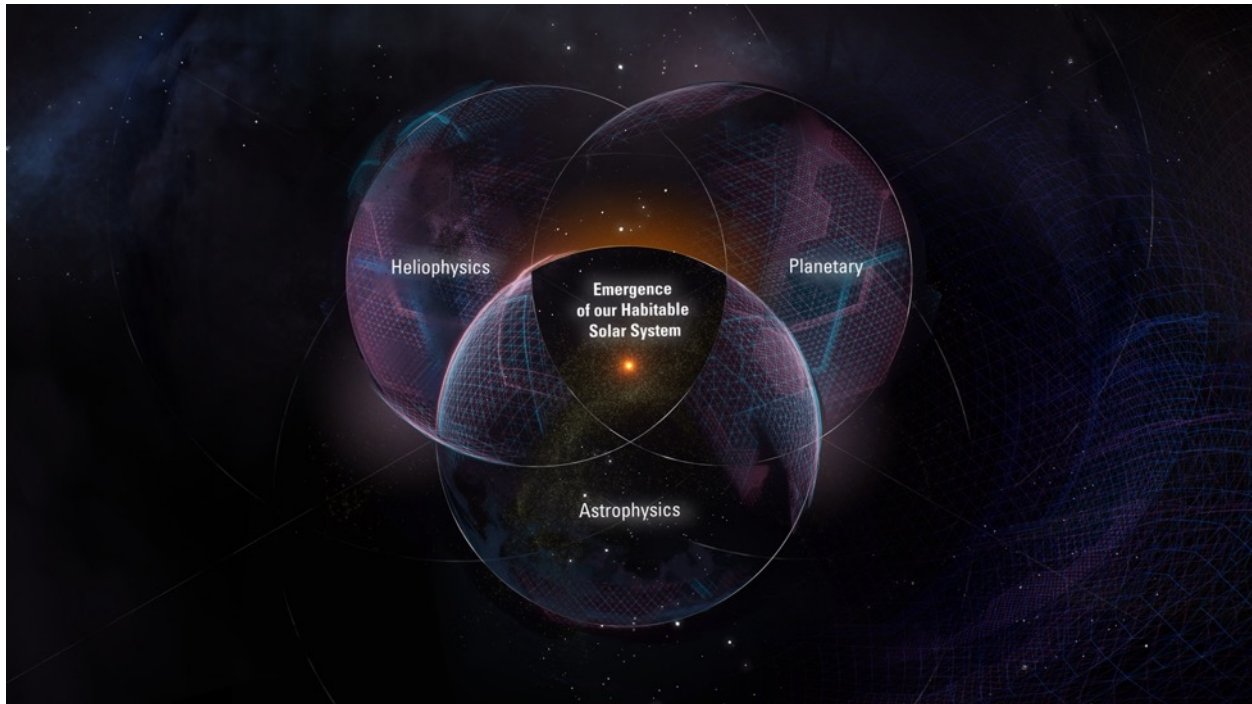


Figure 2-13. Scientific disciplines inevitably become blurred together as our exploration of space pushes outward. The baseline concept of an Interstellar Probe is a pragmatic pathfinder for such a necessary cross-divisional approach, and with only modest augmentations to payload and architecture, it will return science on the level of large individual planetary and astrophysics missions (Appendix A). (Image credit: Johns Hopkins Applied Physics Laboratory.)

The boundaries between predefined disciplines inevitably become blurred as space exploration is pushed outward. The heliophysics primary goal, and its investigations outlined above, unavoidably have components of astrophysics and planetary disciplines. Understanding our heliosphere also requires exploration of the VLISM, and understanding our home in the galaxy requires new insight into the evolutionary path of our heliosphere through the variable galactic environments. Interstellar Probe will serve as a bridge to span the divide between heliophysics and astrophysics by providing the first in situ observations from an astrophysical regime (interstellar space), a regime that is also responsible for helping to shape the heliosphere itself. Measurements of interstellar PUIs not only bring us data on the force balance of the heliosheath but also reveal the composition of the VLISM and, in turn, strong constraints on galactic chemical evolution. The direct sampling of the VLISM not only provides an upstream environment important for the heliospheric interaction but also allows us to gain insight into the physics of our surrounding interstellar clouds and local

bubble. An interstellar probe is therefore a pathfinder for the inevitable cross-divisional science approach necessary for pushing the boundaries of space exploration.

An outward trajectory through the outer solar system also provides natural opportunities for planetary science and astrophysics (Jaffe et al., 1979) with relatively modest augmentations to payload and mission architecture (Appendix A). The exploration of the outer solar system is just beginning to uncover the Kuiper Belt with discoveries that will revise our understanding of planetary system formation. Over 100 dwarf planets and thousands of planetesimals in the Kuiper Belt have now been detected using ground-based surveys such as the Deep Ecliptic Survey, Pan-STARRS1 (Panoramic Survey Telescope and Rapid Response System 1), the Dark Energy Survey, the Outer Solar System Origins Survey, and others (e.g., Bannister et al., 2016; Bernardinelli, 2021; Chambers, 2016; Elliot et al., 2005), with the expectation of increasing the number of known objects by an order of magnitude in the 2020s (Schwamb et al., 2019). At Pluto, New Horizons revealed a planet that was far from inactive but instead hosted active geological phenomena, atmospheric haze, and a potential subsurface ocean (e.g., Nimmo & Pappalardo, 2016; Stern et al., 2015). The flyby observations of 2014 MU69 Arrokoth uncovered an oblate contact binary with far-reaching implications for planetary formation and the collisional history of the Kuiper Belt (Stern et al., 2019).

Any of the fly-out directions dictated by the heliophysics investigation will offer at least one flyby of a compelling planetesimal or dwarf planet in the Kuiper Belt. For example, Orcus with its moon Vanth lies $\sim 80^\circ$ west of the nose direction just some 20° south of the ecliptic and potentially hosts an icy world with cryovolcanism. Quaoar with its moon Weywot is $\sim 40^\circ$ east of the nose just 12° south of ecliptic and is believed to be a world that is in its final stages of losing its atmosphere. Multiple other flyby options exist, any of which would provide an order-of-magnitude increase in our understanding of the formation of our solar system by enabling comparative planetology among dwarf planets.

In the context of all other exoplanetary systems discovered in the past decade, the distant vantage point offered by an interstellar probe would be a natural observation platform to understand our solar system as an analog of a habitable exoplanetary system. A dedicated “family portrait” of the solar system from afar, supported by scientific observations such as light curves and spectra, would provide an important, but accessible, ground truth to better inform other exoplanetary observations.

As a planetary system accretes into larger bodies, it leaves behind an imprint of the formation processes in its large-scale dust disk surrounding the star. Recent observations of protoplanetary disks have revealed planetary formation taking place already at less than one million years from the birth of the star, which has necessitated a complete revision of planetary formation theories. The 4.6-billion-year-old dust disk surrounding the solar system represents an example of a mature system. With the increasingly detailed information about processes in our own solar system, the large-scale distribution of our circumsolar dust disk, or “zodiacal cloud,” is extremely valuable in understanding the formation in other star systems. However, the distribution of the circumsolar dust disk is still largely unknown because observations thus far have only been made from the

inside. An interstellar probe equipped with a dust analyzer and an infrared (IR) detector would provide one of the most critical observations to date of planetary system formation.

Beyond a few tens of astronomical units, the foreground IR emissions from the zodiacal cloud drop to levels where the so-called extragalactic background light (EBL) (Cooray, 2016) becomes detectable. The EBL represents all the red-shifted, diffuse emissions from all galaxies and stars that have ever shone and therefore holds a large missing piece of information for understanding the early galaxy and star formation some 200 million years after the Big Bang. Unobscured measurements of the EBL will provide a crucial test of models of reionization, including the characteristics of early stars and protogalaxies, the nature and thermodynamics of the gas, as well as its scattering and absorption properties.

Interstellar Probe is a mission traditionally anchored in heliophysics, where the predominant science return would lie. However, its outward trajectory would also provide a scientific return on the level of a full planetary and astrophysics mission with only modest instrument augmentations to the existing Interstellar Probe baseline concept.

2.9 Section 2 References

- Alexashov, D.B., Katushkina, O.A., Izmodenov, V.V., Akaev, P.S. (2016) Interstellar dust distribution outside the heliopause: Deflection at the heliospheric interface. *Monthly Notices of the Royal Astronomical Society* 458, 2553. doi: 10.1093/mnras/stw514
- Allegrini, F., Schwadron, N.A., McComas, D.J., Gloeckler, G., Geiss, J. (2005) Stability of the inner source pickup ions over the solar cycle. *Journal of Geophysical Research (Space Physics)* 110. Retrieved from <https://ui.adsabs.harvard.edu/abs/2005JGRA..110.5105A>
- Bannister, M.T., Kavelaars, J.J., Petit, J.-M., et al. (2016) The Outer Solar System Origins Survey. I. Design and first-quarter discoveries. *The Astronomical Journal* 152, 70. doi: 10.3847/0004-6256/152/3/70
- Baranov, V.B., Malama, Y.G. (1993) Model of the solar wind interaction with the local interstellar medium numerical solution of self-consistent problem. *Journal of Geophysical Research* 98, 15157-15164. Retrieved from <https://ui.adsabs.harvard.edu/abs/1993JGR....9815157B>
- Baranov, V.B., Zaitsev, N.A. (1998) On the problem of the heliospheric interface response to the cycles of the solar activity. *Geophysical Research Letters* 25, 4051. doi: 10.1029/1998gl900044
- Bernardinelli, P.H. (2021) *Characterizing the outer Solar System with the Dark Energy Survey*. Retrieved from <https://ui.adsabs.harvard.edu/abs/2021PhDT.....18B>
- Bildsten, L., Brown, E.F., Matzner, C.D., Ushomirsky, G. (1997) Lithium depletion in fully convective pre-main-sequence stars. *The Astrophysical Journal* 482, 442. doi: 10.1086/304151

- Burlaga, L.F., Ness, N.F., Acuña, M.H., Lepping, R.P., Connerney, J.E.P., Richardson, J.D. (2008) Magnetic fields at the solar wind termination shock. *Nature* 454, 75. doi: 10.1038/nature07029
- Burlaga, L.F., Ness, N.F., Gurnett, D.A., Kurth, W.S. (2013) Evidence for a shock in interstellar plasma: Voyager 1. *The Astrophysical Journal* 778, L3. doi: 10.1088/2041-8205/778/1/L3
- Burlaga, L.F., Ness, N.F. (2016) Observations of the interstellar magnetic field in the outer heliosheath: Voyager 1. *The Astrophysical Journal* 829. Retrieved from <https://ui.adsabs.harvard.edu/abs/2016ApJ...829..134B>
- Burlaga, L.F., Ness, N.F., Berdichevsky, D.B., Park, J., Jian, L.K., Szabo, A., Stone, E.C., Richardson, J.D. (2019) Magnetic field and particle measurements made by Voyager 2 at and near the heliopause. *Nature Astronomy* 3, 1007. doi: 10.1038/s41550-019-0920-y
- Chalov, S.V., Alexashov, D.B., McComas, D., Izmodenov, V.V., Malama, Y.G., Schwadron, N. (2010) Scatter-free pickup ions beyond the heliopause as a model for the Interstellar Boundary Explorer Ribbon. *The Astrophysical Journal* 716, L99. doi: 10.1088/2041-8205/716/2/L99
- Chambers, J.E. (2016) Pebble accretion and the diversity of planetary systems. *The Astrophysical Journal* 825, 63. doi: 10.3847/0004-637x/825/1/63
- Chassefiere, E., Bertaux, J.L., Sidis, V. (1986) Elastic collisions of solar wind protons with interstellar neutrals (H and He) inside the heliosphere - A new approach. *Astronomy and Astrophysics* 169, 298. Retrieved from <https://ui.adsabs.harvard.edu/abs/1986A&A...169..298C>
- Clarke, J.T., Mayyasi, M., Bhattacharyya, D., et al. (2017) Variability of D and H in the Martian upper atmosphere observed with the MAVEN IUVS echelle channel. *Journal of Geophysical Research: Space Physics* 122(2), 2336-2344. doi: <https://doi.org/10.1002/2016JA023479>
- Cooray, A. (2016) Extragalactic background light measurements and applications. *Royal Society Open Science* 3, 150555. Retrieved from <https://ui.adsabs.harvard.edu/abs/2016RSOS....350555C>
- Cummings, A.C., Stone, E.C., Heikkila, B.C., Lal, N., Webber, W.R., Jóhannesson, G., Moskalenko, I.V., Orlando, E., Porter, T.A. (2016) galactic cosmic rays in the local interstellar medium: Voyager 1 observations and model results. *The Astrophysical Journal* 831(1), 18. doi: 10.3847/0004-637x/831/1/18
- Dachev, T., Horneck, G., Häder, D.-P., Schuster, M., Richter, P., Lebert, M., Demets, R. (2012) Time profile of cosmic radiation exposure during the EXPOSE-E mission: The R3DE instrument. *Astrobiology* 12, 403. doi: 10.1089/ast.2011.0759
- Decker, R.B., Krimigis, S.M., Roelof, E.C., Hill, M.E., Armstrong, T.P., Gloeckler, G., Hamilton, D.C., Lanzerotti, L.J. (2005) Voyager 1 in the foreshock, termination shock, and heliosheath. *Science* 309(5743), 2020-2024. doi: 10.1126/science.1117569

- Dialynas, K., Krimigis, S.M., Mitchell, D.G., Decker, R.B., Roelof, E.C. (2017) The bubble-like shape of the heliosphere observed by Voyager and Cassini. *Nature Astronomy* 1(5). doi: 10.1038/s41550-017-0115
- Dialynas, K., Krimigis, S.M., Decker, R.B., Mitchell, D.G. (2019) Plasma pressures in the heliosheath from Cassini ENA and Voyager 2 measurements: Validation by the Voyager 2 heliopause crossing. *Geophysical Research Letters* 46, 7911. doi: 10.1029/2019gl083924
- Dialynas, K., Galli, A., Dayeh, M.A., et al. (2020) Combined ~ 10 eV to ~ 344 MeV particle spectra and pressures in the heliosheath along the Voyager 2 trajectory. *The Astrophysical Journal* 905, L24. doi: 10.3847/2041-8213/abcaaa
- Dialynas, K., Krimigis, S.M., Decker, R.B., Hill, M.E. (2021) Ions measured by Voyager 1 outside the heliopause to 28 au and implications thereof. *The Astrophysical Journal* 917, 42. doi: 10.3847/1538-4357/ac071e
- Draine, B.T. (2009a) Perspectives on interstellar dust inside and outside of the heliosphere. *Space Science Reviews* 143, 333. doi: 10.1007/s11214-008-9411-7
- Drake, J.F., Swisdak, M., Che, H., Shay, M.A. (2006) Electron acceleration from contracting magnetic islands during reconnection. *Nature* 443, 553. doi: 10.1038/nature05116
- Drake, J.F., Opher, M., Swisdak, M., Chamoun, J.N. (2010) A magnetic reconnection mechanism for the generation of anomalous cosmic rays. *The Astrophysical Journal* 709, 963. doi: 10.1088/0004-637x/709/2/963
- Elliot, J.L., Kern, S.D., Clancy, K.B., et al. (2005) The Deep Ecliptic Survey: A search for Kuiper Belt objects and Centaurs. II. Dynamical classification, the Kuiper Belt plane, and the core population. *The Astronomical Journal* 129, 1117. doi: 10.1086/427395
- Elliott, H.A., McComas, D.J., Zirnstein, E.J., et al. (2019) Slowing of the solar wind in the outer heliosphere. *The Astrophysical Journal* 885, 156. doi: 10.3847/1538-4357/ab3e49
- Ergun, R.E., Ahmadi, N., Kromyda, L., et al. (2020) Observations of particle acceleration in magnetic reconnection-driven turbulence. *The Astrophysical Journal* 898, 154. doi: 10.3847/1538-4357/ab9ab6
- Fisk, L.A., Kozlovsky, B., Ramaty, R. (1974) An interpretation of the observed oxygen and nitrogen enhancements in low-energy cosmic rays. *The Astrophysical Journal* 190, L35. doi: 10.1086/181498
- Fisk, L.A., Gloeckler, G. (2009) The acceleration of anomalous cosmic rays by stochastic acceleration in the heliosheath. *Advances in Space Research* 43, 1471. doi: 10.1016/j.asr.2009.02.010
- Florinski, V., Pogorelov, N.V., Zank, G.P., Wood, B.E., Cox, D.P. (2004) On the possibility of a strong magnetic field in the local interstellar medium. *The Astrophysical Journal* 604, 700. doi: 10.1086/382017
- Forbush, S.E. (1938) On world-wide changes in cosmic-ray intensity. *Physical Review* 54, 975. doi: 10.1103/PhysRev.54.975

- Fraternale, F., Gallana, L., Iovieno, M., Opher, M., Richardson, J.D., Tordella, D. (2016) Turbulence in the solar wind: Spectra from Voyager 2 data at 5 AU. *Physica Scripta* 91, 023011. doi: 10.1088/0031-8949/91/2/023011
- Frisch, P.C., Redfield, S., Slavin, J.D. (2011) The interstellar medium surrounding the Sun. *Annual Review of Astronomy and Astrophysics* 49, 237. doi: 10.1146/annurev-astro-081710-102613
- Frisch, P.C., Bzowski, M., Livadiotis, G., et al. (2013) Decades-long changes of the interstellar wind through our solar system. *Science* 341, 1080. doi: 10.1126/science.1239925
- Galli, A., Wurz, P., Fichtner, H., Futaana, Y., Barabash, S. (2019) An empirical model of energetic neutral atom imaging of the heliosphere and its implications for future heliospheric missions at great heliocentric distances. *The Astrophysical Journal* 886, 70. doi: 10.3847/1538-4357/ab4e94
- Geiss, J., Gloeckler, G., Fisk, L.A., von Steiger, R. (1995) C⁺ pickup ions in the heliosphere and their origin. *Journal of Geophysical Research* 100, 23373-23378. Retrieved from <https://ui.adsabs.harvard.edu/abs/1995JGR...10023373G>
- Geiss, J., Gloeckler, G. (2003) Isotopic composition of H, HE and NE in the protosolar cloud. *Space Science Reviews* 106, 3. doi: 10.1023/a:1024651232758
- Geiss, J., Gloeckler, G., Fisk, L.A. (2006) Interstellar gas inside the heliosphere. *ISSI Scientific Reports Series* 5, 137. Retrieved from <https://ui.adsabs.harvard.edu/abs/2006ISSIR...5..137G>
- Gloeckler, G., Geiss, J., Balsiger, H., et al. (1992) The Solar Wind Ion Composition Spectrometer. *Astronomy and Astrophysics Supplement Series* 92, 267-289. Retrieved from <https://ui.adsabs.harvard.edu/abs/1992A&AS...92..267G>
- Gloeckler, G., Geiss, J. (1996) Abundance of ³He in the local interstellar cloud. *Nature* 381, 210-212. Retrieved from <https://ui.adsabs.harvard.edu/abs/1996Natur.381..210G>
- Gloeckler, G., Geiss, J. (1998) Interstellar and inner source pickup ions Observed with SWICS on Ulysses. *Space Science Reviews* 86(1-4), 127-159. doi: 10.1023/a:1005019628054
- Gloeckler, G., Fisk, L.A. (2007) Johannes Geiss' investigations of solar, heliospheric and interstellar matter. *Space Science Reviews* 130, 489. doi: 10.1007/s11214-007-9226-y
- Gloeckler, G., Fisk, L.A., Geiss, J., Hill, M.E., Hamilton, D.C., Decker, R.B., Krimigis, S.M. (2009) Composition of interstellar neutrals and the origin of anomalous cosmic rays. *Space Science Reviews* 143, 163. doi: 10.1007/s11214-008-9482-5
- Gloeckler, G., Fisk, L.A. (2015) More evidence that Voyager 1 is still in the heliosphere. *The Astrophysical Journal* 806(2). doi: 10.1088/2041-8205/806/2/127
- Godenko, E.A., Izmodenov, V.V. (2021) Effects of dispersion of the dust velocity in the LISM on the interstellar dust distribution inside the heliosphere. *Astronomy Letters* 47, 50. doi: 10.1134/s1063773721010047

- Gruntman, M., Roelof, E.C., Mitchell, D.G., Fahr, H.J., Funsten, H.O., McComas, D.J. (2001) Energetic neutral atom imaging of the heliospheric boundary region. *Journal of Geophysical Research* 106, 15767. doi: 10.1029/2000ja000328
- Gurnett, D.A., Kurth, W.S., Stone, E.C., Cummings, A.C., Krimigis, S.M., Decker, R.B., Ness, N.F., Burlaga, L.F. (2015) Precursors to interstellar shocks of solar origin. *The Astrophysical Journal* 809. Retrieved from <https://ui.adsabs.harvard.edu/abs/2015ApJ...809..121G>
- Gurnett, D.A., Kurth, W.S. (2019) Plasma densities near and beyond the heliopause from the Voyager 1 and 2 plasma wave instruments. *Nature Astronomy* 3, 1024. doi: 10.1038/s41550-019-0918-5
- Hill, M.E., Allen, R.C., Kollmann, P., et al. (2020) Influence of solar disturbances on galactic cosmic rays in the solar wind, heliosheath, and local interstellar medium: Advanced Composition Explorer, New Horizons, and Voyager observations. *The Astrophysical Journal* 905(1), 69. doi: 10.3847/1538-4357/abb408
- Izmodenov, V., Malama, Y., Gloeckler, G., Geiss, J. (2004) Filtration of interstellar H, O, N atoms through the heliospheric interface: Inferences on local interstellar abundances of the elements. *Astronomy and Astrophysics* 414, L29. doi: 10.1051/0004-6361:20031697
- Izmodenov, V., Malama, Y., Ruderman, M.S. (2005) Solar cycle influence on the interaction of the solar wind with local interstellar cloud. *Astronomy & Astrophysics* 429(3), 1069-1080. doi: 10.1051/0004-6361:20041348
- Izmodenov, V.V., Geiss, J., Lallement, R., Gloeckler, G., Baranov, V.B., Malama, Y.G. (1999) Filtration of interstellar hydrogen in the two-shock heliospheric interface: Inferences on the local interstellar cloud electron density. *Journal of Geophysical Research* 104, 4731. doi: 10.1029/1998ja900122
- Izmodenov, V.V., Gruntman, M., Malama, Y.G. (2001) Interstellar hydrogen atom distribution function in the outer heliosphere. *Journal of Geophysical Research* 106, 10681. doi: 10.1029/2000ja000273
- Izmodenov, V.V., Malama, Y.G., Ruderman, M.S. (2008) Modeling of the outer heliosphere with the realistic solar cycle. *Advances in Space Research* 41(2), 318-324. doi: 10.1016/j.asr.2007.06.033
- Izmodenov, V.V. (2009) Local interstellar parameters as they are inferred from analysis of observations inside the heliosphere. *Space Science Reviews* 143, 139-150. Retrieved from <https://ui.adsabs.harvard.edu/abs/2009SSRv..143..139I>
- Izmodenov, V.V., Alexashov, D.B. (2020) Magnitude and direction of the local interstellar magnetic field inferred from Voyager 1 and 2 interstellar data and global heliospheric model. *Astronomy and Astrophysics* 633, L12. doi: 10.1051/0004-6361/201937058
- Jaffe, L.D., Ivie, C.V., Khodakovsky, I.L., Volkov, V.P., Sidorov, Y.I., Borisov, M.V., Lomonosov, M.V. (1979) Science aspects of a mission beyond the planets. *Icarus* 39, 486. doi: 10.1016/0019-1035(79)90156-8

- Katushkina, O.A., Quémerais, E., Izmodenov, V.V., Lallement, R., Sandel, B.R. (2017) Voyager 1/UVS Lyman α measurements at the distant heliosphere (90–130 AU): Unknown source of additional emission. *Journal of Geophysical Research: Space Physics* 122(11). doi: 10.1002/2017ja024205
- Kollmann, P., Hill, M.E., McNutt, R.L., Jr., et al. (2019) Suprathermal ions in the outer heliosphere. *The Astrophysical Journal* 876, 46. doi: 10.3847/1538-4357/ab125f
- Krimigis, S.M., Mitchell, D.G., Hamilton, D.C., et al. (2004) Magnetosphere Imaging Instrument (MIMI) on the Cassini mission to Saturn/Titan. *Space Science Reviews* 114, 233-329. Retrieved from <https://ui.adsabs.harvard.edu/abs/2004SSRv..114..233K>
- Krimigis, S.M., Mitchell, D.G., Roelof, E.C., Hsieh, K.C., McComas, D.J. (2009) Imaging the interaction of the heliosphere with the interstellar medium from Saturn with Cassini. *Science* 326(5955), 971-973. doi: 10.1126/science.1181079
- Krimigis, S.M., Decker, R.B., Roelof, E.C., Hill, M.E., Armstrong, T.P., Gloeckler, G., Hamilton, D.C., Lanzerotti, L.J. (2013) Search for the exit: Voyager 1 at heliosphere's border with the galaxy. *Science* 341(6142), 144-147. doi: 10.1126/science.1235721
- Krimigis, S.M., Decker, R.B., Roelof, E.C., Hill, M.E., Bostrom, C.O., Dialynas, K., Gloeckler, G., Hamilton, D.C., Keath, E.P., Lanzerotti, L.J. (2019) Energetic charged particle measurements from Voyager 2 at the heliopause and beyond. *Nature Astronomy* 3, 997. doi: 10.1038/s41550-019-0927-4
- Li, H., Wang, C., Richardson, J.D. (2008) Properties of the termination shock observed by Voyager 2. *Geophysical Research Letters* 35, L19107. doi: 10.1029/2008gl034869
- Li, W., Hudson, M.K. (2019) Earth's Van Allen radiation belts: From discovery to the Van Allen Probes era. *Journal of Geophysical Research (Space Physics)* 124, 8319. doi: 10.1029/2018ja025940
- Linsky, J.L., Wood, B.E. (1996) The α Centauri line of sight: D/H ratio, physical properties of local interstellar gas, and measurement of heated hydrogen (the "hydrogen wall") near the heliopause. *The Astrophysical Journal* 463, 254. doi: 10.1086/177238
- Linsky, J.L., Redfield, S., Tilipman, D. (2019) The interface between the outer heliosphere and the inner local ISM: Morphology of the local interstellar cloud, its hydrogen hole, Strömgren shells, and ^{60}Fe accretion. *The Astrophysical Journal* 886, 41. doi: 10.3847/1538-4357/ab498a
- Linsky, J.L., Redfield, S. (2021) Could the local cavity be an irregularly shaped Strömgren sphere? *The Astrophysical Journal* 920, 75. doi: 10.3847/1538-4357/ac1feb
- McComas, D.J., Schwadron, N.A. (2006) An explanation of the Voyager paradox: Particle acceleration at a blunt termination shock. *Geophysical Research Letters* 33, L04102. doi: 10.1029/2005gl025437
- McComas, D.J., Allegrini, F., Bochsler, P., et al. (2009) Global Observations of the interstellar interaction from the Interstellar Boundary Explorer (IBEX). *Science* 326(5955), 959-962. doi: 10.1126/science.1180906

- McComas, D.J., Alexashov, D., Bzowski, M., et al. (2012) The heliosphere's interstellar interaction: No bow shock. *Science* 336(6086), 1291-1293. doi: 10.1126/science.1221054
- McComas, D.J., Zirnstein, E.J., Bzowski, M., et al. (2017) Seven years of imaging the global heliosphere with IBEX. *The Astrophysical Journal Supplement Series* 229(2), 41. doi: 10.3847/1538-4365/aa66d8
- McComas, D.J., Christian, E.R., Schwadron, N.A., et al. (2018) Interstellar Mapping and Acceleration Probe (IMAP): A new NASA mission. *Space Science Reviews* 214(8), 116. doi: 10.1007/s11214-018-0550-1
- McComas, D.J., Bzowski, M., Dayeh, M.A., et al. (2020) Solar cycle of imaging the global heliosphere: Interstellar Boundary Explorer (IBEX) observations from 2009-2019. *The Astrophysical Journal Supplement Series* 248, 26. doi: 10.3847/1538-4365/ab8dc2
- McComas, D.J., Swaczyna, P., Szalay, J.R., Zirnstein, E.J., Rankin, J.S., Elliott, H.A., Singer, K., Spencer, J., Stern, S.A., Weaver, H. (2021) Interstellar pickup ion observations halfway to the termination shock. *The Astrophysical Journal Supplement Series* 254, 19. doi: 10.3847/1538-4365/abee76
- McCracken, K.G., Beer, J. (2007) Long-term changes in the cosmic ray intensity at Earth, 1428-2005. *Journal of Geophysical Research (Space Physics)* 112, A10101. doi: 10.1029/2006ja012117
- Mewaldt, R.A. (2013) Cosmic rays in the heliosphere: Requirements for future observations. *Space Science Reviews* 176, 365. doi: 10.1007/s11214-012-9922-0
- Müller, H.-R., Florinski, V., Heerikhuisen, J., Izmodenov, V.V., Scherer, K., Alexashov, D., Fahr, H.-J. (2008) Comparing various multi-component global heliosphere models. *Astronomy and Astrophysics* 491, 43. doi: 10.1051/0004-6361:20078708
- Müller, H.-R., Frisch, P.C., Fields, B.D., Zank, G.P. (2009) The heliosphere in time. *Space Science Reviews* 143, 415. doi: 10.1007/s11214-008-9448-7
- Nimmo, F., Pappalardo, R.T. (2016) Ocean worlds in the outer solar system. *Journal of Geophysical Research (Planets)* 121, 1378. doi: 10.1002/2016je005081
- Ocker, S.K., Cordes, J.M., Chatterjee, S., Gurnett, D.A., Kurth, W.S., Spangler, S.R. (2021) Persistent plasma waves in interstellar space detected by Voyager 1. *Nature Astronomy*. doi: 10.1038/s41550-021-01363-7
- Opher, M., Drake, J.F., Zieger, B., Gombosi, T.I. (2015) Magnetized jets driven by the Sun: The structure of the heliosphere revisited. *The Astrophysical Journal* 800. Retrieved from <https://ui.adsabs.harvard.edu/abs/2015ApJ...800L..28O>
- Opher, M., Loeb, A., Drake, J., Toth, G. (2018) A predicted small and round heliosphere. *arXiv e-prints*. Retrieved from <https://ui.adsabs.harvard.edu/abs/2018arXiv180806611O>
- Pesses, M.E., Jokipii, J.R., Eichler, D. (1981) Cosmic ray drift, shock wave acceleration, and the anomalous component of cosmic rays. *The Astrophysical Journal* 246, L85. doi: 10.1086/183559

- Pogorelov, N.V., Borovikov, S.N., Zank, G.P., Ogino, T. (2009) Three-dimensional features of the outer heliosphere due to coupling between the interstellar and interplanetary magnetic fields. III. The effects of solar rotation and activity cycle. *The Astrophysical Journal* 696, 1478. doi: 10.1088/0004-637x/696/2/1478
- Pogorelov, N.V., Heerikhuisen, J., Zank, G.P., Borovikov, S.N., Frisch, P.C., McComas, D.J. (2011) Interstellar Boundary Explorer measurements and magnetic field in the vicinity of the heliopause. *The Astrophysical Journal* 742, 104. doi: 10.1088/0004-637x/742/2/104
- Pogorelov, N.V., Heerikhuisen, J., Roytershteyn, V., Burlaga, L.F., Gurnett, D.A., Kurth, W.S. (2017) Three-dimensional features of the outer heliosphere due to coupling between the interstellar and heliospheric magnetic field. V. The bow wave, heliospheric boundary layer, instabilities, and magnetic reconnection. *The Astrophysical Journal* 845, 9. doi: 10.3847/1538-4357/aa7d4f
- Quémerais, E., Sandel, B.R., Bertaux, J.L., Lallement, R. (2000) Outer heliosphere Ly- α measurements: 1993 to 1998. *Astrophysics and Space Science* 274, 123. doi: 10.1023/a:1026591705751
- Quémerais, E., Izmodenov, V. (2002) Effects of the heliospheric interface on the interplanetary Lyman alpha glow seen at 1 AU from the Sun. *Astronomy and Astrophysics* 396, 269. doi: 10.1051/0004-6361:20021396
- Quémerais, E., Lallement, R., Ferron, S., Koutroumpa, D., Bertaux, J.L., Kyrölä, E., Schmidt, W. (2006) Interplanetary hydrogen absolute ionization rates: Retrieving the solar wind mass flux latitude and cycle dependence with SWAN/SOHO maps. *Journal of Geophysical Research: Space Physics (1978–2012)* 111(A9). doi: 10.1029/2006ja011711
- Rankin, J.S., McComas, D.J., Richardson, J.D., Schwadron, N.A. (2019a) Heliosheath properties measured from a Voyager 2 to Voyager 1 transient. *The Astrophysical Journal* 883, 101. doi: 10.3847/1538-4357/ab3d9d
- Rankin, J.S., Stone, E.C., Cummings, A.C., McComas, D.J., Lal, N., Heikkilä, B.C. (2019b) Galactic cosmic-ray anisotropies: Voyager 1 in the local interstellar medium. *The Astrophysical Journal* 873. Retrieved from <https://ui.adsabs.harvard.edu/abs/2019ApJ...873...46R>
- Rankin, J.S., McComas, D.J., Schwadron, N.A. (2020) Galactic cosmic-ray anisotropies: Electrons observed by Voyager 1 in the Very Local Interstellar Medium. *The Astrophysical Journal* 895, 103. doi: 10.3847/1538-4357/ab8eb2
- Reisenfeld, D.B., Bzowski, M., Funsten, H.O., et al. (2021) A three-dimensional map of the heliosphere from IBEX. *The Astrophysical Journal Supplement Series* 254, 40. doi: 10.3847/1538-4365/abf658
- Richardson, J.D., Paularena, K.I., Lazarus, A.J., Belcher, J.W. (1995) Evidence for a solar wind slowdown in the outer heliosphere? *Geophysical Research Letters* 22, 1469. doi: 10.1029/95gl01421
- Richardson, J.D., Smith, C.W. (2003) The radial temperature profile of the solar wind. *Geophysical Research Letters* 30, 1206. doi: 10.1029/2002gl016551

- Richardson, J.D., Kasper, J.C., Wang, C., Belcher, J.W., Lazarus, A.J. (2008) Cool heliosheath plasma and deceleration of the upstream solar wind at the termination shock. *Nature* 454(7200), 63. doi: 10.1038/nature07024
- Roelof, E.C. (2012) *Importance of the Compton-Getting Factor in Energetic Neutral Atom Imaging of the Heliosheath*. <https://ui.adsabs.harvard.edu/abs/2012AGUFMSH11B2208R>.
- Scherer, K., Fahr, H.J. (2003) Solar cycle induced variations of the outer heliospheric structures. *Geophysical Research Letters* 30(2). doi: 10.1029/2002gl016073
- Schwadron, N.A., Geiss, J., Fisk, L.A., Gloeckler, G., Zurbuchen, T.H., von Steiger, R. (2000) Inner source distributions: Theoretical interpretation, implications, and evidence for inner source protons. *Journal of Geophysical Research* 105, 7465-7472. Retrieved from <https://ui.adsabs.harvard.edu/abs/2000JGR...105.7465S>
- Schwadron, N.A., Gloeckler, G. (2007) Pickup ions and cosmic rays from dust in the heliosphere. *Space Science Reviews* 130, 283. doi: 10.1007/s11214-007-9166-6
- Schwamb, M.E., Fraser, W.C., Bannister, M.T., et al. (2019) Col-OSSOS: The colors of the Outer Solar System Origins Survey. *The Astrophysical Journal Supplement Series* 243, 12. doi: 10.3847/1538-4365/ab2194
- Slavin, J.D., Frisch, P.C. (2008) The boundary conditions of the heliosphere: photoionization models constrained by interstellar and in situ data. *Astronomy and Astrophysics* 491, 53-68. Retrieved from <https://ui.adsabs.harvard.edu/abs/2008A&A...491...53S>
- Slavin, J.D., Frisch, P.C., Müller, H.-R., Heerikhuisen, J., Pogorelov, N.V., Reach, W.T., Zank, G. (2012) Trajectories and distribution of interstellar dust grains in the heliosphere. *The Astrophysical Journal* 760, 46. doi: 10.1088/0004-637x/760/1/46
- Steigman, G., Tosi, M. (1992) Galactic evolution of D and ³He. *The Astrophysical Journal* 401, 150. doi: 10.1086/172048
- Sterken, V.J., Altobelli, N., Kempf, S., Schwehm, G., Srama, R., Grün, E. (2012) The flow of interstellar dust into the solar system. *Astronomy and Astrophysics* 538, A102. doi: 10.1051/0004-6361/201117119
- Stern, S.A., Bagenal, F., Ennico, K., et al. (2015) The Pluto system: Initial results from its exploration by New Horizons. *Science* 350, aad1815. doi: 10.1126/science.aad1815
- Stern, S.A., Weaver, H.A., Spencer, J.R., et al. (2019) Initial results from the New Horizons exploration of 2014 MU₆₉, a small Kuiper Belt object. *Science* 364, aaw9771. doi: 10.1126/science.aaw9771
- Stone, E.C., Cummings, A.C., McDonald, F.B., Heikkila, B.C., Lal, N., Webber, W.R. (2005) Voyager 1 explores the termination shock region and the heliosheath beyond. *Science* 309, 2017. doi: 10.1126/science.1117684
- Stone, E.C., Cummings, A.C., McDonald, F.B., Heikkila, B.C., Lal, N., Webber, W.R. (2008) An asymmetric solar wind termination shock. *Nature* 454, 71. doi: 10.1038/nature07022

- Swaczyna, P., McComas, D.J., Zirnststein, E.J., Heerikhuisen, J. (2019) Angular scattering in charge exchange: Issues and implications for secondary interstellar hydrogen. *The Astrophysical Journal* 887, 223. doi: 10.3847/1538-4357/ab5440
- Turner, D.L., Wilson, L.B., Liu, T.Z., et al. (2018) Autogenous and efficient acceleration of energetic ions upstream of Earth's bow shock. *Nature* 561, 206. doi: 10.1038/s41586-018-0472-9
- Vasyliunas, V.M. (1968) A survey of low-energy electrons in the evening sector of the magnetosphere with OGO 1 and OGO 3. *Journal of Geophysical Research* 73, 2839. doi: 10.1029/JA073i009p02839
- Wallner, A., Feige, J., Fifield, L.K., et al. (2020) ⁶⁰Fe deposition during the late Pleistocene and the Holocene echoes past supernova activity. *Proceedings of the National Academy of Science* 117, 21873. doi: 10.1073/pnas.1916769117
- Wang, C., Richardson, J.D., Gosling, J.T. (2000) Slowdown of the solar wind in the outer heliosphere and the interstellar neutral hydrogen density. *Geophysical Research Letters* 27, 2429. doi: 10.1029/2000gl000058
- Washimi, H., Zank, G.P., Hu, Q., Tanaka, T., Munakata, K., Shinagawa, H. (2011) Realistic and time-varying outer heliospheric modelling. *Monthly Notices of the Royal Astronomical Society* 416, 1475. doi: 10.1111/j.1365-2966.2011.19144.x
- Wiedenbeck, M.E., Binns, W.R., Cummings, A.C., Davis, A.J., de Nolfo, G.A., Israel, M.H., Leske, R.A., Mewaldt, R.A., Stone, E.C., von Rosenvinge, T.T. (2007) An overview of the origin of galactic cosmic rays as inferred from observations of heavy ion composition and spectra. *Space Science Reviews* 130, 415. doi: 10.1007/s11214-007-9198-y
- Wiedenbeck, M.E. (2013) Cosmic-ray energy spectra and time variations in the local interstellar medium: Constraints and uncertainties. *Space Science Reviews* 176, 35. doi: 10.1007/s11214-011-9778-8
- Wood, B.E., Müller, H.R., Zank, G.P., Izmodenov, V.V., Linsky, J.L. (2004) The heliospheric hydrogen wall and astrospheres. *Advances in Space Research* 34(1), 66-73. doi: 10.1016/j.asr.2003.01.035
- Zank, G.P., Pauls, H.L., Cairns, I.H., Webb, G.M. (1996) Interstellar pickup ions and quasi-perpendicular shocks: Implications for the termination shock and interplanetary shocks. *Journal of Geophysical Research* 101, 457. doi: 10.1029/95ja02860
- Zank, G.P. (1999) Interaction of the solar wind with the local interstellar medium: A theoretical perspective. *Space Science Reviews* 89(3-4), 413-688. doi: 10.1023/a:1005155601277
- Zank, G.P., Müller, H.R. (2003) The dynamical heliosphere. *Journal of Geophysical Research: Space Physics (1978–2012)* 108(A6). doi: 10.1029/2002ja009689
- Zank, G.P., Pogorelov, N.V., Heerikhuisen, J., Washimi, H., Florinski, V., Borovikov, S., Kryukov, I., Müller, H.R. (2009) Physics of the solar wind-local interstellar medium interaction: Role of magnetic fields. *Space Science Reviews* 146, 295. doi: 10.1007/s11214-009-9497-6

- Zank, G.P., Heerikhuisen, J., Wood, B.E., Pogorelov, N.V., Zirnstien, E., McComas, D.J. (2013) Heliospheric structure: The bow wave and the hydrogen wall. *The Astrophysical Journal* 763, 20. doi: 10.1088/0004-637x/763/1/20
- Zank, G.P., Adhikari, L., Zhao, L.-L., Mostafavi, P., Zirnstien, E.J., McComas, D.J. (2018) The pickup ion-mediated solar wind. *The Astrophysical Journal* 869, 23. doi: 10.3847/1538-4357/aaebfe
- Zhang, M., Pogorelov, N.V., Zhang, Y., Hu, H.B., Schlickeiser, R. (2020) The original anisotropy of TeV cosmic rays in the local interstellar medium. *The Astrophysical Journal* 889, 97. doi: 10.3847/1538-4357/ab643c
- Zhao, L.-L., Zank, G.P., Hu, Q., Chen, Y., Adhikari, L., leRoux, J.A., Cummings, A., Stone, E., Burlaga, L.F. (2019) ACR proton acceleration associated with reconnection processes beyond the heliospheric termination shock. *The Astrophysical Journal* 886, 144. doi: 10.3847/1538-4357/ab4db4
- Zhukovska, S., Gail, H.-P., Tieloff, M. (2008) Evolution of interstellar dust and stardust in the solar neighbourhood. *Astronomy and Astrophysics* 479, 453-480. Retrieved from <https://ui.adsabs.harvard.edu/abs/2008A&A...479..453Z>
- Zieger, B., Opher, M., Schwadron, N.A., McComas, D.J., Tóth, G. (2013) A slow bow shock ahead of the heliosphere. *Geophysical Research Letters* 40, 2923. doi: 10.1002/grl.50576
- Zirnstien, E.J., Heerikhuisen, J., Funsten, H.O., Livadiotis, G., McComas, D.J., Pogorelov, N.V. (2016) Local interstellar magnetic field determined from the Interstellar Boundary Explorer ribbon. *The Astrophysical Journal* 818(1). doi: 10.3847/2041-8205/818/1/L18

3. High-Level Mission Concept

The Interstellar Probe concept presented here implements the science objectives detailed in Section 2, as well as the requirements provided by NASA as inputs to the study. In addition to developing a concept to meet the science objectives, the mission concept should provide

- Readiness for launch no later than 2030. This requirement bounds the technology readiness that can be assumed for use in the mission. Technology generally should be at high technology readiness level (TRL), with a requirement that all technology should be at TRL 6 by 2025.
- Capability of performing significant science at 1000 au. This requirement is intended to define the minimum downlink rate at the farthest expected distance from Earth and is not a requirement on system lifetime (for example, radioisotope thermoelectric generator [RTG] lifetime).
- Spacecraft power requirement at 50 years not less than 300 W. Spacecraft power is provided by RTGs, and this requirement encapsulates the expected performance of the RTGs at 50 years.
- Lifetime not less than 50 years. This requirement defines the reliability and longevity of the mission, and drives considerations such as redundancy and fault tolerance, as well as component/materials lifetime.

Initial trade studies identified three possible trajectory designs to accomplish the science objectives and concept study requirements, as well as several possible science augmentations that would expand the scope of science objectives while resulting in an increase in mission and flight system complexity. The mission concept presented here is the result of trade studies that optimized the mission with regard to factors such as science objectives, concept study requirements, space environment constraints, and risk. Issues associated with implementing augmented science objectives are discussed in Appendix A. The trajectory design trade study is presented in Appendix B, with implications for the flight system for the solar Oberth maneuver (SOM) trajectory described in Appendix D.

3.1 Mission Design Summary

3.1.1 Mission Design

3.1.1.1 Overview

The Interstellar Probe concept seeks to analyze the heliosphere and the nearby interstellar medium within a plausible mission lifetime (~50 years) employing near-current technology for launch in the 2030s. Because the distances to the edge of the heliosphere are quite long (roughly 100 au), a high heliocentric escape speed remains a primary goal for developing trajectory and mission architectures. Three primary methods exist to generate a high-speed departure from the solar system, with each involving some form of a Jupiter gravity assist (JGA).

1. *Ballistic (passive) JGA*: Using a super heavy-lift four-stage rocket, launch the spacecraft into a direct-to-Jupiter arc with a high-speed transfer (roughly 8–10 months) and perform a low-altitude Jupiter flyby aligned to maximize heliocentric escape speed.
2. *Powered JGA*: Using a similar super heavy-lift four-stage rocket, deploy three stages during launch to a slightly slower direct-to-Jupiter transfer (roughly 10–14 months) and take the fourth-stage solid rocket motor (SRM) to Jupiter. Then, the SRM fires (creating ΔV_p or a velocity change at perijove) during a low-altitude JGA to enhance the speed gain after the Jupiter flyby.
3. *SOM*: With a super heavy-lift vehicle, launch a spacecraft with an SRM and a protective solar shield to Jupiter for a JGA that lowers perihelion to a few solar radii. The SRM executes at perihelion to create orbital conditions with high escape speed.

The Option 1 ballistic JGA was selected for its competitive solar system exit speed while minimizing spacecraft complexity. Details regarding the other options are included in Appendices C and D. Appendix H gives the initial analysis of potential launch vehicle combinations that provide input into the mission design trade. Additional detail of the mission design trade can be found in Schlei et al. (2021).

3.1.1.2 Trajectory Trade Space

Given a likely launch analysis timeline from 2030 to 2042 (i.e., a complete Jupiter year), a sky map has been generated for each year in the analysis window and aggregated via a maximal speed comparison to produce the trajectory design trade space for a particular option. Each possible launch year creates an orange-to-red high-speed zone, or *hot-zone*, to a particular portion of the sky based on Jupiter alignment. Sky maps outline where on the celestial sphere high-speed options exist, as well as the relative location to other pertinent science objectives.

Through binned trajectory information available utilizing sky maps, possible destinations of interest for a heliophysics concept can be honed considering notional science objectives and iterations on likely mass values. The notional objectives for heliophysics science culminate into three elements (or design drivers) that strongly influence the trajectory selection:

1. Reach the heliopause and interstellar medium quickly to perform science studies within an acceptable mission duration (<50 years).
2. Capture a side view of the heliopause to characterize shape, preferably near 45° off of the heliopause nose direction at (7°N, 252°E) in Earth ecliptic coordinates.
3. Travel to the Interstellar Boundary Explorer (IBEX) ribbon for compelling and interesting force-balancing observations.

The sky map representing Option 1 trajectory possibilities with a wet mass of 860 kg ($C3 = 304.07 \text{ km}^2/\text{s}^2$) appears in Figure 3-1, where the wet mass was chosen to correspond to the flight system described in Section 5. Similarly, hot-zone areas are desired with near-ecliptic destinations typically being the overall fastest speeds within a given launch year. To demonstrate side-view

the IBEX ribbon at (−22°S, 180°E). The launch period spans from 28 August to 18 September 2036. Shown in Figure 3-3, the system exit speed varies throughout the launch period, with a minimum solar system exit speed of 6.8 au/year and peak at 6.97 au/year on 11 September 2036. Note that the chosen target trades exit speed for the ability to intersect the IBEX ribbon. The concept requires less than 15 years’ time of flight to the heliopause. Table 3-1 provides a high-order mission event timeline. The flight system can continuously take and relay measurements as it travels throughout the heliosheath and beyond into the VLISM (very local interstellar medium).

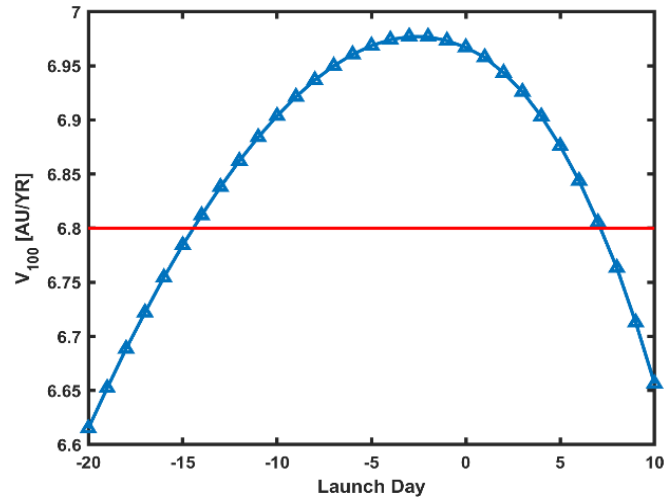


Figure 3-3. Solar system exit speed variation throughout launch period. (Image credit: Johns Hopkins Applied Physics Laboratory.)

3.1.1.4 Alternative Launch Opportunities

As stated before, because the flyout direction is dependent solely on Jupiter position without additional planetary alignment requirements, viable launch opportunities for Interstellar Probe exist annually from 2036 to 2041 while it is still traveling through the IBEX ribbon. Table 3-2 provides high-level details for each launch opportunity.

Table 3-1. Event timeline.

Event	Met
Launch	11 September 2036
JGA	0.78 year
100 au	14.8 years
344 au	50.0 years
1000 au	144.7 years

3.2 Concept of Operations

3.2.1 Mission Timeline

The baseline mission for Interstellar Probe consists of launch, a Jupiter flyby, and then phases through the heliosphere and interstellar space as the spacecraft journeys farther from Earth. The baseline mission timeline with the duration for each phase is shown in Table 3-3.

After the Jupiter flyby, the baseline operations begin. Operations are simple with predefined sequences that are consistent throughout the mission.

Table 3-2. Alternative launch options for the Interstellar Probe mission.

Launch Period	Ecliptic Longitude (Degrees)	Ecliptic Latitude (Degrees)	Peak Exit Speed (au/Year)	Time of Flight to 100 au (Years)
August 2036	180	−22	6.97	14.8
2037	212	−25	6.87	15.0
2038	241	−20	7.03	14.7
2039	270	−9.0	7.30	14.1
December 2040	295	0.0	7.32	14.1

Table 3-3. Interstellar Probe mission phases.

Mission Phase	Time Period	Duration (Months)	Duration (Years)
Launch and checkout	Commissioning	2	0.17
Cruise to Jupiter	Cruise to Jupiter	7	0.58
Wire antenna deployment	Prior to Jupiter flyby	1	0.08
JGA	–5 weeks to +3 weeks around Jupiter closest approach	2	0.17
Heliosphere phase	Jupiter–90 au	142.29	11.86
Heliosheath phase	90–120 au	49.43	4.12
Interstellar phase to 50 years*	120–352.4 au	396.40	33.03
Interstellar phase >50 years	352.4–1000 au	1110.17	92.51

*End of nominal mission

3.2.1.1 Launch and Checkout Phase

Launch and checkout is a 2-month period that begins at launch. There is continuous 24-hour communication with the spacecraft using Deep Space Network (DSN) 34-m antennas for the first week after launch. Then the communication coverage drops to daily 8-hour contacts using DSN 34-m antennas for 3 weeks. For the second month, communication is reduced further to an 8-hour contact 5 days per week, also using DSN 34-m antennas. The launch correction maneuver, spacecraft commissioning, and some instrument commissioning, including deploying the magnetometer boom, will be performed during this phase.

3.2.1.2 Cruise to Jupiter Phase

During the cruise to Jupiter phase, spacecraft and instrument commissioning continues. The DSN coverage decreases further to three 8-hour contacts with DSN 34-m antennas per week. During this phase, the team will prepare for the JGA.

3.2.1.3 Wire Antenna Deployment/Final Commissioning

During cruise, the 50-m wire antennas will be deployed and final instrument commissioning will be completed. It is estimated that it will take approximately 1 month to deploy the 50-m wire antennas based on the 2-week deployment time for the 50-m wire antennas on the Van Allen Probes and the longer round-trip light time (RTLTL) for Interstellar Probe. Continuous communication during the deployments will be performed using DSN 34-m antennas.

3.2.1.4 Jupiter Gravity Assist Phase

Statistical targeting trajectory-correction maneuvers (TCMs) are assumed at –30 days and –10 days before the JGA, with a statistical cleanup maneuver at +10 days after the Jupiter flyby. To support the statistical maneuvers, DSN communication coverage increases 5 weeks before the Jupiter flyby for navigation tracking—increasing back to five 8-hour tracks per week for 4 weeks, then increasing again to seven 8-hour tracks the week before the flyby and continuing through the week after the flyby (3 weeks total).

For the ballistic Jupiter flyby, and if a subset of the instruments are allowed to be on during a powered Jupiter flyby, the instruments will be passively taking science measurements, and no specific spacecraft pointing is required. After the Jupiter flyby is complete, the science data will be played back using the DSN 34-m antennas and the spacecraft high-gain antenna (HGA).

3.2.1.5 Heliosphere Phase (Jupiter to 90 au)

Once commissioning is complete after the JGA, Interstellar Probe enters the heliosphere phase. The mission remains in this phase for the next 11.86 years. During the heliosphere phase, Interstellar Probe is operating continuously with all instruments on and collecting data. Minimal instrument and spacecraft commanding is required and is planned to be performed approximately once a month during this phase. Examples of expected nominal spacecraft activities include periodic spacecraft spin-axis reorientation for telecommunications, spin-rate adjustments, periodic redundant side avionics health checks, ephemeris uplinks, time-tag command load uplinks, and time-keeping updates. There will be some periodic calibrations and table or parameter changes at the boundaries of the mission phases for the instruments.

Science data will be downlinked using three 8-hour contacts per week using DSN 34-m antennas until Interstellar Probe reaches 70 au, then communication will switch to using the Next Generation Very Large Array (ngVLA). There will be a phase-in period for using the ngVLA leading up to 70 au before switching. During the phase-in period, contacts will be taken using both the ngVLA and DSN. In addition, before switching, the ngVLA arrays of DSN 34-m antennas or DSN 70-m antennas, when available, will have to be used to maintain the downlink rate. The DSN antenna arraying will be managed to maintain the downlink rate above 10 kbps. The downlink rate increases after switching to using the ngVLA, so the number of downlink contacts may be reduced. Using one 8-hour ngVLA contact every 2 weeks, the science data volume downlinked decreases from 1.79 Gbit/week at 70 au to 1.06 Gbit/week at 90 au.

3.2.1.6 Heliosheath Phase (90–120 au)

The heliosheath phase lasts for 4.12 years. Similar to the heliosphere phase, during the heliosheath phase, Interstellar Probe will operate continuously with all instruments on and collecting data. There will be minimal commanding approximately once per month, continuing the same activities listed above during the heliosphere phase. Science data will be downlinked using one 8-hour ngVLA contact every 2 weeks. The downlink data rate continues to decline as Interstellar Probe travels farther from Earth. The downlink data volume reduces from 1.06 Gbit/week at the beginning of the heliosheath phase to 0.614 Gbit/week at 120 au.

3.2.1.7 Interstellar Phase to 50 Years

Once Interstellar Probe reaches 120 au, it will transition to the interstellar phase for the next 33 years, at which time it will reach 352.4 au at the nominal end of the mission at 50 years. Similar to the heliosphere/heliosheath phases, during the interstellar phase Interstellar Probe will operate continuously with all instruments on and collecting data. There will be minimal commanding approximately once per month. As Interstellar Probe moves farther away from Earth, the downlink

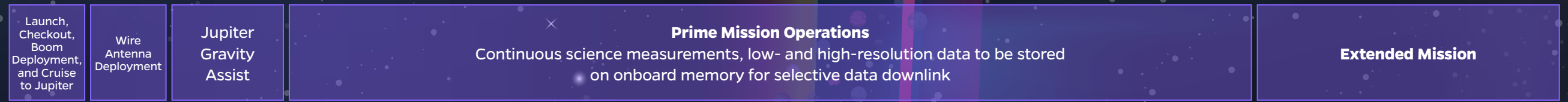
MISSION SCIENCE INVESTIGATIONS

Baseline Heliophysics Science Objectives
(See Section 2)

Cross-divisional Augmented Science Opportunities
(See Appendix A)



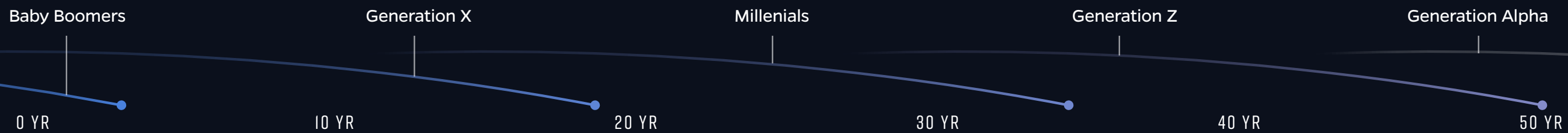
BASELINE MISSION OPERATIONS



DOWNLINK RESOURCE AND RATES



GENERATIONS



rate decreases. Science data will be downlinked using one 8-hour ngVLA contact per week. At 50 years, Interstellar Probe will still be downlinking 0.142 Gbit of data per week.

3.2.1.8 Interstellar Phase to 1000 au

After operating for 50 years, Interstellar Probe will continue farther into interstellar space. It will take approximately another 92.5 years to reach 1000 au. During that time, Interstellar Probe will continue to operate continuously with instruments on and collecting data as described in Section 2 for as long as possible as system performance allows. There will be minimal commanding approximately once per month. Science data will be downlinked using one 8-hour ngVLA contact per week. At 1000 au, Interstellar Probe will be able to return 17.7 Mbit/week of science data using one 8-hour ngVLA contact per week.

3.2.2 Telecommunications

3.2.2.1 Downlink

The expected spacecraft antenna, ground stations, and contact plans for the mission phases are shown in Table 3-4.

The following radio frequency (RF) assumptions were used to develop the Interstellar Probe concept of operations:

- The LGA antenna will be used at launch and for first contact.
- The MGA will be used during the cruise to Jupiter and to monitor the JGA.
- Interstellar Probe switches to using the HGA after the JGA.
- The DSN 34-m antennas are used for the first 10 years of the mission out to a solar distance of 70 au.

Table 3-4. Interstellar Probe telecommunications coverage.

Mission Phase	Spacecraft Antenna	Ground Station	Contact Plan
Launch and checkout	Low-gain antenna (LGA), medium-gain antenna (MGA)	DSN 34 m	Continuous for 1 week, daily contacts 8 hours for 3 weeks, 5× 8 hours/week for 1 month
Cruise to Jupiter	MGA	DSN 34 m	3× 8 hours/week
JGA	MGA, HGA	DSN 34 m	5× 8 hours/week for 4 weeks 7× 8 hours/week for 3 weeks (week before, week of, and week after)
Wire antenna deployment	HGA	DSN 34 m	Continuous coverage during deployments
Heliosphere phase	HGA	DSN 34 m, 2× 34 m, 4× 34 m, ngVLA (>70 au)	3× 8 hours/week (DSN) 1× 8 hours every 2 weeks (ngVLA)
Heliosheath phase	HGA	ngVLA	1× 8 hours every 2 weeks
Interstellar phase to 50 years	HGA	ngVLA	1× 8 hours every 1 week
Interstellar phase >50 years	HGA	ngVLA	1× 8 hours every 1 week

- DSN 34-m antennas arraying using two stations beginning in the fifth year of the mission at a solar distance of 31 au.
- DSN 34-m antennas arraying using four stations beginning in the seventh year of the mission at a solar distance of 40 au. (70-m stations may also be used when available.)
- The ngVLA is available for use after the first 10 years of the mission.

3.2.2.2 Uplink

Estimated uplink for the mission phases is shown in Table 3-5.

Through the 50-m wire antenna deployment, uplink commanding will be performed as required for the commissioning and JGA-related activities. After Interstellar Probe begins the heliosphere phase, the need for commanding becomes more infrequent. Uplink is currently planned for once a month based on the nominal 8- to 10-week negotiated DSN schedule cadence. However, given that Interstellar Probe operations are simple and infrequent, the 1-month time between uplinks may be able to be increased if the schedule is known farther in advance. For example, the most frequent activities in the command sequence will be configuring the spacecraft for downlink contacts and playing back science data. If the times of the downlink contacts in the negotiated schedule could be guaranteed earlier than the normal 8–10 weeks, the duration of the command sequence could be extended and fewer uplink contacts would be required. Using less frequent uplink contacts should be phased in as the mission continues. This also assumes that long-range downlink contact schedules may be negotiated with the ngVLA. The uplink data rate will be 2 kbps through 375 au, which encompasses the entire 50-year nominal mission. After 375 au, the uplink data rate decreases and will be 250 bps at 1000 au. These uplink data rates at range assume the use of an 80-kW, 70-m DSN station as well as uplink forward error correction.

Table 3-5. Interstellar Probe uplink plan.

Mission Phase	Uplink Plan
Launch and checkout	Daily (1 month) 5 days per week (1 month)
Cruise to Jupiter	1 per month (for baseline command loads)
Jupiter flyby	As required for targeting TCMs
Wire antenna deployment	1 month as required for wire antenna deployments
Heliosphere phase	1 per month
Heliosheath phase	1 per month
Interstellar phase to 50 years	1 per month
Interstellar phase >50 years	1 per month

3.2.3 Data Management

Science data are recorded on or transferred to the spacecraft solid-state recorder by the instruments. Data are played back during every contact with the ground. Much more science data will be recorded than can be played back. Because of this, a science data selection plan will be required. The data to be downlinked may be selected autonomously onboard the spacecraft based on selection criteria or by downlinking survey data, then requesting the data of interest to be downlinked. The expected science data volume downlinked as Interstellar Probe travels farther away from Earth is shown in Table 3-6. The data in the table assume 8-hour contacts.

Table 3-6. Interstellar Probe downlink volume.

Mission Phase	Downlink Data Volume (Bits/Week)	Solar Distance (au)	Contacts
Heliosphere phase	1.98E+10	5.4 (post-JGA)	3 contacts per week, using DSN 34-m antennas
	5.87E+08	70	3 contacts per week, using an array of four DSN 34-m antennas
	1.79E+09	70	1 ngVLA contact every 2 weeks
Heliosheath phase	1.06E+09	90	1 ngVLA contact every 2 weeks
	6.14E+08	120	1 ngVLA contact every 2 weeks
	1.43E+08	250	1 ngVLA contact every 2 weeks
Interstellar phase	2.83E+08	250	1 ngVLA contact every week
	1.42E+08	352 (50 years)	1 ngVLA contact every week
	1.77E+07	1000	1 ngVLA contact every week

In addition, CCSDS File Delivery Protocol (CFDP) or a similar protocol will be used for downlinking so that automatic retransmit requests are used for dropped data.

3.2.4 Concept Maturity Level

Concept maturity levels (CMLs) are used by NASA to provide a tool to effectively advance mission concept designs as well as to assess the current state of mission concepts (Wessen et al., 2013). The Interstellar Probe concept is at CML 4, a specific design and cost that returns the desired science selected within the trade space and defined down to the level of major subsystems with acceptable margins and reserves. CML 4 is consistent with expectations for concept studies considered in Decadal Surveys.

3.2.5 Technology Readiness Level

Generally, the flight system included in the Interstellar Probe concept is at high TRL (NASA, 2012), and nearly all components have flight heritage. Exceptions to this are as follows:

- Payload: While all elements of the example payload are based on previously flown instruments, improvements to some instruments are required or desired for Interstellar Probe. Descriptions of development efforts, if any, for each instrument are included in Section 4.
- Spinning Star Tracker: The Interstellar Probe flight system is a spinning spacecraft that includes star trackers. No manufacturer currently offers a star tracker designed for use on a spacecraft spinning at a few revolutions per minute as discussed in this concept study; however, at least one manufacturer is working to rebuild and modify a previously existing star tracker intended for spinning spacecraft based on the star tracker used on the New Horizons mission. We expect that this unit will be available in the next several years, well before it would be needed for Interstellar Probe.
- Galvanic SpaceWire Implementation: The Interstellar Probe concept includes a galvanically isolated SpaceWire bus implementation for fault tolerance; galvanic isolation prevents a failing component from causing a bus failure, allowing other components to continue communicating across that data bus. Currently, galvanic SpaceWire implementations have

been demonstrated in a laboratory environment, and so are at TRL 4. We expect that Interstellar Probe will achieve TRL 6 by Preliminary Design Review (PDR) with minimal difficulty, but if unforeseen technical challenges occur, the mission can use the standard TRL 9 SpaceWire bus implementation to accomplish the mission.

- **Next-Generation Radioisotope Generator:** NASA is currently developing the Next-Generation Radioisotope Thermoelectric Generator (NextGen RTG) through the Radioisotope Power Systems (RPS) Program at Glenn Research Center. The RPS Program is on track to provide the first flight-qualified NextGen RTG by 2028, well before the 2036–2041 time frame when Interstellar Probe would require units. The NextGen RTG is based on the general-purpose heat source (GPHS) RTG most recently flown on New Horizons.
- **Electronics Lifetime:** As discussed in Appendix F, methods for screening and qualifying electronic components to the Interstellar Probe lifetime are in development. These sections provide more detail on how the Interstellar Probe project will address this issue.

3.3 Launch Vehicle

The intended Interstellar Probe mission trajectory would require a very high C3 range (200–400 km²/s²) with either existing or near-existing launch vehicles and upper stages. The Space Launch System (SLS) will provide the highest super heavy-lift performance available with near-existing launch vehicles (Creech, 2019; Creech et al., 2019; Stough et al., 2019). Based on experience with New Horizons and Parker Solar Probe, the Atlas V and Delta IV Heavy launch vehicles were shown to perform insufficiently to accomplish Interstellar Probe and were therefore eliminated from further study. Several upper-stage configurations with a proven flight record were examined to determine the highest possible launch mass for a likely interstellar probe concept (with the performance results in Figure 3-4). Over the very high C3 ranges, one clear curve (red dashed line in Figure 3-4) emerges with the highest usable payload system mass (or possible Interstellar Probe spacecraft mass) over other configurations. Thus, the preferred launch vehicle configuration consists of an SLS Block 2 with an Atlas V Centaur third stage and a Northrop Grumman STAR 48BV fourth stage. Figure 3-5 shows possible stacks of the stages in an SLS Long Shroud with a significant volume remaining in the shroud for a spacecraft such as the concept developed for Interstellar Probe.

Other super heavy launch vehicles are in development and may be operational in the time frame needed for Interstellar Probe, including launch vehicles from SpaceX, Blue Origin, and United Launch Alliance. To date, performance information for these planned systems has been difficult to obtain and will likely not be determined in the immediate future. Because the SLS Block 2 has proven sufficient to meet the requirements of Interstellar Probe and is on track for use before the needed time frame, we have baselined use of the SLS as described above. However, if another launch vehicle does become available and is selected for Interstellar Probe, the mission concept presented here can be performed with no significant modification.

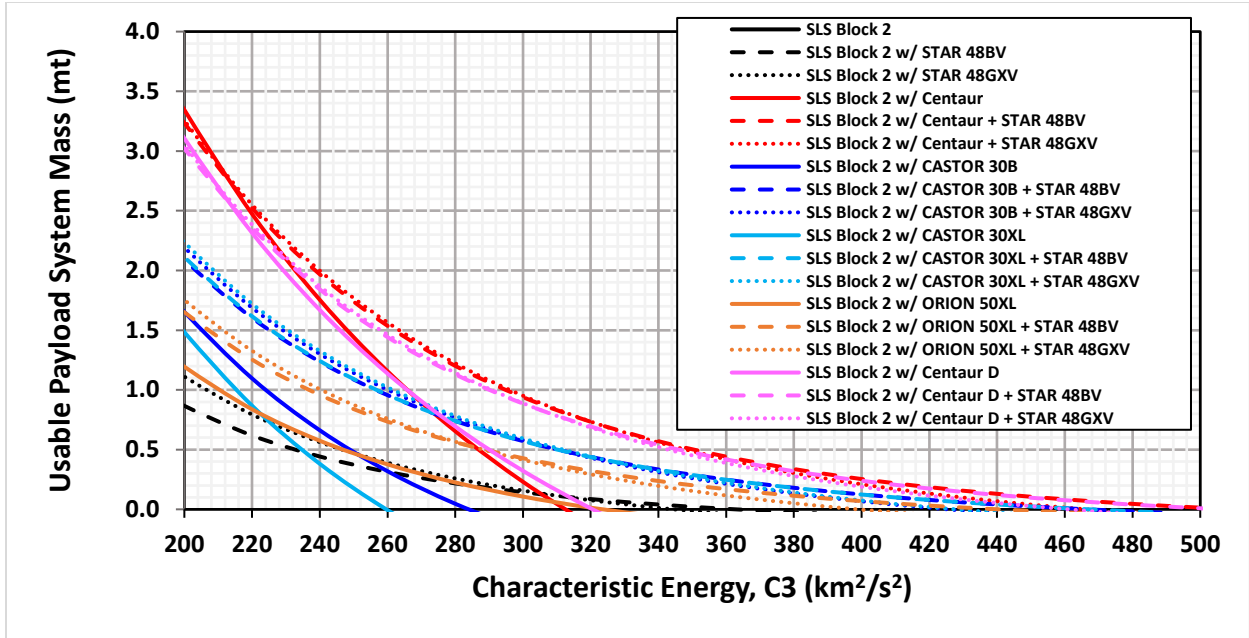


Figure 3-4. SLS Block 2 high-range launch curves expected for a likely Interstellar Probe mission (Creech et al., 2019; Creech et al., 2020). (Reprinted from Kinnison et al. (2021) with permission; © IEEE.)

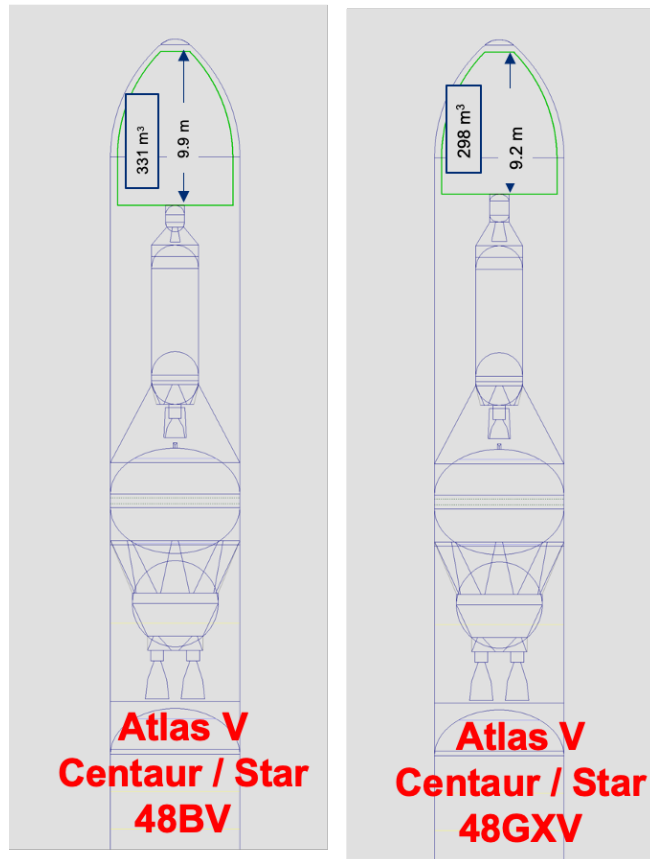


Figure 3-5. SLS stack configurations including possible third and fourth stages. (Reprinted from Kinnison et al. (2021) with permission; © IEEE.)

3.4 Section 3 References

- Creech, S.D. (2019) *Space Launch System - Payload opportunities for lunar exploration, science missions* (Funding Grant NM07AA70C). Washington, D.C.: Center, M.S.F.
- Creech, S.D., Robinson, K.F., Stough, R.W. (2019) *NASA's Space Launch System - Payload opportunities for lunar exploration, science Missions*. Paper presented at the International Astronautical Congress (IAC), Washington, D.C.
<https://ntrs.nasa.gov/citations/20190033316>.
- Kinnison, J., Schlei, W., Rogers, G., Copeland, D., Ashtari, R., Rose, C., Congdon, E., Napolillo, D., Cocoros, A., Brandt, P. (2021) *Interstellar Probe: A Practical Mission to Escape the Heliosphere*. In 2021 IEEE Aerospace Conference (50100), IEEE.
- McComas, D.J., Allegrini, F., Bochsler, P., et al. (2009) Global Observations of the Interstellar Interaction from the Interstellar Boundary Explorer (IBEX). *Science* 326(5955), 959-962.
doi: 10.1126/science.1180906
- NASA (2012) Technology Readiness Level. Retrieved from
https://www.nasa.gov/directorates/heo/scan/engineering/technology/technology_readiness_level.
- Schlei, W., Atchison, J., Gomez-Cano, B., Lathrop, B., Villac, B. (2021) *Pragmatic Trajectory Options Applicable to an Interstellar Probe Mission*. In 2021 IEEE Aerospace Conference.
doi: 10.1109/AERO50100.2021.9438398
- Stough, R.W., Hitt, D., Holt, B., Philips, A., Patrick, M. (2019) *Supporting Material for APL's Interstellar Probe Final Report* (M20-7868). NASA Technical Reports Server.
- Wessen, R.R., Borden, C., Ziemer, J., Kwok, J. (2013) *Space Mission Concept Development Using Concept Maturity Levels* Jet Propulsion Laboratory.

4. Science Implementation

The primary goal and objectives of Interstellar Probe outlined in Section 2 flow to investigations and measurement requirements that can all be addressed by measurements using existing technologies. In this section, we outline each measurement, including its relevant objectives, measurement and mission requirements, example instrumentation, associated trades, and suggestions for enhancing instrument technology developments to maximize the science return. Mass and power allocations were fixed in the 3rd Interstellar Probe Exploration Workshop (November 2020) using the example instrumentation outlined here. Fixed resource allocations are enforced to ensure a realistic exercise in trades to better serve a future Science and Technology Definition Team (STDT) where such trades will be part of the charter to define a payload that ultimately will fly. Science trades associated with different flyout directions are addressed. The notional, fixed resource allocation in mass has led to an example trade study that is documented here together with the resulting example scientific payload. Here we also summarize the accommodation study. Notional science operations throughout the course of the prime mission and beyond are laid out. As discussed in the previous section, the data volume is ultimately constrained by the onboard communication and ground network. In this section, we demonstrate how the resulting available data rates and volumes are sufficient to make sure all required data are downlinked.

Instrument *technologies* that exist today are sufficient to address the science. However, because Interstellar Probe is exploring a new territory of space, none of the developed instruments to date are completely optimized for this new environment. Optimizations include geometrical factor, sensitivity, signal-to-noise ratio (SNR), field of view (FOV) and collimation. It is important to note that it is beyond the scope of this study to define and design specific instrumentation (that is the task of a future STDT); instead, we outline example heritage instrumentation to inform the current capabilities and resource allocations, against which we describe trades and optimizations.

4.1 Measurements

4.1.1 Magnetic Fields

- Weak fields of the very local interstellar medium (VLISM) require low-field, sensitive, and stable measurements.
- This is achieved by two fluxgate magnetometers on a 10-m boom with a robust cleanliness program.

Magnetic Field Subsystem (MAG)

Measurement Objectives	Magnetic field magnitude and direction from the inner heliosphere out to the VLISM
Dynamic Range	0.01–100 nT (three components)
Sensitivity	0.01 nT
Cadence	≤60 s

Sampling Rate	≤100 Hz turbulence and reconnection
Mass Allocation	0.6 kg for two fluxgates, 4.2 kg for 10-m boom
Power Allocation	5.7 W, including two survival heaters
Data Rate	10–1000 bps
Mission Requirement	Spinning spacecraft with spin period ≤60 s
Accommodation	Two fluxgate magnetometers (FGMs) on 10-m boom with cleanliness program

4.1.1.1 *Magnetometer (MAG) Investigation*

Measuring the vector magnetic fields in the outer heliosphere and the local interstellar medium (LISM) is critical for understanding the global shape and nature of the heliosphere (Science Question 1.1) and its interaction with the VLISM (Science Question 1.2). The Voyager 1 and 2 in situ magnetic field measurements in the VLISM revealed smooth but strongly draped field lines. Measurements of the magnetic field strength and direction well beyond the heliopause (HP) are essential to identify the interstellar magnetic field (ISMF) properties (Science Question 1.3) and the detailed mechanisms of how the heliosphere interacts with the VLISM (Science Question 1.2). Measuring the magnetic field orientation in the VLISM is also critical to distinguish between different ribbon-generation mechanisms (Objective 1.1.5). In general, magnetic field measurements are critical to properly understand charged-particle properties. The relative angle between the particle propagation and the local magnetic field, known as pitch angle, provides important information on the source and distance of the particle energization.

4.1.1.2 *Measurement Requirements*

The lowest fields measured by the Voyager spacecraft reached as low as 0.05 nT. Therefore, vector components as low as 0.01 nT have to be measured reliably and even lower to address the role of turbulence. To identify the mechanisms responsible for the interaction of the heliosphere with the interstellar medium (Clarke et al., 2017) and determine the pitch-angle distribution of charged particles, the full vector magnetic field has to be measured. The outer heliosheath magnetic field has relatively low variability on the 48-second scale of the Voyager measurements (see Figure 4-1). Thus, a uniform 10- to 60-second measurement cadence is sufficient. In addition, the decades-long mission necessitates a very high temporal stability of the instruments.

To measure the extremely small magnetic fields of the outer heliosphere, a stringent magnetic cleanliness program has to be implemented for the spacecraft and for all the instruments.

Such a program has been successfully executed recently for the Magnetospheric Multiscale (MMS) mission (Russell et al., 2016) and for the outer heliospheric mission Cassini (Narvaez, 2004). To further reduce the impact of spacecraft-generated fields on the science data, magnetometers are typically mounted on a boom away from the spacecraft. The 13-m Voyager magnetometer booms with two fluxgate magnetometers at different distances to observe the differential spacecraft fields were sufficient to reach an accuracy of ~0.1 nT. Occasional spacecraft rolls around the spacecraft–Earth axis provide additional calibration points for two of the three components. The Voyager spacecraft needed to perform such roll maneuvers every 30–60 days to maintain the required accuracy.

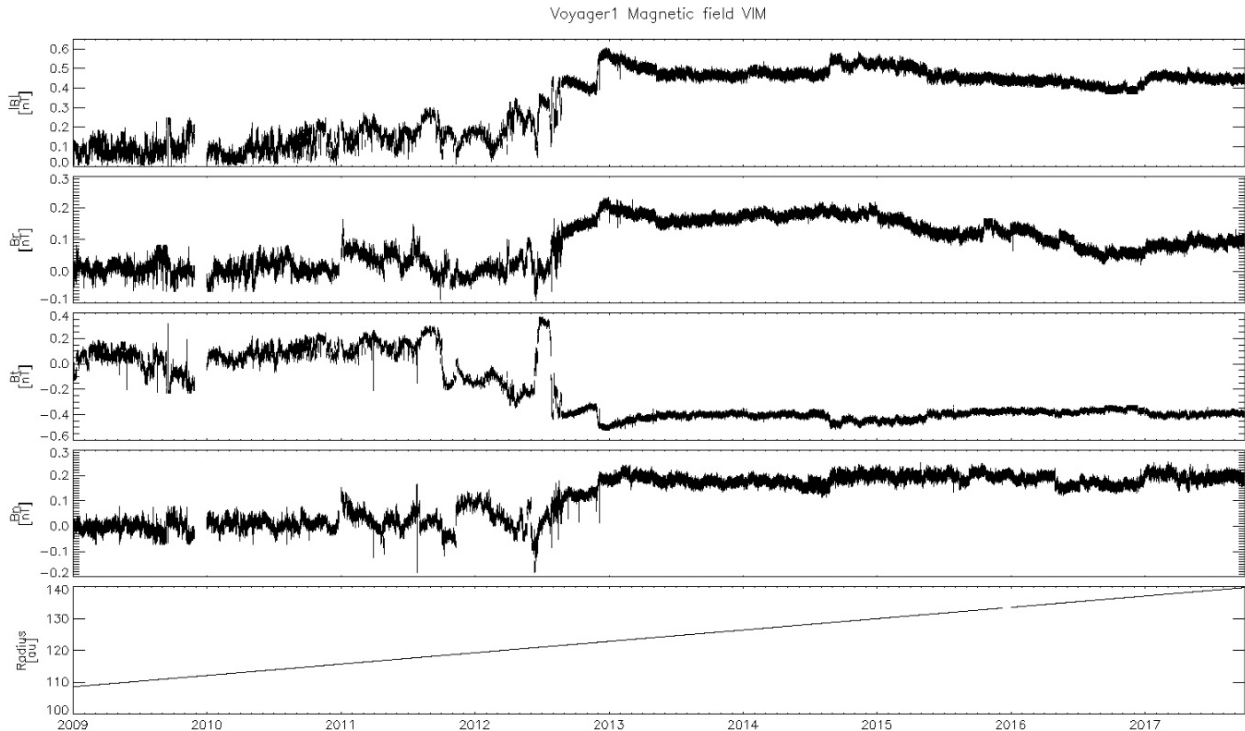


Figure 4-1. Voyager 1 magnetic field measurements from 2009 to 2018 covering both the inner and outer heliosheath. (Image courtesy of A. Szabo.)

4.1.1.3 Example Instrumentation

Traditional fluxgate magnetometers are reliable instruments for long-term, low-power operation and can meet the requirement to measure low field levels at high cadence. However, they cannot provide absolute measurements and require periodic in-flight calibration to mitigate their intrinsic drifts. Atomic helium, rubidium, and Overhauser magnetometers can measure the magnetic field in an absolute sense with a high sensitivity of 1 pT/VHz and an absolute accuracy of 0.01 nT (Acuña et al., 2002; Gilles et al., 2001) but can only do so at high field strengths (hundreds to thousands of nanoteslas), and their long-term operation in space has yet to be demonstrated. A dual fluxgate magnetometer configuration such as on Voyager would therefore be a reliable option on an interstellar probe.

The heritage for MAG mass and power allocations comes from MMS, which flew two fluxgate magnetometers that totaled 0.6 kg and used 1.7 W of power (Russell et al., 2016). Survival heaters would require ~4 W, for a total of 5.7 W for the instrument. The estimated mass for the boom (4.2 kg) was scaled from the Mercury Surface, Space Environment, Geochemistry, and Ranging (MESSENGER) magnetometer boom, which was 3.6 m and 2.66 kg (Anderson et al., 2007; Bale et al., 2016). Of note, Cassini also flew a vector helium and fluxgate magnetometer (Dougherty et al., 2004; Smith et al., 2001).

4.1.1.4 Instrument Trades

Ideally, at least two fluxgate magnetometers would be flown on the spacecraft, located on the same boom well-spaced from the spacecraft and with a small distance between the two sensors,

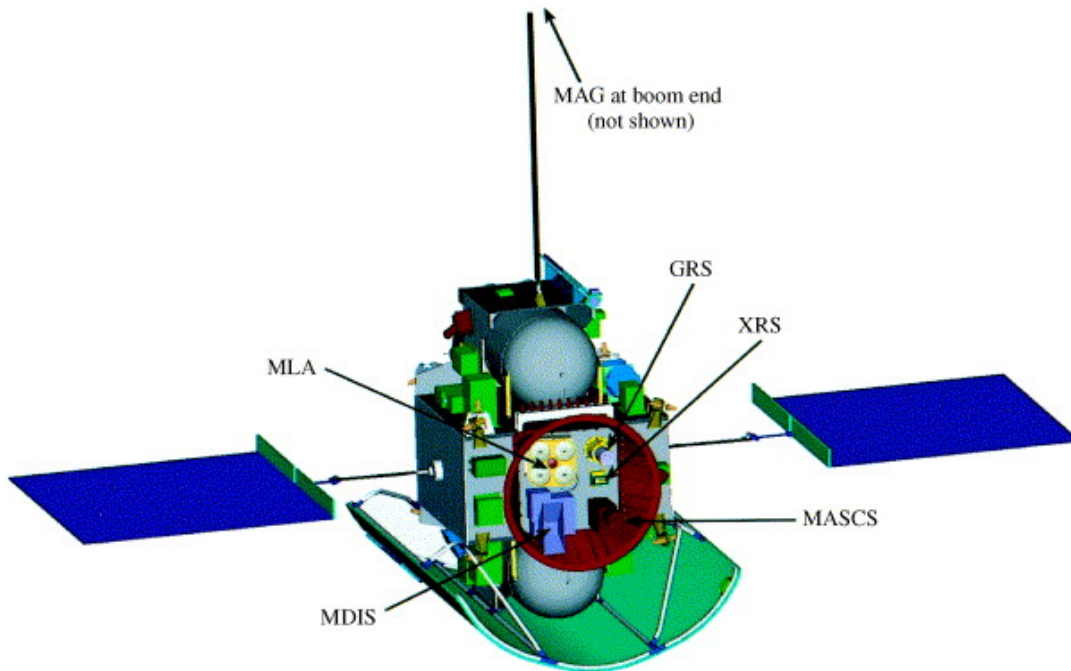
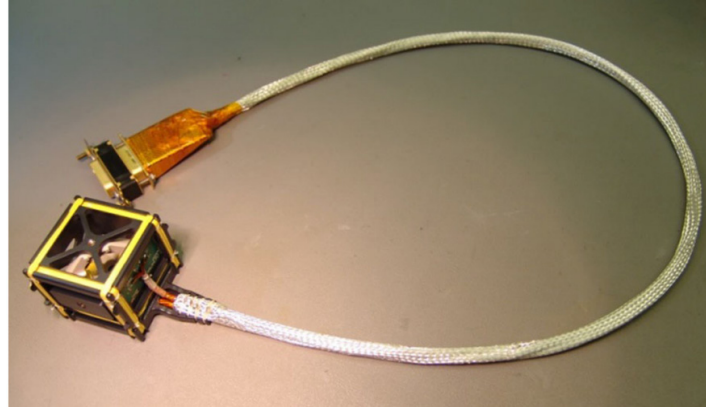


Figure 4-2. (Top) MMS fluxgate sensor with harness, as shown in Figure 3 of Russell et al. (2016). (Bottom) MESSENGER spacecraft with the magnetometer boom deployed, along with other labeled payload instruments, as shown in Figure 7 in Gold et al. (2001) (reprinted with permission from Elsevier). GRS, Gamma-Ray Spectrometer; MAG, Magnetometer; MASCS, Mercury Atmospheric and Surface Composition Spectrometer; MDIS, Mercury Dual Imaging System; MLA, Mercury Laser Altimeter; XRS, X-Ray Spectrometer.

because the ability to correct for spacecraft-generated fields will be limited with one sensor. The type and configuration of the fluxgate magnetometers and accompanying electronics should be chosen such that they provide the lowest noise measurements with the greatest long-term offset stability, because Interstellar Probe will be sampling increasingly smaller magnetic fields during its long transit to the VLISM. However, given the length of the mission, it should be noted that long-duration observations could allow for the calibration of spacecraft-generated fields without the second sensor, should one sensor fail. Another avenue of consideration for calibration and correction of spacecraft-generated fields is the use of gradiometry via multiple lower-grade magnetometers flying with an outboard high-precision fluxgate magnetometer.

4.1.1.5 Enhancing Technology Development

The main issues for magnetometers that arise include the noise levels and long-term stability as the Interstellar Probe encounters weaker and weaker magnetic fields in the journey through the heliosphere and out to the VLISM. With the exception of planetary magnetospheres and bow shocks, as well as transient events such as merged interplanetary coronal mass ejections (ICMEs) and corotating interaction regions, the weak VLISM fields are challenging to measure. The stability of the fluxgate internal zero levels could contribute to limitations on measurements. Low-field absolute magnetometers are the subject of active research and may become an option in the future, serving as a mitigation for these issues.

4.1.2 Charged Particles

Among the top scientific objectives of an interstellar probe mission is the characterization of the complex interactions of the plasma, magnetic field, and neutral interstellar gas taking place from ~ 30 au (the distant supersonic solar wind), through the heliosheath, out to the pristine ISM. The Voyagers' in situ measurements of the magnetic field and plasma waves, as well as their observations of charged particles (suprathermal tails, anomalous cosmic rays [ACRs], and galactic cosmic rays [GCRs]), provided a glimpse of these phenomena but also uncovered more surprises, as discussed above. Ultimately, the Voyager observations were only partial and sometimes of low resolution, leaving great observational gaps in energy and composition considering what we now know about the dynamic ranges and complexity of the particle environments, spanning fully from thermal and suprathermal populations to pickup ions (PUIs) to accelerated energetic particles and cosmic rays, in the outer heliosphere and VLISM. Collectively, the charged-particle suite contributes to all the scientific objectives called out in the science traceability matrix (STM). Whether investigating the nature of the heliospheric termination shock (TS) and its role in ACR acceleration, turbulence in the heliosheath, magnetic reconnection and the force balance at the HP, the nature of plasma in the pristine ISM, or the isotopic tracers of GCR source regions, charged-particle observations are required, and such instrumentation is critical to a future interstellar probe mission funded by NASA's Heliophysics Division.

Solar wind plasma floods the heliosphere in an ever-present outward stream of supersonic, turbulent flow until it reaches the TS (a reverse shock) and suddenly transitions to a slower, but still supersonic, flow in the heliosheath. Large-scale solar wind transients, such as ICMEs and corotating stream interaction regions (CIRs/SIRs) complicate this picture, enabling shock–shock interactions and periodically bursting out through the heliopause into the VLISM, extending the heliosphere's influence into interstellar space. We know now *indirectly* (e.g., Smith, 2001) from Voyager observations that PUIs play a dominant role in the force balance at the TS, in the heliosheath, and at the HP. That evidence is supported by observations beyond Pluto by the Solar Wind Around Pluto (SWAP) instrument on New Horizons (e.g., Zank et al., 2018). PUIs are created throughout the heliosphere by direct photoionization and electron impact ionization of interstellar neutrals (ISNs) in the heliosphere or charge exchange between solar wind plasma and ISN gas particles in both the heliosphere and the VLISM. Once ionized, PUIs get “picked up” by the solar wind convection electric field and rapidly accelerated up to twice the solar wind speed. PUIs are mostly singly charged and have unique velocity distribution functions, with a sharp cutoff at twice the bulk speed of the local

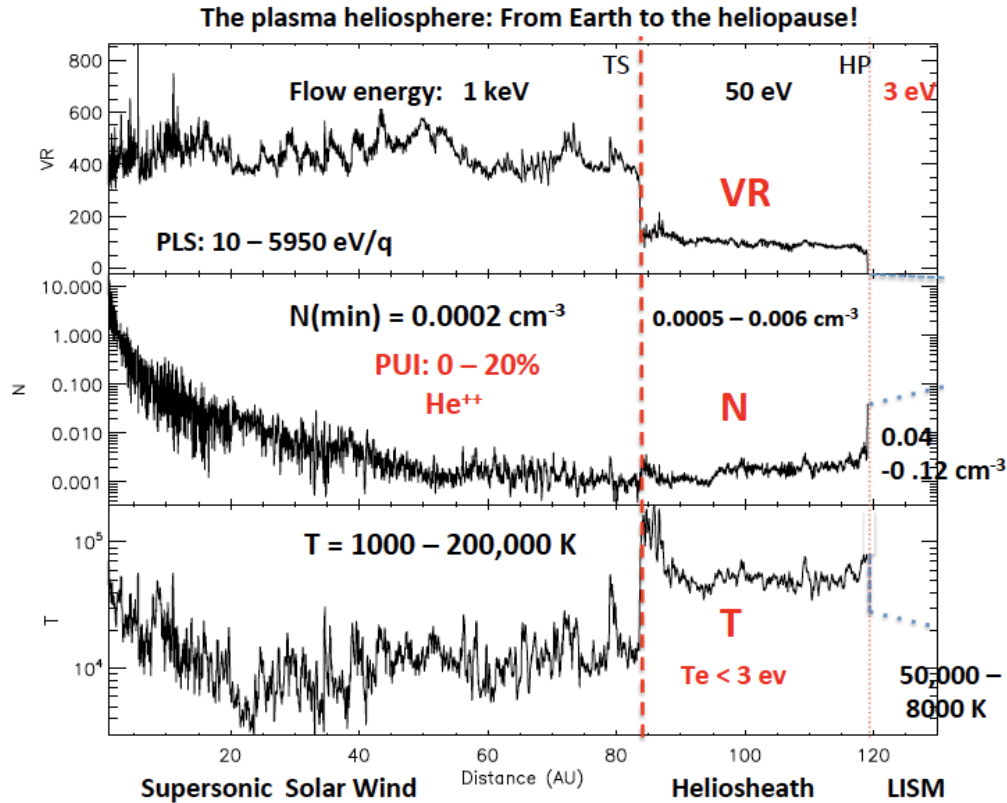


Figure 4-3. Voyager observations of plasma radial velocity, density, and temperature from Earth to the heliopause. (Figure courtesy of John Richardson, MIT.)

plasma. PUIs play a dominant role in the dynamics of the outer heliosphere and LISM because they carry most of the particle pressure in the increasingly tenuous solar wind at such large heliocentric distances (Gloeckler & Fisk, 2015). Their crucial role in the dynamics of the outer heliosphere and the LISM could not be studied with Voyager 1 and 2 because PUIs were and are not measured by those spacecraft. Therefore, it is essential for Interstellar Probe to determine the relative roles between the thermal plasma, PUIs, and the energetic particles in driving forces governing the balance between the solar wind and plasma in the outer heliosphere and VLISM as well as identify any other thermal populations over the energy range of electronvolts to hundreds of kiloelectronvolts, considering also that Voyager left a gap at 5–30 keV.

Thermal and suprathermal plasmas (up to tens of kiloelectronvolts) are traditionally measured by Faraday cups (FCs) to determine plasma flux and moments or electrostatic analyzers (ESAs) to determine the intensity versus energy per unit charge (E/q) of incident ions and electrons. When post-acceleration and time-of-flight (TOF) measurements are added after an ESA's electrostatic deflection to determine an incident ion's velocity, the ion's mass, energy, and charge can be uniquely identified. After Voyager 2 crossed the HP, its FCs—the Plasma Subsystem (PLS) (Bridge et al., 1977; Richardson & Wang, 2012) were not pointed directly into the ram direction and so the observed currents were close to the instrument threshold, resulting in uncertain estimates of the flow velocity, temperature (≤ 3 eV), and density. A future plasma instrument must be sensitive enough to measure the very cold interstellar plasma while still offering the dynamic range required to observe the solar wind. Fortunately, preliminary analysis has shown that the expected level of

spacecraft charging on the baseline design of the Interstellar Probe spacecraft is only approximately +5 V and very steady, meaning that it is feasible to be able to measure the cold interstellar plasma, especially when measuring in the ram direction (accounting for both spacecraft motion and the flow of the interstellar plasma). To measure both the cold, tenuous plasma in the ISM and the solar wind *plus* PUIs into the suprathermal energy range, two dedicated instruments have been baselined to ensure the thermal plasma (baselined plasma subsystem [PLS] instrument) and PUIs (baselined PUI instrument) are *both* measured sufficiently to satisfy the top-level science requirements for Interstellar Probe.

Particles with energies above ~ 20 keV can be detected directly by their energy deposits in solid-state detectors (SSDs), which can be built into finite FOV, stacked-detector telescopes using multiple detectors that enable directional distributions over an extended energy range. The upper energy range is directly related to mass because material is needed to totally stop the particle in the detector to obtain the measurement. Maximum angular coverage could be achieved by using a spinning platform and multiple telescopes to cover several look directions simultaneously. Mass of incident particles can be determined when such SSD systems are further combined with TOF segments (providing a measure of incident particle velocity that, combined with the measured energy from the SSDs, uniquely identifies the particle mass) or differential energy deposits in stacks of two or more SSDs (because those energy deposits follow distinct, mass-dependent distributions versus distance in a material, predicted accurately for ions above ~ 1 MeV by the Bethe-Bloch formula). Several such instruments have flown, such as the Solar Isotope Spectrometer on Advanced Composition Explorer (ACE; Stone et al., 1998), EPI-Lo and EPI-Hi on Parker Solar Probe (McComas et al., 2016), Pluto Energetic Particle Spectrometer Science Investigation (PEPSSI) on New Horizons (McNutt et al., 2008), and Low-Energy Charged Particle (LECP) on Voyager (Krimigis et al., 1977).

4.1.2.1 Plasma Subsystem (PLS)

- Accurate thermal to suprathermal solar wind and ISM plasma distributions
- Derived moments critical to the physics of the outer heliosphere, TS, heliosheath, heliospheric interaction with the VLISM, and nature of the LISM

Plasma Subsystem (PLS)

Measurement Objectives	Plasma moments of major species and electrons in the solar wind, heliosheath and VLISM, light PUIs
Geometrical Factor	$>1e-3 \text{ cm}^2 \text{ sr}$
Signal-to-Noise Ratio	>10
Cadence	From 60 s at shock crossings
Composition	e, H ⁺ , He ⁺ , He ⁺⁺ , C ⁺ , N-O ⁺ , $\Delta m/m \leq 30\%$, 1–10 amu/e
Energy Range/Resolution	$<3 \text{ eV/e}$ to 20 keV/e , $\Delta E/E \leq 10\%$
Angular Coverage/Instantaneous Field of View/Resolution	$4\pi \text{ sr}$, $\geq 180^\circ \times 10^\circ$, $\sim 20^\circ$
Mass Allocation	8.0 kg
Power Allocation	10 W
Data Rate	0.1–2000 bps
Mission Requirement	Spinning spacecraft

Accommodation

Aperture plane perpendicular to spin axis
 Conductive spacecraft surfaces to minimize potential differences

4.1.2.1.1 PLS Investigation

Plasma physics forms the core of Interstellar Probe’s prime science objectives, and thus, accurate plasma observations are one of the highest priority investigations. Thermal plasma consists of the electrons and ions that are effectively “frozen in” to the local magnetic field and interact self-consistently with the electric and magnetic fields in the plasma. Plasma distribution functions and moments (i.e., density, velocity, temperature, pressure) are required for determining fundamental physical processes such as boundary layer physics (e.g., at the TS and HP), plasma wave generation and propagation, wave-particle interactions, plasma turbulence, magnetic reconnection, transient and embedded plasma structures, and many aspects of particle acceleration.

4.1.2.1.2 Measurement Requirements

The ability to determine plasma moments for major ions and electrons in the VLISM drives the measurement requirements for the PLS example instrument. The net ram speed of VLISM plasma (and gas) lies in the range between 30 and 60 km/s depending on direction. For the first launch opportunity in 2036, 80° off the nose direction, the net ram will be ~30 km/s, which means that proton energy threshold must start at ~5 eV and preferentially <3 eV.

The required geometrical factor can be derived from the estimated proton density, temperature, and ram speed in the regions of interest. For the VLISM, we assume that with a proton density of 0.1 cm^{-3} , temperature of 8500 K, and ram speed of ~30 km/s, the differential intensity js would be in the range of 1^6 at a few electronvolts down to $1e-2 \text{ (cm}^2 \text{ sr s keV)}^{-1}$ at a few tens of kiloelectronvolts. The expected foreground signal count rate S depends on the energy resolution dE and the geometry factor G_s : $S = js * G_s * dE$. Assuming dE to be 10% of the measured energy and a geometry factor of $1e-3 \text{ cm}^2 \text{ sr}$, we get count rates S of 0.5/s and $3e-5/s$. With these assumptions, low energies can be resolved with nearly second resolution, while changes in the higher energies will only be notable on the timescale of days. Given that we do not expect fast changes in the VLISM, such long integration is acceptable.

Given that flow speeds are so slow in the VLISM, PLS may also be able to measure PUIs or nonthermal ions in the VLISM. For ^{20}Ne in the VLISM, we can assume that with a density of $3.25E-5 \text{ cm}^{-3}$ from interstellar PUI measurements (Gloeckler & Geiss, 2004), the ram flux lies in the $100\text{--}200 \text{ cm}^{-2} \text{ s}$ range depending on flyout direction. With an estimated temperature of ~6300 K and accounting for PUIs showing at twice the bulk speed, the resulting differential intensity peaks just below 1 keV with $\sim 1e2 \text{ (cm}^2 \text{ sr s keV)}^{-1}$. With a geometry factor of $\sim 1e-3 \text{ cm}^2 \text{ sr}$ and 30% energy resolution, this would imply a count rate of ~0.03/s, which is sufficient as long as the instrument background rates are ten times lower.

For the heliosheath, we assume a density of 0.004 cm^{-3} , temperature of 10,000 K, and ram speed of 100 km/s (Richardson et al., 2008, 2019). The spectral peak at a few tens of electronvolts will

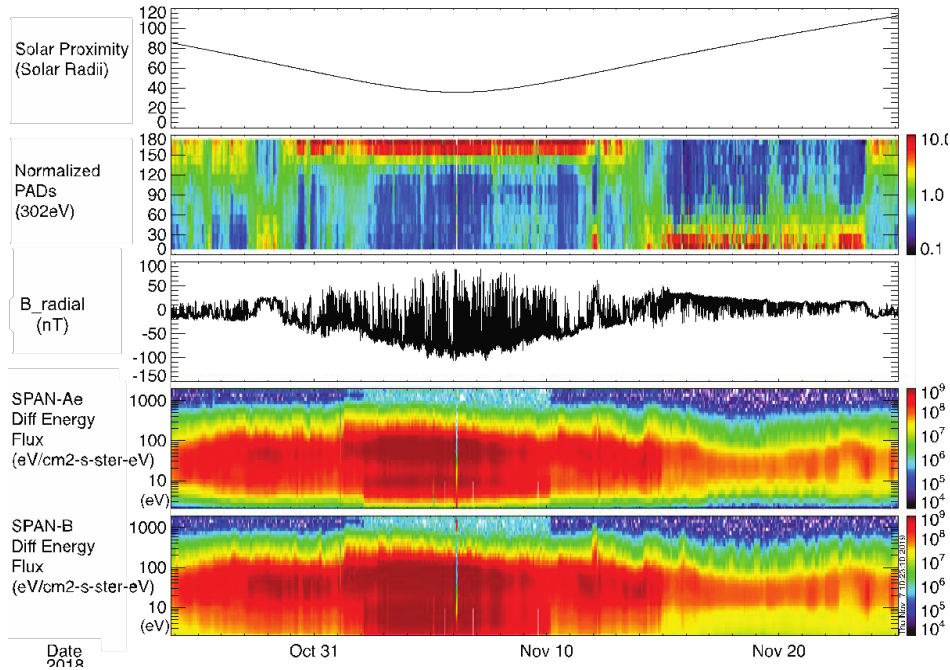


Figure 4-4. The Voyager Faraday cups obtained the only existing plasma measurement in the heliosheath and VLISM, but their pointing made it difficult to accurately determine the required plasma moments of electrons and major ions. Although generally less sensitive, an optimized ESA instrument for electrons and ions can also obtain plasma moments. Although designed for the solar wind, the Solar Wind Electrons Alphas and Protons (SWEAP)/Solar Probe Analyzers (Ocker et al., 2021) dual-head ESA has sufficient resolution and range for this task, as seen from the example data from this first pass of Parker Solar Probe (Whittlesey et al., 2020).

be at $1e5 \text{ (cm}^2 \text{ sr s keV)}^{-1}$, equivalent to a count rate of 500/s. With such a rate, we can expect to calculate plasma moments with a time resolution of ~ 1 second.

For instruments that count particles, such as ESAs (compared to instruments that measure currents, such as FCs), it is important to compare the foreground count rate S with the background noise count rates N , especially in regions such as the VLISM where S will be small. N depends on the penetrating background in the respective environment. We assume here the fit to GCR protons from Burger (2000), which we extend down to 10 MeV as an approximation of the energies where protons penetrate to the detectors. Integrating this function from 10 MeV to infinity yields an integral intensity of $I = 20 \text{ (cm}^2 \text{ sr s)}^{-1}$.

The noise rate also depends on various instrumental details that at this stage can only be estimated. It scales with the geometrical factor G_n of the single detectors used for the omnidirectional detection of penetrating particles. In the case of slab detectors such as a microchannel plate (MCP), G_n is equal to the detector area A_n times 2π (Sullivan, 1971). We assume $G_n = 2 \text{ cm}^2 * 2\pi$. The noise rate on the single detector is then $N_1 = G_n * I \approx 300/\text{s}$. The SNR for VLISM protons is $\approx 1e-3$ and $1e-7$ for $\sim eV$ and $\sim 10\text{-keV}$ energies, respectively. Such low SNR indicates that coincidence measurements will be required to achieve a reasonable SNR.

The overall noise rate for a system that combines measurements from several detectors results from accidental coincidences between the detectors. We assume a triple coincidence system that not just detects a particle but also measures its TOF. The accidental background rate between three detectors that have similar noise rates $N1$ is $N = N3 = 4 * N1^3 * TOF * T$ (Eckart & Shonka, 1938). TOF is the maximum TOF that the instrument can measure. We assume 1000 ns, which can resolve low-energy heavy ions with a TOF path on the order of 1 cm. T is the pulse width of the detectors that we assume as $T = 1$ ns. With these values, we get a triple coincidence background rate of $N \approx 6e-8$, equivalent to $SNR = S/N \approx 1e7$ and $1e3$ for $\sim eV$ and $\sim 10\text{-keV}$ VLISM protons, respectively. This means a triple coincidence system may be needed when using an ESA-type instrument instead of an FC. Even though high energies will need to be integrated for days, they still yield a clean signal.

A sanity check for the above accidental noise rate can be done by comparing to New Horizons/Solar Wind Around Pluto (SWAP), which has a background rate of $N2 = 0.07/s$ (Randol et al., 2013) and uses only a double coincidence. When assuming the instrument values from above, which are different from SWAP's values and its environment, we get $N2 = 3 * N1^2 * TOF \approx 0.2/s$, which is of the same order of magnitude.

The requirement on energy resolution is primarily driven by the required accuracy of the flow speed. In the cold VLISM, 10% energy resolution translates into 10% energy in the bulk flow energy.

The requirement on mass coverage is driven by the objective to determine the distribution function of major thermal ions (and electrons) across the TS and in the heliosheath. The distribution of the major ion species and electrons in the VLISM is also an important measurement to investigate the interstellar plasma flows, densities, and temperatures of major species and electrons that may be an important ionization source.

4.1.2.1.3 Example Instrumentation

Thermal and suprathermal plasmas (up to tens of kiloelectronvolts) are traditionally measured by ESAs to determine the energy per unit charge (E/q) of incident ions and electrons. To resolve mass per charge, post-acceleration and TOF measurements are added after the electrostatic deflection system. FCs should also be considered as a robust alternative, in particular for the VLISM (see details below).

To measure both the cold, tenuous plasma in the ISM and the solar wind *plus* PUIs into the suprathermal energy range, two dedicated example instruments have been chosen for the model payload to ensure the thermal plasma (example PLS instrument) and PUIs (example PUI instrument) are *both* measured sufficiently to satisfy the top-level science requirements for Interstellar Probe.

An ESA+TOF system is used here as an example within the fixed mass allocation of the model payload because it allows for direct composition measurements and because it can likely reach the desired SNR. However, a set of FCs provides a very strong alternative because of their robustness and large geometry factors. See discussion in Section 4.1.2.1.4 below.

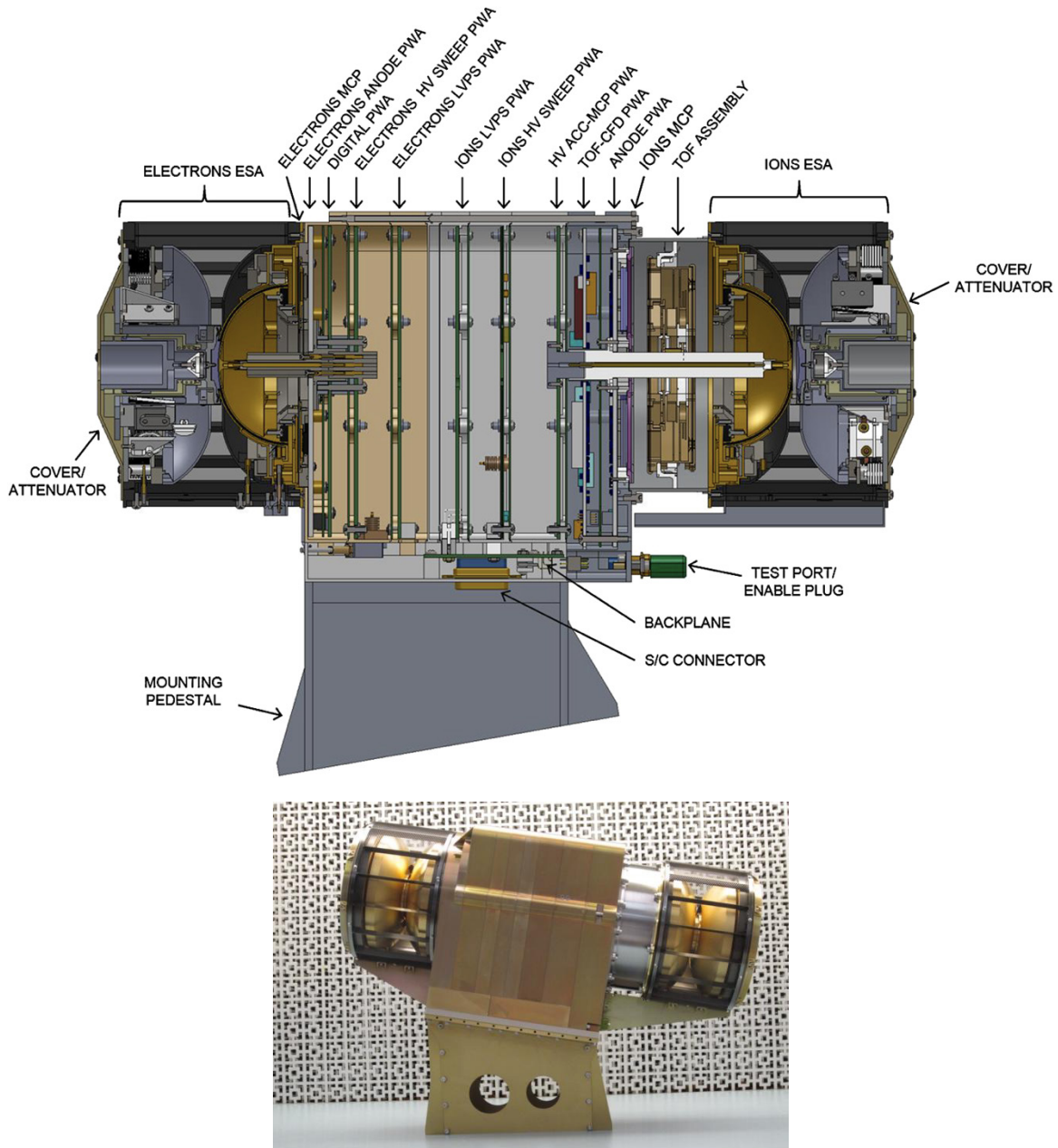


Figure 4-5. (Top) Cross-sectional view of an example ESA measuring plasma electrons and ions with electrostatically sweeping entrance aperture (Kasper et al., 2016). (Bottom) The SPAN-A heads on board Parker Solar Probe (image credit: [Parker Solar Probe SWEAP website](#)).

4.1.2.1.4 Instrument Trades

Maximizing SNR is a high priority for any PLS development. A high SNR can be achieved either by a complex ESA that uses several coincidences or by an FC that includes three cups accommodated at appropriate angles. The SNR is driven by the requirement to resolve major ion species in the VLISM and their bulk properties.

While the geometry factor and SNR ideally should even be larger than required, increasing them also increases mass and complexity and therefore increases cost and lowers reliability.

Considerations of instrument longevity (≥ 50 -year operational lifetime), electronics miniaturization and efficiency, and mass and volume minimization must be detailed and documented.

Careful trades are needed to find an optimum instrument type (ESA versus FC) and design, but the key takeaway is that the PLS observations required for the baseline Interstellar Probe science can be achieved with existing instrument technology.

	Electrostatic Analyzer	Faraday Cup
Geometry factor	Generally small (few $1e-3 \text{ cm}^2 \text{ sr}$, for example, (McComas & Schwadron, 2006). A large geometry factor and high energy resolution are mutually exclusive.	Generally large (tens of $\text{cm}^2 \text{ sr}$, for example, (Grey et al., 2018). Scales with instrument size. Large geometry factor will ensure that bulk properties can be determined, which is critical.
SNR	Measurement technique is sensitive to background, which needs to be compensated through coincidences. ESA likely needs to be combined with a TOF system, to achieve required SNR; see main text.	Measurement technique is not very sensitive to background. High SNR is critical.
Robustness	Complex system.	Simpler system.
Composition	Direct composition measurement when adding a TOF system.	Only indirect composition measurement possible when making assumptions and when the plasma temperature is cold enough. With VLISM parameters, we expect to distinguish elements such as He from Li and Ne from Al, but distinguishing isotopes such as He-3 from He-4 or Ne-20 from Ne-22 may be challenging because Maxwellian peaks of the species overlap.

4.1.2.1.5 Enhancing Technology Development

Although an ESA+TOF system provides direct composition measurements, the geometry factor is relatively small, with room for improvement on SNR for proper measurements in the VLISM. Therefore, enhancements in geometry factor are desirable, as are the implementation of additional coincidence systems to increase SNR. On the other hand, FCs have superior geometry factor and are relatively insensitive to background but provide indirect composition measurements, in particular in the hot heliosheath. Any enhancements in resolving composition in FC measurements would be desirable.

4.1.2.2 Pickup Ion Subsystem (PUI)

- Key to understanding the force balance of the heliosphere, but never directly measured in the heliosheath or VLISM
- Critical for understanding the source of the enigmatic energetic neutral atom (ENA) “ribbon” and “belt”
- Source population of the elusive ACRs
- Geometry factor and SNR need to be enhanced over current-day instrumentation for optimized measurements in the VLISM

Pickup Ion Subsystem (PUI)

Measurement Objectives	Interstellar and inner-source PUI evolution, force balance, heliospheric and VLISM plasma composition, ribbon/belt formation processes
Dynamic Range	1e-1 to 1e4 (cm ² sr s keV) ⁻¹
Geometrical Factor	≥1e-3 cm ² sr (goal >1e-2 cm ² sr)
Signal-to-Noise Ratio	>10
Cadence	0.1–6000 bps
Composition	H, ² H, ³ He, ⁴ He, ⁷ Li, ¹² C, ¹⁴ N, ¹⁶ O, ²⁰ Ne, ²² Ne, Ar, Mg, Si, Fe; distinguish charge states
Energy Range/Resolution	~0.5–78 keV/e, ΔE/E ≤ 10%
Instantaneous Field of View/Angular Coverage	≥90 × 15°, coverage of near-solar wind direction and net ram direction
Mass Allocation	5.5 kg
Power Allocation	7 W
Data Rate	See Section 4.5
Mission Requirement	Spinning spacecraft
Accommodation	Aperture plane perpendicular to spin axis Accommodation to cover PUI in heliosphere and interstellar ram direction

4.1.2.2.1 PUI Investigation

While the physics of PUIs within the inner heliosphere has been previously addressed with Ulysses/Solar Wind Ion Composition Spectrometer (SWICS) and ACE/Solar Wind Ion Composition Spectrometer (SWICS) observations (Allegrini et al., 2005; Geiss et al., 1995; Gloeckler et al., 1992; Schwadron et al., 2000), lack of full 3D velocity distribution function measurements (i.e., arrival directions of ions) and the small geometrical factor of SWICS inhibited the progress and understanding of the particle processes in the heliosphere. For example, neither the origin nor the production mechanism for “inner-source” PUIs has been established (Allegrini et al., 2005; Gloeckler & Geiss, 1996), and although the cosmologically important density of pickup ³He⁺ was measured for the first time with Ulysses/SWICS (Gloeckler et al., 1992), this value had a large uncertainty. New Horizons’ PEPSSI and SWAP instruments are making PUI observations (e.g., Kollmann et al., 2019; Randol et al., 2012), but these instruments were never intended for these measurements. The PEPSSI and SWAP instruments are limited to hydrogen and helium, have limited directional information, and cannot be set in context with coinciding fields or wave measurements. New Horizons should make PUI observations out to around the TS, but even the data there will be difficult to interpret without magnetic field observations detailing the shock itself. Also, New Horizons is not expected to continue operating far into the heliosheath because of power constraints on the spacecraft.

The Interstellar Probe PUI investigation targets the PUIs inside the heliosphere and heliosheath as well as the heavier thermal and nonthermal ion plasma composition of the VLISM, something that is partially enabled by the high plasma ram speeds that range from 30 to 60 km/s for flyout directions perpendicular to the nose to straight out through the nose direction.

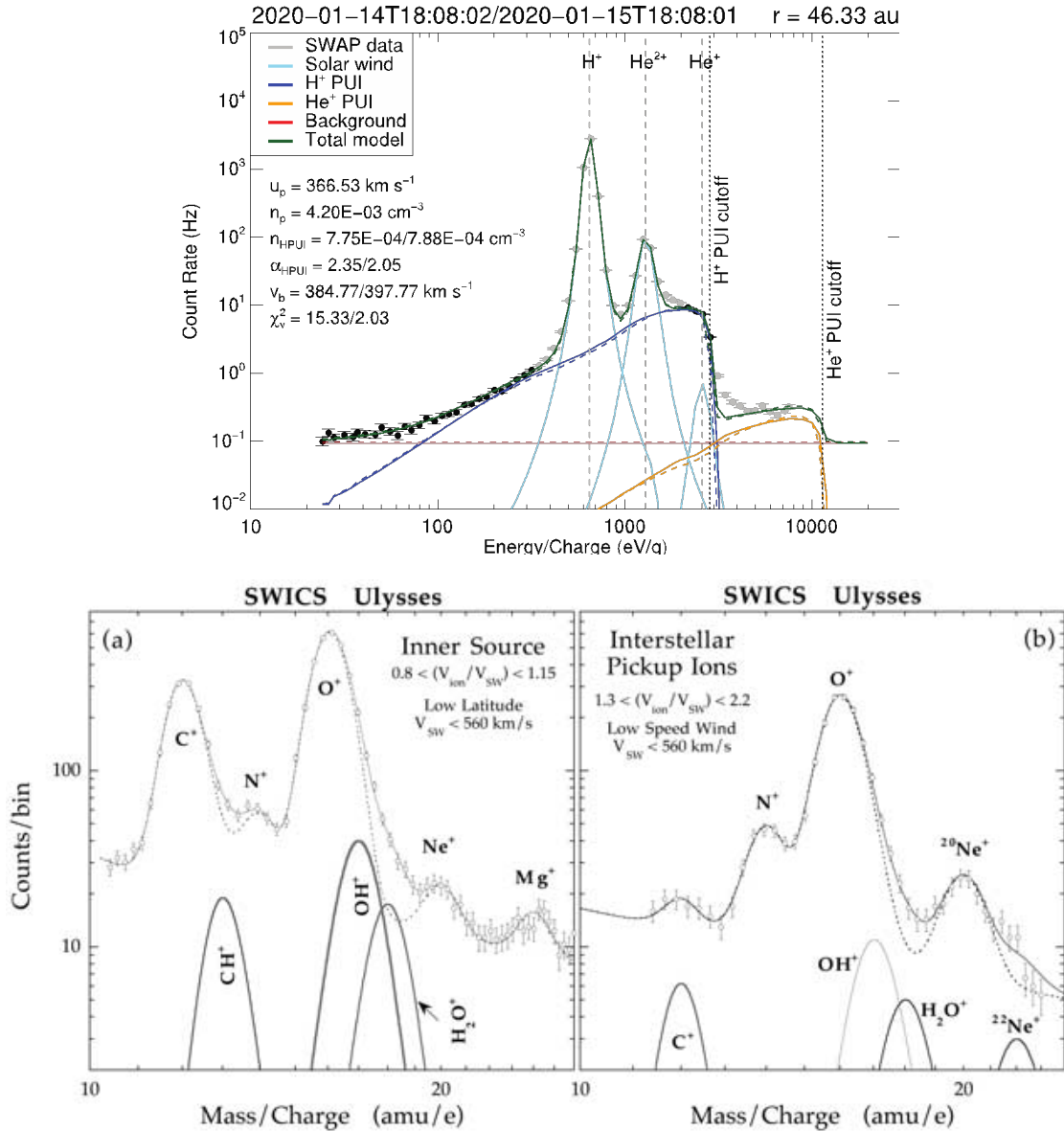


Figure 4-6. (Top) PUI measurements halfway to the termination shock by New Horizons (McComas et al., 2021). (Bottom) PUI measurements by Ulysses/Solar Wind Ion Composition Spectrometer (SWICS) (reprinted from Geiss & Gloeckler (2001) with permission; © 2001 Springer Nature Limited).

4.1.2.2.2 Measurement Requirements

The PUI geometrical factor is driven by the requirement to resolve structures in the heliosheath and to measure interstellar elemental and isotopic composition. Protons in the heliosheath with energies in the 1- to 100-keV range and intensities in the range of 0.1 to 1000 (cm 2 sr s keV) $^{-1}$ (Dialynas et al., 2020), providing an upper bound for what to expect for the heavier PUIs, which have not been measured well to date. With a geometry factor of ~ 0.001 cm 2 sr and 30% energy resolution, we can expect count rates between 0.3 and 0.003/s, meaning that we can resolve protons with minute-to-hour resolution. Extrapolating the suprathermal helium (Krimigis et al., 2003) suggests about a factor of 100 less for pickup helium, which degrades the time resolution

to hours and days. Provided known estimates of PUI in the outer heliosphere and heliosheath, it is likely that a larger geometrical factor will be desirable for better temporal resolution.

In the VLISM, kiloelectronvolt ions are at least an order of magnitude below heliosheath levels. Voyager measurements go to background (e.g., Krimigis et al. (2013)), so no measurements are available. Therefore, the issue is not the geometry factor but the SNR, which will depend on details of the instrument design and can be estimated as described above. We assume here that the PUI instrument detects particles through a combined TOF and SSD measurement. We base our assumptions on SWICS (Gloeckler et al., 1998) and similar instruments, and if we assume areas for the MCPs and SSDs of 10 cm^2 , a TOF window of 1000 ns, and an SSD pulse rise time of $T = 10 \text{ ns}$, we get a triple coincidence rate of $8e-5/s$. Based on the count rate estimates above, we can expect $\text{SNR} \approx 1000$ for kiloelectronvolt protons in the VLISM and ~ 10 for kiloelectronvolt helium, which meets our requirements. However, the SNR is less for heavier or more energetic species, which is insufficient, indicating that careful instrument design is needed.

Energy resolution is driven by resolving the PUI cutoff, which changes ion intensity over a range of 70% of the cutoff energy (e.g., Gloeckler et al., 1995). To measure several points over this range, we require a resolution of 10%.

An adequate FOV is required to cover both the PUIs within the heliosphere and the net plasma ram once in the VLISM. This implies an FOV coverage from near the solar wind direction to the ram direction. For the baseline example trajectory of 80° off the nose, this means an instantaneous field of view (iFOV) of at least 90° to cover both PUIs in the solar wind and plasma composition in the VLISM. However, an iFOV of 180° is preferred such that full-sky angular coverage can be achieved with a spinning spacecraft. For a SWICS-type instrument, this implies a two-head configuration. Future development efforts should also include maximizing iFOV while minimizing mass.

PUI as well as the energetic particle subsystem (EPS) (described below) are required to have a mass resolution of 20%. Such a resolution allows the Li-Be-B group to be distinguished from He and C. This distinction is critical because it allows us to identify when Interstellar Probe enters the VLISM. This is because the abundance of Li-Be-B is five orders of magnitude higher in the VLISM compared to the heliosphere (Wiedenbeck et al., 2007). The ISM abundance is known from cosmic ray abundances in the several to hundreds of megaelectronvolts range and known sources of Li-Be-B (i.e., cosmic ray spallation in the ISM, as well as dying low-mass stars for Li (Bildsten et al., 1997); note: fusion in the Sun is *not* a source of Li, Be, or B because of their nuclear binding energies compared to solar temperatures). Thus, observations of significant abundances of Li-Be-B ions by PUI (and EPS, below) can be used by Interstellar Probe to indicate plasma access and remote or direct connectivity to the VLISM in the outer heliosheath. Twenty percent mass resolution will automatically allow other species to be distinguished, such as ^3He from ^4He , ^4He from Li, Li from C, and O from C.

4.1.2.2.3 Example Instrumentation

To resolve heavier interstellar ions at these low energies, a post-acceleration voltage and a long TOF path are required. Both interstellar PUIs inside the heliosphere and heavier plasma species in the VLISM are relatively low in abundance. Therefore, a g-factor larger than that of a PLS is generally

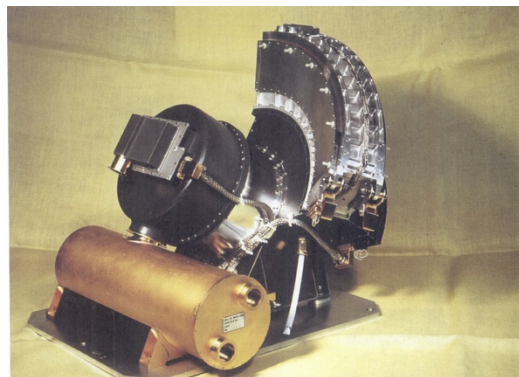
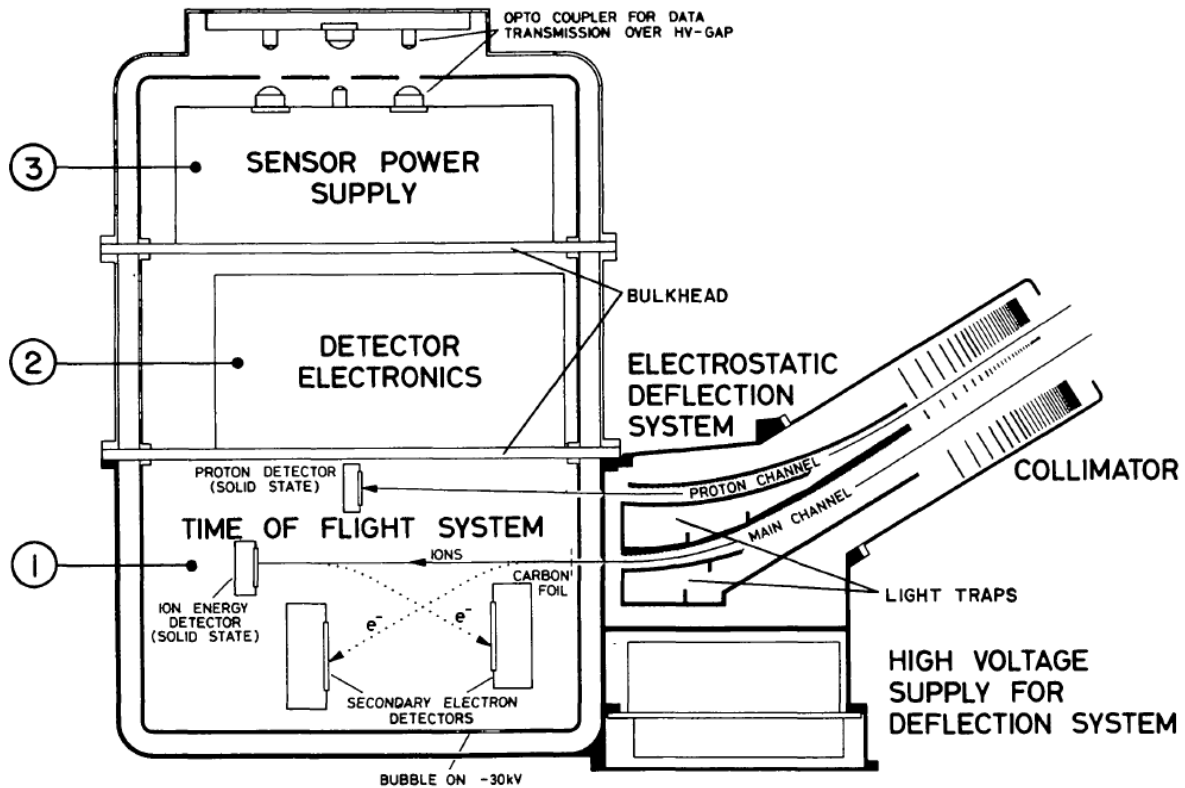


Figure 4-7. Although small, Ulysses/SWICS provides a functional example of a PUI instrument. (Top) Functional overview. (Bottom) Photo of SWICS. (Both images reprinted from Gloeckler et al. (1992) with permission; © ESO.)

required. This can be accomplished by an entrance aperture that is larger than the common ESA style can afford. Ulysses/SWICS (Gloeckler et al., 1992) implemented such a system, although the g -factor made it a challenge to accurately resolve the ^{20}Ne and ^{22}Ne abundances of interstellar PUIs. We baseline the resources of Ulysses/SWICS here. A newer iteration of this instrument with current heritage is Solar Orbiter/Heavy Ion Sensor (HIS) (Owen et al., 2020). Its resources are higher, which follows from the mission's requirements, for example, of operating on a three-axis-stabilized spacecraft, which requires a deflection system. Post-acceleration will still increase the power needs, which is why we allocate 7 W instead of the 4 W for Ulysses/SWICS. We also allocate a mass of 5.5 kg, which can be redistributed among the payload allocation depending on need.

4.1.2.2.4 Instrument Trades

Instrument mass has to be traded carefully with an iFOV and angular coverage sufficient to cover both the PUIs in the solar wind and the VLISM plasma ram. This may require two heads or one head with an extended iFOV, both of which may require more mass. The same type of trade needs to be considered to possibly increase the geometry factor. However, an enhanced SNR is more important (see below).

4.1.2.2.5 Enhancing Technology Development

No new technology needs to be developed for PUI instrumentation. However, enhancements in primarily SNR are desirable. SNR can be improved by reducing the MCP areas, which may be possible without decreasing the geometry factor. Another method is choosing sufficiently thick SSDs: GCR protons that penetrate the instrument and detector all deposit a similar “minimum ionizing energy” in the detector, which only depends weakly on their energy. If a detector is made of silicon and at least 400 μm thick, cosmic rays will deposit >100 keV, which is above the energy range of the PUI instrument, so that such counts can be discarded.

4.1.2.3 Energetic Particle Subsystem (EPS)

- Particle acceleration to high energies is ubiquitous in space plasmas.
- It is critical to understand the acceleration processes responsible for the transition from suprathermal tails to cosmic ray energies.
- Energetic particles serve as remote sensors of distant plasma boundaries and dynamic processes (e.g., reconnection).

Energetic Particle Subsystem (EPS)

Measurement Objectives	Energetic particles in the solar wind and heliosheath, force balance
Dynamic Range	1×10^{-7} to $1 \times 10^{+3}$ ($\text{cm}^2 \text{ sr s keV}^{-1}$)
Geometrical Factor	$\geq 0.1 \text{ cm}^2 \text{ sr}$ (goal $\sim 1 \text{ cm}^2 \text{ sr}$)
Signal-to-Noise Ratio	>10
Cadence	60 s for solar wind and shock crossings
Composition	H, ^3He , ^4He , Li, C, O, Ne, Mg, Si, Ar, Fe; $\Delta m/m \leq 20\%$, electrons (goal)
Energy Range/Resolution	20 keV to 20 MeV; $\Delta E/E \leq 30\%$
Angular Coverage/Instantaneous Field of View/Resolution	$4\pi \text{ sr}$, $\geq 180^\circ \times 10^\circ$, $\leq 20^\circ \times 10^\circ$
Mass Allocation	5.1 kg
Power Allocation	5 W
Data Rate	0.1–1000 bps
Mission Requirement	Spinning spacecraft
Accommodation	Central boresight perpendicular to spin axis

4.1.2.3.1 EPS Investigation

Just like the Low-Energy Charged Particle (LECP) experiment on Voyager, the EPS would target the major energetic ion population of the solar wind and heliosheath up through low-energy cosmic

rays (S. M. Krimigis et al., 1977). This includes shock acceleration in the solar wind and the acceleration processes across the TS. EPS would also follow the energization of ACRs from their seed populations. Within the heliosheath, energetic ions are an important part of the force balance (Dialynas et al., 2020). The angular and spectral distribution of energetic ions can also be used to derive the bulk flow by applying the Compton–Getting effect (Ipavich, 1974) that has been used by LECP to derive flow velocities in the heliosheath (Decker et al., 2012). During the HP encounter, EPS measurements will be critical for characterizing the HP and the nature of the instabilities (Krimigis et al., 2019). Beyond the HP, EPS measurements will be important for characterizing and discovering any upwind “leakage” into the VLISM (Dialynas et al., 2021).

4.1.2.3.2 Measurement Requirements

The lower energy threshold is required to overlap with the PLS and PUI measurements to measure major ion species in the heliosheath to determine the full spectrum of the force balance, meaning ~ 30 keV/nuc. The upper energy threshold is required to overlap with the low-energy end of the Cosmic Ray Subsystem (CRS) of approximately tens of megaelectronvolts of total ion energy.

The energy resolution is not a strong driver of instrument design, given that the expected energy distribution in the heliosheath generally follows a power law. For example, a 30% energy resolution would be sufficient for determining the flow velocity using the Compton–Getting effect (Decker et al., 2012).

The primary driver for geometrical factor is to resolve major energetic ions in the VLISM. Just before the HP, the proton intensities detected by LECP on board Voyager 2 were approximately $0.06 \text{ (cm}^2 \text{ sr s keV)}^{-1}$ at ~ 109 keV (Dialynas et al., 2020; Krimigis et al., 2019), but once in the VLISM, a “leakage” of ions from the HP was detected at about $7 \times 10^{-4} \text{ (cm}^2 \text{ sr s keV)}^{-1}$ at ~ 109 keV (Dialynas et al., 2021). Therefore, a total geometrical factor similar to or higher than that of LECP ($\sim 0.12 \text{ cm}^2 \text{ sr}$) is required. It is strongly desired to increase the geometrical factor even up to $\sim 1 \text{ cm}^2 \text{ sr}$ to ensure adequate statistics. Here one can also make use of the ENA camera (see below), which can successfully be operated as a very sensitive energetic ion spectrometer because of its large geometrical factor.

Energetic electrons up to ~ 1 MeV were measured in the heliosheath by LECP and showed different profiles than those of ions in the heliosheath (Decker et al., 2008). Energetic electron measurements remain a capability that was both achieved by LECP and is achieved by an instrument like EPI-Lo. Therefore, in this example, no dedicated energetic electron sensor is planned.

SNR can be determined as done above and scales with details of the instrument. We assume that the measurement occurs through a TOF system using an MCP with anodes of area 1 cm^2 in coincidence with SSDs of area 0.1 cm^2 (see below for implementation). These detectors receive background rates of $N_{\text{MCP}} \approx 100/\text{s}$ and $N_{\text{SSD}} \approx 10/\text{s}$, respectively. The latter can be compared with the noise on the detectors of New Horizons/PEPSSI, which is $6/\text{s}$ (Hill et al., 2020) and therefore comparable. The triple coincidence accidental background noise is $N = 4 * N_{\text{MCP}}^2 * N_{\text{SSD}} * \text{TOF} * T$. We assume $\text{TOF} = 1000 \text{ ns}$ and $T = 10 \text{ ns}$, which yields $\text{SNR} = S/N \approx 1e6$ for protons.

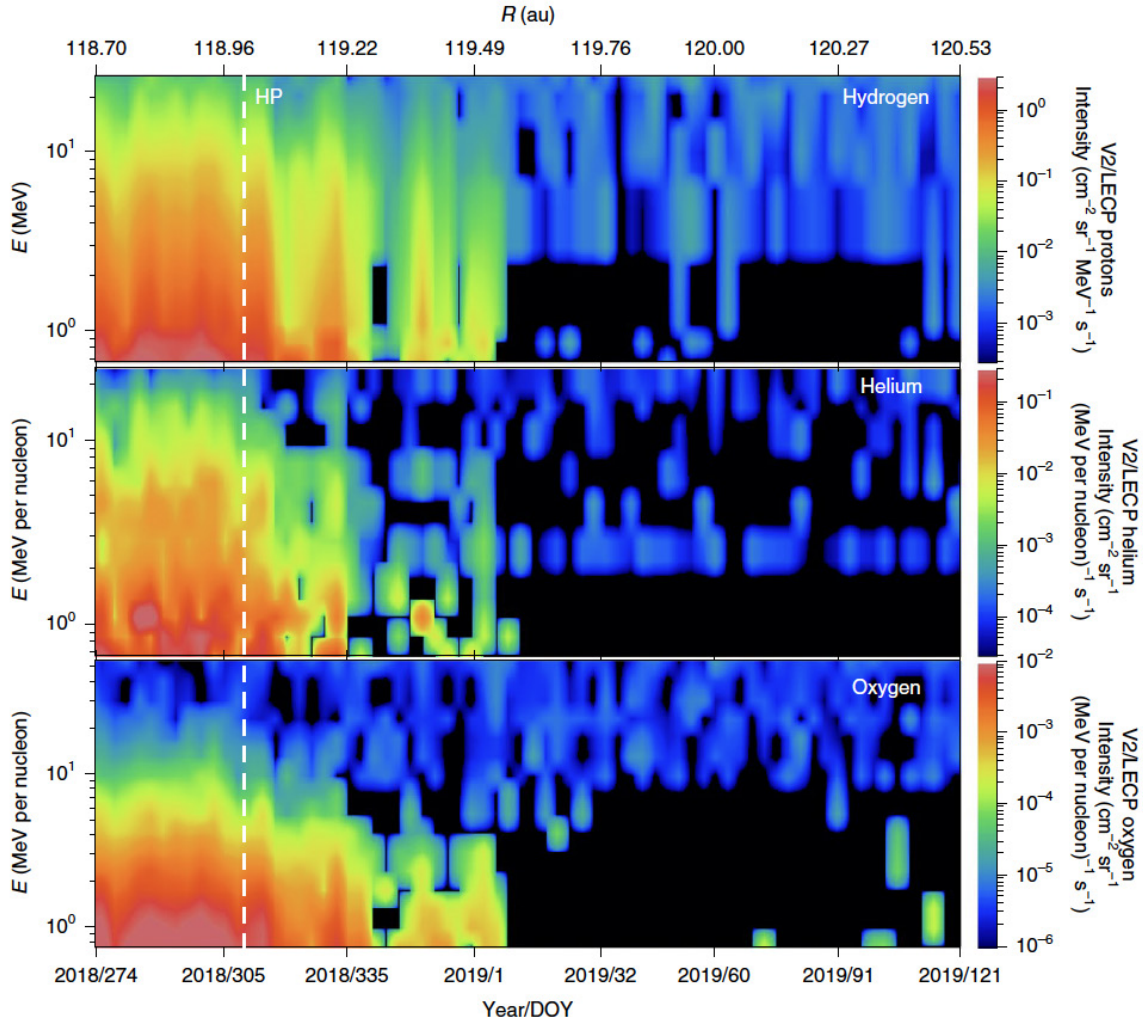


Figure 4-8. Major ions of the heliosheath as measured by Voyager/Low-Energy Charged Particle (LECP) (reprinted from Krimigis et al. (2019) with permission; © 2019 Springer Nature Limited).

Angular coverage and resolution are required for resolving pitch-angle distributions to study shock acceleration mechanisms, which drives the requirement for full-sky coverage. Such coverage would also allow for accurate bulk flow velocity determination in the heliosheath and across the instabilities of the HP, where Voyager relied on only a few angular sectors and the stepper motor of LECP.

4.1.2.3.3 Example Instrumentation

At energies above a few tens of kiloelectronvolts, a foil-based TOF instrument can be used without the complication of post-acceleration. Resolving species is enabled by SSDs so that TOFxE analysis can be performed. Alternatively, a stacked SSD telescope such as LECP (Krimigis et al., 1977) could be used.

TOF-based instruments have been flown or are in development, including EPI-Lo on Parker Solar Probe, Radiation Belt Storm Probes Ion Composition Experiment (RBSPICE) on the Van Allen Probes mission, Jupiter Energetic-particle Detector Instrument (JEDI) on the Juno mission, and

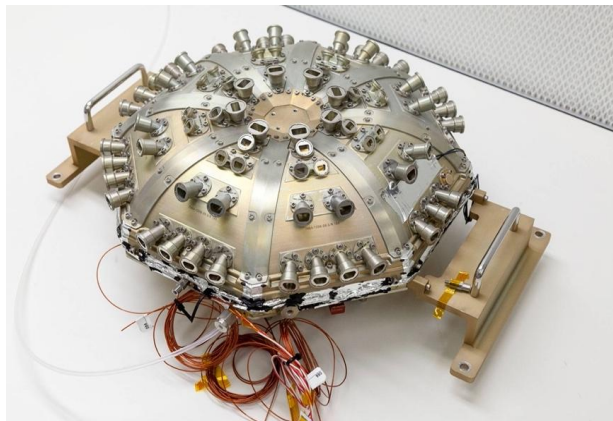
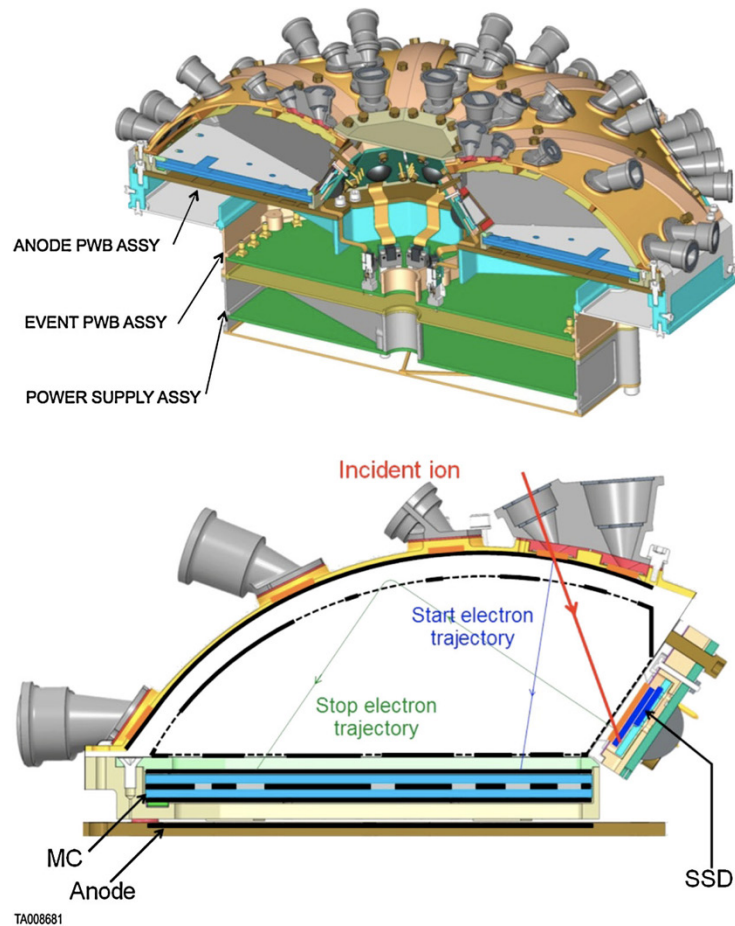


Figure 4-9. (Top) Functional overview of the EPI-Lo sensor as an example of heritage instrumentation, although an LECP-type instrument can also be considered (McComas et al., 2016). PWB, printed wiring board. (Bottom) EPI-Lo sensor as part of the ISOIS suite (image credit: Johns Hopkins Applied Physics Laboratory).

PEPSSI on the New Horizons mission. The advantage of an EPI-Lo-type instrument is the instantaneous near- 2π FOV for maximizing the duty cycle and the fact that it also has a capability to measure energetic electrons. EPI-Lo has been chosen as an example heritage instrument to inform the resource allocations; however, EPI-Lo's geometrical factor was tailored for the high-

intensity region near the Sun and is $\sim 0.05 \text{ cm}^2 \text{ sr}$ summed over all 80 entrance apertures, smaller than the requirement by a factor of two. A future EPS will have to be optimized for maximum geometrical factor, which is feasible with existing instrument technology within the 5.1-kg example allocation. Operating a large-geometrical-factor ENA camera in ion mode is a straightforward method for measuring the low-intensity ions in the VLISM that must be considered (McComas et al., 2016).

4.1.2.3.4 Instrument Trades

Thanks to the LECP observations from Voyager 1 and 2, the energetic-particle environments in the outer heliosphere, heliosheath, and VLISM are relatively well characterized. Trades include examining modifications necessary to existing TOF-based instrument designs, such as EPI-Lo, that consider geometrical factor, angular resolution, SNR, and look directions versus instrument power, mass, and volume. Furthermore, an LECP-type SSD solution can be considered, but it would require several telescopes and/or reliable stepping mechanisms. To avoid an undesirable gap in the electron distribution, another trade should involve examining whether the EPS instrument can accommodate measuring electrons in the $\sim 20\text{-keV}$ to 1-MeV range.

4.1.2.3.5 Suggested Technology Enhancements

No new technology developments are required for energetic particles. However, it is desirable to enhance the geometry factor for resolving the unshielded low-energy GCRs in the VLISM. Considerations of instrument longevity (≥ 50 years of operational lifetime), electronics miniaturization and efficiency, and mass and volume minimization must be detailed and documented.

4.1.2.4 Cosmic Ray Subsystem (CRS)

- Cosmic rays are the most energetic particles in the universe and represent a bridge between heliophysics and astrophysics.
- Voyager 1 and 2 have measured the distribution of some elemental species of GCRs in the VLISM, but only a few data points exist at low energies.
- Many key answers to outstanding questions on cosmic ray sources, acceleration, and heliospheric shielding can be answered with new observations enabling isotopic analysis (e.g., cosmic ray “clocks”) and comprehensive angular distributions (e.g., mysterious GCR anisotropies).

Cosmic Ray Subsystem (CRS)

Measurement Objectives	GCRs and ACRs
Dynamic Range	1e-6 to 1e2 /m ² -s-sr-MeV/nuc for H through Sn 1e-1 to 1e3 for electrons
Geometry Factor	>2 cm ² sr
Signal-to-Noise Ratio	>10
Cadence	≥ weekly in the VLISM
Composition	H-Sn, isotopes, $\Delta m/m < 10\%$

Energy Range/Resolution	10 MeV/nuc to 1 GeV/nuc (ions), 1–10 MeV (electrons), $\Delta E/E \leq 30\%$
Angular Coverage/Instantaneous Field of View	2 perpendicular directions; $\leq 15^\circ$ opening angle
Mass Allocation	8.0 kg
Power Allocation	6.7 W
Data Rate	0.1–1000 bps
Mission Requirement	Spinning spacecraft
Accommodation	Perpendicular mounting and spinning to cover anisotropies in the VLISM

4.1.2.4.1 CRS Investigation

The CRS investigation starts within the heliosphere with the modulation of ACR and GCR electrons and ions interacting with the solar-cycle variability of the solar wind and solar transient structures (e.g., coronal mass ejections [CMEs]). Combined with PUI and EPS observations, CRS will investigate the exact mechanisms of ACR acceleration at the TS and in the heliosheath and test the hypothesis of an offset and asymmetric TS posed by (McComas & Schwadron, 2006; McComas et al., 2017). Throughout the heliosheath, measurements will continue to explore the source and acceleration of ACRs. Nearing the HP, the CRS instrumentation will be a significant part of the HP campaign for understanding the magnetic barrier and shielding that appear to affect GCRs over distances shorter than their gyroradii (Krimigis et al., 2019). Once beyond the HP, the elemental and isotopic composition of unshielded GCRs will be measured in detail, including rare isotopes of GCRs (e.g., cosmic ray “clocks”) that can be used to determine the sources of GCR acceleration and production. Furthermore, CRS on Interstellar Probe will also extend the mass range of GCRs beyond that provided by Voyager, to $M \sim 120$ amu (i.e., Sn - tin), which will provide critical measurements to test and constrain astrophysical models of nuclear synthesis and cosmic ray production. With unprecedented angular resolution and multiple, simultaneous look directions, CRS on Interstellar Probe will also answer outstanding questions concerning the mysterious anisotropies of GCRs observed in the VLISM by the Voyagers (e.g., Krimigis et al., 2013, 2019; Rankin et al., 2019).

4.1.2.4.2 Measurement Requirements

Geometry factor is a central requirement for any CRS instrument and is driven here by the requirement to resolve heavier species and rare isotopes beyond the HP in the important energy range of 5 MeV/nuc to a few GeV/nuc. For cosmic ray science, Interstellar Probe will benefit greatly from long integration times made possible by the longevity of the mission. Using dE/dx in a stack of many ultrathin silicon detectors, isotopic mass resolution is possible with extremely low background levels. Combined with low intensities and the possibility of long integration times, data recorded from all individual events of heavy species and rare isotope GCRs can be telemetered back to Earth, optimizing the scientific return and potential from CRS.

The intensities of elemental species of GCRs in the VLISM range from $\sim 10^{-7}$ ($m^2 \text{ s sr MeV/nuc}^{-1}$) for GeV/nuc Ni to $\sim 100/m^2\text{-s-sr-MeV/nuc}$ for 10-MeV protons, based on the Voyager measurements in the VLISM (Cummings et al., 2016; Figure 4-10). With a nominal geometry factor of $2 \text{ cm}^2 \text{ sr}$ and an energy resolution of 30%, we can expect count rates of 0.1/s to 1/year,

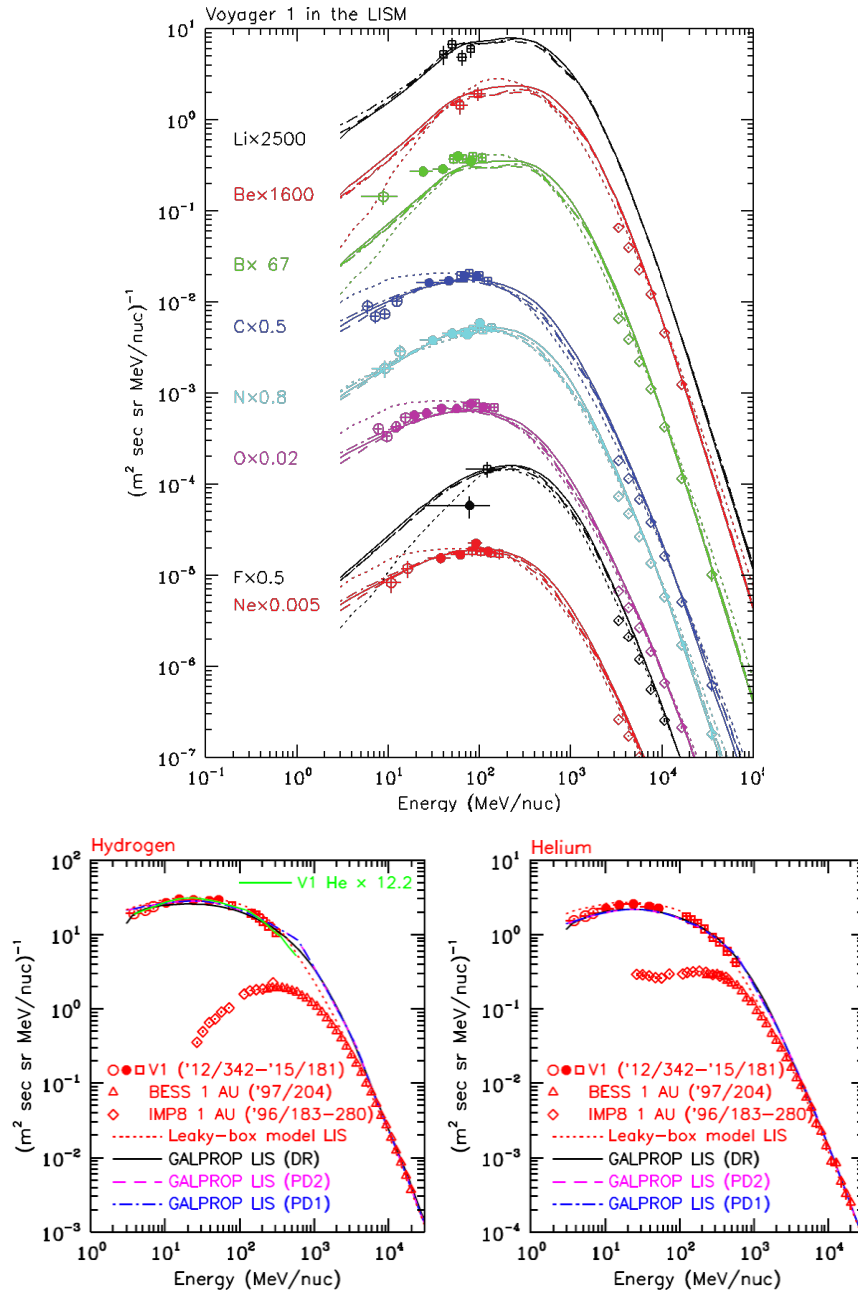


Figure 4-10. Voyager 1 provided only a few points over a relatively narrow range of energies of the important Li, Be, and B (top panel; reproduced from Cummings et al. (2016) with permission; © AAS). This has left an important gap in the spectrum for constraining the production of light elements in stars and the role of spallation on heavy ions in the VLISM. Note: The intensities of Li, Be, and B are comparable to those of C, N, and O. Cosmic ray proton (hydrogen) and helium spectra in the VLISM from Voyager 1 are shown in the bottom two panels for comparison. (Reproduced from Cummings et al. (2016) with permission; © AAS.)

respectively, which is sufficient to address the critical science questions. Innovative application of existing state-of-the-art SSD technology, however, can enable large geometrical factors while still delivering on the required angular resolution. With a realistic G-factor of 100–1000 $\text{cm}^2 \text{ sr}$, CRS could deliver count rates of ~ 200 – 6000 per minute for protons, 4–100 per minute for helium, and,

with longer integration times of up to 400 per day for lithium, ~1000 per day for carbon and ~100 per day for neon. At even longer integration times of 10–100 days (up to nickel) and longer (≥ 1 year) for heavier species and rare isotopes, statistically significant counts can still be accumulated with such a large geometrical factor instrument.

Important to all this is that background rates will be lower than the respective foreground rates, which can be achieved through the stacking of detectors and running them in coincidence. This was demonstrated by Voyager/High-Energy Telescope System (HETS) that provided clean measurements for <300 MeV/nuc up to 56 nuc with a very low background thanks to the up to eight coincidences applied across its multiple stacked detectors (Stone et al., 1977).

Voyager/CRS consists of two nearly perpendicular high-energy telescopes and four low-energy telescopes, all within a mass of 7.5 kg and 5.35 W (Stone et al., 1977). Although Voyager was not a spinning platform, CRS performed excellent measurements of GCR anisotropies. The spinning platform of Interstellar Probe offers a far superior angular coverage and therefore only two, or more, simultaneous perpendicular look directions are required. As will be seen below, this is a requirement that can be exceeded within the mass allocation.

4.1.2.4.3 *Example Instrumentation*

SSD technology has improved drastically since the Voyager CRS was developed. For Interstellar Probe, the EPI-Hi instrument has been baselined as an example of a state-of-the-art instrument that could be modified to satisfy the Interstellar Probe CRS measurement requirements. Details of EPI-Hi from Parker Solar Probe are shown in Figure 4-11. EPI-Hi consists of three solid-state telescopes, each with a different stack of various thickness and diameter detectors to target different species and energy ranges. Ion species are determined very accurately using dE/dx logic of energy deposited as a function of distance through the detector stacks. While the EPI-Hi design is optimized for solar energetic particles, the concept is directly applicable to CRS for Interstellar Probe, with only the number of telescopes plus the number, thickness, and size of the detectors needing to be optimized for cosmic ray science based on known and estimated intensities of ACRs and GCRs in the outer heliosphere and VLISM. With three large FOVs and a large geometrical factor, the telescopes should be oriented such that the entire 4π sr is mapped out over the course of one rotation, which is well beyond the requirements for measuring anisotropies.

4.1.2.4.4 *Instrument Trades*

Thanks to CRS observations from Voyager 1 and 2, the cosmic ray environments in the outer heliosphere, heliosheath, and VLISM have been relatively well characterized. Further trades include modifications to existing designs, such as EPI-Hi, considering required geometrical factor, angular resolution, and instantaneous look directions versus instrument power, mass, and volume. Trade studies on instrument design and component selection should also be made considering instrument longevity for a ≥ 50 -year baseline mission in deep space.

Fig. 28 EPI-Hi mechanical configuration including E-Box and telescopes

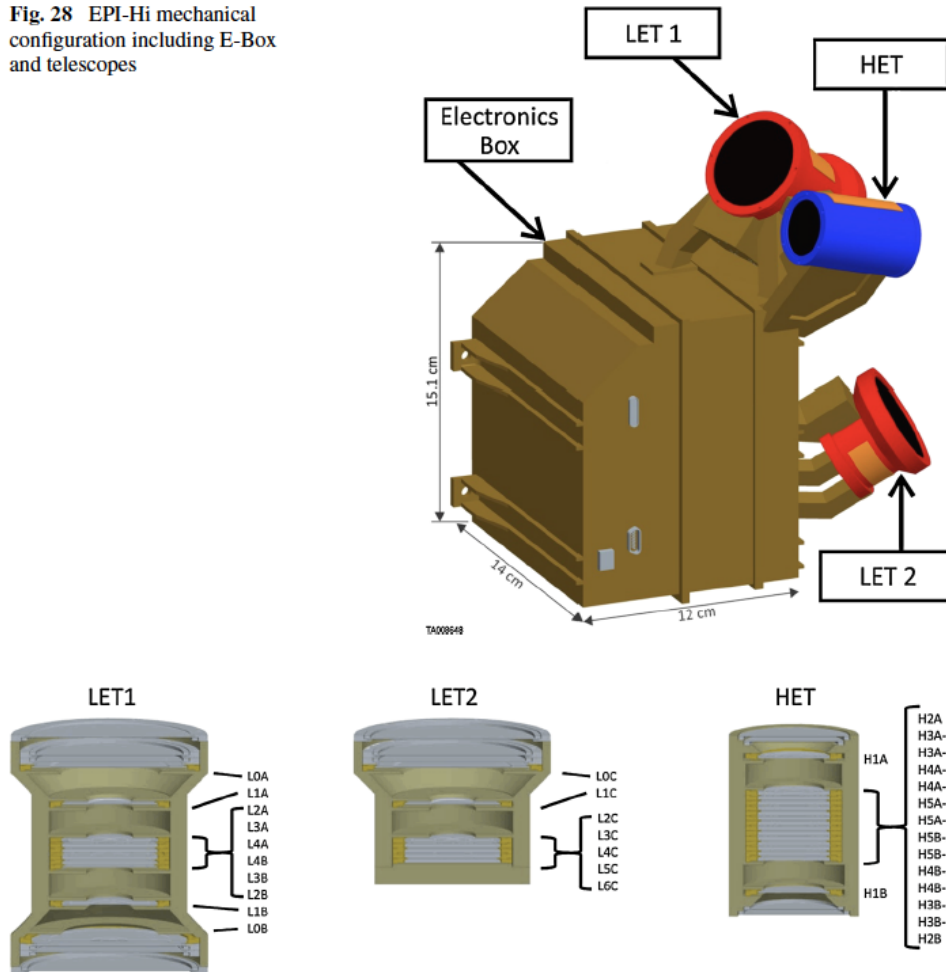


Fig. 29 Cut-away illustration of the EPI-Hi telescope designs and detector naming

Figure 4-11. (Top) EPI-Hi instrument on Parker Solar Probe (Figure 28 from McComas et al. (2016)). (Bottom) Details of the EPI-Hi LET1, LET2, and HET telescope configurations (Figure 29 from McComas et al. (2016)).

4.1.2.4.5 Suggested Technology Enhancements

No new technology developments are required for cosmic ray measurements. However, solutions are needed to optimize performance, mass, power, and data volume to meet the large required dynamic range of particle intensities, energies, and angular distributions within the resource constraints of an interstellar probe mission. Primarily increases in geometrical factor and low-energy thresholds are desired to optimize the measurements of the heavier species of GCRs in the VLISM.

4.1.3 Plasma Wave Measurements

- Powerful remote diagnostic of electron density gradients in the heliospheric boundary
- Provides in situ measurements of total electron density and temperature independent of spacecraft potential

Plasma Wave Subsystem (PWS)

Measurement Objectives	Stable, precision measurements of plasma density and electron temperature, radio emissions from outer heliospheric boundaries, and dust impacts
Range	Approximately a few hertz to 1 MHz (5 MHz for turbulence)
Sensitivity	$\leq 0.7 \text{ uV/m}$ at 10 kHz
Spectral Resolution	$\Delta f/f < 4\%$
Cadence	1 spectrum/60 s, commandable cadence
Mass Allocation	3.3 kg + 8.2 kg (antennas)
Power Allocation	11 W
Data Rate	1–100 bps (burst modes excluded)
Mission Requirement	Spinning spacecraft preferred, EMC program
Accommodation	4 × 50-m spin-plane wire antennas; centrifugally deployed

4.1.3.1 Plasma Wave Subsystem (PWS) Investigation

Voyager has demonstrated the importance of low-frequency radio and plasma wave measurements for an interstellar probe mission. Even as close as 15 au to the Sun, the Voyager PWS instruments were able to detect radio emissions in the range of $\sim 1.8\text{--}3.6$ kHz that we now know are generated in the ISM near and beyond the HP (Gurnett et al., 1993; Kurth et al., 1984). The emissions are generated at the local plasma frequency by mode conversion from electron plasma oscillations, similar to type III radio emissions or narrowband radio emissions from Earth’s bow shock. Furthermore, we know that the radio emissions are triggered by disturbances originating in solar transient events that propagate through the heliosphere and inner heliosheath until they interact with the HP, where shocks or pressure pulses are transmitted through the HP into the ISM.

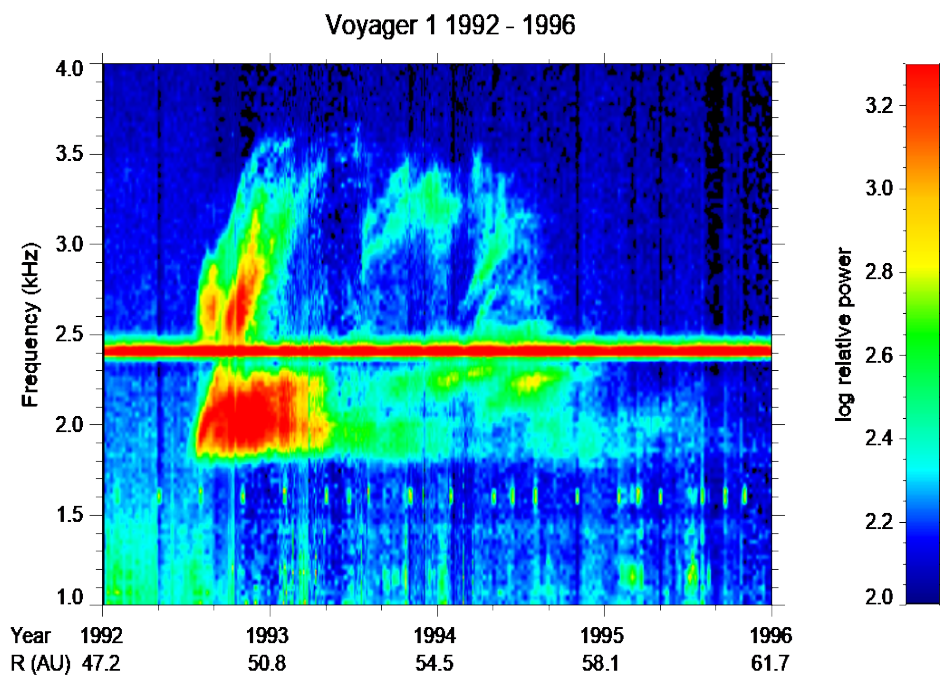


Figure 4-12. Low-frequency radio emissions generated at and beyond the heliopause via mode conversion from electron plasma oscillations in the foreshock of shocks and pressure pulses moving through the ISM. (Image courtesy of W. Kurth.)

Once in the ISM, Voyager 1 and 2 detected narrowband, bursty electron plasma oscillations at the local electron plasma frequency (Figure 4-13), providing accurate measurements of the plasma density, even to the extent of showing density jumps that match the jump in the magnetic field at shocks and pressure fronts (Burlaga et al., 2021; Gurnett et al., 2013). Hence, whether by radio emissions detected within the heliosphere or by plasma oscillations in the heliosphere and ISM, the wave signatures provide evidence of the influence of the Sun on the LISM and independent diagnostics of the interstellar plasma density, even in the absence of a working plasma instrument such as in the case of Voyager 1. Also, radio direction finding can localize the source of radio emissions from locations beyond ~ 15 au (Kurth & Gurnett, 2003) and could complement a dust investigation by detecting hypervelocity dust impacts from all directions (Gurnett et al., 1997).

Recently, a very weak quasi-continuous line at the plasma frequency has been observed with the Voyager 1 wideband receiver from about 2016 onward (Burlaga et al., 2021; Ocker et al., 2021). This measurement, coupled with the much more intense electron plasma oscillations (Figure 4-14) provides evidence of a large-scale radial density gradient with scale lengths on the order of 10 au. Gurnett et al. (2021) have shown that this weak emission is consistent with the quasi-thermal noise (QTN) spectrum of an electron population that includes a significant suprathermal population and may be a persistent feature of the VLISM. A PWS instrument can provide a highly accurate, stable plasma density measurement in the low-density environment of the VLISM.

Onboard spectrum analysis of digitized waveforms could be used to optimize the data volume significantly. Such capabilities already exist in missions such as Van Allen Probes, Juno, and Parker Solar Probe. For example, onboard spectral line detection would enable the onboard identification of radio emissions or plasma oscillations, allowing an onboard determination of n_e in the latter case. Onboard QTN spectrum analysis would enable fitting the plasma wave spectrum to an electron density and bi-Maxwellian temperature distribution, enabling the ability to downlink n_e , T_c , and T_h as opposed to high-resolution spectra on an ongoing basis. The addition of a sounder capability to stimulate the plasma frequency would provide electron densities in the inner heliosheath where the Debye length is much too large to allow for QTN spectroscopy with a

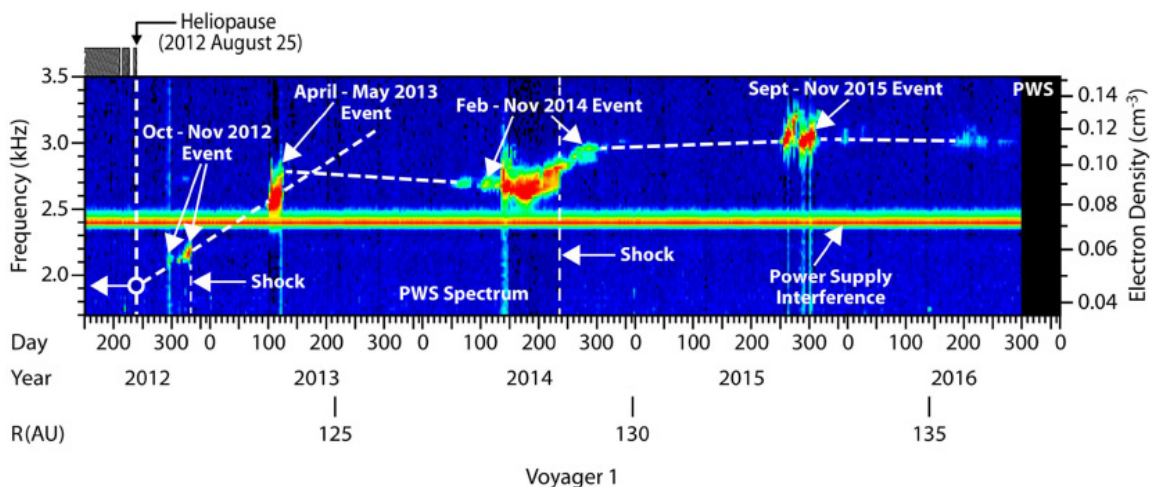


Figure 4-13. Electron plasma oscillations observed beyond the HP showing the increase in interstellar plasma density in the LISM. (Reproduced from Pogorelov et al. (2017) with permission; © AAS.)

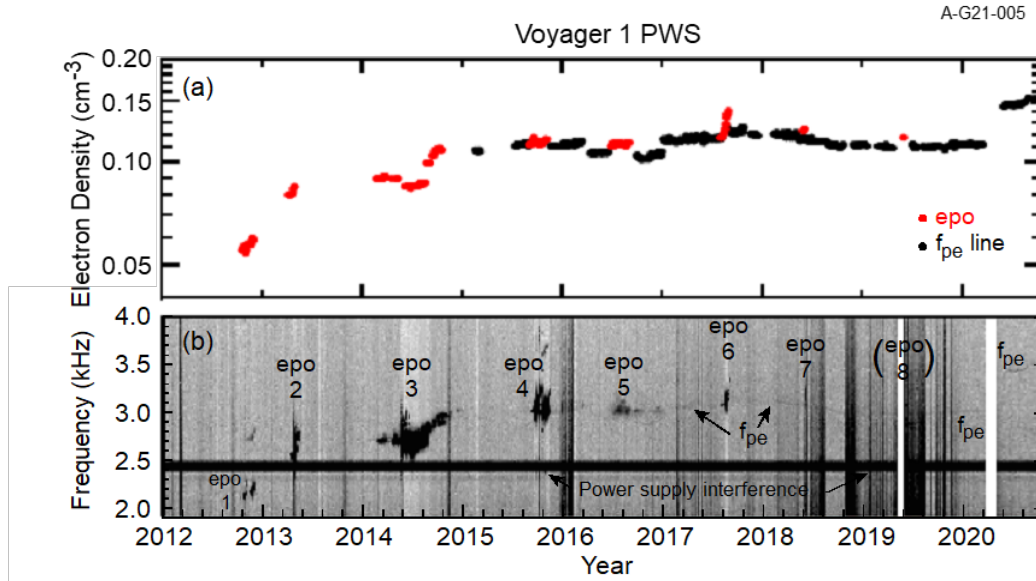


Figure 4-14. The recent discovery of the “hum” showing up as a quasi-continuous line at the plasma frequency, implying a significant and unexpected suprathermal electron population of the VLISM (Burlaga et al., 2021; Gurnett et al., 2021; Ocker et al., 2021). (Top panel courtesy of W. Kurth. Bottom panel taken from Burlaga et al. (2021).)

reasonable antenna length. And finally, onboard dust detection would enable a much higher duty cycle for identifying impulses due to hypervelocity dust impacts rather than by downlinking voluminous waveforms. The resulting data set would be a time tag and amplitude of detected impulses. Such software was implemented in the Cassini Radio and Plasma Wave Science (RPWS) instrument (Gurnett et al., 2005) and Parker Solar Probe FIELDS suite (Bale et al., 2016).

4.1.3.2 Measurement Requirements

In summary, a radio and plasma wave investigation would require a frequency range from a few hertz to ~ 5 MHz with 4% spectral resolution, corresponding to an equivalent of 8% density resolution. The range up to 10 kHz is required to observe the electric field components of radio emissions generated at HP and beyond, and plasma oscillations for $\leq 1 \text{ cm}^{-3}$. This requires a sensitivity of about $\leq 0.7 \mu\text{V/m}$ at 10 kHz. To study turbulence in the plasma, an extension of the frequency range to 5 MHz would be required. During the Jupiter gravity assist, a range up to 40 MHz would be desired. One spectrum every 60 s is required, which is easily varied depending on telemetry constraints, and should not be synchronous with the spin period. Ability to capture burst-mode waveforms up to 10 kHz is required for constructing high-resolution QTN spectra and plasma waves. A waveform data product could be telemetered at low duty cycle, and onboard processing would provide plasma electron frequency and dust detection at low “survey” telemetry rates. A spinning and electromagnetically clean spacecraft would be required, with antenna lengths of at least 10 m, with 50 m preferred.

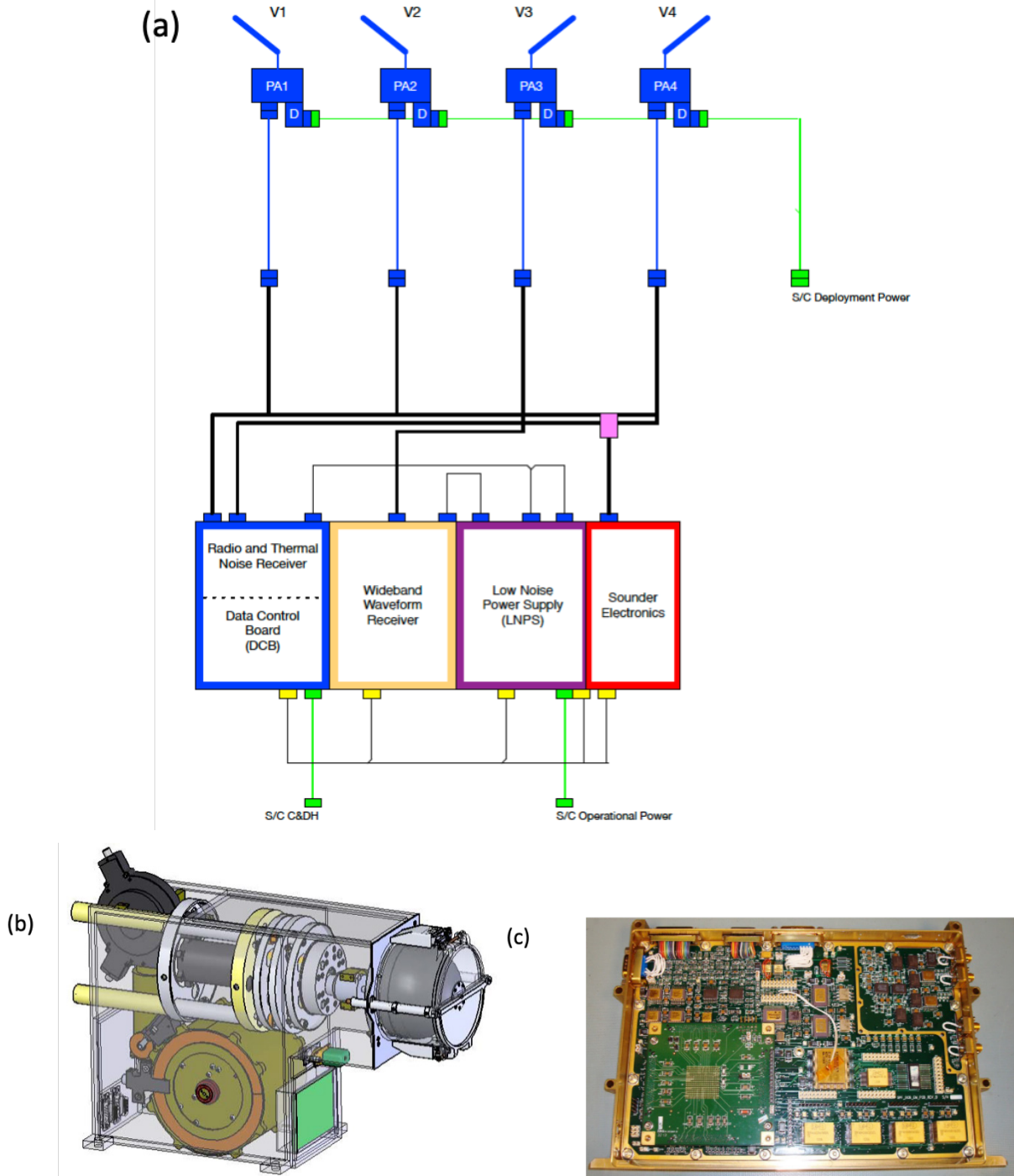


Figure 4-15. (a) PWS functional block diagram. (b) PWS deployment mechanism. (c) Parker Solar Probe/FIELDS radio/thermal noise board. (All images courtesy of S. Bale.)

4.1.3.3 Instrumentation

A baseline PWS instrument would consist of a tightly integrated receiver system (both spectral and waveform), low-noise power supply, preamplifiers, and antennas. A data controller system with dedicated solid-state memory and command and data handling (C&DH) capability can be

integrated into the receiver system electronics. The full system would represent three small electronics boards (stacked together) and four antenna deployment units with integrated preamplifiers. The antenna deployers would be mounted to deploy the wires radially away from the spacecraft (i.e., at its outer edge) and at 90° around the spacecraft body, to deploy the four wires into two orthogonal colinear pairs (i.e., dipoles). High heritage for all subsystems lies in designs that have been flown recently on the Parker Solar Probe and Van Allen Probes missions.

4.1.3.4 Instrument Trades

The primary PWS instrument trade is the length of the deployable wire antennas, including a potential hybrid (rigid+wire) antenna system if the Interstellar Probe spacecraft is three-axis stabilized during a Jovian flyby. The overall sensitivity of the instrument scales simply with antenna length L and requires at least 10-m wires (for ~20 m tip-to-tip). To achieve sensitivity for QTN measurements, the wire antennas should be longer than the local Debye length, which suggests ~50-m antenna elements in the LISM. Other trades on bandwidth, frequency resolution, and measurement cadences do not have a major impact on the spacecraft/mission design.

4.1.3.5 Enhancing Technology Development

Demonstration of a hybrid rigid-wire antenna system that could be fully deployed several years after launch (post-Jovian flyby) would reduce risk and allow increased instrument capability for both Jovian and heliospheric science. A highly durable Kevlar-core wire antenna system might benefit from a development and demonstration program, although there do not appear to be fundamental challenges.

4.1.4 Energetic Neutral Atom (ENA) Imaging

- Remote imaging of the global structure, dynamics, energy spectra, and relative velocity field of the heliosphere
- First images of our heliosphere from the outside

Energetic Neutral Atom Imager (ENA)

Measurement Objectives	Global heliospheric structure, force balance, ribbon/belt, dynamics
Energy Range	1–100 keV
Energy Resolution	50%
Angular Resolution	<5°
Dynamic Range	10^{-3} to 10^3 ($\text{cm}^2 \text{ s sr keV}^{-1}$)
Mass Resolution	Protons (He, O goal)
Cadence	Weeks
Angular Coverage	Near 4π ster
Geometrical Factor	$\geq 1.2 \text{ cm}^2 \text{ sr}$ (total), triple coincidence
Foreground to Background Ratio	>10
Mass Allocation	12 kg
Power Allocation	9 W
Data Rate	0.001–3000 bps, varying through mission timeline
Mission Requirement	Spinning, $\geq 45^\circ$ from nose, through ribbon

Accommodation

 Placement perpendicular to spin axis with Sun exclusion zone and unobstructed FOV

4.1.4.1 ENA Investigation

The ENA measurements provide large-scale measurements of plasma structures via spectral imagery. The imagery acquired from Interstellar Probe will provide measurements information about the shape and singly charged ion distributions of the heliosheath (Objectives 1.1.4, 1.2.1) and the ribbon and belt structures (Question 1.1.5). These are structures that have been mapped from the inner heliosphere with the Interstellar Boundary Explorer (IBEX) and Cassini/Ion and Neutral Camera (INCA) instruments and will be measured with greater precision with the Interstellar Mapping and Acceleration Probe (IMAP) instruments to be located at L1. These vantage points closer to the Sun are helpful to establish the spatial scales and energy ranges required for Interstellar Probe measurements. It should be noted, however, that these measurements have been made from what is essentially a single vantage point within the heliosphere, and they are not sufficient to resolve the above-referenced questions. Because Interstellar Probe will take measurements from multiple vantage points as it flies through and out of the heliosphere, its ENA measurements will be able to resolve the ambiguity about the 3D structure of the heliosphere sufficient to address Objectives 1.1.4, 1.1.5, and 1.2.1.

4.1.4.1.1 Objectives 1.1.4 and 1.2.1

The primary ENA measurement addressing these objectives will be images of the heliosheath acquired from beyond the HP at a distance of ~ 250 au from the Sun. This is a measurement of the PUIs/nonthermal plasma charge exchanging with ISN hydrogen. In addition to providing the mechanism for the measurement, charge exchange plays an important role in determining the ion lifetime as a function of energy. The lifetime increases monotonically above 10 keV as the charge-exchange cross-section decreases; thus, the higher-energy ions persist for a much longer time. Therefore, at lower energies, we see the ions closer to the acceleration source (e.g., the TS), whereas we see the higher energies show us ions farther away from the acceleration regions, yielding a much better view of the entire shape of the heliosheath (see Figure 3-34 [from the 2019 report]). For this reason, the imagery for this global external view should be taken over an energy range from 10 to 100 keV. To measure spatial structure on the same scale as the radial thickness of the heliosheath (i.e., ~ 30 – 40 au), these images should have $\sim 10^\circ$ spatial resolution. To view the entire heliosphere, the FOV must be at least 65° oriented in the anti-ram direction.

In addition to the images acquired from beyond the HP, Objectives 1.1.4 and 1.2.1 are also addressed by ENA images acquired on the outbound trajectory—images taken from multiple viewpoints that can be used to infer the 3D structure of the heliosheath. The overall structure, including regions of acceleration, requires measurements from PUI energies through 50 keV or so where the charge-exchange lifetimes are reasonably long. The goal of this measurement is to look at the same volume elements from various points of view and observation angles; for this reason, a very large FOV (the entire sky, if possible) is highly desirable. Characterizing the tail regions on the outward trajectory, however, requires a higher resolution (5°) because these regions are farther away. Following (Schwadron et al., 2014), the structure of the heliotail can be studied at energies between 0.5 and

10 keV with which the approach of “cooling lengths” can be applied. Further, the data presented in (Schwadron et al., 2014) show that the tail/lobe regions in the IBEX images extend over most of the downwind hemisphere, suggesting that a very large FOV is desirable.

Objective 1.2.1 addresses the time dependence of these measurements. We expect time dependences to be driven by the solar cycle, so measurements taken on the scale of 6 months to 1 year would be sufficient. However, the vantage point provided by Interstellar Probe will be changing faster than 0.5 au/month. Thus, to avoid smearing, single images should be acquired on a timescale of several weeks to a month.

4.1.4.1.2 Objective 1.1.5

This question involves characterizing the IBEX ribbon ($E < 5$ keV) and the INCA belt ($E > 5$ keV), although it is not clear whether they arise from the same mechanism. The ENA measurements will acquire imagery of these structures from multiple vantage points, thus resolving the ambiguities involved with measurements very near the Sun (i.e., within 10 au or so). The required measurements are similar to those made by IBEX and INCA (i.e., covering energies across both structures [0.5–100 keV] at similar spatial resolutions [i.e., $< 5^\circ$]). Again, the measurement cadence is determined by the timescale of the changing vantage point rather than the temporal variation of the ribbon or belt (i.e., the images should be acquired on the timescale of several weeks to a month). It is important that the energy region where the ribbon and the belt overlap (4–10 keV) be continuously covered.

4.1.4.2 Measurement Requirements

The energy range of the measurements (1–100 keV) is derived from the ability to detect both PUIs from the core of the solar wind (1 keV) as well as ions in the tail of the energy spectrum with very long lifetimes that allow us to image the plasma very far away from the TS and other acceleration mechanisms in the heliosheath (~ 100 keV). This results in a very wide dynamic range requirement (10^{-3} to 10^3 [$\text{cm}^2 \text{ s sr keV}^{-1}$]) based on the spectra shown in Figure 4-16. This rather large dynamic range requirement is mitigated by the ability to accumulate data counts for several weeks, a time period that is driven primarily by the velocity of the spacecraft and the changing vantage point (~ 0.13 au/week), which is substantially shorter than the timescales for change expected in the source regions.

The angular resolution requirement is primarily driven by observations of the IBEX ribbon, which has a full width at half maximum (FWHM) of $\sim 15^\circ$ at 1 AU. Measuring the ribbon at $\leq 5^\circ$ resolution provides the sampling required to track changes in its apparent width as the vantage point changes along the trajectory.

For all the measurements described above, an energy resolution ($\Delta E/E$) of 0.5 is required such that appropriate power law coefficients can be determined among the various energy channels. The measurement of hydrogen ENAs is sufficient to address the requirements described here; measurements of other species are useful but not necessary.

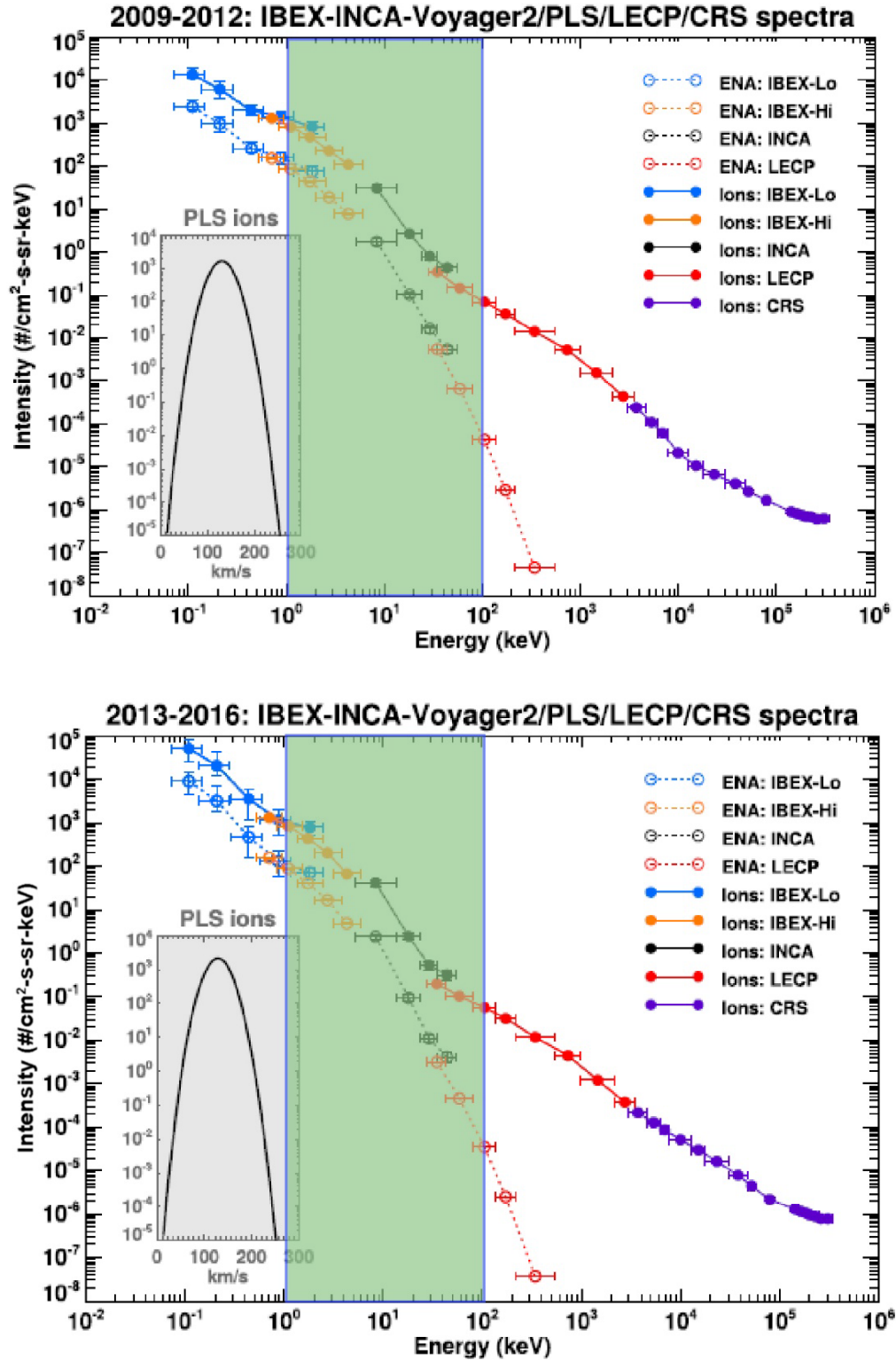


Figure 4-16. Reference ion (solid) and ENA (dotted) intensity spectra in the heliosheath (Dialynas et al., 2020). The green box in each panel shows the required energy range of the ENA measurements. (Reproduced from Dialynas et al. (2020) with permission; © AAS.)

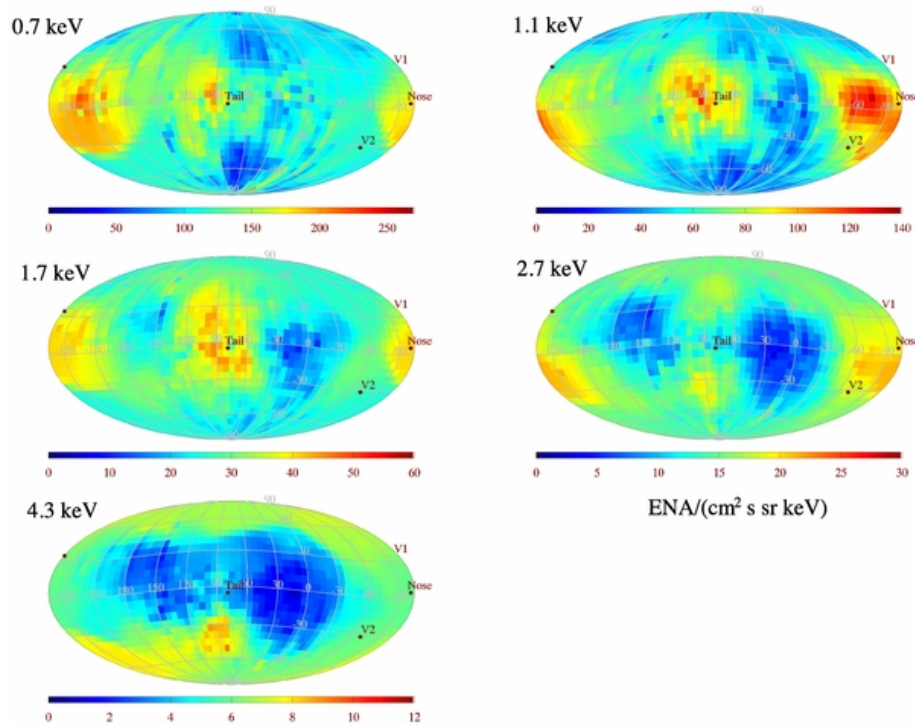


Figure 4-17. ENA maps from IBEX of the tail and lobe regions. (Reproduced from Schwadron et al. (2014) with permission; © AAS.)

4.1.4.3 Instrumentation

Using current technology, this energy range would be covered, as it is on the IMAP mission, with the combination of an instrument like IMAP-Hi (0.5–15 keV) and IMAP-Ultra (3–300 keV). IMAP-Hi measures ENAs in a single direction and in a single energy interval at a given time, whereas IMAP-Ultra measures a substantial portion of the sky ($90^\circ \times 120^\circ$) and the entire energy range simultaneously. On the IMAP mission, these cameras both cover the entire sky over large portions of the year through the precession of the spinning spacecraft. On Interstellar Probe, the spin axis is fixed by communications requirements to point toward Earth (i.e., sunward), so the instruments cannot take advantage of a change in direction of the spin axis to cover the sky. This is particularly important for an IMAP-Hi-style, single-pixel instrument, which would require a scanning mechanism to cover more than a ring around the spin axis. In contrast, an IMAP-Ultra-like instrument could sweep out a substantial portion of the sky with the fixed spin axis.

Including an instrument like IMAP-Hi in the example payload would enable us to measure charge-exchanged PUIs at solar wind energies (0.5–3 keV), which are certainly important to the pressure in the heliosheath. Further, the IBEX ribbon peaks at these energies.

4.1.4.4 Instrument Trades

The current IMAP-Ultra technology is limited at lower energies because of the scattering and efficiency loss in the entrance foil. That is, at these lower energies, the instrument is much less efficient and the spatial resolution is significantly degraded.

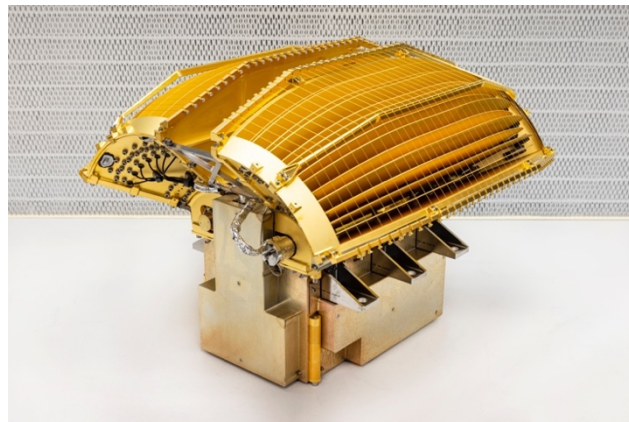
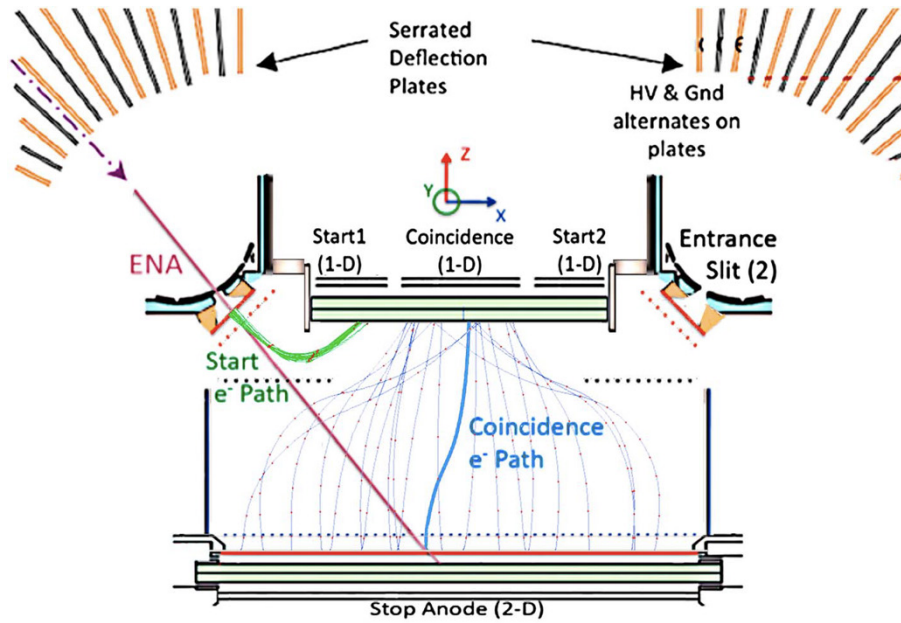


Figure 4-18. (Top) The example IMAP-Ultra camera with triple coincidences including a tight 4-ns timing window (Mitchell et al., 2016). (Bottom) The JUPIter ICy Moons Explorer (JUICE)/Jovian Energetic Neutrals and Ions (JENI) flight model without thermal blankets (image credit: Johns Hopkins Applied Physics Laboratory).

The IMAP-Hi instrument has not been included in the example payload because of the mass required to accommodate a scan table. There is a penalty to the ribbon and tail science. However, the ribbon is visible and distinct in the IMAP-Ultra energy range, and spectral indices in the tail can also be constructed (up to 10 keV). These measurements can be made with degraded spatial resolution, and an increase in the ENA intensities at these lower energies somewhat offsets the loss of efficiency.

4.1.4.5 Enhancing Technology Development

The combination of requirements for ENA measurements requires spatial coverage over most of the sky and coverage of energies from 0.5 to 100 keV with a $\Delta E/E$ of 50%. With the current technology, these requirements would be satisfied with a minimum of two instruments (as is the

case for the IMAP mission). In the example payload, we have included only one of these instruments because of mass constraints, with some impact to the science. To mitigate the science impact, technology developments that would allow the extension of the lower energy boundary of the IMAP-Ultra-style of instrument could be implemented. Conversely the IMAP-Hi-style instrument's upper energy boundary could be raised coupled with a low-mass scan platform.

The IMAP-Ultra-style of instrument is limited by the entrance foil where the passage of an ENA is first detected. As the ENA passes through the foil, electrons are ejected and the location of the ejection is measured via electron optics and position-sensitive detectors. At moderate-to-high energies, the ENA passes through the foil with a very small change in direction and is subject to another positional measurement. The combination of the two positional measurements allows the inference of the incident direction of the ENA. At energies of <10 keV, the entrance foil more significantly scatters the ENA, and information about the incident direction is obscured. This can be mitigated by a thinner entrance foil, but that can reduce the electron production efficiency and poses engineering challenges in managing these delicate foils. To mitigate this, a collimator can be placed before the entrance foil in such a way that the incident direction can be inferred directly from the position in which it encounters the entrance foil. Such a collimation scheme would necessarily reduce the geometric area of the system. A collimated system with foils of appropriate thickness with a suitable detection area/efficiency could be developed.

As noted above, switching off the deflection system of an ENA camera allows it to operate as a very sensitive ion spectrometer with large ($\sim 1 \text{ cm}^2 \text{ sr}$) geometrical factor. Such operations would be particularly useful for measuring the low-intensity ions in the VLISM that were very difficult to detect from Voyager.

Alternatively, an IMAP-Hi-like instrument could be paired with a lightweight scan platform to cover a larger energy and spatial range. This would require two distinct technology developments. First, the lightweight scan platform must be very carefully balanced in such a way that it imparts very little or no momentum to the spacecraft. The attitude constraints on Interstellar Probe are very stringent for the purposes of communication, and large moving systems such as this pose a significant risk to the mission, given the lifetime requirements. Second, the ENA detection system must be extended upward from 10 to 100 keV with the required large geometrical factor to resolve the global shape, which can be difficult to achieve with the general ESA design. This would require an ESA to operate over a very large dynamic range at substantially higher voltages and/or increased volume/mass.

4.1.5 In Situ Interplanetary and Interstellar Dust Detection and Compositional Analysis

-
- First measurements of the composition of dust particles in the heliosphere outside 10 au and in the nearby LISM
 - Predicted vast size range of interplanetary and interstellar dust (ISD) particles
-

Interstellar Dust Analyzer (IDA)

Measurement Objectives	Measure interplanetary and interstellar dust grain densities and compositions within the heliosphere and the LISM
Elemental Composition	1–500 amu
Dust Mass Range	10 ⁻¹⁹ to 10 ⁻¹⁴ g (IDA) 10 ⁻¹⁸ to 10 ⁻¹¹ g (dust counter)
Uncertainty	<100%
Sensitive Area	400 cm ² (IDA); 10,000 cm ² (dust counter)
Atomic Mass Resolution	m/Δm > 200
Angular Coverage	~2π sr
Mass Allocation	10 kg (IDA) 1 kg (dust counter)
Power Allocation	12 W (IDA) 2 W (dust counter)
Mission Requirement	Heliospheric noseward hemisphere preferred such that Interstellar Probe flies roughly into the local interstellar dust stream
Accommodation	FOV must cover the local ram direction of the interstellar flow; dust analyzer and counter should be coboresighted

4.1.5.1 *In Situ Dust Investigation*

The in situ dust measurements will study interplanetary dust (IPD) and ISD distributions in situ both within and outside of the heliosphere. ISD grains flow from the local galactic environment through the solar system because of the solar system’s relative motion through the LISM (e.g., Gruen et al., 1994; Krüger et al., 2007; Krüger & Grün, 2009). These grains carry vital information about the galactic kinematics of our solar system, the structure of the outer heliosphere, and the nature and makeup of our local interstellar and galactic environment (e.g., Altobelli et al., 2016; Sterken et al., 2012; Westphal et al., 2014). Because of filtering effects from solar radiation pressure and electromagnetic perturbations from the heliosphere (e.g., Slavin et al., 2012), the ISD size distribution observed in the inner solar system is highly distorted from that expected in the pristine ISM. Perhaps most importantly for Interstellar Probe’s prime science goals, the amount of dust in the outer heliosphere and heliosheath and the effects of these dust populations on the complex interplay of outflowing solar wind plasma and inflowing ISM material remain unknown.

ISD grains erode the surfaces of airless bodies at the outer reaches of our solar system, such as Oort cloud comets and Kuiper Belt objects (KBOs), potentially contributing to the production of the outer IPD disk (Yamamoto & Mukai, 1998). Each ISD grain also carries critical compositional information, delivering matter that may resemble the original solid building blocks of our solar system (Horányi et al., 2019). Our solar system filters the flow of ISDs, primarily through solar radiation pressure and electromagnetic forces over long timescales (Landgraf et al., 2002; Sterken et al., 2012, 2013). Radiation pressure alone prevents much of the flux from reaching inside 5 au. The filtering mechanism(s) may be sensitive to ISD composition(s); hence, ISD fluxes in the inner solar system may not be representative of the unperturbed, pristine upstream flow from local interstellar space.

Understanding the ISD flux, including its directional variability, remains an unfinished and challenging task (e.g., Krüger et al., 2015; Sterken et al., 2015; Strub et al., 2015) that is directly addressable by an Interstellar Probe/IDA instrument flown through the heliosphere and into the VLISM. In situ measurements of ISD grains taken across a large range of heliocentric distances out past the Kuiper Belt are critical for fully understanding and characterizing the flux and composition of ISD as well as how the solar system filters and interacts with this material. For example, the size distribution of ISD entering the heliosphere measured by Ulysses (Figure 4-19; Landgraf, 2000) contradicts both optical observations and expectations of the required abundance of elements based on current models (Draine, 2009, 2011).

The bottom panel of Figure 4-19 displays the detectable dust grain mass ranges of different instrument components, including IDA, a neutral mass spectrometer (NMS), and an additional dust counter (DC), showing how each would contribute to our understanding of ISM and IPD.

Knowledge of IPD distributions is critical for understanding a multitude of processes throughout the solar system. For example, the flux of IPD grains to planetary systems is responsible for the formation of tenuous rings (e.g., Verbiscer et al., 2009), impact ejecta clouds (e.g., Horányi et al., 2015; Krüger et al., 1999), and neutral exospheres around airless planetary bodies (e.g., Colaprete et al., 2016; Pokorný et al., 2017; Szalay et al., 2016). IPD flux contributes to the spatial and compositional evolution of the main ring system of Saturn (e.g., Cuzzi & Estrada, 1998; Estrada et al., 2015), the injection of meteoric material into planetary magnetospheres (e.g., Christon et al., 2015, 2020), and the alteration of neutral and ionospheric chemistry in planetary atmospheres (Carrillo-Sánchez et al., 2016; Moses et al., 2000; Moses & Poppe, 2017). Determination of the production rates of IPD grains can inform us about the physical evolution of their parent bodies, including, for example, the fading times of Jupiter-family comets (e.g., Nesvorný et al., 2010) or the current-day collisional state of the Edgeworth-Kuiper Belt (EKB; e.g., Abedin & Kavelaars, 2019; Singer et al., 2019; Stern 1995, 1996).

Our solar system’s debris disk also provides “ground-truth” comparison to the multitude of observations of exozodiacal debris disks around other stars (e.g., Bryden et al., 2006, 2009; Chen et al., 2014; Eiroa et al., 2013; Ertel et al., 2018; Hughes et al., 2018; Koerner et al., 2010; Kral et al.,

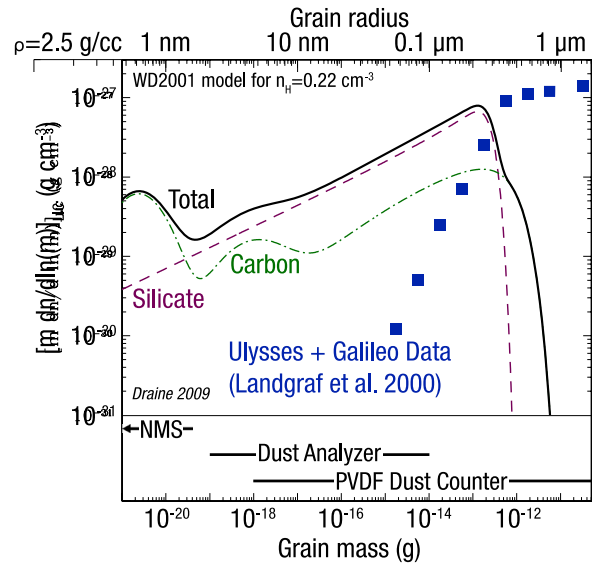


Figure 4-19. Predicted ISM dust population distribution that Interstellar Probe should encounter (solid black curve from Draine (2009)). The dust consists of both silicate and carbonaceous dust grains formed from the thick stellar winds of asymptotic giant branch (AGB) stars and supernovae outflows (Draine, 2011). These predictions, based on the best Earth-based remote-sensing measurements of the VLISM, are in strong conflict with the inflowing ISM particles measured in situ by Ulysses and Galileo in the inner heliosphere (Landgraf, 2000, blue squares), which resemble much more the 0.3- to 100- μm dust grains found from interplanetary sources. (Reprinted from Draine (2009) with permission; © 2009 Springer Nature Limited.)

2017; Millan-Gabet et al., 2011; Montesinos et al., 2016; Trilling et al., 2008), where hidden planets may warp and/or perturb their debris disks in manners similar to how Neptune and/or Jupiter may affect the equilibrium distribution of IPD in our solar system (e.g., Holmes et al., 2003; Liou & Zook, 1999; Moro-Martín & Malhotra, 2002).

Compositional information on the makeup of IPD grains in the outer solar system is also extremely sparse, for the simple reason that when viewed from near 1 au, the inner solar system grains obscure much of the signal from outer solar system dust. Analysis of sample returns by the Stardust mission from comet 81P/Wild 2, which is thought to originate from the EKB, has provided evidence of large-scale radial mixing of material in the solar nebula (e.g., Ishii et al., 2008). On its interplanetary cruise to Saturn, the Cassini Cosmic Dust Analyzer (CDA) recorded TOF mass compositional spectra of only two IPD grains, both iron-rich and surprisingly silicate-poor (Hillier et al., 2007); however, both grains most likely originated from inside 2.5 au and thus are not necessarily representative of outer solar system grain compositions. Further analyses of potential IPD grain compositions detected by the Cassini CDA instrument while in orbit around Saturn continue (e.g., Kempf et al., 2017), yet questions remain about the dominant composition of IPD dust in the outer solar system.

The IDA will make its historic contribution by the simple process of flying the first-ever in situ dust composition analyzer past 10 au from the Sun. Despite previous in situ investigations out to the orbit of Saturn (e.g., Cassini/CDA) and through the Kuiper Belt (e.g., New Horizons/Student Dust Counter [SDC]), as well as Earth-based remote telescopic observations out into the galaxy, the full shape and structure of the solar system's outer debris disk beyond Jupiter is poorly understood because we live inside it. We do not fully understand how much dust is produced from the EKB or how that dust migrates through the outer solar system because near-Sun cometary contributions dominate near-Earth space and only one spacecraft, New Horizons, has ever flown a dedicated dust counter through the EKB (e.g., Piquette et al., 2019).

In situ dust measurements will provide critical information regarding the distribution and structure of IPD grains in the outer heliosphere. While multiple models have been constructed of the outer solar system dust disk (e.g., Figure 4-19; Kuchner & Stark, 2010; Poppe et al., 2019; Vitense et al., 2012), in situ measurements are required to validate these global solar-system-wide models of the IPD density distribution. Based on New Horizons measurements, recent modeling has in fact suggested that dust generated outside of 30 au from EKB objects and Oort cloud comets accounts for ~99% of the total mass of all dust grains in the solar system (Poppe et al., 2019). In other words, the zodiacal light seen from Earth, which is dominated by Jupiter-family comets, comprises only ~1% of the picture. Further validation of this claim requires next-generation follow-up instrumentation capable of building upon and extending the in situ measurements made by New Horizons.

Observing the density and size distributions, flux, and composition of IPD and ISD in the outer solar system, through the transition region, and beyond the heliosphere will bring closure to several critical questions in planetary sciences, heliophysics, and astrophysics.

4.1.5.2 Measurement Requirements

The measurement requirements are summarized in the IDA callout at the beginning of Section 4.1.5. Interplanetary dust particle (IDP) detection is maximized when IDA points into the ram direction of the spacecraft, while ISD detection is most efficient when IDA points into the relative velocity vector of ISD flow as seen from Interstellar Probe.

Ideally, IDA, in combination with other instruments that are capable of measuring in situ dust, must be capable of measuring the full range of expected IPD and ISD grain masses, ranging from 10^{-21} g to 10^{-10} g, to an uncertainty of 100%. For the composition measurements, the atomic mass range should be 1–500 amu with a resolution of $m/\Delta m > 200$ in order to distinguish isotopic variability. Note that because of the very high speed of Interstellar Probe, nearly all dust grains that impact IDA will be reduced to their atomic form, and thus, molecular species are not expected.

4.1.5.3 Instrumentation

An impact-ionization, TOF dust impact instrument composition analyzer similar to that shown in the left panel of Figure 4-20 would measure both the impact rate and the chemical composition of dust submicron-sized grains. This “next-generation” dust instrument would yield vast improvements in our knowledge of the density and chemical compositions of interstellar, and potentially interplanetary, dust grains. This instrument is accounted for on the example payload.

4.1.5.4 Instrument Trades

Other instrumentation should be considered beyond the dust analyzer in order to detect a wider mass range of dust grains.

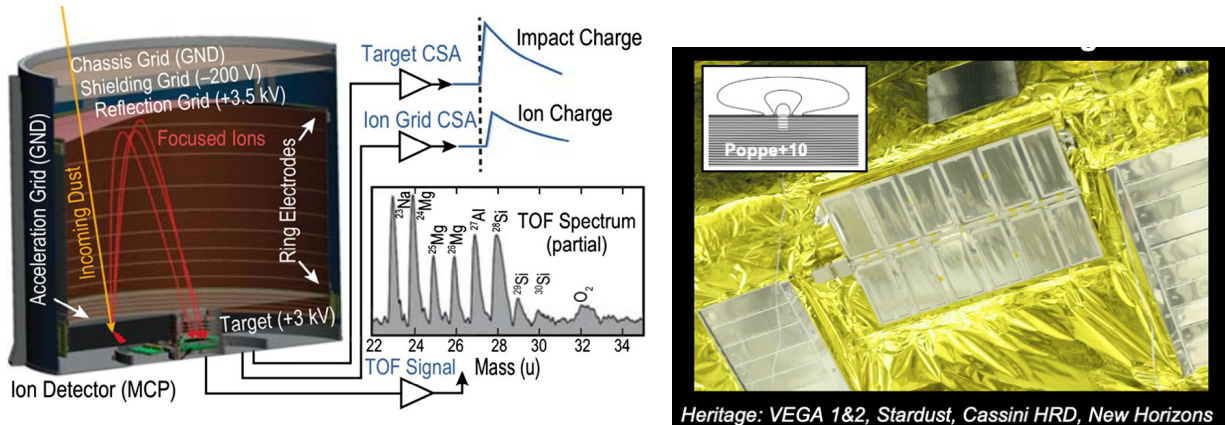


Figure 4-20. (Left) IDA cutaway diagram of the Interstellar Dust Experiment (IDEX) on the IMAP mission (McComas et al., 2018). IDEX detects dust impacts via impact-ionization-produced charge (left) and concurrently produces high-mass-resolution compositional spectra. (Right) Dust counter for detection of the largest (and thus, rarest) particles impinging on the spacecraft (image credit: NASA/Johns Hopkins Applied Physics Laboratory/Southwest Research Institute). The detector relies on the impact-generated removal of polarized material, creating an electrical signal proportional to the amount of plastic removed (and thus the particle's mass). A heritage instrument, the Student Dust Counter, has most recently been flown on the New Horizons spacecraft out beyond 50 au (Piquette et al., 2019; Poppe et al., 2019). HRD, High Rate Detector.

Dust Counter: Less-prevalent micron-sized and larger particles found along Interstellar Probe’s trajectory through the circumsolar dust cloud could be detected by using an instrument similar to the New Horizons/SDC impact Dust Counter (DC). The DC uses thin polyvinylidene fluoride (PVDF) films that are lightweight and can be attached to the back side of the communication high-gain antenna (or other flat surface), as was done on board the Pioneer 10 and 11 “beer can” experiments (Humes, 1980). Although this instrument is not accounted for on the example payload, it should be simple to add.

Neutral Mass Spectrometer (as described in Section 4.1.6): Extremely small nanodust particles may exist in the interstellar flow and can be measured by the NMS instrument. Their elemental composition (volatile and refractory species) can be observed by a type of NMS as proposed in Section 4.1.6 via the collection foil measurement approach, but additional calibration of the fragmentation pattern of nanograins at impact speeds relevant for the Interstellar Probe may be needed. This instrument is accounted for on the example payload.

Of note, the plasma wave antennas (see Section 4.1.3) will also be able to detect dust grains, although this is not their primary function. This instrument is accounted for on the example payload.

4.1.5.5 *Enhancing Technology Development*

The technology development needs of Interstellar Probe/NMS mainly concern the accumulation method for nanodust grains. The collection foil method that has been optimized for neutral gas detection (see NMS description, Section 4.1.6) must be fully tested and then modified for nanodust grain optimization.

The technology development needs of IDA are minimal. Similar instruments are currently under development at the University of Colorado/Laboratory for Atmospheric and Space Physics (CU/LASP): the SURface Dust Analyzer (SUDA) instrument on Europa Clipper and the Interstellar Dust Experiment (IDEX) on IMAP. As of September 2021, SUDA’s flight version is nearing completion and is ready for its environmental testing, with delivery to spacecraft integration at the end of the year. Concurrently, IDEX has passed its preliminary design review (PDR), and its critical design review (CDR) is scheduled for spring 2022. The instrument will be delivered by mid-2024, for launch in 2025. Although neither of these instruments can be used as a build-to-print approach for Interstellar Probe (SUDA is designed for heavy radiation shielding, and IDEX is a very large instrument to detect ISD at L1), the mass/power versus sensitive surface area versus the desired spatial resolution can be readily optimized. Figure 4-21 shows an example impact-ionization TOF mass spectrum from a laboratory version of an Interstellar Probe/IDA, demonstrating clear detection of multiple, well-separated mass peaks from the impacting dust grain.

Despite the high level of existing heritage instrumentation for the IDA, technology development could be leveraged to implement a “gain-switching” mechanism for IDA TOF detection. The IDA electronics currently limit composition measurements to a range of five orders of magnitude in grain mass (e.g., see Figure 4-19); grains below this range do not register sufficient charge, while grains larger than the upper limit saturate the electronics. Such a limited range is suitable for

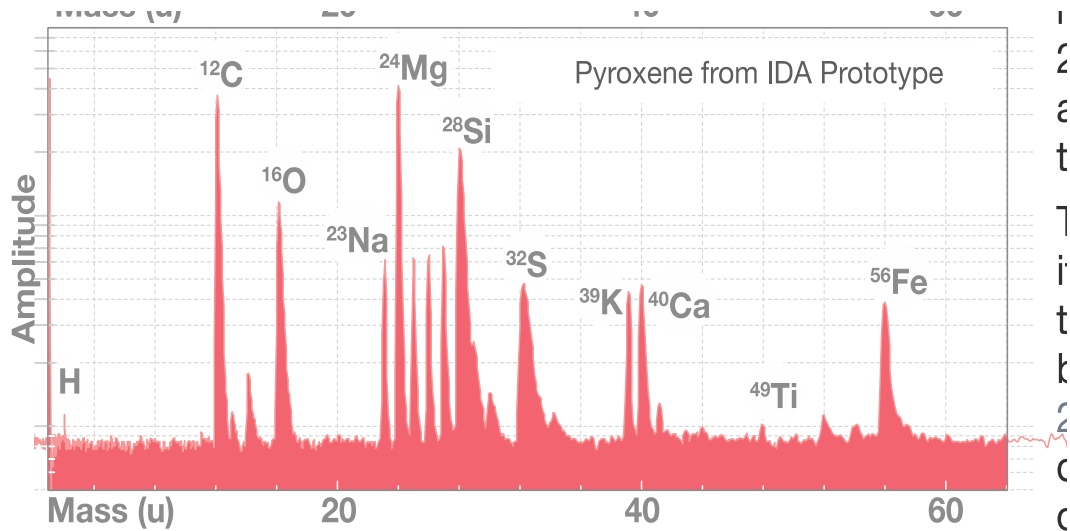


Figure 4-17. An example mass spectrum of a pyroxene particle (radius ~ 30 nm, speed ~ 18 km/s) as recorded in the IDA lab model at the CU/LASP dust accelerator facility. The mass resolution of $m/\Delta m > 100$ clearly resolves several isotopes of Mg and Si, for example. (Image courtesy of M. Horanyi.)

measuring either ISD grain compositions ($< \sim 0.3$ μm) or heliospheric dust grain composition ($> \sim 0.3$ μm); however, compositional measurements of both populations are highly desired. The development of a settable gain for the IDA TOF section could allow the instrument to measure the composition of both interplanetary and interstellar populations, albeit not simultaneously. Namely, within the IPD-dominated region ($< \sim 75$ au), the gain would be set low, such that the IDA TOF does not saturate for the expected large, micrometer-sized impacts of IDP grains. Beyond ~ 75 au, the gain could be set to high to obtain compositional spectra of the much smaller ISD grains.

The technology development needs of the DC are also minimal. The Cosmic Dust Experiment (CDE) on board the Earth-orbiting Aeronomy of Ice in the Mesosphere (AIM) satellite and the SDC instrument on board New Horizons were PVDF-type impact detectors built at CU/LASP. The desire to fly a PVDF sensor as big as reasonably possible stems from the desire to extend the mass range of the detectable ISD/IDPs to include the rarer large (> 0.5 μm) particle population that has been observed in the Kuiper Belt. The existence of such a large particle population in the VLISM also remains an open question (e.g., see Figure 4-19). Since the development of the CDE and SDC instruments, LASP has developed improved electronics designs that reduce the power consumption of PVDF-based instruments by over an order of magnitude. The envisioned large surface area (on the order of a few square meters) could be accommodated on the ram-facing back side of the high-gain communication antenna, as it was for the Pioneer 10 and 11 dust experiments. Although the CDE and SDC instruments consisted of small individually framed PVDF patches, the new approach enables individual patches with much larger surface areas that can be directly attached to exposed spacecraft surfaces.

4.1.6 Neutral Gas

- A neutral gas mass spectrometer is crucial to study the physics of the heliosphere and for sampling the unaltered chemical composition of the ISM for the first time.
- High-sensitivity measurements at a cadence of weeks or months over several decades will be obtained as Interstellar Probe moves out to toward our galactic neighborhood.

Neutral Mass Spectrometer (NMS)

Measurement Objectives	Neutral gas and/or sum of all neutrals and ionized particles in the heliosphere and VLISM
Elemental Composition	H to Fe
Molecular Composition	Masses from 1 to 300 u/e (goal 1-1000 u/e)
Major Isotope Ratios	D/H, ³ He/ ⁴ He, ¹³ C/ ¹² C, ¹⁸ O/ ¹⁶ O, ²² Ne/ ²⁰ Ne, ³⁸ Ar/ ³⁶ Ar
Mass Resolution	m/Δm > 100
Sensitivity	10 ⁻³ cm ⁻³ (direct daily sampling), 10 ⁻⁶ cm ⁻³ (collection method)
Cadence	1x week (10 s for planetary augmentation)
Angular Coverage	Minimum 10° cone around ram direction; maximum conical FOV with 120° opening angle for antechamber mode without pre-collimator
Mass Allocation	10 kg
Power Allocation	11 W
Data Rate	Minimum 1 bps
Mission Requirement	Noseward hemisphere preferred
Accommodation	FOV must cover the local ram direction of the neutral gas, local gas flow must not hit any part of the spacecraft before entering the NMS, and the NMS should be coboresighted with the IDA

4.1.6.1 Neutral Mass Spectrometer (NMS) Investigation

As long as in situ measurements are restricted to heliocentric distances deep inside the heliosphere, only a heavily processed, filtrated, and distorted leftover of the ISM will be observed. This is an intrinsic limitation to near-Earth heliosphere missions such as IBEX and IMAP. Only at heliocentric distances >5 au can more than 50% of the neutrals of all major ISN species be sampled (Sokół et al., 2019), but these neutrals are still far from their pristine condition in the VLISM. This holds even for the most abundant neutral species measured inside the heliosphere, neutral helium: an ISN He atom collides four times on average between the pristine LISM and measurement near Earth (Swaczyna et al., 2021). Living deep inside an astrosphere is beneficial in terms of habitability (Smith & Scalo, 2009), but to gain access to the pristine environment of our local neighborhood (neutrals, plasma, and dust), we need to leave the heliosphere. This will give us the necessary context on our heliosphere and its relation to our local interstellar neighborhood.

With the Interstellar Probe traveling from the inner solar system outward into the VLISM, we will be able to determine the absolute values of neutral species in different regions of the heliosphere and its neighborhood, determine the absolute density in the VLISM, and, by comparison of inside versus outside, quantify the loss and filtration effects including the solar modulation of those effects. We will determine in situ neutral gas temperature and density along the trajectory throughout the heliosphere and beyond, measuring the spatial distributions and identifying

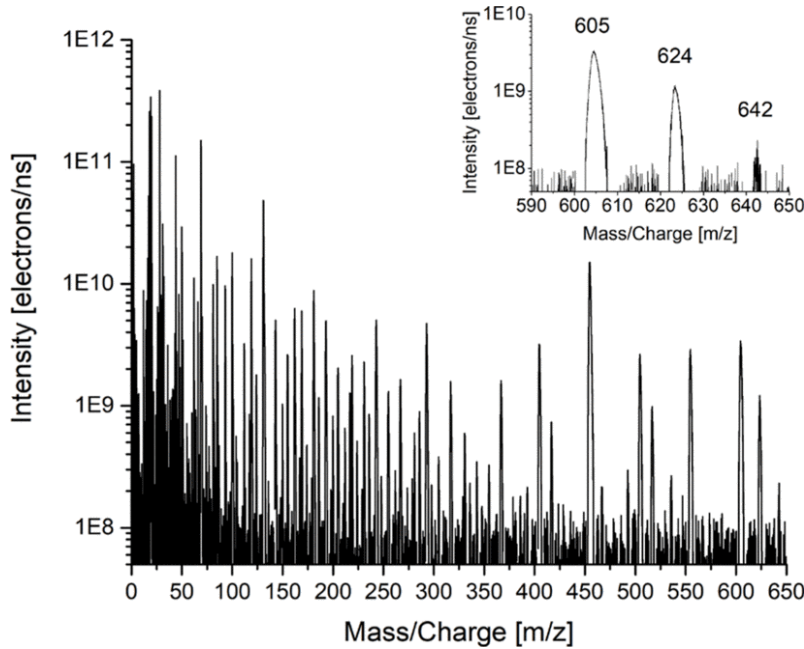


Figure 4-22. Mass spectrum recorded with JUper ICy Moons Explorer’s (JUICE) Neutral gas and Ion Mass spectrometer (NIM) with FC5311 as calibration gas. (Reprinted from Föhn et al. (2021) with permission; © 2021 IEEE.)

potential variations with time. The dominant species are H, He, Ne, O, and C (see the measurement requirements table at the beginning of this section), but all masses from H to Fe will be measured. Measuring neutral H also provides a crucial ground truth to interpret ENA observations and other remote-sensing observations of the heliosphere boundaries. Measuring absolute densities, abundance ratios, and isotopic ratios of neutral matter in the LISM will characterize the VLISM in terms of chemistry and will also quantify filtration effects for the various species. Some of the target species (e.g., ISN carbon) will be detected for the very first time, because they cannot cross into the heliosphere (Müller & Zank, 2004). Regarding the isotopic ratios in the VLISM, the most interesting ratios for cosmology and comparison of solar abundances with its local neighborhood (Frisch et al., 2011) that can be identified with a present-day spaceborne NMS are likely D/H, $^3\text{He}/^4\text{He}$, $^{13}\text{C}/^{12}\text{C}$, $^{18}\text{O}/^{16}\text{O}$, $^{22}\text{Ne}/^{20}\text{Ne}$, and $^{38}\text{Ar}/^{36}\text{Ar}$. On the other hand, the Interstellar Probe trajectory allows for imaging the primary and secondary populations of the most abundant ISN species (H, He, and O) as they enter the heliosphere to determine their densities and temperature distributions.

4.1.6.2 Measurement Requirements

The science drivers listed in the previous section led to the measurement requirements summarized in the table at the beginning of this section (e.g., Mass Resolution, Elemental Composition, and Molecular Composition). The mass range could be restricted to 1–150 amu in most cases, because intact large molecules and nanograins are rare and will likely fragment to smaller masses upon hitting the NMS entrance. However, the ability to cover the mass range 1–1000 u/e is rather simple for present-day mass spectrometers and can thus easily be included (Fausch et al., 2018; Föhn et al., 2021).

The required sensitivity derives from the composition of the VLISM (predominantly neutral hydrogen) with abundances of the interesting trace elements of Na and Fe amounting to a few parts per million with respect to H (e.g., Frisch et al., 2011) and a total neutral VLISM density on the order of 0.1 cm^{-3} (e.g., Heerikhuisen et al., 2014). Thus, a sensitivity of at least 10^{-6} cm^{-3} is required (at least for integration times of at least 1 month).

The required cadence is a trade-off between data rate constraints, obtainable SNR, and required spatial resolution of changes in neutral gas composition along the Interstellar Probe trajectory. Assuming a speed of 8 au/year, acquisition of one spectrum per month corresponds to a spatial resolution of ~ 1 au, which can be considered the minimum requirement given the expected length scales of neutral densities in the VLISM (Heerikhuisen et al., 2014). A longer accumulation time of several months (with the accumulation foil approach) may be needed to detect rare species. Cadences faster than one spectrum per day are only strictly required for planetary augmentation (KBO flybys, etc.)

Mass and power allocation estimates are taken from existing Neutral gas and Ion Mass spectrometer (NIM; Föhn et al., 2021) and Neutral Gas Mass Spectrometer (NGMS) instruments (Fausch et al., 2018); the older quadrupole mass spectrometer Ion and Neutral Mass Spectrometer (INMS) also had a mass of 9.25 kg (Waite et al., 2004). Regarding power, 11 W is realistic for weekly measurements: 1 day out of 7 we would do the measurements with the antechamber, and a total of 24 measurements would be transmitted. A total of 19 W is realistic for the measurements involving the collection foils (twice-a-year measurement); this measurement needs to heat a collection foil to set free the collected material, so it needs more power.

The assumed minimum data rate of 1 bps corresponds to one mass spectrum per day with 20,000 entries, 32 bits per entry, and $m/z = 1-1000$, including housekeeping and a compression factor of 10 for the Particle Environment Package (PEP)/NIM instrument (Föhn et al., 2021).

4.1.6.3 Instrumentation

Two different types of instruments with high heritage from previous space missions can be used to measure neutrals on board the Interstellar Probe in situ. Their capabilities and shortcomings are complementary, and both would allow for synergies with a Lyman- α ultraviolet (UV) spectrometer on board the Interstellar Probe for remote sensing of neutral hydrogen densities along a line of sight.

1. Neutral gas mass spectrometer: A TOF detector combined with a dual entrance system (closed source for volatile species, accumulation foils for all species and ionization states) can identify elemental and isotopic abundances of all neutral species, covering all atomic species up to Fe. Masses up to 1000 amu can easily be achieved, and (rare) larger molecules or dust fragments can be handled as well. Densities along the trajectory can be measured to obtain time series, but no information on velocity, temperature, or flow direction of particles is obtained. The main challenge for NMS will be to accumulate sufficient neutrals for a good SNR, in particular when mounting and trajectory imply that NMS will only be in the ram direction of neutrals for a short period of each spin. To collect the neutrals, NMS will likely rely on two modes to collect or accumulate neutrals: (1) an antechamber design (also called “closed source” in literature, appropriate for volatiles, one

of the two accumulation modes demonstrated by NIM/PEP on JUperiter ICy Moons Explorer [JUICE]; see Föhn et al., 2021) and (2) in particular for refractory species, a set of foils on a carousel; here, all impacting particles will be accumulated over several months before the foil is heated and the released gas is analyzed. The carousel can be a simple turn mechanism similar to the LECP instrument or the LASMA (laser ablation mass spectrometer) instrument on Luna-Glob and Luna-Resurs, with Luna-Glob scheduled for launch in October 2021 (Peter Wurz, personal communication, 2021; Fausch et al., 2018).

2. Low-energy ENA camera: An ENA-Lo imager (similar to instruments flown on IBEX and IMAP; see McComas et al. (2018)) can measure intensities, energies, and directions of ISNs and heliosheath ENAs between 10 eV and 1 keV energy, usually distinguishing between the three major species H, He, and O&Ne (the latter two are difficult to separate). If a scanning FOV is used, these measurements enable 2D sky maps of the primary and secondary populations of ISN H, He, and O&Ne, from which spatial and temperature distributions of the different populations can be derived.

4.1.6.4 Instrument Trades

There are two different ways of detecting in situ ISNs on board the Interstellar Probe: an NMS and an ENA-Lo imager. Both offer unique science opportunities that cannot be fully covered by the other or by any other instrument in the model payload. Both types of instruments have been flown or will soon be flown on space missions with technical performances similar to what is needed for the Interstellar Probe. An NMS can measure elemental and isotopic abundances of all ISN species. The threshold goal is all atomic species up to Fe, but current-generation NMSs for space missions, such as NIM/PEP on board JUICE, can measure up to 1000 amu to also handle (rare) larger molecules and nanodust grain fragments. However, an NMS of a reasonable size and mass will need to collect/thermalize samples, thus eliminating information about in situ velocity distribution. Therefore, the information on velocity, temperature, and flow direction is lost. NMS will measure neutral densities of all species along trajectory, which implies time series, but no maps. To retrieve some level of direction information, one could combine a collimator with the scanning over the flow (introduced by the spinning spacecraft), at the cost of dynamic range for the composition measurements, or extra days of measurements.

An ENA-Lo camera or imager, on the other hand, registers the energy and direction of a neutral particle (at moderate resolutions of $\Delta E/E \sim 0.7$ and $6^\circ \times 6^\circ$ angular resolution in the case of the IBEX-Lo imager) but can only distinguish between a few mass groups H, He, and heavier species (O&Ne). At the typical energy range of 10 eV to 1 keV (IBEX-Lo, IMAP-Lo), an ENA-Lo imager collects both ISNs and heliosheath ENAs, yielding moderately resolved 2D sky maps of ISNs and ENAs. From the spatial distribution, the temperature and velocity of the primary and secondary interstellar populations of the dominant species (H, He, Ne&O) can be derived. The challenges for interpretation of such low-energy data are similar but not worse on the Interstellar Probe compared with the IBEX and IMAP missions in the case of ram observations. For both types of instruments, the ram direction of the ISNs relative to the spacecraft must be covered by spinning or using a scanning platform along with a prudent choice of trajectory.

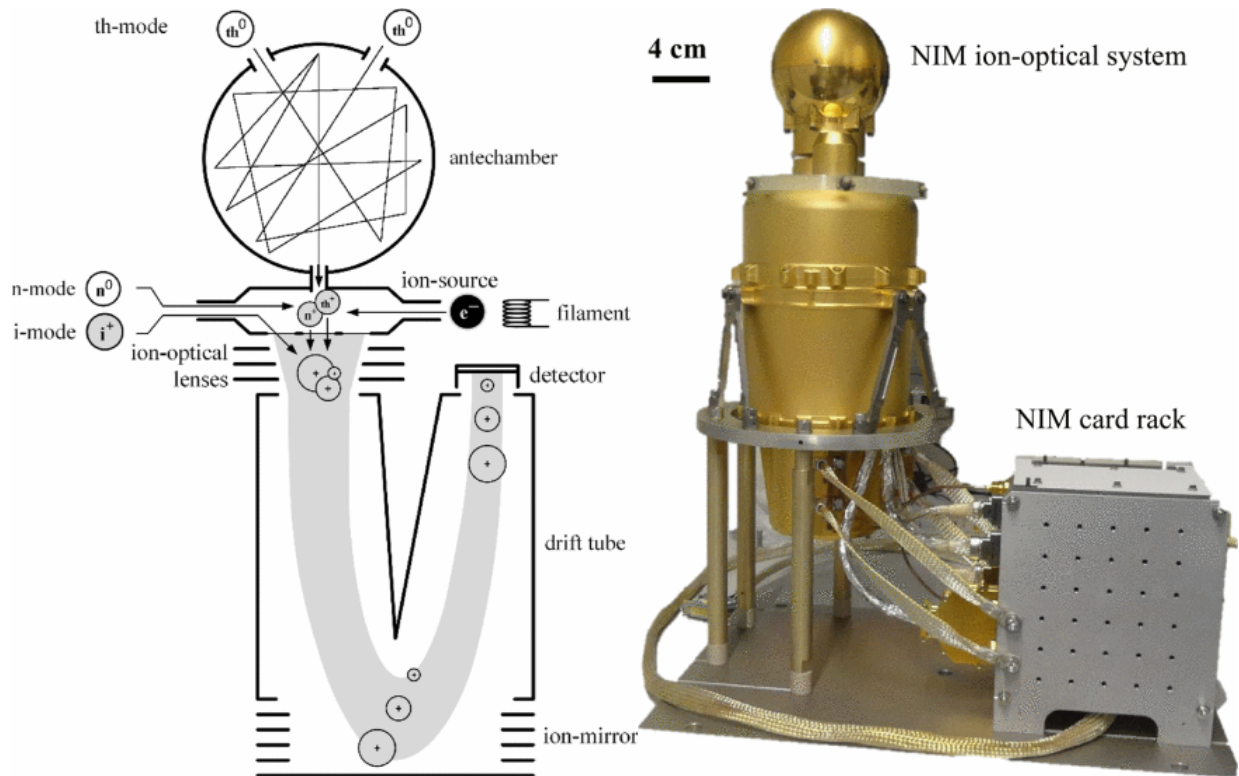


Figure 4-24. Schematics (left) and photograph (right) of the NIM TOF mass spectrometer designed for the JUper ICy Moons Explorer (JUICE) mission. (Both images reprinted from Föhn et al. (2021) with permission; © 2021 IEEE.)

In summary, an ENA-Lo imager would give us more insight into the interaction of the ISM with the heliosphere (the secondary ISN He, H, and O populations are created by these interactions), whereas an NMS is mandatory to sample the ISM itself, including rare species and at least some of the isotopic ratios, which is one of the unique selling points of an interstellar mission from the point of astronomy and cosmology. Limitations in mass and power as well as lifetime considerations led the team to include only the NMS in the example model payload. One could attempt to recover part of the science lost due to the absence of an ENA-Lo imager by operating the NMS with a narrow-field pre-collimator (in front of the antechamber) in combination with the spinning of the spacecraft to obtain a 2D scan from a given point. But this option would come with the trade-off of a sensitivity loss or lower duty cycle.

4.1.6.5 Enhancing Technology Developments

Generally, NMSs meeting the requirements for the Interstellar Probe mission already exist and have been or will be flown on planetary missions lasting more than a decade (Cassini and JUICE for instance). The main technical development to prepare for specific use on the Interstellar Probe will be directed at the way the neutrals hitting the Interstellar Probe will be collected and accumulated before analyzing them with the TOF system. The main driver of development for NMS will be the required instrument sensitivity (10^{-3} cm^{-3} for daily or weekly sampling via the antechamber and 10^{-6} cm^{-3} for the accumulation method where integration is approximately months. Currently, the two options foreseen for NMS to accumulate neutrals are the antechamber

and accumulation foils on a carousel. The longevity of the second mode of operation should be further investigated.

An additional option to be investigated is the use of a switchable high voltage (HV) deflection in front of the NMS entrance to switch between accepting neutrals and plasma and only accepting neutrals. This would allow us to recover some science otherwise lost if the Interstellar Probe does not have a dedicated instrument to measure heavy plasma species; the ion composition would then be the difference between an NMS measurement with and without ion rejection. To measure ions directly at these velocities (and thus energies), one would need a dedicated ion instrument. If we assume the ions all have the same speed, then a simple energy analyzer can already be quite useful (see Cassini negative ions); if not, an approach similar to the Mass-Time-of-Flight (MTOF) experiment on Solar and Heliospheric Observatory (SOHO) or some other linear electric field mass spectrometer might be necessary.

4.1.7 Lyman-Alpha

- Interaction of the interstellar hydrogen with plasma from the VLISM to the inner heliosphere is not understood.
- The nature of the hydrogen wall remains unknown.
- High-resolution measurements of Lyman- α spectra on the Interstellar Probe are required to characterize properties of interstellar hydrogen across hundreds of astronomical units from the Sun.

4.1.7.1 Lyman-Alpha (LYA) Investigation

UV Spectrograph (LYA)

Measurement Objectives	Lyman- α line profiles from nose-to-tail directions to quantify velocity distribution of interstellar hydrogen
Wavelength Range	120–130 nm
Wavelength Resolution	5–10 km/s (0.002–0.004 nm)
Sky Coverage	At least half-sky covering nose and tail directions
Cadence	Monthly
Mass Allocation	12.5 kg
Power Allocation	12 W
Data Rate	0.01–600 bps
Mission Requirement	Spinning platform at ≤ 60 s
Accommodation	Pointing away from the Sun

Interstellar hydrogen atoms are the dominant constituent of the interstellar gas and play a major role in the interaction of the solar wind with the VLISM and, hence, in the global structure of the heliosphere. However, the properties of interstellar hydrogen in the VLISM such as density, velocity, and temperature and their modification as hydrogen flows into the heliosphere through its complex boundary remain poorly constrained observationally.

Measuring solar Lyman- α (1215.67 Å) emission backscattered from interstellar H atoms is a powerful technique to probe interstellar H atoms. A spectral shape of the Lyman- α emission line holds key information on spatial and velocity distribution of interstellar hydrogen and enables us to infer momentum exchange between hydrogen and plasma.

Twenty-five years of SOHO/SWAN Lyman- α observations from 1 au brought many discoveries: a detection of secondary, warmer, and slower interstellar hydrogen created beyond the heliosphere (Costa et al., 1999); deflection of interstellar hydrogen flow in the heliosphere (Lallement et al., 2005, 2010); variations of the interstellar hydrogen velocity and temperature in the heliosphere due to the solar-cycle effects (Quémerais et al., 2006); and stability of interstellar hydrogen inflow longitude (Koutroumpa et al., 2017). However, limited spectral data obtained from a hydrogen cell on SOHO/SWAN left many open questions such as: (1) What is a spatial and velocity distribution of the interstellar hydrogen in the heliosphere, and what does it tell us about the charge-exchange coupling at the heliosphere boundary and beyond? (2) What are the effects of various hydrogen populations on the global interaction? (3) What are the structure and properties of the hydrogen wall, and what is the relation to similar structures existing around other astrospheres? (4) Are there any inhomogeneities in the LISM on scales of tens of astronomical units or hundreds of astronomical units?

Measurements on Voyager/Ultraviolet Spectrometer (UVS) (Katushkina et al., 2017) and New Horizons/Alice (Gladstone et al., 2018) showed a surprising behavior of Lyman- α intensity with distance from the Sun, implying an additional emission of few tens of Rayleigh (Figure 4-25). A question about the source of this emission remains unanswered. Resolving a spectrum of Lyman- α emission is required to distinguish a possible contribution from the galactic background.

The Interstellar Probe mission with a UV spectrograph on board will answer the compelling questions by making high-spectral-resolution measurements of Lyman- α emission on outward trajectory from the Sun. Spectral measurements on the Interstellar Probe would enable us to (1) determine the properties of interstellar hydrogen flow such as density, velocity, and temperature; (2) discover a position of the hydrogen wall and 3D structure of this unique unexplored global feature; (3) determine the properties of hot hydrogen atoms created in the heliosheath and their spatial variations (enabling an additional diagnostic of the global heliosheath structure); (4) determine a deflection of interstellar hydrogen flow in the heliosphere compared to pristine interstellar flow and discover any deviations from the previously reported deflection of 4° (Lallement et al., 2005, 2010); and (5) identify galactic and extragalactic components of Lyman- α (Gladstone et al., 2018; Katushkina et al., 2017; Lallement et al., 2011). Spectra taken at different distances from the Sun and in different look directions will for the first time enable global diagnostics of the non-Maxwellian velocity distribution function of the interstellar hydrogen and therefore understanding of plasma–hydrogen coupling processes in the context of the global heliosphere–LISM interaction.

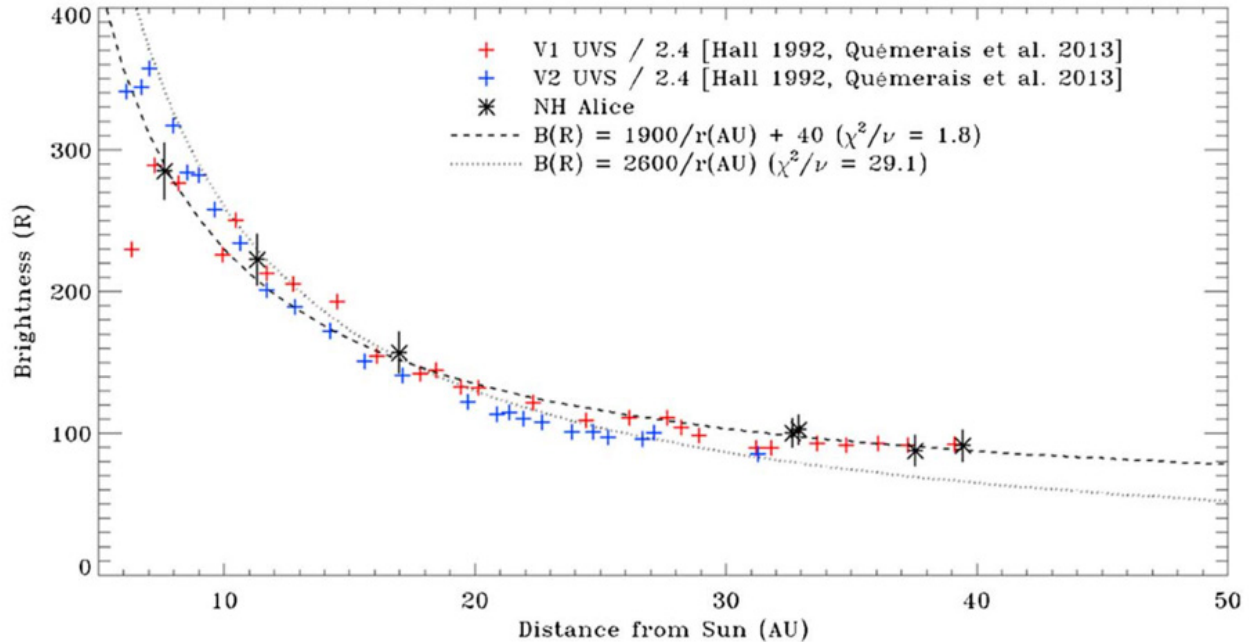


Figure 4-25. Observed falloff in brightness of interplanetary Lyman- α emission viewed in the upwind direction as measured by the UVS on Voyager 1 (red crosses) and Voyager 2 (blue crosses) scaled downward by 2.4 \times , and by Alice on New Horizons (black asterisks, with 3- σ error bars). Additional distant upstream brightness of 40 R to the expected 1/r dependence is needed to explain Alice data. (Figure from Gladstone et al. (2018).)

4.1.7.2 Measurement Requirements

To distinguish contributions to the Lyman- α emission line of different hydrogen populations created in the heliosheath or hydrogen wall or coming from the pristine VLISM as well as the galactic emission component, a Doppler velocity resolution of a few to 10 km/s is required. This corresponds to a wavelength resolution of 0.002–0.004 nm or resolving power $R \sim 30,000$ –60,000. A resolution of 0.008 nm was achieved on Mars Atmosphere and Volatile Evolution (MAVEN)/Imaging Ultraviolet Spectrograph (IUVS) in echelle mode (Mayyasi et al., 2017). A sample spectrum of interplanetary hydrogen Lyman- α emission obtained during the cruise to Mars is shown in Figure 4-26. Previous measurements of line widths and line shifts on SOHO/SWAN with the hydrogen absorption cell during half of the solar cycle in 1996–2002 showed noticeable variability of spectral characteristics on yearly timescales (Quémerais et al., 2006). Therefore, a several-months cadence of spectral measurement by LYA will be sufficient to investigate possible variations within a year due to solar effects. To infer spatial variations of line-of-sight hydrogen velocity distributions, multiple look directions are required, in particular toward the nose, toward the tail of the heliosphere, and sidewise, covering at least half of the sky.

4.1.7.3 Instrumentation

UV instruments that are capable of resolving a line profile of backscattered Lyman- α emission include a high-resolution spectrograph and a spatial heterodyne spectrometer (SHS). MAVEN/IUVS is an example of a spectrograph that includes a far-UV spectral channel that uses an echelle grating (Figure 4-26) to resolve H and D Lyman- α lines (echelle channels were also implemented in the

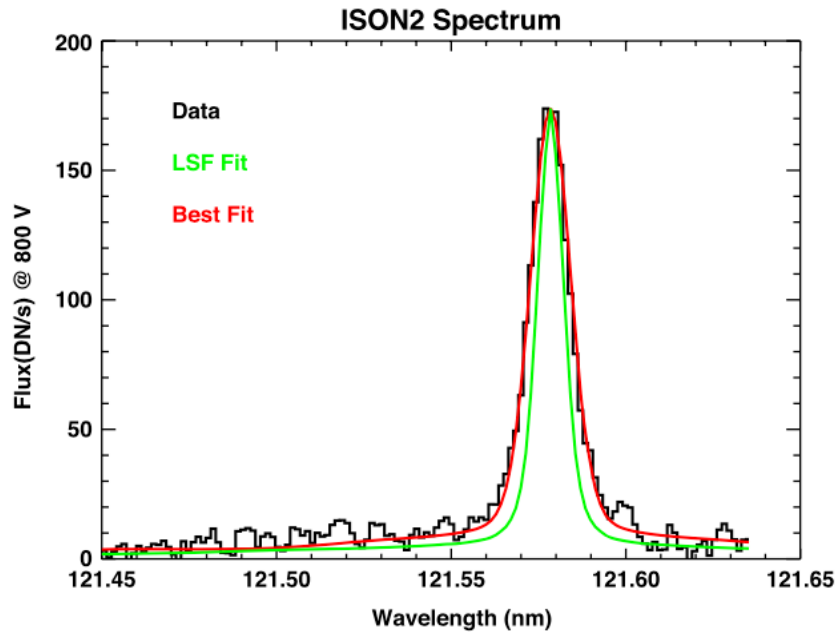


Figure 4-26. Spectrum of interplanetary hydrogen Lyman- α emission observed by IUVS echelle on MAVEN in December 2013 during the cruise to Mars. The black line is a coadded spectrum from the total 3 hours of integration. Instrument line spread function (green) and best fit to the data (red) are shown. (Figure from Mayyasi et al. (2017).)

Hubble Space Telescope [HST]/Goddard High Resolution Spectrograph [GHRS] and the HST/Space Telescope Imaging Spectrograph [STIS]; Clarke et al. (1998)). These instrument packages are typically large. A compact spectrograph design with a high spectral resolution and a high sensitivity is a subject of the technology development for a UV instrument on the Interstellar Probe. An alternative to grating spectrographs is an SHS with a high resolving power ($R \sim 10^5$) and a compact design that recently has been under development for laboratory tests and sounding rocket flights (Harris & Corliss, 2018). SHS is a self-scanning Fourier transform spectrometer. An all-reflective SHS design uses a grating serving as a beam-splitter and a dispersing element and mirrors translating beams back to the grating where they interfere and exit the system (Harris et al., 2005). An SHS optical layout is shown in Figure 4-28.

Another approach is to use a hydrogen absorption cell to reconstruct the Lyman- α line profile. The cells were implemented on the Prognoz 5 and 6, NOZOMI, and SOHO/SWAN missions (Bertaux et al., 1995). The absorption cell uses its internal H atoms as a narrowband absorption feature. The motion of a spacecraft provides a Doppler shift of this narrow absorption feature against the observed Lyman- α line profile. Continuous measurements with the cell ON and OFF in any chosen direction on a solar orbiting SOHO/SWAN enabled a Doppler scanning of a line profile (Qu  merais et al., 1999, 2000). While a photodetector approach with a hydrogen absorption cell can be made with low mass, power, and data rates, it only provides indirect information on the line shape and only for a limited range of Doppler shifts controlled by the spacecraft orbit design.

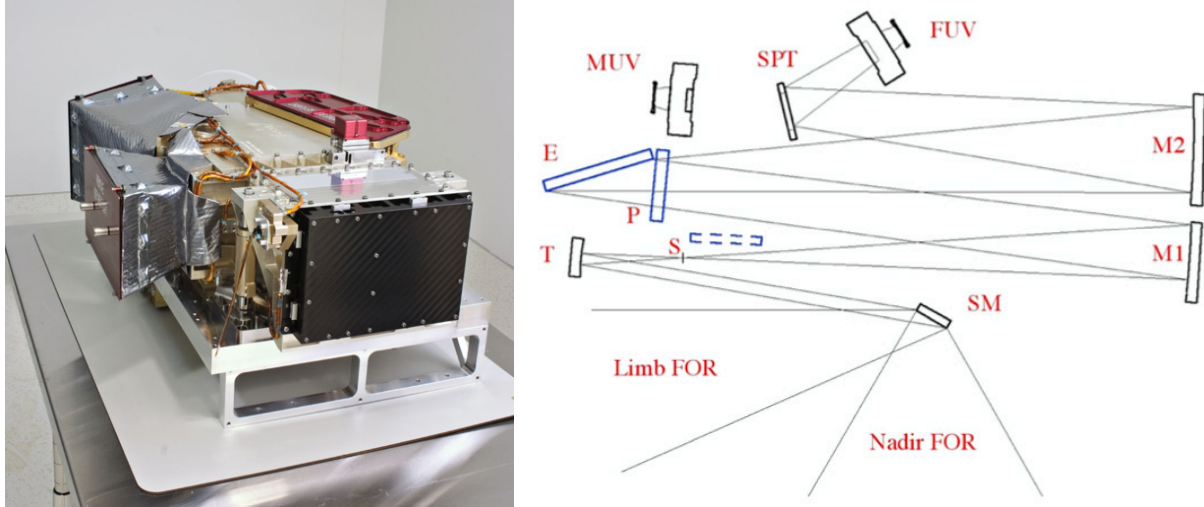


Figure 4-27. (Left) MAVEN Imaging Ultraviolet Spectrograph (IUVS) instrument image taken during instrument testing at the Laboratory for Atmospheric and Space Physics (Bale et al., 2016) at the University of Colorado (reprinted from McClintock et al. (2015) with permission; © 2015 Springer Nature Limited). (Right) IUVS optical schematic showing the light path through a prism-echelle grating combination (P-E) in the echelle mode enabling resolution of H and D Lyman- α emission lines (Clarke et al., 2017). FUV, far ultraviolet; MUV, middle ultraviolet; note that other labels indicate different optical components of the instrument.

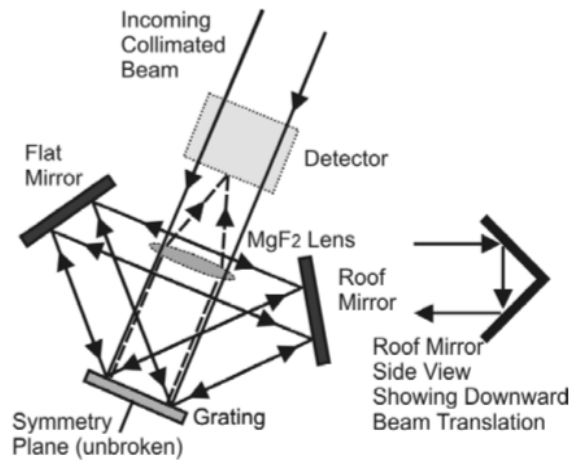


Figure 4-28. Optical layout of an all-reflective spatial heterodyne spectrometer. (Reprinted from Harris et al. (2004) with permission; © 2004 SPIE.)

4.1.7.4 Instrument Trades

4.1.7.4.1 High-Resolution Spectrograph versus Photometer

Using different instrument options affects the extent to which science objectives for interstellar hydrogen investigation can be achieved. Measurements of Lyman- α line profiles with a high-resolution spectrograph enable us to determine the density, velocity, and temperature of different hydrogen populations from the heliosphere through the boundary to the VLISM; to determine trace variations in different H contributions and deviations from Maxwellian distributions as a

function of a distance from the Sun and look directions; and thus to understand complex coupling processes between interstellar hydrogen and plasma in regions with different properties (heliosheath, hydrogen wall, pristine VLISM). Taking Lyman- α spectra in different look directions through the hydrogen wall, a 3D structure of the wall will be determined.

Photometric observations enable us to measure Lyman- α emission intensity in different directions on the sky, allowing us to determine hydrogen density; however, because of a lack of spectral information, the ability to determine velocity and temperature would be eliminated. A position of a maximum hydrogen density in the hydrogen wall and its extent along the spacecraft trajectory can still be determined by using kinetic hydrogen models.

4.1.7.4.2 *High-Resolution Spectrograph versus Spatial Heterodyne Spectrometer (SHS)*

State-of-the-art technological developments and instrument concepts for obtaining high-spectral-resolution far-UV emission spectra include an SHS or a reduced-size echelle spectrograph. The SHS would be ideal for measurements >300 nm, but it is not currently possible to obtain the required resolution at Lyman- α because of insufficient fringe contrast from limitations imposed by grating surface roughness (e.g., Harris et al., 2004). This approach would require significant technology development. By contrast, the approach of using an echelle spectrograph is feasible today, although it will require downsizing.

4.1.7.5 *Enhancing Technology Development*

The size and mass constraints for an LYA instrument in the heliophysics baseline mission payload for the Interstellar Probe are considerably smaller than prior instruments flown to perform high-resolution spectroscopy at Lyman- α . The best current example is the MAVEN IUVS echelle channel, part of the IUVS instrument that is $62 \times 54 \times 23$ cm and 22 kg. The instrument size and mass can be greatly reduced by incorporating only an echelle channel and folding the optics with flat mirrors. The optical system is constrained to be $f/15$ - 20 to maintain the high spectral dispersion, and there will be a trade-off between sensitivity and size of the instrument package that needs to be studied in detail. Fortunately, the long integration times available in the Interstellar Probe mission can lead to high sensitivity to faint emissions if a suitably low background detector is used.

4.2 **Trajectory Science Trades**

Given a direct launch to Jupiter for either a passive or a powered Jupiter gravity assist (JGA), the heliospheric boundary and VLISM can be reached through the leading hemisphere of the heliosphere through a series of launch opportunities beginning around 2036, as shown in Figure 4-29. The speed map was computed assuming an SLS Block 2 launch with an Atlas V Centaur and Star 48BV kick stage that are all used shortly after launch for a direct injection to Jupiter, where a passive (“ballistic”) JGA follows. Speed maxima arise from the dependence on the relative orbital velocity between locations of Earth and Jupiter with a recurrence of roughly every 13 months. The decade-long modulation seen across the maxima arises from Jupiter’s position in its 11.86-year orbit around the Sun. For a detailed description of the construction of this map, please see Appendix B.

(~30 au) in all directions, IBEX observations imply a distance of the HP of ~150–200 au in this direction (Reisenfeld et al., 2021). Models predict a distance to the TS of 91 au and a distance to the HP of 148 au (Shresta, personal communication), which corresponds to a heliosheath thickness of 57 au. Thus, this direction places a particularly important constraint on models. The angle of exit relative to the nose direction of ~80° also offers a clear side view for ENA and UV imaging of the heliosphere once beyond the HP that could discern a possible existence of any extended tail structures. And lastly, the ecliptic latitude has been chosen to intersect the ribbon, although somewhat weaker on this side of the nose. As will be discussed in Appendix A, this is also the general direction toward the dwarf planet Orcus with its moon Vanth that provide a very compelling flyby target at only 30 au for potential planetary augmentation of the mission concept. All directions in the leading hemisphere and their individual trades are summarized in Table 4-1.

Trajectories in the downwind direction provide valuable exploration of the possible tail structure, turbulent regions of potential jets, and directions toward strong extreme ultraviolet (EUV) stars to explore the ionization process in the local interstellar cloud. However, the distances to the HP in these downwind directions generally result in high uncertainties on the order of hundreds of astronomical units, and the net ram speed of interstellar material would be low, making it more challenging for in situ measurements of interstellar gas, dust, and plasma.

Table 4-1. Four flyout directions across the sky have been identified, each with its own benefits and trades. Flyout time estimates to 100 au of the Interstellar Probe are given.

Direction	Launch	Trade	Target Flight Time
180° elon, -20° elat (Option A)	2036	<ul style="list-style-type: none"> ▪ Early launch ▪ External side view ▪ ACR flank measurements ▪ Intersects ribbon ▪ Smallest net ram speed 	TS: 13–14 years HP: 17–29 years
205° elon, 0° elat (Option B)	2037	<ul style="list-style-type: none"> ▪ Adequate external side view ▪ Moderate net ram speed ▪ Does not intersect ribbon 	TS: 12 years HP: 16 years
Nose	2038	<ul style="list-style-type: none"> ▪ Intersects maximum ENA globally distributed flux (GDF) intensity region ▪ Maximum net ram speed ▪ Does not intersect ribbon ▪ No side view external viewpoint 	TS: 13 years HP: 17 years
295° elon, 0° elat (Option C)	2041	<ul style="list-style-type: none"> ▪ Late launch ▪ Adequate external side view ▪ Moderate net ram speed ▪ Intersects ribbon ▪ Longitude similar to Voyager 2 ▪ Direction similar to New Horizons 	TS: 12 years HP: 16–20 years

4.3 Example Model Payload

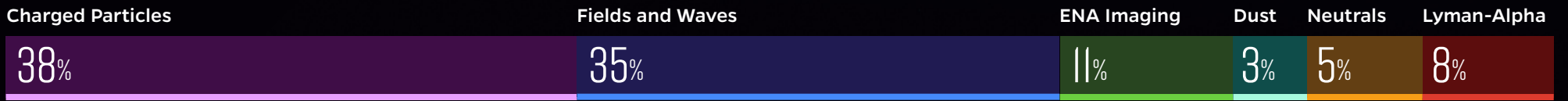
One of the many challenges of Interstellar Probe includes selecting instrumentation that will collectively meet science requirements over a long baseline. To accomplish this, a variety of instruments will need to be included in the payload, while keeping in mind size, mass, and power

EXAMPLE MODEL BASELINE PAYLOAD

Payload Mass and Power

87.4 KG | 86.7 W

PERCENTAGE OF SCIENCE OBJECTIVES ADDRESSED



PERCENTAGE OF PAYLOAD MASS



INSTRUMENT <i>Heritage</i>	MEASUREMENT REQUIREMENTS	MISSION REQUIREMENTS	SCIENCE DRIVER
Magnetometer (MAG) (MMS/DFG)	0.01–100 nT; 0.01 nT (1e–8 nT ² /Hz turb.)	≤60 s; (100 Hz)	Two FG, 10-m boom LISM (turbulence)
Plasma Waves (PWS) (Van Allen/EFW)	~1 Hz – 5 MHz; Δf/f ≤ 4% ≤ 0.7 μV/m @ 3 kHz	≤60 s (≤4 s at TS)	4 x 50 m wire; spin plane LISM n _e , T _e (QTN), turbulence
Plasma Subsystem (PLS) (PSP/SWEAP/SPAN-A)	< 3 eV/e to 20 keV/e. e, H ⁺ , He ⁺ , He ²⁺ , C ⁺ , N-O ⁺	~4π; ≤60 s	Spinning Flows, n _e , T _e , n _i , T _i Force balance
Pick-Up Ions (PUI) (Ulysses/SWICS)	0.5–78 keV/e H, ² H, ³ He, ⁴ He, ⁶ Li, ¹² C, ¹⁴ N, ¹⁶ O, ²⁰ Ne, ²² Ne, Mg, Si, Ar, Fe, charge states	iFOV ≥ 90° x 15°	Spinning Interstellar, inner PUI Force balance
Energetic Particles (EPS) (PSP/EPI-Lo)	20 keV – 20 MeV H, ³ He, ⁴ He, Li, C, O, Ne, Mg, Si, Ar, Fe	~4π; ≤60 s	Spinning S/W, HS and ACRs Force balance
Cosmic Rays (CRS) (PSP/EPI-Hi, in development)	H to Sn; 10 MeV/nuc – 1 GeV/nuc; m/Δm ≥ 10 electrons; 1–10 MeV	2 directions; hours	Spinning ACRs, GCRs LiBeB cosmic story
Interstellar Dust Analyzer (IDA) (IMAP/IDEX, in development)	1e–19 to 1e–14 g, 1–500 amu; m/Δm ≥ 200	iFOV ≥ 90°	Ram direction Coboresighted NMS ISDs, galactic heavy ion composition
Neutral Mass Spectrometer (NMS) (LunaResurs/NGMS, JUICE/NMS)	H, ³ He, ⁴ He, ¹⁴ N, ¹⁶ O, ²⁰ Ne, ²² Ne, ³⁶ Ar, ³⁸ Ar, m/Δm ≥ 100	iFOV ≥ 10°; weekly	Ram direction Coboresighted IDA LISM composition
Energetic Neutral Atom Imager (ENA) (IMAP/Ultra, in development)	~1–100 keV H	iFOV: ≥ 170°	Spinning, 2 heads Shape, force balance, ribbon/belt
Lyman-Alpha Spectrograph (LYA) (MAVEN/IUVS, in development)	±100 km/s Doppler range, <10 km/s resolution	iFOV: ≤ 5°; 140° monthly	Spinning LISM and heliosheath H

Deployed Antennas



constraints for the mission. Instruments in the payload may include particle and field sensors, imaging spectrometers, spectrographs, mass spectrometers, and dust analyzers, for example.

Magnetometers (MAG), placed on a boom away from the spacecraft, are generally accepted to be one of the most critical instruments in the payload. With the exception of composition analysis and particle detection, magnetometers are capable of answering many questions related to the nature of the heliosphere, the VLISM, and the interactions between the two. Although both vector helium magnetometers and fluxgate magnetometers have heritage, because of the lengthy duration of this mission, fluxgates may prove to be the more reliable instrument.

Another set of critical instruments will be a particle suite that covers a wide range of energies. Particle sensors will play a key role in learning more about our heliosphere and the VLISM, providing insight into everything but the neutral hydrogen wall. The suite would most likely include four sensors. First, a plasma subsystem (PLS) would detect thermal ions and electrons up through light PUIs with energies in the 10s to 10,000s of eV. Detecting energetic ions, electrons, inner-source PUIs, and PUIs in the ISM would require an energetic-particle system for particles with energies in the 10s to 1000s of keV (EPS) and a dedicated PUI instrument sensitive to ~100s of eV to 100 keV (PUI). A cosmic ray subsystem (CRS) would account for the highest energy particles, observing ACRs and GCRs with energies most likely ranging from 1 to 1000 MeV. Each of these systems would need as close to full coverage of the sky as possible, most likely achieved through angular coverage provided by a spinning spacecraft.

The final particle and field sensor that might be included on such a mission is a plasma wave subsystem (PWS). This would support measurements made by the magnetometers and particle suite, enabling a better understanding of the size and shape of the heliosphere, particle acceleration in shock regions and the heliosheath, the structure and nature of the HP, and properties of the VLISM and GCR spectra outside the HP. Although the measurements would most likely be made with four components spaced 90° from each other, all perpendicular to ram direction, determining the length and type of antenna used for this instrument is a trade between plasma wave science, guidance navigation and control capabilities, and mission operations.

Another critical sensor suite would involve ENA imagers, where the suite might include one or more imagers designed to image at different energy levels (a low-energy ENA-L at 10–2000 eV, a medium-energy ENA-M at 0.5–15 keV, and a high-energy ENA-H at 1–100 keV). ENA imagers would result in a better understanding of the force balance and ENA ribbon, as well as solar/heliosphere/VLISM interaction and their influence on each other. In particular, an ENA-H that has the capability to point back at our heliosphere once we are well into the VLISM would allow scientists to gain insight into what our astrosphere looks like from the outside. While the two lower-energy ENA imagers would only require noseward hemisphere angular coverage, to view the definitive shape of the heliosphere from the outside, the ENA-H would need full-sky coverage with a Sun exclusion zone.

An NMS would provide key compositional insight during the mission by measuring neutral gas and dust in the VLISM, as well as the neutral hydrogen wall and neutral ISM gas and dust inside the heliosphere. Direct measurements of elemental and isotopic gas compositions of the VLISM would place important constraints on models of stellar nucleosynthesis, which holds implications for the

formation of matter in the galaxy. This would enable a much better understanding of the properties and potential history of the ISM as a whole. The instrument would be placed facing the ram direction. Coboresighted to perform complementary measurements to the NMS could be an Interstellar Dust Analyzer (IDA), which would further establish properties of the VLISM and how it affects our heliosphere. It would also provide important insight into the formation of planetary systems through the examination of IPD.

To round out a heliophysics-focused payload, a Lyman- α spectrograph (LYA) would provide vital information about interplanetary and LISM hydrogen phase-space density. This would enable studies of the neutral hydrogen wall and the properties of the LISM as well as the influence of the Sun and heliosphere on them. LYA would characterize the diffuse galactic Lyman- α emission to constrain radiation transfer in galaxies. The spectral resolution of the instrument would need to be sufficient to resolve ideally ≤ 3 km/s, with a sensitivity of < 1 rayleigh/resolution element. The FOV would maximize angular coverage ($> 2\pi$ sr) while maintaining a Sun exclusion zone, with a placement of the spectrograph on the ram side of the spacecraft. Heritage for such an instrument includes instruments already flying on missions such as MAVEN.

In this study, an example payload was chosen, balancing science requirements that flow from the STM with engineering constraints requiring a payload between 80 and 90 kg. We assumed a spinning spacecraft at a few revolutions per minute, to keep antennas deployed and also provide angular coverage for many of the instruments. Given these parameters, 10 representative instruments were selected for the heliophysics baseline payload to provide a solution to the consensus STM with an engineering implementation approach that “closes.” Top-level mission details are given in Section 3, and spacecraft details are discussed in Section 5.

Two main field sensors were chosen. Two fluxgate magnetometers (MAG) were accommodated on a 10-m boom, spaced at an appropriate distance apart to capture the magnetic fields accurately (Figure 4-30). The closest sensor is outside the spacecraft near field, which allows for the assumption that the spacecraft field is a dipole. The magnetometer boom is deployed shortly after the spacecraft’s separation from the fourth stage and is accommodated in an axial alignment. The payload also includes a plasma wave instrument (PWS), which comprises four 50-m wire boom antennas placed perpendicular to the spacecraft ram direction and 90° apart from each other, to capture two components of the electric field (Figure 4-31). These antennas would be deployed shortly after the magnetometer boom, and the spacecraft spin rate ensures the antennas stay properly deployed throughout the remainder of the mission. Deploying the antennas would require ~ 1 – 2 kg of propellant.

Most of the particle sensor suite, which includes a PLS, a PUI sensor (PUI), and an energetic particle subsystem (EPS), had to be accommodated out on a rigid boom, to achieve full-sky angular coverage for PLS and EPS and avoid having the high-gain antenna in the FOV (Figure 4-32). The fourth particle sensor, which comprises two cosmic ray telescopes (CRS), is accommodated with one telescope on the particle suite boom, pointing 135° away from spacecraft ram direction, and the other telescope pointing 45° away from spacecraft ram direction, accommodated on the body of the spacecraft near the base of the particle suite boom. This 90° angle between the sensors should be sufficient to measure the anisotropies expected in cosmic ray detection. Pointing

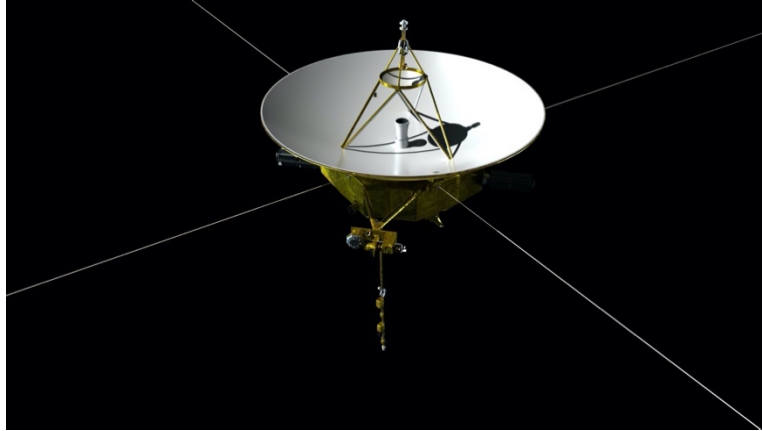


Figure 4-30. Artistic rendering of the spacecraft, showing a clear view of the magnetometer boom. (Image credit: Johns Hopkins Applied Physics Laboratory.)

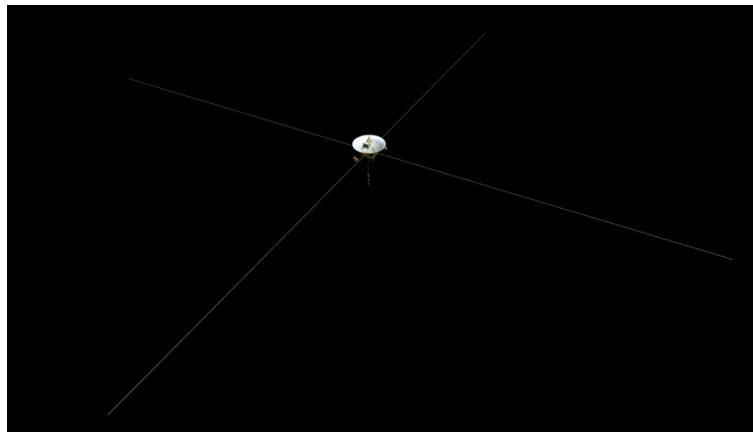


Figure 4-31. A view of the spacecraft showing the full length of the plasma wave antennas. (Image credit: Johns Hopkins Applied Physics Laboratory.)

accuracy for these instruments is assumed to be $\sim 1^\circ$. The spacecraft surface, particularly any obstacles close to the iFOV, needs to be conducting to avoid the buildup of strong charges that may deflect the measured particles and therefore disturb the measurement.

Only one energetic neutral atom imager (ENA) was accommodated, assuming an energy measurement range of ~ 1 –100 keV. Lower energy ranges require telescopes with small FOVs on heavy scanning platforms to achieve appropriate angular coverage. The ENA imager was placed on a boom to achieve full-sky coverage with a Sun exclusion zone of 10° half-angle FOV, assuming an iFOV of $170^\circ \times 90^\circ$. Two instrument heads were assumed in order to achieve this angular coverage. This boom also conveniently aids in balancing the particle suite boom on the other side of the spacecraft. Next to the ENA boom is the LYA, placed on the side of the spacecraft pointing away from the Sun, to achieve more than half-sky coverage in the anti-sunward direction, achieved with an iFOV of 5° that is able to capture 140° over the course of a month (Figure 4-33). We assume a pointing accuracy of 0.4° for this instrument.

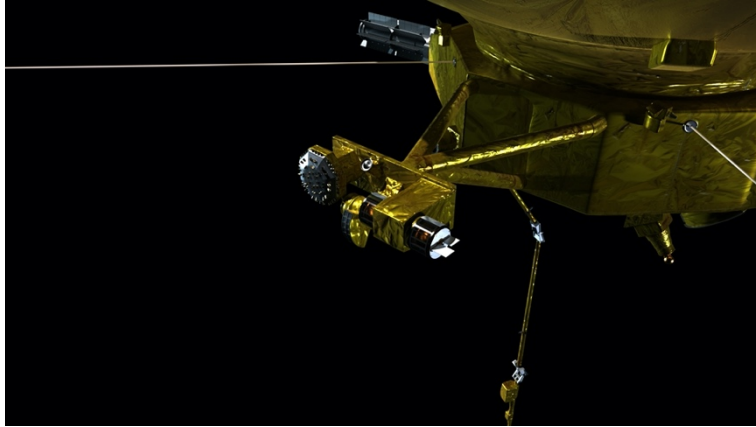


Figure 4-32. A close-up of the particle suite boom. From left to right and top to bottom, EPS, one of the CRS telescopes, PUI, and PLS. The other CRS telescope is to the left of the base of the boom. (Image credit: Johns Hopkins Applied Physics Laboratory.)

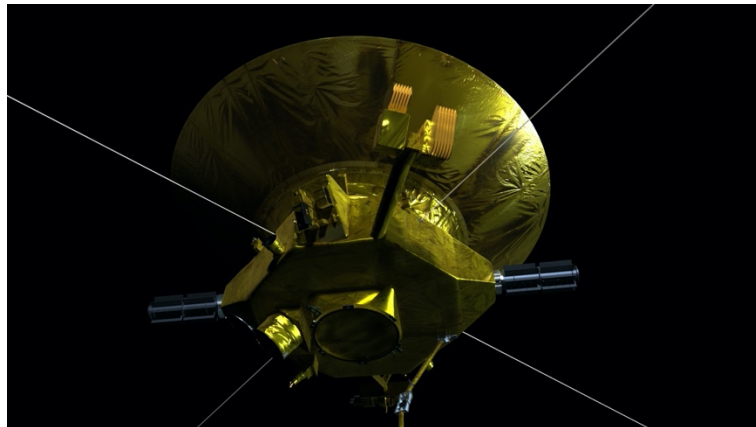


Figure 4-33. ENA out on a boom, with LYA to the left. (Image credit: Johns Hopkins Applied Physics Laboratory.)

The NMS and IDA are cobe-sighted and accommodated on the bottom of the spacecraft (Figure 4-34). They are pointing 38.5° away from spacecraft ram direction, optimized toward the inflow direction of dust and neutrals assuming a flyout direction that takes us 45° off of the nose and remains near the ecliptic plane. This angle was also chosen to avoid FOV obstructions with other instruments and spacecraft structures such as the magnetometer boom. IDA has a 90° FOV, and NMS has a 10° FOV with an antechamber that increases the acceptance cone to 90° . Both instruments are assumed to have a pointing accuracy of $\sim 1^\circ$.

4.4 Science Operations

The baseline Interstellar Probe primary science mission uses a simple concept of operations to autonomously operate 10 instruments and continuously for long periods (see also Section 3). Interstellar Probe science instruments do not require specific pointing of the spacecraft, and the payload does not depend on mechanisms operated by the spacecraft after the magnetometer boom and the 50-m wire antennas are deployed. Measurement sequences are self-contained and are performed simultaneously with little or no impact on the spacecraft or other instruments.

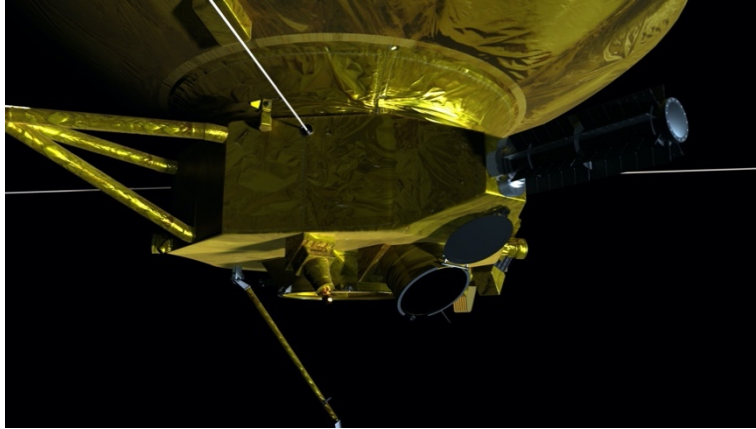


Figure 4-34. NMS and IDA located on the bottom of the spacecraft. (Image credit: Johns Hopkins Applied Physics Laboratory.)

Instrument calibrations and table or parameter changes are infrequent and mainly occur when crossing from one mission phase to the next. Science operations for the mission phases are summarized in Table 4-2, which shows that the majority of the prime mission is conducted over the course of three nominal phases, consisting of operation inside the inner heliosphere ($\sim 1\text{--}90$ au), through the heliosheath/boundary layer(s) ($\sim 90\text{--}120$ au), and into the VLISM itself (>120 au) (Figure 4-35). These phases are elaborated on below. There may also be some periodic instrument calibrations and activities when transitioning between phases to switch to updated tables or parameters for science data collection. Anticipated major scientific events along the mission timeline are summarized in Table 4-3.

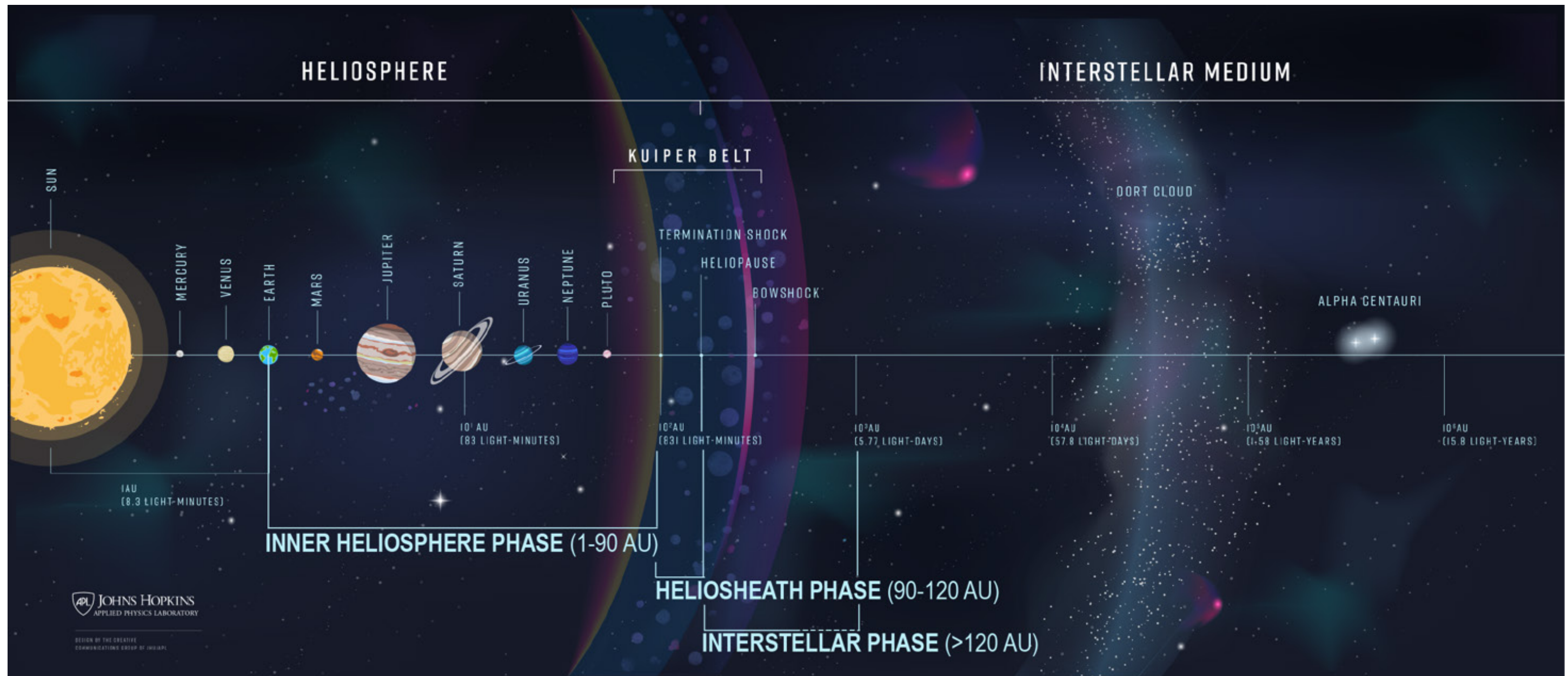


Figure 4-35. Science starts soon after launch with investigations of how the heliospheric boundary is formed by processes deep in the heliosphere and continues throughout the heliospheric boundary (heliosheath) and into the VLISM. (Image credit: Johns Hopkins Applied Physics Laboratory.)

Table 4-2. Interstellar Probe science operations.

Mission Phase	Science Operations
Launch and Checkout	<ul style="list-style-type: none"> ▪ Magnetometer boom deployment ▪ Instrument commissioning
Cruise to Jupiter	<ul style="list-style-type: none"> ▪ In situ particle instrumentation solar wind measurements for checkout ▪ ENA imaging of Jupiter’s magnetosphere and heliosheath for instrument checkout ▪ All science instruments on continuous operations after commissioning with MAG and PWS as allowed
Wire Antenna Deployment	<ul style="list-style-type: none"> ▪ 50-m wire antenna deployment
Jupiter Gravity Assist (ballistic)	<ul style="list-style-type: none"> ▪ ENA imaging of Jupiter on approach starting at 1000 R_J ▪ Continuous operations of all instruments during JGA (pending dust impact and radiation assessment)
Heliosphere Phase	<ul style="list-style-type: none"> ▪ Continuous science measurements ▪ Instruments simultaneously streaming low- and high-resolution data to solid-state mass memory (SSMM)
Heliosheath Phase	<ul style="list-style-type: none"> ▪ Continuous science measurements ▪ Instruments simultaneously streaming low- and high-resolution data to SSMM
Interstellar Phase to 50 Years	<ul style="list-style-type: none"> ▪ Continuous science measurements ▪ Instruments simultaneously streaming low- and high-resolution data to SSMM
Interstellar Phase >50 Years	<ul style="list-style-type: none"> ▪ Continuous science measurements ▪ Instruments simultaneously streaming low- and high-resolution data to SSMM

4.4.1 Heliosphere Phase

Traversing the heliosphere on an outward trajectory offers unique observations of how the heliospheric boundary is already forming from processes deep in the heliosphere. ISNs penetrate close to the Sun where solar EUV radiation ionizes the neutrals to form the so-called interstellar PUIs that are picked up by the magnetized solar wind. As a result, the mass-loaded solar wind eventually slows down as it expands outward (Elliott et al., 2019) until it encounters the TS. Therefore, the first phase of the mission is the heliosphere phase from after commissioning out to the TS, which is predicted to be ~84 au in the example baseline direction. With a speed of ~7.0 au/year, the spacecraft will traverse the TS in a little less than 12 years from launch. During commissioning and checkout of nominally 30–60 days, the magnetometer boom will be deployed followed by centrifugal deployment of the 50-m plasma wave antennas, which can remain deployed for the passive JGA. All scientific instruments should operate shortly after commissioning, but with no requirement to operate during the JGA, during which spacecraft health and safety are the priority. In several previous missions, the mission operations team has found ways to maximize science return while keeping the spacecraft safe even during gravity assists and critical burns (e.g., during Cassini’s Jupiter flyby as well as Saturn orbit insertion).

Measurements include all the magnetic fields, plasma waves, in situ charged-particle measurements, neutral gas composition, and dust. Remote imaging in ENAs along the outward trajectory will offer a unique change of vantage point that will provide important constraints on the 3D structure of the heliosphere and the location of the ribbon. Remote Lyman- α imaging will provide line profiles for deriving temperature and flow velocities of interstellar hydrogen across the boundary region, and for determining the distribution of the solar wind mass flow, which will be important for relating dynamics in the remotely observed ENA emissions.

4.4.2 Heliosheath Phase

This phase starts with the crossing of the TS, where turbulent, small-scale physics may be decisive for the heating of the PUIs in the TS that subsequently will dominate the force balance in the heliosheath. Here, selected burst modes for high-resolution plasma, PUI, and fields and waves measurements may be used and would fit within the available data volume allocation. Selective data downlink can be implemented to maximize the science return.

The baseline direction with launch in 2036 will provide 4–9 years of measurements in the heliosheath and will ensure that large-scale solar-cycle variations can be captured in situ as well. During this traversal, instrumentation will generally be in the same mode as in the previous phase, with selected and intermittent high-resolution modes during shock encounters and for brief sampling of the turbulent spectra in electric and magnetic fields. Remote ENA observations will continue depending on image patterns (spacecraft may be inside the ENA emitting source region, which may confuse interpretation). Lyman- α observations will continue and will be important for resolving the hydrogen wall from the galactic background.

This phase will end with a campaign leading up to the HP crossing and beyond by a few tens of astronomical units. Here, it will be important to plan for any high-resolution data-taking and use the onboard memory to select periods of interest.

4.4.3 Interstellar Phase

Once the HP is crossed as defined by changes in plasma densities, energetic particles, and GCRs, as seen by the Voyagers, the interstellar phase will begin. All measurements will continue in this phase, including plasma moments, such as flows, densities, and temperatures that will be down to at least 3 eV and perhaps lower. The lower energy threshold of direct plasma measurements will be limited by the spacecraft potential, but beyond the HP, the spacecraft potential may be as low as +5 V because of the ion deposition being higher than the electron deposition. The positive potential implies that one would be able to measure the plasma electron distribution and estimate the electron temperature. By using analysis of the QTN obtained by the plasma wave antennas, one would obtain an independent estimate of electron density and temperature as well. Intermittent, brief intervals of high-resolution magnetic field and wave measurements can be made to sample the turbulence spectrum. Remote ENA and Lyman- α imaging would continue and would be particularly important given the vantage point far away from the Sun that would provide the first external view of our heliosphere in ENAs and Lyman- α observations closer to the optically thick UV emissions from the hydrogen wall.

Measurements of the unperturbed interstellar plasma, neutral gas, dust, and GCRs will be particularly important in this phase. With a baseline trajectory 80° off the nose direction, the NMS and the IDA must be mounted such that they point into the net gas and dust ram once per spin. See Section 4.3 for more details.

No one really knows how far the heliosphere extends in all directions, and the completely unperturbed VLISM may lie as far away as beyond 600 au (Izmodenov & Alexashov, 2020; Kim et al., 2017). Within the design life of 50 years, Interstellar Probe would reach more than twice the

projected distance of Voyager 1, more than 350 au. Operation out to 1000 au may be possible. Although the design life has been determined assuming all instruments operating simultaneously, running only the most critical instruments would ensure operation to larger distances. Instrument power includes survival heater power that in some cases draws as much power as the operational power, so switching off noncritical instruments would mean also switching off survival heaters, which ultimately would terminate those instruments. Similar approaches are being taken on Voyager and may ultimately be taken on New Horizons.

Table 4-3. Scientific events along the trajectory.

Target/Event	Distance	Flight Time
Hydrogen ionization cavity	~3 au	~6 months
Change in ribbon view	~10 au	~1 year
Solar wind slowdown	30 au (5% decrease line) (Elliott et al., 2019)	~4 years
Termination shock	84 au ± 10 au	13–14 years
Heliopause	120–200 au ± 10 au (Krimigis et al., 2019; Reisenfeld et al., 2021)	17–29 years
Bow wave (existence)/hydrogen wall	200–300 au (Zank et al., 2013)	29–43 years
Unperturbed (pristine) VLISM	~600 au (Izmodenov & Alexashov, 2020; Kim et al., 2017)	~86 years

4.5 Data Volume

Assuming the use of the telecommunications subsystem laid out in Section 5, an analysis was performed to determine whether the desired data downlink can be accommodated, so that the contemplated science analyses can be successfully performed. The available downlink data rate is represented by the red curve in Figure 4-36. The data rates of each instrument were bounded using realistic values for the beginning and end of the mission. These estimates are meant to test feasibility, rather than serving as data allocations.

Simplifications were needed to determine the minimum rates at a stage where instruments are not even selected. In particular, to maintain the spirit of a pragmatic near-term mission, a continuous recording of standard data products such as time series of binned measurements was assumed. Although not required and therefore not included in the analysis, nonstandard data products (for example, snippets of data in the native resolution) could be traded against the standard products, and onboard processing may adaptively change resolutions to allow for more science from the same data allocation.

Available data downlink rates change by three orders of magnitude over the course of the mission. For simplicity, the data rates for each instrument are separated into five representative time periods, based on different phases of the mission that delineate changing measurement needs: early mission (<20 au), “inner” heliosphere (20–70 au), “outer” heliosphere (70–250 au), ISM (250–350 au), and extension (350 au+, representative of operation past the prime nominal mission, taken as ending at 50 years). For each period, representative available data rates are calculated as the logarithmic average of the data rate extremes. The data recorder on Interstellar Probe is presumed to be able to hold at a minimum data from the early solar system accumulated over the course of a year, or ~600 Gbit. To bound the representative rates, a useful range for each

instrument is determined using the rate needed for Voyager-equivalent science at the low end and a nominal operating rate based on heritage instruments making comparable measurements near the beginning of the mission at the high end.

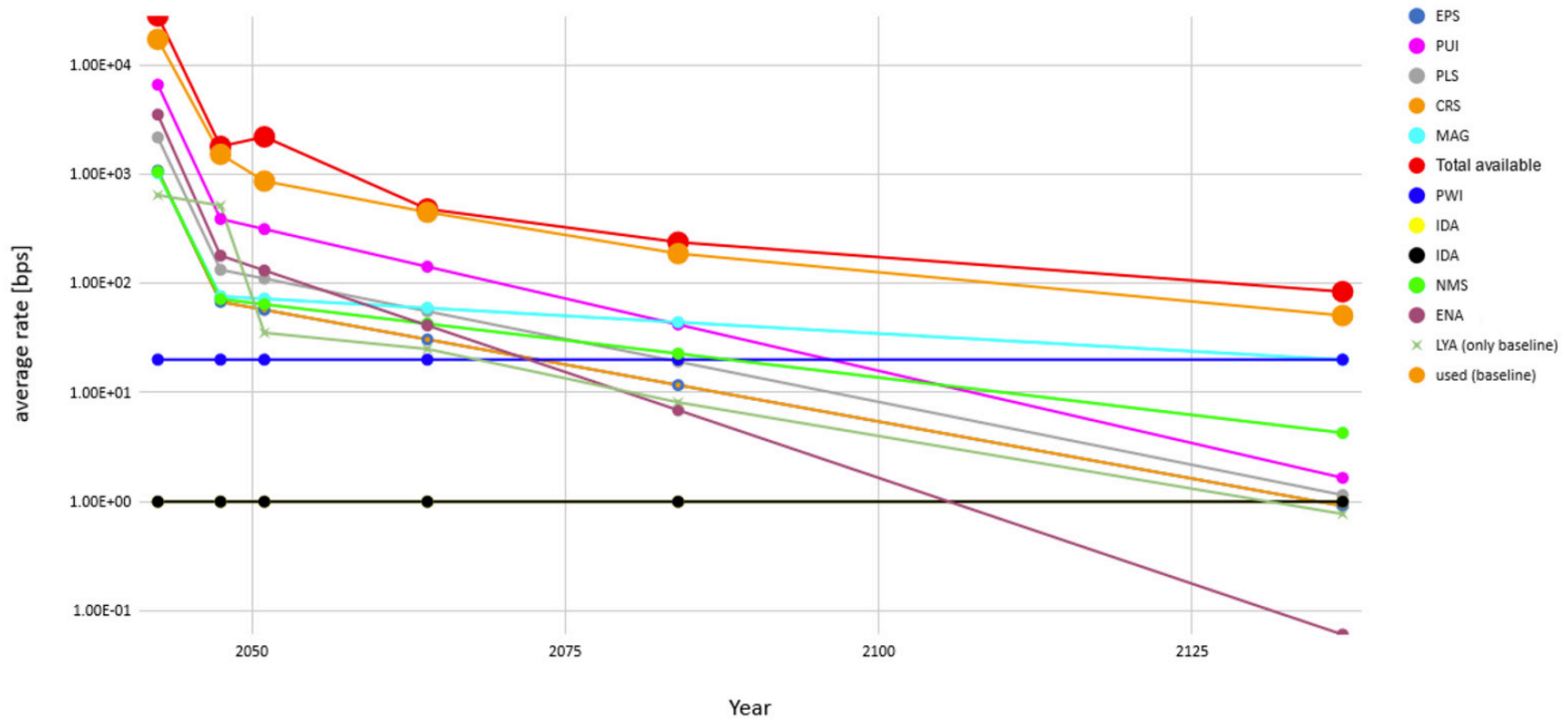


Figure 4-36. Data rates for each instrument as a function of time. These rates are not allocations. Rates in the early mission are based on what has been used within the solar system, while rates in and beyond the outer heliosphere are representative of what is required to address the science. Summing up these rates (orange) demonstrates that the available downlink capacity (red) is sufficient to perform the required science. Note the increase in available downlink capacity around 2050 is concurrent with the switch to the Next Generation Very Large Array (ngVLA) (see Section 3.2.4 for more details). (Image credit: Johns Hopkins Applied Physics Laboratory.)

The rates at the beginning of the mission through the inner heliosphere are based on what has been used when operating similar instruments within the solar system. Although the available data rates for the inner heliosphere are an order of magnitude lower in comparison with the rates at the beginning of the mission, this order of magnitude decrease is relative to the generous values of the early mission, and the scaled values are all well above the established minimum rate. Data rates are scaled for each instrument such that they decay exponentially from the value in the inner heliosphere to the minimum established for the extended mission. This scaling is shown as the orange curve in Figure 4-36. These data rates fit within what is available, even though instruments will need to run at or close to the minimum established for the respective regions. In the outer heliosphere, defined in this analysis as 70–250 au, the need to gain as much insight as possible into structures and boundaries must be balanced with the decreasing capacity for data downlink. To capture this, separate minimum rates were defined for key instruments. The rates at the end of the prime mission are based on estimates of minimum measurements that are needed, often equivalent to what has been done with Voyager. Although relatively low, these rates are sufficient because fast changes are not expected in the ISM, allowing for long averages. Overall, the available data rates are sufficient to achieve the contemplated science goals throughout the entire mission.

Table 4-4 sketches the rationale for the data rates illustrated in Figure 4-36. For the particle suite (PLS, PUI, EPS, CRS), 10 bits per sample is assumed, where the number of channels and directions for the minimum values are provided in Table 4-4. More detailed estimates using more exact numbers for channels and directions that follow from the instrument requirements have yielded similar data rates. In particular, CRS also needs to accumulate the spectrum of rare species. The respective data rate is in the noise, requiring only 0.01 bps from 100 energies, 100 species, 10 directions, and 10 bits over the course of 1 year. For MAG, 18 bits per directional field measurement is assumed, with 32 bits per time tag. For the other fields instrument, PWS, a Voyager reference of 20 bps on average was used for spectra and wave forms. The minimum rate is based on four spectra with 100 bins and 10 bits and histograms with 1000 bins and 10 bits, each once per day. More detailed estimates (accounting for data products for power spectra with two channels, cross spectra with real and imaginary parts, summary histogram for wave peaks, summary histogram for dust detection, plasma density, and waveform burst) yield similar data rates. It should be noted that PWS will need to write with ~ 400 kbps to a recorder, independent of what is downlinked. The IDA allocation assumes that a full spectrum of a dust hit requires 30 kbit. With a 0.06-m^2 typical detection area and 1 bps, a flux of $5\text{e-}4/(\text{s m}^2)$ can be fully sampled, which is five times larger than what should be needed. For NMS, one full mass spectrum is assumed to have 20,000 entries for $m/z = 1\text{--}1000$ with 32 bits per entry, which adds up to a total of 10^5 bits including housekeeping and a compression factor of 10. The ENA data allocation includes a full set, which has 20×20 pixels, 10 energies, and 12 bits per sample. Lastly, for LYA, a single full data set has 512 wavelengths \times 256 directions and 16 bits/pixel.

Table 4-4. Columns group nominal instruments, range of reasonable data rates, and representative rates during different mission phases. Values are in bits per second. Each instrument line includes a data rate and, where applicable, a justification. More details on the justification are in the main text. Green cells are fixed values, and gray cells are calculated from scaling as described in the text.

Instrument	Instrument Inst. Data Rate (bps)						
	Useful Range (bps)		Data Rate at Representative Times (bps)				
	Voyager Equivalent Science	Nominal Rate when Operating at <10 au	Early Mission (<20 au)	Inner Heliosphere (20–70 au)	Outer Heliosphere (70–250 au)	ISM (250–350 au)	Extension (350–1000 au)
			2043	2048	2064	2084	2137
EPS	1.00E-01	1.00E+03	1.07E+03	6.76E+01	3.06E+01	1.17E+01	9.14E-01
	10 energies & 10 species & 10 directions per day	Nominal: Parker Solar Probe/EPI-Lo Lowest: Magnetospheric Multiscale (MMS)/Energetic Ion Spectrometer (EIS) Highest: Juno/Jupiter Energetic-particle Detector Instrument (JEDI)			10 energies & 10 species & 10 directions per hour		
PUI	1.00E-01	6.00E+03	6.57E+03	3.88E+02	1.42E+02	4.19E+01	1.65E+00
	10 energies & 10 species & 10 directions per day	Solar Orbiter/Solar Wind Analyser (SWA)/Heavy Ion Sensor (HIS)			10 energies & 10 species & 10 directions per hour		
PLS	1.00E-01	2.00E+03	2.17E+03	1.33E+02	5.53E+01	1.91E+01	1.15E+00
	100 energies & 5 directions per day	Approximately Van Allen Probes/Helium Oxygen Proton Electron (Ishii et al.)			100 energies & 5 directions per hour		

Instrument	Instrument Inst. Data Rate (bps)						
	Useful Range (bps)		Data Rate at Representative Times (bps)				
	Voyager Equivalent Science	Nominal Rate when Operating at <10 au	Early Mission (<20 au)	Inner Heliosphere (20–70 au)	Outer Heliosphere (70–250 au)	ISM (250–350 au)	Extension (350–1000 au)
			2043	2048	2064	2084	2137
CRS	1.00E-01	1.00E+03	1.07E+03	6.76E+01	3.06E+01	1.17E+01	9.14E-01
	10 energies & 10 species & 10 directions per day	Approximately Advanced Composition Explorer (ACE)/Cosmic Ray Isotope Spectrometer (CRIS)			10 energies & 10 species & 10 directions per hour		
MAG	1.00E+01	1.00E+03	1.02E+03	7.59E+01	5.93E+01	4.40E+01	1.99E+01
	1-s resolution for 5.4/24 of day, otherwise 1 min	Rounded down Cassini and Van Allen Probes					
PWS	1.00E+00	1.00E+02	2.00E+01	2.00E+01	2.00E+01	2.00E+01	2.00E+01
	4 spectra types	10× Voyager	2× Voyager	2× Voyager	2× Voyager	2× Voyager	2× Voyager
IDA	1.00E+00	5.00E+02	1.00E+00	1.00E+00	1.00E+00	1.00E+00	1.00E+00
	Composition for 3e-5 dust/s	Cassini/Cosmic Dust Analyzer (CDA) at dusty Saturn	Composition for 3e-5 dust/s	Composition for 3e-5 dust/s	Composition for 3e-5 dust/s	Composition for 3e-5 dust/s	Composition for 3e-5 dust/s
NMS	1.00E+00	1.00E+03	1.05E+03	7.16E+01	4.26E+01	2.27E+01	4.26E+00
	1 spectrum per day	1 spectrum per 100 s					
ENA	1.00E-03	3.06E+03	3.50E+03	1.79E+02	4.11E+01	6.89E+00	6.07E-02
	One set per year	Interstellar Mapping and Acceleration Probe (IMAP)/Ultra					
LYA	1.00E-01	6.00E+02	6.41E+02	5.14E+02	2.50E+01	8.12E+00	7.71E-01
	One set per year	One set per hour	One set every few hours	One set every few hours	One set per day		

Instrument	Instrument Inst. Data Rate (bps)						
	Useful Range (bps)		Data Rate at Representative Times (bps)				
	Voyager Equivalent Science	Nominal Rate when Operating at <10 au	Early Mission (<20 au)	Inner Heliosphere (20–70 au)	Outer Heliosphere (70–250 au)	ISM (250–350 au)	Extension (350–1000 au)
			2043	2048	2064	2084	2137
Total available (bps)			2.80E+04	1.79E+03	4.78E+02	2.37E+02	8.37E+01
Total used BASELINE (bps)			1.71E+04	1.52E+03	4.47E+02	1.87E+02	5.06E+01
Total used BASELINE (fraction)			6.11E-01	8.48E-01	9.35E-01	7.88E-01	6.05E-01

4.6 Section 4 References

- Abedin, A., Kavelaars, J.J. (2019) *Collisions in the classical Kuiper belt*. Paper presented at the AGU Fall Meeting.
- Acuña, M.H., Anderson, B.J., Russell, C.T., Wasilewski, P., Kletetschka, G., Zanetti, L., Omid, N. (2002) NEAR magnetic field observations at 433 Eros: First measurements from the surface of an asteroid. *Icarus* 155(1), 220-228. doi: <https://doi.org/10.1006/icar.2001.6772>
- Allegrini, F., Schwadron, N.A., McComas, D.J., Gloeckler, G., Geiss, J. (2005) Stability of the inner source pickup ions over the solar cycle. *Journal of Geophysical Research: Space Physics* 110(A5). doi: <https://doi.org/10.1029/2004JA010847>
- Altobelli, N., Postberg, F., Fiege, K., et al. (2016) Flux and composition of interstellar dust at Saturn from Cassini's Cosmic Dust Analyzer. *Science* 352(6283), 312-318. doi: [doi:10.1126/science.aac6397](https://doi.org/10.1126/science.aac6397)
- Anderson, B.J., Acuña, M.H., Lohr, D.A., Scheifele, J., Raval, A., Korth, H., Slavin, J.A. (2007) The Magnetometer Instrument on MESSENGER. *Space Science Reviews* 131(1), 417-450. doi: [10.1007/s11214-007-9246-7](https://doi.org/10.1007/s11214-007-9246-7)
- Bale, S.D., Goetz, K., Harvey, P.R., et al. (2016) The FIELDS Instrument Suite for Solar Probe Plus. *Space Science Reviews* 204(1), 49-82. doi: [10.1007/s11214-016-0244-5](https://doi.org/10.1007/s11214-016-0244-5)
- Bertaux, J.L., Kyrölä, E., Quémerais, E., et al. (1995) SWAN: A study of solar wind anisotropies on SOHO with Lyman alpha sky mapping. In B., F., V., D., A., P. (Eds.), *The SOHO Mission*. Dordrecht: Springer.
- Bildsten, L., Brown, E.F., Matzner, C.D., Ushomirsky, G. (1997) Lithium depletion in fully convective pre-main-sequence stars. *The Astrophysical Journal* 482, 442. doi: [10.1086/304151](https://doi.org/10.1086/304151)
- Boelter, L.M.K., Stever, H.G., Summerfield, M., et al. (1959) *Space Technology* (Seifert, H.S. Ed.). New York: John Wiley and Sons, Inc.
- Bridge, H.S., Belcher, J.W., Butler, R.J., Lazarus, A.J., Mavretic, A.M., Sullivan, J.D., Siscoe, G.L., Vasyliunas, V.M. (1977) The plasma experiment on the 1977 Voyager mission. *Space Science Reviews* 21, 259. doi: [10.1007/bf00211542](https://doi.org/10.1007/bf00211542)
- Bryden, G., Beichman, C.A., Trilling, D.E., et al. (2006) Frequency of debris disks around solar-type stars: First results from a Spitzer MIPS survey. *The Astrophysical Journal* 636(2), 1098-1113. doi: [10.1086/498093](https://doi.org/10.1086/498093)
- Bryden, G., Beichman, C.A., Carpenter, J.M., et al. (2009) Planets and debris disks: Results from a Spitzer/MIPS search for infrared excess. *The Astrophysical Journal* 705(2), 1226-1236. doi: [10.1088/0004-637x/705/2/1226](https://doi.org/10.1088/0004-637x/705/2/1226)
- Burger, R.A. (2000) Galactic cosmic rays in the heliosphere. *AIP Conference Proceedings* 516(1), 83-102. doi: [10.1063/1.1291470](https://doi.org/10.1063/1.1291470)

- Burlaga, L.F., Kurth, W.S., Gurnett, D.A., Berdichevsky, D.B., Jian, L.K., Ness, N.F., Park, J., Szabo, A. (2021) Magnetic field and plasma density observations of a pressure front by Voyager 1 during 2020 in the very local interstellar medium. *The Astrophysical Journal* 911, 61. doi: 10.3847/1538-4357/abeb6a
- Carrillo-Sánchez, J.D., Nesvorný, D., Pokorný, P., Janches, D., Plane, J.M.C. (2016) Sources of cosmic dust in the Earth's atmosphere. *Geophysical Research Letters* 43(23), 11,979-911,986. doi: <https://doi.org/10.1002/2016GL071697>
- Chen, C.H., Mittal, T., Kuchner, M., Forrest, W.J., Lisse, C.M., Manoj, P., Sargent, B.A., Watson, D.M. (2014) The Spitzer Infrared Spectrograph Debris Disk Catalog. I. Continuum Analysis of Unresolved Targets. *The Astrophysical Journal Supplement Series* 211, 25. doi: 10.1088/0067-0049/211/2/25
- Christon, S.P., Hamilton, D.C., Plane, J.M.C., Mitchell, D.G., DiFabio, R.D., Krimigis, S.M. (2015) Discovery of suprathermal Fe⁺ in Saturn's magnetosphere. *Journal of Geophysical Research: Space Physics* 120(4), 2720-2738. doi: <https://doi.org/10.1002/2014JA020906>
- Christon, S.P., Hamilton, D.C., Mitchell, D.G., Plane, J.M.C., Nylund, S.R. (2020) Suprathermal magnetospheric atomic and molecular heavy ions at and near Earth, Jupiter, and Saturn: Observations and identification. *Journal of Geophysical Research: Space Physics* 125(1), e2019JA027271. doi: <https://doi.org/10.1029/2019JA027271>
- Clarke, J.T., Lallement, R., Bertaux, J.L., Fahr, H., Quemerais, E., Scherer, H. (1998) HST/GHRS observations of the velocity structure of interplanetary hydrogen. *The Astrophysical Journal* 499(1), 482-488. doi: 10.1086/305628
- Clarke, J.T., Mayyasi, M., Bhattacharyya, D., et al. (2017) Variability of D and H in the Martian upper atmosphere observed with the MAVEN IUVS echelle channel. *Journal of Geophysical Research: Space Physics* 122(2), 2336-2344. doi: <https://doi.org/10.1002/2016JA023479>
- Colaprete, A., Sarantos, M., Wooden, D.H., Stubbs, T.J., Cook, A.M., Shirley, M. (2016) How surface composition and meteoroid impacts mediate sodium and potassium in the lunar exosphere. *Science* 351(6270), 249-252. doi: 10.1126/science.aad2380
- Costa, J., Lallement, R., Quémerais, E., Bertaux, J.-L., Kyrölä, E., Schmidt, W. (1999) Heliospheric interstellar H temperature from SOHO/SWAN H cell data. *Astronomy and Astrophysics* 349, 660. Retrieved from <https://ui.adsabs.harvard.edu/abs/1999A&A...349..660C>
- Cummings, A.C., Stone, E.C., Heikkila, B.C., Lal, N., Webber, W.R., Jóhannesson, G., Moskalenko, I.V., Orlando, E., Porter, T.A. (2016) Galactic cosmic rays in the local interstellar medium: Voyager 1 observations and model results. *The Astrophysical Journal* 831(1), 18. doi: 10.3847/0004-637x/831/1/18
- Cuzzi, J.N., Estrada, P.R. (1998) Compositional evolution of Saturn's rings due to meteoroid bombardment. *Icarus* 132(1), 1-35. doi: <https://doi.org/10.1006/icar.1997.5863>

- Decker, R.B., Krimigis, S.M., Roelof, E.C., Hill, M.E., Armstrong, T.P., Gloeckler, G., Hamilton, D.C., Lanzerotti, L.J. (2008) Mediation of the solar wind termination shock by non-thermal ions. *Nature* 454(7200), 67. doi: 10.1038/nature07030
- Decker, R.B., Krimigis, S.M., Roelof, E.C., Hill, M.E. (2012) No meridional plasma flow in the heliosheath transition region. *Nature* 489(7414), 124. doi: 10.1038/nature11441
- Dialynas, K., Galli, A., Dayeh, M.A., et al. (2020) Combined ~ 10 eV to ~ 344 MeV particle spectra and pressures in the heliosheath along the Voyager 2 trajectory. *The Astrophysical Journal* 905, L24. doi: 10.3847/2041-8213/abcaaa
- Dialynas, K., Krimigis, S.M., Decker, R.B., Hill, M.E. (2021) Ions measured by Voyager 1 outside the heliopause to 28 au and implications thereof. *The Astrophysical Journal* 917, 42. doi: 10.3847/1538-4357/ac071e
- Dougherty, M.K., Kellock, S., Southwood, D.J., et al. (2004) The Cassini Magnetic Field Investigation. *Space Science Reviews* 114(1), 331-383. doi: 10.1007/s11214-004-1432-2
- Draine, B.T. (2009) Perspectives on interstellar dust inside and outside of the heliosphere. *Space Science Reviews* 143(1), 333-345. doi: 10.1007/s11214-008-9411-7
- Draine, B.T. (2011) *Physics of the Interstellar and Intergalactic Medium*. Retrieved from <https://ui.adsabs.harvard.edu/abs/2011piim.book.....D>
- Eckart, C., Shonka, F.R. (1938) Accidental coincidences in counter circuits. *Physical Review* 53(9), 752-756. doi: 10.1103/PhysRev.53.752
- Eiroa, C., Marshall, J.P., Mora, A., et al. (2013) DUst around NEarby Stars. The survey observational results. *Astronomy and Astrophysics* 555, A11. doi: 10.1051/0004-6361/201321050
- Elliott, H.A., McComas, D.J., Zirnstein, E.J., et al. (2019) Slowing of the solar wind in the outer heliosphere. *The Astrophysical Journal* 885, 156. doi: 10.3847/1538-4357/ab3e49
- Ertel, S., Defrère, D., Hinz, P., et al. (2018) The HOSTS Survey—Exozodiacal dust measurements for 30 stars. *The Astronomical Journal* 155(5), 194. doi: 10.3847/1538-3881/aab717
- Estrada, P.R., Durisen, R.H., Cuzzi, J.N., Morgan, D.A. (2015) Combined structural and compositional evolution of planetary rings due to micrometeoroid impacts and ballistic transport. *Icarus* 252, 415-439.
- Fausch, R., Wurz, P., Lase, D., Tulej, M., Cabane, M., Szopa, C., Sapgir, A., Gerasimov, M. (2018) *In-Situ Analysis of Lunar Regolith with the Gas Chromatograph-Neutral Gas Mass Spectrometer on the Luna-Resurs Lander*. In European Planetary Science Congress 2018, held 16-21 September 2018 at TU Berlin, Berlin, Germany, <https://ui.adsabs.harvard.edu/abs/2018EPSC...12.1028F>.
- Föhn, M., Galli, A., Vorburger, A., et al. (2021, 6-13 March 2021) *Description of the Mass Spectrometer for the Jupiter Icy Moons Explorer Mission*. In 2021 IEEE Aerospace Conference (50100). doi: 10.1109/AERO50100.2021.9438344

- Frisch, P.C., Redfield, S., Slavin, J.D. (2011) the interstellar medium surrounding the Sun. *Annual Review of Astronomy and Astrophysics* 49, 237. doi: 10.1146/annurev-astro-081710-102613
- Geiss, J., Gloeckler, G., Fisk, L.A., von Steiger, R. (1995) C+ pickup ions in the heliosphere and their origin. *Journal of Geophysical Research: Space Physics* 100(A12), 23373-23377. doi: <https://doi.org/10.1029/95JA03051>
- Geiss, J., Gloeckler, G. (2001) Heliospheric and interstellar phenomena deduced from pickup ion observations. *Space Science Reviews* 97. doi: 10.1023/A:1011867320416
- Gilles, H., Hamel, J., Chéron, B. (2001) Laser pumped 4He magnetometer. *Review of Scientific Instruments* 72(5), 2253-2260. doi: 10.1063/1.1364667
- Gladstone, G.R., Pryor, W.R., Stern, S.A., et al. (2018) The Lyman- α sky background as observed by New Horizons. *Geophysical Research Letters* 45(16), 8022-8028. doi: <https://doi.org/10.1029/2018GL078808>
- Gloeckler, G., Geiss, J., Balsiger, H., et al. (1992) The Solar Wind Ion Composition Spectrometer. *Astronomy and Astrophysics Supplement Series* 92, 267-289. Retrieved from <https://ui.adsabs.harvard.edu/abs/1992A&AS...92..267G>
- Gloeckler, G., Roelof, E.C., Ogilvie, K.W., Berdichevsky, D.B. (1995) Proton phase space densities (0.5eV<E_p<5MeV) at midlatitudes from Ulysses SWICS/HI-SCALE measurements. *Space Science Reviews* 72(1), 321-326. doi: 10.1007/BF00768798
- Gloeckler, G., Geiss, J. (1996) Abundance of 3He in the local interstellar cloud. *Nature* 381(6579), 210-212. doi: 10.1038/381210a0
- Gloeckler, G., Cain, J., Ipavich, F.M., et al. (1998) Investigation of the composition of solar and interstellar matter using solar wind and pickup ion measurements with SWICS and SWIMS on the ACE spacecraft. *Space Science Reviews* 86(1), 497-539. doi: 10.1023/A:1005036131689
- Gloeckler, G., Geiss, J. (2004) Composition of the local interstellar medium as diagnosed with pickup ions. *Advances in Space Research* 34, 53. doi: 10.1016/j.asr.2003.02.054
- Gloeckler, G., Fisk, L.A. (2015) More evidence that Voyager 1 is still in the heliosphere. *The Astrophysical Journal* 806(2). doi: 10.1088/2041-8205/806/2/l27
- Gold, R.E., Solomon, S.C., McNutt, R.L., et al. (2001) The MESSENGER mission to Mercury: Scientific payload. *Planetary and Space Science* 49(14), 1467-1479. doi: [https://doi.org/10.1016/S0032-0633\(01\)00086-1](https://doi.org/10.1016/S0032-0633(01)00086-1)
- Grey, M., Westlake, J., Liang, S., Hohlfeld, E., Crew, A., McNutt, R. (2018, 3-10 March 2018) *Europa PIMS prototype faraday cup development*. In 2018 IEEE Aerospace Conference. doi: 10.1109/AERO.2018.8396522
- Gruen, E., Gustafson, B., Mann, I., Baguhl, M., Morfill, G.E., Staubach, P., Taylor, A., Zook, H.A. (1994) Interstellar dust in the heliosphere. *Astronomy and Astrophysics* 286, 915. Retrieved from <https://ui.adsabs.harvard.edu/abs/1994A&A...286..915G>

- Gurnett, D.A., Kurth, W.S., Allendorf, S.C., Poynter, R.L. (1993) Radio emission from the heliopause triggered by an interplanetary shock. *Science* 262(5131), 199-203. doi: doi:10.1126/science.262.5131.199
- Gurnett, D.A., Ansher, J.A., Kurth, W.S., Granroth, L.J. (1997) Micron-sized dust particles detected in the outer solar system by the Voyager 1 and 2 plasma wave instruments. *Geophysical Research Letters* 24(24), 3125-3128. doi: <https://doi.org/10.1029/97GL03228>
- Gurnett, D.A., Kurth, W.S., Hospodarsky, G.B., et al. (2005) Radio and plasma wave observations at saturn from cassini's approach and first orbit. *Science* 307(5713), 1255-1259. doi: doi:10.1126/science.1105356
- Gurnett, D.A., Kurth, W.S., Burlaga, L.F., Ness, N.F. (2013) In situ observations of interstellar plasma with Voyager 1. *Science* 341(6153), 1489-1492. doi: doi:10.1126/science.1241681
- Gurnett, D.A., Kurth, W.S., Stone, E.C., Cummings, A.C., Heikkila, B., Lal, N., Krimigis, S.M., Decker, R.B., Ness, N.F., Burlaga, L.F. (2021) a foreshock model for interstellar shocks of solar origin: Voyager 1 and 2 observations. *The Astronomical Journal* 161, 11. doi: 10.3847/1538-3881/abc337
- Harris, W., Roesler, F., Harlander, J., Ben-Jaffel, L., Mierkiewicz, E., Corliss, J., Oliverson, R. (2004) *Applications of reflective spatial heterodyne spectroscopy to UV exploration in the solar system* (Vol. 5488): SPIE. Retrieved from <https://doi.org/10.1117/12.553107>
- Harris, W., Roesler, F., Ben-Jaffel, L., Mierkiewicz, E., Corliss, J., Oliverson, R., Neef, T. (2005) Applications of spatial heterodyne spectroscopy for remote sensing of diffuse UV–vis emission line sources in the solar system. *Journal of Electron Spectroscopy and Related Phenomena* 144-147, 973-977. doi: <https://doi.org/10.1016/j.elspec.2005.01.223>
- Harris, W., Corliss, J. (2018, 2018/11/05) *Development of a Reflective Spatial Heterodyne Spectrometer (SHS) for Spaceflight Applications from the Extreme UV to Near IR*. In Light, Energy and the Environment 2018 (E2, FTS, HISE, SOLAR, SSL), Optical Society of America, Singapore. doi: 10.1364/FTS.2018.FM3B.3
- Heerikhuisen, J., Zirnstein, E.J., Funsten, H.O., Pogorelov, N.V., Zank, G.P. (2014) The effect of new interstellar medium parameters on the heliosphere and energetic neutral atoms from the interstellar boundary. *The Astrophysical Journal* 784(1), 73. doi: 10.1088/0004-637x/784/1/73
- Hill, M.E., Allen, R.C., Kollmann, P., et al. (2020) Influence of solar disturbances on galactic cosmic rays in the solar wind, heliosheath, and local interstellar medium: Advanced Composition Explorer, New Horizons, and Voyager observations. *The Astrophysical Journal* 905(1), 69. doi: 10.3847/1538-4357/abb408
- Holmes, E.K., Dermott, S.F., Gustafson, B.A.S., Grogan, K. (2003) Resonant structure in the Kuiper disk: An asymmetric Plutino disk. *The Astrophysical Journal* 597(2), 1211-1236. doi: 10.1086/378509

- Horányi, M., Hoxie, V., James, D., Poppe, A., Bryant, C., Grogan, B., . . . Westfall, J. (2008). The Student Dust Counter on the New Horizons mission. *Space Science Reviews*, 140, 387. doi:10.1007/s11214-007-9250-y
- Horányi, M., Szalay, J.R., Kempf, S., Schmidt, J., Grün, E., Srama, R., Sternovsky, Z. (2015) A permanent, asymmetric dust cloud around the Moon. *Nature* 522(7556), 324-326. doi: 10.1038/nature14479
- Horányi, M., Kempf, S., Sternovsky, Z., Tucker, S., Pokorný, P., Turner, N.J., Castillo-Rogez, J.C., Bálint, T., West, J.L., Szalay, J.R. (2019, 2-9 March 2019) *Fragments from the Origins of the Solar System and our Interstellar Locale (FOSSIL): A Cometary, Asteroidal, and Interstellar Dust Mission Concept*. In 2019 IEEE Aerospace Conference. doi: 10.1109/AERO.2019.8742223
- Hughes, A.M., Duchêne, G., Matthews, B.C. (2018) Debris Disks: Structure, Composition, and Variability. *Annual Review of Astronomy and Astrophysics* 56(1), 541-591. doi: 10.1146/annurev-astro-081817-052035
- Humes, D.H. (1980) Results of Pioneer 10 and 11 meteoroid experiments: Interplanetary and near-Saturn. *Journal of Geophysical Research: Space Physics* 85(A11), 5841-5852. doi: https://doi.org/10.1029/JA085iA11p05841
- Ipavich, F.M. (1974) The Compton-Getting Effect for low energy particles. *Geophysical Research Letters* 1, 149. doi: 10.1029/GL001i004p00149
- Ishii, H.A., Bradley, J.P., Dai, Z.R., Chi, M., Kearsley, A.T., Burchell, M.J., Browning, N.D., Molster, F. (2008) Comparison of Comet 81P/Wild 2 dust with interplanetary dust from comets. *Science* 319(5862), 447-450. doi: doi:10.1126/science.1150683
- Izmodenov, V.V., Alexashov, D.B. (2020) Magnitude and direction of the local interstellar magnetic field inferred from Voyager 1 and 2 interstellar data and global heliospheric model. *Astronomy and Astrophysics* 633, L12. doi: 10.1051/0004-6361/201937058
- Kasper, J.C., Abiad, R., Austin, G., et al. (2016) Solar Wind Electrons Alphas and Protons (SWEAP) investigation: Design of the Solar Wind and Coronal Plasma Instrument Suite for Solar Probe Plus. *Space Science Reviews* 204, 131. doi: 10.1007/s11214-015-0206-3
- Katushkina, O.A., Quémerais, E., Izmodenov, V.V., Lallement, R., Sandel, B.R. (2017) Voyager 1/UVS Lyman α measurements at the distant heliosphere (90–130 AU): Unknown source of additional emission. *Journal of Geophysical Research: Space Physics* 122(11), 10,921-910,937. doi: https://doi.org/10.1002/2017JA024205
- Kempf, S., Altobelli, N., Srama, R., Cuzzi, J.N., Estrada, P.R. (2017) *The Age of Saturn's Rings Constrained by the Meteoroid Flux Into the System*. https://ui.adsabs.harvard.edu/abs/2017AGUFM.P34A..05K.
- Kim, T.K., Pogorelov, N.V., Burlaga, L.F. (2017) Modeling shocks detected by Voyager 1 in the local interstellar medium. *The Astrophysical Journal* 843, L32. doi: 10.3847/2041-8213/aa7b2b

- Koerner, D.W., Kim, S., Trilling, D.E., Larson, H., Cotera, A., Stapelfeldt, K.R., Wahhaj, Z., Fajardo-Acosta, S., Padgett, D., Backman, D. (2010) New debris disk candidates around 49 nearby stars. *The Astrophysical Journal* 710, L26. doi: 10.1088/2041-8205/710/1/L26
- Kollmann, P., Hill, M.E., McNutt, R.L., et al. (2019) Suprathermal ions in the outer heliosphere. *The Astrophysical Journal* 876(1), 46. doi: 10.3847/1538-4357/ab125f
- Koutroumpa, D., Quémerais, E., Katushkina, O., Lallement, R., Bertaux, J.-L., Schmidt, W. (2017) Stability of the interstellar hydrogen inflow longitude from 20 years of SOHO/SWAN observations. *A&A* 598, A12. Retrieved from <https://doi.org/10.1051/0004-6361/201629840>
- Kral, Q., Krivov, A.V., Defrère, D., van Lieshout, R., Bonsor, A., Augereau, J.-C., Thébault, P., Ertel, S., Lebreton, J., Absil, O. (2017) Exozodiacal clouds: hot and warm dust around main sequence stars. *Astronomical Review* 13(2), 69-111. doi: 10.1080/21672857.2017.1353202
- Krimigis, S.M., Armstrong, T.P., Axford, W.I., Bostrom, C.O., Fan, C.Y., Gloeckler, G., Lanzerotti, L.J. (1977) The Low Energy Charged Particle (LECP) experiment on the Voyager spacecraft. *Space Science Reviews* 21(3), 329-354. doi: 10.1007/BF00211545
- Krimigis, S.M., Decker, R.B., Hill, M.E., Armstrong, T.P., Gloeckler, G., Hamilton, D.C., Lanzerotti, L.J., Roelof, E.C. (2003) Voyager 1 exited the solar wind at a distance of ~ 85 au from the Sun. *Nature* 426(6962), 45-48. doi: 10.1038/nature02068
- Krimigis, S.M., Decker, R.B., Roelof, E.C., Hill, M.E., Armstrong, T.P., Gloeckler, G., Hamilton, D.C., Lanzerotti, L.J. (2013) Search for the exit: Voyager 1 at heliosphere's border with the galaxy. *Science* 341(6142), 144-147. doi: doi:10.1126/science.1235721
- Krimigis, S.M., Decker, R.B., Roelof, E.C., Hill, M.E., Bostrom, C.O., Dialynas, K., Gloeckler, G., Hamilton, D.C., Keath, E.P., Lanzerotti, L.J. (2019) Energetic charged particle measurements from Voyager 2 at the heliopause and beyond. *Nature Astronomy* 3, 997. doi: 10.1038/s41550-019-0927-4
- Krüger, H., Krivov, A.V., Hamilton, D.P., Grün, E. (1999) Detection of an impact-generated dust cloud around Ganymede. *Nature* 399(6736), 558-560. doi: 10.1038/21136
- Krüger, H., Landgraf, M., Altobelli, N., Grün, E. (2007) Interstellar dust in the Solar System. *Space Science Reviews* 130(1), 401-408. doi: 10.1007/s11214-007-9181-7
- Krüger, H., Grün, E. (2009) Interstellar dust inside and outside the heliosphere. *Space Science Reviews* 143, 347. doi: 10.1007/s11214-008-9431-3
- Krüger, H., Strub, P., Grün, E., Sterken, V.J. (2015) Sixteen years of ulysses interstellar dust measurements in the Solar System. I. Mass Distribution and Gas-to-Dust Mass Ratio. *The Astrophysical Journal* 812(2), 139. doi: 10.1088/0004-637x/812/2/139
- Kuchner, M.J., Stark, C.C. (2010) Collisional grooming models of the Kuiper Belt dust cloud. *The Astronomical Journal* 140(4), 1007-1019. doi: 10.1088/0004-6256/140/4/1007

- Kurth, W.S., Gurnett, D.A., Scarf, F.L., Poynter, R.L. (1984) Detection of a radio emission at 3 kHz in the outer heliosphere. *Nature* 312(5989), 27-31. doi: 10.1038/312027a0
- Kurth, W.S., Gurnett, D.A. (2003) On the source location of low-frequency heliospheric radio emissions. *Journal of Geophysical Research: Space Physics* 108(A10). doi: <https://doi.org/10.1029/2003JA009860>
- Lallement, R., Quémerais, E., Bertaux, J.L., Ferron, S., Koutroumpa, D., Pellinen, R. (2005) Deflection of the interstellar neutral hydrogen flow across the heliospheric interface. *Science* 307(5714), 1447-1449. doi: doi:10.1126/science.1107953
- Lallement, R., Quémerais, E., Bertaux, J.-L., Sandel, B.R., Izmodenov, V. (2011) Voyager measurements of hydrogen Lyman- α diffuse emission from the Milky Way. *Science* 334(6063), 1665-1669. doi: doi:10.1126/science.1197340
- Landgraf, M. (2000) Modeling the motion and distribution of interstellar dust inside the heliosphere. *Journal of Geophysical Research: Space Physics* 105(A5), 10303-10316. doi: <https://doi.org/10.1029/1999JA900243>
- Landgraf, M., Liou, J.-C., Zook, H.A., Grün, E. (2002) Origins of Solar System Dust beyond Jupiter. *The Astronomical Journal* 123, 2857. doi: 10.1086/339704
- Liou, J.-c., Zook, H.A. (1999) Signatures of the giant planets imprinted on the Edgeworth-Kuiper Belt dust disk. *The Astronomical Journal* 118, 580-590.
- Mayyasi, M., Clarke, J., Quémerais, E., et al. (2017) IUVS echelle-mode observations of interplanetary hydrogen: Standard for calibration and reference for cavity variations between Earth and Mars during MAVEN cruise. *Journal of Geophysical Research: Space Physics* 122(2), 2089-2105. doi: <https://doi.org/10.1002/2016JA023466>
- McClintock, W.E., Schneider, N.M., Holsclaw, G.M., Clarke, J.T., Hoskins, A.C., Stewart, I., Montmessin, F., Yelle, R.V., Deighan, J. (2015) The Imaging Ultraviolet Spectrograph (IUVS) for the MAVEN Mission. *Space Science Reviews* 195(1), 75-124. doi: 10.1007/s11214-014-0098-7
- McComas, D.J., Schwadron, N.A. (2006) An explanation of the Voyager paradox: Particle acceleration at a blunt termination shock. *Geophysical Research Letters* 33(4). doi: <https://doi.org/10.1029/2005GL025437>
- McComas, D.J., Alexander, N., Angold, N., et al. (2016) Integrated Science Investigation of the Sun (ISIS): Design of the energetic particle investigation. *Space Science Reviews* 204(1), 187-256. doi: 10.1007/s11214-014-0059-1
- McComas, D.J., Zirnstein, E.J., Bzowski, M., et al. (2017) Seven years of imaging the global heliosphere with IBEX. *The Astrophysical Journal Supplement Series* 229(2), 41. doi: 10.3847/1538-4365/aa66d8
- McComas, D.J., Christian, E.R., Schwadron, N.A., et al. (2018) Interstellar Mapping and Acceleration Probe (IMAP): A new NASA mission. *Space Science Reviews* 214(8), 116. doi: 10.1007/s11214-018-0550-1

- McNutt, R.L., Jr., Livi, S.A., Gurnee, R.S., et al. (2008) The Pluto Energetic Particle Spectrometer Science Investigation (PEPSSI) on the New Horizons mission. *Space Science Reviews* 140(1), 315-385. doi: 10.1007/s11214-008-9436-y
- Millan-Gabet, R., Serabyn, E., Mennesson, B., et al. (2011) Exozodiacal dust levels for nearby main-sequence stars: A survey with the Keck Interferometer Nuller. *The Astrophysical Journal* 734, 67. doi: 10.1088/0004-637x/734/1/67
- Mitchell, D.G., Brandt, P.C., Westlake, J.H., Jaskulek, S.E., Andrews, G.B., Nelson, K.S. (2016) Energetic particle imaging: The evolution of techniques in imaging high-energy neutral atom emissions. *Journal of Geophysical Research: Space Physics* 121(9), 8804-8820. doi: 10.1002/2016ja022586
- Montesinos, B., Eiroa, C., Krivov, A.V., et al. (2016) Incidence of debris discs around FGK stars in the solar neighbourhood. *Astron. Astrophys.* 593, A51. Retrieved from <https://doi.org/10.1051/0004-6361/201628329>
- Moro-Martín, A., Malhotra, R. (2002) A study of the dynamics of dust from the Kuiper Belt: Spatial distribution and spectral energy distribution. *The Astronomical Journal* 124, 2305. doi: 10.1086/342849
- Moses, J.I., Lellouch, E., Bézard, B., Gladstone, G.R., Feuchtgruber, H., Allen, M. (2000) Photochemistry of Saturn's atmosphere: II. Effects of an influx of external oxygen. *Icarus* 145(1), 166-202. doi: <https://doi.org/10.1006/icar.1999.6320>
- Moses, J.I., Poppe, A.R. (2017) Dust ablation on the giant planets: Consequences for stratospheric photochemistry. *Icarus* 297, 33-58. doi: <https://doi.org/10.1016/j.icarus.2017.06.002>
- Müller, H.-R., Zank, G.P. (2004) Heliospheric filtration of interstellar heavy atoms: Sensitivity to hydrogen background. *Journal of Geophysical Research: Space Physics* 109(A7). doi: <https://doi.org/10.1029/2003JA010269>
- Narvaez, P. (2004) The Magnetostatic Cleanliness Program for the Cassini spacecraft. *Space Science Reviews* 114(1), 385-394. doi: 10.1007/s11214-004-1433-1
- Nesvorný, D., Jenniskens, P., Levison, H.F., Bottke, W.F., Vokrouhlický, D., Gounelle, M. (2010) Cometary origin of the zodiacal cloud and carbonaceous micrometeorites. Implications for Hot Debris Disks. *The Astrophysical Journal* 713, 816. doi: 10.1088/0004-637x/713/2/816
- Ocker, S.K., Cordes, J.M., Chatterjee, S., Gurnett, D.A., Kurth, W.S., Spangler, S.R. (2021) Persistent plasma waves in interstellar space detected by Voyager 1. *Nature Astronomy* 5(8), 761-765. doi: 10.1038/s41550-021-01363-7
- Owen, C.J., Bruno, R., Livi, S., et al. (2020) The Solar Orbiter Solar Wind Analyser (SWA) suite. *Astronomy and Astrophysics* 642, A16. doi: 10.1051/0004-6361/201937259
- Piquette, M., Poppe, A.R., Bernardoni, E., et al. (2019) Student dust counter: Status report at 38 AU. *Icarus* 321, 116. doi: 10.1016/j.icarus.2018.11.012

- Pogorelov, N.V., Heerikhuisen, J., Roytershteyn, V., Burlaga, L.F., Gurnett, D.A., Kurth, W.S. (2017) Three-dimensional features of the outer heliosphere due to coupling between the interstellar and heliospheric magnetic field. V. The bow wave, heliospheric boundary layer, instabilities, and magnetic reconnection. *The Astrophysical Journal* 845(1), 9. doi: 10.3847/1538-4357/aa7d4f
- Pokorný, P., Sarantos, M., Janches, D. (2017) Reconciling the dawn-dusk asymmetry in Mercury's exosphere with the micrometeoroid impact directionality. *arXiv: Earth and Planetary Astrophysics*.
- Poppe, A.R., Lisse, C.M., Piquette, M., Zemcov, M., Horányi, M., James, D., Szalay, J.R., Bernardoni, E., Stern, S.A. (2019) Constraining the solar system's debris disk with in situ new horizons measurements from the Edgeworth–Kuiper Belt. *The Astrophysical Journal* 881(1), L12. doi: 10.3847/2041-8213/ab322a
- Quémerais, E., Bertaux, J.-L., Lallement, R., Berthé, M., Kyrölä, E., Schmidt, W. (1999) Interplanetary Lyman α line profiles derived from SWAN/SOHO hydrogen cell measurements: Full-sky Velocity Field. *Journal of Geophysical Research: Space Physics* 104(A6), 12585-12603. doi: <https://doi.org/10.1029/1998JA900101>
- Quémerais, E., Bertaux, J.-L., Lallement, R., Berthé, M., Kyrölä, E., Schmidt, W. (2000) SWAN/SOHO H cell measurements: The first year. *Advances in Space Research* 26(5), 815-818. doi: [https://doi.org/10.1016/S0273-1177\(00\)00012-0](https://doi.org/10.1016/S0273-1177(00)00012-0)
- Quémerais, E., Izmodenov, V. (2002) Effects of the heliospheric interface on the interplanetary Lyman α glow seen at 1 AU from the Sun. *A&A* 396(1), 269-281. Retrieved from <https://doi.org/10.1051/0004-6361:20021396>
- Quémerais, E., Lallement, R., Bertaux, J.-L., Koutroumpa, D., Clarke, J., Kyrölä, E., Schmidt, W. (2006) Interplanetary Lyman α line profiles: variations with solar activity cycle. *A&A* 455(3), 1135-1142. Retrieved from <https://doi.org/10.1051/0004-6361:20065169>
- Randol, B.M., Elliott, H.A., Gosling, J.T., McComas, D.J., Schwadron, N.A. (2012) Observations of Isotropic Interstellar Pick-up Ions at 11 and 17 AU From New Horizons. *The Astrophysical Journal* 755(1), 75. doi: 10.1088/0004-637x/755/1/75
- Randol, B.M., McComas, D.J., Schwadron, N.A. (2013) Interstellar pick-up ions observed between 11 and 22 AU by New Horizons. *The Astrophysical Journal* 768(2), 120. doi: 10.1088/0004-637x/768/2/120
- Rankin, J.S., Stone, E.C., Cummings, A.C., McComas, D.J., Lal, N., Heikkila, B.C. (2019) Galactic cosmic-ray anisotropies: Voyager 1 in the local interstellar medium. *The Astrophysical Journal* 873(1), 46. doi: 10.3847/1538-4357/ab041f
- Reisenfeld, D.B., Bzowski, M., Funsten, H.O., et al. (2021) A three-dimensional map of the heliosphere from IBEX. *The Astrophysical Journal Supplement Series* 254(2), 40. doi: 10.3847/1538-4365/abf658

- Richardson, J.D., Kasper, J.C., Wang, C., Belcher, J.W., Lazarus, A.J. (2008) Cool heliosheath plasma and deceleration of the upstream solar wind at the termination shock. *Nature* 454(7200), 63-66. doi: 10.1038/nature07024
- Richardson, J.D., Wang, C. (2012) Voyager 2 observes a large density increase in the heliosheath. *The Astrophysical Journal* 759, L19. doi: 10.1088/2041-8205/759/1/L19
- Richardson, J.D., Belcher, J.W., Garcia-Galindo, P., Burlaga, L.F. (2019) Voyager 2 plasma observations of the heliopause and interstellar medium. *Nature Astronomy* 3(11), 1019-1023. doi: 10.1038/s41550-019-0929-2
- Russell, C.T., Anderson, B.J., Baumjohann, W., et al. (2016) The Magnetospheric Multiscale Magnetometers. *Space Science Reviews* 199(1), 189-256. doi: 10.1007/s11214-014-0057-3
- Schwadron, N.A., Geiss, J., Fisk, L.A., Gloeckler, G., Zurbuchen, T.H., Steiger, R.v. (2000) Inner source distributions: Theoretical interpretation, implications, and evidence for inner source protons. *Journal of Geophysical Research: Space Physics* 105(A4), 7465-7472. doi: <https://doi.org/10.1029/1999JA000225>
- Schwadron, N.A., Moebius, E., Fuselier, S.A., et al. (2014) Separation of the ribbon from globally distributed energetic neutral atom flux using the first five years of IBEX observations. *The Astrophysical Journal Supplement Series* 215(1), 13. doi: 10.1088/0067-0049/215/1/13
- Singer, K.N., McKinnon, W.B., Gladman, B., et al. (2019) Impact craters on Pluto and Charon indicate a deficit of small Kuiper belt objects. *Science* 363(6430), 955-959. doi: doi:10.1126/science.aap8628
- Slavin, J.D., Frisch, P.C., Müller, H.-R., Heerikhuisen, J., Pogorelov, N.V., Reach, W.T., Zank, G. (2012) Trajectories and distribution of interstellar dust grains in the heliosphere. *The Astrophysical Journal* 760(1), 46. doi: 10.1088/0004-637x/760/1/46
- Smith, D.S., Scalo, J.M. (2009) Habitable zones exposed: Astrosphere collapse frequency as a function of stellar mass. *Astrobiology* 9(7), 673-681. doi: 10.1089/ast.2009.0337
- Smith, E.J. (2001) The heliospheric current sheet. *Journal of Geophysical Research: Space Physics* 106(A8), 15819-15831. doi: <https://doi.org/10.1029/2000JA000120>
- Smith, E.J., Dougherty, M.K., Russell, C.T., Southwood, D.J. (2001) Scalar helium magnetometer observations at Cassini Earth swing-by. *Journal of Geophysical Research: Space Physics* 106(A12), 30129-30139. doi: <https://doi.org/10.1029/2001JA900115>
- Sokół, J.M., Kubiak, M.A., Bzowski, M. (2019) Interstellar neutral gas species and their pickup ions inside the heliospheric termination shock: The large-scale structures. *The Astrophysical Journal* 879(1), 24. doi: 10.3847/1538-4357/ab21c4
- Sterken, V.J., Altobelli, N., Kempf, S., Schwehm, G., Srama, R., Grün, E. (2012) The flow of interstellar dust into the solar system. *Astronomy and Astrophysics* 538, A102. doi: 10.1051/0004-6361/201117119

- Sterken, V.J., Altobelli, N., Kempf, S., Krüger, H., Srama, R., Strub, P., Grün, E. (2013) The filtering of interstellar dust in the solar system. *Astronomy and Astrophysics* 552, A130. doi: 10.1051/0004-6361/201219609
- Sterken, V.J., Strub, P., Krüger, H., von Steiger, R., Frisch, P. (2015) Sixteen Years of Ulysses interstellar dust measurements in the Solar System. III. Simulations and data unveil new insights into local interstellar dust. *The Astrophysical Journal* 812(2), 141. doi: 10.1088/0004-637x/812/2/141
- Stern, S.A. (1995) Collisional time scales in the kuiper disk and their implications. *The Astronomical Journal* 110, 856. doi: 10.1086/117568
- Stern, S.A. (1996) Signatures of collisions in the Kuiper Disk. *Astronomy and Astrophysics* 310, 999. Retrieved from <https://ui.adsabs.harvard.edu/abs/1996A&A...310..999S>
- Stone, E.C., Vogt, R.E., McDonald, F.B., Teegarden, B.J., Trainor, J.H., Jokipii, J.R., Webber, W.R. (1977) Cosmic ray investigation for the Voyager missions; energetic particle studies in the outer heliosphere—and beyond. *Space Science Reviews* 21, 355. doi: 10.1007/bf00211546
- Stone, E.C., Frandsen, A.M., Mewaldt, R.A., Christian, E.R., Margolies, D., Ormes, J.F., Snow, F. (1998) The Advanced Composition Explorer. In Russell, C.T., Mewaldt, R.A., Rosenvinge, T.T. (Eds.), *The Advanced Composition Explorer Mission* (pp. 1-22): Springer Netherlands.
- Strub, P., Krüger, H., Sterken, V.J. (2015) Sixteen years of Ulysses interstellar dust measurements in the Solar System. II. Fluctuations in the dust flow from the data. *The Astrophysical Journal* 812(2), 140. doi: 10.1088/0004-637x/812/2/140
- Sullivan, J.D. (1971) Geometric factor and directional response of single and multi-element particle telescopes. *Nuclear Instruments and Methods* 95(1), 5-11. doi: [https://doi.org/10.1016/0029-554X\(71\)90033-4](https://doi.org/10.1016/0029-554X(71)90033-4)
- Swaczyna, P., Rahmanifard, F., Zirnstein, E.J., McComas, D.J., Heerikhuisen, J. (2021) Slowdown and heating of interstellar neutral helium by elastic collisions beyond the heliopause. *The Astrophysical Journal Letters* 911(2), L36. doi: 10.3847/2041-8213/abf436
- Szalay, J.R., Horányi, M., Colaprete, A., Sarantos, M. (2016) Meteoritic influence on sodium and potassium abundance in the lunar exosphere measured by LADEE. *Geophysical Research Letters* 43(12), 6096-6102. doi: <https://doi.org/10.1002/2016GL069541>
- Trilling, D.E., Bryden, G., Beichman, C.A., Rieke, G.H., Su, K.Y.L., Stansberry, J.A., Blaylock, M., Stapelfeldt, K.R., Beeman, J.W., Haller, E.E. (2008) Debris disks around sun-like stars. *The Astrophysical Journal* 674(2), 1086-1105. doi: 10.1086/525514
- Verbiscer, A.J., Skrutskie, M.F., Hamilton, D.P. (2009) Saturn's largest ring. *Nature* 461(7267), 1098-1100. doi: 10.1038/nature08515
- Vitense, C., Krivov, A.V., Kobayashi, H., Löhne, T. (2012) An improved model of the Edgeworth-Kuiper debris disk. *A&A* 540, A30. Retrieved from <https://doi.org/10.1051/0004-6361/201118551>

- Waite, J.H., Lewis, W.S., Kasprzak, W.T., et al. (2004) The Cassini Ion and Neutral Mass Spectrometer (INMS) investigation. *Space Science Reviews* 114(1), 113-231. doi: 10.1007/s11214-004-1408-2
- Westphal, A.J., Stroud, R.M., Bechtel, H.A., et al. (2014) Evidence for interstellar origin of seven dust particles collected by the Stardust spacecraft. *Science* 345(6198), 786-791. doi: doi:10.1126/science.1252496
- Whittlesey, P.L., Larson, D.E., Kasper, J.C., et al. (2020) The Solar Probe ANalyzers—Electrons on the Parker Solar Probe. *The Astrophysical Journal Supplement Series* 246(2), 74. doi: 10.3847/1538-4365/ab7370
- Wiedenbeck, M.E., Binns, W.R., Cummings, A.C., Davis, A.J., de Nolfo, G.A., Israel, M.H., Leske, R.A., Mewaldt, R.A., Stone, E.C., von Roseninge, T.T. (2007) An overview of the origin of galactic cosmic rays as inferred from observations of heavy ion composition and spectra. *Space Science Reviews* 130(1), 415-429. doi: 10.1007/s11214-007-9198-y
- Yamamoto, S., Mukai, T. (1998) Dust production by impacts of interstellar dust on Edgeworth-Kuiper Belt objects. *Astronomy and Astrophysics* 329, 785. Retrieved from <https://ui.adsabs.harvard.edu/abs/1998A&A...329..785Y>
- Zank, G.P., Heerikhuisen, J., Wood, B.E., Pogorelov, N.V., Zirnstien, E., McComas, D.J. (2013) Heliospheric structure: The bow wave and the hydrogen wall. *The Astrophysical Journal* 763, 20. doi: 10.1088/0004-637x/763/1/20
- Zank, G.P., Adhikari, L., Zhao, L.L., Mostafavi, P., Zirnstien, E.J., McComas, D.J. (2018) The pickup ion-mediated solar wind. *The Astrophysical Journal* 869(1), 23. doi: 10.3847/1538-4357/aabfe

5. Technical Implementation

The science objectives given in the baseline science traceability matrix foldout and the example payload, along with the high-level mission requirements, derive a robust flight system that is relatively independent of specific trajectory target or launch date. The physical spacecraft concept (Kinnison et al., 2021) developed for the example payload and target trajectory is shown in Figure 5-1, and the major components are shown on the block diagram in Figure 5-2. The spacecraft bus is a 2-m octagonal structure that supports a 5-m high-gain antenna (HGA), two radioisotope thermoelectric generators (RTGs), and the payload mounted either on booms or on the ram-facing deck of the spacecraft; other spacecraft components are located inside the structure. Interface to the launch vehicle is opposite the HGA. Physically, the system is balanced for spin-stabilized control for the example payload, as the 50-m PWI wire antennas require a spinning spacecraft for deployment and control. A top-level master equipment list (MEL) for this configuration is shown in Table 5-1.

The example payload includes a number of instruments with wide fields of view, as described in Section 4. These instruments are accommodated by mounting them on booms that extend beyond the edge of the HGA to provide clear fields of view. Spinning the spacecraft also allows these fields of view to be swept through 360° to give the full coverage needed for these measurement types.

Electrically, the spacecraft consists of an avionics suite that provides control of all spacecraft systems, interfaces with the payload, and provides for communication with the ground system. As SpaceWire has been adopted throughout the industry, we have chosen to require that all payload and spacecraft components communicate via a redundant, robust SpaceWire bus, as shown in the block diagram (Figure 5-2). Power is provided by two 16-module Next-Generation RTGs (NextGen RTGs), with characteristics shown in Table 5-2. Given the beginning-of-life power and degradation specifications for the NextGen RTG, the worst-case power condition will be at the end of the mission’s design life (50 years) with instruments and telecommunications simultaneously using power; we have designed the system to fit within the anticipated power at 50 years with margin, as shown in Table 5-3.

The engineering team conducted a significant trade study (Ashtari et al., 2021) to optimize downlink rates, with the goal of providing more than 500 bps at 50 years and downlink rates sufficient to allow significant science at 1000 au. The design for significant downlink rates to 1000 au is not a lifetime requirement on the flight system; rather, it is intended to allow for additional science beyond the 50-year lifetime as flight system performance allows. As a result of this trade, telecommunications is based around an X-band system with multiple antennas, including low-gain antennas (LGAs) used just after launch, a medium-gain antenna (MGA) that can support operations through the inner heliosphere with less stringent pointing requirements, and a large HGA for operations later in the mission at the cost of more restrictive guidance and control requirements to maintain Earth-pointing and optimizing downlink.

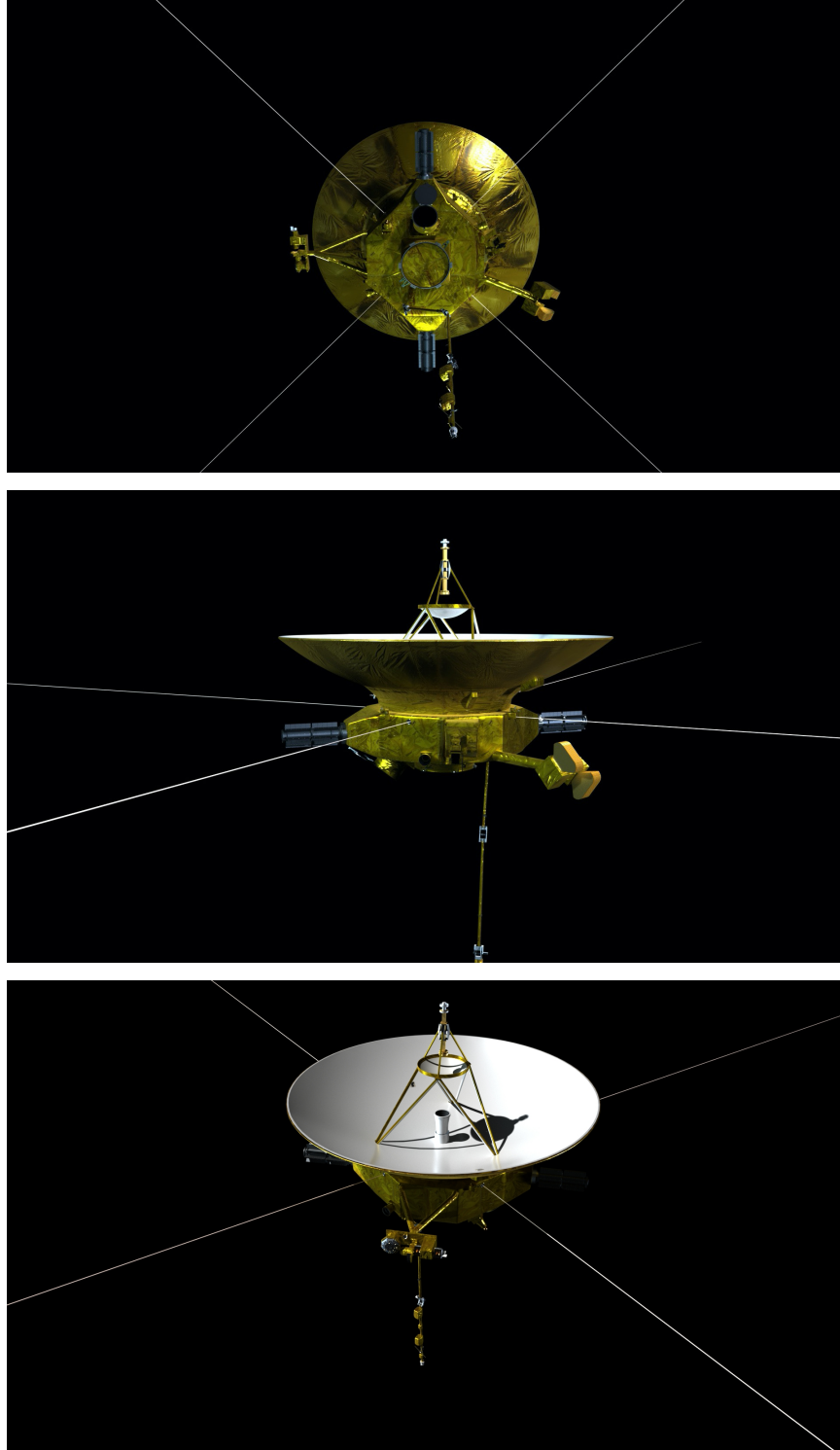


Figure 5-1. Conceptual Interstellar Probe spacecraft in science configuration. (Image credit: Johns Hopkins Applied Physics Laboratory.)

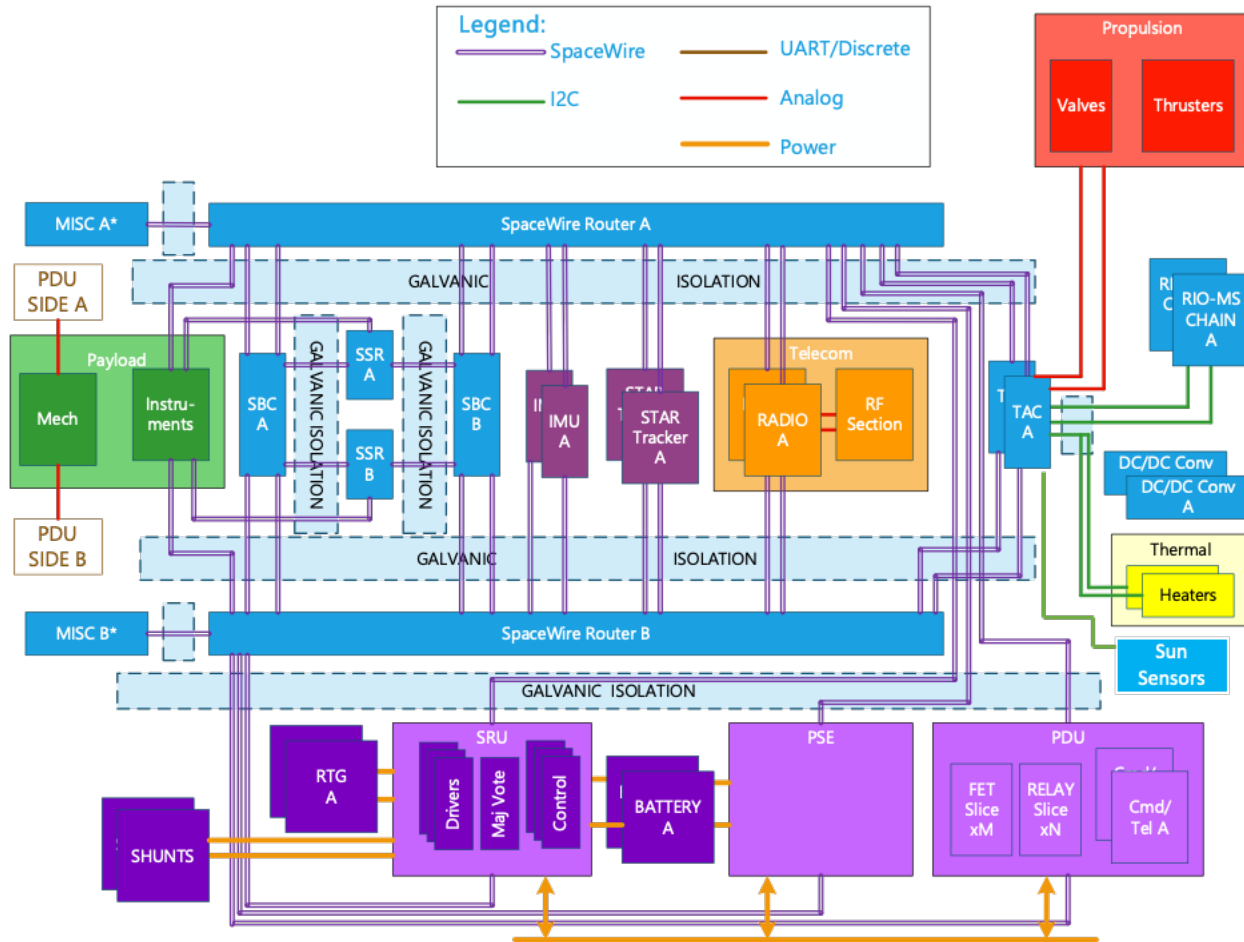


Figure 5-2. Conceptual block diagram of baseline spacecraft. Note: Batteries are included as an optional element and are not required for the mission. (Image credit: Johns Hopkins Applied Physics Laboratory.)

5.1 Critical Subsystems

5.1.1 Guidance and Control

The guidance and control (G&C) subsystem consists of two star trackers that can operate in spin mode, a fully internally redundant inertial measurement unit (IMU) with no life-limiting items, and a sun sensor assembly optimized for spin-mode operations. Actuation is provided solely by attitude control thrusters, which are coupled to minimize residual ΔV . The algorithms and subsystem design are heritage from the New Horizons (Fountain et al., 2008), Van Allen Probes (Stratton et al., 2013), and Interstellar Mapping and Acceleration Probe (IMAP; McComas et al., 2018) missions.

Table 5-1. Baseline concept spacecraft MEL summary.

	Mass (kg) (Includes Contingency)
Payload (including accommodation hardware)	100.5
Telecommunications	83.4
Guidance and control	16.8
Power	169
Thermal control	70.8
Avionics	12.8
Propulsion	37.2
Mechanical/structure	150
Harness	29.3
Propellant	106
Total	776
Margin	84
Launch mass	860

The G&C system is required to maintain the HGA pointing to less than 0.2° to Earth. Accomplishing this will require periodic precession maneuvers to adjust the spacecraft system momentum vector to better than 0.05° from the commanded vector and to then allow Earth to drift off until another precession maneuver is required. Thus, the G&C attitude knowledge must be much better than the control requirement, and heritage star trackers used on New Horizons could provide attitude knowledge to better than 0.027° up to 10 rpm. The hemispherical resonating gyroscopes in the IMU provide high-frequency body rate information, useful to determine how the system momentum state is aligned to the central hub state. This information is used to calibrate the star tracker and sun sensor alignment after launch. The IMU also contains accelerometers, which are needed for trajectory-correction maneuvers (TCMs). Attitude knowledge will also be used by the science team to correlate their data.

Table 5-2. Assumed RTG characteristics.

Assumed RTG Characteristics (1 unit)	
Power at the beginning of life (We)	300
Mass (kg)	60
Power at the end of life (We)	150
Voltage (V)	22–34
Launch availability	2030

Table 5-3. End-of-life power mode.

Worst-Case Power (W)	
Payload	87.9
Spacecraft	139
Margin	73
Total	300
Available RTG power (2 units, end of mission)	300

The long flexible booms introduce kinematic motion that makes controlling the system momentum vector problematic (Rogers et al., 2021). Coupling between the hub and boom nutation modes can confuse the control system, so algorithms developed for Van Allen Probes and IMAP will be used to perform those maneuvers.

The sun sensors are required in the event the spacecraft loses inertial attitude knowledge, or its positional state with respect to Earth. They allow the control system to point the HGA toward the Sun to try to reestablish commanding and telemetry to recover the spacecraft. A variable gain setting in the electronics allows them to be used from 1 au to greater than 60 au. When the spacecraft distance exceeds the detection threshold, an inertial pointing scheme developed by New Horizons can be used.

5.1.2 Avionics

The avionics subsystem provides control of all spacecraft systems, interfaces with the payload, and provides for communication with the ground system. The subsystem is based on redundant single-board computers, with data storage provided by solid-state recorders (SSRs) and links to other subsystems through a redundant SpaceWire bus. We have not chosen a specific architecture for the single-board computers; however, processors flown on current missions are well within the capability range needed for Interstellar Probe.

The SpaceWire protocol, with its rich flight heritage, is used to simplify and standardize interfaces. SpaceWire includes multiple levels of error detection and correction and is reliable over a broad range of operating conditions. Its physical layer uses low-power differential signaling, for low power, low electromagnetic interference (EMI), and low switching noise. At the protocol layer, both remote memory access protocol (RMAP) and Consultative Committee for Space Data Systems (CCSDS) are supported for flexibility.

Increased longevity is a primary goal of the avionics design. Redundant components are cross-strapped across redundant SpaceWire buses, allowing an autonomy function to rapidly reconfigure the spacecraft from healthy reserves. Alternating current (AC)-coupled implementations will allow components with SpaceWire interfaces to operate in galvanic isolation, eliminating the risk of ground drift. Galvanic isolation particularly will reduce the complexity of mounting instruments on booms.

Additional care is being given at the component and board levels to assess and mitigate long-term failure modes such as metal migration and joint fatigue. Appendix F provides more details about these concerns. Field-programmable gate arrays (FPGAs) may be reprogrammed periodically to remove accumulated upsets, if necessary. SSRs may require extra redundancy or interleaving to ensure functionality in this high-radiation environment.

Power use is also a major design constraint for avionics. Radiation-tolerant multicore processors are used to reduce the dynamic power use when less processing effort is required. A sleep mode with auxiliary watchdog may be engaged when further power reduction is necessary. SpaceWire rates will be tuned to the bandwidth required for individual data links.

5.1.3 Telecommunications

The baseline telecommunications subsystem is an X-band fully redundant system, as shown in Figure 5-3. The hardware in this subsystem represents mature technology with heritage in deep space. The antenna complement includes the 5-m HGA, a 0.4-m MGA coboreshielded with the HGA, and fore and aft LGAs. The MGA will be used early in the mission to allow high data rates without the high pointing constraints of the HGA.

The subsystem uses redundant and cross-strapped X-band radios, based on the APL Frontier radio. It is assumed that these radios provide turbo-rate 1/6 downlink coding, low-density parity check (LDPC) uplink decoding, regenerative ranging, delta differential one-way ranging (D-DOR), and coherent turnaround. These radios in turn feed redundant traveling-wave tube amplifiers (TWTAs), diplexers, and a simple switch matrix. The TWTA output power is constrained by direct current (DC) power available after 50 years: the baseline design assumes that each TWTA is capable of 52 W, which is well within currently flying capabilities. The overall topology maintains redundant paths to the HGA and MGA, which are dual-polarized.

Specifications for the telecommunications subsystem (Ashtari et al., 2021) are given in Table 5-4 along with a comparison with similar deep-space missions. We have considered multiple ground stations for communicating with Interstellar Probe, and ground stations that can support the mission at the required uplink/downlink capability are given in link difficulty, which is the data rate in megabytes multiplied by the distance in astronomical units squared. Values are based on regenerative ranging.

Table 5-5 and Figure 5-4 show downlink rates as a function of range for the stations of interest. From this, we have calculated the available downlink volume per week across the baseline mission, as shown in Figure 5-5. This data volume mission profile is consistent with the derived measurement requirements to meet the science objectives.

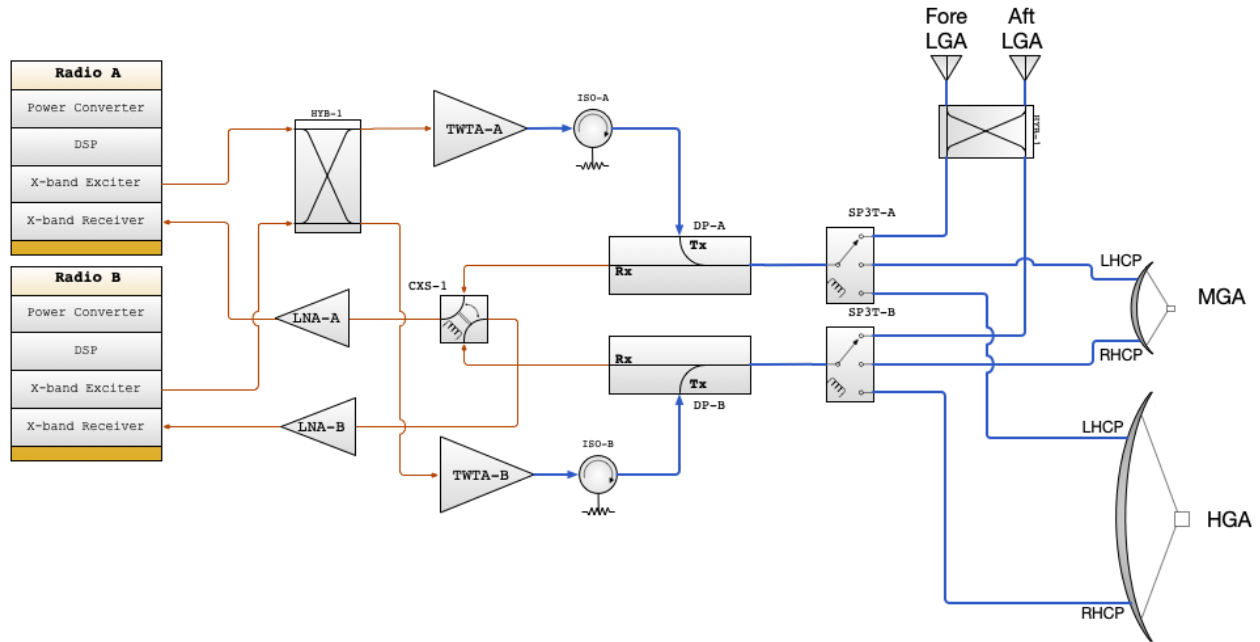


Figure 5-3. Baseline telecommunications subsystem. (Image credit: Johns Hopkins Applied Physics Laboratory.)

Table 5-4. Communications specifications compared to notable deep-space missions.

	New Horizons	Voyager	Interstellar Probe
Frequency	8.4 GHz	8.4 GHz	8.4 GHz
Range	45 au	145 au	375 au 1000 au
Transmitter antenna diameter	2.1 m	3.7 m	5 m
Transmit power	12.61 W	21.3 W	52 W
Ground station	Deep Space Network (70 m)	DSN (70 m)	Next Generation Very Large Array (ngVLA)
Maximum data rate	800 bps	160 bps	2592 365 bps
Link difficulty*	1.62	3.36	364.5

*Link difficulty = $\text{DataRate (MB)} \times \text{Distance (au)}^2$. Values based on regenerative ranging.

Table 5-5. Ground station alternatives for Interstellar Probe.

	Deep Space Network (DSN)		Green Bank Telescope (GBT)	Next Generation Very Large Array (ngVLA)
Antennas (m)	34	4 × 34	100	244 × 18
Effective aperture (m ²)	481	2523	6351	47,141
Gain (dBic)	66.8	72.8	78.0	86.2
System noise temperature (K)	28*	28*	29**	27**
Sensitivity (dBic)	52.3	58.5	63.4	71.9

Notes:

*Values shown are for X-band downlink frequencies, DSS-14, -43, -63—20° elevation (90% CD).

**System noise temperatures of National Radio Astronomy Observatory (NRAO) facilities assume 45° elevation.

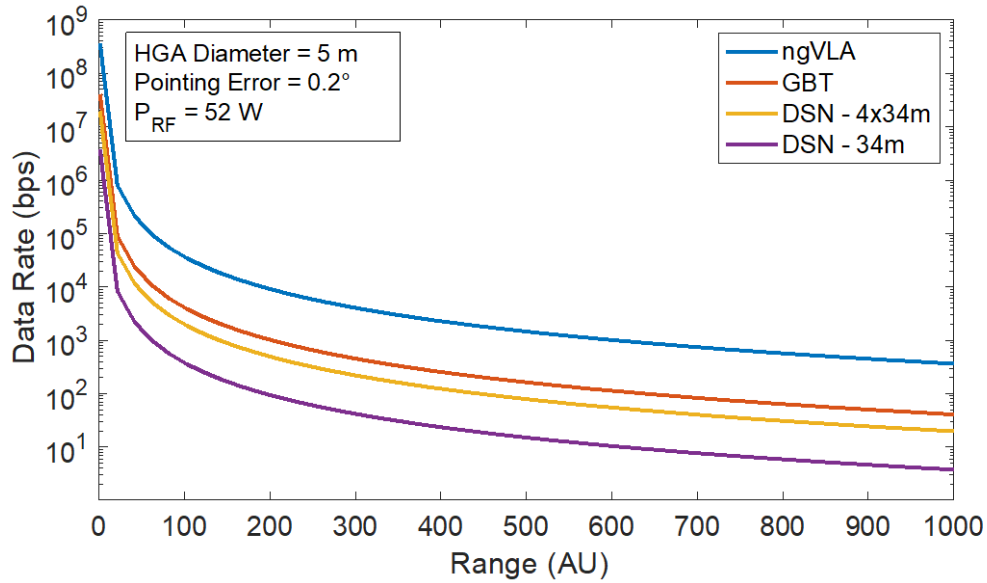


Figure 5-4. Downlink performance for ground stations. DSN, Deep Space Network; GBT, Green Bank Telescope; ngVLA, Next Generation Very Large Array. (Reprinted from Kinnison et al. (2021) with permission; © IEEE.)

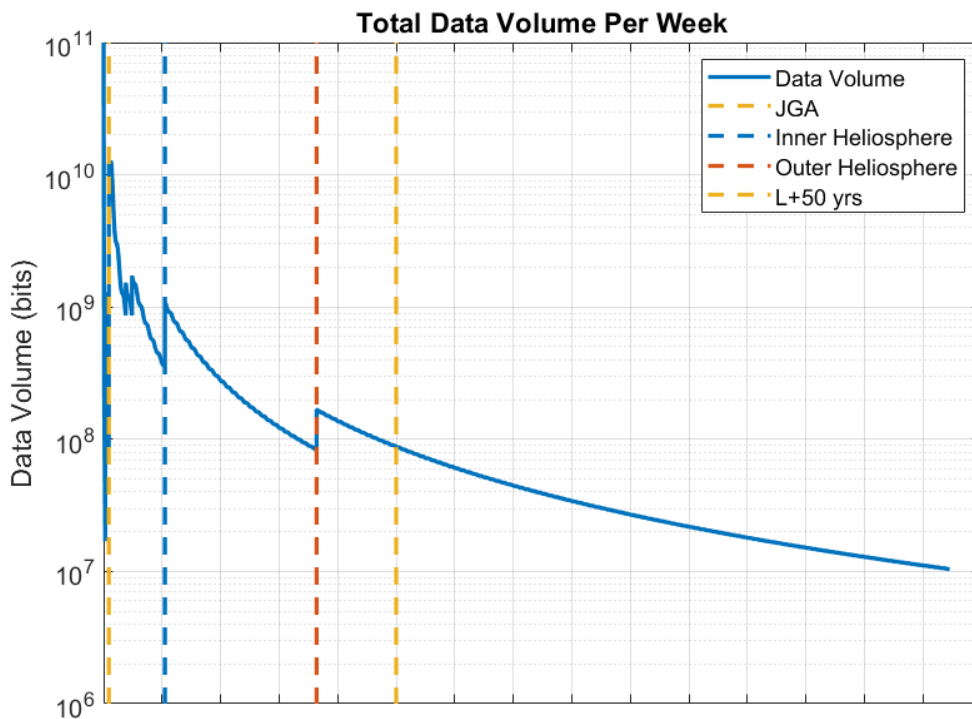


Figure 5-5. Expected data volume per week through the mission. JGA, Jupiter gravity assist. (Reprinted from Kinnison et al. (2021) with permission; © IEEE.)

5.1.4 Power

The spacecraft is powered by two 16-module NextGen RTGs, which produce ~600 We at the beginning of the mission. Primary power is regulated through a system of shunts controlled by the

shunt regulation unit (SRU) and provided to the power supply electronics (PSE), which regulate the main bus to 22–34 V. Power is distributed to all components through relays and switches in the power distribution unit (PDU). The PSE and PDU also use SpaceWire interfaces to receive commands from and provide telemetry to the avionics. A battery is included in the architecture but is not necessary; if a long-lived battery is available, it can be included in the flight system to simplify operations late in the mission. This architecture is similar to that on New Horizons, which is also powered by an RTG with shunt regulation, and Parker Solar Probe (Kinnison et al., 2020), which uses the PSE/PDU architecture for highly reliable control of power regulation and distribution.

5.1.5 Propulsion

The propulsion subsystem is a blowdown monopropellant hydrazine design that provides ΔV and attitude control capability for the spacecraft. Monopropellant systems are well characterized, are well understood, and have significant flight history. The system consists of four 4.4-N (1.0-lbf) and twelve 1.0-N (0.2-lbf) thrusters and components required to control the flow of propellant and monitor system health and performance. Propellant and pressurant are stored in a single tank. As propellant is expelled, the pressure of the pressurant decreases; thus, the thrust and specific impulse of the thrusters decrease as the mission progresses. Several flight-proven options exist for each component of the propulsion system, although delta-qualification testing of some components may be required.

The thrusters are of the catalytic monopropellant hydrazine type; when the thruster valves open, propellant flows through the thruster into a catalyst bed, where the hydrazine spontaneously decomposes into hot gases, which then expand through a nozzle and exit the thruster, producing thrust. For the purposes of this study, performance data for OSIRIS-REx (Origins, Spectral Interpretation, Resource Identification, Security-Regolith Explorer)-heritage Aerojet Rocketdyne MR-111G 4.4-N thrusters and New Horizons-heritage Aerojet Rocketdyne MR-103H 1.0-N thrusters were used, but alternative options exist.

Propellant will be stored in a 186-liter spherical titanium tank with Earth Radiation Budget Satellite (ERBS) flight heritage manufactured by Northrop Grumman Innovation Systems. This 71.1-cm (28-in.) inner-diameter tank contains an elastomeric diaphragm separating propellant from pressurant. The maximum expected operating pressure (MEOP) for the mission is 380 psi. Remaining components used to monitor and control the flow of propellant—latch valves, filters, orifices, service valves, and pressure and temperature transducers—will be selected in Phase A from a large catalog of components with substantial flight heritage on many spacecraft.

5.1.6 Thermal

The thermal control subsystem (TCS) provides a stable, near-room-temperature environment for the Interstellar Probe spacecraft bus based on the successful implementation of a similar design for New Horizons. Like New Horizons, Interstellar Probe avoids inner solar system cruise with a minimum solar distance greater than 1.0 au simplifying the TCS. The HGA and insulation on the Sun-facing surfaces, along with the short time spent close to the Sun, provide a nearly constant thermal environment for the spacecraft that allows the thermal design to be tailored for the deep-

space environment. Most of the spacecraft components are thermally coupled to the bus, using their heat dissipation to minimize the need for heater power in all spacecraft modes.

The principal heat source for the Interstellar Probe spacecraft is the two RTGs. Both the electrical power and thermal waste heat of the RTGs are used in the TCS to support spacecraft bus temperatures. The RTGs are mounted to a thermally isolated pyramid structure that provides a large thermal resistance, but with an internal cavity that allows the heat flow into the bus region to be tailored by adjusting the internal multilayer insulation (MLI). The final tailoring of the RTG heat input can be implemented and verified very late in the schedule, similar to New Horizons, after system-level thermal-vacuum (TV) testing.

MLI covers the entire spacecraft, except for the louvers and instrument apertures, providing a thermos-bottle environment for the internal subsystems. The spacecraft bus temperatures are controlled by measuring the internal currents and adjusting the power shunts to maintain a constant dissipation inside the thermal bus. This thermos-bottle approach, demonstrated in flight on New Horizons, depends on the heat leak through the MLI, which will be tested in Phases B/C to ensure that as-built MLI required effectiveness is achieved.

Spacecraft bus components are controlled to near room temperatures throughout the mission by controlling the power dissipation inside the bus. Heat is spread around the bus cavity by conduction and radiation, providing a nearly isothermal bus environment. Heat is shunted away from high-dissipation components, such as the transmitters, using high-conductivity doublers. Components sensitive to low temperature, such as the propulsion system, are kept above 20°C using the internal bus environment. Other components with smaller operating ranges, such as the battery, are cooled using an external louver to below the bus environment. Interstellar Probe will need about 155 W inside the thermal bus to maintain its allowable temperature.

The instruments mounted off the spacecraft have lower temperature limits. They draw some heat from the spacecraft and also have survival heaters to keep them within their allowable ranges. The instruments and the structure supporting them are wrapped in MLI to minimize their heat leak. Heat-loss testing for these instruments, and all thermally isolated components, is conducted during the component-level TV testing and checked again at the system-level test.

5.2 Ground System

The Interstellar Probe ground system is used to plan, test, and uplink commands and downlink, process, and distribute telemetry and science data. A simple block diagram of the ground system is shown in Figure 5-6. Green arrows represent the flow of commands. Blue arrows represent the flow of telemetry and science data. Yellow, pink, and purple arrows represent various data products that are produced and distributed among the team. Contact scheduling and telecommunications begin using the Deep Space Network (DSN) initially; downlink tasks will be performed by the Next Generation Very Large Array (ngVLA) equivalent.

At the center of the ground system is the Mission Operations Center (MOC). The MOC interfaces with the spacecraft engineering team, the Science Operations Center (SOC), navigation, mission design, the DSN (or ngVLA), and the contact scheduler (DSN or ngVLA equivalent) to plan, test, and

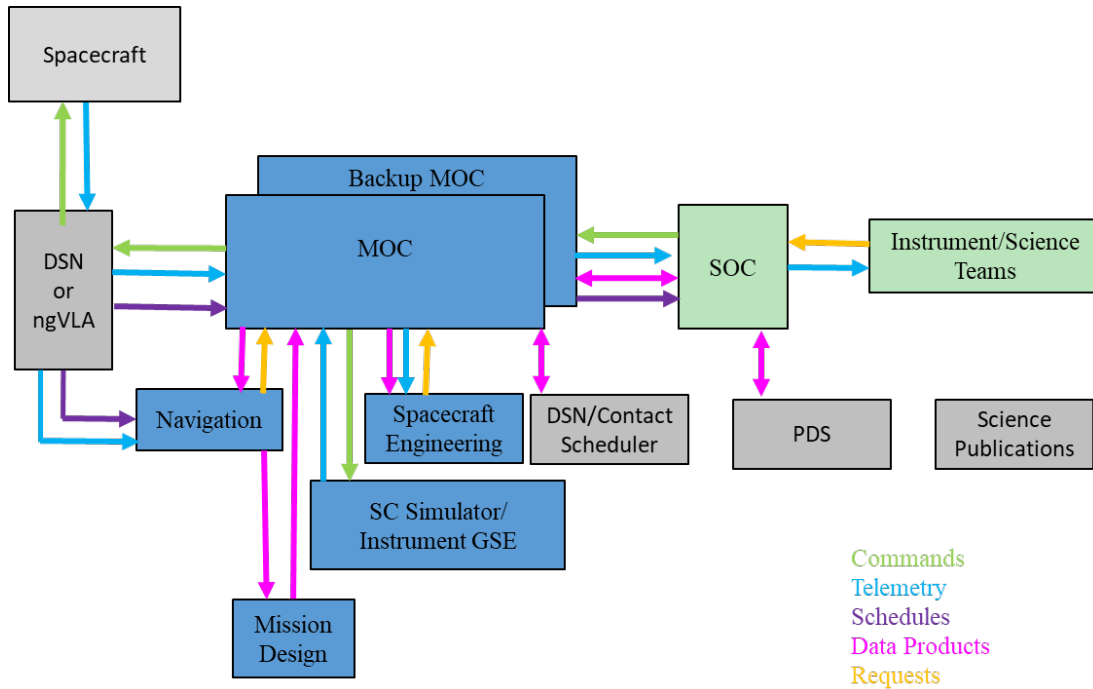


Figure 5-6. Interstellar Probe example ground system. (Reprinted from Kinnison et al. (2021) with permission; © IEEE.)

execute all spacecraft activities, monitor spacecraft and instrument health and safety, and downlink spacecraft and science data. In addition, the SOC interfaces with the instrument and science teams to plan instrument activities, science data collection, and science data distribution. A single SOC is shown in the diagram, but this function could be split into multiple SOCs for individual or groups of instruments.

5.2.1 Automation and Unattended Contact Operations

Outside of events such as spacecraft and instrument commissioning, TCMs, and the Jupiter gravity assist, the MOC is capable of supporting the downlink of science data and uplink of nominal command sequences during contacts through the DSN or ngVLA without the need for staffing within the MOC. The ground system will monitor spacecraft health and status and support remote notification of predefined alarm conditions to Mission Operations Team members. It will also support autonomously uplinking command sequences using contact plans generated by the planning and scheduling software. The automated and unattended operations concept has been successfully used on the STEREO and Van Allen Probes missions.

5.3 Section 5 References

Ashtari, R., Copeland, D., Kinnison, J., Rogers, G., McNutt, R. (2021, 6-13 March 2021) *Interstellar Communications*. In 2021 IEEE Aerospace Conference (50100). doi: 10.1109/AERO50100.2021.9438311

Fountain, G.H., Kusnierkiewicz, D.Y., Hersman, C.B., et al. (2008) The New Horizons Spacecraft. *Space Science Reviews* 140(1), 23-47. doi: 10.1007/s11214-008-9374-8

- Kinnison, J., Vaughan, R., Hill, P., Raouafi, N., Guo, Y., Pinkine, N. (2020, 7-14 March 2020) *Parker Solar Probe: A Mission to Touch the Sun*. In 2020 IEEE Aerospace Conference. doi: 10.1109/AERO47225.2020.9172703
- Kinnison, J., Schlei, W., Rogers, G., et al. (2021, 6-13 March 2021) *Interstellar Probe: A Practical Mission to Escape the Heliosphere*. In 2021 IEEE Aerospace Conference (50100). doi: 10.1109/AERO50100.2021.9438249
- McComas, D.J., Christian, E.R., Schwadron, N.A., et al. (2018) Interstellar Mapping and Acceleration Probe (IMAP): A New NASA Mission. *Space Science Reviews* 214(8), 116. doi: 10.1007/s11214-018-0550-1
- Rogers, G.D., Kinnison, J.D., Brandt, P.C., Cocoros, A.A., Paul, M.V. (2021, 6-13 March 2021) *Dynamic Challenges of Long Flexible Booms on a Spinning Outer Heliospheric Spacecraft*. In 2021 IEEE Aerospace Conference (50100). doi: 10.1109/AERO50100.2021.9438510
- Stratton, J.M., Harvey, R.J., Heyler, G.A. (2013) Mission Overview for the Radiation Belt Storm Probes Mission. *Space Science Reviews* 179(1), 29-57. doi: 10.1007/s11214-012-9933-x

6. Programmatics/Mission Management

6.1 High-Level Mission Schedule

The mission schedule is based on the actual timelines of two previous missions: Parker Solar Probe and New Horizons. Parker Solar Probe, as the most recent Heliophysics Large Strategic Mission, is a suitable model for the programmatic process (Fox et al., 2016) that Interstellar Probe might follow, including allowances for the broad competition for individual science instruments, excepting the need for prolonged development of Parker’s heat shield. New Horizons (Fountain et al., 2008; Harmon & Bohne, 2007) is powered by NASA’s most recently launched general-purpose heat source radioisotope thermoelectric generator (GPHS-RTG) and has operational and flight system considerations similar to Interstellar Probe (whereas NASA’s other recent ²³⁸Pu-powered missions, the Mars rovers, have very different flight system designs and operational parameters). The Interstellar Probe project phase durations are shown in Table 6-1, and the schedule is shown in Table 6-2. Table 6-2 designates key mission dates, including life-cycle reviews that require standing review boards (SRBs), as specified by NASA Procedural Requirement (NPR) 7120.005E.

6.2 Mission Life-Cycle Cost

The cost estimates for Interstellar Probe were prepared consistent with the *Planetary Decadal Mission Study Ground Rules* (a copy of this document can be provided upon request) in detail sufficient to identify and understand the likely summary costs and major cost drivers. For payloads and spacecraft, the use of parametric cost models considers the technical and performance characteristics of hardware and software down to key components where appropriate. Cost estimates for science, mission operations (MOps), and ground data system (GDS) elements, whose costs

Table 6-1. Interstellar Probe project phase durations.

Project Phase	Duration (Months)
Phase A – Conceptual Design	12
Phase B – Preliminary Design	24
Phase C – Detailed Design	24
Phase D – Integration and Testing	36
Phase E – Primary Mission Operations	600
Phase F – Closeout	12
Start of Phase B to Preliminary Design Review (PDR)	22
Start of Phase B to Critical Design Review (CDR)	38
System-Level Integration and Testing	34.5

Table 6-2. Interstellar Probe project schedule with key milestones.

Project Milestones	Date
Phase A Start	September 2028
System Readiness Review (SRR)	March 2029
Mission Design Review (MDR)	August 2029
Phase B Start	September 2029
Preliminary Design Review (PDR)	July 2031
Phase C Start	September 2031
Critical Design Review (CDR)	November 2032
System Integration Review (SIR)	August 2033
Phase D Start	September 2033
Operational Readiness Review (ORR)	February 2034
Pre-Environmental Review (PER)	March 2035
Pre-Ship Review (PSR)	March 2036
Mission Readiness Review (MRR)	April 2036
Launch Readiness Date (LRD)	August 2036
Phase E Start	September 2036
Phase F Start	September 2086
Phase F End	September 2087

are driven by labor requirements, are based on the Phase A–D schedule and planned activities and are comparable to cost trends for prior missions. Phase E costs are based on lessons learned from Voyager and New Horizons as they consider the long duration of the mission and the need for knowledge management as well as successive ground system updates over the course of Phase E. The life-cycle cost (LCC) estimates for the Interstellar Probe mission apply to the concept maturity level-4 (CML-4) mission concept described in this report. The life-cycle Interstellar Probe estimates cover all major work breakdown structure (WBS) elements listed in NPR 7120.5 E except for Launch Vehicle and Services (WBS 08).

To quantify program risk, a range was generated for each WBS element, to reflect current best estimates in quantities, design, and manufacturing heritage, mass, and power, along with the uncertainties and design evolution that are likely to occur before authorization to proceed.

The Interstellar Probe Phase A–F mission estimate covers an 8-year development cycle and 50 years of MOps. It does not include launch vehicle and services but does include unencumbered cost reserves of 50% on Phases A–D and 25% reserves on Phases E and F. Table 6-3 presents the details. The baseline mission cost estimate is \$3144M in fiscal year 2025 (FY25) dollars. For Phases A–D, the baseline cost estimate is \$1689M FY25, including 50% reserves. For Phases E and F, because the proposed length of Interstellar Probe’s mission operations exceeds that of almost all NASA robotic missions, a parametric estimating tool developed for NASA called the Mission Operations Cost Estimating Tool (MOCET; Hayhurst et al., 2021) was used to extrapolate a rough order of magnitude (ROM) estimate for 50 years of Phase E/F operations of \$1455M FY25, which for Phase E is approximately \$230.9M FY25 per decade. That estimate includes 25% unencumbered reserves but excludes Deep Space Network (DSN) charges.

Table 6-3. Interstellar Probe life-cycle cost estimate (FY25\$M).

WBS	Interstellar Probe	Baseline
1	Project Management (PM)	\$169
2	Systems Engineering (SE)	
3	Mission Assurance (MA)	
4	Science	\$50
5	Payload	\$361
6	Spacecraft (S/C)	\$388
7/9	Mission Operations & Ground Data Systems (MOps/GDSs)	\$37
8	Nuclear Launch Approval	\$26
10	Integration & Testing (I&T)	\$95
	Subtotal	\$1126
	Phase A–D Unencumbered Reserves (50%)	\$563
	<i>Phase A–D Total</i>	<i>\$1689</i>
	Phase E Subtotal	\$1164
	Phase E Unencumbered Reserves (25%)	\$291
	<i>Phase E Total</i>	<i>\$1455</i>
	Total Project Cost	\$3144

6.3 Mission Ground Rules and Assumptions

The cost, schedule, and program structure for Interstellar Probe are based the following:

- Cost-estimating ground rules and assumptions are derived from Revision 4 of the *Planetary Decadal Mission Study Ground Rules*. A copy of this document can be provided upon request.

- Mission development costs are reported at WBS Level 2 (and Level 3 where appropriate) per NPR 7120.5E. Phase E costs are reported at WBS Level 1.
- Participation in the mission is assumed to be distributed throughout the NASA community. Cost estimates do not assume which NASA institutions will build the spacecraft, provide the instruments, or manage the program. However, they do assume that payloads will be competed while the spacecraft and operations will be directed.
- Cost estimates are reported in FY25 dollars. Historical costs used for analogous costing are inflated using the NASA New Start Inflation indices.
- This estimate assumes no development delays and an on-time launch between 28 August and 18 September 2036.
- Phase A–D unencumbered cost reserves are calculated as 50% of the estimated costs of all components excluding Launch Vehicle and Services, and Phase E–F cost reserves are calculated as 25% of the estimated costs of all Phase E elements excluding DSN charges.

6.4 Cost Benchmarking

The study team used several solar system exploration missions as comparators while developing the cost estimate for Interstellar Probe. None of the comparator missions have exactly the same architecture or programmatic considerations as Interstellar Probe, but each shares similarities that make the group of missions a useful set to understand the *scale* of Interstellar Probe’s cost. New Horizons, for example, has a very similar mission architecture (direct launch to Jupiter for the gravity assist, and then onward, out of the solar system), but New Horizons’ science operations (Stern et al., 2015) were focused around the Pluto system flyby and not the ongoing science collection described above for Interstellar Probe’s multi-decade lifetime. Like Interstellar Probe’s plan, Parker Solar Probe’s instruments were turned on within 2 months of the 2018 launch and are expected to operate in different modes until the end of the mission, but that spacecraft’s constant proximity to Earth (<2 au from the moment of launch; Guo et al., 2021) allows for a more familiar operational cadence. On the other hand, Parker’s extreme proximity to the Sun requires unique operational considerations that are very different from Interstellar Probe’s, which are driven by Interstellar Probe’s unprecedented remoteness. The collection of missions below allowed the study team to scale the Phase A–D complexity and risk, and to estimate the Phase E and F level of effort in accordance with NASA’s past missions of similar scale, although further refinement is needed to decrease cost uncertainty.

Figure 6-1, which compares the estimated Phase A–D costs of the Interstellar Probe concept against the reported costs of several NASA solar system exploration missions, shows that it falls mid-range for these comparator missions. The Interstellar Probe A–D estimate with 50% reserves is 85% higher than the Phase A–D cost of Parker Solar Probe. Without cost reserves, the baseline Interstellar Probe A–D estimate is 23% higher than the Phase A–D cost of Parker Solar Probe. This cost delta is driven by a difference in mission lifetime requirements and the number of instruments

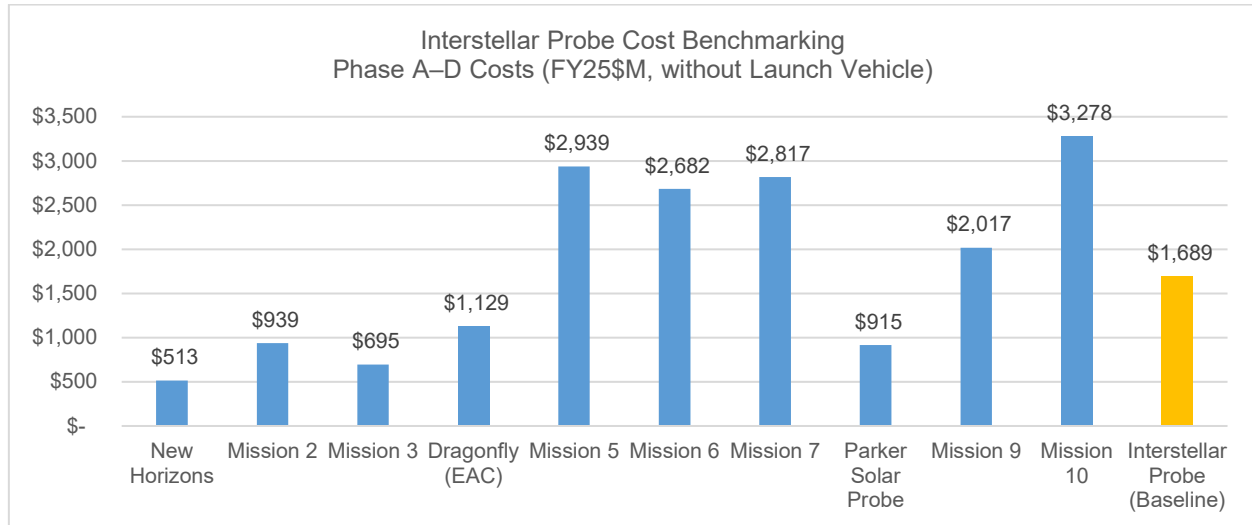


Figure 6-1. Interstellar Probe Phase A–D cost benchmarking. Mission names are listed only for APL-managed missions; missions managed by other organizations are indicated by number. Source: NASA’s Cost Analysis Data Requirement Database (CADRe). EAC, estimate at completion.

in the Interstellar Probe payload. The Interstellar Probe concept falls mid-range among solar system exploration missions of similar complexity in terms of science scope, engineering scope, and, as shown, cost.

Because of the unique length of Interstellar Probe’s prime mission, the study team compared this mission’s annual and 10-year Phase E/F costs to the prime mission costs of the other NASA robotic scientific missions. The average annual cost per year for Interstellar Probe during Phase E is \$22.7M/year. Figure 6-2 compares the average annual Phase E cost of Interstellar Probe to that of other New Frontiers and large strategic-class science missions. The comparison shows that Interstellar Probe is in line with the annual Phase E costs of other comparable large strategic science missions.

6.5 Costing Methodology and Basis of Estimate

Interstellar Probe cost estimates were generated with a combination of high-level parametric models and analog techniques. They incorporate cost, schedule, and technical uncertainty in the estimating process. No adjustments were made to remove the historical cost of manifested risk from the heritage data underlying the baseline estimate. Therefore, before unencumbered cost reserves are applied, the estimated costs already include a historical average of the cost of risk. This approach is appropriate for capturing risk and uncertainty commensurate with the early stages of a mission. The following paragraphs describe the basis of estimate (BOE) for each element.

6.5.1 Phases A–D

Phase A Interstellar Probe development costs include the budget for a 12-month Phase A (see Table 6-1). Planned Phase A activities include the following:

- Development of project plans: project management plan, systems engineering management plan, mission assurance requirements document, etc.

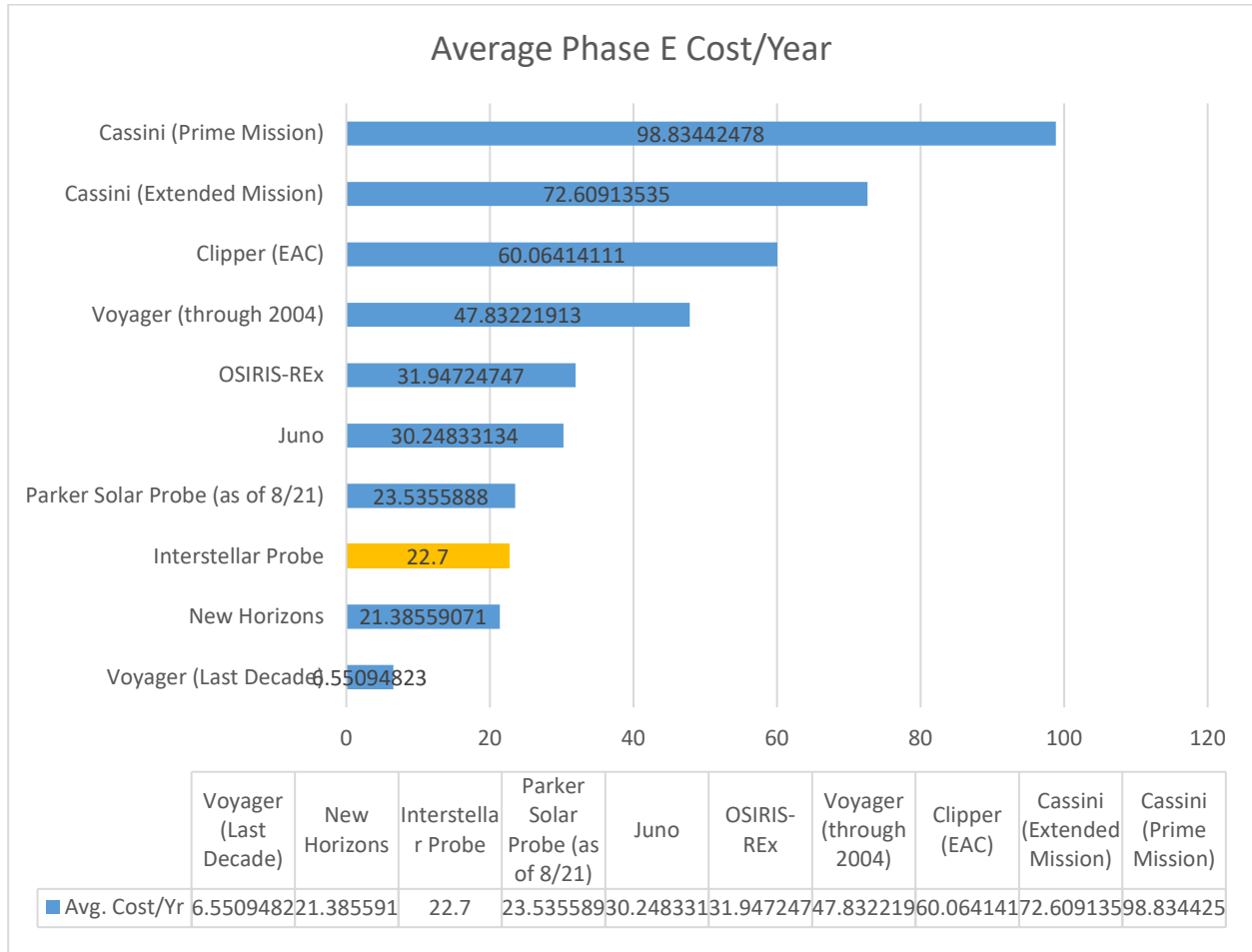


Figure 6-2. Interstellar Probe Phase E cost benchmarking. Source: The Planetary Society Planetary Exploration Budget Dataset, Johns Hopkins Applied Physics Laboratory.

- Development of project schedule
- Completion of any remaining trade studies
- Payload definition and selection
- Accommodation of selected payload
- Definition of system requirements to subsystem and instrument level
- Development of interfaces and interface control documents
- Definition of environment requirements
- Mission concept development
 - Trajectory and navigation
 - Propellant budget

- Initial flight system concept
- Any technical budgets (mass, power, pointing, alignments, etc.)
- Concept of operations
- Conduct System Requirements Review (SRR) and Mission Concept Review (MCR) (gates to entering Phase B)

WBS 1, 2, 3: Project Management, Systems Engineering, and Mission Assurance (PMSEMA). These activities depend on multiple mission- and organization-specific characteristics (Hahn, 2014). Therefore, cost estimates derived from analogous historical missions are preferred over cost model outputs that do not take the mission characteristics into account. Existing analyses demonstrate that hardware costs are a reliable predictor of these critical mission function costs. The Johns Hopkins Applied Physics Laboratory (APL) has conducted thorough and rigorous analyses of PMSEMA costs, both for historical APL missions and for analogous missions. The BOE relies on analysis of PM, SE, and MA practices on recent NASA large strategic science missions managed under current NASA requirements. The analysis finds that PMSEMA cost is, on average, 20% of the flight system. To represent uncertainty within the estimate, both cost percentage and predicted hardware cost (used as the cost basis) are allowed to vary.

WBS 4: Science. This element is largely level of effort. It covers the management and planning of the science investigation during the 8-year Interstellar Probe development period. For Interstellar Probe, Phase A–D Science is estimated with ROM estimates derived from analysis of historical costs expended during prelaunch on science on New Frontiers and large strategic science missions. Missions analogous to Interstellar Probe spent between \$3M and \$6M annually. The baseline cost for Interstellar Probe’s prelaunch Science is ~\$6M annually, or \$50M FY25 for Phases A–D.

WBS 5: Payload. This element includes the costs for a notional baseline payload. An estimated cost for the augmented payload option can be found in Appendix G. Because we assume that Interstellar Probe payloads will be competed, we predict that WBS element 5 has the highest degree of uncertainty. As such, it is also the cost element with the most cost risk.

All instrument costs underwent an iterative effort between cost, science, and engineering to ensure an estimate that adequately captures the true effort required to develop these instruments. This exercise involved the analysis of analogous costs and parametric modeling. The parametric models used to estimate the payload were SEER for Space and the NASA Instrument Cost Model (NICM) 9 with technical inputs captured in the Master Equipment List (MEL). These two models are most appropriate for the level of concept maturity of Interstellar Probe. The baseline cost estimate is shown in in Table 6-4. It is assumed that all instruments are technology readiness level (TRL) 4/5 and will require some level of technology development. Table 6-4 summarizes the estimates by instrument for the Interstellar Probe baseline payload (as described in Sections 4.1 and 4.3).

WBS 6: Spacecraft. The baseline Interstellar Probe spacecraft bus cost estimate covers delivery of hardware and flight software. Also included are the costs for spacecraft management, systems engineering, and safety and mission assurance. Costs of the baseline Interstellar Probe spacecraft bus

hardware were estimated using historical cost-per-kilogram factors. These factors were derived from New Horizons and Parker Solar Probe. New Horizons was selected for its similarity in architecture, and Parker Solar Probe was selected because it is the most recent APL large strategic science mission with complete, finalized cost data. The results from a parametric model, PRICE® TruePlanning® 16, served as a cross-check to the Interstellar Probe baseline estimate and to validate cost realism. Because of similarities in spacecraft hardware and mission, New Horizons spacecraft cost actuals were also analyzed. As a recently built and launched spacecraft with operational complexities to design for, Parker Solar Probe is also included as a comparison point.

Table 6-4. Interstellar Probe payload cost summary (FY25\$M).

Instrument	Cost Estimate
Payload PMSEMA	\$27
Fluxgate Magnetometer (2) + Boom	\$15
Plasma Wave Instrument + Boom	\$51
Solar Wind	\$22
Pickup Ion (PUI)	\$17
Suprathermals and Energetic Ions	\$23
Cosmic Ray Spectrometer	\$35
Interstellar Dust Analyzer	\$20
Neutral Ion Mass Spectrometer	\$74
Energetic Neutral Atom (ENA)	\$31
Lyman-α Spectrograph	\$47
Total (FY25\$M)	\$361

The Interstellar Probe estimate begins with the currently CML-4 design captured by the technical description presented in this report (Section 5) and the numerical description of the design captured in the MEL. Unlike the payload, almost all the spacecraft hardware is already at or near TRL 6, the one exception being the star tracker. Accordingly, the percentage of nonrecurring engineering (NRE) activity still to be completed for that component was increased to account for development of a star tracking capability that will operate outside the heliopause for multiple decades. Flight software development costs cover licenses and design/implementation/testing activities for avionics software, autonomy rules, and testbed software. Estimate costs are generated by the APL flight software team based on cost data from prior APL missions for development of analogous software modules.

The baseline spacecraft cost estimate is \$388M FY25. Table 6-5 compares the spacecraft estimate by spacecraft subsystem to actuals from New Horizons and Parker Solar Probe. It includes \$95M FY25 for the use of two Next Generation Radioisotope Power Sources (NGRPSs).

While the Interstellar Probe spacecraft design is more mature than that of many of the CML-4 designs presented in recent Planetary Decadal Studies, there are several uncertainties that are yet

Table 6-5. Interstellar Probe spacecraft estimate by subsystem (FY25\$M).

Subsystem	Interstellar Probe Baseline Estimate	New Horizons	Parker Solar Probe
<i>Spacecraft PMSEMA</i>	\$35	\$-	\$-
<i>Mechanical and Structures</i>	\$41	\$16	\$43
<i>Electrical Power (EPS)</i>	\$148	\$133	\$95
<i>Thermal Control</i>	\$5	\$2	\$8
<i>Avionics</i>	\$57	\$29	\$48
<i>Telecommunications</i>	\$52	\$27	\$54
<i>Guidance, Navigation, and Control</i>	\$16	\$14	\$34
<i>Propulsion</i>	\$15	\$10	\$11
<i>Flight Software</i>	\$18	\$14	\$25
<i>Specialized Hardware</i>	\$-	\$-	\$96
Total (FY25\$M)	\$388	\$245	\$416

to be resolved, especially in terms of avionics. Specifically, the Interstellar Probe estimate attempts to account for recent parts costs inflation as well as parts longevity. The Interstellar Probe mission must ensure that protocols, procedures, and material solutions provide the means for electronic components and assemblies to survive and function at a high reliability for multiple decades. Likely solutions are starting to be identified and assessed, but it is premature to predict their efficacy (see Appendix F). Related to these is the configuration and operation of testbeds and a long-term mission operations system. The inclusion of 50% unencumbered cost reserves should be sufficient to cover normal design revisions before mission confirmation and new solutions for virtual operations of the Interstellar Probe mission in the 21st century.

As a cross-check, the results of the PRICE® TruePlanning estimate compared to Interstellar Probe are summarized by subsystem in Table 6-6. The TruePlanning model and the cost-per-kilogram estimates used maximum expected value (MEV) mass and power values as inputs. Table 6-6 shows some variance in subsystem costs, but the total TruePlanning estimate is 2% below the baseline Interstellar Probe estimate.

WBS 7 and 9: Mission Operations (MOPs) and Ground Data Systems (GDSs). This element covers prelaunch MOPs and GDS efforts and includes mission operations planning and development and GDS development. An analysis of prelaunch MOPs and GDS costs on previous APL efforts, including New Horizons, Mercury Surface, Space Environment, Geochemistry and Ranging (MESSENGER) and Parker Solar Probe, provided analogies. These missions represent a typical expenditure on prelaunch MOPs for projects of comparable scope and complexity. The baseline estimate for Interstellar Probe varies with the low and high end of the costs in an analysis of prelaunch MOPs and GDS costs for several recent large strategic science missions.

WBS 8: Launch Vehicle and Services (LV&S). As with other Planetary Decadal Science missions, the Interstellar Probe estimate assumes that the required launch vehicle will be provided as government-furnished equipment (GFE). A cost estimate of \$26M FY25\$ has been included for nuclear launch approval costs associated with the use of RTGs. This estimate is derived from the *Planetary Decadal Mission Study Ground Rules*. A copy of this document can be provided upon request.

Table 6-6. Interstellar Probe parametric cross-check results (FY25\$M).

Subsystem	Interstellar Probe Baseline Estimate	PRICE® TruePlanning Cross-Check	Delta (%)
<i>Spacecraft PMSEMA</i>	\$35	\$34	-2%
<i>Mechanical and Structures</i>	\$41	\$21	-50%
<i>Electrical Power (EPS)</i>	\$148	\$171	15%
<i>Thermal Control</i>	\$5	\$6	23%
<i>Avionics</i>	\$57	\$51	-11%
<i>Telecommunications</i>	\$52	\$44	-16%
<i>Guidance, Navigation, and Control</i>	\$16	\$17	4%
<i>Propulsion</i>	\$15	\$17	19%
<i>Flight Software</i>	\$18	\$18	0%
<i>Specialized Hardware</i>	\$-	\$-	
<i>Total (FY25\$M)</i>	\$388	\$379	-2%

WBS 10: System Integration and Testing (I&T). This element covers the efforts to assemble, integrate, and test the flight system. The costs are based on a detailed analysis of cost actuals from previous APL missions, including MESSENGER, New Horizons, Solar Terrestrial Relations Observatory (STEREO), Van Allen Probes, and Parker Solar Probe. Furthermore, the WBS 10 complexity and risk levels were informed by the study team’s firsthand experience with New Horizons’ integration of the ²³⁸Pu power source. The Interstellar Probe I&T effort is estimated as, on average, 12.7% of the hardware. Given the use of cost-to-cost factors to estimate I&T, both the cost-estimating relationship (CER) and the underlying cost drivers are allowed to vary so that all sources of uncertainty can be quantified. As hardware cost varies, the cost-to-cost factor I&T estimate also varies. This approach allows the estimate to maintain a conservative risk posture given the historical complexity of I&T.

6.5.2 Phase E

The current Phase E estimate includes all the standard aspects of Phase E: PMSEMA, MOps and GDS, and Science. It does not include DSN costs. The estimate is derived using the MOCET parametric model. The study team recognizes that planning for a five-decade operation has unique challenges with both personnel as well as ground system maintenance and replenishment, but no costs have been added to the model output for longevity. More work must be done to understand the requirements for such a long-lived mission and how use this knowledge to estimate the cost of longevity, and move toward a higher-fidelity baseline estimate.

The MOCET model output and Interstellar Probe Phase E estimate by mission activity are summarized in Table 6-7. It covers all of Phase E from the defined schedule generated by the MOps subject-matter expert. Excluding DSN usage fees, the average cost per year for Interstellar Probe is \$22.7M (FY25). MOCET does not output at WBS Level 2, so costs are shown at WBS Level 1. However, a summary of cost by year for the first decade of Interstellar Probe’s Phase E is presented in Table 6-8.

Although not explicitly costed because of the ROM nature of the current Phase E estimate, the Interstellar Probe team is actively engaging in discussions and analysis on the cost impact longevity

Table 6-7. Interstellar Probe MOCET results (FY25\$M).

Description	Duration (Months)	Cost/Month (FY25\$M)	Total Cost (FY25\$M)
Launch and Checkout	2	3.36	6.52
Cruise to Jupiter	7	2.95	20.72
Jupiter Flyby	2	5.23	10.50
Jupiter Flyby Science Data Downlink	1	3.01	3.07
Wire Antenna Deployment	1	3.01	3.06
Inner Heliosphere Phase	142	1.83	259.81
Switch to ngVLA	12	3.01	36.16
Outer Heliosphere (Heliosheath) Prep/Commanding	2	2.34	4.76
Outer Heliosphere (Heliosheath) Phase	49	1.83	89.54
Interstellar Prep/Commanding	2	2.34	4.69
Interstellar Phase to 50 Years	396	1.83	725.00
End of Mission		Total	\$1163.83

Table 6-8. Interstellar Probe Phase E: first decade (FY25\$M).

FY	2036	2037	2038	2039	2040	2041	2042	2043	2044	2045	2046
Cost (FY25\$M)	\$3.4	\$40.5	\$22.0	\$22.0	\$22.0	\$22.0	\$22.0	\$22.0	\$22.0	\$22.0	\$22.0

will have on Phase E. In particular, the team has identified unique roles that will be vital to ensuring success over the long duration of the mission. These roles include mission librarian, technology maven, and science archivist. A multigenerational approach to key roles (emeritus, practitioner, apprentice) is also recommended. Interstellar Probe will also need to carefully plan for GDS upgrades, record retention and the archiving and storage of data, uplink/command encryption (as required, as well as preparing for changes in navigation, mission design, and ground communications infrastructure. More details on the impact of longevity on the design and planning of Interstellar Probe can be found in Appendix F.

WBS 1, 2, 3: Project Management, Systems Engineering, and Mission Assurance (PMSEMA). This element covers the management, engineering and mission assurance of Interstellar Probe during Phase E. In addition to the traditional PMSEMA activities, Interstellar Probe will have an unconventional staffing plan involving multiple people in similar roles for guaranteeing required knowledge transfer. It will also have to budget for a technology maven to manage the technology the mission depends on and a mission librarian for archiving and data migration.

WBS 4: Science. This element covers the managing, directing, and controlling of the science investigation. The best analog for the baseline science expenditure on Interstellar Probe would be New Horizons. Although costs are not compared at WBS Level 2, Interstellar Probe’s average costs per year are very comparable to those for New Horizons, and Interstellar Probe’s longevity planning will build on that of New Horizons. Interstellar Probe’s average cost per year is \$22.7M FY25, while New Horizons’ is \$21.4M FY25. While Interstellar Probe will spend much of its journey in quiescent cruise, similar to New Horizons, Interstellar Probe will have a more complex payload than New Horizons.

WBS 7 & 9: Mission Operations (MOps) and Ground Data Systems (GDSs). This element covers mission operations, network security, data processing, and mission management. It does not include DSN charges. As part of the Interstellar Probe Phase E GDS effort, Interstellar Probe will need to perform ground refreshes every 5 years. Although this is not explicitly modeled, the costs for this are in the underlying data set that MOCET is based on. In particular, New Horizons is a data point used in the MOCET model, and New Horizons spent ~\$800K FY25 on ground system upgrades during its cruise phase.

6.5.3 Cost Risk and Cost Reserves

The Interstellar Probe cost risk analysis is performed on the Phase A–D baseline cost estimate, using inputs from the cross-checks and additional historical and parametric data. The cost risk ranges by major WBS element as inputs for the Interstellar Probe probabilistic cost risk analysis to quantify total cost risk are described below.

PMSEMA. Given the use of cost-to-cost factors to estimate these functions, both the CER and underlying cost drivers are allowed to range so that all sources of uncertainty can be quantified.

Science Ground Data Systems and Mission Operations. These are low-risk cost elements but are subject to cost growth as part of the cost risk analysis. Cost uncertainty is based on the historical range of uncertainty as a percentage of the average actual science cost in NASA missions.

Payload. The baseline cost estimate for each instrument is taken from a range of parametric estimates and historical analogies. Using these parameters, a log-normal distribution was generated for each instrument. These distributions were used to inform the Interstellar Probe payload risk model and to capture uncertainty given the CML-4 level design phase.

Spacecraft. Each subsystem is subject to data-driven risk analysis based on historical analogies and parametric model estimates. Mass inputs in the parametric models are allowed to vary up to 30% over current best estimate, consistent with early design programs.

Integration and Testing. I&T as a percentage of the payload and spacecraft from the baseline cost estimate is used to inform the risk analysis, allowing I&T to vary with hardware cost.

These cost ranges were used to quantify total cost risk to Interstellar Probe’s development costs. A Monte Carlo simulation of Interstellar Probe’s development costs produced the cumulative distribution function (CDF) used to quantify Interstellar Probe’s cost risk with reserves. The results of this analysis are detailed in Table 6-10 and Figure 6-3.

Table 6-9. Development cost summary results.

Interstellar Probe				Reserve Allocation
WBS		Baseline Estimate	68th Percentile	
1	Project Management (PM)	\$169	\$236	40%
2	Systems Engineering (SE)			
3	Mission Assurance (MA)			
4	Science	\$50	\$75	51%
5	Payload	\$361	\$573	58%
	<i>Payload Management</i>	\$28	\$46	67%
	<i>Fluxgate Magnetometer (2) + Boom</i>	\$15	\$21	42%
	<i>Plasma Wave Instrument + Boom</i>	\$51	\$83	63%
	<i>Solar Wind</i>	\$23	\$32	37%
	<i>Pickup Ion (PUI)</i>	\$18	\$24	37%
	<i>Suprathermals and Energetic Ions</i>	\$23	\$33	47%
	<i>Cosmic Ray Spectrometer</i>	\$35	\$51	45%
	<i>Interstellar Dust Analyzer</i>	\$20	\$33	60%
	<i>Neutral Ion Mass Spectrometer</i>	\$74	\$129	75%
	<i>Energetic Neutral Atom (ENA)</i>	\$33	\$46	37%
	<i>Lyman-α Spectrograph</i>	\$47	\$76	62%
6	Spacecraft (S/C)	\$388	\$564	45%
7/9	Mission Operations and Ground Data Systems (MOps/GDSs)	\$37	\$47	28%
8	Nuclear Launch Approval	\$26	\$31	20%
10	Integration and Testing (I&T)	\$95	\$163	71%
Subtotal		\$1126	\$1689	50%

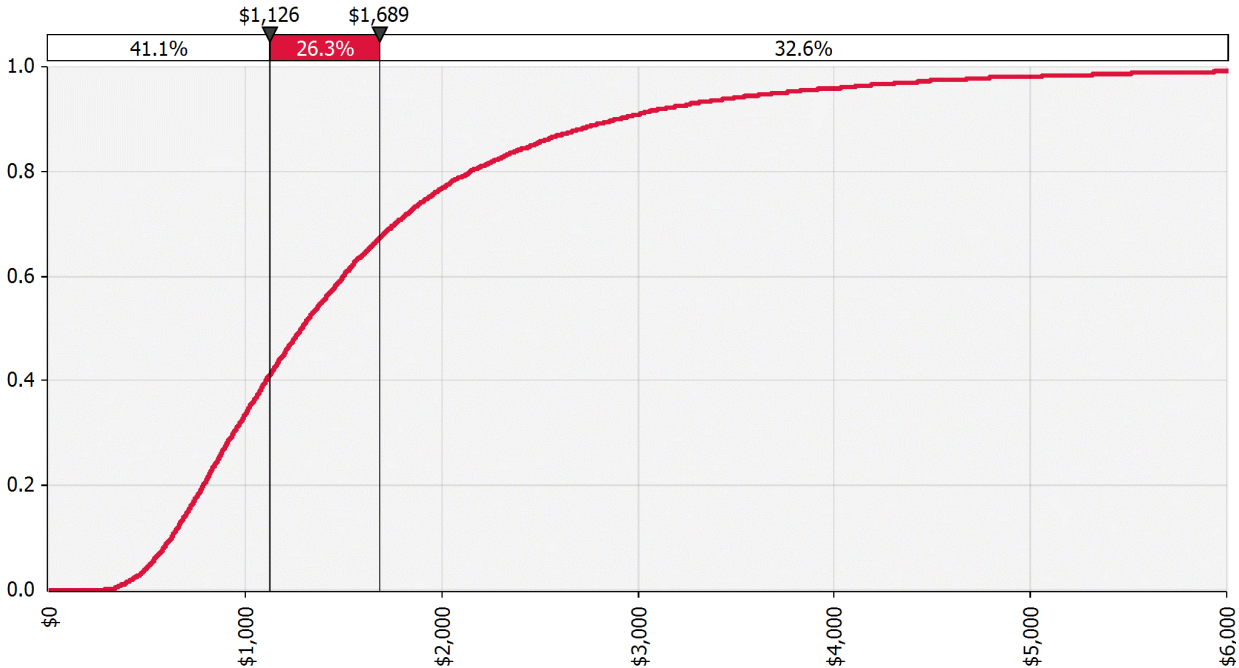


Figure 6-3. Interstellar Probe cost risk cumulative distribution function/S-curve. (Image credit: Johns Hopkins Applied Physics Laboratory.)

Similar to the *Planetary Decadal Mission Study Ground Rules*, the Interstellar Probe estimate includes unencumbered cost reserves of 50% of the estimated costs of all Phase A–D elements except the launch vehicle. The probabilistic cost risk analysis shows 68% confidence that the Phase A–D mission is achievable within the estimated costs of this study, including reserves. A 50th- to 70th-percentile confidence level is expected and reasonable for a pre-Phase A concept with this level of reserves.

While reserves would be used to cover Interstellar Probe cost growth, regardless of the source of the risk, the team has taken into consideration performance on past missions, design maturity level, and the level of risk in each WBS element in the anticipated allocation of reserves (see Table 6-11). This gives the Interstellar Probe team an early understanding of where project reserves may be needed, enabling more robust management of costs and risks.

During its operational phase, Interstellar Probe faces many of the same challenges other missions face, plus several specific risks of its own. Quantifying the cost risk during Phase E is essential, but it presents several challenges. Recent experience with significant cost growth during the operations phase in NASA missions highlights the importance of, first, approaching the baseline estimate with appropriate rigor and, second, understanding the cost risk associated with the Phase E estimate. Because the

Table 6-10. Interstellar Probe reserves (FY25\$M).

Description	Value (FY25\$M)	Confidence Level
Baseline Point Estimate Before Reserves	\$1126	41%
Mean	\$1591	
Standard Deviation	\$1140	
Cost Reserves (50%)	\$563	
Total Phase A–D	\$1689	68%

Phase E baseline cost estimate was derived using the MOCET tool, which is based on actual spent costs from historical missions, it is not subject to the same estimating error that a buildup estimate would be. McNeill (2014) identified eight leading indicators of Phase E cost growth:

1. Insufficient budget for sustaining engineering
2. Insufficient budget for PMSEMA
3. Long cruise phase
4. Having a large number of Phase E maneuvers
5. Operational dependence on launch dates
6. Insufficiently robust mission planning
7. Inexperienced staff
8. Insufficient staffing during cruise and maneuvers

Indicators 1, 2, and 8 are mitigated by the use of MOCET as an estimating tool, because actual staff levels from historical missions feed the cost output. Indicator 7 is mitigated by adhering to this report's recommendations on personnel planning for Phase E, elucidated in Section F.4 of Appendix E. The remaining concerns are Interstellar Probe's unprecedentedly long cruise phase, its dependence on a specific launch date, the trajectory maneuvers required early during the operations phase, and sufficiency of planning to ensure success during 50 years of operations.

The team also identified several specific risks unique to Interstellar Probe. First, cybersecurity requirements are likely to increase between now, when the estimate is generated, and the time that Interstellar Probe launches. Second, unexpected environmental challenges, which could affect any mission, increase in likelihood the longer a mission is in operations. Third, design errors/flaws and degradation can be expected to affect the cost of Phase E to a greater extent than a mission with a shorter operational life. And finally, the team noted that, during the course of 50 years, the likelihood that some members of the international science team could lose political or institutional support and require alternative sources of funding is high.

These risks fed into a ROM risk analysis to determine whether 25% reserves are sufficient to ensure success for Interstellar Probe. The resulting S-curve is shown in Figure 6-4, with 23% confidence that the baseline Phase E cost of \$1.164B (FY25) is sufficient. Confidence rises to 84% with an additional 25% reserves, for a total Phase E cost of \$1.455B (FY25). Unsurprisingly, the curve is steeper than what we observe for development cost risk. Phase E does not face schedule risk, and most of its risks are uncorrelated with each other. The analysis supports the recommendation of 25% reserves on Phase E costs.

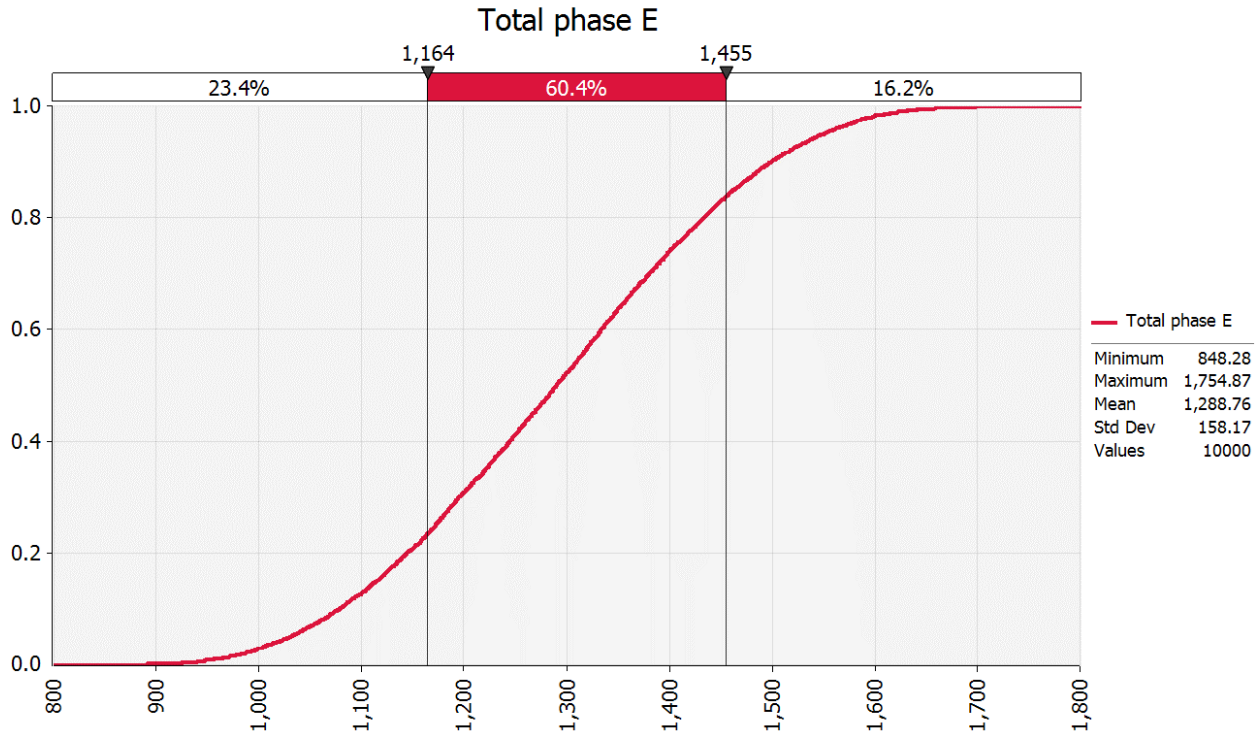


Figure 6-4. Twenty-five percent reserves on the estimated cost of Phase E covers cost risk sufficiently during operations. (Image credit: Johns Hopkins Applied Physics Laboratory.)

6.5.4 Cost Validation

The cost-estimating process for Phases A–F provides a credible basis for generating an accurate forecast of costs associated with Interstellar Probe. All elements of the cost estimate are cross-checked with historical analogies, and parametric model results are within a reasonable range.

6.5.5 Conclusion

The Interstellar Probe concept establishes that a cost-effective, multi-decadal interstellar mission is feasible. Based on the notional baseline payload and baseline spacecraft design, the Interstellar Probe development cost is estimated at \$1689M FY25 (Phases A–D). Operations costs are estimated at \$1455M FY25 for a 50-year Phase E. This brings the total mission cost, excluding DSN charges and assuming a GFE launch vehicle, to \$3144M FY25 including reserves. The development costs and the Phase E cost profile are in family with other New Frontiers and large strategic science missions.

Downsizing of the payload would provide cost savings with respect to these estimates. Such an exercise could be examined, e.g., by a future NASA Science and Technology Definition Team. Other downsizing (and upsizing) options are, no doubt, possible. That said, these estimates do provide a solid starting point for such further considerations and accompanying cost analyses.

Table 6-11. Development costs by work breakdown structure and fiscal year.

FY25\$M		Phase A		Phase B			Phases C/D					
		2028	2029	2029	2030	2031	2031	2032	2033	2034	2035	2036
	Phase A	\$0.8	\$9.2									
1	PM			\$0.1	\$5.4	\$6.1	\$0.6	\$7.9	\$8.3	\$8.7	\$9.1	\$8.4
2	SE			\$0.1	\$4.4	\$5.3	\$0.8	\$7.4	\$8.3	\$9.6	\$11.4	\$10.9
3	MA			\$0.2	\$6.0	\$10.1	\$0.1	\$5.4	\$7.1	\$8.1	\$8.6	\$7.4
4	Science			\$0.1	\$1.8	\$3.2	\$0.3	\$4.3	\$6.4	\$8.6	\$10.8	\$13.3
5	Payload			\$0.4	\$18.6	\$39.9	\$2.9	\$56.2	\$79.1	\$80.2	\$59.4	\$22.8
6	Spacecraft			\$0.8	\$21.7	\$36.3	\$2.5	\$56.6	\$88.9	\$91.7	\$63.2	\$24.0
7/9	MOps/GDS			\$0.0	\$0.9	\$1.5	\$0.1	\$5.4	\$7.4	\$8.0	\$7.0	\$5.7
8	NEPA			\$-	\$-	\$-	\$26.0	\$-	\$-	\$-	\$-	\$-
10	I&T			\$0.0	\$1.4	\$2.3	\$0.5	\$3.2	\$5.0	\$14.1	\$30.4	\$37.1
	Subtotal	\$0.8	\$9.2	\$1.8	\$60.1	\$104.7	\$33.9	\$146.4	\$210.5	\$229.0	\$200.0	\$129.7
	Reserves	\$0.4	\$4.6	\$0.9	\$30.1	\$52.4	\$16.9	\$73.2	\$105.3	\$114.5	\$100.0	\$64.9
	Total	\$1.3	\$13.8	\$2.7	\$90.2	\$157.1	\$50.8	\$219.6	\$315.8	\$343.5	\$300.1	\$194.6

NEPA, National Environmental Policy Act

6.5.6 Development Cost by WBS and Fiscal Year

To assist with planning and budgeting for Interstellar Probe during development, the notional costs for Phases A–D for the baseline heliophysics mission are presented by WBS and fiscal year in Table 6-12. Phasing is based on expenditure patterns from previous APL missions.

6.6 Risks of Implementing

The Interstellar Probe mission has a unique set of risks in that the implementation of a pragmatic design concept reduces the development risks to very nominal levels; the risks of operating a mission for a minimum of 50 years become dominant. The risk consequences follow NASA management practices (NASA, 2011) in defining likelihood of and consequence for risks as identified by the study team and are provided in Table 6-13 and Table 6-14. Cost risk is discussed in Section 6.7. Schedule risks are not addressed because they are inappropriate until an implementation plan is developed and approved. The primary risks addressed here are technical and programmatic. Programmatic risk is defined as a risk that capabilities that exist might not be available because of NASA decisions (e.g., the unavailability of the needed launch service, or insufficient PuO₂ to fuel the NextGen RTGs) and would require action by NASA to mitigate.

Table 6-12. Risk consequence definitions.

Cf	Cost Impact	Schedule Impact	Technical or Science Impact
5 Unacceptable	Exceeds project reserves	Precludes primary and backup launch dates	Total loss of spacecraft or instruments, or failure to achieve minimum mission success (Level 1) requirements
4 Major	Exceeds segment reserves	Precludes primary launch date but not backup launch date	Major loss of spacecraft or instrument capability, or failure to achieve full mission success (Level 1) requirements

Cf	Cost Impact	Schedule Impact	Technical or Science Impact
3 Significant	Within project managed segment reserves	Affects critical path but not primary launch date	Significant loss of spacecraft or instrument capability, or failure to achieve some Level 2 science objectives
2 Moderate	Within management allocated segment reserves	Reduces slack to the lesser of 1 month per year or 50% of the remaining schedule	Moderate loss of spacecraft or instrument capability needing requirement redefinition or design/implementation work-around, or failure to achieve some Level 3 science objectives
1 Minimal	No impact to cost reserves	Reduces slack, but still more than 1 month per year or 50% of remaining schedule	Loss of spacecraft or instrument capability within planned margin or redundancy, or science objectives achieved via work-around

Table 6-13. Risk likelihood definitions.

Likelihood	Consequence				
	1 Minimal	2 Moderate	3 Significant	4 Major	5 Unacceptable
5: Very High (>80% chance of occurring)	(1,5)	(2,5)	(3,5)	(4,5)	(5,5)
4: High (60–80% chance of occurring)	(1,4)	(2,4)	(3,4)	(4,4)	(5,4)
3: Medium (40–60% chance of occurring)	(1,3)	(2,3)	(3,3)	(4,3)	(5,3)
2: Low (5–40% chance of occurring)	(1,2)	(2,2)	(3,2)	(4,2)	(5,2)
1: Very Low (<5% chance of occurring)	(1,1)	(2,1)	(3,1)	(4,1)	(5,1)

6.7 Risks

The risks have been assessed by the study team, and the top 10 risks are shown in Table 6-15. Their definition and mitigations plans are shown in Table 6-16.

Table 6-14. Risk matrix.

Likelihood	Consequence				
	1 Minimal	2 Moderate	3 Significant	4 Major	5 Unacceptable
5: Very High (>80% chance of occurring)					
4: High (60–80% chance of occurring)					
3: Medium (40–60% chance of occurring)					
2: Low (5–40% of occurring)				R3, R4, R5, R6	R1, R2
1: Very Low (<5% of occurring)			R10	R7, R8, R9	

Table 6-15. Risk list.

#	Risk	Type	L	C	Mitigation
1	If latent electronic parts vulnerabilities exist in the flight system, then the spacecraft reliability risk may exceed a level that is not acceptable, or the spacecraft may fail.	T	2	5	Mitigate through physics of failure analysis and test.
2	If NASA processes are in conflict with requirements of a 50-year mission, then the mission may not be confirmed.	P	2	5	The community will need to develop the rationale for the acceptability of long-term missions, including the Interstellar Probe. This should be a focus for the decadal survey.
3	If the launch vehicle performance or availability the study assumes cannot be achieved, then the flight velocity assumed in the study would not be met.	P	2	4	Any future Interstellar Probe Project will need to survey launch vehicle options other than the Space Launch System (SLS) as assumed in this study to ensure a launch energy sufficient to achieve 200 au in 50 years as a minimum.
4	If required subsystems that are typically procured from vendors with the appropriate skills will not meet the mission lifetime requirements, then the mission may not be able to meet its 50-year lifetime requirement.	T	2	4	Mitigate by (1) identifying system elements that require improvement in lifetime needed to support multiple (community) mission concepts, (2) developing relationships with vendors to procure elements that meet the lifetime requirement, and/or (3) ensuring that budgets and schedules allow for working with vendors to develop appropriate technologies that will meet the lifetime requirement, and/or (4) developing a robust system design that limits the impact.
5	If critical team members are lost to the mission without proper backup to the critical skills of these team members, then the mission could fail prematurely.	T	2	4	If the longevity plan is supported during Phase E, the risk is reduced to a 1 × 4.
6	If the ground communication facilities are not adequate to meet the requirements stated in the report, then the data rate from the spacecraft will not meet the science requirements as the spacecraft reaches the desired region of space 50 years after launch.	P	2	4	Enhanced DSN capability (or an equivalent such as the National Science Foundation next generation Very Large Array) is required. The community must support NASA's continued investment into the DSN asset or find an alternative equivalent.
7	If the reliability of the flight system cannot be acceptably demonstrated for a 50-year mission, then the risk to proceed to development may cause the mission to not be confirmed.	T	1	4	Build a case based on analysis of historical missions and appropriate reliability analysis to provide the information necessary to convince NASA that the longevity risk is acceptable. The analysis will provide the guidance using physics of failure methodology for a test program to provide the necessary data to support the analysis.
8	If models used to manage consumables (thruster cycles, power on/off cycles [including especially heater cycles], etc.) are not correct, then a key subsystem may fail before reaching the 50-year operational requirement.	T	1	4	Mitigate by developing a robust design that provides sufficient redundancy to ensure that model margin uncertainties are covered. Also develop potential operational work-arounds to mitigate.
9	If the radioisotope power source does not deliver the performance the study assumes or there is insufficient PuO ₂ , then the power available will not be adequate at end of mission (50 years).	P	1	4	Mitigate through analysis and accelerated life testing.
10	If ground system technological changes are not compatible with the initial system implementation without adequate robustness in both hardware and software, then the ground system may not be able to support mission operations for the required 50-year duration.	T	1	3	If the longevity plan as documented in this report includes a technology "maven" and librarian who will be proactive in mitigating technology obsolescence, the risk becomes a 1 × 2.

C, consequence; L, likelihood; P, programmatic risk; T, technical risk

6.8 Section 6 References

- Fountain, G.H., Kusnierkiewicz, D.Y., Hersman, C.B., et al. (2008) The New Horizons Spacecraft. *Space Science Reviews* 140, 23-47. Retrieved from <http://adsabs.harvard.edu/abs/2008SSRv..140...23F>
- Fox, N.J., Velli, M.C., Bale, S.D., et al. (2016) The Solar Probe Plus Mission: Humanity's First Visit to Our Star. *Space Science Reviews* 204(1), 7-48. doi: 10.1007/s11214-015-0211-6
- Guo, Y., Thompson, P., Wirzburger, J., et al. (2021) Execution of Parker Solar Probe's unprecedented flight to the Sun and early results. *Acta Astronautica* 179, 425-438. doi: <https://doi.org/10.1016/j.actaastro.2020.11.007>
- Hahn, M. (2014) *Higher Fidelity Estimating: Program Management, Systems Engineering, and Mission Assurance*. Paper presented at the 2014 NASA Cost Symposium
- Harmon, B.A., Bohne, W.A. (2007) A Look Back at Assembly and Test of the New Horizons Radioisotope Power System. *AIP Conference Proceedings* 880(1), 339-346. doi: 10.1063/1.2437472
- Hayhurst, M.R., Wood, B.W., Daniels, C.L., Jordin, L.M., Sasamoto, W.A., Rodriguez, W.J. (2021, 6-13 March 2021) *Mission Operations Cost Estimation Tool (MOCET) 2020/2021 Updates*. In 2021 IEEE Aerospace Conference (50100). doi: 10.1109/AERO50100.2021.9438301
- McNeill, J., Jr. (2014) *An Examination of the Leading Indicators of Phase E Cost and Staffing Growth and Methods for Their Use* (ATR-2014-02799). The Aerospace Corporation.
- NASA (2011) *NASA Risk Management Handbook* (NASA/SP-2011-3422). Washington, D.C.: NASA.
- Stern, S.A., Bagenal, F., Ennico, K., et al. (2015) The Pluto system: Initial results from its exploration by New Horizons. *Science* 350(6258), aad1815. doi: doi:10.1126/science.aad1815

Appendix A. Augmented Science Mission

A.1 Science Goals and Objectives

In the following sections, the science goals and science objectives refer to those in the science traceability matrix (STM) for the augmented mission. See Section A.1.4.

A.1.1 Science Rationale of an Augmented Mission

To date, only five spacecraft have left or are leaving the solar system: Pioneer 10 and 11, Voyager 1 and 2, and New Horizons. Exo-solar system missions are inherently cross-disciplinary, and these missions have made groundbreaking discoveries not only in heliophysics but also in planetary science. As shown in Figure A-1, the potential bonanza of new science in astrophysics and planetary science from Interstellar Probe, the potential next exo-solar system mission, is too enticing to ignore. Flying by a planetary “cousin” of Pluto on the way out of the solar system and observing dust clouds and the galaxy from a unique vantage point represent exceedingly rare opportunities begging for inclusion on Interstellar Probe. Beyond the primary science goal related to the heliosphere’s interaction with the very local interstellar medium (VLISM), we present the option of two additional goals in planetary science and astrophysics.

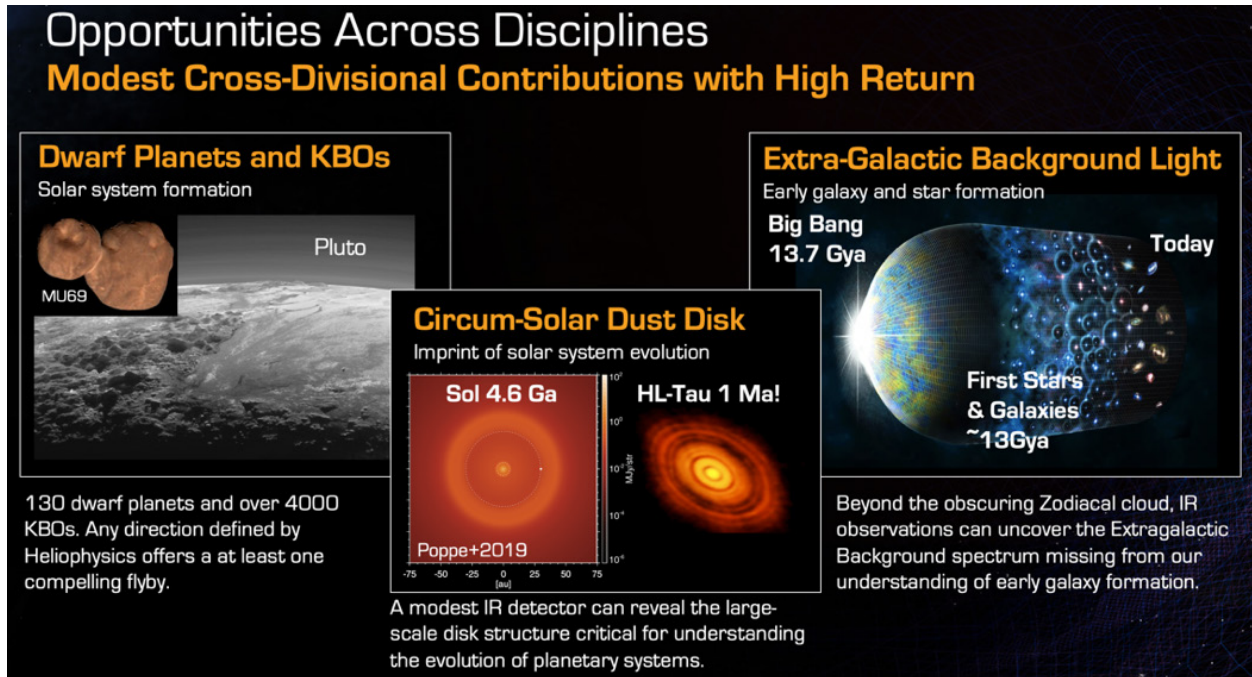


Figure A-1. A wide range of unique, transformational science can be done from the Interstellar Probe spacecraft heading out of the solar system with modern purpose-built instrumentation, including close flybys of outer-solar-system planetesimals and dwarf planets, imaging of our solar system’s entire circumstellar debris disk and planets as exoplanets, and accurate measurement of the cosmic background light. Note: IR, infrared; KBO, Kuiper Belt object. (Image credit: Johns Hopkins Applied Physics Laboratory.)

A.1.2 Goal 2: Understand the Origin and Evolution of Planetary Systems

Understanding the origin and evolution of our solar system, and of planetary systems around other stars, is fundamental to achieving science goals for the NASA Planetary Science and Astrophysics divisions. Interstellar Probe has the potential to advance our understanding on its way out of the solar system by taking direct measurements of small bodies it passes by and of the dust it encounters before reaching the heliopause and even beyond the heliopause. Small outer-solar-system bodies and dwarf planets, relic leftovers from the earliest ages of our solar system, are detectable not only by direct telescopic measurement but also by the dust they are creating via collisional grinding.

A.1.2.1 Science Question 2.1: *How did the solar system form and evolve compared to other planetary systems?*

Because Interstellar Probe must cross through the Kuiper Belt and broader trans-Neptunian region to reach interstellar space, opportunities may arise to fly by a trans-Neptunian object (TNO), especially a dwarf planet. Dwarf planets, defined here as planetary bodies larger than 400 km in diameter up to roughly Pluto-sized (2377-km diameter; Nimmo et al. (2017)), are now known to number ~130 (Brown, 2021) in the trans-Neptunian region and thus represent the largest category of planet, far outnumbering giant and terrestrial planets in the solar system. Many of these planets may be or may have been ocean worlds—targets of great astrobiological interest. Although many tens of thousands of smaller planetesimals exist, we prioritize dwarf planets because of their more complex geology and greater potential to have once been habitable. Visible-infrared mapping flybys of planetesimal-sized TNOs and other small bodies, such as Centaurs, will be prioritized lacking dwarf planet flyby opportunities and otherwise opportunistically. Figure A-2 shows the distribution of select dwarf planets and other TNOs in the time span 2030–2042 (see Section A.1.6 for detailed explanation).

Additionally, the Interstellar Probe trajectory will include a Jupiter gravity assist (JGA) flyby and could include a flyby of another giant planet depending on the flyout direction chosen. During a flyby of a giant planet, passive observations of the magnetosphere with the full suite of Interstellar Probe instruments would provide valuable information about the structure and dynamics of the magnetosphere as well as the interaction with the solar wind. Furthermore, imaging of giant planet moons could provide valuable data on surface processes, the potential for subsurface oceans, and moon–magnetosphere interactions.

A.1.2.2 Science Question 2.2: *What dynamical and chemical processes produced the structure and composition of the circumsolar dust disk?*

Observations of interplanetary dust (IPD) clouds throughout the heliosphere and at distances beyond the heliopause enable transformative science that is impossible to obtain from inner-system platforms. In particular, completing a census of all IPD and ice permeating the solar system, with direct comparison of its distribution to exo-circumstellar disks, is important for advancing our understanding of the origin and evolution of our solar system.

Planetesimal belts and dusty debris disks are known as the “signposts of planet formation” in exo-systems. The overall brightness of a disk provides information on the amount of sourcing

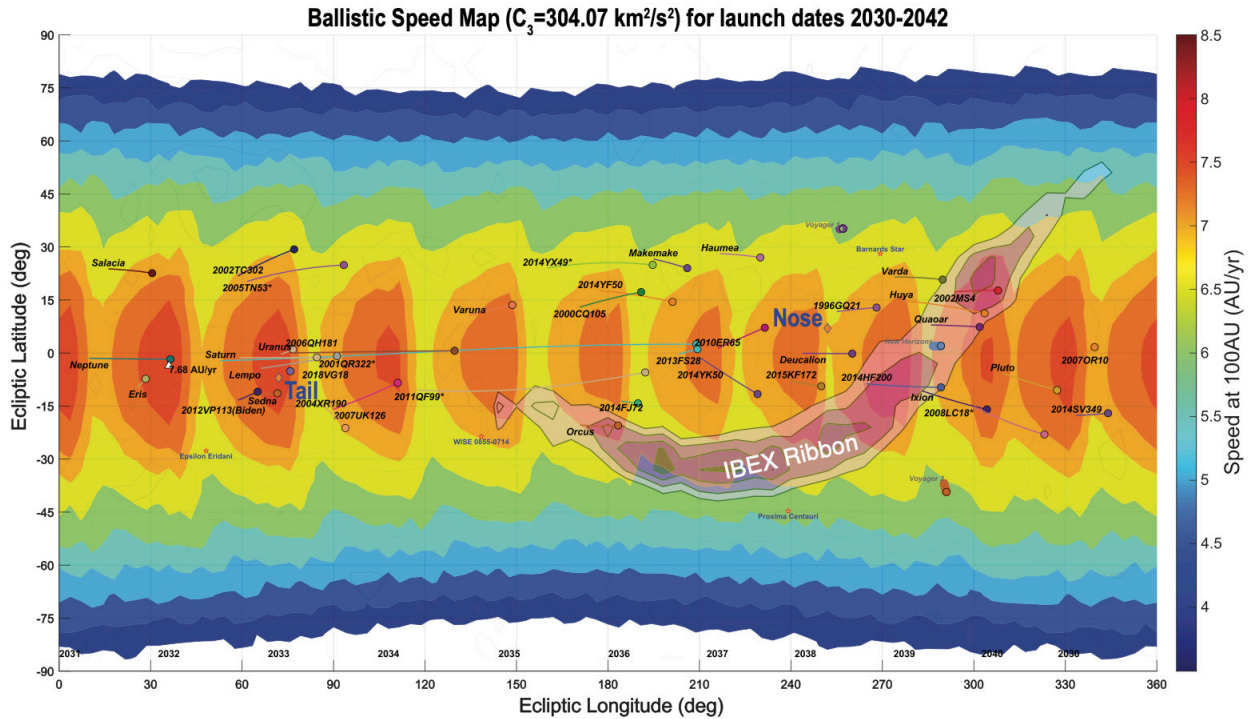


Figure A-2. Trajectory “heat map” showing solar system exit velocities (color bar) as a function of year (2030–2042), illustrating which dwarf planets and Kuiper Belt objects are in which part of the sky during 2030–2042 (paths move left to right). The heliosphere nose and tail are marked on the figure. Additionally, the region of highest fluxes of energetic neutral atoms in the IBEX ribbon are shown with contours and labeled as “IBEX Ribbon” in the figure. A flyby of Orcus or Quaoar in particular balances exit direction and energetic neutral atom ribbon science with compelling planetary science. (Image credit: Johns Hopkins Applied Physics Laboratory.)

planetesimal material, while asymmetries in the shape of the disk can be used to search for perturbing planets. The solar system is known to house two such belts, the inner Jupiter-family comet (JFC) + asteroid belt and the outer Edgeworth-Kuiper Belt (EKB), and at least one debris cloud, the zodiacal cloud, sourced by planetesimal collisions and comet evaporative sublimation.

Both the composition and the structure of our circumsolar dust cloud are relatively well understood locally to the Earth (e.g., Leinert et al., 1998; Kelsall et al., 1998; Rowan-Robinson & May, 2013; Tsumura et al., 2013). Instruments on solar-orbiting spacecraft such as Spitzer have helped by providing zodiacal light (ZL) measurements along alternate lines of sight (LOSs) that are not constrained to originate at Earth, and have highlighted the presence of local density enhancements in the ZL dust cloud at 1 au (Krick et al., 2012).

However, beyond 1 au, we have little understanding of the structure of the circumsolar dust disk. These regions are poorly understood because we live deep inside them. For example, it is not well understood how much dust is produced from the EKB because the near-Sun comet contributions dominate the inner cloud and the only spacecraft to have flown any dust measurement capability through the EKB are New Horizons (Piquette et al., 2019) and the Voyagers via the Plasma Wave System (Gurnett, 1997). New estimates from the New Horizons

results put the EKB disk mass at 30–40 times the inner disk mass (Poppe et al., 2019). Better understanding how much dust is produced in the EKB will improve our estimates of the total number of bodies in the belt, especially the smallest ones, and their dynamical collisional state. Even for the innermost zodiacal cloud, questions remain concerning its overall shape and orientation with respect to the ecliptic and invariable plane of the solar system.

Lack of knowledge of our own system is a major hindrance as we begin to probe the equivalent structures in exoplanetary systems (e.g., review by Hughes et al., 2018). Models indicate that there should be structures associated with Neptune and the EKB (Figure A-3, left panels; Poppe et al. (2019)), to which we see many analogs in the circumstellar disks around other stars. We have virtually no understanding of how these disks map to our own, where we can hope to study composition and small-scale structure directly. Observations probing IPD emission at a variety of wavelengths along different sight lines, as we pass through and emerge from the cloud, are necessary to develop a 3D understanding of the morphology of our own dust disk and to contrast it with those of exoplanetary systems.

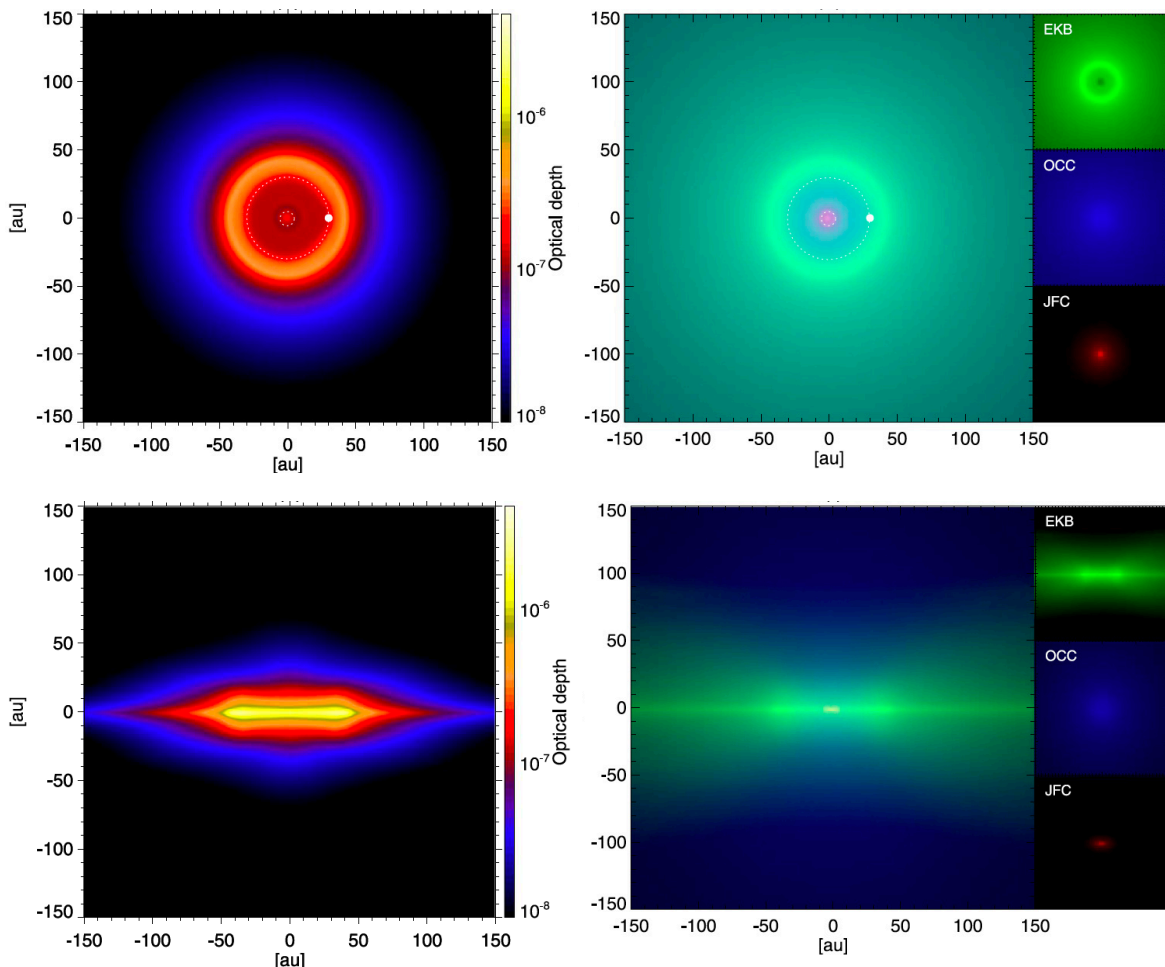


Figure A-3. Predicted dust cloud morphologies arising from solar system Jupiter-family comet (JFC), Oort cloud comet (OCC), and Edgeworth-Kuiper Belt (EKB) sources. (Top) Looking down on the solar system. (Bottom) Looking through the plane of the solar system. (Reproduced from Poppe et al. (2019) with permission; © AAS.)

A.1.3 Goal 3: Explore the Universe beyond Our Circumsolar Dust Cloud

Astrophysical measurements at distances outside of 10 au from the Sun enable transformative science that is impossible to obtain from within the solar system because of the influence of the IPD cloud. Purpose-built, sensitive, visible through infrared (VISIR) and dust instrumentation taken to far distances from the Sun outside the heliosphere will produce unique, novel results pertaining to the origin and evolution of our solar system in the galaxy and universe. For example, once Interstellar Probe is outside the bulk of the “zodiacal” circumsolar dust cloud enveloping the Earth, past 10 au from the Sun, the outer solar system is a unique, quiet vantage point from which to observe the extragalactic background light (EBL) around us. At VISIR (0.4–100 μm) wavelengths, the sensitivity of an instrument near Earth is limited by scattered light and thermal emission light from the circumsolar dust cloud. Reductions in this bright foreground permit tremendous gains in sensitivity and temporal stability that permit new kinds of observations of both the solar system and the universe beyond it (Zemcov et al., 2018, 2019).

A.1.3.1 Science Question 3.1: What role do the composition, evolution, and thermodynamics of the nearby and distant interstellar medium (ISM) play in determining the habitability of planetary bodies?

At the outermost edges of our solar system, the role dust plays in shaping and energizing the heliosphere’s boundary with the local galactic medium is almost completely unknown. Estimates range to up to one-third of the energy density in the heliopause and heliosheath being in the dust. Current models of the heliopause and heliosheath do not allow for the physics of a dusty plasma because the dust component is so poorly known. We do know that submicrometer-sized interstellar dust is streaming into the solar system opposite the direction the solar system is taking through the local interstellar medium (LISM), and the discrepancy between remote-sensing models of LISM dust and ISM dust measured inside the solar system suggests a large amount of energy is involved in diverting much of the impinging dust around the edges of the solar system in the heliosheath. Because the solar system was built from ISM dust, measuring it in its pristine galactic condition will greatly improve our understanding of stellar and solar system formation. Pristine galactic dust studies will also produce cosmological findings because species made in the early universe—such as ^2H , ^7Li , and ^8Be —can be directly measured.

A.1.3.2 Science Question 3.2: What is the total diffuse red-shifted light emitted by all the stars and galaxies in the universe since the beginning of cosmic time?

The EBL is the cumulative sum of all radiation produced over cosmic time, including light from the first stars, galaxies, and planets, as well as any truly diffuse extragalactic sources (Figure A-1, right; Cooray, 2016; Hauser & Dwek, 2001; Tyson, 1995). Measurements of the EBL can constrain galaxy formation and the evolution of cosmic structure, provide unique constraints on the epoch of reionization, and allow searches for beyond-standard model physics (Tyson, 1995). The absolute brightness of the EBL has been established from Earth at many radio and X-ray wavelengths, but at most infrared (IR), optical, and ultraviolet (UV) wavelengths, a precise assessment of the sky brightness has been hampered by reflected and emitted light from IPD, which results in an irreducible >50% uncertainty (and, at some wavelengths, significantly larger) on the absolute

emission from the EBL (e.g., Hauser et al., 1998). By observing beyond the IPD, observations from the outer solar system can eliminate these uncertainties and definitively determine the absolute brightness of the EBL (Zemcov et al., 2018, 2019). However, to date there has been only one mission, New Horizons (Stern & Trafton, 2008), that has ever carried visible light (VIS) imaging instrumentation past 50 au. No highly sensitive, useful IR imaging or spectral mapping has ever been done beyond 10 au, despite being the subject of multiple mission proposals over the last few decades. With Interstellar Probe observing beyond the IPD, a series of simple, repeated observations from the outer solar system can eliminate these uncertainties and definitively determine the absolute brightness of the EBL for the very first time.

A.1.4 Science Traceability for Augmentation

The Interstellar Probe augmented mission has two science goals beyond the heliospheric baseline mission: understanding the origin and evolution of planetary systems and understanding space beyond our circumsolar dust cloud from the nearby galaxy to the edges of the early universe.

To advance understanding of the origin and evolution of planetary systems, observations within the solar system of small bodies and the interplanetary dust disk must be placed in the context of models for planet formation. This approach is embodied in the two science questions under objective 2, where the first science question is focused on understanding the formation and evolution of small bodies in the outer solar system and the second is focused on understanding the processes that shaped the IPD disk.

Advancing understanding of the universe beyond our circumsolar-dust cloud requires observations of the dust outside our solar system as well as measurements in wavelengths that provide information about the formation of early galaxies, nucleosynthesis, and star-formation processes. This approach is outlined in two science questions under objective 3. The first question is to understand the local interstellar dust, and the second is to provide the first-ever measurements of diffuse red-shifted light beyond the solar system.

As illustrated on the augmented mission science traceability matrix (STM) foldout, each of the science questions is addressed by a set of objectives, which, in turn, flow directly to four overarching science investigations, as discussed below, that define the important bridge between the science and the implementation with measurement and mission requirements (Section A.3). The overarching investigations start with a flyby of a dwarf planet during the first decade of the mission and include observations of the dust disk during this time and beyond the dwarf planet flyby. The third investigation focuses on ISM dust, and, lastly, the fourth investigation focuses on the EBL. Each overarching science investigation is detailed in a set of more-specific investigations, each of which drive measurement and mission requirements. Although many investigations map to unique measurement requirements, the most stringent measurement requirements that would drive instrument design are listed in a stand-alone column with color coding referring to the applicable investigation. This column also contains the next-level instrument requirements, with specific requirements toward the spacecraft in the next column (to the right). The specific derivations of measurement requirements are laid out in Section A.3.

SCIENCE QUESTIONS	OBJECTIVES	INVESTIGATIONS
2.1 How did the solar system form and evolve compared to other planetary systems?	2.1.1 Determine current state, evolution, and potential habitability of dwarf planets and satellites	Multispectral, panchromatic images <1 km/px hemispherically, <500s m/px regionally, phase angles few to 180°; Thermal IR of hotspots 10–30 km/pixel
		In-situ sampling of magnetic fields, plasma, and neutrals during flyby
		High phase angle (>90–180°) “look-back” resolved at <1 km/px and unresolved observations
		Distant (>1 million km) unresolved photometric and panchromatic observations and searches, at hours-days cadence
		Pickup ion spatial distribution and composition variation with distance from the Sun
2.1.2 Determine how and how fast Solar Nebula processes gave rise to current properties, and dynamical and compositional states of solar system small bodies	2.1.3 Constrain role of space weathering of planetary targets beyond the heliopause	Distant (>1 million km) unresolved photometric and panchromatic observations and searches, at hours-days cadence
		Panchromatic multi-phase angle, unresolved observations across the trans-Neptunian region
2.1.4 Characterize structure and dynamics of Jupiter’s magnetosphere during JGA	2.1.5 Determine ground truth solar system characteristics relevant to exoplanets	In-situ magnetic, particle, energetic particle, and field measurements
		Distant (>10 au) panchromatic and multispectral observations at different wavelengths of terrestrial and giant planets
		Distant (>10 au) panchromatic and multispectral observations at different wavelengths of terrestrial and giant planets
2.2 What dynamical and chemical processes produced the structure and composition of the interplanetary dust disk?	2.2.1 Determine total dust mass and dust grain composition in inner and outer heliosphere	In-situ dust properties
		Remote forward hemisphere mapping >1x/50% change in rh cadence
		In-situ dust properties
2.2.2 Constrain the size distribution of interplanetary dust grains and their production mechanisms	2.2.3 Characterize the structures and processes in the Sun’s circumstellar debris disk due to solar system formation and evolution as compared to nearby exodisks	Remote forward hemisphere and lookback mapping of dust extinction, >1x/50% change in rh cadence for tomography Ancillary IR imagery and spectroscopy of nearby exodisks
		Remote forward hemisphere and lookback mapping of dust extinction, >1x/50% change in rh cadence for tomography Ancillary IR imagery and spectroscopy of nearby exodisks

GOAL 3: Explore the Universe Beyond Our Circumsolar Dust Cloud

3.1 What role do the composition, evolution, and thermodynamics of the nearby and distant interstellar medium (ISM) play in determining the habitability of planetary bodies?	3.1.1 Determine the origin and evolution of ISM dust based on its properties	NIR spectrum of diffuse galactic light covering > 5,000 deg ² on and away from galactic disk at resolution < 30 arcsec, with 1 sigma uncertainty < 1 nW m ⁻² sr ⁻¹
		FIR brightness of galactic emission in discrete bands covering > 5,000 deg ² on and away from galactic disk
3.2 What is the total diffuse red-shifted light emitted by all the stars and galaxies in the universe since the beginning of cosmic time?	3.2.1 Determine contribution from first light galaxies (optical/NIR) to total sky brightness	In-situ interstellar dust density, size, and composition outside heliosphere compared to remote emission and absorption observations of distant dust populations
		3.2.2 Constrain energy released by process of nucleosynthesis in the universe
		3.2.3 Characterize variability of emission from nucleosynthesis and star formation as a function of redshift

MEASUREMENT REQUIREMENTS	SPACECRAFT REQUIREMENTS
Magnetometer (MAG) 0.01–100 nT; 0.01 nT sensitivity, ≤60 s Two fluxgate magnetometers spaced 1/3 of boom	10-m boom, spinning, cleanliness program
Plasma Subsystem (PLS) e, H ⁺ , He ⁺ , He ⁺⁺ , C ⁺ , N-O ⁺ , <3 eV/e–20 keV/e; E/E≤10%, ≤60 s iFOV≥180°x20°, GF>1e-3 cm ² sr, ESA+Postacceleration+TOF Analysis or Faraday Cups	Spinning for full sky coverage
Pick-Up Ions (PUI) 0.5–78 keV/e, E/E≤10%, H, ² H, ³ He, ⁴ He, ⁶ Li, ¹² C, ¹⁴ N, ¹⁶ O, ²⁰ Ne, ²² Ne, Mg, Si, Ar, Fe, charge states iFOV≥90°x15°, GF≥1e-3 cm ² sr, ESA+Postacceleration and TOF analysis	Spinning to maximize angular coverage Accommodation to cover PUI in heliosphere and interstellar ram direction
Energetic Particle Subsystem (EPS) 20 keV–20 MeV, H, ³ He, ⁴ He, Li, C, O, Ne, Mg, Si, Ar, Fe, ΔE/E≤30%, ≤60 s iFOV≥180°, GF≥0.1 cm ² sr, TOFxE or SSD stack	Spinning for full sky coverage
Cosmic Ray Subsystem (CRS) 1–10 MeV/e, 10 MeV/nuc–1 GeV/nuc H-Sn, isotopes, m/Δm ≥ 10; ΔE/E ≤ 30%, hours GF≥2 cm ² sr, two directions, 15°, SSD telescopes	Perpendicular mounting and spinning to cover anisotropies in the VLISM
Plasma Wave Subsystem (PWS) ≤10 kHz, ≤0.7 μV/m @ 3 kHz, Δf/f≤15%, ≤60 s	4x2.5m stacers + sounder; 4x50m wire deployable antennas (optional)
Energetic Neutral Atom Camera (ENA) ~1–100 keV H, ΔE/E≤50%, ≤5°, ~weeks iFOV≥170°, ultra-thin foils and TOF	Spinning to maximize angular coverage Accommodation to cover full sky except Sun exclusion zone
Interstellar Dust Analyzer (IDA) 1e-19 to 1e-14 g, 1–500 amu, m/Δm≥200 iFOV ≥90°, impact based TOF with reflectron	Mount at angle to spin axis to cover interstellar dust ram direction Coboresighted with NMS
Neutral Mass Spectrometer (NMS) H, ³ He, ⁴ He, ¹⁴ N, ¹⁶ O, ²⁰ Ne, ²² Ne, ³⁶ Ar, ³⁸ Ar, m/Δm≥100, 1e-3 cm ⁻³ sensitivity, weekly iFOV≥10°, 120° antechamber, ionization source+TOF+reflectron	Mount at angle to spin axis to cover interstellar gas ram direction Coboresighted with IDA
Visible-Near Infrared Mapper (VIR) : ~0.4–3 μm; ≥5 channels, 2.3–5.7° in the cross-track, ~10 μrad	3-axis stabilized spacecraft during observations, coboresighted with IRM
Infrared Spectral Mapper (IRM) : 0.5–15 μm, R ~ 20, for spectral observations; 20, 30, 40–50 μm (±3 μm) for photometry; l/Dl=3 for broad band measurements 30–200 μm	3-axis stabilized or slowly rotating spacecraft during observations, coboresighted with VIR

HELIOSPHERE <TS										HELIOSHEATH TS THROUGH HP										INTERSTELLAR MEDIUM >HP										MISSION REQUIREMENT	ANALYSIS PRODUCT	CLOSURE
MAG	PLS	PUI	CRS	PWS	ENA	IDA	NMS	VIR	IRM	MAG	PLS	PUI	CRS	PWS	ENA	IDA	NMS	VIR	IRM	MAG	PLS	PUI	CRS	PWS	ENA	IDA	NMS	VIR	IRM			
																														3-axis, precise pointing	Photomosaic and compositional maps; shape models and/or topographic maps	Interpreted geologic, compositional, and topographic maps with cross-sections
●	●	●					●				●	●	●					●												Passive magnetic and plasma measurements before, during, and after flybys	Magnetic field, plasma distribution function	Magnetic field strength of minor bodies, if present, and constraints on subsurface ocean presence
																														3-axis, on- and off-target look-back post-flyby, solar eclipse, phase angles 90–180°	Images and spectra of surface, potential atmosphere, and rings	Atmosphere upper limits, ring detection and grain size estimates or upper limits
																														3-axis, precise pointing	Ring images if present, time series of ring occultations	Detection of rings, grain size estimates or upper limits on ring density
		●																												Passive magnetic and plasma measurements before, during, and after flybys	Plasma distribution function, composition	Detection of pickup ions from atmosphere
							●																							All-sky coverage, 1–100 au, IDA and NMS co-aligned, canted at ~20 deg to ram	Mass measurement of interplanetary dust	Bulk composition of solar system vs. heliocentric distance
																														3-axis, precise pointing knowledge	TNOs colors across different dynamical classes	Surface color differences influence by time outside the heliopause
●	●	●	●	●	●	●	●	●	●																					Spinning, passive observations	Magnetic field, plasma distribution function, comp., waves, ENA	Magnetosphere conditions during Jupiter gravity assist
																														Lookback from Kuiper belt and beyond, no Sun pointing	Plots of DN vs. time and observation phase	Planetary characteristics relevant to exoplanet observations
																														Slowly (<0.1 RPM) spinning or 3-axis, in situ 1–100 au, high spatial resolution, IDA and NMS co-aligned, ~20 deg to ram	Dust SFD, kind, abundance, composition	Dust mass and composition vs distance in heliosphere, processes influencing dust in solar nebula
																														Spinning, 1–100 au, IDA and NMS co-aligned, canted at ~20 deg to ram	Dust SFD, kind, abundance	Dust size distribution and production mechanisms
																														Slowly (<0.1 RPM) spinning or 3-axis, forward hemisphere 1–100 au, lookback outside 250 au	Maps of dust structure in the heliosphere and exodisks	Zodiacal disk residual structures from solar system formation and evolution
																														Slowly (<0.1 RPM) spinning or 3-axis, >150 au	Scattered light maps of ISM dust	Origin and evolution of ISM dust
																															Thermal emission maps of ISM dust	Improved understanding of ISM dust properties
																														Slowly (<0.1 RPM) spinning or 3-axis, in situ 120 to >400 au IDA and NMS co-aligned, ~20 deg to ram	Galaxy dust chemical maps tied to in situ VLISM composition	Comparison of local ISM dust and gas with what is known about ISM material throughout the galaxy
																														Slowly (<0.1 RPM) spinning or 3-axis, r = 5–10 au	All-sky Diffuse Galactic + Cosmic NIR background maps	Contribution first light galaxies to the total sky brightness
																															All-sky Diffuse Galactic + Cosmic FIR background maps	Energy released by nucleosynthesis in the universe
																															All-sky Diffuse Galactic + Cosmic 0.5–50 μm IR background maps	Variability of nucleosynthesis and star formation emission vs redshift

The applicability of specific measurements to different phases of the baseline mission is laid out across the heliosphere phase from launch to the termination shock, the heliosheath phase including the termination shock crossing through the heliopause, and, lastly, the interstellar phase beyond the heliopause. Filled circles denote the primary measurements.

The right-hand side of the augmented mission STM traces the investigations into mission requirements. The last two columns describe the analysis products of each investigation and the closure, or science results, refers to the higher-order results that allow one to meet the objectives and therefore also answer the science question.

A.1.5 Technical Implementation of the Augmented Mission

Here, we present science considerations for the augmented mission; the operational considerations are covered in Section A.4 (Science Operations) and are driven by the need to track a dwarf planet during a flyby.

An augmented Interstellar Probe mission is similar in most aspects to the baseline mission from an implementation perspective. Using the approach to keep the total payload mass and power usage roughly the same for the augmented mission as it is for the baseline, the mission trajectory is essentially the same as for the baseline, with the same potential options, to the target point selected to accomplish the augmented mission science objectives.

Physically, the spacecraft configuration is much the same for the augmented and baseline missions, with the primary difference being the types and layout of instruments on the spacecraft. Spacecraft systems themselves are identical, with the exception that the guidance and control system is designed for both spinning and three-axis control for the augmentation case.

After completing the JGA, the instruments conduct a regular series of measurements to characterize the heliosphere as the Interstellar Probe travels toward and into the VLISM. In situ dust measurements can be conducted in the spinner mode along with particles and fields measurements, as can the largest (~10') scale EBL and dust-cloud, far-IR observations. Depending on the specific augmentations selected, additional important individual observation activities will be planned and executed, as, for example, when encountering an individual Kuiper Belt object (KBO) or making pointed observations of the circumstellar dust cloud and EBL at short wavelengths. These events would (1) spin down the spacecraft and establish three-axis control, (2) execute a series of attitude changes and measurements to collect the desired data, and (3) spin up the spacecraft and transition back to regular science collection. Data from these activities will be stored on a solid-state recorder, and extra downlink contacts will be added to the telecommunications schedule as needed to return these data to Earth.

A.1.6 Science Investigations

A.1.6.1 Dwarf Planet Investigation

The science goals we seek to pursue with a dwarf planet flyby are summarized in the STM in the augmented science traceability matrix foldout. Broadly, the goals are to characterize the geophysical and compositional characteristics and their spatial variation on a dwarf planet and its

satellite (if applicable) or, alternatively, a smaller body such as a Centaur or TNO. Imaging at least one hemisphere of a dwarf planet (Figure A-4) and its satellite at ≤ 1 km/pixel resolution across multiple visible and near-infrared wavelengths would satisfy the broad science objectives. In particular, observations of this quality would permit (1) detailed photogeologic maps of at least the planet’s encounter hemisphere, (2) topographic digital terrain models of the varied landscape from parallax across images (stereo photogrammetry), and (3) composition maps as a function of position and geologic setting. Such quality of observations will enable high-quality comparative planetology across other dwarf planets (or similar worlds) such as Pluto, Charon, and Triton.

Volatiles on the surface and in the atmosphere of a KBO are also of great interest, but only larger KBOs are predicted to have retained sufficient volatiles to form an atmosphere (Schaller & Brown, 2007a; Young et al., 2020). If the KBO selected for a close flyby is predicted to have retained volatiles and be exposed to sufficient insolation to form an atmosphere, a UV spectrometer would be a valuable addition to the augmented payload. An instrument like New Horizons’ Alice (Stern et al., 2009) would be able to characterize global or regional atmospheres and haze, as well as outgassing around a dwarf planet or a planetesimal. For example, an atmosphere around a dwarf planet with a methane partial pressure of 10 nanobars at the surface and a surface temperature of 50 K would have a surface density of $\sim 10^{12}$ atoms/cm³, several orders of magnitude greater than the minimum densities observed at Pluto by Alice (Young et al., 2018).

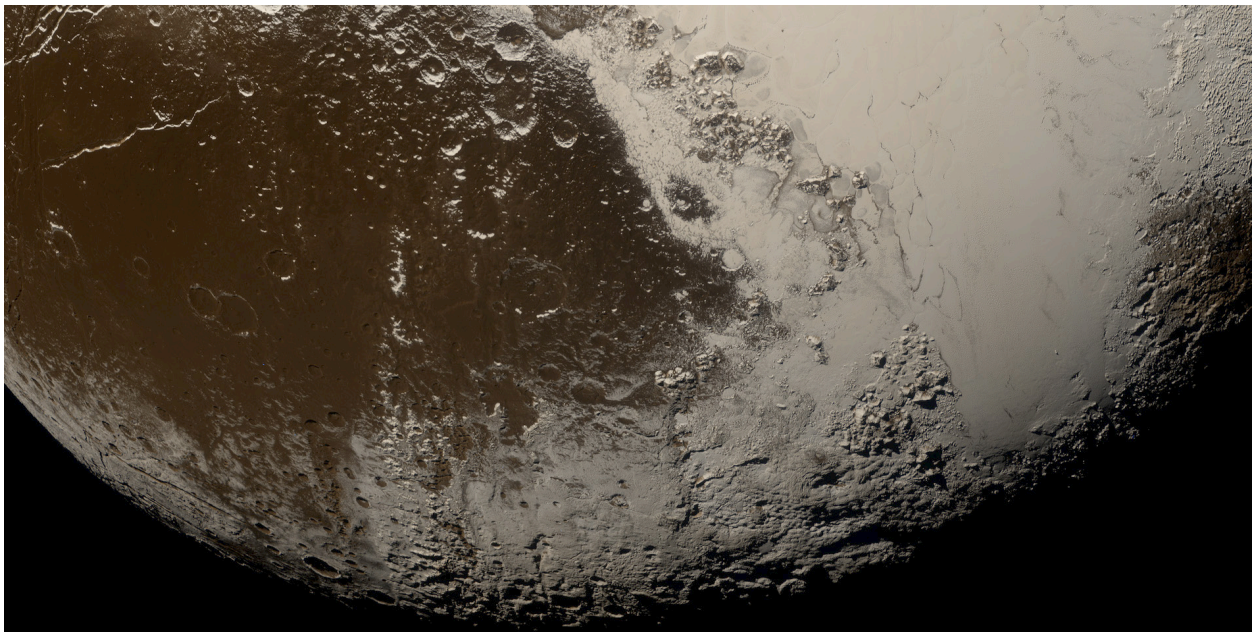


Figure A-4. Pluto’s southern encounter hemisphere from New Horizons, shown at slightly coarser than 1 km/pixel. This level of detail or finer is necessary for interpreting geologic features on planets’ surfaces. For instance, a flowing nitrogen ice glacier fills in the low-lying areas around towering water-ice mountains. (Image credit: NASA/Johns Hopkins Applied Physics Laboratory/Southwest Research Institute [http://pluto.jhuapl.edu/Galleries/Featured-Images/image.php?page=1&gallery_id=2&image_id=543&keyword=42&search_cat=1].)

Comparative planetology: “One of these things is not like the other.” Below, we have briefly described a number of potential dwarf planet targets that represent the largest diameters and the most

diversity. A large range of targets are reachable for a variety of launch dates and thus ecliptic longitudes as Jupiter orbits the Sun. These targets necessarily cover a larger range of ecliptic longitudes and also have a larger range of orbital inclinations, leading to a wider distribution in ecliptic latitude. Possible flyby targets include the two currently known Uranian Trojan asteroids, along with other well-known TNOs. The optimal launch dates are listed after each target description.

Quaoar is a large, hot classical KBO that presents the opportunity to study a world that is representative of many other TNOs covering different sizes, orbits, and compositions. Quaoar, at ~ 1110 km in diameter, is among the larger TNOs and by most definitions is considered a dwarf planet (Braga-Ribas et al., 2014). However, it is not quite large enough to have retained the entirety of its original inventory of volatile ices over the age the solar system (Schaller & Brown, 2007a). Spectral absorption features suggest volatile methane (CH_4) and/or nonvolatile ammonia (NH_3) ices mixed with water ice on Quaoar's surface (Schaller & Brown, 2007b). As predicted by the volatile retention models, Quaoar straddles the line between CH_4 -rich and H_2O -rich TNOs, possibly allowing the study of both surface types on one object. Quaoar is classified as moderately red, making it representative of the TNO population as a whole (Belskaya et al., 2015). The surface is not expected to change much over the course of a single orbit because of Quaoar's low orbital eccentricity ($\sim 4\%$), removing the effects of seasons on the study of its surface properties and composition. Similarly, any atmosphere might be relatively constant in pressure over the course of its year; any such atmosphere would be below 10 nbar and would require a spacecraft flyby to detect and characterize it (Arimatsu et al., 2019). Quaoar's satellite Weywot would come for free as part of such a flyby. It is estimated to have a diameter of ~ 170 km (Kretlow, 2020), placing it in a size class never before studied by spacecraft in the trans-Neptunian region. Quaoar's largest deviation from "average" is its high density of nearly 2 g cm^{-3} (Braga-Ribas et al., 2014), making it denser (more rock-rich) than Pluto and second only to Eris (e.g., Holler et al., 2021; Stern et al., 2015). This difference provides its own opportunity for exploration: evaluation of the origins of Quaoar and Weywot and comparison to other large TNOs with satellites. The wealth of investigations afforded by a spacecraft flyby of Quaoar, the "renaissance TNO," are extensive and would be much more than incremental. **Launch date: 2030 or 2042.**

Gonggong (2007 OR₁₀) is a large, scattered disk object and is among the more distant known TNO dwarf planets. It has a small satellite named Xiangliu on a surprisingly eccentric orbit. Gonggong is comparable in size to Pluto's largest moon Charon (~ 1250 km), while Xiangliu is smaller than ~ 100 km in diameter (Kiss et al., 2019). The surface of Gonggong may support CH_4 ice (Brown et al., 2011), as predicted by volatile retention models (Schaller & Brown, 2007a), and its surface is extremely red (Boehnhardt et al., 2014). The surface of Xiangliu is much less red, however, leading to one of the largest color dichotomies among the components of a TNO binary system. When combined with Xiangliu's surprisingly high orbital eccentricity of ~ 0.3 , which should be negligible under most physical assumptions for the system (Kiss et al., 2019), these two pieces of evidence lend credence to a capture hypothesis. However, the high eccentricity of Xiangliu could instead be due to Gonggong itself being a semi-contact binary (Kiss et al., 2019). If true, Gonggong would be the largest such object known, which would raise new questions and challenge our thinking on the formation of planetesimals in the outer solar system. Definitely confirming the nature of

Gonggong is not currently possible with Earth-based telescopes and would require imaging from a spacecraft flyby. **Launch date: 2030 or 2042.**

Pluto was the first TNO ever discovered and was the primary target of the New Horizons spacecraft; it remains a viable target for future robotic reconnaissance. Because of the short duration of the New Horizons flyby and the long rotation period of Pluto, ~ 6.5 days, only one hemisphere of Pluto was observed in significant detail (e.g., Stern et al., 2015). Pluto's non-encounter hemisphere exhibits multiple dark splotches, nicknamed the "brass knuckles" and possibly similar to Cthulhu Macula on the encounter hemisphere; evidence for additional "bladed terrain" similar to penitentes on Earth; as well as a large impact crater (Stern et al., 2021). The study of Pluto's evolving atmosphere (e.g., Meza, 2019) would benefit significantly from another flyby 20+ years later, with Pluto approaching northern hemisphere summer as it continues to move farther from the Sun. Additionally, a second flyby could also plan to more closely approach the minor satellites, particularly Styx and Kerberos, which were only observed at low spatial resolution (e.g., Weaver et al., 2016). New Horizons raised no shortage of additional questions during its 2015 flyby. **Launch date: 2030 or 2042.**

Eris is a scattered disk object and the most massive and distant TNO dwarf planet known (Brown & Schaller, 2007; Holler et al., 2021). It is also extremely bright, with an albedo of $\sim 96\%$ (Sicardy, 2011). But even at 96 au, it may still host a local atmosphere around the subsolar point (Hofgartner et al., 2019). The prospect of any atmosphere depends on the presence of nitrogen (N_2) ice on the surface, which has yet to be confirmed directly from the ground (e.g., Tegler et al., 2010). Methane ice signatures dominate Eris' spectrum, preventing direct identification of the weaker N_2 signatures (e.g., Licandro et al., 2006a). Eris' light-curve amplitude is very small, indicating a uniformly bright surface (Holler et al., 2020), so if N_2 is present, which could require in situ observations to confirm, the entire surface could be similar to Sputnik Planitia on Pluto. Eris' large satellite Dysnomia (~ 700 km in diameter; Brown & Butler, 2018) would also be worth a flyby. Dysnomia's albedo is only $\sim 4\%$, presenting an enormous contrast with Eris. The spatial distribution of light and dark materials on both objects would reveal the physical and chemical processes at work in this system, as well as help settle the debate about how the Eris/Dysnomia system formed. **Launch date: 2031.**

Manwë is a cold classical KBO with a large satellite, Thorondor, and the two components were expected to undergo mutual events between 2014 and 2019, where they would take turns passing directly in front of each other, as seen from Earth. However, no mutual events were observed (Rabinowitz et al., 2019). The most reasonable explanation is that the observations were not timed correctly to catch the mutual events, because of uncertainties, but a different explanation could point to a bizarre system. Light-curve data suggest that Manwë is a very elongated contact binary, sort of like a long peanut. Additionally, Thorondor has shown large changes in the amplitude of its light curve, which, combined with the non-detection of the mutual events, could mean that it is an extremely flattened object that was viewed edge-on between 2014 and 2019. Similar flattening was observed for one of the lobes of Arrokoth, the New Horizons extended mission flyby target, and may be a common process among the cold classical KBOs (Porter et al., 2019; Stern et al., 2019). Cold classical KBOs represent leftover building blocks of the solar system, and a close encounter with the Manwë/Thorondor system would contribute to our understanding of how these building blocks formed. **Launch date: 2031.**

Salacia is a member of the hot classical Kuiper Belt, which is home to a rich diversity of TNOs. It occupies the same orbital parameter space as the Haumea family members but is more than likely an interloper because of its lack of strong water-ice signatures present in the spectra of confirmed family members (Snodgrass et al., 2010). It is also extremely dark, with an albedo lower than that of asphalt (Fornasier et al., 2013; Brown & Butler, 2018). This low albedo is surprising for an object so large (~850 km; Grundy et al., 2019). The orbit of its satellite, Actaea (~290 km; Fornasier et al., 2013), is also the tightest known in the trans-Neptunian region, and both components have similar colors, strongly hinting at a giant-impact formation scenario (Stansberry et al., 2012). In situ geological and compositional studies would provide further context for Pluto and other large TNO binary systems thought to have formed through giant impacts. **Launch date: 2032.**

Sedna was the first inner Oort cloud candidate object discovered and also happens to be approaching perihelion in 2076 (Brown, 2004). Sedna ranges from 76 au to nearly 900 au over the course of its ~10,000-year orbit, with most of its time spent outside the heliopause in interstellar space. Studies of Sedna's surface composition have been limited from Earth-based facilities because of its large distance (Barucci et al., 2005, 2008a), but it is clear that Sedna represents a valuable case study for retention of volatile ices in the low-temperature regime as well as a probe of the radiation environment of interstellar space. Indeed, Sedna is a very red object (Sheppard, 2010), possibly due to bombardment of its surface ices by radiation and charged particles. **Launch date: 2033.**

Lempo is similar to Pluto in that it is in a 3:2 resonance with Neptune and is a system composed of more than two objects. A small satellite, Paha, was discovered orbiting the primary in 2001, and the primary itself was later revealed to be a comparably sized, small-separation binary, given the names Lempo and Hiisi (Benecchi et al., 2010). The Lempo system is, in fact, the only known hierarchical triple in the solar system. Two theories—gravitational capture and collision—attempt to describe the origin of the system, but both have issues (Benecchi et al., 2010). Paha is orbiting in the same plane as Lempo and Hiisi, which is highly unlikely as part of a capture mechanism. The angular momentum of the system is also much higher than other collisionally produced TNO multiples, specifically Pluto and Haumea. However, the fact that there is only one known hierarchical triple system means that the co-planar orbit of Paha could be due to a selection effect. Such an event could possibly have disrupted the primary, which may have been a contact binary before the capture of Paha. The formation of contact binaries is thought to be a relatively gentle event, with the collision occurring at human walking speed (e.g., McKinnon et al., 2020); thus, it makes sense that a contact binary could be easily separated. A flyby of the Lempo system could therefore present the opportunity to study the geological signatures of a disrupted contact binary. **Launch date: 2033.**

2011 QF₉₉ is a minor body and one of only two known Uranus Trojans, both of which are in temporary orbits that last on the order of 100,000 years (Alexandersen et al., 2013; de la Fuente Marcos, 2017). The temporary nature of 2011 QF₉₉'s orbit suggests it was captured from the Centaur population and will return there when its time as a Uranus Trojan is up. A flyby of this object would enable the study of a true solar system wanderer, having likely originated in the trans-Neptunian region (Volk & Malhotra, 2008) before transitioning into the region of the giant planets. (The other known Uranus Trojan, 2014 YX₄₉, is a possible target for a 2036 launch.) **Launch date: 2034–2036.**

Varuna is a hot classical KBO that has lately been the subject of many investigations that have raised more questions than answers. Varuna’s rotation period is only ~6.3 hours, and nonperiodic variations in its light curve potentially point to a very close-in satellite (Fernández-Valenzuela et al., 2019). No satellite has yet been detected. The fast rotation period agrees with the ellipsoidal shape determined from a stellar occultation (Sicardy et al., 2010). It is worth noting that Haumea, which is also ellipsoidal with a fast rotation period, supports rings (Ortiz et al., 2017). The most puzzling aspect of Varuna is the tentative detection of volatile CH₄ ice on its surface (Lorenzi et al., 2014). Based on volatile loss and retention models (e.g., Schaller & Brown, 2007a), Varuna should have lost its volatile ice inventory long ago, presenting a valuable test of these models. **Launch date: 2035.**

2003 AZ₈₄, a 3:2 resonant TNO, briefly had a satellite. The erstwhile satellite was detected in 2007, but subsequent efforts to recover it have been unsuccessful. Without a confirmed satellite and calculated orbit, it is not possible to calculate 2003 AZ₈₄’s mass or density, which are useful for understanding the formation of TNOs. A flyby would help recover the satellite or put the idea to rest entirely. 2003 AZ₈₄, which is about two-thirds the size of Charon, also has a potential chasm on its surface, as detected by a stellar occultation (Dias-Oliveira et al., 2017). For such a detection to be made, the chasm must be very deep, between 8 and 13 km. Such features have also been detected on Charon; in situ study of 2003 AZ₈₄ would therefore help provide context for the geologic evolution of large TNOs (e.g., Beyer et al., 2017). **Launch date: 2035.**

Makemake’s near-infrared spectrum exhibits the strongest CH₄ absorption features of any TNO, even stronger than Pluto and Eris (Licandro et al., 2006b). Its observed surface is quite uniform, similar to Eris (Hromakina et al., 2019; Holler et al., 2020), but it is redder than Eris (e.g., Snodgrass et al., 2010). Fitting into this story, Makemake’s spectrum presents signatures of radiation-processed hydrocarbons such as ethane (C₂H₆) and ethylene (C₂H₄) that tend to darken and redden TNO surfaces (Brown et al., 2015). With an upper limit on the atmospheric pressure of only ~10 nbar (Ortiz et al., 2012), comparable to that of Quaoar, the surface of Makemake is directly subjected to radiation and cosmic rays that alter CH₄ to create these ice species. Makemake therefore presents a unique laboratory for studying the processing of ices at cryogenic temperatures; indeed, it is the first solar system object on which solid C₂H₄ has been detected. In situ spectroscopy of the surface could reveal even more exotic ices and chemical processes that cannot be recreated by experiments on Earth. **Launch date: 2036.**

Orcus is sometimes called the “anti-Pluto” because of its similar but anti-aligned orbit, but this 3:2 resonant TNO is actually more akin to Charon than Pluto. It has a neutral color and strong water-ice absorption features, along with an unidentified spectral feature that could be due to either ammonia hydrates or methane (e.g., Barucci et al., 2008b; Carry et al., 2011; Delsanti et al., 2010; Fornasier et al., 2004). Detection of ammoniated species would make it the only TNO outside the Pluto system with such ices and could indicate past or present cryovolcanic episodes. Some have even suggested that the presence of NH₃ and water ice provides evidence for a subsurface ocean (Hussmann et al., 2006). Geologic information obtained as part of a flyby would be useful for comparison to the surface of Charon and could even be used to look for short-timescale resurfacing processes. Active cryovolcanic eruptions or the detection of a magnetic field would be strong evidence for a subsurface ocean below Orcus’ crust. **Launch date: 2036.**

Haumea is the largest member of its eponymous collisional family, which includes its two satellites Hi'iaka and Namaka and a handful of other TNOs (Brown et al., 2007). The ancient collision that produced the family also likely spun up Haumea and produced its highly ellipsoidal shape (e.g., Ortiz et al., 2017). Haumea's ~3.9-hour rotation period is among the fastest in the solar system (e.g., Lacerda et al., 2008). Haumea is also the only TNO with a confirmed ring system (Ortiz et al., 2017). Investigating the dynamics of Haumea's rings, satellites, and possible shepherd moons would be a primary goal of a spacecraft flyby. All of the confirmed members of the Haumea family have high albedos, neutral colors, and strong water-ice absorption features in their spectra (Brown et al., 2007; Snodgrass et al., 2010); however, Haumea also appears to support a "Great Dark Spot" (Lacerda, 2009). The origin and composition of this feature are unknown but could be associated with an impact crater and radiation-processed hydrocarbons. Haumea is the largest TNO for which volatile ices have not been detected (e.g., Pinilla-Alonso et al., 2009; Trujillo et al., 2007), and studying the composition of the revealed subsurface would be an investigation uniquely suited for a spacecraft flyby. It is possible that Haumea may have retained some its original volatile inventory, as predicted by loss and retention models (e.g., Schaller & Brown, 2007a), but high spatial resolution is required to identify them. **Launch date: 2037 or 2038.**

Ixion, a 3:2 resonant TNO, provides evidence that heterogeneous surfaces can exist on TNOs lacking volatile ices. Two different sets of observations returned two broadly different color results, one indicating Ixion was moderately red and the other indicating it was bluer (Doressoundiram et al., 2007; DeMeo et al., 2009). This stark contrast is best explained by a surface with longitudinal or perhaps hemispherical variations. The tentative detection of water ice on the surface could also be due to surface heterogeneities (Barkume, 2008; Licandro et al., 2002). Without mobile volatile ices depositing and sublimating from different regions on seasonal timescales, it is not immediately clear what could cause these detectable heterogeneities. Confirmation of a varied surface would be possible through spacecraft observations leading up to and including a close encounter with Ixion, allowing comparison of colors, albedos, and spectra across at least one full rotation period. **Launch date: 2039 or 2040.**

2002 MS₄ is a hot classical KBO and the largest object in the solar system without a name or a known satellite. It is a ~1000-km-diameter object with a relatively low albedo for an object so large (Vilenius et al., 2012). An object this large would be expected to support water ice on its surface (e.g., Barucci et al., 2011), but the low albedo suggests possible tholin deposits. However, its surface composition remains a mystery, largely due to its current superposition in front of a dense Milky Way star field, which complicates spectroscopic measurements. TNOs in this size range are currently exemplified by Charon, but this could be misleading because of Charon's unique formation and history; 2002 MS₄ would more generally reveal the surface and interior evolution of 1000-km TNOs. Ultimately, the allure of flying by this object would be to study one of the top-10 largest TNOs and acquire basic information that cannot currently be obtained from Earth-based facilities. **Launch date: 2040 or 2041.**

A.1.6.2 *Small Bodies Investigation*

For purposes of this study, we have scientifically prioritized dwarf planets (planetary bodies at least 400 km in diameter and therefore likely to be round) ahead of smaller, irregular planetesimals

as the primary flyby target. In addition to a dwarf planet flyby, distant (i.e., unresolved; usually greater than ~ 0.1 au from the spacecraft) observations of TNOs would easily be within the camera and spacecraft’s capabilities. Although such observations would not resolve Centaurs or TNOs as more than a pixel, they would be unique observations able to constrain rotation rates, magnitudes (and thus size), spectra, binarity status, and photometric properties in the manner of New Horizons (Verbiscer et al., 2019) as a result of the closer range and especially the unique phase angles not possible from Earth (i.e., $>2^\circ$).

A.1.6.3 Exoplanet Analogs Investigation

Interstellar Probe’s unique vantage point beyond the orbits of the ice-giant planets Uranus and Neptune will permit high-phase-angle ($>90^\circ$) observations not possible near Earth. Model phase curves for Uranus and Neptune are limited to Voyager images up to $\sim 90^\circ$ (Pollack et al., 1986). Exoplanet studies predict that for the Nancy Grace Roman Space Telescope, we can optimistically expect to detect exoplanets at phase angles up to 120° (Carrión-González et al., 2021), and thus this solar system point of reference is necessary to detect exo-Neptunes and place them in context with Uranus and Neptune. By combining near-contemporaneous high-phase-angle, unresolved data from Interstellar Probe with low-phase-angle, resolved data from near-Earth observatories, various Neptune models can be constrained, enabling their expanded use for their exoplanet counterparts (such as the evolution of Marley et al. (1999) and Marley & McKay (1999) into the growing field of exoplanet modeling today). We will also be able to measure their color variations as a function of phase angle, which has been proposed as a method of classifying exoplanets and distinguishing them from background stars in observation (Seager et al., 2015). Constraining these characteristics could aid in discriminating between Neptunes, Jupiters, and terrestrial exoplanets (Cahoy et al., 2010; Hegde & Kaltenegger, 2013; Mayorga et al., 2016; Sudarsky et al., 2005). In particular, Uranus presents an unusual case study of what a planet with high obliquity looks like in either transit or direct imaging. While rotational information for Neptune could tell us about the presence of a dark spot, mapping of a Uranus-like planet (see Mayorga et al. (2020) and Luger et al. (2019) for examples of exoplanet mapping) may not be so straightforward. A cadence of look-back observations once a year for several years involving imaging the planets for one or two of their rotation periods would not only allow us to improve our understanding of Uranus’ and Neptune’s phase functions and emission/scattering properties but also lay the groundwork for exoplanet comparison with upcoming instruments like the Roman Space Telescope, Large Ultraviolet Optical Infrared Surveyor (LUVOIR)/Habitable Exoplanet Observatory (HabEx), and beyond.

A.1.6.4 Space Physics Investigation during Flyby

The New Horizons spacecraft made the first particle measurements near TNO objects and provided a glimpse of the interaction of Pluto and Arrokoth with their environment (Bagenal et al., 2021; Stern et al., 2019). Interstellar Probe may complement the New Horizons results by visiting another TNO with different instrumentation that could characterize the fields in the object’s environment.

The magnetic field is critical to determine whether a body stands off the surrounding plasma as a result of internal magnetic fields, magnetic induction, the pickup of atmospheric ions, or other processes. An internal magnetic field may be unlikely based on the relatively small size of the

known TNOs; however, given the challenges in numerical modeling of planetary dynamos, it cannot be ruled out, and finding such an intrinsic field would be a breakthrough.

Particle measurements will contribute to determining the weathering processes that act on the surface of the TNO. Especially for TNOs far from the Sun, and potentially even beyond the heliopause, it will be important to characterize the cosmic ray radiation, which may modify surfaces differently than what we find within the heliosphere or planetary magnetospheres. Understanding the weathering is critical to relate the remote measurements of surface properties with the properties and history of the bulk material of the body itself.

A possible atmosphere would raise questions about its nature and how it is maintained. The combination of particles and fields measurements will inform on a possible atmosphere on the TNO in different ways. The composition of ions that are removed from the atmosphere can be directly measured in situ. Plasma waves created by the conversion of neutral atmosphere into ions that ultimately escape will inform about the stability of the atmosphere. Although neutral measurements with the Neutral Mass Spectrometer (NMS) would also help with understanding any atmosphere, any thruster firings during the flyby may interfere with these observations. NMS observations should be done on a best-effort basis so as not to interfere with the primary observational operations. Accommodation of the flyby cameras and an NMS should be such that NMS will be measuring in the ram direction during closest approach.

The space physics measurements are not just beneficial for space physics itself, such as determining how a solid body interacts with its plasma environment, but should be considered an integral part of the planetary science investigation, such as characterizing how surfaces and atmospheres are weathered.

A.1.6.5 Dust Disk Investigation

The primary goals of the dust disk investigations are to carry out in situ and remote observations to search for evidence of solar nebula chemical processing in dust mass and composition, determine dust grain production mechanisms, and observe whether remnant structures from the formation of the solar system can be found in the structure of the IPD disk. The potential KBO flyby targets listed in the last section are all sources of outer-solar-system dust, created by KBO–KBO grinding and ISM dust sputtering. Thus, directly measuring the dust abundance and composition in situ (i.e., locally along Interstellar Probe’s trajectory) while also simultaneously remotely mapping the dust cloud from 0.5 to 100 μm in the forward direction will allow for accurate large-scale remote mapping of the dust cloud calibrated using real encountered particles. Adding in “look-back spectral mapping” of the backward hemisphere once Interstellar Probe is far enough from the Sun to view the entire expected extent of the cloud (and also have the instrument survive looking back toward the Sun) will complete the all-sky dust cloud mapping objectives.

The dust measurements will produce (1) maps of the dust abundance and size-frequency distribution, (2) dust composition versus distance from the Sun, and (3) maps of the dust disk structure in the heliosphere and exodisk. These measurements could all be made using a VISNIR spectral mapper flown on Interstellar Probe (hereafter referred to as the IRM) based on a CubeSat-class instrument for measuring the ZL from near Earth.

Three-dimensional cloud mapping would occur during flythrough of the disk via tomographic inversion, and via look-back imaging once the spacecraft is beyond 200 au. The look-back imaging will allow Interstellar Probe to measure for the first time in history the entire extent of the zodiacal cloud, and determine whether its inner JFC/asteroidal and outer KBO parts connect smoothly, as predicted by (Stark & Kuchner, 2008, 2009) and detected by Poppe (2016), Poppe & Horányi (2012), and Piquette et al. (2019) using New Horizons dust counts along one chord (Figure A-5 and Figure A-6). This would also allow direct comparison of the solar system’s debris disks with those observed around other nearby stars, and test theories that suggest that our solar system is planet-rich but dust-poor (Greaves & Wyatt, 2010).

The goal of these observations is twofold. By taking repeated stares at specified “dark” regions of the sky along Interstellar Probe’s trajectory and examining the differences between them, Interstellar Probe will obtain measurements of the emission column density of the LOS vector difference through the solar system’s circumstellar dust cloud, as well as better and better measures of the final asymptotic “O Zody” background flux measurement. By differencing IRM repeated measurements in the ram direction, Interstellar Probe will provide the differential column emission flux through the cloud in that direction since the last measurement. And by making great circles on the sky while it is in spin-stabilized mode, the spacecraft will obtain multiple measurements of the cloud’s shell of emission as a function of heliocentric distance on the $\sim 10'$ scale, which, when combined with the far-off cloud look-back mapping, will allow for accurate 3D modeling of the cloud’s structure on scales of a few astronomical units, enough to search for large resonant structures such as the “Neptune Ring,” the main asteroid belt’s bands, and the Jovian dust streams’ inflows.

Model estimates using the latest New Horizons Student Dust Counter in situ outer dust cloud particle density measurements indicate that the galactic diffuse background + EBL should dominate the background signal for wavelengths of $>10 \mu\text{m}$ and Interstellar Probe distances from the Sun of $>10 \text{ au}$. All these measurements—when coupled with the direct $>10\text{-}\mu\text{m}$ look-back mapping of the circumstellar dust cloud when Interstellar Probe is at $>200 \text{ au}$ from the Sun and the direct sampling, in situ dust particle measurements made by the interstellar dust analyzer (IDA) (see Section 4.1.5) along Interstellar Probe’s trajectory—will provide the best 3D reconstruction of the outer large-scale structure of the solar system’s circumstellar dust cloud ever produced.

Using mapping observations with the IRM from 0.5 to $50 \mu\text{m}$ and at high phase angle by looking back toward the Sun from $>400 \text{ au}$, we will be able to perform deep searches for the presence of rings and dust clouds around discrete sources, and thus we will be able to search for possible strong individual sources of the debris clouds, such as Planet X, the Haumea family of icy collisional fragments, the rings of the Centaur Chariklo, or dust emitted from spallation off the larger KBOs. Large-scale structure determination of the cloud should help inform us about ancient events such as planetary migration and planetesimal scattering (as in the Late Heavy Bombardment), and measurement of the cloud’s total brightness will allow improved removal of its signal in near-Earth cosmological measurements looking out into the universe.

Interstellar Probe will also carry the first-ever IDA past the orbit of Saturn. Based on the Europa Clipper SURface Dust Analyzer (SUDA) instrument (see Section 4.1.5), the IDA, in tandem with the

IRM, will compositionally and directionally characterize the solar system’s dust clouds and help isolate their sources, like the rocky asteroidal dust bands and the icy Haumea family fragments. Using measured dust particle masses and velocities, dust input and loss rates from these sources will be derived. Direct dust sampling will return the first-ever in situ chemical analysis of dust in the EKB, provide the first-ever in situ sampling of dust beyond 50 au, and provide calibrated ground truth for cloud models produced from our imagery.

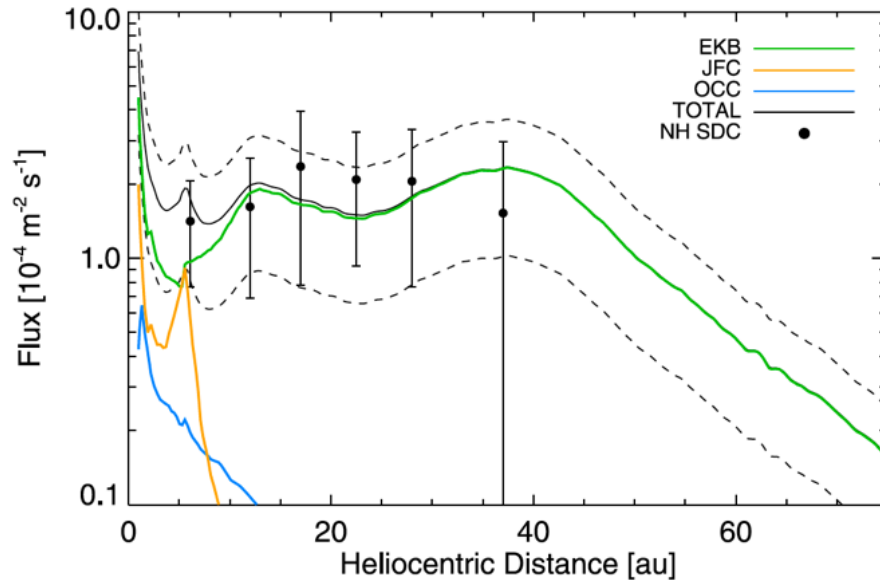


Figure A-5. In situ measurements (black data points) and predicted dust flux contributions (colored curves) for the solar system’s debris disks (Poppe et al., 2019; Greaves & Wyatt, 2010). The overall relative shapes of the inner and outer disks scale well, and the predicted crossover at ~10 au from JFC-dominated to EKB-dominated is seen. Interstellar Probe will help determine whether another crossover from EKB-dominated to OCC-dominated occurs at ~100 au and whether the EKB dust is rich in ice, rock, and organics like KBOs and comets. Note: NH SDC, New Horizons Student Dust Counter. (Reproduced from Poppe et al. (2019) with permission; © AAS.)

A.1.6.6 Near and Far ISM Investigation

The IDA will make the first direct measurements of unaltered galactic ISM solids. In tandem with the IRM, it will compositionally and directionally characterize the dust inflowing from the VLISM into the solar system. Thus, it should directly resolve the tension between the expected makeup of inflowing ISM dust as determined by remote sensing and the measured ISM dust component found at Jupiter and Saturn by Galileo, Ulysses, and Cassini (Weingartner & Draine, 2001; Draine & Hensley, 2016; and Figure A-6). This is also the raw material that the young solar system was made from, and because of the probable size and compositional dust sorting mentioned above, taking a direct census of the “original solid input material” for the solar system will greatly advance models of early solar system formation.

Further, work by Redfield and Linsky using LOS observations to background stars through the VLISM has produced extinction maps of the local clouds with interesting structure (Section 2).

Coupled with direct IRM measurements of the local VLISM dust by the IRM, the IDA in situ dust measurements will provide “local ground truth” of how real ISM dust particles interact with the ISM radiation field and emit light, thus providing an LISM calibration for further IRM measurements of far-off regions of the galaxy (i.e., beyond 1000 au from the Sun), where Interstellar Probe will not venture. That is, the IDA will directly census dust particles that the IRM will observe remotely, and knowing the size and composition of the emitting dust particles will greatly improve our radiative models of their behavior.

A.1.6.7 Extragalactic Background Light Investigation

The outer solar system is a unique, quiet vantage point from which to observe the universe around us. The emission, both in scattered light and in direct thermal emission, from the IPD that sources, for example, the ZL is a particularly pernicious foreground, and the 1000-fold reductions in foreground brightness from the outer solar system to studies of the faint and distant universe would permit measurements of unprecedented accuracy. Unfortunately, we have been slow to take advantage of this resource. Since Pioneer 10, there have been a relative handful of astrophysical studies using data from beyond the Earth’s orbit, including measurements of diffuse light from the galaxy (Gordon et al., 1998; Toller et al., 1987), the brightness of the cosmic optical background (Lauer et al., 2021; Matsuoka et al., 2011; Toller, 1983; Zemcov et al., 2017) and the cosmic UV background (Edelstein et al., 2000; Holberg, 1986; Murthy et al., 1991, 1999), exoplanet mass determination using gravitational lensing (Muraki et al., 2011), and the UV emission from specific objects (Holberg, 1985), including studies of their spectral features (Murthy, 1993, 2001). In total, this amounts to a meager three results per decade.

A field where transformational improvements in scientific capability would be enabled by measurements from the outer solar system is the study of the total emissive history of all sources in the cosmos (Figure A-7). The EBL is the cumulative sum of all radiation released over cosmic time, including light from galaxies throughout cosmic history, as well as any truly diffuse extragalactic sources (Cooray, 2016; Hauser & Dwek, 2001). Measurements of the EBL can constrain galaxy formation and the evolution of cosmic structure, provide unique constraints on the epoch of reionization, and even allow searches for beyond-standard model physics (Tyson, 1995). Ultimately, precise measurements of the EBL allow a stringent “cosmic consistency test” wherein the observed brightness strongly constrains future structure formation models and simulations as well as informs surveys for faint objects that may be missing in our current census of galaxies (Conselice et al., 2016).

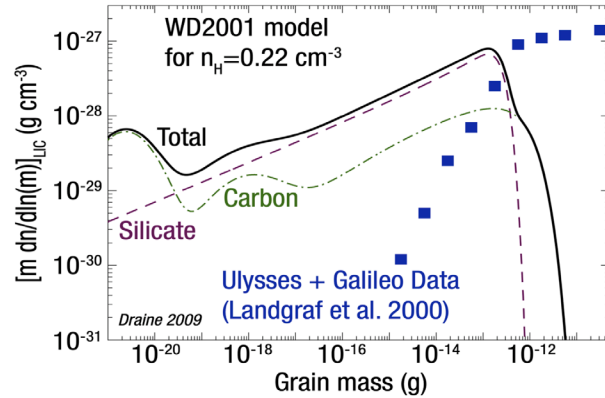


Figure A-6. Disconnect between the nearby ISM dust size distribution predicted from remote-sensing measurements (black) and ISM dust counts measured inside the solar system (blue) (Weingartner & Draine, 2001; Draine & Hensley, 2016). Further, only evidence for siliceous ISM-derived dust has been found to date inside the heliosphere, suggesting some process has preferentially removed carbonaceous solids from dust instreaming from the VLISM. (Reprinted from Draine (2009) with permission; © 2001 Springer Nature Limited.)

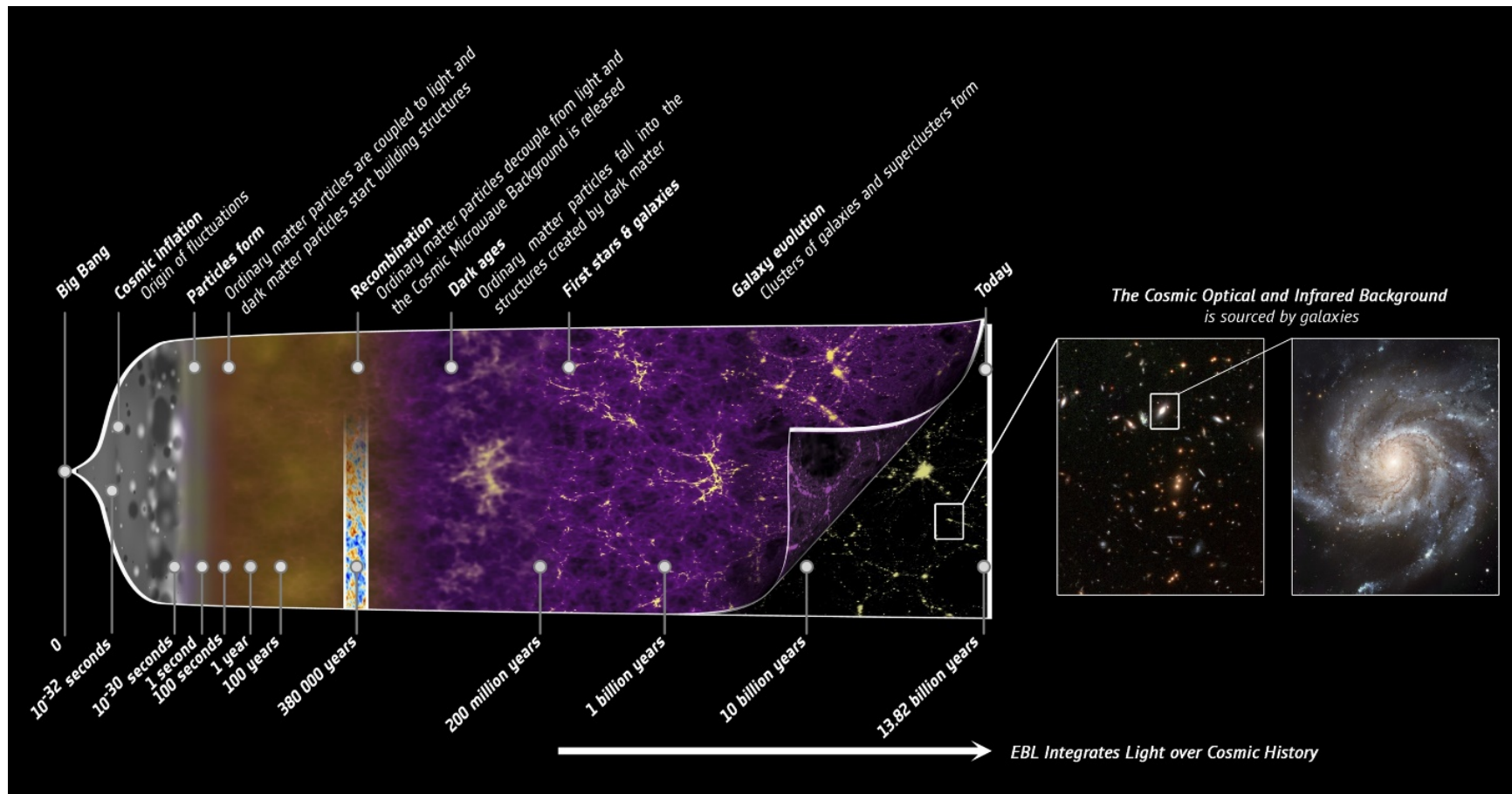


Figure A-7. Our current understanding of the thermal history of the universe, beginning at the Big Bang and running through 13.8 Gyr to today. Measurements of the EBL integrate the emission from all sources whose rest-frame emission falls into a given region of the spectrum. At optical and near-IR wavelengths, direct emission from stars sources most of the light, while at mid- and far-IR wavelengths, star formation in cold nebulae is the source. Together, both trace the history of stars and nucleosynthesis since the very first generation of stellar objects. (Image credit: C. Carreau, European Space Agency.)

As shown in Figure A-8, the absolute brightness of the EBL has been established from Earth at many radio and X-ray wavelengths, but at most IR, optical, and UV wavelengths, a precise

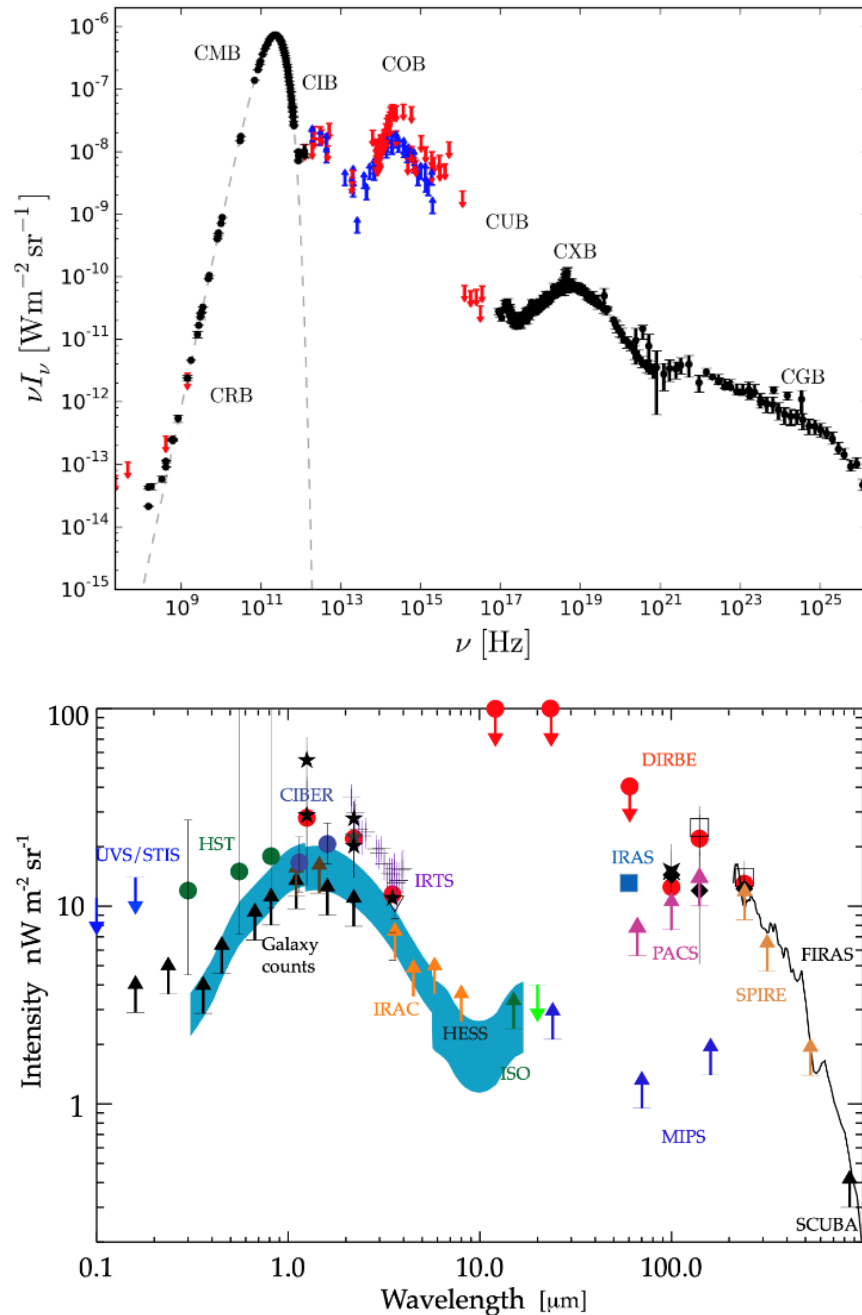


Figure A-8. The cosmic EBL over all wavelengths (bottom; adapted from Hill et al., 2018) and at wavelengths falling between the UV and far-IR (top; adapted from Cooray, 2016). The cosmic radio, microwave, X-ray, and gamma-ray backgrounds (CRB, CMB, CXB, and CGB, respectively) are well measured and understood. On the other hand, the cosmic IR, optical, and UV backgrounds (CIB, COB, CUB, respectively) have large uncertainties due to the interplanetary dust that is 100–1000 \times brighter than the astrophysical backgrounds. This has led to a wide range of constraints, as highlighted in the bottom panel, which only data taken in the outer solar system will be able to discriminate.

assessment of the sky brightness has been hampered by reflected and emitted light from IPD, which results in an irreducible >50% uncertainty—and at some wavelengths significantly larger—on the absolute emission from the EBL (e.g., Hauser et al., 1998). Notwithstanding the great success of Spitzer and its various predecessor cryogenic space missions, Earth’s position within the solar system severely constrains the sensitivity that can be achieved at UV, optical, and IR wavelengths, both for point source observations and for measurements of diffuse emission. By observing beyond the IPD, observations from the outer solar system can eliminate these uncertainties and definitively determine the absolute brightness of the EBL.

The Optical/Near-IR EBL. The optical/near-IR EBL encodes direct emission from stars integrated over time and thus constrains the aggregate stellar population of the universe and nucleosynthesis in stars through cosmic history. By measuring the intensity and spectrum of the diffuse optical/near-IR EBL between 0.3 and 5 μm , we can perform a census of the total mass density in stars and the fraction of them in diffuse structures, search for sources of diffuse emission that might arise from dark-matter annihilation, determine the fraction of baryons that have been processed through stars and active galactic nuclei during the epoch of reionization, and understand the rate at which stars and supermassive black holes build up over cosmic time. Based on measurements near Earth, the optical/near-IR is not known to within a factor of three, and current measurements from more distant vantage points are systematics-error dominated. Better designed, more capable instrumentation is required to make a definitive measurement.

The Mid-IR/Far-IR. Here the EBL is dominated by thermal emission from small dust grains in galaxies, with high redshift sources from cosmic noon making the largest contribution (Lagache et al., 2005). Despite pioneering work on source counts with Spitzer, Herschel, and ground-based millimeter/submillimeter surveys, our census of the total EBL at mid-IR wavelengths (>5 μm) is incomplete. This is largely because of the brightness of the IPD at these wavelengths, which does not approach the level of the EBL until well beyond the orbit of Uranus.

Observations in the far-IR (>50 μm) can reveal the contribution from low-mass star-forming galaxies and thereby result in a complete census of obscured star formation, measure obscured active galactic nuclei activity, and trace the growth of dust and its evolution as a function of metallicity and cosmic time. This is particularly important because there is evidence, based on the spectra of distant quasi-stellar objects, that low-metallicity dust has extinction properties different from those of dust in local star-forming regions (e.g., Maiolino et al., 2010). Ultimately, this measurement offers a way to trace the evolution of the stellar initial mass function over time, which is one of the key uncertain parameters required in the conversion of luminosity to baryonic matter density.

The Ultraviolet EBL. In the far-ultraviolet (FUV), the diffuse astrophysical background is thought to be largely due to light from local Milky Way O and B stars scattered by dust in the ISM. Isolating the extragalactic component that quantifies the ionizing intergalactic radiation field from the VLISM galactic and scattered local solar UV components is the challenge. As a result, advanced spectral decomposition techniques over the broad 500- to 2000-Å wavelength grasp of Interstellar Probe’s augmented payload UV spectral mapper (such as the one referenced in the search for dwarf planet atmosphere during a planetary flyby) will be required to separate the extragalactic component from local dust and atomic scattering, as well as other emission processes (e.g., Murthy, 2009). However,

such measurements, conducted far from the Sun and its scattered light, will help elucidate the origin of the galactic and extragalactic UV backgrounds, including any locally dominant sources (such as Epsilon Canis Majoris; see Linsky & Redfield, 2014), a secondary source of galactic scattering (Henry et al., 2014), or exotic dark-matter physics that may be present (Henry et al., 2018).

A.1.6.8 *Giant Planet Flyby Investigation*

A JGA provides an opportunity to learn more about the Jupiter system, including Jupiter itself as well as its magnetosphere and moons. Even though Jupiter and its magnetosphere have been explored by a variety of spacecraft, Interstellar Probe may be able to make unprecedented measurements thanks to its unique trajectory and instrumentation.

Jupiter’s magnetotail is known to extend over several astronomical units (e.g., Lepping et al., 1983), yet how this tail merges with the interplanetary medium and to what extent its plasma is magnetically connected to Jupiter are unknown. New Horizons measurements were consistent both with particles flowing along field lines connected with the magnetosphere (Hill et al., 2009) as well as with plasmoids that may be magnetically closed in themselves (e.g., Nicolao et al., 2015). By carrying a magnetometer and flying along Jupiter’s deep magnetotail, Interstellar Probe may answer these questions. While it would be most valuable to traverse the magnetotail for several astronomical units, new data can already be collected beyond 200R_J downtail (e.g., Krupp et al., 2004).

Jupiter is also known to accelerate electrons to higher energies than any other planet (Mauk & Fox, 2010), yet there are very few measurements that resolve that high-energy population in energy and direction. Most current results are based on measurements that integrate over large energy ranges or along an LOS (e.g., Roussos et al., 2019). Depending on the details of Interstellar Probe’s payload, its cosmic ray instrumentation may close this measurement gap and thereby provide valuable signatures of possible acceleration processes. Such a measurement does not require passing through the intense radiation belts because greater-than-megaelectronvolt electrons can be found throughout the magnetosphere (Kollmann et al., 2018).

Lastly, it needs to be understood that the Jupiter system varies on many timescales, meaning that even a repetition of previously done measurements will be valuable and may indicate changes on the decade timescale that cannot be determined through shorter missions and that may be related, for example, to the solar cycle or the changing geologic activity of its moons. If, on the other hand, other spacecraft are already present at Jupiter, such as the Jupiter Icy moons Explorer (JUICE) mission, Interstellar Probe will allow coordinated observations that could provide multipoint observation in Jupiter’s magnetosphere, which is critical to distinguish temporal versus spatial changes, especially in a system as large as Jupiter’s.

If the trajectory design allows for a flyby of one of the ice giants, Uranus or Neptune, observations of the magnetospheres similar to what is described for Jupiter would be of very high value. The Voyager flybys showed that the magnetospheres of Uranus and Neptune are drastically different from any other in our solar system (e.g., Paty et al. 2020). Both magnetospheres are highly asymmetric and have complex interactions with the solar wind that were only briefly sampled during the Voyager flybys. A second flyby of either planet would help to improve understanding

of the geometry of each magnetosphere and to constrain which observations made by Voyager were inherent to the system versus transient phenomena.

A.1.7 *Space Physics Measurements during Flyby*

All of the known TNO planets are currently embedded within the heliosphere, which determines the field, plasma, particle, dust, and UV environment, while some are on highly eccentric orbits taking them out through boundary regions into local interstellar space. Different aspects of these environments can affect TNO surfaces and atmospheres in various, sometimes ambiguous ways (e.g., Hendrix et al., 2012). Knowledge of these varying environments is needed to determine and understand the structure, evolution, and composition of planetary atmospheres and surfaces. For example, chemical reaction rates (e.g., for tholins) scale with UV and electron irradiation and determine atmospheric structure and surface weathering. Also, measurable surface reflectance spectra depend on composition but also on grain size (e.g., Hapke, 1981) that, in turn, is affected by galactic cosmic rays (e.g., Raut et al., 2008).

The planetary orbits fall within three regions: (1) the supersonic heliosphere of direct solar wind flow from the Sun to the solar wind termination shock, (2) the heliosheath boundary layer where the solar wind slows down and plasma heats up, and (3) the VLISM environment dominated by the inflow of interstellar fields, plasma, and particles. A classical KBO resides only within the first region (direct solar wind flow), while objects on more elliptical orbits pass through region 2 (heliosheath) and, in the most extreme cases (e.g., Sedna, 2012 VP₁₁₃, and Leleākūhonua), region 3 (VLISM). In region 1, the solar plasma and energetic particle irradiation effects fall off outward from the Sun into the classical TNO region beyond the giant planets. Conversely, objects are progressively more exposed to galactic cosmic rays moving from region 1 to region 3. Interstellar Probe instrumentation could systematically track the different effects that this has on surface and atmosphere composition. Intermittently throughout the Sun's history, the heliosheath may have been pushed inward by external pressure from dense molecular clouds and supernova shocks (Müller et al., 2006). Thus, TNO depth profiles may not only reflect the history of solar activity but also provide insight into the Sun's journey through the galaxy.

The space environment of dwarf planets in the outer heliosphere and beyond is very different from the environment of most other well-studied planetary bodies. Dwarf planets in regions 1 and 2 are embedded in a population of interstellar pickup and suprathermal ions that originate from neutral gas in interstellar space and acceleration after ionization in the heliosphere. Given that the gyromotion of these particles is larger than the size of a dwarf planet or its magnetosphere (hundreds to thousands of kilometers), it is not obvious that these particles would be affected by the presence of a planet. Yet, New Horizons measurements found that these particles are deflected around Pluto and show a wealth of phenomena like flow turbulence and waves that may be unique to dwarf planets (Bagenal et al., 2016; Kollmann et al., 2019). Simulations suggest that interstellar pickup ions in turn play a critical role in shaping the structure of a dwarf planet's space environment, including its wake and suggested bow shock (Barnes et al., 2019). Dwarf planets in the outer heliosphere therefore offer a unique opportunity to study critical aspects of space physics that are not accessible through measurements in the inner solar system.

The broad extent of Pluto’s atmosphere hints at the possibility that other TNO planets could have atmospheres. A flyby of another TNO planet with Interstellar Probe, especially if carrying a magnetometer and imaging UV spectrometer, would provide invaluable information on how geologic, atmospheric, interplanetary, and interstellar processes interact with small planets. Stern & Trafton (2008) suggest that processes driving atmospheric evolution for terrestrial planets, such as Jeans and hydrodynamic escape, operate on TNO planets. Constraining bulk composition and trace gas species in these atmospheres would provide a rich data set applicable to a broad swath of worlds and even exoplanets, and even without the detection of another atmosphere, characterizing a TNO planet’s surface would put upper limits on the particles and radiation experienced by the planets, and by extension, the solar system as a whole, as well as potential atmospheric longevity.

A.2 Science Implementation of Augmentation

A.2.1 *Changes to the Flight System*

If an augmented science mission is chosen for Interstellar Probe, the payload described below must be accommodated. Although much of the flight system remains unchanged because of this payload, some adaptation is needed to meet the requirements of the mission when science augmentations are included. These adaptations are as follows:

- The instruments selected must be reaccommodated. The basic approach remains the same in that instruments are located on booms with clear fields of view (FOVs) around the high-gain antenna (HGA) or on the ram-facing deck oriented to allow observations as required. Figure A-9 (also see the augmented payload foldout) shows an example of the physical configuration of the spacecraft with example augmented instruments.
- The guidance and control (G&C) system will be required to operate for at least part of the mission in three-axis mode to accommodate events such as observation of planetary bodies during flybys. Although this is not expected to require additional G&C instrumentation, the capability must be included in flight software. In addition, there may be an increase in propellant needed for attitude control during three-axis observations and for spin-up and spin-down of the spacecraft for these events.
- The strategy used to downlink science data must incorporate increased data volumes associated with the extra observations in the augmented mission scenario. The baseline heliophysics-centered payload produces data at a relatively constant rate; in the augmented mission, events will produce a burst of data in a short time that must be stored and downlinked over a longer period of time. The augmented scenario is very similar to the situation with New Horizons, so that mission will be used as a model for the Interstellar Probe data downlink strategy in a mission that includes augmented science.
- A crucial, overarching difference between the baseline heliophysics-only design and the augmented design relates to spacecraft attitude control. In the heliophysics baseline configuration, the spacecraft would be a Sun-pointed, spin-stabilized spacecraft. In the augmented configuration, the spacecraft would spend most of the mission as a Sun-

pointed spinner but would also have three-axis attitude control to enable pointing imagers at planetary and astrophysical targets.

The changes to the flight system are relatively modest and represent little change in flight system concept. We expect that these changes would not significantly increase mission cost or risk and that the decision to include augmented science objectives in Interstellar Probe should not be based on concerns with the flight system.



Figure A-9. The VIR and IRM are circled to show their inclusion on the augmented payload. Note the shorter Plasma Wave Subsystem (PWS) antenna to the left. (Image credit: Johns Hopkins Applied Physics Laboratory.)

A.2.2 Science Implementation

A.2.2.1 VISNIR Flyby Imaging

- Will acquire multispectral images of a dwarf planet’s geologic features.
- Enables unique comparative planetology among dwarf planets—the most common type of planet.
- New Horizons’ Pluto flyby serves as an excellent standard.

A.2.2.1.1 VIR Investigation

Flying by one of the ~130 dwarf planets (bodies > 400 km) or countless small-body planetesimals will require the spacecraft to fly within several thousand to several tens of thousands of kilometers of its surface. Imaging the target across multiple visible and IR wavelengths will permit detailed

geophysical studies of its surface, allowing geoscientists to infer the target’s evolutionary history and internal makeup. The flyby by New Horizons of Pluto and 2014 MU69/Arrokoth provides an excellent analog for the concept of operations (ConOps) and types of measurements Interstellar Probe could make at a dwarf planet.

A.2.2.1.2 Measurement Requirements

Table A-1. Measurement requirements for the Visible-Near Infrared Imager (VIR).

Visible-Near Infrared Mapper (VIR)	
Measurement Objective	Multispectral images of planetary surface features and distant planetary and astrophysical observations
Instantaneous (Pixel) Field of View	5–20 μ rad
Field of View	2.3° × 1.2° (framing area for EIS) or 5.7° (in the cross-track direction)
Channels	≥5
Mass Allocations	10.5 kg
Power Allocations	7.1 W
Data Rate (or Volume)	20 Gbit for planetary encounter
Mission Requirements	Three-axis-stabilized spacecraft, precise pointing knowledge, tens of thousands of kilometers from planetary surface Pointing accuracy: <1000 mrad Pointing knowledge: <7.5 μ rad Jitter: <10 μ rad over 0.05 seconds
Accommodations	Coboresighted with IRM; ~90° from ram point away from Sun; spacecraft clear of FOV

To address science goals related to geological and compositional characterization across the surface of a dwarf planet, the main planetary measurement requirements are to image the encounter hemisphere of the planet at ≤ 1 km/pixel across multiple visible and near-IR (VISNIR) wavelengths (Table A-1). At 1 km/pixel or better pixel scales, landforms such as ridges, craters, plains, faults, and cryolava flows reveal their details sufficiently to permit detailed geological interpretations. At pixel scales coarser than several kilometers per pixel, there is insufficient spatial data to permit useful geological interpretation. We chose these pixel scales based on experience with planetary image data from the likes of Voyager, Galileo, Cassini, and New Horizons. Repeat imagery over as much of the target as possible would enable stereo observations for topography derivations. Topographic data are commonly several multiples coarser pixel scale than the original images, thus further necessitating <1 km/pixel images.

A.2.2.1.3 Instrumentation

As an example, we used New Horizons’ Ralph visible/near-IR camera and imaging spectrometer (Figure A-10; Reuter et al., 2008) as our flyby camera and acknowledge that other cameras, such as the Europa Imaging System (EIS) camera (Turtle, 2019), may be similarly well-suited.

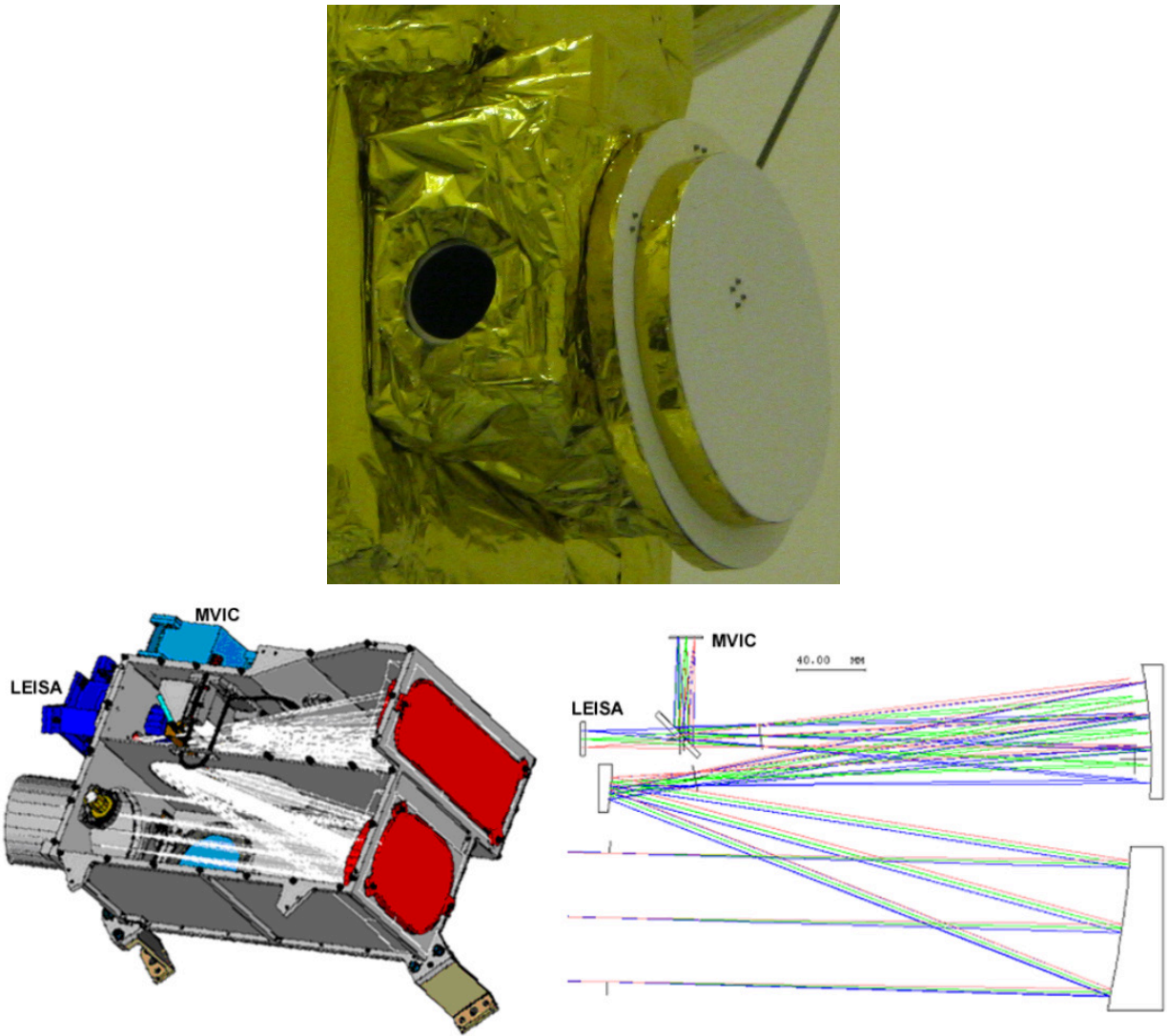


Figure A-10. Top, Ralph camera integrated on the New Horizons spacecraft (image credit: Johns Hopkins Applied Physics Laboratory). Bottom, Ray-trace schematic for Ralph (image credit: Reuter et al., 2008). Note: LEISA, Lisa Hardaway Infrared Mapping Spectrometer (formerly Linear Etalon Imaging Spectral Array); MVIC, Multispectral Visible Imaging Camera.

While we used the full FOVs and instantaneous fields of view (IFOVs) of Ralph for our augmented payload design (5.7° cross-track and $20 \mu\text{rad}$, respectively; Reuter et al., 2008), we highlight the dual framing ($2.3 \times 1.2^\circ$)/pushbroom (2.3° cross-track) capability of the EIS camera as a possible modification to a Ralph-like camera. Panchromatic framing would best serve the needs of optical navigation (OpNav) and stereophotogrammetric planetary observations used to derive topography, whereas pushbroom imaging enables multispectral observations in a way that minimizes smear due to the spacecraft's high speed. We envision something like Figure A-11 below.

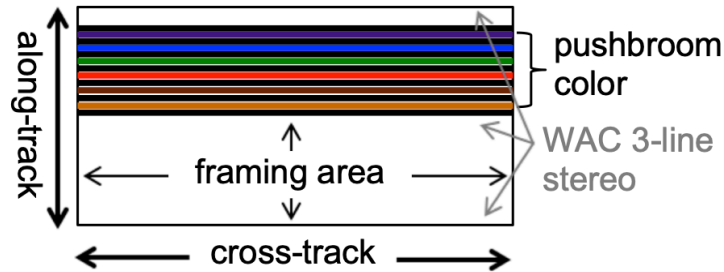


Figure A-11. The focal plane conceptual schematic for the Europa Imaging System camera showing its panchromatic framing area and multispectral pushbroom area. The pushbroom section enables non-smeared images at high speed across multiple color channels, allowing for compositional information and single-track stereo. The framing area is useful for optical navigation, panchromatic, and certain stereophotogrammatic observations. Conceptually, this design is ideal for flyby dwarf planet VISNIR reconnaissance. WAC refers to the EIS Wide Angle Camera. (Image credit: Johns Hopkins Applied Physics Laboratory, <https://www.hou.usra.edu/meetings/lpsc2019/eposter/3065.pdf>.)

The VIR and IRM should be coboresighted so they can both acquire complementary data of the same features, whether a planetary surface or an astrophysical target. A planetary target would be imaged on approach, near closest approach, and on departure, requiring the spacecraft to slew nearly 180°.

A.2.2.2 IRM Imaging

Table A-2. Measurement requirements for the Infrared Spectral Mapper (IRM).

Infrared Spectral Mapper (IRM)	
Measurement Objective	Multispectral mapping of planetary surface features, the circumsolar dust disk, the diffuse galactic light, and the extragalactic background light
Instantaneous (Pixel) Field of View	30 μ rad at 0.55 μ m, 1.7 mrad at 100 μ m
Field of View	3.6° × 3.6°
Channels	5 (one 0.5- to 15- μ m spectral at R > 30, 40/60/100/150 μ m at R > 3 far-IR imaging)
Mass Allocations	4 kg
Power Allocations	<10 W
Data Rate (or Volume)	1 Gbit for each in situ sky survey, repeated at 2, 5, 10, 20, 50, 100 au...5 Gbit at KBO planetary encounter
Mission Requirements	Three-axis-stabilized spacecraft, precise pointing knowledge, tens of thousands of kilometers from planetary surface. Pointing accuracy: <1000 μ rad Pointing knowledge: <7.5 μ rad Jitter: <10 μ rad over 0.05 seconds
Accommodations	Coboresighted with VISNIR; point away from Sun; spacecraft clear of FOV

A.2.2.2.1 Investigation

A suitably designed instrument for Interstellar Probe operating in the outer solar system could revolutionize our understanding of a variety of astrophysical and planetary science questions—building a definitive understanding of the cosmic EBL at optical and IR wavelengths, providing a unique and robust probe of structure formation in the universe, determining the properties of

dust and ice throughout our own solar system to allow direct comparison to equivalent measurements in exo-systems, observing during planetary flybys to map the IR spectral properties of a wide range of objects in the distant solar system, and more. Crucially, these science cases require only a 10-cm-class telescope and passively cooled, high-heritage detectors, allowing a single instrument to be a scientific “Swiss Army knife.” Measurements of the EBL and IPD to ~ 20 au are enabled through low-resolution spectra at near-IR wavelengths, while studies of the cold, distant dust disk in our solar system require a low-spatial-resolution far-IR camera. Planetary science observations from the same instrument could help us understand the geology and evolution of bodies across a range of masses, including their ice and chemical compositions, landform type and distribution, the impact of solar irradiation interactions, and the details of sublimation of ices or organic concentrations. In this report, we outline a compact and lightweight instrument concept that allows us to perform trade studies and develop detailed requirements for the Interstellar Probe mission concept.

A.2.2.2.2 Measurement Requirements

Objective 2.2. Mapping the emission from dust as a function of heliocentric distance informs us about the structure and processes generating micrometer-scale dust in the solar system—be it collisional grinding of main belt asteroids, sublimation of passing comets, resonant dust trapping by the planets, or sputtering of KBO surfaces (Figure A-12). Mapping over a broad wavelength range ensures we will measure the light scattered by the zodiacal cloud at $0.5\text{--}3.0\ \mu\text{m}$, the thermal emission from the warm inner (asteroidal) dust cloud at $3.0\text{--}30\ \mu\text{m}$, and the cold outer (Kuiper

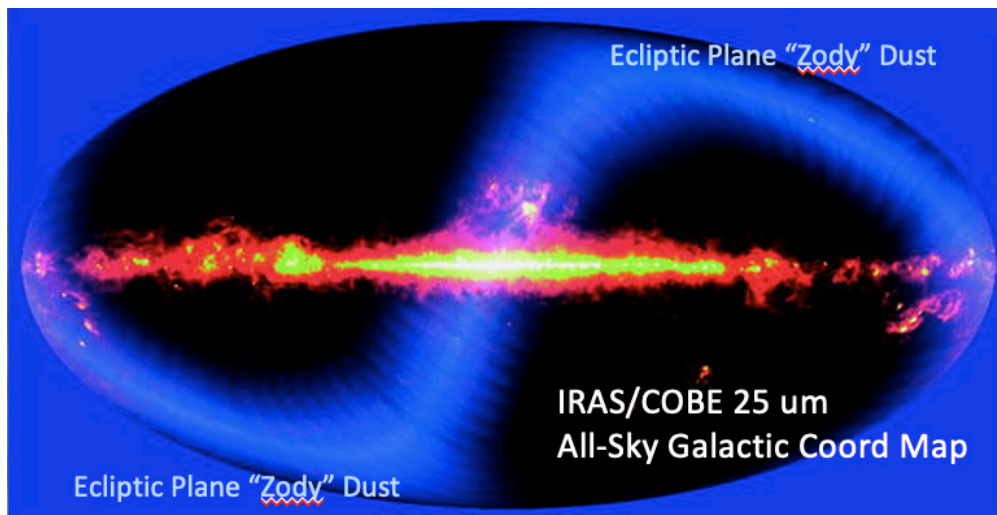


Figure A-12. Observed distributions on the sky of $25\text{-}\mu\text{m}$ thermal emission from the galaxy (bright yellow/red structure spanning left to right) and the circumsolar dust disk (light-blue sideways S-shaped structure going from bottom left to upper right). Note how bright the galaxy appears, even though it contains mainly very cold ($T = 15\text{--}30\ \text{K}$) dust; this is because it contains a massive amount of this dust. By contrast, the circumsolar (or “zodiacal”) emission is much fainter, even though it is dominated by emission from $T \sim 260\ \text{K}$ dust near the Earth. It is these two “foreground” components that Interstellar Probe will be mapping using the IRM in order to also accurately measure the much fainter EBL flux in the sky created by the light of all the stars in all the galaxies since the beginning of the universe (dark black regions). (Image credit: NASA/Cosmic Background Explorer [COBE] Science Team.)

Belt [KB]) dust cloud at 20–100 μm (Poppe et al., 2019). An ideal measurement would map the entire sky at both near-IR and far-IR wavelengths at $\geq 20'$ resolution with $\lambda/\Delta\lambda = R \sim 3$ as a function of heliocentric distance. Because this is unrealistic given the total integration time required to map the entire sky even at $20' \times 20'$ resolution (4 months assuming 30-second exposures for each $10' \times 10'$ field), we define “complete” science to be imaging enough of the sky during flight to perform a 3D tomographic reconstruction of the IPD spatial distribution in the solar system. Doing this will also require obtaining good look-back imagery of the entire cloud complex once Interstellar Probe is clear of it at $r_h > 100$ au.

Objective 3.1. As for circumsolar dust, light is also scattered and emitted by dust orbiting around and located between other stars in our galaxy. Unless pointing directly at a star, the ISM-created component dominates; we call this the diffuse galactic light (DGL), and studies of it teach us directly about the distribution and composition of dust in the galaxy at large, and indirectly about the physics controlling the dust. An ideal measurement would map the galaxy across all longitudes and to galactic latitudes $>30^\circ$ of the plane using the entire 0.5- to 100- μm passband with spectral resolution $\lambda/\Delta\lambda = R \approx 30$ in $20' \times 20'$ pixels. The shortest 0.5- to 5.0- μm portion of the passband is required to fully inventory scattered galactic starlight, while the longest 50- to 100- μm portion of the passband will be required to fully measure thermal emission from cold (15–30 K) ISM dust that is re-radiating absorbed galactic starlight.

Note that the same measurements made to map the circumsolar dust disk will also measure the DGL, as long as they are taken sufficiently far away from the Sun so that the Zody light contribution is small compared to the DGL. We thus define “complete” science to be a complete half-sky image of the dust emission acquired beyond 10 au.

Objective 3.2. Mapping the aggregate emission from galaxies in the universe is a critical test of cosmological structure formation theories. Light created by all the stars in all the galaxies of the universe has been created by gravitational accretion and fusion reactions since redshifts Z of 10–20. Thus, the VISNIR, 0.3- to 3.0- μm light we see dominating current stellar emission would be observable as 6- to 60- μm light from the very first stars. The 30- to 100- μm light dominating our galaxy’s dust-created DGL would appear as 600- to 2000- μm light from the very first galaxies. An ideal measurement would thus map the entire sky across the entire 0.5- to 100- μm waveband with spectral resolution $\lambda/\Delta\lambda = R \approx 30$ in $2''$ pixels, and also map large regions of the sky in approximately four far-IR spectral channels at $20''$ resolution with wavelengths centered at 30–200 μm . Because this idealized scenario places unrealistic requirements on a variety of systems, we define “complete” science to be imaging six fields over several square degree fields at least once beyond 10 au.

A.2.2.2.3 Instrumentation

The conceptual IRM instrument is illustrated in Figure A-13. It includes a modest 7-cm clear aperture (10-cm total aperture) telescope, 1D spectroscopic + four-channel photometric detector focal plane arrays (FPAs), and all of the flight systems required to measure VISIR cosmic backgrounds and planetary surfaces in a <4 -kg, <10 -W package. Its imaging capabilities are similar to those flown as

the New Horizons/MVIC+LEISA (Multispectral Visible Imaging Camera + Lisa Hardaway Infrared Mapping Spectrometer [formerly Linear Etalon Imaging Spectral Array]) instrument package to Pluto and 2014 MU69/Arrokoth (Reuter et al., 2008) but with a greatly expanded longer wavelength range out to $50\ \mu\text{m}$. We plan to use an $\sim 10\text{-cm} \times 20\text{-cm} \times 20\text{-cm}$ volume to house the scientific instrument and rely on the spacecraft for data telemetry, power, and attitude sensing and control subsystems. We would minimize risk by using commercially available, high-heritage, flight-tested systems, components, and subsystems, requiring no new technologies. Low-resolution near-IR spectrophotometry ($R = 300$ corresponds to $0.0055\text{-}\mu\text{m}$ spectral resolution at the $1.65\text{-}\mu\text{m}$ crystalline water absorption feature) will be performed through the use of linear variable filters, and the telescope and detector can be cooled to $30\ \text{K}$ through entirely passive means. Integration times will be configurable from milliseconds to kiloseconds to obtain four-orders-of-magnitude sensitivity on cosmic backgrounds and planetary surfaces. Planetary observations will be performed in time delay integration (TDI) mode, with active control of the fine instrument pointing, implemented through a scan mirror, gimble, and/or spacecraft slew. Data will be stored and returned as gigabyte-sized $1\text{K} \times 1\text{K}$ hyperspectral cubes.

IRM will use an off-axis free-form telescope design with three optical elements, as shown in Figure A-13.

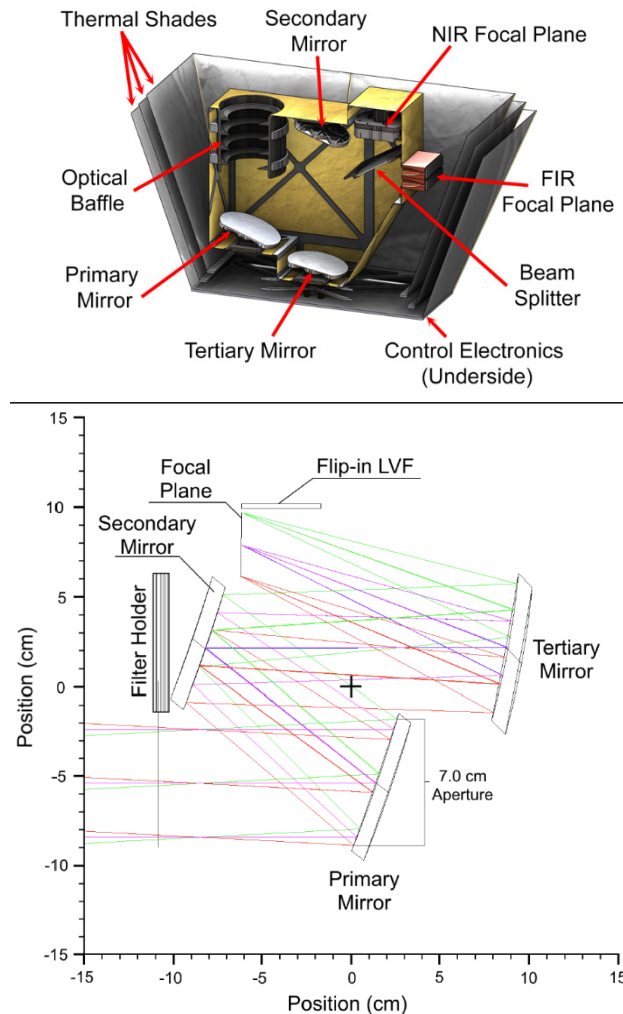


Figure A-13. Top, Schematic representation of our strawman IRM mapper instrument design. The telescope uses an off-axis three-element design and couples to a standard VISNIR HgCdTe detector patterned with a linear variable filter (LVF) for spectroscopic mapping, with the option for broadband far-IR channels through the use of a beamsplitter. Nested thermal shields efficiently reject radiant heat and help passively cool the FPA to $<10\ \text{K}$. The instrument would weigh $<5\ \text{kg}$ and require $\sim 5\ \text{W}$ to power. The current technology readiness level (TRL) of the instrument's components would support a 2030 launch. Bottom, A schematic representation of the Interstellar Probe IRM mapper optical chain. Low spectral resolution is achieved with an LVF that will be flipped into or out of the optical path as needed. The shutter in the filter mechanism could be used to verify the dark current of the system, and (space permitting) broadband filters for calibration purposes. Note: FIR, far-infrared; NIR, near-infrared. (Images courtesy of M. Zemcov.)

With a 7.0-cm effective aperture (10-cm primary optic), we calculate this telescope can image, at best resolution, 6" pixels over a $3.4^\circ \times 3.4^\circ$ FOV. We specify a longwave-enhanced 2048 \times 2048 pixel H2RG detector (Blank et al., 2011) or equivalent to increase flight heritage. The detector and telescope will be passively cooled to <10 K (beyond 50 au) using radiation shields, which have high heritage for astrophysics applications (e.g., Tauber et al., 2004). We will use a SIDECAR application-specific integrated circuit (Loose et al., 2005) to clock and read out the detector at the ambient temperature, simplifying the data-processing chain. The current instrument technology readiness level (TRL) at the component level is 9 except for the filter and passive cooling design, which is TRL = 5 until the SPHEREx launch in 2024 raises it to TRL = 9.

A custom onboard flight computer would be responsible for the following tasks: (1) processing the detector output, (2) passing the processed data to the spacecraft computers for later telemetry, and (3) executing a preprogrammed observing sequence. The onboard processing would be based on that described in Zemcov et al. (2016), and the data storage would be based on that developed by the Zemcov group for various sounding rockets (Park et al., 2018). We expect that commercially available radiation-hardened field-programmable gate arrays would be more than adequate to meet our computational requirements. Most of the rest of the spacecraft subsystems are available from the Interstellar Probe bus: data telemetry, power generation and storage, and attitude control during science observations.

A.2.2.3 *Instrument Trades*

A.2.2.3.1 *Possibility for Merging Astrophysics and Planetary Science Instruments*

The Visible-Infrared Mapper (VIR) is optimized for enabling geological and compositional analysis of the surface of a dwarf planet, and the Infrared Mapper (IRM) is optimized for astrophysics investigations, including measurements of the EBL from 0.5- to 100- μm wavelength. The IRM instrument has a full-instrument FOV of $3.6^\circ \times 3.6^\circ$, which is comparable to EIS and New Horizons/Ralph. The instantaneous (i.e., pixel) FOV is 30 μrad , enabling 300 m/pixel spatial scale on the surface of a dwarf planet from a 10,000-km flyby distance from the surface. Across 30 spectral channels, this would satisfy the planetary science requirements. However, as a purely framing camera and not a pushbroom, there may be several pixels of smear near closest approach, and the shortest wavelength end of 0.5 would ideally be reduced to 0.4 μm to include the entire visible spectrum to show a planetary target in true color.

Intensive observing campaigns built around several days of closest approach of these bodies will produce science data returns similar to the spectacular findings of the New Horizons mission at Pluto and 2014 MU69/Arrokoth, so we can expect multispectral compositional maps co-registered to high-angular-resolution photogeological maps of these new worlds. Like the New Horizons results of Pluto and Charon, these maps will revolutionize our understanding of the formation and evolution of these bodies with measurements unobtainable except via close (approximate distance of tens of thousands of kilometers) flyby.

The main difference between the astrophysical and planetary requirements will be the inclusion of high-speed (milliseconds to seconds) readout times, rapid slew and pointing capability ($>1^\circ/\text{s}$ and $<5''$), and high-precision pointing stability ($<1''$ over 10 seconds) to resolve landforms. These

can be included either in a gimbaled instrument or as augmentations of the spacecraft bus; for the sake of this study, we assumed they are provided as part of a stand-alone gimbaled IRM instrument. If the IRM assumed the planetary imaging capability alone, the impact to science would be lower (but still acceptable) spatial resolution, a loss of wavelength sensitivity shortward of 0.5 μm , and a loss of imaging redundancy.

If the VIR and IRM capabilities are absorbed into a single instrument, a future Science and Technology Definition Team (STDT) could consider re-manifesting the UV imager (see Section A.2.2.4.1 on the UV instrument) to study gases, hazes, and atmospheres around a dwarf planet, if they exist.

A.2.2.3.2 *Enhancing Technology Development: IRM Far-IR Channel*

The cooled far-IR detectors will require some form of active cooling to achieve ~ 4 K temperatures where they are optimally sensitive. Given the tight resource envelope of Interstellar Probe, this will require advances in miniature cryocooler technologies from the state of the art. We plan to investigate and develop solutions to this over the next 5 years, but if no solution is found, we can remove the far-IR channels at the loss of the far-IR science.

A.2.2.4 *Other Instrument Options*

Here we describe other instruments that we considered in the trades but did not fit into the mass, power, and ConOps constraints. We describe these to assist a future STDT. These instruments could be added to the existing payload or traded against the instruments, and we consider these instruments to be enhancing but not required. The options we consider here are an Ultraviolet Imager, a Solar System Lookback Camera, and a nose-mounted planetary imager for a purely spin-stabilized spacecraft.

A.2.2.4.1 *Ultraviolet Imager*

- Ultraviolet observations should be included for any dwarf planet with the potential for an atmosphere
- Adding UVS would enable studies of the cosmic UV background and hydrogen in the ISM
- Can be accommodated by spinning or three-axis spacecraft

UV Imager

Measurement Objective	Dwarf planet atmospheres; solar and stellar occultations; cosmic UV background; ISM hydrogen
Field of View	$2^\circ \times 2^\circ$ plus $4^\circ \times 0.1^\circ$
Instantaneous FOV	5 mrad/pixel
Channels	786 (46.5–188 nm)
Mass Allocations	4.35 kg
Power Allocations	5 W
Mission Requirements	Point near anti-ram after passage of dwarf planet
Accommodations	Coboresighted with IRM and VIR

An ultraviolet imaging spectrometer (UVS) would provide important information about dwarf planet atmospheres, the cosmic UV background, and hydrogen in the ISM, while also allowing for potential solar and stellar occultations. An imager with capabilities in the FUV would be ideal, with a wavelength range of ~50–200 nm. Although a UVS could reveal the composition of any hazes or atmospheres, we did not include this instrument in the augmented payload for this study because collisional gases are not expected around most known smaller dwarf planets. However, discovery of a tenuous atmosphere around a dwarf planet would be groundbreaking, so an additional future trade looking at the potential for including a UVS would be of high value.

A.2.2.4.2 *Solar System Lookback Camera*

- Acquire unresolved views of solar system planets
- Wide-field, color-framing camera
- Can be accommodated by spinning or three-axis spacecraft
- Part of the spacecraft could be in the FOV for “you are there” public engagement views

A simple, wide-angle framing camera could provide three- or four-channel views of giant planets using a Bayer pattern of filters over the imaging detector. The Rosetta Lander’s Comet Infrared and Visible Analyser (CIVA) camera offers suitable example heritage (Bibring et al., 2007). Such views could enable simple giant planet observations for the sake of exoplanet analog science as well as serve as a public engagement camera. This simple instrument could be accommodated on either the spinning or hybrid stabilized spacecraft and could be included regardless of whether Interstellar Probe flies by a planetary target. Beyond mentioning it here as a possible trade, we have not considered this camera further.

Solar System Lookback/Public Engagement Camera

Measurement Objective	Color images of unresolved planets
Field of View	60° × 60°
Channels	4
Mass Allocations	0.8 kg
Power Allocations	2.3 W
Data Rate (or Volume)	20 Mbit for planetary encounter
Mission Requirements	Spin-stabilized or three-axis-stabilized spacecraft, pointed toward the inner solar system when the spacecraft is in nominal cruise attitude; point away from Sun
Accommodations	Potentially mounted on rim of HGA; not cobsighted with other imagers

A.2.2.4.3 *Camera for Heliophysics Spinning Spacecraft for Planetary Reconnaissance*

- Planetary flyby imaging could be possible with a Sun-pointed spinner
- The ConOps for imaging is very different than for a three-axis-controlled spacecraft

SpinCam

Measurement Objective	Multispectral images of planetary surface features and distant planetary and astrophysical observations
Field of View	2.85°
Channels	10 (0.4–0.9 μm; 1.25–3.5 μm)
Mass Allocations	10 kg
Power Allocations	10 W
Data Rate (or Volume)	20 Gbit for planetary encounter
Mission Requirements	Spin-stabilized (~1 rpm) spacecraft only; fly within one planetary diameter of a dwarf planet’s surface (~1000 km)
Accommodations	Pointed in ram, clear of spacecraft structures. ½ FOV off from spacecraft spin-axis

Investigation. While most of our considerations for a planetary flyby assume a spacecraft that can operate in both spin and three-axis stabilization modes (the “augmented payload”), we also consider a planetary encounter using a small modification of the “heliophysics-only” payload in which the spacecraft lacks a three-axis mode and is only spin-stabilized. This “Helio+” configuration, which was not designed, represents a compromise between the heliophysics and augmentation payloads. Here, an imaging spectrometer (“SpinCam”) would be fixed, staring along the ram direction, and would use the spacecraft’s rotation to build up images on approach to a very close flyby of Orcus (or any dwarf planet). In this scenario, in which the camera stares nearly straight ahead, the precise timing of the B-plane crossing is much less important than in the three-axis mode because the target will be in the FOV during the entire approach.

Like its imaging counterpart on the three-axis/hybrid version of the spacecraft, this imaging system could conduct searches for satellites, rings, and hazards; create planet and satellite rotation movies; create parallax sequences; and image the approach hemisphere at ≤ 1 km/pixel (see technical specifications below). However, unlike its counterpart on the three-axis/hybrid version of the spacecraft, this camera would be incapable of creating high-resolution strips of images, or “noodles,” across cords of the target(s); it would only view the terminator obliquely and not face-on, and it would not be able to take look-back images after approach and thus would be limited in its ability to search for high-scattering atmospheric hazes. Such an imaging scenario would be equivalent to New Horizons lacking its highest-resolution Long Range Reconnaissance Imager (LORRI) camera and only returning color and hyperspectral imaging data from ~35,000 km away from Pluto (about three times its closest approach). Although not as detailed as what New Horizons ultimately captured of Pluto and Charon, such data, if they had been the only data returned at Pluto by New Horizons, would still have been sufficient for a hemispheric geologic map and otherwise revolutionary for our geophysical and compositional understanding of Pluto, Charon, and dwarf planets in general. This follows the adage, “most of something is better than all of nothing.”

Background. SpinCam will be a two-band imaging system with a multispectral VIS camera with a hyperspectral (450-channel) short-wave infrared (SWIR) camera. Both cameras will share the same telescope. The system will be forward-looking as part of a spin-stabilized spacecraft at 1 rpm (Figure A-14, below). It could operate from 42 au to 90 au, with the design baselined for 47-au operation for Orcus.



Figure A-14. The basic concept of operations for a camera on a spinning spacecraft, staring ahead and approximately aligned with the spin axis. This illustration uses a fictional instrument on a digital model of New Horizons. Top row: sunward of the spacecraft looking outward with the SpinCam rotating on the disc of a dwarf planet. Bottom row: anti-sunward of the spacecraft looking back to the inner solar system. Each subsequent frame shows the spacecraft and SpinCam rotated in a different direction.

Instrument Requirements. The instrument requirements have been designed to match New Horizons’ Ralph (Reuter et al., 2008), with the exception of the SWIR camera.

Requirement	Value
Field of View	2.85°
Instantaneous Field of View	VIS: 20 μ rad SWIR: 72 μ rad
Passband	VIS: 0.4–0.9 μ m SWIR: 1.25–3.5 μ m
Spatial Resolution	VIS: 20% modulation transfer function (MTF) at to-be-determined cycle/ μ rad SWIR: 20% MTF at to-be-determined cycle/ μ rad
Spectral Resolution	VIS: five channels \sim 100 nm wide and panchromatic SWIR: 5 nm/channel
Signal-to-Noise Ratio	VIS: 50:1 or greater at 42 au, 30% reflectivity SWIR: 10:1 at 42 au, 30% reflectivity
Scan Rate	1 rpm at 45,000 km
Size	To be determined
Mass	10 kg (to be determined)
Power	10 W (to be determined)

Optical System. To support the large focal plane and wide FOV, the optical system will consist of a telescope designed to provide a truncated ring field, with image sensors mounted in a circular pattern perpendicular to the scan direction. The ring-field geometry provides a large FOV

perpendicular to the scan direction, while simplifying the optical design by reducing the number of field angles it must be optimized over.

To meet the signal-to-noise ratio (SNR) at 42 au, the telescope needs have a fast focal ratio of $f/4$. All mirrors will be coated with a high-reflectivity silver for maximum throughput over the entire passband. The focal length shall be 500 mm to provide a $20\text{-}\mu\text{rad}$ IFOV with $10\text{-}\mu\text{m}$ pixels.

To make the system as light as possible and insensitive to thermal variations, an M55J-composite structure with lightweight Zerodur mirrors is assumed. This is similar to the Didymos Reconnaissance & Asteroid Camera for OpNav (DRACO) instrument on Double Asteroid Redirection Target (DART), which was chosen because of the large thermal gradients that are created as a consequence of being buried within the spacecraft. If the thermal environment allows, an athermal all-beryllium system could also be used for greater weight savings.

VIS Camera. The VIS camera will consist of six linear complementary metal–oxide semiconductor (CMOS) image sensors supporting up to 64 stages of on-chip TDI. The notional sensor will be similar to the Teledyne e2v CIS125 CMOS-charge-coupled device (CCD; Pralong et al., 2019; Figure A-15) with $10\text{-}\mu\text{m}$ pixels and 2048 columns with fully digital output and low read noise. The CIS125 is a CMOS but reads out of a CCD register, and the CCD is fabricated using the CMOS process.

While Figure A-15 shows a large array with multiple pan and spectral channels, the device for the SpinCam will only require one panchromatic and five spectral channels. Assuming a backside illuminated configuration with good antireflection coating, a high average quantum efficiency of $>80\%$ can be assumed for the 400- to 800-nm bands, and $>50\%$ can be assumed for the 800- to 900-nm band.

Exposure between channels will be adjusted by modifying the number of TDI stages required while synchronizing the readout rate to image motion; the sensors can be clocked for any reasonable rate. The expected performance is listed in Table A-3. Because of the differences in linear velocity from the center to the edge of the FOV, a higher amount of blur will be present in the outer ring. This may be mitigated by increasing the angle from the spin-axis center (creating a “donut” image with a small blind spot in the center), which would eliminate the columns of essentially stationary

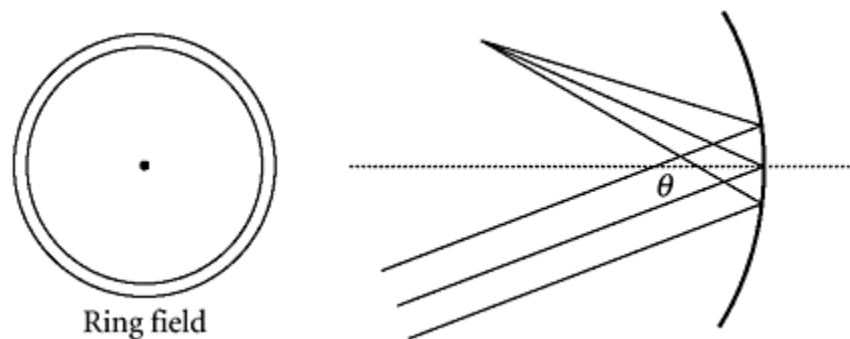


Figure A-15. The ring-field geometry. Note that although an image sensor (or set of image sensors) can be placed anywhere within the ring, the field angle is always the same. (Image credit: Johns Hopkins Applied Physics Laboratory.)

pixels at the inside of the FOV. The goal would be to optimize this off-axis distance against loss of on-spin-axis FOV to reduce the velocity variation across the image plane as much as possible. This will also improve the SNR. However, such donut imaging may be deleterious to OpNav and other long-range imaging along the spacecraft’s velocity vector.

Another option for eliminating smear in the multispectral bands would be to use multiple image sensors staggered across the field and clocked at different TDI rates, such that they are physically short enough in the cross-track direction to not have significant velocity variation.

SWIR Camera. The SWIR-channel camera will notionally use an HgCdTe sensor like the Teledyne CHROMA-D, with an 18- μm pitch, 1024 \times 512 pixels, and fully digital output (Jerram & Beletic, 2019). This image sensor also provides the high frame rate required for line scanning operation.

This camera will consist of a Dyson spectrometer to split the incoming light into at least 450 channels (Lobb, 1997), which will be cooled by a multistage radiator on the anti-sunward side of the spacecraft. A relay train will be used in the camera to reduce the focal ratio to f/1. While this decreases the spatial resolution, it increases the focal plane irradiance by a factor of eight. Even with this, pixel binning will still be required to achieve a high SNR when at distances of >42 au.

Table A-3. Estimated camera performance at 90 au, with 64 stages of TDI and a spacecraft-to-target distance of 45,000 km.

Channel	Estimated Signal-to-Noise Ratio
PAN	>50
400–500 nm	>50
500–600 nm	>55
600–700 nm	>55
700–800 nm	>50
800–900 nm	>20

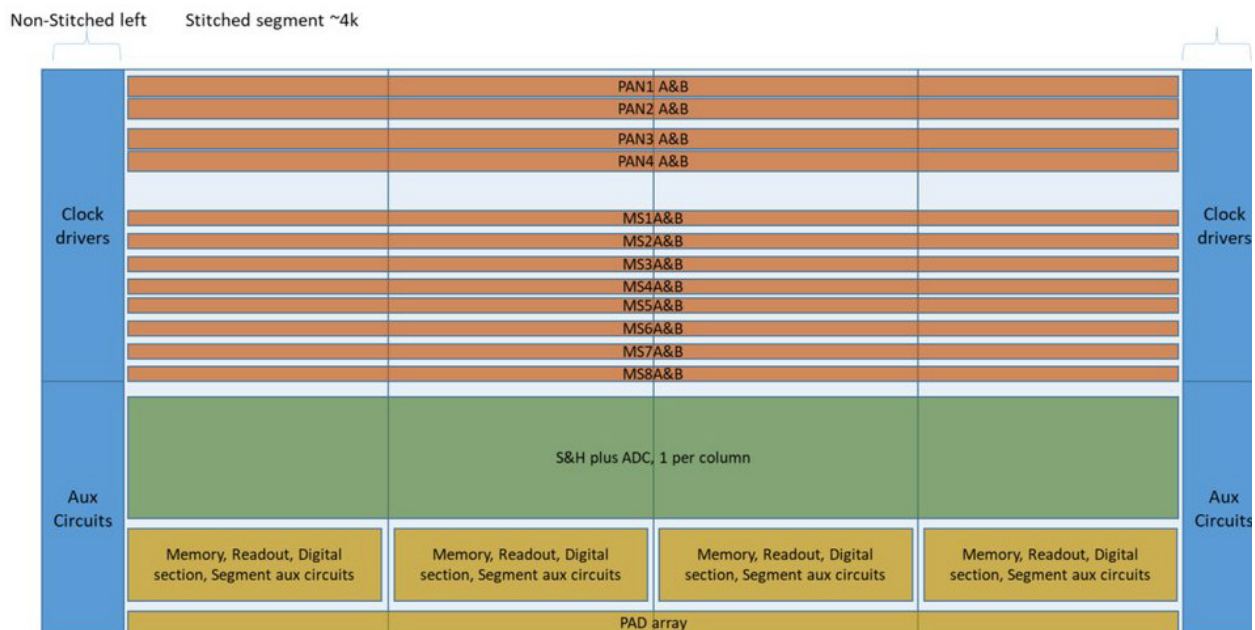


Figure A-16. The CIS125 visible imaging sensor chip as designed for the Centre for Earth Observation Instrumentation (CEOI) program of the UK Space Agency. Note the use of stitching (a method to create semiconductors of arbitrary size by patterning a mask across the wafer), allowing the number of channels and size of the array to be customized. Pixels on the CMOS are read out at the column level. (Image credit: Johns Hopkins Applied Physics Laboratory.)

Because of the narrower spectral bands, 2-pixel binning and multiple scans will be required to meet the necessary SNR of the instrument when at 42 au, as shown in Table A-3, above. While this means the SWIR camera will have lower spatial resolution, it is anticipated that techniques such as panchromatic sharpening will be used to improve the image quality of the final data product.

A.3 Augmented Example Payload and Trades

A.3.1 Example Payload and Accommodation Trades

The baseline example payload was adjusted to account for an augmented payload that could capture planetary science and astrophysics, while maintaining the engineering constraint requiring a payload between 80 and 90 kg. In this case, we assume a spinning spacecraft that is also able to despin and perform measurements in a three-axis state. Given these parameters, 11 representative instruments were selected for the augmented payload.

There were a range of cameras to choose from. One could fly a VISNIR imager (VIR), which would enable observations of planetary surface features, distant (i.e., unresolved) planets and TNOs, and the cosmic background, as well as sensing of the ISM in this wavelength band. The wavelength range would be $\sim 0.4\text{--}4\ \mu\text{m}$. Missions such as New Horizons would provide heritage for these instruments. An interstellar probe would also be able to observe the diffuse red-shifted light emitted by the universe beyond the dominant zodiacal cloud foreground that obfuscates such studies when performed within our heliosphere. To examine this EBL, a visible-infrared spectral mapper (IRM) with two wavelength ranges of $0.5\text{--}15\ \mu\text{m}$ and $30\text{--}100\ \mu\text{m}$ would complement the payload. Heritage for an instrument such as this can be found in missions like Spitzer and New Horizons.

The VIR imager (Figure A-17) was chosen to focus on planetary science for the augmented payload. Observations would require the spacecraft to operate in three-axis mode, and the location of the camera would need to be relatively cold. The camera would need to point away from the Sun as well as the spacecraft ram direction and would need to avoid having any other instrument or piece of the spacecraft in its FOV. It would be cobsighted with any other camera onboard (other than the potential Solar System Lookback Camera) so that flyby observations could be made by all cameras, and would ideally be $\sim 90^\circ$ away from the NMS so that the camera could take images during the flyby



Figure A-17. VIR and IRM shown above the particle suite boom, respectively. They are pointed 90° to the spacecraft ram direction. (Image credit: Johns Hopkins Applied Physics Laboratory.)

EXAMPLE MODEL AUGMENTED PAYLOAD

Payload Mass and Power

89.1 KG | 90.2 W

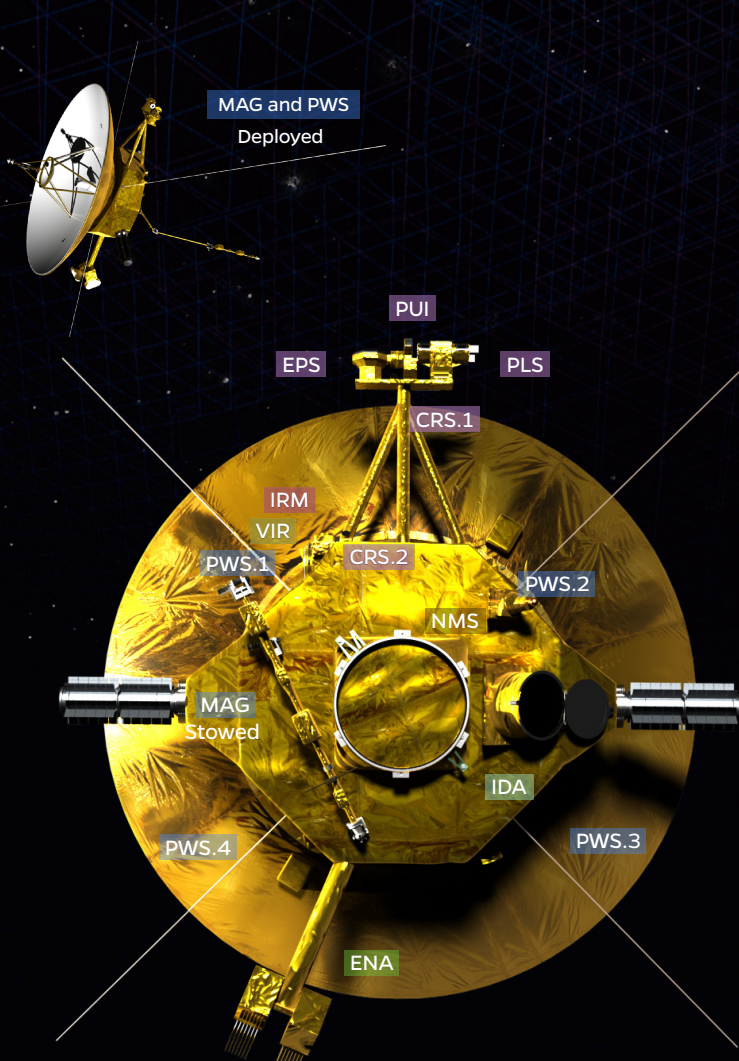
PERCENTAGE OF SCIENCE OBJECTIVES ADDRESSED



PERCENTAGE OF PAYLOAD MASS



INSTRUMENT <i>Heritage</i>	MEASUREMENT REQUIREMENTS	MISSION REQUIREMENTS	SCIENCE DRIVER
Magnetometer (MAG) (MMS/DFG)	0.01–100 nT; 0.01 nT (1e–8 nT ² /Hz turb.)	≤60 s; (100 Hz)	Two FG, 10m boom LISM (turbulence)
Plasma Waves (PWS) (Van Allen/EFW)	~1 Hz–5 MHz; Δf/f ≤ 4% (≤0.7 μV/m @ 3 kHz)	≤60 s ≤4 s at TS	4 x 2.5 m stacers + sounder; (4 x 50 m wire deployables—high mission risk)
Plasma Subsystem (PLS) (PSP/SWEAP/SPAN-A)	< 3 eV/e to 20 keV/e e, H ⁺ , He ⁺ , He ²⁺ , C ⁺ , N-O ⁺	~4π; ≤60 s	Spinning Flows, n _e , T _e , n _i , T _i Force balance
Pick-Up Ions (PUI) (Ulysses/SWICS)	0.5–78 keV/e H, ² H, ³ He, ⁴ He, ⁶ Li, ¹² C, ¹⁴ N, ¹⁶ O, ²⁰ Ne, ²² Ne, Mg, Si, Ar, Fe, charge states	iFOV ≥ 90° x 15°	Spinning Interstellar, inner PUI Force balance
Energetic Particles (EPS) (PSP/EPI-Lo)	20 keV–20 MeV H, ³ He, ⁴ He, Li, C, O, Ne, Mg, Si, Ar, Fe	~4π; ≤60 s	Spinning S/W, HS and ACRs Force balance
Cosmic Rays (CRS) (PSP/EPI-Hi, in development)	H to Sn; 10 MeV/nuc–1 GeV/nuc; m/Δm ≥ 10 electrons; 1–10 MeV	2 directions; hours	Spinning ACRs, GCRs LiBeB cosmic story
Interstellar Dust Analyzer (IDA) (IMAP/IDEX, in development)	1e–19 to 1e–14 g, 1–500 amu; m/Δm ≥ 200	iFOV ≥ 90°	Ram direction Coboresighted NMS ISDs, galactic heavy ion composition
Neutral Mass Spectrometer (NMS) (LunaResurs/NGMS, JUICE/NMS)	H, ³ He, ⁴ He, ¹⁴ N, ¹⁶ O, ²⁰ Ne, ²² Ne, ³⁶ Ar, ³⁸ Ar, m/Δm ≥ 100	iFOV ≥ 10°; weekly	Ram direction Coboresighted IDA LISM composition
Energetic Neutral Atom Imager (ENA) (IMAP/Ultra, in development)	~1–100 keV H	iFOV: ≥ 170°	Spinning, 2 heads Shape, force balance, ribbon/belt
Visible–Near–IR (VIR) (New Horizons/Ralph)	0.4–4 μm; ≥ 5 ch. ≤0.975 μm; >240 ch. >0.975 μm	iFOV: 5–20 μrad FOV: 2.3–5.7°	3-axis; perp. to spin Coboresighted IRM Planetary flyby surface geology & composition
Visible–IR Mapper (IRM) (New Horizons/LEISA, CIBER-2, in development)	0.5–15 μm 30–100 μm	NIR: 0.075 mrad/1° FIR: 3 mrad/0.2°	3-axis; perp. to spin Coboresighted VIR Dust disk, surface comp., ISM dust, EBL



while the NMS is pointed to ram to maximize inflow of planetary atmosphere, assuming an atmosphere exists on the flyby target. The above requirements resulted in accommodating the camera on the side of the spacecraft, pointing perpendicular to spacecraft ram. The pointing accuracy would need to be $<1024 \mu\text{rad}$, while the pointing knowledge would need to be $<471 \mu\text{rad}$.

Coboresighted with the VIR is the IRM spectral mapper (Figure A-17), included in the augmented payload in order to meet astrophysics and planetary flyby requirements in the STM. Depending on the camera design, observations could either be made on a slowly spinning spacecraft or would require pointing in three-axis modes. If the camera is to include a far-IR channel, a cryocooler will be needed to get down to 4–15 K, while the near-IR channel would only need thermal shades to passively cool to ~ 30 K. The camera pointing is consistent with requirements, including avoiding staring at the Sun and pointing the umbrella of the camera out to cold space, as well as being properly angled to accomplish the desired science and avoid FOV conflicts. The camera is located close to the VIR, and boresighted with it, in order to be as far from the radioisotope thermoelectric generator heat as possible. Pointing accuracy and pointing knowledge are both estimated at $<1000 \mu\text{rad}$ and $<7.5 \mu\text{rad}$, respectively, while jitter requirements would be $<10 \mu\text{rad}$ over 0.05 seconds.

The requirements outlined in the baseline payload remain the same for MAG, PLS, PUI, EPS, CRS, NMS, IDA, and ENA in the augmented payload, while LYA is not included in the augmented payload. However, the PWS instrument needed to be adjusted to account for the three-axis phases of the augmented ConOps. Replacing the 50-m wire antennas are four 2.5-m rigid stacers (Figure A-18), still perpendicular to the spacecraft ram direction and 90° apart from each other to measure two of the field components. Additionally, a sounder is accommodated to enhance the instrument.

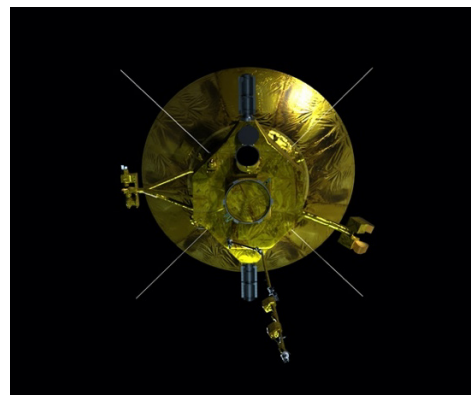


Figure A-18. A view of the bottom of the spacecraft, showing the shorter, rigid PWS antennas. (Image credit: Johns Hopkins Applied Physics Laboratory.)

A.3.2 Science Trades against Baseline Mission

A.3.2.1 Plasma Wave Subsystem

Centrifugally deployed Plasma Wave Subsystem (PWS) wire boom antennas will not work during a three-axis-stabilized flyby unless they are rigid. Several rigid antenna designs exist, including the “tape-measure” design of Voyager 1 and 2 (Lang & Peltzer, 1977) and the “whip” antennas of Parker Solar Probe (Bale et al., 2016). Because PWS performance depends on the ratio between the antenna length and cross section, the performance of thin, centrifugally deployed wire boom antennas is far superior. The 10-m Voyager/PWS rigid antennas were able to provide measurements of electron density during shock waves in the VLISM (Gurnett & Kurth, 2019). However, measurements of the hot, tenuous plasma of the heliosheath were not possible using the Voyager antennas.

Centrifugal deployment of long wire antennas after a three-axis-stabilized flyby of a KBO or dwarf planet has been considered but poses severe risks to the mission given the round-trip light time of 11 hours at 40 au and the fact that the flyby would be autonomous, like what was done on New Horizons. In the current example augmented payload, four 2.5-m rigid root stacers mounted in the spin plane have been considered for Jovian science. While centrifugal deployment of longer wire antennas from those root stacers is technically possible for a near-Earth mission, such a deployment in the outer solar system remains a Level-5 mission risk rating, but could be studied in future trades.

A.3.2.2 *Lyman- α Science*

Mapping observations of Lyman- α emission backscattered from hydrogen in the heliosphere and beyond is a powerful technique to probe the properties of interstellar hydrogen atoms and their modification due to coupling with heliospheric plasma. Study of the hydrogen wall is a primary science investigation, with the Lyman- α measurements enabling for the first time the ability to determine its location and 3D structure. As interstellar hydrogen meets the heliosphere, it charge exchanges with plasma in different regions to form, for example, the hydrogen wall region with heated and decelerated ISM plasma, the heliosheath with hot slowed-down solar wind, and the region inside the termination shock with the supersonic solar wind. Hence, the hydrogen velocity distribution function not only reveals how the pristine hydrogen flow is changed by the interaction with the heliosphere boundary region but also holds information about the global heliosphere structure and dynamics. Observations of the spectral shape of the Lyman- α emission line along different directions in the sky enable us to quantify properties of various populations of hydrogen atoms, such as density, velocity, and temperature, and understand their origin and variations across the heliosphere boundary and with the solar cycle. See Section 4.1.7 for more information on Lyman- α measurements.

The lack of Lyman- α measurements on the Interstellar Probe because of a trade resulting from the augmented payload will result in a loss of ability to perform the following investigations: (1) provide constraints on the hydrogen velocity distribution in the heliosphere; (2) understand the origin of hydrogen atoms with different properties and their evolution; (3) constrain the density of hot hydrogen originating in the heliosheath and probe a topology of the heliospheric boundary with independent diagnostics with Lyman- α measurements; and (4) separate local Lyman- α emission from interstellar hydrogen and the galactic emission, and also identify galactic and extragalactic components of Lyman- α .

The NMS will measure densities and elemental abundances along the Interstellar Probe trajectory; however, this science will be recovered with a loss of any information on the velocity or temperature of neutral gas. For example, NMS observations will enable determination of the location of the peak neutral density in the hydrogen wall and gas composition in this region but will still leave a gap in understanding the velocity and temperature distribution of hydrogen and mapping the 3D structure of the wall. See Section 4.1.6 for more information on neutral gas measurements.

A.4 Science Operations

A.4.1 Mission Timeline

The augmented mission for Interstellar Probe consists of launch, a Jupiter flyby, and then phases through the heliosphere, heliosheath, and interstellar space as the spacecraft journeys farther from Earth (see mission timeline foldout). Planetary augmentations to the baseline mission include a possible flyby of an outer-solar-system body, which would occur in the heliosphere phase as described below. Astrophysics augmentation activities would occur in the heliosphere through interstellar phases of the mission and will be conducted at high spatial resolution during three-axis-pointed mode and at low resolution at far-IR wavelengths during spin-stabilized mode.

We consider a range of actual launch readiness years of 2036–2041 (which does not negate 2030 as the year for all technology to be sufficiently mature). The first augmented mission measurements, pointed observations of the circumsolar dust disk, will occur within the first few months after launch at 2 au and again at 5 au from the Sun. The first complete augmented scientific studies, of the DGL and EBL, will be conducted within 2 years from launch when the spacecraft has passed by 10 au from the Sun; performing these studies as soon as possible will take advantage of the highest data relay rates available while Interstellar Probe is closest to Earth. DGL and EBL studies can continue along with further circumsolar mapping activities at 10-, 20-, and 50-au heliocentric distance, preferably in three-axis-pointed mode. Key EBL measurements will be made within 2 years of any launch date. Once Interstellar Probe is past 30 au, KBO flybys become available. Reaching any dwarf planet is possible—depending on launch year—depending on the position of Jupiter. In 2036, reaching Orcus and its moon Vanth could be possible; in 2041, Quaoar and its moon Weywot would be reachable. Interim years have other dwarf planet flyby potentials, as discussed in Section A.1.6.1.

A potential augmented mission timeline with the duration for each phase is shown in Table A-4.

Table A-4. Interstellar Probe mission phases.

Mission Phase	Time Period	Duration (Months)	Duration (Years)
Launch and Checkout	Commissioning	2	0.17
Cruise to Jupiter	Cruise to Jupiter (includes boom and payload deployments)	7	0.58
Jupiter Gravity Assist	–5 weeks to +3 weeks	2	0.17
Heliosphere Phase (includes possible outer-solar-system-body encounter)	Jupiter to 90 au	143.29	11.94
Heliosheath Phase	90–120 au	49.43	4.12
Interstellar Phase to 50 Years* (includes possible astrophysics augmentations)	120–352.4 au	396.40	33.03
Interstellar Phase >50 Years	352.4–1000 au	1110.17	92.51

*End of nominal mission

The augmented mission will substitute shorter rigid antennas for the wire boom antennas used in the baseline mission, so payload deployments and instrument calibration can occur before the JGA for the powered JGA option depending on detail of the magnetometer boom. Other than IRM

mapping of the circumsolar dust disk at $r_h \sim 2$ au, most primary science operations begin after the JGA. As with the baseline mission, operations are simple with predefined sequences that are consistent throughout the mission, with the addition of specific activities for possible planetary encounter and/or astrophysical investigations such as imaging of the heliosphere.

A.4.1.1 Launch and Checkout Phase

Launch and checkout is a 2-month period that begins at launch. There is continuous 24-hour communication with the spacecraft using Deep Space Network (DSN) 34-m antennas for the first week after launch. Then the communication coverage drops to daily 8-hour contacts using DSN 34-m antennas for 3 weeks. For the second month, communication is reduced further to an 8-hour contact 5 days per week, also using DSN 34-m antennas. The launch correction maneuver, spacecraft commissioning, and instrument commissioning, including deploying the magnetometer boom, will be performed during this phase.

A.4.1.2 Cruise to Jupiter Phase

The early cruise from Earth to Jupiter is expected to last less than a year, and spacecraft and instrument commissioning continues, including additional payload deployments such as for the rigid antennas. The DSN coverage decreases further to three 8-hour contacts with DSN 34-m antennas per week. During this phase, the team will prepare for the JGA.

During these months, observations of the diffuse sky and of the system will serve as checkouts, operational tests, and calibration of the remote-sensing instrument suite. Novel science may result from these observations, although the main intent is to gain familiarity with instrument and spacecraft performance and ConOps as a dress rehearsal for the next DGL/EBL, circumsolar dust disk, and future dwarf planet flyby activities, much as New Horizons did during its Jupiter encounter in 2007.

These observations of the Jovian system could include planet and satellite rotation curves and photometry observations, atmospheric changes on Jupiter, volcanic changes on Io, plume searches above Europa, and any observations that could be complementary to other missions, such Europa Clipper and/or JUICE. Distant observations of other solar system planets could serve as exoplanet analog observations.

A.4.1.3 Jupiter Gravity Assist Phase

Statistical targeting trajectory-correction maneuvers (TCMs) are assumed at -30 days and -10 days before the JGA, with a statistical cleanup maneuver at $+10$ days after the Jupiter flyby. To support the statistical maneuvers, DSN communication coverage increases 5 weeks before the Jupiter flyby for navigation tracking, increasing back to five 8-hour tracks per week for 4 weeks, then increasing again to seven 8-hour tracks the week before the flyby and continuing through the week after the flyby (3 weeks total).

There are opportunities for science measurements during the JGA, in particular if the JGA is unpowered. Such science could include planet, ring, and/or satellite observations. However, certain mission rules such as power and radiation requirements may dictate keeping instruments

turned off during the Jupiter encounter. After the Jupiter flyby is complete, the science data will be played back using the DSN 34-m antennas and the spacecraft HGA.

A.4.1.4 Heliosphere Phase (Jupiter to 90 au)

Once commissioning is complete after the JGA, Interstellar Probe enters the heliosphere phase. During the heliosphere phase, Interstellar Probe is operating continuously with all instruments on and collecting data; this is similar to the baseline mission from an operational perspective.

The first augmented mission measurements, pointed observations of the circumsolar dust disk, will occur within a few months after launch at 2 au. Calibration and start-up activities will also be occurring during this time, and the inner Zody Cloud is relatively well mapped and understood from Earth-based observations, so we do not regard the first ~ 2 -au circumsolar dust disk measurements as absolutely critical; they can also be conducted as far out as 3 au. By contrast, the next set of circumsolar dust disk measurements at ~ 5 au from the Sun are critical because they will return some of the best evidence for the effects of being outside the main asteroid belt dust source but close to the Jovian dust stream and Trojan cloud sources. Whether to conduct these measurements before or after the JGA remains to be determined; after might be better to allow the mission to better focus on JGA ConOps and scientific activities planning. At ~ 10 au, the first complete augmented scientific studies of the DGL and EBL will be conducted within 2 years from launch when the spacecraft has passed by 10 au from the Sun; while these measurements can be taken anytime after (and, in fact, will only improve as we leave more and more of the Zody dust behind the spacecraft), performing them as soon as possible will take advantage of the highest data relay rates available while Interstellar Probe is closest to Earth. DGL and EBL studies can continue along with further circumsolar mapping activities at 10-, 20-, and 50-au heliocentric distance, preferably in three-axis pointed mode.

Once Interstellar Probe is past ~ 30 au, KBO flybys become available. These activities are unique events, the most likely of which is a flyby of an outer-solar-system body, such as a dwarf planet. In this case, the activity will include several months of detailed planning and command load development, rehearsals, distant observations, and the execution of the flyby. After the event, data recorded during the flyby will be downlinked, possibly requiring a period of several months of modestly increased contact time with the spacecraft. Opportunistic multispectral and multiphase image sequences of solar system giant planets will serve as analog observations for exoplanet observations (see Section A.1.6.3).

Other opportunistic observations during the inner heliosphere phase could include small-body observations. Small-body observations need not necessarily involve propellant because some could be obtained from staring. We expect many opportunities to exist: after the first few years of the Vera C. Rubin Observatory's Legacy Survey of Space and Time (LSST), it is expected that $>45,000$ TNOs will be known (e.g., Schwamb et al., 2018). Assuming that current population statistics hold, 35% of that number will be cold classical Kuiper Belt objects (CCKBOs), which have orbital inclinations $<5^\circ$ and semimajor axes between 42 and 47 au. If the resulting 16,000 CCKBOs are taken to be uniformly distributed in a flat ring, the chance of making a serendipitous flyby

comparable to that of New Horizons' flyby of Pluto (~15,000 km), following a trajectory radially outward from the Sun, is ~1 in 100,000.

It is unlikely that both a planetary and small-body flyby could occur. For fast planetary flyby missions, altering the spacecraft's trajectory is expensive with regard to propellant. New Horizons offers an instructive analogy: To reach the KBO Arrokoth after the Pluto system flyby at ~14 km/s, a 0.1° TCM was required, which consumed 12 kg of hydrazine propellant out of New Horizons' original 77 kg of usable hydrazine. For Interstellar Probe's much faster speed and comparable propellant quantities, second targets would be even more resource intensive. To visit both the dwarf planets Quaoar (42 au) and Gonggong (92 au) with an angular separation of ~7° in the mid-2030s, an untenable 4.1 km/s of velocity change would be required. Thus, we anticipate that Interstellar Probe could only fly by one planetary target. A future science definition team could elect to prioritize a small body over a dwarf planet. If a small-body flyby does occur, the imaging ConOps would be essentially the same as described for a dwarf planet flyby (see Section A.3 [Augmented Example Payload and Trades] and Section A.4 [Science Operations]).

Outside of these special events, the communications plan during this phase is similar to the baseline mission.

Mission Operations Planning

Command loads are sequences of software commands that the spacecraft's onboard computer executes to control the spacecraft, and controllers upload them from the ground during flight. Different phases of the mission use specially built command loads; they are developed on the ground, tested and refined on ground-based duplicates of the flight computer, and only then transmitted ("radiated") to the spacecraft. Once successfully uploaded, the option exists for the spacecraft to execute the command load as practice, before the load is needed for a specific event. For instance, New Horizons executed its Pluto–Charon flyby command load before the actual encounter, even going so far as to fire its thrusters to point the spacecraft and its imagers as though it were flying by its future targets. We anticipate similar command load ConOps for Interstellar Probe.

Command loads can be for arbitrarily long or short portions of the mission. For New Horizons, four loads were built before Pluto system closest approach, which accounted for between 4 and 9 days during this highly dynamic time. Because of New Horizons' limited onboard memory, up to 50% of memory could be used for a given load. Interstellar Probe will not be as limited with regard to memory.

A.4.1.5 *Heliosheath Phase (90–120 au)*

The heliosheath phase in the augmented mission is similar to this phase in the baseline mission from an operational perspective. During this phase, specific activities, such as look-back circumsolar dust disk imaging, could be planned to meet augmented science objectives, with these activities expected to cover relatively short time periods of weeks to a few months. However, considering the high-priority heliospheric science studies to be performed during the heliosheath phase by Interstellar Probe as well as the lack of identified critical science activities, augmented

science activities can easily “take a back seat” and become secondary to heliophysics primary science measurement goals. Some increased planning will be conducted as part of each activity, and some modest increase in downlink time may be needed after each activity for a short time to allow for downlink of data recorded during that activity.

A.4.1.6 Interstellar Phase to 50 Years

The interstellar phase in the augmented mission is similar to this phase in the baseline mission from an operational perspective, with the addition of circumsolar dust disk measurement activities. These activities include the usual forward hemisphere in situ mapping but also a new activity: turnaround look-back mapping of the entire cloud in its full extent. Because the edges of the KB are currently poorly determined, it is unknown exactly how far out Interstellar Probe will need to be to obtain a map of the full extent, so preliminary planning has look-back imaging occurring at 130 au, 200 au, and greater. These cloud measurement activities are expected to cover relatively short time periods of weeks to months. Some increased planning will be conducted as part of each activity, and some modest increase in downlink time may be needed after each activity for a short time to allow for downlink of data recorded during that activity.

A.4.1.7 Interstellar Phase to 1000 au

After operating for 50 years, Interstellar Probe will continue into interstellar space. It will take approximately another 92.5 years to reach 1000 au. During that time, the augmented mission will be similar to the baseline mission, with special activities planned to fit within available resources. As with other phases, these activities will be relatively short and can be accommodated within the overall operations of the mission.

A.4.2 Telecommunications

Telecommunications for the augmented mission are similar to, and use the same resources as, the baseline heliospheric mission. No additional ground stations with regard to the baseline requirements are needed, and the onboard telecommunications subsystem is identical to the baseline heliospheric mission.

For most activities for augmented science objectives, the change in data volume to be downlinked can be accommodated within the downlink schedule developed for the baseline mission. However, if a planetary body flyby is included in the augmented mission, some increase in the downlink schedule will be needed.

A.4.3 Operations

For a mission as long as Interstellar Probe, the key to keep Phase E operations costs low is to keep the operations as simple as possible. Day-to-day operations for the augmented mission are similar to the baseline mission; although specific activities may be different, the operations team and systems to support them are the same.

A.4.3.1 *Coupled versus Decoupled Operations*

The augmented mission will use decoupled operations similar to Parker Solar Probe as planned for the baseline mission for all activities except a planetary body flyby. For this event, a high degree of coordination is needed, and we will use planning and activity validation/verification processes similar to those used on New Horizons to plan, practice for, and execute the flyby.

A.4.4 *Data Management*

Science data are recorded on or transferred to the spacecraft solid-state recorder by the instruments in the augmented mission just as for the baseline mission. Many more science data will be recorded than can be played back. Because of this, a science data selection plan will be required that may differ from the baseline plan in details. As discussed above, the augmented mission activities fit within the data volumes for the payload as a whole in the baseline mission, although individual instrument allocations differ. The exceptions of a planetary body flyby and distant planetary observations are also discussed above.

A.4.5 *Flyby Imaging*

Unlike the all-sky astrophysics measurements, for which the target object “is always there,” to reach a specific dwarf planet via a JGA, Interstellar Probe would need to launch in a specific year. Precise knowledge of the dwarf planet’s position is necessary to successfully execute a reconnaissance flyby. While a planet’s right ascension and declination are well known, its solar distance is less well constrained. The plane where the spacecraft reaches closest approach is called the body plane, or B-plane, and for a fast flyby, this point could be almost directly above the terminator (boundary between light and dark). The uncertainty in the target’s solar distance propagates to uncertainty as to when the spacecraft “pierces” the B-plane; however, this uncertainty can be significantly reduced by stellar occultation observation campaigns from Earth-based assets as well as observations from the spacecraft during approach, called optical navigation (OpNav). These will also inform where to point to image any moons. Refinements in the dwarf planet’s orbital elements will translate to higher certainty for the timing of flyby observations and for calculating the ΔV required for any TCMs by the spacecraft.

Spacecraft OpNav imaging campaigns would need to begin ~ 1.5 years before closest approach of the target dwarf planet. Such refinements in knowledge of the target’s orbit relative to the spacecraft are necessary to allow for precise aiming and timing for imaging the planet. This updated state information will allow for any TCMs to be planned and executed. As the flyby uncertainty is reduced, so too are the imager pointing and timing. Earth-based stellar occultation campaigns can be used to refine their orbit solutions. Such a ground observation campaign was used by the New Horizons mission to constrain the size, rotation, and orbital characteristics of the TNO Arrokoth (2014 MU69). The New Horizons team deployed 25 small telescopes around South America and southern Africa to record occultation chords as the body passed in front of a star (e.g., Buie et al., 2020; Porter et al., 2021).

A.4.5.1 Dwarf Planet Approach

Based on New Horizons' encounter with Pluto, 2–3 days before closest approach has been considered the last safe time to update sequence pointing and timing (Harch et al., 2017). Closed-loop autonomous navigation could obviate human-in-the-loop sequence updating. Closest flyby distance will be chosen to optimize image coverage and surface pixel scale and will likely range from several thousand to several tens of thousands of kilometers. In the days to weeks leading to closest approach to the dwarf planet, a VISNIR imager could search for previously undiscovered satellites and rings, both of scientific interest and for documenting and avoiding hazards to the spacecraft. Rotation movies and photometry measurements of the planet and any moons will also occur during this time.

A.4.5.2 Dwarf Planet Flyby

The flyby to the dwarf planet could range from ~5000- to 40,000-km distance from the surface, comparable to Pluto's flyby distance of Arrokoth (~3000 km) and Pluto (~12,000 km). Assuming a ~5000-km distance, which was chosen to allow mass spectroscopy measurements of any exosphere, the spacecraft will switch from spin-stabilized to three-axis control to allow tracking of the planet and any moon by the imaging spectrometer. Because of the relatively fast rotation period of many dwarf planets (several to a few tens of hours; much faster than Pluto's 6.39-day period), more of the encounter hemisphere will be observed, and with more spin-enhanced parallax imaging than was possible during New Horizons' encounter with slow-spinning Pluto. Repeat imaging with parallax offset is necessary for deriving the 3D topography and terrain models required for achieving the geological and geodetic science goals. Parallax caused by spacecraft motion will also allow multiphase-angle (Sun–target–spacecraft angle) images of the targets to better constrain the geology, composition, and photometric properties. Much like New Horizons at Pluto, imaging (Figure A-19) will cover the entire encounter hemisphere, becoming higher-resolution rectangular image mosaics and, at even closer distances, very-high-resolution strips or “noodles” across chords of the planet and any moons. Around closest approach, imaging at the planet's terminator will reveal topography through the low-Sun-angle images. Spatial resolutions would range from 80 to 500 m/pixel, which is sufficient for detailed geologic mapping and characterization and better than the <1 km/pixel requirement.

A.4.5.3 Looking Back

After the flyby of the dwarf planet, look-back observations would observe the planet and any atmospheric hazes at high phase angle (>90°). These observations would help establish the photometric properties of the surface, and the effects of forward scattering could reveal the presence of an atmosphere, hazes, plumes, and/or rings. An important future trade is a UV imaging spectrometer, not included in the augmented example payload. A UV imaging spectrometer could reveal the composition of any hazes or atmospheres.

A.4.6 Dust Disk Imaging and EBL Observations

The IRM will be used to measure the solar system's circumsolar dust cloud (aka the “Zody” or “Zody Cloud”) and the EBL by staring repeatedly, during three-axis orientation periods, at selected “dark” portions of the sky that are in the forward-looking hemisphere of the sky with respect to

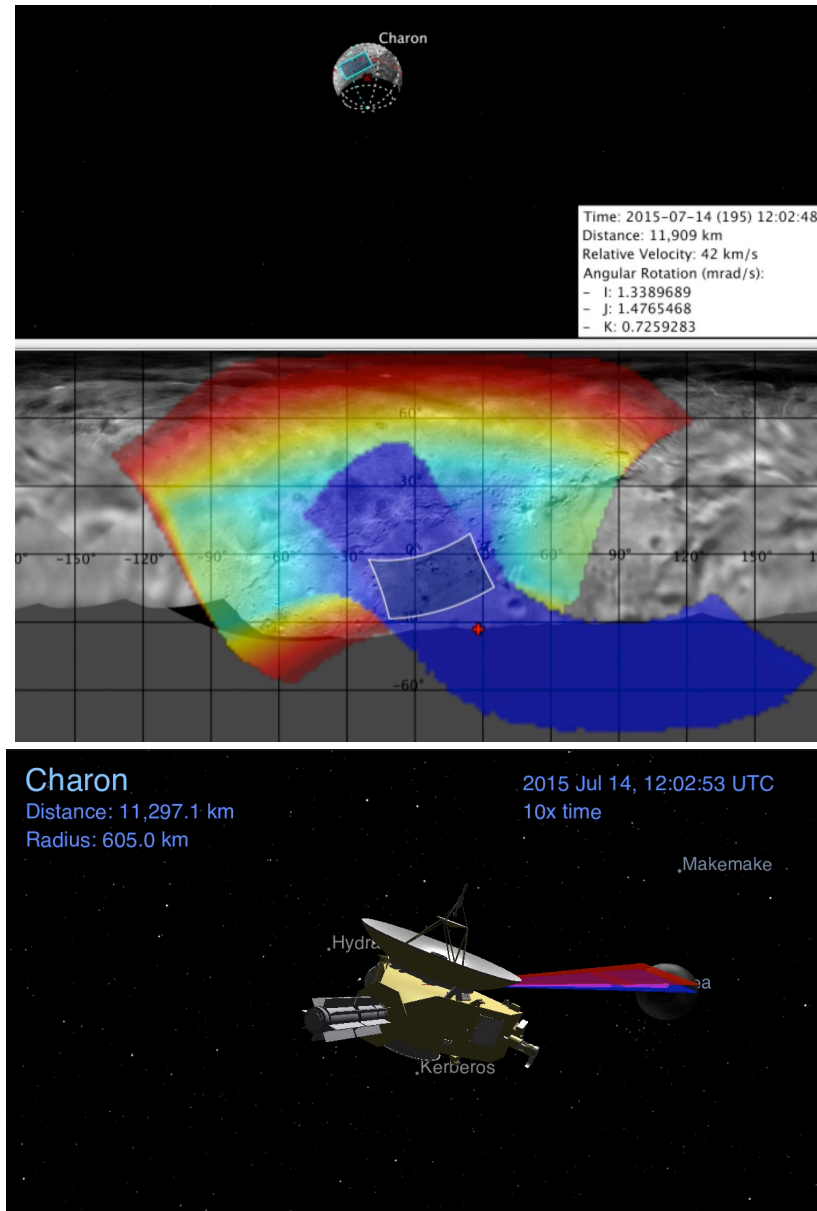


Figure A-19. Using New Horizons' flyby of Charon (comparable in size to many dwarf planets), we have modeled the type of images that Interstellar Probe could acquire of a dwarf planet. This modeling uses the Europa Imaging System – Narrow Angle Camera (EIS-NAC) boresight with an FOV of 2.3° in the cross-track direction. For ~1 minute around closest approach, the boresight slews off the planet to allow for a high-resolution, multiphase-angle strip or noodle. The slew would be ~1500 $\mu\text{rad/s}$. Top, Approach to a dwarf planet with the imager's FOV superimposed as a cyan box. Middle, Imaging footprint on the planet during approach. The color ranges from 500 to 80 m/pixel from red to blue. Bottom, View of the New Horizons spacecraft scanning Charon with three of its imagers (LORRI, Ralph, and Alice). This is comparable to what Interstellar Probe could do at a dwarf planet. (Image credit: Johns Hopkins Applied Physics Laboratory.)

Interstellar Probe's direction of flight away from the Sun. These dark regions, generally at high ecliptic and galactic latitudes (so as to minimize foreground signals) are well known from previous

deep field and cosmic background efforts, and will include the so-called Lockman Hole and the Hubble and Chandra Deep and Ultra-Deep Field sites.

In addition, repeated measurements will be made in the Interstellar Probe spacecraft's forward ram direction, once this has steadied down to its asymptotic location on the sky. When in spinner mode, the expected majority duty cycle of the mission, the IRM will take great circle measurements of the sky in logarithmic steps (i.e., when Interstellar Probe is at 2, 5, 10, 20, 50, and 100 au from the Sun; the logarithmic steps ensure good coverage of changes with heliocentric distance from the Sun while minimizing data volume and maximizing data return rates while the spacecraft is closest to Earth). IDA and NMS will measure dust abundance, mass, and composition to complement the IRM observations.

A.4.6.1 *Despun Three-Axis Operations*

In this design, we would not operate the near-IR channel while the spacecraft is spinning. We would, however, continuously operate the far-IR channel beyond ~5 au when the instrument is cooled enough to permit long wavelength operation. This would permit complete EBL science and retain the far-IR IPD and DGL science, as detailed below.

Minimum Survey Requirements: For the EBL science, measurement of six fields is required to demonstrate statistical isotropy on the sky. Each field would be observed in each independent wavelength band, requiring 85 integrations per field. We assume pointing jitter of <10 μ rad over 0.05 seconds. Absolute pointing would need to be <1000 μ rad. For the IPD and DGL science, only the far-IR channels would be used. They would acquire data continuously during the spun periods of the mission.

The ConOps for Pointed Survey can be outlined as follows.

1. At 2, 5, 10, 20, 50, and 100+ au from the Sun, we despin the spacecraft for an observing campaign.
2. On despin, we slew to the first of six targets:
 - a. Point the camera at the target for a 150-second integration.
 - b. Step the camera by 24 pixels = 2.6 arcmin to the next wavelength band.
 - c. Perform 85 such steps to complete the spectral coverage of one full 3.5×3.5 square degree target.
3. We slew to the next such target and repeat.
4. After six such observations, we spin up the spacecraft again.

Ignoring slew times, such an observation campaign would require $150 \text{ seconds} \times 85 \times 6 / (3600 \text{ s/h}) = 21.25$ hours of integration time (so including slews ~30 hours of wall clock time).

A.4.6.2 Accommodations for Pure-Spinner Operations

In this design, we would use pushbroom-style detectors for the IRM to continuously generate images in the near-IR, not operating the near-IR channel while the spacecraft is spinning. We would, however, continuously operate the far-IR channel beyond ~5 au when the instrument is cooled enough to permit long wavelength operation. This would permit small maps to be built at near-IR wavelengths, which could be built up into larger images over time.

The effective integration time per 6.5 arcsec pixel for a 2048-format pushbroom camera would be $(3.7^\circ/1 \text{ rpm}) = (3.7^\circ/6^\circ/\text{s}) = 0.6$ seconds. Our ideal integration time per field would be 150 seconds, meaning $(150 \text{ s}/0.6 \text{ s}) = 250$ such images would need to be co-added to reach our desired depth per pixel. At a revisit time of once per minute per field, 4.2 hours would be required to build to this depth. At this point, the image could be stepped up by a small amount and the integration could begin again. In 1 year, we could map ~2048 such steps. By performing this procedure every 0.6 seconds in 97 patches over the entire great circle traced by the instrument pointing, the whole $(180^\circ \times 3.4^\circ)$ great circle could be filled in. Alternatively, if a mechanism to tip the pointing of the instrument orthogonal to the rotation were implemented, we could fill in the spectral direction using the same 85 steps mentioned above. This would require 357 hours per 6-arcsec survey line, permitting a full spectral sampling in 97 images of $(3.4^\circ \times 2.5 \text{ arcmin})$ regions. Various trades like this exist.

Minimum Survey Requirements: We would require at least six “line map” images to make any kind of measurement of EBL. Because of the integration time permitted at 1 rpm, the trade space available here is between the size of the 97 survey regions and the spectral coverage. If we require building up a total survey region of ~70 square degrees $(6 \times 3.4^\circ \times 3.4^\circ)$, each region would require an edge length of 0.21° . This corresponds to 127 lines of 6-arcsec pixels, which at 4.2 hours/line would require 535 hours to build up. As a result, we would only be able to survey 16 spectral steps in 1 year, as opposed to 85 to build up the entire spectral coverage. To ensure the detector is being sampled over the same patches of sky during each rotation, we would require $1/(6^\circ/\text{s} * 3600 \text{ arcsec/degree}/3 \text{ arcsec pointing}) = 0.14\text{-ms}$ attitude knowledge to coherently sample the detector.

ConOps for Pointed Survey: In a pure spinner, we would continuously sample the sky at a regular cadence and co-add the images onboard. Over 97 different patches of the sky, we could build up individual $6 \text{ arcsec} \times 3.4^\circ$ “line maps” at near-IR wavelengths. The images would be generated on board, and co-added images would be telemetered periodically.

A.5 Data Volume

We performed a study similar to that in Section 4.5 on the feasibility of downlinking measurements for the augmented mission. This concept assumes one planetary flyby and no distant (i.e., unresolved) small-body or planet observations. This mission concept replaces the LYA instrument with the IRM and VIR instruments. The new instruments yield data rates that are significant but comparable to some of the other instruments, so that the net difference in data rates is minor.

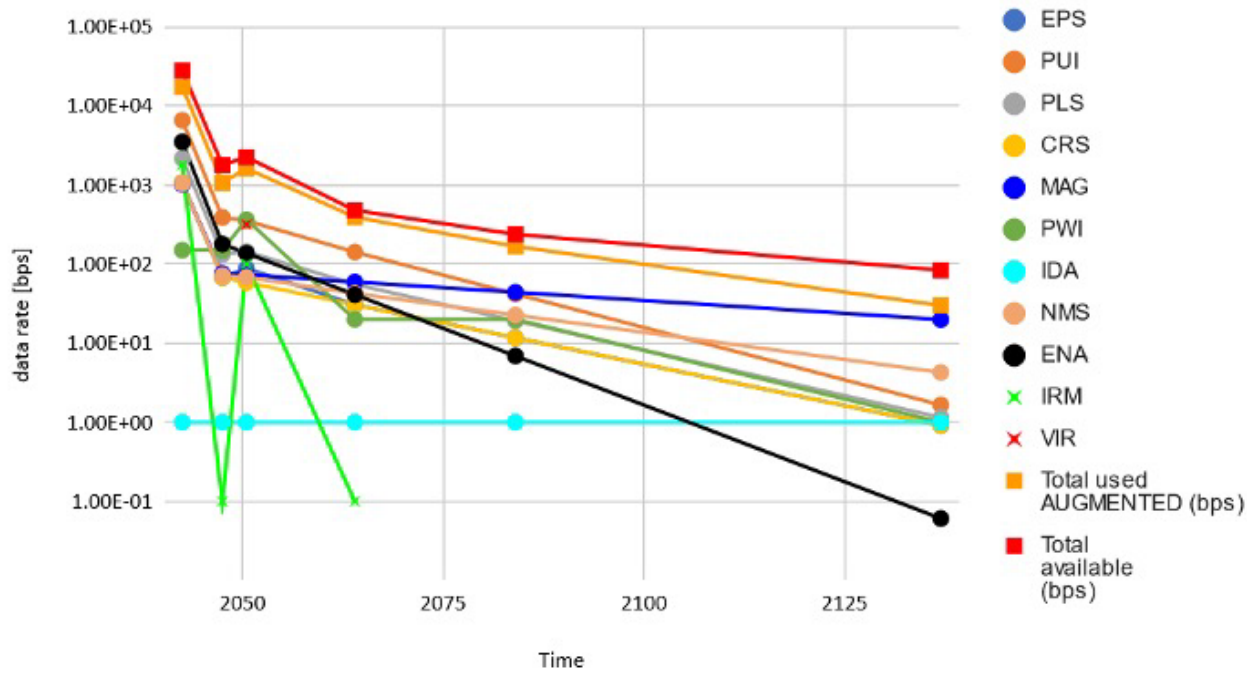


Figure A-20. Comparison of the available data rates (red) with the sum of minimum data rates of all instruments (orange). Table A-5 provides a brief rationale for the assumed data rates. More details are provided below.

To estimate the available data to downlink flyby data, we bracket it over the range between 40 and 90 au (i.e., within the heliosphere phase). The later the planetary flyby occurs in the mission, the more time will be required to complete downlink because of decreasing data rates with distance.

Table A-5. Formatting is equivalent to Table 4-4. The augmented mission has the same instruments as discussed in Table 4-4 except LYA, and includes the IRM and VIR.

Instrument	Instrument Inst. Data Rate (bps)							
	Useful Range (bps)		Data Rate at Representative Times (bps)					
	Voyager Equivalent Science	Nominal Rate when Operating at <10 au	Early Mission (<20 au)	Heliosphere (20–70 au)	Flyby	Outer Heliosphere (70–250 au)	ISM (250–350 au)	Extension (350–1000 au)
			2043	2048	2051	2064	2084	2137
EPS	1.00E-01	1.00E+03	1.07E+03	6.76E+01	8.85E+01	3.06E+01	1.17E+01	9.14E-01
	10 energies & 10 species & 10 directions per day	Nominal: Parker Solar Probe/EPI-Lo Lowest: Magnetospheric Multiscale (MMS)/ Energetic Ion Spectrometer (EIS) Highest: Juno/Jupiter Energetic-particle Detector Instrument (JEDI)			Scaling + 1-s resolution for 1 day	10 energies & 10 species & 10 directions per hour		
PUI	1.00E-01	6.00E+03	6.57E+03	3.88E+02	3.53E+02	1.42E+02	4.19E+01	1.65E+00
	10 energies & 10 species & 10 directions per day	Solar Orbiter/Solar Wind Analyser (SWA)/Heavy Ion Sensor (HIS)			Scaling + 1-s resolution for 1 day	10 energies & 10 species & 10 directions per hour		
PLS	1.00E-01	2.00E+03	2.17E+03	1.33E+02	1.43E+02	5.53E+01	1.91E+01	1.15E+00
	100 energies & 5 directions per day	approximately Van Allen Probes/Helium Oxygen Proton Electron (HOPE)			Scaling + 1-s resolution for 1 day	100 energies & 10 directions per hour		

Instrument	Instrument Inst. Data Rate (bps)							
	Useful Range (bps)		Data Rate at Representative Times (bps)					
	Voyager Equivalent Science	Nominal Rate when Operating at <10 au	Early Mission (<20 au)	Heliosphere (20–70 au)	Flyby	Outer Heliosphere (70–250 au)	ISM (250–350 au)	Extension (350–1000 au)
			2043	2048	2051	2064	2084	2137
CRS	1.00E-01	1.00E+03	1.07E+03	6.76E+01	5.85E+01	3.06E+01	1.17E+01	9.14E-01
	10 energies & 10 species & 10 directions per day	approximately Advanced Composition Explorer (ACE)/ Cosmic Ray Isotope Spectrometer (CRIS)				10 energies & 10 species & 10 directions per hour		
MAG	1.00E+01	1.00E+03	1.02E+03	7.59E+01	7.36E+01	5.93E+01	4.40E+01	1.99E+01
	1-s resolution for 5.4/24 of day, otherwise 1 min	Rounded down Cassini and Van Allen Probes			Scaling + 1s resolution for 1day			
PWS	1.00E+00	1.50E+02	1.50E+02	1.50E+02	3.64E+02	2.00E+01	2.00E+01	1.00E+00
	6 spectra/ histograms with 100 bins per day	6 spectra/ histograms with 100 bins per min	6 spectra/ histograms with 100 bins per min	6 spectra/ histograms with 100 bins per min	1-min resolution+ 10× higher for 1 au	2× Voyager	2× Voyager	6 spectra/ histograms with 100 bins per day
IDA	1.00E+00	5.00E+02	1.00E+00	1.00E+00	1.00E+00	1.00E+00	1.00E+00	1.00E+00
	Composition for 3e-5 dust/s	Cassini/Cosmic Dust Analyzer (CDA) at dusty Saturn	Composition for 3e-5 dust/s	Composition for 3e-5 dust/s		Composition for 3e-5 dust/s	Composition for 3e-5 dust/s	Composition for 3e-5 dust/s
NMS	1.00E+00	1.00E+03	1.05E+03	7.16E+01	6.82E+01	4.26E+01	2.27E+01	4.26E+00
	1 spectrum per day	1 spectrum per 100 s			Scaling + 100-s resolution for 1 day			
ENA	1.00E-03	3.06E+03	3.50E+03	1.79E+02	1.37E+02	4.11E+01	6.89E+00	6.07E-02
	One set per year	Interstellar Mapping and Acceleration Probe (IMAP)/Ultra						

Instrument	Instrument Inst. Data Rate (bps)							
	Useful Range (bps)		Data Rate at Representative Times (bps)					
	Voyager Equivalent Science	Nominal Rate when Operating at <10 au	Early Mission (<20 au)	Heliosphere (20–70 au)	Flyby	Outer Heliosphere (70–250 au)	ISM (250–350 au)	Extension (350–1000 au)
			2043	2048	2051	2064	2084	2137
LYA	1.00E-01	6.00E+02	6.41E+02	5.14E+02	3.60E+01	2.50E+01	8.12E+00	7.71E-01
	One set per year	One set per hour	One set every few hours	One set every few hours	One set per day	One set per day		
IRM	1.00E-01		1.80E+03	1.00E-01	1.00E+02	1.00E-01		
	1.2 kB far-IR per 62 h		5 campaigns	1.2 kB far-IR per 62 h	85 images over 2 years	1.2 kB far-IR per 62 h		
VIR		3.17E+02			3.17E+02			
		20 Gbit over 2 years			20 Gbit over 2 years			
Total available (bps)			2.80E+04	1.79E+03	2.25E+03	4.78E+02	2.37E+02	8.37E+01
Total used BASELINE (bps)			1.84E+04	1.13E+03	1.70E+03	4.22E+02	1.79E+02	3.09E+01
Total used AUGMENTED (fraction)			6.57E-01	6.34E-01	7.58E-01	8.83E-01	7.53E-01	3.69E-01

Based on New Horizons, we expect to collect 20 Gbit during the planetary flyby from VIR. For IRM, each campaign observes EBL in six directions and takes 4.3 GB that we assume compresses by a factor of 2. There are five campaigns within <20 au that are downlinked over the course of the ~3-year period at these distances. These campaigns assume that IRM only operates in three-axis-stabilized periods. Operation during spinning would yield lower data rates but requires technology development. A planetary flyby is expected to collect 10 Gbit of IRM data, which could augment or replace VIR data.

For the near-IR channel, the 2048×1 near-IR array pixels would be sampled at 0.6-second intervals, which would be co-added over time. The data to be transmitted would be photocurrent estimates for $97 \times 2048 \times 15$ pixels in each data-taking period. At 16 bits/pixel, this observation campaign would produce 6 MB of data per data period (presumably we could have a further gain of 2 in compression). These data would need to be transmitted near the beginning of the mission when the available data bandwidth is larger.

For the far-IR channel, the ~600 detectors will be sampled using “correlated double sampling” (CDS) with a cadence of ~1/6 second, which at a spin rate of 1 rpm will lead to images with a spatial resolution of ~1°. The data will need to be co-added on board into ~0.3° pixels, and ideally one such ($360^\circ/0.3^\circ =$) 600-pixel map would need to be transmitted every 62-hour data-taking period. At 16-bit depth, this image would require a maximum of 1.2 kB every period.

Even though in situ observations are not required for the planetary flyby, we estimated the respective data rates for such observations and found that they pose no significant burden. This behavior was also found for the New Horizons flybys. For PLS, PUI, and EPS, on top of the heliospheric observations, 1-second resolution data would be collected over 1 day and downlinked over a year, yielding an additional 30 bps per instrument. PWI would use 10× of heliosphere resolution for 1 au around the KBO. On top of the heliospheric observations, MAC would collect 1-second resolution data over 1 day and downlink over a year, yielding an additional 1 bps. Finally, in addition to the heliospheric data, NMS would take one spectrum over 100 seconds and downlink over 2 years, yielding an additional 3 bps.

A.6 Appendix 6 References

- Alexandersen, M., Gladman, B., Greenstreet, S., Kavelaars, J.J., Petit, J.M., Gwyn, S. (2013) A Uranian Trojan and the frequency of temporary giant-planet co-orbitals. *Science* 341(6149), 994-997.
- Arimatsu, K., Ohsawa, R., Hashimoto, G.L., Urakawa, S., Takahashi, J., Tozuka, M., et al. (2019) New constraint on the atmosphere of (50000) Quaoar from a stellar occultation. *The Astronomical Journal* 158(6), 236.
- Bagenal, F., Horányi, M., McComas, D.J., et al. (2016) Pluto’s interaction with its space environment: Solar wind, energetic particles, and dust. *Science* 351(6279).
- Bagenal F., McComas D.J., Elliott H.A., et al. (2021) Solar wind interaction with the Pluto system. In *The Pluto System After New Horizons* (S.A. Stern, J.M. Moore, W.M. Grundy, L.A. Young,

- and R.P. Binzel, eds.), pp. 379-392. Tucson, AZ: Univ. of Arizona Press. doi: 10.2458/azu_uapress_9780816540945-ch016
- Bale, S.D., Goetz, K., Harvey, P.R., et al. (2016) The FIELDS instrument suite for Solar Probe Plus. Measuring the coronal plasma and magnetic field, plasma waves and turbulence, and radio signatures of solar transients. *Space Science Reviews* 204, 49-82. doi:10.1007/s11214-016-0244-5
- Barkume, K.M. (2008) *Surface Properties of Kuiper Belt Objects and Centaurs*. California Institute of Technology.
- Barnes, N.P., Delamere, P.A., Strobel, D.F., et al. (2019) Constraining the IMF at Pluto using New Horizons SWAP data and hybrid simulations. *Journal of Geophysical Research: Space Physics* 124(3), 1568-1581.
- Barucci, M.A., Cruikshank, D.P., Dotto, E., et al. (2005) Is Sedna another Triton? *Astronomy & Astrophysics* 439(2), L1-L4.
- Barucci, M.A., Merlin, F., Guilbert, A., et al. (2008) Surface composition and temperature of the TNO Orcus. *Astronomy & Astrophysics* 479(1), L13-L16.
- Barucci, M.A., Brown, M.E., Emery, J.P., Merlin, F. (2008) Composition and surface properties of transneptunian objects and centaurs. In *The Solar System Beyond Neptune*, 143.
- Barucci, M.A., Alvarez-Candal, A., Merlin, F., et al (2011) New insights on ices in Centaur and Transneptunian populations. *Icarus* 214(1), 297-307.
- Belskaya, I.N., Barucci, M.A., Fulchignoni, M., Dvognopol, A.N. (2015) Updated taxonomy of trans-Neptunian objects and centaurs: Influence of albedo. *Icarus*, 250, 482-491.
- Benecchi, S.D., Noll, K.S., Grundy, W.M., Levison, H.F. (2010) (47171) 1999 TC36, a transneptunian triple. *Icarus* 207(2), 978-991.
- Beyer, R.A., Nimmo, F., McKinnon, W.B., et al. (2017) Charon tectonics. *Icarus* 287, 161-174.
- Bibring, J.P., Lamy, P., Langevin, Y., et al. (2007) CIVA. *Space Science Reviews* 128(1-4), 397-412.
- Blank, R., Anglin, S., Beletic, J.W., et al. (2011) The HxRG family of high performance image sensors for astronomy. In J.R. Kuhn, D.M. Harrington, H. Lin, S.V. Berdyugina, J. Trujillo-Bueno, S.L. Keil, and T. Rimmele, editors, *Solar Polarization 6*, 437 of *Astron. Soc. Pacific Conf. Series*, p. 383.
- Boehnhardt, H., Schulz, D., Protopapa, S., Götz, C. (2014) Photometry of Transneptunian objects for the Herschel Key Program 'TNOs Are Cool.' *Earth, Moon, and Planets* 114(1-2), 35-57.
- Braga-Ribas, F., Vieira-Martins, R., Assafin, M., Camargo, J.I.B., Sicardy, B., Ortiz, J.L. (2014, October) Stellar occultations by Transneptunian and Centaurs objects: Results from more than 10 observed events. In *Revista Mexicana de Astronomia y Astrofisica Conference Series* 44, 3-3.
- Brown, M. (2021) How many dwarf planets are there in the outer solar system? Accessed Aug. 1. <http://web.gps.caltech.edu/~mbrown/dps.html>

- Brown, M.E., Butler, B.J. (2018). Medium-sized satellites of large Kuiper belt objects. *The Astronomical Journal* 156(4), 164.
- Brown, M.E., Schaller, E.L. (2007) The mass of dwarf planet Eris. *Science* 316, 1585.
- Brown, M.E., Trujillo, C., Rabinowitz, D. (2004) Discovery of a candidate inner Oort cloud planetoid. *The Astrophysical Journal* 617(1), 645.
- Brown, M.E., Barkume, K.M., Ragozzine, D., Schaller, E.L. (2007) A collisional family of icy objects in the Kuiper belt. *Nature* 446(7133), 294-296.
- Brown, M.E., Burgasser, A.J., Fraser, W.C. (2011) The surface composition of large Kuiper Belt object 2007 OR10. *The Astrophysical Journal* 738(2), L26. doi: 10.1088/2041-8205/738/2/L26
- Brown, M.E., Schaller, E.L., Blake, G.A. (2015) Irradiation products on dwarf planet Makemake. *The Astronomical Journal* 149(3), 105.
- Buie, M.W., Porter, S.B., Tamblyn, P., et al. (2020) Size and shape constraints of (486958) Arrokoth from stellar occultations. *The Astronomical Journal* 159(4), 130.
- Cahoy, K.L., Marley, M.S., Fortney, J.J. (2010) Exoplanet albedo spectra and colors as a function of planet phase, separation, and metallicity. *The Astrophysical Journal* 724(1), 189.
- Carrión-González, Ó., García Muñoz, A., Santos, N.C., Cabrera, J., Cizmadia, S., Rauer, H. (2021) Catalogue of exoplanets accessible in reflected starlight to the Nancy Grace Roman Space Telescope. Population study and prospects for phase-curve measurements. *Astronomy & Astrophysics* 651, A7.
- Carry, B., Hestroffer, D., DeMeo, F.E., et al. (2011) Integral-field spectroscopy of (90482) Orcus-Vanth. *Astronomy & Astrophysics* 534, A115.
- Conselice, C.J., Wilkinson, A., Duncan, K., Mortlock, A. (2016) The evolution of galaxy number density at $z < 8$ and its implications. *The Astrophysical Journal* 830(2), 83.
- Cooray, A. (2016) Extragalactic background light measurements and applications. *Royal Society Open Science* 3, 150555. Doi: 10.1098/rsos.150555
- de la Fuente Marcos, C., de la Fuente Marcos, R. (2017) Asteroid 2014 YX49: A large transient Trojan of Uranus. *Monthly Notices of the Royal Astronomical Society* 467(2), 1561-1568. doi: 10.1093/mnras/stx197
- Delsanti, A., Merlin, F., Guilbert-Lepoutre, A., Bauer, J., Yang, B., Meech, K.J. (2010) Methane, ammonia, and their irradiation products at the surface of an intermediate-size KBO? *Astronomy & Astrophysics* 520, A40. Retrieved from <https://doi.org/10.1051/0004-6361/20101429>
- DeMeo, F.E., Fornasier, S., Barucci, M.A., et al. (2009) Visible and near-infrared colors of Transneptunian objects and Centaurs from the second ESO large program. *Astronomy & Astrophysics* 493(1), 283-290. Retrieved from <https://doi.org/10.1051/0004-6361:200810561>

- Dias-Oliveira, A., Sicardy, B., Ortiz, J.L., et al. (2017) Study of the plutino object (208996) 2003 AZ84 from stellar occultations: Size, shape, and topographic features. *The Astronomical Journal* 154(1), 22. doi: 10.3847/1538-3881/aa74e9
- Doressoundiram, A., Peixinho, N., Moullet, A., Fornasier, S., Barucci, M.A., Beuzit, J.L., Veillet, C. (2007) The Meudon Multicolor Survey (2MS) of Centaurs and trans-Neptunian objects: From visible to infrared colors. *The Astronomical Journal* 134(6), 2186-2199. doi: 10.1086/522783
- Draine, B.T. (2009) Perspectives on interstellar dust inside and outside of the heliosphere. *Space Science Reviews* 143, 333–345.
- Draine, B.T., Hensley, B.S. (2016) Quantum suppression of alignment in ultrasmall grains: Microwave emission from spinning dust will be negligibly polarized. *The Astrophysical Journal* 831(1), 59. Doi: 10.3847/0004-637x/831/1/59
- Edelstein, J., Bowyer, S., Lampton, M. (2000) Reanalyses of Voyager Ultraviolet Spectrometer limits to the EUV and FUV diffuse astronomical flux. arXiv preprint astro-ph/0003208.
- Fernández-Valenzuela, E., Ortiz, J. L., Morales, N., et al. (2019) The changing rotational light-curve amplitude of Varuna and evidence for a close-in satellite. *The Astrophysical Journal Letters* 883(1), L21.
- Fornasier, S., Dotto, E., Barucci, M. A., Barbieri, C. (2004) Water ice on the surface of the large TNO 2004 DW. *Astronomy & Astrophysics* 422(2), L43-L46.
- Fornasier, S., Lellouch, E., Müller, T., et al. (2013) TNOs are cool: A survey of the trans-Neptunian region-VIII. Combined Herschel PACS and SPIRE observations of nine bright targets at 70–500 μm . *Astronomy & Astrophysics* 555, A15.
- Gordon, K.D., Witt, A.N., Friedmann, B.C. (1998) Detection of extended red emission in the diffuse interstellar medium. *The Astrophysical Journal* 498(2), 522.
- Greaves, J.S., Wyatt, M.C. (2010) Debris discs and comet populations around Sun-like stars: the Solar system in context. *Monthly Notices of the Royal Astronomical Society* 404(4), 1944-1951. doi: 10.1111/j.1365-2966.2010.16415.x
- Grundy, W.M., Noll, K.S., Roe, H.G., et al. (2019) Mutual orbit orientations of transneptunian binaries. *Icarus* 334, 62-78.
- Gurnett, D.A., Huff, R.L., Kirchner, D.L. (1997) The wide-band plasma wave investigation. In: Escoubet C.P., Russell C.T., Schmidt R. (eds) *The Cluster and Phoenix Missions*. Dordrecht: Springer. https://doi.org/10.1007/978-94-011-5666-0_8
- Gurnett, D.A., Kurth, W.S. (2019) Plasma densities near and beyond the heliopause from the Voyager 1 and 2 plasma wave instruments. *Nature Astronomy* 3, 1024. Doi:10.1038/s41550-019-0918-5
- Hapke, B. (1981) Bidirectional reflectance spectroscopy: 1. Theory. *Journal of Geophysical Research: Solid Earth* 86(B4), 3039-3054.

- Harch, A., Carcich, B., Rogers, G., et al. (2017) Accommodating Navigation Uncertainties in the Pluto Encounter Sequence Design. In *Space Operations: Contributions from the Global Community* (pp. 427-487). Springer, Cham. https://doi.org/10.1007/978-3-319-51941-8_21
- Hauser, M.G., Arendt, R.G., Kelsall, T., et al. (1998). The COBE diffuse infrared background experiment search for the cosmic infrared background. I. Limits and detections. *The Astrophysical Journal* 508(1), 25. Doi: 10.1086/306379
- Hauser, M.G., Dwek, E. (2001) The cosmic infrared background: Measurements and implications. *Annual Review of Astronomy and Astrophysics*, 39(1), 249-307. Doi: 10.1146/annurev.astro.39.1.249
- Hegde, S., Kaltenegger, L. (2013) Colors of extreme exo-Earth environments. *Astrobiology* 13(1), 47-56.
- Hendrix, A.R., Cassidy, T.A., Buratti, B.J., et al. (2012) Mimas' far-UV albedo: Spatial variations. *Icarus* 220(2), 922-931.
- Henry, R.C., Murthy, J., Overduin, J., Tyler, J. (2014) The mystery of the cosmic diffuse ultraviolet background radiation. *The Astrophysical Journal* 798(1), 14.
- Henry, R.C., Murthy, J., Overduin, J. (2018) Discovery of an ionizing radiation field in the universe. arXiv preprint arXiv:1805.09658.
- Hill, M.E., Haggerty, D.K., McNutt, R.L., Jr., Paranicas, C.P. (2009) Energetic particle evidence for magnetic filaments in Jupiter's magnetotail. *Journal of Geophysical Research* 114, A11201. doi:10.1029/2009JA014374
- Hill, R., Masui, K.W., Scott, D. (2018) The spectrum of the universe. *Applied Spectroscopy* 72(5), 663. doi: 10.1177/0003702818767133
- Hofgartner, J.D., Buratti, B.J., Hayne, P.O., Young, L.A. (2019) Ongoing resurfacing of KBO Eris by volatile transport in local, collisional, sublimation atmosphere regime. *Icarus* 334, 52-61.
- Holberg, J.B. (1985, March) Photometric standard stars for the far UV. *Bulletin of the American Astronomical Society* 17, 554.
- Holberg, J.B. (1986) Far-ultraviolet background observations at high galactic latitude. II-Diffuse emission. *The Astrophysical Journal* 311, 969-978.
- Holler, B., Grundy, W., Murray, K., Young, L., Porter, S., Buie, M., et al. (2020, January). New Insights into the Eris/Dysnomia System. In *American Astronomical Society Meeting*, Abstracts 235, 278-06.
- Holler, B., Bannister, M., Singer, K., Stern, S.A., Benecchi, S., Ore, C., et al. (2021) Prospects for future exploration of the trans-Neptunian region. *Bulletin of the AAS* 53(4).
- Hromakina, T.A., Belskaya, I.N., Krugly, Y.N., et al. (2019) Long-term photometric monitoring of the dwarf planet (136472) Makemake. *Astronomy & Astrophysics* 625, A46.
- Hughes, M., Duchêne, G., Matthews, B.C. (2018) Debris disks: Structure, composition, and variability. *Ann. Rev. of Astron & Astrophys* 56, 541. doi: 10.1146/annurev-astro-081817-052035

- Hussmann, H., Sohl, F., Spohn, T. (2006) Subsurface oceans and deep interiors of medium-sized outer planet satellites and large trans-Neptunian objects. *Icarus* 185(1), 258-273.
- Jerram, P., Beletic, J. (2019, July). Teledyne's high performance infrared detectors for space missions. In *International Conference on Space Optics—ICSO 2018* 11180, 111803D. International Society for Optics and Photonics.
- Kelsall, T., Weiland, J.L., Franz, B.A., et al. (1998) The COBE Diffuse Infrared Background Experiment search for the cosmic infrared background. II. Model of the interplanetary dust cloud. *Astrophysical Journal* 508, 44. doi: 10.1086/306380
- Kiss, C., Marton, G., Parker, A.H., Grundy, W.M., Farkas-Takacs, A., Stansberry, J., et al. (2019) The mass and density of the dwarf planet (225088) 2007 OR10. *Icarus* 334, 3-10.
- Kollmann, P., Roussos, E., Paranicas, C., et al. (2018) Electron acceleration to MeV energies at Jupiter and Saturn. *Journal of Geophysical Research: Space Physics* 123. <https://doi.org/10.1029/2018JA025665>
- Kollmann, P., Hill, M.E., Allen, R.C., et al. (2019) Pluto's interaction with energetic heliospheric ions. *Journal of Geophysical Research: Space Physics* 124(9), 7413-7424.
- Kretlow, M. (2020) Beyond Jupiter-(50000) Quaoar. *Journal for Occultation Astronomy* 10(1), 24-31.
- Krick, J.E., Glaccum, W.J., Carey, S.J., et al. (2012) A Spitzer/IRAC measure of the zodiacal light. *Astrophysical Journal* 754, 53. Doi: 10.1088/0004-637X/754/1/53
- Krupp, N., Vasyliunas, V.M., Woch, J., et al. (2004) Dynamics of the Jovian magnetosphere. In *Jupiter – The Planet, Satellites and Magnetosphere*, Cambridge University Press.
- Lacerda, P. (2009) Time-resolved near-infrared photometry of extreme Kuiper belt object Haumea. *The Astronomical Journal* 137(2), 3404.
- Lacerda, P., Jewitt, D., Peixinho, N. (2008) High-precision photometry of extreme KBO 2003 EL61. *The Astronomical Journal* 135(5), 1749.
- Lagache, G., Puget, J.-L., Dole, H. (2005) Dusty infrared galaxies: Sources of the cosmic infrared background. *Annual Review of Astronomy and Astrophysics* 43, 727. doi: 10.1146/annurev.astro.43.072103.150606.
- Lang, G.J., Peltzer, R.G. (1977) Planetary radio astronomy receiver. *IEEE Transactions on Aerospace and Electronic Systems* 5, 466-472.
- Lauer, T.R., Postman, M., Weaver, H.A., et al. (2021) New Horizons observations of the cosmic optical background. *The Astrophysical Journal* 906(2), 77.
- Leinert, C., Bowyer, S., Haikala, L.K., et al. (1998) The 1997 reference of diffuse night sky brightness. *Astron. Astrophys. Suppl.* 127, 1. doi: 10.1051/aas:1998105
- Lepping, R.P., Desch, M.D., Sittler, E.C., Jr., et al. (1983) Structure and other properties of Jupiter's distant magnetotail. *Journal of Geophysical Research* 88, 8801-8815. doi:10.1029/JA088iA11p08801

- Licandro, J., Ghinassi, F., Testi, L. (2002) Infrared spectroscopy of the largest known trans-Neptunian object 2001 KX. *Astronomy & Astrophysics* 388(1), L9-L12.
- Licandro, J., Grundy, W.M., Pinilla-Alonso, N., Leisy, P. (2006a) Visible spectroscopy of 2003 UB313: Evidence for N₂ ice on the surface of the largest TNO? *Astronomy & Astrophysics* 458(1), L5-L8.
- Licandro, J., Pinilla-Alonso, N., Pedani, M., Oliva, E., Tozzi, G.P., Grundy, W.M. (2006b) The methane ice rich surface of large TNO 2005 FY9: A Pluto-twin in the trans-Neptunian belt? *Astronomy & Astrophysics* 445(3), L35-L38.
- Linsky, J.L., Redfield, S. (2014) The local ISM in three dimensions: Kinematics, morphology and physical properties. *Astrophysics and Space Science* 354(1), 29-34.
- Lobb, D.R. (1997, October). Imaging spectrometers using concentric optics. In *Imaging Spectrometry III* (Vol. 3118, pp. 339-347). International Society for Optics and Photonics.
- Loose, M., Beletic, J., Blackwell, J., et al. (2005) The SIDECAR ASIC: Focal plane electronics on a single chip. *Proceedings of SPIE 5904*, Cryogenic Optical Systems and Instruments XI, 59040V. <https://doi.org/10.1117/12.619638>
- Lorenzi, V., Pinilla-Alonso, N., Licandro, J., Dalle Ore, C.M., Emery, J.P. (2014) Rotationally resolved spectroscopy of (20000) Varuna in the near-infrared. *Astronomy & Astrophysics* 562, A85.
- Luger, R., Agol, E., Foreman-Mackey, D., Fleming, D.P., Lustig-Yaeger, J., Deitrick, R. (2019) starry: Analytic occultation light curves. *The Astronomical Journal* 157(2), 64. doi: 10.3847/1538-3881/aae8e5
- Maiolino, R., Mannucci, F., Cresci, G., (2010) AMAZE and LSD: Metallicity and dynamical evolution of galaxies in the early universe. *The Messenger* 142, 36-39.
- Marley, M.S., & McKay, C.P. (1999) Thermal structure of Uranus' atmosphere. *Icarus* 138(2), 268-286.
- Marley, M.S., Gelino, C., Stephens, D., Lunine, J.I., Freedman, R. (1999) Reflected spectra and albedos of extrasolar giant planets. I. Clear and cloudy atmospheres. *The Astrophysical Journal* 513(2), 879.
- Matsuoka, Y., Ienaka, N., Kawara, K., Oyabu, S. (2011) Cosmic optical background: The view from Pioneer 10/11. *The Astrophysical Journal* 736(2), 119.
- Mauk, B.H., Fox, N.J. (2010) Electron radiation belts of the solar system. *Journal of Geophysical Research* 115, A12220. doi:10.1029/2010JA015660
- Mayorga, L.C., Jackiewicz, J., Rages, K., West, R.A., Knowles, B., Lewis, N., Marley, M.S. (2016). Jupiter's phase variations from Cassini: A testbed for future direct-imaging missions. *The Astronomical Journal* 152(6), 209.
- Mayorga, L.C., Charbonneau, D., Thorngren, D.P. (2020) Reflected light observations of the Galilean satellites from Cassini: A test bed for cold terrestrial exoplanets. *The Astronomical Journal* 160(5), 238.

- McKinnon, W.B., Richardson, D.C., Marohnic, J.C., et al. (2020) The solar nebula origin of (486958) Arrokoth, a primordial contact binary in the Kuiper Belt. *Science* 367(6481), eaay6620. doi:10.1126/science.aay6620
- Meza, E., Sicardy, B., Assafin, M., Ortiz, J.L., Bertrand, T., Lellouch, E., et al. (2019) Lower atmosphere and pressure evolution on Pluto from ground-based stellar occultations, 1988–2016. *Astronomy & Astrophysics* 625, A42.
- Müller, H.R., Frisch, P.C., Florinski, V., Zank, G.P. (2006) Heliospheric response to different possible interstellar environments. *The Astrophysical Journal* 647(2), 1491.
- Muraki, Y., Han, C., Bennett, D.P., et al. (2011) Discovery and mass measurements of a cold, 10 Earth mass planet and its host star. *The Astrophysical Journal* 741(1), 22.
- Murthy, J. (2009) Observations of the near and far ultraviolet background. *Astrophysics and Space Science* 320(1-3), 21-26.
- Murthy, J., Henry, R.C., Holberg, J.B. (1991) Constraints on the optical properties of interstellar dust in the far-ultraviolet: Voyager observations of the diffuse sky background. *The Astrophysical Journal* 383, 198.
- Murthy, J., Im, M., Henry, R.C., Holberg, J.B. (1993) Voyager observations of diffuse far-ultraviolet continuum and line emission in Eridanus. *The Astrophysical Journal* 419, 739.
- Murthy, J., Hall, D., Earl, M., Henry, R.C., Holberg, J.B. (1999) An analysis of 17 years of Voyager observations of the diffuse far-ultraviolet radiation field. *The Astrophysical Journal* 522(2), 904-914.
- Murthy, J., Henry, R.C., Shelton, R.L., Holberg, J.B. (2001) Upper limits on O VI emission from Voyager observations. *The Astrophysical Journal* 557(1), L47-L50.
- Nicolaou, G., McComas, D.J., Bagenal, F., Elliott, H.A., Wilson, R.J. (2015) Plasma properties in the deep Jovian magnetotail. *Planetary and Space Science* 119, 222-232. doi:10.1016/j.pss.2015.10.001
- Nimmo, F., Umurhan, O., Lisse, C. M., Bierson, C. J., Lauer, T. R., Buie, M. W., ... & Ennico, K. (2017). Mean radius and shape of Pluto and Charon from New Horizons images. *Icarus*, 287, 12-29.
- Ortiz, J.L., Sicardy, B., Braga-Ribas, F., et al. (2012) Albedo and atmospheric constraints of dwarf planet Makemake from a stellar occultation. *Nature* 491(7425), 566-569.
- Ortiz, J.L., Santos-Sanz, P., Sicardy, B., et al. (2017) The size, shape, density and ring of the dwarf planet Haumea from a stellar occultation. *Nature* 550(7675), 219-223.
- Park, W.-K., Bang, S.-C., Battle, J., et al. (2018) Development of data storage system and GSE for cosmic infrared background experiment 2 (CIBER-2). *Proceedings of SPIE 10698*, Space Telescopes and Instrumentation 2018: Optical, Infrared, and Millimeter Wave, 1069849. <https://doi.org/10.1117/12.2313184>
- Paty, C., Arridge, C.S., Cohen, I.J., DiBraccio, G.A., Ebert, R.W., Rymer, A.M. (2020) Ice giant magnetospheres. *Philosophical Transactions of the Royal Society A* 378(2187), 20190480.

- Pinilla-Alonso, N., Brunetto, R., Licandro, J., Gil-Hutton, R., Roush, T. L., Strazzulla, G. (2009) The surface of (136108) Haumea (2003 EL61), the largest carbon-depleted object in the trans-Neptunian belt. *Astronomy & Astrophysics* 496(2), 547-556.
- Piquette, M., Poppe, A., Bernardoni, E., Szalay, J., James, D., Horányi, M., Stern, S., Weaver, H., Spencer, J., Olkin, C. (2019) Student dust counter: Status report at 38 AU. *Icarus* 321, 116-125.
- Pollack, J.B., Rages, K., Baines, K.H., Bergstralh, J.T., Wenkert, D., Danielson, G.E. (1986) Estimates of the bolometric albedos and radiation balance of Uranus and Neptune. *Icarus* 65(2), 442-466. doi: [https://doi.org/10.1016/0019-1035\(86\)90147-8](https://doi.org/10.1016/0019-1035(86)90147-8)
- Poppe, A.R. (2016) An improved model for interplanetary dust fluxes in the outer Solar System. *Icarus* 264, 369. doi: 10.1016/j.icarus.2015.10.001
- Poppe, A. R., Horányi, M. (2012) On the Edgeworth-Kuiper Belt dust flux to Saturn. *Geophysical Research Letters* 39, L15104. doi:10.1029/2012GL052530
- Poppe, A.R., Lisse, C.M., Piquette, M., Zemcov, M., Horányi, M., et al. (2019) Constraining the Solar System's debris disk with in situ New Horizons measurements from the Edgeworth-Kuiper Belt. *The Astrophysical Journal Letters* 881(1), L12.
- Porter, S., Beyer, R.A., Bierson, C.J., et al. (2019, December) The shapes of (486958) 2014 MU69 and 14 other Kuiper Belt objects from New Horizons. In *AGU Fall Meeting Abstracts*, P42C-02.
- Porter, S., Spencer, J., Verbiscer, A., et al. (2021, October). Orbits and occultation opportunities of 15 TNOs observed by New Horizons. In *AAS/Division for Planetary Sciences Meeting Abstracts* 53(7), 307-02.
- Pratlong, J., Jerram, P., Tsiolis, G., Arkesteijn, V., Donegan, P., Korthout, L. (2019) *TDI CMOS image sensor for Earth Observation*. In International Conference on Space Optics—ICSO 2018, International Society for Optics and Photonics.
- Rabinowitz, D.L., Benecchi, S.D., Grundy, W.M., Verbiscer, A.J., Thirouin, A. (2019) The complex rotational light curve of (385446) Manwë–Thorondor, a multicomponent eclipsing system in the Kuiper Belt. *The Astronomical Journal* 159(1), 27.
- Raut, U., Famá, M., Loeffler, M.J., Baragiola, R.A. (2008) Cosmic ray compaction of porous interstellar ices. *The Astrophysical Journal* 687(2), 1070.
- Reuter, D.C., Stern, S.A., Scherrer, J., et al. (2008) Ralph: A visible/infrared imager for the New Horizons Pluto/Kuiper Belt mission. *Space Science Reviews* 140, 129.
- Roussos, E., Allanson, O., André, N., et al. (2019) *The in-situ exploration of Jupiter's radiation belts (A White Paper submitted in response to ESA's Voyage 2050 Call)*, arxiv.org/abs/1908.02339.
- Rowan-Robinson, M., May, B. (2013) An improved model for the infrared emission from the zodiacal dust cloud: cometary, asteroidal and interstellar dust. *Monthly Notices of the Royal Astronomical Society* 429, 2894-2902. doi: 10.1093/mnras/sts471

- Schaller, E.L., Brown, M.E. (2007a) Volatile loss and retention on Kuiper Belt objects. *The Astrophysical Journal* 659(1), L61-L64.
- Schaller E.L., Brown, M.E. (2007b) Detection of methane on Kuiper Belt Object (50000) Quaoar. *The Astrophysical Journal* 670(1), L49-L51.
- Schwamb, M.E., Jones, R.L., Chesley, S.R., et al. (2018) Large synoptic survey telescope solar system science roadmap. arXiv preprint arXiv:1802.01783.
- Seager, S., Turnbull, M., Sparks, W., et al. (2015, September). The Exo-S probe class starshade mission. In *Techniques and Instrumentation for Detection of Exoplanets VII* 9605, 96050W. International Society for Optics and Photonics.
- Sheppard, S.S. (2010) The colors of extreme outer solar system objects. *The Astronomical Journal* 139(4), 1394.
- Sicardy, B., Colas, F., Maquet, L., et al. (2010, October). The 2010, February 19 stellar occultation by Varuna. In *AAS/Division for Planetary Sciences Meeting Abstracts* 42, 23-11.
- Sicardy, B., Ortiz, J.L., Assafin, M., Jehin, E., Maury, A., Lellouch, E., et al. (2011) A Pluto-like radius and a high albedo for the dwarf planet Eris from an occultation. *Nature* 478(7370), 493-496.
- Snodgrass, C., Carry, B., Dumas, C., Hainaut, O. (2010) Characterisation of candidate members of (136108) Haumea's family. *Astronomy & Astrophysics* 511, A72.
- Stansberry, J.A., Grundy, W.M., Mueller, M., et al. (2012) Physical properties of trans-Neptunian binaries (120347) Salacia–Actaea and (42355) Typhon–Echidna. *Icarus* 219(2), 676-688.
- Stark, C.C., Kuchner, M.J. (2008) The detectability of exo-earths and super-earths via resonant signatures in exozodiacal clouds. *The Astrophysical Journal* 686(1), 637.
- Stark, C.C., Kuchner, M.J. (2009) A new algorithm for self-consistent three-dimensional modeling of collisions in dusty debris disks. *The Astrophysical Journal* 707(1), 543.
- Stern, S.A., Trafton, L.M. (2008) On the atmospheres of objects in the Kuiper Belt (pp. 365–380). In *The Solar System Beyond Neptune*. Tucson, AZ: University of Arizona Press.
- Stern, S.A., Slater, D.C., Scherrer, J., Stone, J., Dirks, G., Versteeg, M., et al. (2009) ALICE: The ultraviolet imaging spectrograph aboard the New Horizons Pluto–Kuiper Belt mission. *Space Science Reviews* 140, 155-187.
- Stern, S.A., Bagenal, F., Ennico, K., Gladstone, G.R., Grundy, W.M., McKinnon, W.B., et al. (2015) The Pluto system: Initial results from its exploration by New Horizons. *Science* 350(6258).
- Stern, S.A., Weaver, H.A., Spencer, J.R., et al. (2019) Initial results from the New Horizons exploration of 2014 MU₆₉, a small Kuiper Belt object. *Science* 364(6441), eaaw9771. doi: 10.1126/science.aaw9771
- Stern, S.A., White, O.L., McGovern, P.J., Keane, J.T., Conrad, J.W., Bierson, C. J., et al. (2021) Pluto's far side. *Icarus* 356, 113805.

- Sudarsky, D., Burrows, A., Hubeny, I., Li, A. (2005) Phase functions and light curves of wide-separation extrasolar giant planets. *The Astrophysical Journal* 627(1), 520-533.
- Tauber, J.A., ESA Scientific Collaboration & the Planck Scientific Collaboration (2004) The Planck Mission. *Advances in Space Research* 34, 491.
- Tegler, S.C., Cornelison, D.M., Grundy, W.M., et al. (2010) Methane and nitrogen abundances on Pluto and Eris. *The Astrophysical Journal* 725(1), 1296-1305. doi: 10.1088/0004-637x/725/1/1296
- Toller, G.N. (1983) The extragalactic background light at 4400 Å. *The Astrophysical Journal* 266, L79-L82.
- Toller, G., Tanabe, H., Weinberg, J.L. (1987) Background starlight at the north and south celestial, ecliptic, and galactic poles. *Astronomy and Astrophysics* 188, 24-34.
- Trujillo, C.A., Brown, M.E., Barkume, K.M., Schaller, E.L., Rabinowitz, D.L. (2007) The surface of 2003 EL61 in the near-infrared. *The Astrophysical Journal* 655(2), 1172.
- Tsumura, K., Matsumoto, T., Matsuura, S., Sakon, I., Wada, T. (2013) Low-resolution spectrum of the extragalactic background light with the AKARI infrared camera. *Publ. Astron. Soc. Japan* 65, 121. doi: 10.1093/pasj/65.6.121
- Turtle, E., McEwen, A., Bland, M., et al. (2019) The Europa Imaging System (EIS): High-resolution, 3-D insight into Europa's geology, ice shell, and potential for current activity. The Lunar and Planetary Science Conference, The Woodlands, TX, Poster. <https://www.hou.usra.edu/meetings/lpsc2019/eposter/3065.pdf>
- Tyson, J.A. (1995) The optical extragalactic background radiation. In *Extragalactic Background Radiation Meeting* (ed. D. Calzetti, M. Livio, and C. Madau), pp. 103–133.
- Verbiscer, A.J., Porter, S., Benecchi, S.D., et al. (2019) Phase curves from the Kuiper Belt: Photometric properties of distant Kuiper Belt objects observed by New Horizons. *The Astronomical Journal* 158(3), 123.
- Vilenius, E., Kiss, C., Mommert, M., et al. (2012) "TNOs are Cool": A survey of the trans-Neptunian region-VI. Herschel/PACS observations and thermal modeling of 19 classical Kuiper Belt objects. *Astronomy & Astrophysics* 541, A94.
- Volk, K., Malhotra, R. (2008) The scattered disk as the source of the Jupiter family comets. *The Astrophysical Journal* 687(1), 714.
- Weaver, H.A., Buie, M.W., Buratti, B.J., Grundy, W.M., Lauer, T.R., et al. (2016) The small satellites of Pluto as observed by New Horizons. *Science* 351(6279), id.aae0030.
- Weingartner, J.C., Draine, B.T. (2001) Dust grain-size distributions and extinction in the Milky Way, Large Magellanic Cloud, and Small Magellanic Cloud. *The Astrophysical Journal* 548(1), 296-309. doi: 10.1086/318651
- Young, L.A., Kammer, J.A., Steffl, A.J., Gladstone, G.R., Summers, M.E., Strobel, D.F., et al. (2018) Structure and composition of Pluto's atmosphere from the New Horizons solar ultraviolet occultation. *Icarus* 300, 174-199.

- Young, L.A., Braga-Ribas, F., Johnson, R.E. (2020) Volatile evolution and atmospheres of trans-Neptunian objects. In *The Trans-Neptunian Solar System* (pp. 127-151). Elsevier.
- Zemcov, M., Crill, B., Ryan, M., et al. (2016) An algorithm for real-time optimal photocurrent estimation including transient detection for resource-constrained imaging applications. *Journal of Astronomical Instrumentation* 5, 1650007-1881.
- Zemcov, M., Immel, P., Nguyen, C., Cooray, A., Lisse, C.M., Poppe, A.R. (2017) Measurement of the cosmic optical background using the Long Range Reconnaissance Imager on New Horizons. *Nature Communications* 8, 15003.
- Zemcov, M., Arcavi, I., Arendt, R., et al. (2018) Astrophysics with New Horizons: Making the most of a generational opportunity. *Publications of the Astronomical Society of the Pacific* 130(993), 115001.
- Zemcov, M., Arcavi, I., Arendt, R.G., et al. (2019) Opportunities for astrophysical science from the inner and outer Solar System. White paper submitted to the *NAS Astrophysics 2020 Decadal Survey*. arXiv preprint arXiv:1903.05729

Appendix B. Heritage Tables

Table B-1. Flown magnetometer resources and capabilities.

Mission	Instrument	Mass (kg)	Power (W)	Bit Rate (bps)	Capabilities	TRL and Heritage	References/Notes
Cassini	Vector Helium + Fluxgate Magnetometer (MAG)	3.2 without boom (1.22 kg scalar, 1.97 kg vector)	6.8 W (2.3 W scalar, 4.5 W vector)	3600	3 axes Dual configuration 0.01–10 nT, 10–60 s Power includes 1-W heater	9	Dougherty et al. (2004) Smith et al. (2001)
Mercury Surface, Space Environment, Geochemistry, and Ranging (MESSENGER)	Magnetometer with 3.6-m boom (MAG)	4.09	5.13	1130	3 axes	9	Anderson et al. (2007) Bale et al. (2016)
Magnetospheric Multiscale (MMS)	Digital Fluxgate Magnetometer	0.228 (sensor and board)	0.45		Dynamic range: ± 650 nT (low range); $\pm 10,500$ nT (high range) Nonlinearity: $< 3 \times 10^{-5}$ (low range); $< 6 \times 10^{-4}$ (high range) Noise density at 1 Hz: < 8 pT/VHz (low range); < 100 pT/VHz (high range)	9	Russell et al. (2016)

Table B-2. Examples of current charged particle instruments that have flown, are in operation, or are in development.

Mission	Instrument	Mass (kg)	Power (W)	Bitrate (bps)	Capabilities	TRL and Heritage	References/ Notes
Advanced Composition Explorer (ACE)	Solar Wind Electron Proton Alpha Monitor (SWEPAM)	6.8	Nominal: 5.8 Peak: 6.1	1000	Elemental isotopic composition, electron and ion instruments separate H, He, e-; E/Q dist.; ~0.001 MeV/nuc	9	Russell et al. (1998)
ACE	Solar Wind Ion Composition Spectrometer (SWICS)	6	Nominal: 5 Peak: 6.1	504	Chemical/isotopic composition of solar and interstellar medium (ISM) $2 \leq Z \leq 30$; Z, E; ~0.001 MeV/nuc; E/Q, TOF-E	9	Russell et al. (1998) Gloeckler et al. (1998)
ACE	Solar Energetic Particle Ionic Charge Analyzer (SEPICA)	38.3	Nominal: 16.5 Peak: 17.5	608	Ionic charge states of energetic particles from 0.2 MeV/nuc to 5 MeV/nuc $2 \leq Z \leq 30$; Q, Z, E, ~ 1; E/W; dE/dx - E	9	Russell et al. (1998)
Interstellar Mapping and Acceleration Probe (IMAP)	CoDICE (Plasma + Solar Wind)	N/A	N/A	N/A	3D velocity distribution function and ionic charge state/mass composition/arrival direction - 0.5–80 keV/q ions, 0.03–5 MeV/nuc ions, 20–600 keV electrons	6	D. J. McComas et al. (2018)
IMAP	SPICES (Suprathermal + PUI)	N/A	N/A	N/A	In development	~5	Gloeckler, personal communication
Jupiter ICy moons Explorer (JUICE)	Jupiter Energetic Neutrals and Ions (JENI)	7.4 (sensor), 7.0 (shielding)	7.6	500	Combined energetic ion and energetic neutral atom (ENA) camera ~1–300 keV/nuc (ENA), 5 MeV ions, field of view (FOV): 90° × 120°, 2° res (>10 keV H)	8	Brandt (2021)

Mission	Instrument	Mass (kg)	Power (W)	Bitrate (bps)	Capabilities	TRL and Heritage	References/ Notes
JUICE	Jovian Energetic Electrons (JoEE)	1.3 (sensor), 1.9 (shielding)	1.2	<500	Energetic electrons 25 keV – 1 MeV, $\Delta E/E \leq 20\%$, FOV: $12^\circ \times 180^\circ$, $\Delta\omega = 12^\circ \times 22^\circ$	8	Brandt (2021)
New Horizons	Pluto Energetic Particle Spectrometer Science Investigation (PEPSSI)	1.5	2.5	91	Ion detector, FOV: $160^\circ \times 12^\circ$, ion energy detection range 20 keV to 1 MeV	9 Heritage: MESSENGER/Energetic Particle Spectrometer (EPS), Firewheel/ICT, Active Magnetospheric Particle Tracer Explorers (AMPTE)/Charge Composition Explorer (CCE)/Medium-Energy Particle Analyzer (MEPA)	McNutt et al. (2008)
New Horizons	Solar Wind Around Pluto (SWAP)	3.3	2.8	280	Electrostatic analyzer - 35 eV–7.5 keV $\Delta E/E \sim 0.085$	9	D. McComas et al. (2008)
Parker Solar Probe	Solar Wind Electrons Alphas and Protons (SWEAP)	8	10	1500	0.5–30 keV/q $\Delta E/E \sim 0.3$ Interstellar PUIs: $^3\text{He}^+$, $^4\text{He}^+$, N^+ , O^+ , $^{20}\text{Ne}^+$, $^{22}\text{Ne}^+$, Ar^+ Inner-source PUIs: C^+ , O^+ , Mg^+ , Si^+ Mass and charge state of H-Fe ions: $1.4 \times 10^{-3} \text{ cm}^2 \text{ sr eV/eV}$ $6^\circ \times 360^\circ$	9 Heritage: Parker Solar Probe/ SWEAP, ACE/SWICS	Kasper et al. (2016)

Mission	Instrument	Mass (kg)	Power (W)	Bitrate (bps)	Capabilities	TRL and Heritage	References/Notes
Parker Solar Probe	Suprathermals and Energetic Ions (Epi-Lo)	5.1	5	500	0.03–5 MeV/nuc 1 – >60 amu 12° × 10° × 7° over 360° 0.2 cm ² sr	>8 Heritage: Parker Solar Probe, ACE, Juno, MMS, Van Allen Probes, Solar Orbiter	Clark et al. (2016) D. J. McComas et al. (2016) Rodríguez-Pacheco et al. (2020)
ACE	Solar Isotope Spectrometer (SIS)	22.4	Nominal: 17.5 Peak: 22.4	1992	2 ≤ Z ≤ 30; Z, M, E, ~ 20 MeV/nuc; dE/dx - E	9	Russell et al. (1998)
Solar Orbiter	Suprathermal Ion Spectrograph (SIS)	6.8	3.8	400	50 keV/nuc – 14 MeV/n for CNO Two telescopes, pointing 130° apart, FOV 22°, geo factor 0.2 cm ² sr	Heritage: ACE/Ultra-Low-Energy Isotope Spectrometer (ULEIS), Solar Terrestrial Relations Observatory (STEREO)/SIT	Gómez-Herrero et al. (2016) Rodríguez-Pacheco et al. (2020)

Table B-3. Examples of current energetic neutral atom (ENA) instruments that have flown, are in operation, or are in development.

Mission	Instrument	Mass (kg)	Power (W)	Bitrate (bps)	Capabilities	TRL and Heritage	References/Notes
JUICE	JENI	7.4 (sensor), 7.0 (shielding)	7.6	500	Combined energetic ion and ENA camera ~1–300 keV/nuc (ENA), 5-MeV ions, FOV: 90° × 120°, 2° res (>10 keV H)	8	Brandt (2021)

Mission	Instrument	Mass (kg)	Power (W)	Bitrate (bps)	Capabilities	TRL and Heritage	References/Notes
Cassini	Ion and Neutral Camera (INCA)	6.9	3	500	<p>$\geq 1.5^\circ$ (electron optics limit)</p> <p>$90^\circ \times 120^\circ$</p> <p>$< 7 \text{ keV/nuc} - 3 \text{ MeV/nuc}$ (ENA)</p> <p>H, He, O, S</p> <p>GF: $\leq 1.8 \text{ cm}^2 \text{ sr}$</p> <p>Efficiency: 0.2 (H)</p>	9	Krimigis et al. (2004)
Chandrayaan-1	Sub-keV Atom Reflecting Analyser (SARA)/ Chandrayaan-1 Energetic Neutral Analyzer (CENA)	1.98	10	2000	<p>ENA 10 eV–3.2 keV</p> <p>1–56 amu</p> <p>H, O, Na/Mg/Si/Al-group, K/Ca-group, Fe group</p> <p>FOV: $15^\circ \times 160^\circ$</p> <p>Efficiency: 0.01–1%</p> <p>G-factor/sector⁻² $\text{cm}^2 \text{ sr eV/eV}$ at 3.3 keV</p>	9	Barabash et al. (2009)
Interstellar Boundary Explorer (IBEX)	IBEX-Lo	11.5	3.46	100	<p>10–2000 eV (32 energy channels)</p> <p>H, He, O, Ne</p> <p>$45 \times 2^\circ$ pixels using scanning platform</p>	9	<p>D. J. McComas, Allegrini, Bochsler, Bzowski, Christian, et al. (2009)</p> <p>D. J. McComas, Allegrini, Bochsler, Bzowski, Collier, et al. (2009)</p> <p>Fuselier et al. (2009)</p>

Mission	Instrument	Mass (kg)	Power (W)	Bitrate (bps)	Capabilities	TRL and Heritage	References/Notes
IBEX	IBEX-Hi	7.37	0.65	100	0.38–6.0 keV 6.5° $3 \times 10^{-3} \text{ cm}^2 \text{ sr eV/eV}$ at 2.2 keV (double coincidence, incl. eff.)	9	D. J. McComas, Allegrini, Bochsler, Bzowski, Collier, et al. (2009) Funsten et al. (2009)
Imager for Magnetopause-to-Aurora Global Exploration (IMAGE)	High-Energy Neutral Atom Imager (HENA)	19.05	14.6	~1700	Energy range: ~10–300 keV/nuc Energy resolution: ≤ 0.25 Mass resolution: H and Heavies FOV: $120^\circ \times 90^\circ$ Angular resolution: $\geq 3^\circ$ Sensitivity: $0.3 \text{ cm}^2 \text{ sr}$ (H), $1.6 \text{ cm}^2 \text{ sr}$ (O)	9	Mitchell et al. (2000)
IMAGE	Medium-Energy Neutral Atom Imager (MENA)	13.9	22.5	4300	FOV: 140×360 Energy range: 1–70 keV Energy resolution: 80% H, O	9	Pollock et al. (2000)
IMAGE	Low-Energy Neutral Atom Imager (LENA)	20.75	13.1	500	ENA 15–1250 eV E/dE = 1 1–20 amu	9	Moore et al. (2000)
IMAP	Ultra	~7.4	~7.6	~500	Combined energetic ion and ENA camera ~1–300 keV/nuc (ENA), 5-MeV ions, FOV: $90^\circ \times 120^\circ$, 2° (>10 keV H)	8	Brandt, personal communication

Mission	Instrument	Mass (kg)	Power (W)	Bitrate (bps)	Capabilities	TRL and Heritage	References/Notes
IMAP	IMAP-Lo	N/A	N/A	N/A	Energy range: 5–1000 eV Pointing knowledge: 0.1° Angular resolution: 9° full width at half maximum		D. J. McComas et al. (2018)
IMAP	IMAP-Hi	N/A	N/A	N/A	Angular resolution: 4° Energy range: 0.41–15.6 keV Energy resolution: $\leq 0.45 (E_{FWHM}/E)$ Signal-to-noise ratio (SNR): >100 Mass resolution (M/ Δ M): 5		D. J. McComas et al. (2018)

Table B-4. Examples of current neutral mass spectrometers that have flown, are in operation, or are in development.

Mission	Instrument	Mass (kg)	Power (W)	Bit Rate (bps)	Capabilities	TRL and Heritage	References/Notes
Rosetta	Rosetta Orbiter Spectrometer for Ion and Neutral Analysis (ROSINA)	34.8 16 for Double Focusing Mass Spectrometer (DFMS) 15 for Reflectron Time of Flight (RTOF)	49 19 for DFMS 24 for RTOF	20,000	Magnetic mass spectrometer, reflectron-type time-of-flight (TOF) mass spectrometer – molecules up to 300 amu Mass range: 12–150, resolution: $m/dm > 3000$ for DFMS Mass range: 1– 500, resolution > 500 for RTOF	7	Balsiger et al. (2007)

Mission	Instrument	Mass (kg)	Power (W)	Bit Rate (bps)	Capabilities	TRL and Heritage	References/Notes
Lunar Atmosphere and Dust Environment Explorer (LADEE)	Neutral Mass Spectrometer (NMS)	3.5	5	1	Isotope ratios: D/H, ³ He/ ⁴ He, ¹³ C/ ¹² C, ¹⁸ O/ ¹⁶ O, ²² Ne/ ²⁰ Ne, ³⁸ Ar/ ³⁶ Ar Li abundance m/Δm > 100 at 1σ Sensitivity: 0.1 cm ³	9 Cassini, LADEE, Rosetta	Mahaffy et al. (2014) Balsiger et al. (2007) Waite et al. (2004)
Luna-Resurs	Neutral Gas Mass Spectrometer (NGMS)	3.5	6.8–23	1,000,000	Mass range: 1–1000	<9	Fausch et al. (2018)
Cassini	Ion and Neutral Mass Spectrometer (INMS)	10.3	23.3	1495	Mass range: 1–99 Da	9	Waite et al. (2004)
JUICE	Neutral Mass Spectrometer (NMS)	3.1 (sensor only)	11.8–18.5	10–1000	Mass range: 1–1000 amu Mass resolution: m/Δm > 1100 FOV: 10° × 300°	8	P. Wurz, personal communication

Table B-5. Examples of current ultraviolet (UV) instruments that have flown, are in operation, or are in development.

Mission	Instrument	Mass (kg)	Power (W)	Bit Rate (bps)	Capabilities	TRL and Heritage	References/Notes
Voyager	Ultraviolet Spectrometer (UVS)	4.52	3.2	160	Wavelengths: 1.5-nm resolution; 53- to 170-nm range	9	Broadfoot et al. (1977)
Hubble Space Telescope (HST)	Goddard High-Resolution Spectrograph (GHRS)	-	-	-	Spectral range: 110–320 nm Resolution: 0.0012 nm	9	Clarke et al. (1995)

Mission	Instrument	Mass (kg)	Power (W)	Bit Rate (bps)	Capabilities	TRL and Heritage	References/Notes
Defense Meteorological Satellite Program (DMSP)	Special Sensor Ultraviolet Spectrographic Imager (SSUSI)	25.4	28	3800	115–180 nm in 165 bins	9	Paxton et al. (1999) Paxton et al. (1993)
New Horizons	Alice	4.5	4.4	-	Spectral range: 52–187 nm Spectral resolution: 0.36 nm	9	Stern et al. (2008)
Solar and Heliospheric Observatory (SOHO)	Solar Wind Anisotropies (SWAN)	13.25	11	200	Spectral range: 115–180 nm Spectral resolution: 0.001 nm (absorption cell)	9	Bertaux et al. (1995)
Mars Atmosphere and Volatile Evolution (MAVEN)	Imaging Ultraviolet Spectrograph (IUVS)	22	28	-	In Echelle Mode: Spectral range: 116–132 nm Spectral resolution: 0.007 nm	9	McClintock et al. (2015)

Table B-6. Examples of current plasma wave instruments that have flown, are in operation, or are in development.

Mission	Instrument	Mass (kg)	Power (W)	Bit Rate (bps)	Capabilities	TRL and Heritage	References/Notes
Galileo	Plasma Wave Spectrometer (PWS)	7.14	6.8	Low: 240, High: 806,400	Electric: 5.62 Hz to 5.65 MHz, Magnetic: 5.62 Hz to 160 kHz	9	Gurnett et al. (1992)
Parker Solar Probe	Plasma Wave Instrument	6	1.5	100	Includes sensor, wire antennas, shielding, harness	9	Bale et al. (2016)
Voyager	Plasma Wave Subsystem (PWS)	1.4 (without boom)	1.1/1.6	16 bps for typical survey, 115 kbps for burst	E-field spectra to 56 kHz, waveform burst mode	9	Scarf & Gurnett (1977)

Mission	Instrument	Mass (kg)	Power (W)	Bit Rate (bps)	Capabilities	TRL and Heritage	References/Notes
Van Allen Probes	Wave instrument [part of Electric and Magnetic Field Instrument Suite and Integrated Science (EMFISIS) suite]	15.5 (main electronics including MAG electronics and radiation shielding)	14.2 (entire suite)	7.5 kbps survey (full suite), burst modes ranging to 1.3 Mbps	3-channel E, 3-channel B to 12 kHz, 1 channel E to 500 kHz	9	Kletzing et al. (2013)

Table B-7. Examples of current dust instruments that have flown, are in operation, or are in development.

Mission	Instrument	Mass (kg)	Power (W)	Bit Rate (bps)	Capabilities	TRL and Heritage	References/Notes
Cassini	Cosmic Dust Analyzer (CDA)	17.151	12	524	$M/\Delta M > 50$	9	Srama et al. (2004)
LADEE	Dust Detector (LDEX)	3.6	5	579	$M/\Delta M > 200$ $< 1^\circ$ 1–70 km/s $> 0.3 \mu\text{m}$	9	Horányi et al. (2014)
Europa Clipper	SURface Dust Analyzer (SUDA)	-	-	-	200–250 $M/\Delta M$ 1–250 amu	9	S. Kempf, personal communication
In Development	Interstellar Dust Analyzer	9–11	12–15	10	$< 1 \mu\text{m}$ composition	6, Heritage Cassini/CDA, IMAP/Interstellar Dust Explorer (IDEX), Europa Clipper/SUDA	Szalay et al. (2019)
New Horizons	Student Dust Counter (SDC)	1.9	5	900	10^{-12} – 10^{-9} g 0.5 – $10 \mu\text{m}$	9	Szalay et al. (2015)

Table B-8. Examples of current infrared (IR) instruments that have flown, are in operation, or are in development.

Mission	Instrument	Mass (kg)	Power (W)	Bit Rate (bps)	Capabilities	TRL and Heritage	References/Notes
New Horizons	Ralph (Multispectral Visible Imaging Camera [MVIC] and Lisa Hardaway Infrared Mapping Spectrometer, formerly Linear Etalon Imaging Spectral Array [LEISA])	10.5	7.1	Variable; 1–3 kbps	75-mm aperture; 658-mm effective focal length; MVIC panchromatic images (400–975 nm), medium-resolution, high-SNR multispectral imaging; blue, red, IR; methane filters; LEISA is a wedged filter infrared spectral imager (1.25–2.5 μm)	9	Reuter et al. (2008)
Origins, Spectral Interpretation, Resource Identification, Security, Regolith Explorer (OSIRIS-REx)	OSIRIS-REx Visible and Infrared Spectrometer (OVIRS)	17.8	8.8	Variable; 914 kbps (max, OSIRIS-REx)	Wavelength range: 0.4–4.3 μm Resolving power ($\lambda/\Delta\lambda$): 125–560 (higher for longer wavelengths)	9	Reuter et al. (2018)

Mission	Instrument	Mass (kg)	Power (W)	Bit Rate (bps)	Capabilities	TRL and Heritage	References/Notes
In Development	VISIR Spectral Mapper	4	3	10 bps	0.5–15.0 μm , R \sim 100 1D imaging spectrometer, 10 μrad \times 10 μrad + 50–100 μm single-element 10' \times 10' photometer	TRL = 9 for VISNIR flight instrument: Voyager/Infrared Interferometer Spectrometer and Radiometer (IRIS), Galileo/Near Infrared Mapping Spectrometer (NIMS), Cassini/Visible and Infrared Mapping Spectrometer (VIMS), Rosetta/Visible and Infrared Thermal Imaging Spectrometer (VIRTIS), New Horizons/Ralph LEISA using H2RG detector: Deep Impact High-Resolution Instrument/Infrared (HRI/IR), OSIRIS-REx/OVIRS, James Webb Space Telescope (JWST)/Near Infrared Spectrograph (NIRSpec) TRL = 5 using “Speckle” low-Mass/power design: CIBER 2	Hampton et al. (2005) Reuter et al. (2008) Reuter et al. (2018)

Table B-9. Examples of current visible/near infrared (VISNIR) imagers that have flown, are in operation, or are in development.

Mission	Instrument	Mass (kg)	Power (W)	Bit Rate (bps)	Capabilities	TRL and Heritage	References/Notes
Double Asteroid Redirection Test (DART)	Didymos Reconnaissance & Asteroid Camera for OpNav (DRACO)	9	4.95	-	High-resolution, high-SNR panchromatic imaging, 208 aperture, 400–1000 nm, 0.29° full-angle FOV	9	Fletcher et al. (2018)

Mission	Instrument	Mass (kg)	Power (W)	Bit Rate (bps)	Capabilities	TRL and Heritage	References/Notes
New Horizons	Long-Range Reconnaissance Imager (LORRI)	8.6	15	Variable; 1–3 kbps	<p>Panchromatic (~0.3–0.8 μm) and multispectral (~0.3–2 μm) 100 m/pixel at 10,000 km; <5 μrad (baselined ~LORRI optics)</p> <p>Framing (panchromatic) and pushbroom (multispectral) modes (baselined) ~EIS electronics</p> <p>Single-pass pushbroom stereo capability</p> <p>Millisecond to multiple second exposures</p> <p>Tolerance needed to observe planet–Sun transits beyond 30 au as exoplanet analogue. Also could observe moons crossing planets’ disks.</p>	9	Cheng et al. (2009)
New Horizons	MVIC (part of Ralph)	10.5	7.1	Variable; 1–3 kbps	<p>Visible imaging; 400–975 nm (panchromatic); four-color filters (blue, red, methane, near-IR); FOV 5.7° × 0.15° (stare pan) or 5.7° × arbitrary (scan); instantaneous field of view (IFOV) 20 μrad/pixel</p>	9	Reuter et al. (2008)

B.1 Appendix B References

- Anderson, B.J., Acuña, M.H., Lohr, D.A., Scheifele, J., Raval, A., Korth, H., Slavin, J.A. (2007) The Magnetometer Instrument on MESSENGER. *Space Sci. Rev.* 131, 417–450. doi: <https://doi.org/10.1007/s11214-007-9246-7>
- Bale, S.D., Goetz, K., Harvey, P.R., et al. (2016) The FIELDS Instrument Suite for Solar Probe Plus. *Space Sci. Rev.* 204, 49–82. doi: <https://doi.org/10.1007/s11214-016-0244-5>
- Balsiger, H., Altwegg, K., Bochsler, P., et al. (2007) Rosina – Rosetta Orbiter Spectrometer for Ion and Neutral Analysis. *Space Science Reviews* 128(1), 745-801. doi: 10.1007/s11214-006-8335-3
- Barabash, S., Bhardwaj, A., Wieser, M., et al. (2009) Investigation of the Solar Wind-Moon Interaction Onboard Chandrayaan-1 Mission with the SARA Experiment. *Current Science* 96, 526-532.
- Bertaux, J.L., Kyrölä, E., Quémerais, E., et al. (1995) SWAN: A Study of Solar Wind Anisotropies on SOHO with Lyman Alpha Sky Mapping. In Fleck, B., Domingo, V., Poland, A. (Eds.), *The SOHO Mission*. Dordrecht, The Netherlands: Springer.
- Brandt, P.C. (2021) Global Energetic Neutral Atom (ENA) Imaging of Magnetospheres. In Maggiolo, R., André, N., Hasegawa, H., et al. (Eds.), *Magnetospheres in the Solar System* (pp. 673-698).
- Broadfoot, A.L., Sandel, B.R., Shemansky, D.E., et al. (1977) Ultraviolet spectrometer experiment for the Voyager mission. *Space Science Reviews* 21(2), 183-205. doi: 10.1007/BF00200850
- Cheng, A.F., Weaver, H.A., Conard, S.J., et al. (2009) Long-Range Reconnaissance Imager on New Horizons. In Russell, C.T. (Ed.), *New Horizons: Reconnaissance of the Pluto-Charon System and the Kuiper Belt* (pp. 189-215). New York, NY: Springer New York.
- Clark, G., Allegrini, F., McComas, D.J., Louarn, P. (2016) Modeling the Response of a Top Hat Electrostatic Analyzer in an External Magnetic Field: Experimental Validation with the Juno JADE-E Sensor. *Journal of Geophysical Research: Space Physics* 121(6), 5121-5136. doi: <https://doi.org/10.1002/2016JA022583>
- Clarke, J.T., Lallement, R., Bertaux, J.-L., Quemerais, E. (1995) HST/GHRS Observations of the Interplanetary Medium Downwind and in the Inner Solar System. *The Astrophysical Journal* 448, 893. doi: 10.1086/176018
- Dougherty, M.K., Kellock, S., Southwood, D.J., et al. (2004) The Cassini Magnetic Field Investigation. *Space Sci. Rev.* 114, 331-383. doi: 10.1007/s11214-004-1432-2
- Fausch, R.G., Wurz, P., Tulej, M., Jost, J., Gubler, P., Gruber, M., Lasi, D., Zimmermann, C., Gerber, T. (2018, 3-10 March 2018) *Flight Electronics of GC-Mass Spectrometer for Investigation of Volatiles in the Lunar Regolith*. In 2018 IEEE Aerospace Conference, IEEE, Big Sky, MT. doi: 10.1109/AERO.2018.8396788

- Fletcher, Z., Ryan, K., Maas, B., et al. (2018) *Design of the Didymos Reconnaissance and Asteroid Camera for OpNav (DRACO) on the double asteroid redirection test (DART)* (Vol. 10698): SPIE. Retrieved from <https://doi.org/10.1117/12.2310136>
- Funsten, H.O., Allegrini, F., Bochsler, P., et al. (2009) The Interstellar Boundary Explorer High Energy (IBEX-Hi) Neutral Atom Imager. *Space Science Reviews* 146(1-4), 75-103. doi: 10.1007/s11214-009-9504-y
- Fuselier, S.A., Bochsler, P., Chornay, D., et al. (2009) The IBEX-Lo Sensor. *Space Science Reviews* 146(1-4), 117-147. doi: 10.1007/s11214-009-9495-8
- Gloeckler, G., Cain, J., Ipavich, F.M., et al. (1998) Investigation of the Composition of Solar and Interstellar Matter Using Solar Wind and Pickup Ion Measurements with SWICS and SWIMS on the ACE Spacecraft. In Russell, C.T., Mewaldt, R.A., Von Roseninge, T.T. (Eds.), *The Advanced Composition Explorer Mission* (pp. 497-539). Dordrecht, The Netherlands: Springer.
- Gómez-Herrero, R., Rodriguez-Pacheco, J., Wimmer-Schweingruber, R., et al. (2016) *The Solar Orbiter Mission: An Energetic Particle Perspective*. In XXV European Cosmic Ray Symposium, Turin, Italy. Retrieved from arXiv:1701.04057
- Gurnett, D.A., Kurth, W.S., Shaw, R.R., Roux, A., Gendrin, R., Kennel, C.F., Scarf, F.L., Shawhan, S.D. (1992) The Galileo Plasma Wave Investigation. *Space Science Reviews* 60(1), 341-355. doi: 10.1007/BF00216861
- Hampton, D.L., Baer, J.W., Huisjen, M.A., Varner, C.C., Delamere, A., Wellnitz, D.D., A'Hearn, M.F., Klaasen, K.P. (2005) An Overview of the Instrument Suite for the Deep Impact Mission. *Space Science Reviews* 117(1), 43-93. doi: 10.1007/s11214-005-3390-8
- Horányi, M., Sternovsky, Z., Lankton, M., et al. (2014) The Lunar Dust Experiment (LDEX) Onboard the Lunar Atmosphere and Dust Environment Explorer (LADEE) Mission. *Space Science Reviews* 185(1), 93-113. doi: 10.1007/s11214-014-0118-7
- Kasper, J.C., Abiad, R., Austin, G., et al. (2016) Solar Wind Electrons Alphas and Protons (SWEAP) Investigation: Design of the Solar Wind and Coronal Plasma Instrument Suite for Solar Probe Plus. *Space Science Reviews* 204(1), 131-186. doi: 10.1007/s11214-015-0206-3
- Kletzing, C.A., Kurth, W.S., Acuna, M., et al. (2013) The Electric and Magnetic Field Instrument Suite and Integrated Science (EMFISIS) on RBSP. *Space Science Reviews* 179, 127-181. Retrieved from <https://ui.adsabs.harvard.edu/abs/2013SSRv..179..127K>
- Krimigis, S.M., Mitchell, D.G., Hamilton, D.C., et al. (2004) Magnetosphere Imaging Instrument (MIMI) on the Cassini Mission to Saturn/Titan. *Space Science Reviews*, 233-329. doi: 10.1007/s11214-004-1410-8
- Mahaffy, P.R., Richard Hodges, R., Benna, M., et al. (2014) The Neutral Mass Spectrometer on the Lunar Atmosphere and Dust Environment Explorer Mission. *Space Science Reviews* 185(1), 27-61. doi: 10.1007/s11214-014-0043-9
- McClintock, W.E., Schneider, N.M., Holsclaw, G.M., Clarke, J.T., Hoskins, A.C., Stewart, I., Montmessin, F., Yelle, R.V., Deighan, J. (2015) The Imaging Ultraviolet Spectrograph

- (IUVS) for the MAVEN Mission. *Space Science Reviews* 195(1), 75-124. doi: 10.1007/s11214-014-0098-7
- McComas, D., Allegrini, F., Bagenal, F., et al. (2008) The Solar Wind Around Pluto (SWAP) Instrument Aboard New Horizons. *Space Science Reviews* 140(1), 261-313. doi: 10.1007/s11214-007-9205-3
- McComas, D.J., Allegrini, F., Bochsler, P., et al. (2009) Global Observations of the Interstellar Interaction from the Interstellar Boundary Explorer (IBEX). *Science* 326(5955), 959-962. doi: doi:10.1126/science.1180906
- McComas, D.J., Allegrini, F., Bochsler, P., et al. (2009) IBEX—Interstellar Boundary Explorer. *Space Science Reviews* 146(1-4), 11-33. doi: 10.1007/s11214-009-9499-4
- McComas, D.J., Alexander, N., Angold, N., et al. (2016) Integrated Science Investigation of the Sun (ISIS): Design of the Energetic Particle Investigation. *Space Science Reviews* 204(1), 187-256. doi: 10.1007/s11214-014-0059-1
- McComas, D.J., Christian, E.R., Schwadron, N.A., et al. (2018) Interstellar Mapping and Acceleration Probe (IMAP): A New NASA Mission. *Space Science Reviews* 214(8), 116. doi: 10.1007/s11214-018-0550-1
- McNutt, R.L., Livi, S.A., Gurnee, R.S., et al. (2008) The Pluto Energetic Particle Spectrometer Science Investigation (PEPSSI) on the New Horizons Mission. *Space Science Reviews* 140(1-4), 315-385. doi: 10.1007/s11214-008-9436-y
- Mitchell, D.G., Jaskulek, S.E., Schlemm, C.E., et al. (2000) High Energy Neutral Atom (HENA) Imager for the IMAGE Mission. In Burch, J.L. (Ed.), *The IMAGE Mission* (pp. 67-112). Dordrecht, The Netherlands: Springer.
- Moore, T.E., Chornay, D.J., Collier, M.R., Herrero, F.A., Johnson, J., Johnson, M.A., Keller, J.W., Laudadio, J.F., Lobell, J.F., Ogilvie, K.W. (2000) *The Low-Energy Neutral Atom Imager for IMAGE*. Dordrecht, The Netherlands: Springer. Retrieved from [http://scholar.google.com/scholar?q=The low-energy neutral atom imager for IMAGE&btnG=&hl=en&num=20&as_sdt=0%2C22](http://scholar.google.com/scholar?q=The+low-energy+neutral+atom+imager+for+IMAGE&btnG=&hl=en&num=20&as_sdt=0%2C22)
- Paxton, L., Meng, C.-I., Fountain, G., et al. (1993) *SSUSI: Horizon-to-Horizon and Limb-Viewing Spectrographic Imager for Remote Sensing of Environmental Parameters*. In Proceedings of SPIE 1764, Ultraviolet Technology IV, SPIE, San Diego, CA. doi: 10.1117/12.140846
- Paxton, L., Christensen, A., Humm, D., et al. (1999) *Global Ultraviolet Imager (GUVI): Measuring Composition and Energy Inputs for the NASA Thermosphere Ionosphere Mesosphere Energetics and Dynamics (TIMED) Mission* (Vol. 3756): SPIE. 10.1117/12.366380
- Pollock, C.J., Asamura, K., Baldonado, J., et al. (2000) Medium Energy Neutral Atom (MENA) Imager for the IMAGE Mission. In Burch, J.L. (Ed.), *The IMAGE Mission* (pp. 113-154). Dordrecht, The Netherlands: Springer.
- Reuter, D.C., Stern, S.A., Scherrer, J., et al. (2008) Ralph: A Visible/Infrared Imager for the New Horizons Pluto/Kuiper Belt Mission. *Space Science Reviews* 140(1), 129-154. doi: 10.1007/s11214-008-9375-7

- Reuter, D.C., Simon, A.A., Hair, J., et al. (2018) The OSIRIS-REx Visible and InfraRed Spectrometer (OVIRS): Spectral Maps of the Asteroid Bennu. *Space Science Reviews* 214(2), 54. doi: 10.1007/s11214-018-0482-9
- Rodríguez-Pacheco, J., Wimmer-Schweingruber, R.F., Mason, G.M., et al. (2020) The Energetic Particle Detector. *A&A* 642, A7. Retrieved from <https://doi.org/10.1051/0004-6361/201935287>
- Russell, C.T., Mewaldt, R.A., von Roseninge, T.T. (1998) *The Advanced Composition Explorer Mission*. The Netherlands: Springer. 10.1007/978-94-011-4762-0
- Russell, C.T., Anderson, B.J., Baumjohann, W., et al. (2016) The Magnetospheric Multiscale Magnetometers. *Space Science Reviews* 199(1-4), 189-256. doi: 10.1007/s11214-014-0057-3
- Scarf, F.L., Gurnett, D.A. (1977) A Plasma Wave Investigation for the Voyager Mission. *Space Science Reviews* 21(3), 289-308. doi: 10.1007/BF00211543
- Smith, E.J., Dougherty, M.K., Russell, C.T., Southwood, D.J. (2001) Scalar Helium Magnetometer Observations at Cassini Earth Swing-By. *J. Geophys. Res.* 106(A12), 30129-30139. doi: doi:10.1029/2001JA900115
- Srama, R., Ahrens, T.J., Altobelli, N., et al. (2004) The Cassini Cosmic Dust Analyzer. *Space Science Reviews* 114(1), 465-518. doi: 10.1007/s11214-004-1435-z
- Stern, S.A., Slater, D.C., Scherrer, J., et al. (2008) ALICE: The Ultraviolet Imaging Spectrograph Aboard the New Horizons Pluto-Kuiper Belt Mission. *Space Science Reviews* 140, 155-187. Retrieved from <https://ui.adsabs.harvard.edu/abs/2008SSRv..140..155S>
- Szalay, J., Piquette, M., Horanyi, M. (2015) *Dust Measurements by the Student Dust Counter Onboard the New Horizons Mission to Pluto*. In 46th Lunar and Planetary Science Conference, The Woodlands, Texas. Retrieved from <https://www.hou.usra.edu/meetings/lpsc2015/pdf/1701.pdf>
- Szalay, J., Horanyi, M., Sternovsky, Z., Poppe, A., Lisse, C., Draine, B., Zemcov, M., Beichman, C. (2019) *The Interstellar Dust Analyzer: Measuring interstellar and zodiacal dust in-situ*. In 2nd Interstellar Probe Exploration Workshop, New York, New York. Retrieved from https://interstellarprobe.jhuapl.edu/uploadedDocs/presentations/346-szalay_ism_poster_2019.pdf
- Waite, J.H., Lewis, W.S., Kasprzak, W.T., et al. (2004) The Cassini Ion and Neutral Mass Spectrometer (INMS) Investigation. *Space Science Reviews* 114(1), 113-231. doi: 10.1007/s11214-004-1408-2

and the resulting geometric Jupiter alignment to depart toward the intended (0°N, 295°E) direction that, in fact, sits between the 2039 and 2040–2041 hot zones. Other targets for powered JGA meet similar science criteria, including a potential candidate direction at (12°S, 284°E) that starts near the Ixion location in Figure C-1. Launching in December 2039, the powered JGA candidate solution toward (12°S, 284°E) achieves a 7.44 au/year speed but accomplishes only a 37° off-nose angle. At only 8° from the idealized off-nose objective, it is considered to be an acceptable trade reduction on the side-view objective to preserve a high-speed departure.

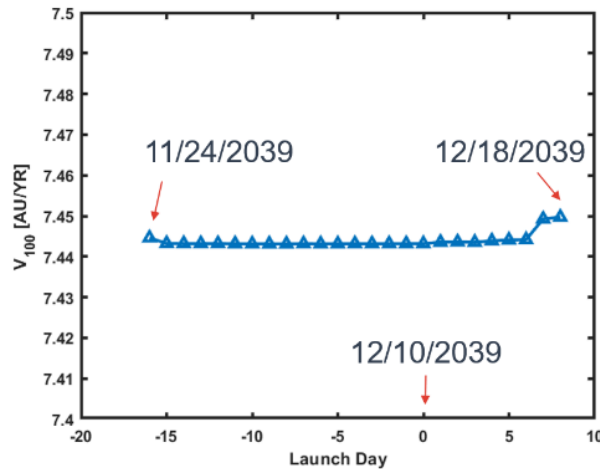
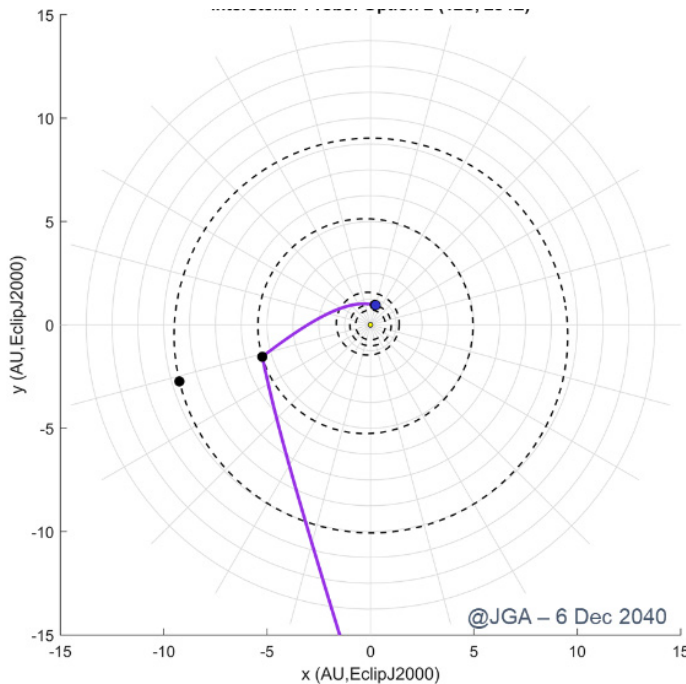


Figure C-2. Escape speed variation across the launch period for the powered JGA option.

Regarding launch period considerations, the powered JGA case uses a variable $C3$ and a slightly variable target ($\pm 1^\circ$ around the (12°S, 284°E) destination) to craft a longer and more stable set of launch options over a multiday period. The resulting powered JGA launch period (Figure C-2) possesses 7.44 au/year over a 25-day range. Note that the slight variance in $C3$ assists in geometric alignment in conjunction with the powered flyby; the $C3$ value peaks at the intended 203.91 km^2/s^2 at the edges but smoothly dips to 193.98 km^2/s^2 during the middle of the launch period. Note that the powered JGA destination moves slightly to (11.68°S, 284.52°E) for a maximized outbound direction.



(a) Interplanetary trajectory

Event	MET
Launch	10 Dec 2039
JGA	0.99 yrs
80 AU	11.2 yrs
100 AU	13.8 yrs
120 AU	16.4 yrs
200 AU	26.8 yrs
377 AU	50.0 yrs
500 AU	66.1 yrs
1000 AU	131.5 yrs

(b) Event timeline

Figure C-3. Heliocentric mission geometry for notional powered JGA to (12°S, 284°E) with associated timeline. Planetary positions in panel (a) correspond to the powered JGA on 6 December 2040.

The powered JGA cases require ~11–13 months of flight time to Jupiter such that the Sun–Earth–probe angle at the Jupiter encounter is comfortably ~40° for most speed-optimal cases. Figure C-3 gives the mission profile for this option.

It is worth noting that the large final acceleration taking place in Jupiter’s gravity well, rather than that of Earth during the normal launch sequence, precludes the plasma wave and magnetometer deployments until after the kick stage used at Jupiter is successfully jettisoned. This delay and deployment at smaller data rates (uplink and downlink) tend to increase overall mission risk. This is in addition to the thermal constraints on the SRM during the Earth-to-Jupiter cruise.

Appendix D. Solar Oberth Maneuver

D.1 Description of the Solar Oberth Maneuver

As described in Appendix H (Mission Architecture), three options for generating a high-speed departure from the solar system were identified. Option 3 is known as the solar Oberth maneuver (SOM) trajectory. For this option, we would use a heavy-lift vehicle to launch a spacecraft with a solid rocket motor (SRM) and a protective solar shield to Jupiter for a Jupiter gravity assist (JGA) that lowers perihelion to a few solar radii. The SRM executes at perihelion to create orbital conditions with high escape speed. A mission using the SOM trajectory can achieve a higher escape speed than either the ballistic or powered JGA options; this mission will incur significant challenges associated with the flight to the Sun, the solar encounter, and the separation of the observatory from the SRM and associated components.

At launch, the flight system will consist of the observatory, SRM, and transition ring with a mechanism to separate the observatory; a thermal protection system to protect flight components from the solar environment; ballast used to balance the thermal protection system; and structures used to connect and support all other components. One possible configuration is shown in Figure D-1. For the purposes of this discussion, the *flight system* is the collection of components in Figure D-1, and the *observatory* is the spacecraft that separates from the rest of the flight system and hosted science payload.

The SOM imposes requirements on the overall flight system and observatory itself. The flight system must:

- Target and complete a JGA such that the desired perihelion is achieved, then target that perihelion, perform the SOM, and maintain trajectory outbound from the Sun
- Provide thermal control of the SRM from launch to firing at perihelion, including thermal gradients across the SRM
- Provide a thermal protection system to protect the flight system components from solar illumination and other solar environment effects as close as 2 solar radii (R_s), measured from the center of the Sun
- Provide attitude control sufficiently well to reliably prevent exposure of vulnerable components to the solar environment
- Provide telecommunications to Earth before observatory separation sufficient to navigate and operate the spacecraft from Jupiter to perihelion and then to observatory separation

In addition to these flight system driving requirements, the observatory is required to meet the science and operational requirements of the post-separation mission, similarly to the baseline mission.

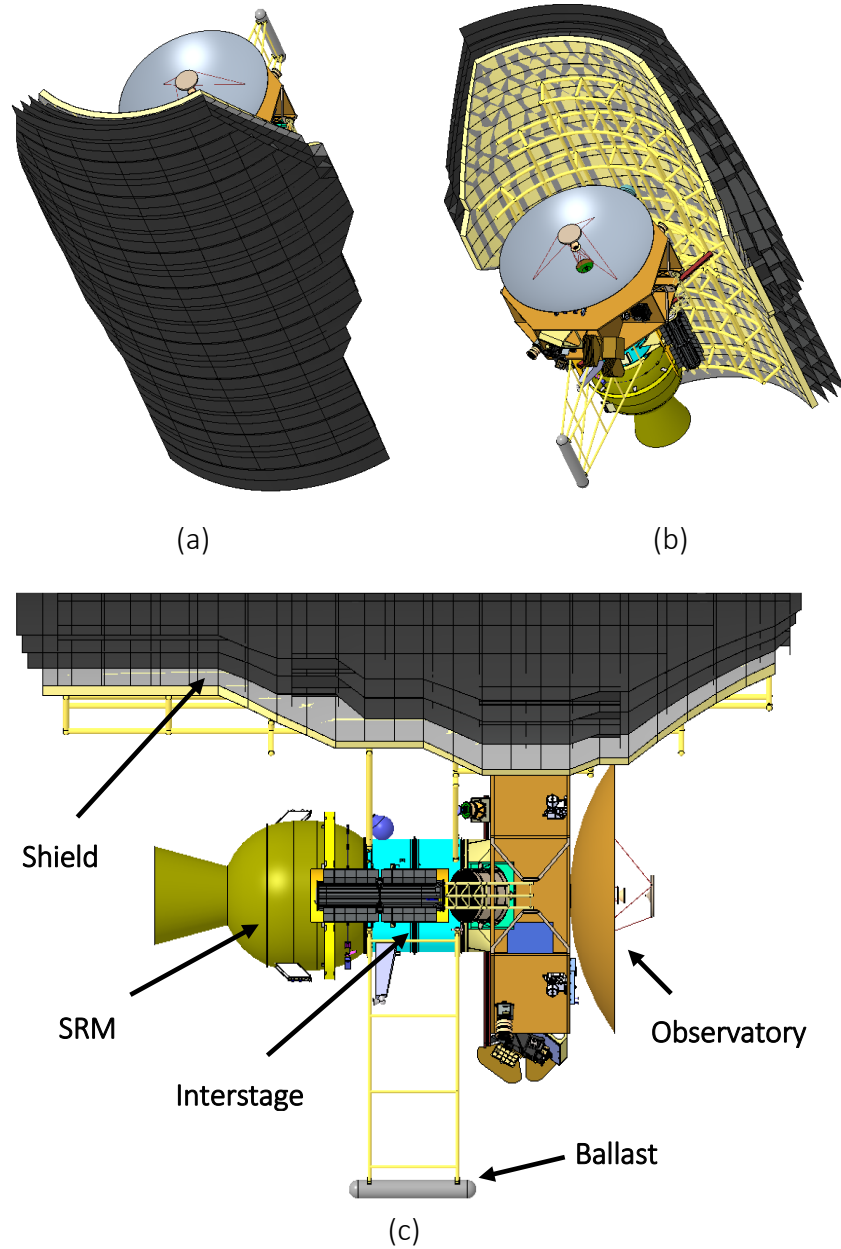


Figure D-1. Views of the SOM flight system for the 2 R_s , Star 48BV case. (a) Sun-facing view showing the thermal protection system. (b) Anti-sunward view. (c) Side view with identification of flight system components. (Image credit: Johns Hopkins Applied Physics Laboratory.)

D.2 Flight System Description

Unique aspects of the near-solar environment mean that the flight system for the SOM case is significantly different from the flight systems used in either Option 1 or Option 2, the JGA-only cases. In particular, the need to protect the observatory from solar illumination during the approach to, perihelion at, and departure from the Sun drives the design. Figure D-1 shows the flight system design that meets the driving requirements above, with the major components identified in Figure D-1(c). Each is described below.

The flight system is composed of five major components: the SRM used to perform the SOM; the observatory used to conduct the science mission itself; an interstage module (IM) to interface the SRM and observatory, support the TPS and ballast, and provide subsystems such as a secondary propulsion system to control the flight system before observatory separation; the TPS and support structure; and ballast used to balance the TPS. Each of these is described below. Masses have been developed for the flight system for each perihelion considered, and these masses were used to develop escape speeds for each perihelion design. Table D-1 gives mass estimates for the individual components and the flight system as a whole for the $3 R_s$ perihelion case.

Table D-1. Mass breakdown of flight system components for a solar Oberth trajectory with perihelion at $3 R_s$.

Flight System Component	Mass (kg)
Spacecraft	900
Interstage	300
Star 48BV Stage	2624
Thermal Protection Shield/Support Structure	788
Ballast/Support Structure	600
Margin	30%
Total	6776
Not-to-Exceed Mass	7000

D.2.1 Solid Rocket Motor

To be most effective, the SOM requires a high-impulse rocket to be fired at perihelion over a short period of time. Based on the launch vehicle trade performed early in the study, the Orion 50 XL and Star 48BV/GXV are candidates for use in this mission design. Both are compatible with the flight system design, with similar characteristics; Figure D-1 shows a Star 48BV.

D.2.2 Thermal Protection Shield

The Interstellar Probe heat shield provides umbra protection for the spacecraft and SRM. Shield design options are limited by high-temperature material availability and the capabilities of high-temperature fabrication and test facilities. The two major shield design issues are thermal and mechanical. Unlike earlier missions, where a shield design was needed for a given Sun distance, the Interstellar Probe challenge is to see how close to the Sun a spacecraft can realistically get. As the solar distance decreases, the umbra angle increases and the size of the shield, relative to the spacecraft, grows significantly. Because a conceptual design effort cannot include all the material design, fabrication, and testing limitations of the full design, the final recommendation of allowable Sun distance is made based on where the design seems to be moving from very difficult to impossible.

Key design criteria for the shield are its external optical properties and insulating capabilities. The limiting factor for any proposed material is its ability to withstand the temperatures experienced during the solar pass. Optical propriety and material conductivity uncertainties in the near-Sun environment preclude the use of standard materials.

The conceptual Interstellar Probe thermal shield consists of four separate sections. The first section is made from several layers of thin, ultra-high material separated from each other. The thin layers provide a series of radial, radiative barriers. Their spacing allows heat to escape along the edges and reduces peak temperatures to ~ 2300 K. The second shield section consists of a Parker

Solar Probe-type carbon–carbon/foam sandwich that drops the rear wall temperatures to <800 K. At this point, the transition to standard materials and designs happens. The third section of the shield is the supporting truss structure, which provides significant thermal resistance between the hot sections and the spacecraft bus. Finally, the last section consists of high-temperature thermal blankets that surround the spacecraft and protect it from the heat radiating from the hot sections. Combining all the shield sections, the near-Sun heat shield has to reduce the incident heat hitting the shield by 99.995% before it reaches the bus. Although analytically the numbers may be shown to work with the proper combination of optical properties and thermal resistances, the actual implementation is nearly impossible to verify.

Other types of design approaches have been suggested and will continue to be put forward. It is hard to assess these options because they reference materials and test capabilities that do not exist. The effort to decide whether these options can be made practical will involve a great amount of time and money before more realistic assessments can be made.

Table D-2. Shield and support masses for a range of SOM trajectory perihelia.

Solar Distance of SOM (R_s)	Star 48BV Configuration (kg)
2	653
3	524
4	444
5	326
6	315

Note that the TPS becomes larger as the perihelion is decreased. Table D-2 gives the estimated mass of the TPS for the range of perihelia considered in this design.

D.2.3 Ballast

A major concern is to keep the thrust vector of the SRM aligned with the center of mass of the flight system to prevent uncontrollable torque as the SRM fires. Using a large propulsion system to provide control authority during the burn is unfeasible, so we have chosen to include ballast to balance the center of mass offset induced by the TPS. This ballast is passive, likely made of tungsten or another high-density material, is supported by a titanium structure that interfaces with the IM, and is pushed to the boundary of the umbra formed by the TPS to reduce the ballast mass as much as possible.

D.2.4 Interstage Module

The IM performs three primary functions: interfacing the SRM and observatory with a separation mechanism at the observatory interface, providing support for the thermal shield and ballast structures, and containing components needed to control the flight system from launch through the SOM to observatory separation. Given the size and mass of the flight system, the observatory propulsion system is insufficient to control the attitude of the stack. The IM will include a secondary propulsion system with propellant tank and thrusters sized to provide attitude control, as well as components used to control the firing and thrust vector control of the SRM during firing.

D.2.5 Observatory

The observatory is intended to perform the science mission—whether heliophysics or with augmentations. As such, it must meet the requirements of the primary mission as well as survive the

SOM and operate the overall flight system before separation. The basic design of the observatory is similar to the baseline design described in Section 5, with several modifications driven by the specific needs of the SOM.

- The 5-m X-band high-gain antenna (HGA) of the baseline design is large and, if kept, drives the thermal shield size and mass to untenable levels. Two options were considered to reduce the size of the HGA: a 2-m Ka-band HGA or deployable 5-m X-band antenna. We chose the smaller Ka-band dish to eliminate concerns over deployment of the HGA more than 5 years after launch; however, use of Ka band inherently limits downlink rates as the observatory reaches the most interesting parts of the mission during the transition to the local interstellar medium.
- The radioisotope thermoelectric generators (RTGs) powering the observatory are long and, in the baseline design, extend away from the body of the spacecraft. This design is favorable for power generation but drives the size and mass of the thermal shield. We have elected to mount the RTGs on mechanisms that deploy after observatory separation to provide the full view of space needed for optimal power generation. This design introduces risk but does have heritage with the Voyager spacecraft, for instance.
- The interface to the SRM through the IM is significantly more complex than in the baseline design. For the SOM, power and data interfaces to and through the IM are required to provide functions that control the flight system. In addition, the flight system will also most likely require a thermal control system that moves waste heat from the RTGs to the SRM to regulate its temperature.

D.3 Mission Design

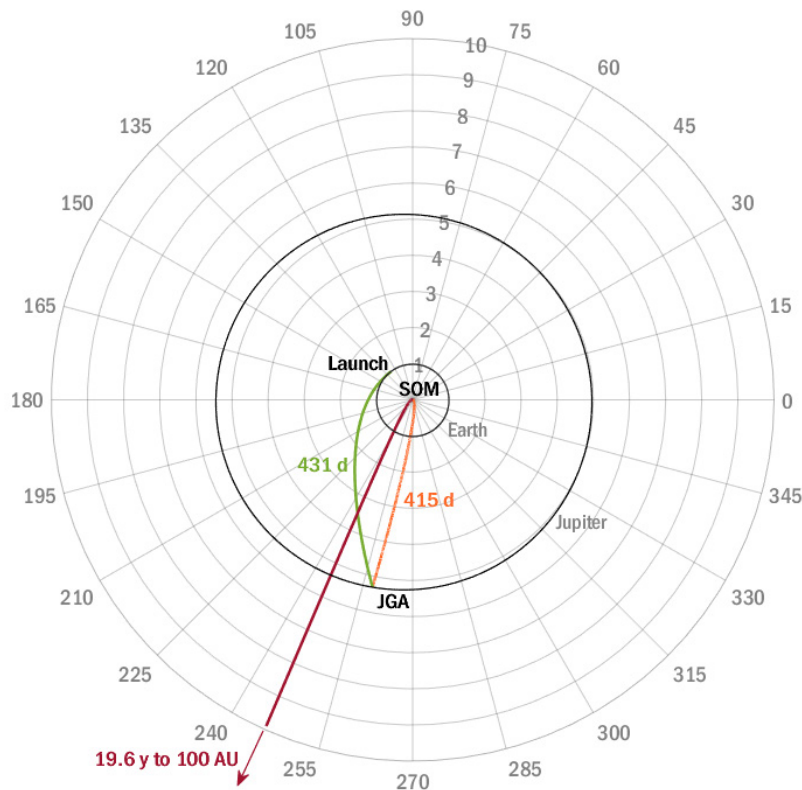
The SOM mission is executed in five phases: launch to JGA, JGA to SOM, perihelion, SOM to observatory separation, and primary science mission. Figure D-2 gives a schematic of the mission. Each phase offers different challenges, as discussed below.

D.3.1 Launch to Jupiter Gravity Assist

The first phase of the SOM mission is an interplanetary cruise to Jupiter for a gravity assist that targets the selected perihelion. This JGA is a critical event for the SOM mission. For the flight system mass and expected performance of the launch vehicle, transit time to Jupiter is $\sim 1\text{--}1.5$ years. During this time, the flight system must control the trajectory to target the JGA aimpoint and keep the SRM within thermal limits. No science will be accomplished during this phase of the mission because the payload cannot be deployed until after observatory separation.

D.3.2 Jupiter Gravity Assist

After completing the JGA to target the desired perihelion, 1–2 years are needed to reach the perihelion and execute the SOM. As with the previous phase, operations during this time are centered on control and protection of the flight system and trajectory as well as preparation for the SOM. No science will be accomplished during this phase of the mission because the payload cannot be deployed until after the observatory separation.



Launch:

- 27 January 2030
- $C_3 = 140.0 \text{ km}^2/\text{s}^2$

Jupiter gravity assist:

- 2 April 2031
- $V_\infty = 16.9 \text{ km/s}$, $1.054 R_J$

Perihelion and SOM:

- 21 May 2032
- $r_p = 2.98 R_s$, $v_p = 358.5 \text{ km/s} = 75.4 \text{ au/year}$
- SOM $\Delta V = 0.971 \text{ km/s}$
- 19.6 years from SOM to 100 au

Science Mission:

- $v_{100 \text{ au}} = 4.87 \text{ au/year}$
- $RA = 247^\circ$

Figure D-2. Example SOM mission scenario. (Image credit: Johns Hopkins Applied Physics Laboratory.)

D.3.3 Solar Oberth Maneuver

The SOM at perihelion is the most critical event for this mission concept, and the environment for this activity is the most challenging. In the period around perihelion (roughly ± 2 months around perihelion), the primary function of the flight stack is to provide tight control of the flight system attitude, not only to prevent catastrophic exposure to solar illumination but also to accurately fire the SRM. No science will be accomplished during this phase of the mission because the payload cannot be deployed until after the observatory separation.

D.3.4 Observatory Separation

After the SOM, the thermal environment remains hazardous until the flight system reaches a significant distance from the Sun. Based on results from Parker Solar Probe, this may be as early as 0.7 au, but 1 au is more likely. The transit to safe thermal conditions requires < 1 month. During the transition to the point at which the thermal shield is no longer needed to protect the observatory, operations will be similar to prior phases in that the primary concern is to protect the flight system from solar illumination and control the flight to the outer solar system. Observatory separation is the final critical event for the SOM mission concept, and after separation, the primary science mission can begin.

D.3.5 Primary Science Mission

After observatory separation, the SOM mission concept is similar to missions developed using the ballistic or powered JGA only. As with those concepts, deployment, checkout, and calibration of the instruments are expected to take several months. Mission constraints and risks are similar to those of the baseline concept.

D.4 SOM Performance and Escape Trade

To evaluate whether a SOM offers advantages in escape speed or mission lifetime, we conducted a two-part study of mission design. First, we used optimistic masses for the flight system stack to understand the range of escape speeds that could be achieved for the launch system/fourth-stage configurations that could be launched based on our initial launch configuration trade study. This represents the best a SOM can do with existing launch vehicle and SRM technology. Second, and after developing a realistic design for the flight system, we developed a specific case to understand what could realistically be accomplished given the constraints induced by the SOM to better directly compare with the baseline Option 1 and 2 cases. The results of these studies indicate that the SOM offers no advantage with regard to escape speed or mission lifetime.

D.4.1 Initial Trade Study

From Oberth’s 1929 book (Oberth, 1970) until the present, the applicability of a powered, near-Sun rocket maneuver to escape the solar system has been a topic of much speculation. While Oberth explored the kinematic requirements, the issues of dealing with the thermal environment while also providing a “suitable” speed change are more perplexing. Although nominally engineering issues, both are ultimately limited by chemistry and physics as well.

Recall that Oberth had allotted his astronaut a rocket with a total ΔV of 6 km/s and orbiting the Sun in a circular orbit at 900 au. He noted that the best scheme is to use 1 km/s to deorbit the vehicle to fall into the Sun and then use the remaining 5 km/s at a perihelion defined by the vehicle speed being 500 km/s. He derives the resulting exit from the solar system to be 70.9 km/s or ~ 15 au/year. He noted the need to bring the craft “to the edge of the solar corona.” It can be shown that a perihelion speed of 500 km/s corresponds to a closest approach of $\sim 1.5 R_s$ from the Sun’s center.

The two auxiliary assumptions are as follows:

1. A total ΔV of 6 km/s can be achieved, presumably with a single stage.
2. Approaching to within $0.5 R_s$ of the photosphere, the Sun’s effective “surface,” is possible.

The threshold for a gravity assist at Jupiter (retrograde or prograde) for the idealized model in place here corresponds to the launch energy for an Earth-to-Jupiter Hohmann transfer orbit: one has to have the energy to reach Jupiter in order to interact with its gravitational field in any case.

Recall that for the limiting retrograde case, we would have (R. L. McNutt Jr., 2021)

$$v_a = v_j - v_\infty, \tag{1}$$

with the spacecraft’s incoming asymptotic speed in Jupiter’s reference frame $\mathbf{v}_{\infty, before}$ and the outgoing spacecraft velocity vector \mathbf{v}_a and Jupiter’s orbital velocity vector \mathbf{v}_j both in the heliocentric frame after the gravity assist. For $\mathbf{v}_a = \mathbf{0}$, the spacecraft literally would fall into the Sun from Jupiter’s orbital distance. Defining Jupiter’s average orbital radius in au as \hat{r}_j , Earth’s average orbital speed as v_E , and the corresponding C_3 as $C_{3, stop}$,

$$\frac{\sqrt{C_{3, stop}}}{v_E} = -\left(1 - \frac{1}{\hat{r}_j^{3/2}}\right) + \sqrt{\frac{1}{\hat{r}_j^3} + 2 - \frac{2}{\hat{r}_j}}, \quad (2)$$

which using $v_E = 29.7859$ yields $C_{3, stop} = 113.8 \text{ km}^2/\text{s}^2$. Smaller values of C_3 correspond to larger perihelion values. It is clear that a fairly narrow range of launch energies can control the perihelion of the spacecraft.

Larger C_3 s with no plane change can actually provide retrograde orbits around the Sun.

Although all this sounds fairly straightforward, the crux of the analysis has always concerned the appropriate thermal shield and how its mass drives the propulsion requirements (because “You can’t go at night”).

Point 1: A starting point of an “asteroid” in a circular orbit at 900 au may be good for this *gedanken* experiment, but a more “realistic” starting point is a direct launch from Earth itself. The launch C_3 combined with an “ideal” retrograde JGA maps deterministically to the perihelion in the orbit at the Sun. In the context of the coplanar, circular orbit model using a patched conic formulation, a perihelion on $9.86 R_s$ (the final planned perihelion of Parker Solar Probe) corresponds to a launch C_3 of $102.1744 \text{ km}^2/\text{s}^2$. Higher C_3 s enable lower perihelia. See Table D-3. For a 450-kg spacecraft + 30% reserve (= 585 kg) on a Fregat kick stage (this work with Fregat in the mix was done in August 2016), the available ΔV is 4.891 km/s.

At face value then, Oberth’s postulate of achieving $\sim 5 \text{ km/s}$ with a kick stage is not a bad one.

However, although these results look impressive, they are far from self-consistent. The total stack mass is 6765 kg (spacecraft plus probe—but less the adaptor masses), and this does not include *any* thermal shield mass. As the perihelion gets closer to the Sun, the thermal shield mass and its connections back to the spacecraft and, especially, the kick stage will increase.

Point 2: If we wanted to posit the ultimate physical limits, then the real question is how close to the photosphere ($R_s = 1$) can one get. The effective solar blackbody temperature is 5772 K (Williams, 2018), which is far in excess of the total failure point of any material (cf., e.g., (Shabalin, 2014)). Ultimately such failure points are driven by the quantum mechanical considerations of the material in question. Some type of matrix combination of hafnium and/or tantalum carbide appears to provide for the highest failure temperature in the vicinity of $\sim 4200 \text{ K}$ (Cedillos-Barraza et al., 2016) (but with no structural strength). This exceeds the melting point of tungsten at $\sim 3695 \text{ K}$. Tungsten has structural strength while the aforementioned carbides have far less, but its mass is problematic for a thermal shield, as are those of the other refractory metals (McNutt et al., 2019).

Table D-3. Perihelia as a function of C_3 for direct-to-Jupiter trajectories.

C_3 (km ² /s ²)	$r_{\text{perihelion}}$ (R_{Sun})	$v_{\text{perihelion}}$ (km/s)	$V_{\text{esc}} = (2E_{\text{final, Oberth}})^{1/2}$ (au/yr)
102.100265	10.0000	194.458922	8.4067
102.174400	9.8600	195.846274	8.4424
102.368106	9.5000	199.554847	8.5372
102.644618	9.0000	205.068572	8.6763
102.930533	8.5000	211.060608	8.8249
103.226696	8.0000	217.604559	8.9845
103.534085	7.5000	224.790907	9.1566
103.853845	7.0000	232.732374	9.3431
104.187326	6.5000	241.571445	9.5464
104.536148	6.0000	251.491427	9.7696
104.902273	5.5000	262.732626	10.0166
105.288122	5.0000	275.617597	10.2925
105.696739	4.5000	290.591126	10.6041
106.132042	4.0000	308.287067	10.9610
106.599218	3.5000	329.646127	11.3769
107.105395	3.0000	356.137858	11.8726
107.660830	2.5000	390.216472	12.4815
108.281264	2.0000	436.372532	13.2617
108.993196	1.5000	503.992132	14.3283
109.848283	1.0000	617.399424	15.9581
110.979882	0.5000	873.330137	19.1328
112.000245	0.2000	1381.039594	24.2296
113.791647	0.0000	Not applicable	Not applicable

From the Stefan–Boltzmann law, the intercepted solar flux is proportional to the fourth power of the absolute temperature, but it also decreases as the inverse square of the distance from a point source. For a thermal power source of strength Q , the thermal power a distance r from the source will raise an ideal blackbody to the temperature T where

$$\sigma T^4 = \frac{Q}{4\pi r^2} \quad (3)$$

and

$$\sigma T_{\text{sun}}^4 = \frac{Q}{4\pi R_s^2} \quad (4)$$

so that

$$r = R_s \left(\frac{T_{\text{sun}}}{T} \right)^2. \quad (5)$$

With $T = 4200$ K, the minimum perihelion can be estimated as $r = 1.892 R_s$. This corresponds to $C_3 = 108.4261$ km²/s². With this very simple scaling (at these distances, the Sun can no longer be considered a “point source”), getting to Oberth’s implied $1.5 R_s$ would require a material failure

temperature of ~ 4720 K, and this exceeds, by ~ 500 K, the highest known failure material of any currently known material at 4232 ± 84 K (for $\text{HfC}_{0.98}$) (Cedillos-Barraza et al., 2016).

Testing to date suggests that a shield with a temperature of 4200 K could last up to 2 hours in hard vacuum near the Sun. Conversely, if we accept $\sim 2 R_s$ as being the closest approach possible, our rough estimate implies a corresponding temperature of ~ 4085 K. Given all the uncertainties, this is perhaps the best estimate in the absence of better thermal data and a better thermal shield design and accounting of the finite size of the solar disk at such small distances:

$$\theta_{subtend} = 2\sin^{-1}\left(\frac{R_s}{r}\right). \quad (6)$$

Hence, solar disk sizes include 84° at $1.5 R_s$, 60° at $2 R_s$, 29° at $4 R_s$, and 12° at $9.86 R_s$, as examples.

One could object that one could “do better” (= “go closer”) with an active cooling unit such as that used to cool the solar arrays on Parker Solar Probe (Fox et al., 2016). However, in addition to added complexity and an even more extreme lack of possible testing in a “relevant environment,” such a system would certainly be more massive, requiring an active pumping system with backup, plumbing, and thermally insulated radiator panels located opposite the thermal protection system (TPS), as are used on Parker Solar Probe. While one can speculate about such systems (Bradbury, 1967), they fall far outside “near-term”/“pragmatic” technology.

Point 3: A full system, which “closes,” must still be assembled from our posited “building blocks.” In particular, as we have argued elsewhere, the only launch system capable of making a direct-to-Jupiter trajectory is of the super heavy-lift launch vehicle (SHLLV) class. Otherwise one must add the additional complexity and costs associated with a custom propulsion system required for at least one deep-space maneuver (DSM) and/or Earth/Mars and/or Venus flybys. The only vehicle of this class with publicly released high C_3 data is the Space Launch System (SLS) Block 2 Cargo configuration. At this time, this is the only vehicle of the Saturn V (U.S.)/N-1 (Soviet) class with sufficiently characterized and publicly available injected mass capabilities to allow for detailed system studies. Similarly, there are a finite number of kick stages, with well-known characteristics and very high success-rate performance, to combine with such a launch vehicle for the purpose of constructing a solid engineering design.

Allowing for a Centaur-3 (Atlas V second stage) for the third stage of an SLS Block 2 Cargo stack and adopting a C_3 of $108.3 \text{ km}^2/\text{s}^2$ (Table D-3 entry for a $2 R_s$ perihelion), we can estimate an injected mass from:

$$C_3 \cong -77.68341 \ln m + 292.35354, \quad (7)$$

with C_3 in km^2/s^2 and the injected mass m (including current Manager’s reserves) in metric tons (mt). The fit has an R -square of >0.999 from C_3 of -40 to $420 \text{ km}^2/\text{s}^2$ and can be inverted with high fidelity in this range to yield

$$m \cong e^{\left(\frac{292.35354}{77.68341}\right)} e^{-\frac{C_3}{77.68341}} = 42.47517 e^{-\frac{C_3}{77.68341}}. \quad (8)$$

Using Equation 8 for C_3 of $108.3 \text{ km}^2/\text{s}^2$ yields $m = 10.54 \text{ mt}$ for the stack delivered to a perihelion at $2 R_s$.

Point 4. The next step is to determine the largest ΔV consistent with a total stack mass of 10.54 mt , including the observatory (separated spacecraft) and kick stage. The latter must include engine plus guidance and control systems plus any heating loops using reject radioisotope power system (RPS) thermal power required to maintain the kick-stage engine and propellant within required thermal limits for up to ~ 3 years total cruise time: Earth to Jupiter plus Jupiter to Sun. This mass must also include the TPS for the spacecraft plus kick stage, the thermal structure assembly (TSA) to connect the TPS to the rest of the perihelion stack, and the required adaptor hardware for the Centaur to stack as well as adaptor hardware for the kick stage to the observatory.

Point 5. Given all the aforementioned mass liens and a 500-kg (New Horizons class) to 1000-kg (Voyager-class) observatory, we are limited to an existing, proven solid rocket engine to maximize the ΔV . Custom liquid systems will increase costs significantly. Nuclear thermal propulsion (NTP) systems do not exist, would be too massive (compare the “initiative” for the “small nuclear rocket” (Schnitzler & Borowski, 2007, 2008; Schnitzler et al., 2009)), and would require deep-space storage of liquid hydrogen (LH_2) with minimal boiloff (an oft-promised technology, the most recent being the Atlas-Vulcan system, but never demonstrated). Cryogenic systems using liquid oxygen (LOX) and LH_2 suffer from the same LH_2 storage problem, and custom space-storable bipropellant (e.g., nitrogen tetroxide [NTO] plus hydrazine – anhydrous, unsymmetrical dimethyl hydrazine [UMDH], or monomethyl hydrazine [MMH], or derivatives, e.g., Aerozine-50 [half UMDH and half MMH]) or monopropellant [hydrazine]) have cost plus “complexity mass,” which limit their effectiveness while not providing significantly larger specific impulse (I_{sp}) (Greenwood, 1975) over solid systems. Minimization of protracted burn times (introducing significant gravity losses in the burn) also shift considerations in favor of the higher-thrust, solid engines.

The real question is whether a SOM (Option 3) offers any technical advantage over simpler trajectories using a prograde JGA only (Options 1 and 2). To enable such comparisons, we need to include explicit staging and perihelion/thermal shield requirements. A more subtle point is that even if Option 3 provides a larger asymptotic speed, it may not propel the spacecraft to the largest distance within the required 50-year design lifetime: at the same launch date, Option 1 and 2 trajectories simply move outward with additional speed from their respective Jupiter flybys. In carrying the heaviest possible kick stage to perihelion, the Option 3 trajectory will take longer to get to Jupiter and require more time to fall back to the Sun, and then the “fast” trajectory starts from a heliocentric distance of essentially zero. If the SOM only offers a marginally larger speed, it may not overtake an Option 1 or 2 launch over the 50 years beginning at the launch.

To illustrate the logic of looking at the various trades, within the confines of our simplified analytic trajectory model, consider the limiting performance for a nominal stack consisting of a Centaur-3 (Atlas V second stage) and a Star 48BV carrying a 250-kg separated spacecraft (about the mass of Pioneer 10 (about the mass of Pioneer 10; McNutt Jr et al., 2014). For Option 1, we have $C_3 = 400.0 \text{ km}^2/\text{s}^2$, asymptotic speed with no JGA of 5.6 au/year , asymptotic speed with passive gravity assist at the cloud tops of 8.4 au/year , and corresponding flight times to 500 au of 88.1 years and 60.0 years, respectively. For Option 2, $C_3 = 220.4 \text{ km}^2/\text{s}^2$ and $\Delta V = 4.46 \text{ km/s}$. For these parameters, the

alignment of the outgoing asymptotic velocity vector with Jupiter’s orbital velocity vector implies a closest approach of less than one Jupiter radius. So, fixing the closest approach at $1 R_J$ (i.e., $r_p/r_0 = 1$) yields an asymptotic speed with gravity assist at the cloud tops of 8.9 au/year, and corresponding flight time to 500 au of 57.0 years, three years less than for Option 1.

We can also make an initial, but not quite self-consistent, comparison with results for a SOM using the tungsten shield approach and the form for a “New Horizons” spacecraft (McNutt et al., 2019), but at approximately half the mass (250 kg versus 478.3 kg). Locating the solution space for Option 3 is inherently more complex: the spacecraft mass drives the minimum obtainable perihelion distance, but that drives the shield requirement and, hence, the overall spacecraft mass, so a self-consistent perihelion and spacecraft mass must be determined for a given separated spacecraft mass and kick-stage engine such that the implied shield can withstand the thermal loading at the perihelion. Typically, the three-stage configurations are superior to the four-stage configurations because the latter configurations are traveling too fast at Jupiter to enable sufficient “breaking” during the retrograde gravity assist.

For example, using the first two stages of the SLS to launch a third stage plus the 250-kg spacecraft on a SOM-enabled trajectory yields the following. Note that the use of either a Castor 30XL or a Castor 30B as the third stage makes the stack too heavy to reach Jupiter.

Table D-4. SOM performance versus kick stage for 250-kg observatory mass.

Kick Stage	Thermal Shield Design (R_s)	Launch C_3 (km^2/s^2)	ΔV (km/s)	Perihelion	V_{esc} (au/yr)	Time to 500 au (years)
Orion 50XL	12	101.3	4.41	11.5	7.54	69.3
Star 48BV	3	106.9	2.07	3.16	6.99	74.3
Star 48GXV	4	105.6	3.46	4.64	8.57	61.4

All other combinations provide worse performance. Both Option 1 and Option 2 using a Centaur-3/Star 48BV stack provide better (= faster) trajectories.

For comparison, consider the case with the New Horizons spacecraft with a separated wet mass of 478.3 kg.

Option 1 best performance is again with the SLS plus Centaur-3 plus Star 48BV.

This time, $C_3 = 349.6 \text{ km}^2/\text{s}^2$, asymptotic speed with no JGA is 5.1 au/year, asymptotic speed with gravity assist at the cloud tops is 7.9 au/year, and corresponding flight times to 500 au are 97.2 years and 63.3 years, respectively.

Option 2 best performance is again with the SLS plus Centaur-3 plus Star 48BV.

For Option 2, $C_3 = 214.6 \text{ km}^2/\text{s}^2$ and $\Delta V = 3.69 \text{ km/s}$. For these parameters, the alignment of the outgoing asymptotic velocity vector with Jupiter’s orbital velocity vector implies a closest approach of less than one Jupiter radius. So, fixing the closest approach at $1 R_J$ (i.e., $r_p/r_0 = 1$) yields an asymptotic speed with gravity assist at the cloud tops of 8.4 au/year and a corresponding flight time to 500 au of 59.8 years.

Table D-5. SOM performance versus kick stage for 478.3-kg observatory mass.

Kick Stage	Thermal Shield Design (R_s)	Launch C_3 (km^2/s^2)	ΔV (km/s)	Perihelion	V_{esc} (au/yr)	Time to 500 au (years)
Orion 50XL	12	100.2	3.98	14.1	6.61	78.5
Star 48BV	3	105.7	1.91	4.47	5.87	87.6
Star 48GXV	4	104.4	3.14	6.24	7.37	70.1

Option 3: going through the same methodology as before

Again, all other combinations provide worse performance. Both Option 1 and Option 2 using a Centaur-3/Star 48BV stack provide better (= faster) trajectories.

From working through this trade space, the methodology consists of the following:

1. Select a spacecraft mass.
2. For all the launch vehicle stacks with “valid” solutions (e.g., sufficient launch C_3 to reach Jupiter), locate the “best” cases by examining the asymptotic flyout speeds and corresponding flight times to some “target” distance (we have been using 500 au).
3. For each “selected case,” check that the design perihelion is less than the actual perihelion achieved.
4. For the cases in item 3, choose the one for which the two numbers are closest; this will be the “optimal” solution for that vehicle stack.
5. Compare across stacks and pick the best.
6. Compare with best-performing Option 1 and best-performing Option 2 cases for the given, separated spacecraft mass.
7. Use this “best” solution as the starting point for more detailed trajectory analyses, including actual planetary orbits, finite launch windows, and backup launch windows.

For a New Horizons or smaller mass with tungsten as a thermal shield material, we conclude that the best solution is either Option 1 or Option 2—as dictated by risk posture—using a Centaur-3 and Star 48BV combined stack.

The next step is to look at the heavier heliospheric baseline spacecraft using the less massive metal carbide shields rather than tungsten.

D.4.1.1 “Baseline” Spacecraft

Both the (heliospheric) baseline spacecraft and the (planetary and astrophysics) augmented spacecraft have wet launch masses (including contingency and allocated and unallocated margins) of 860.0 kg. The “working mass” for the heliospheric baseline spacecraft for use with the SOM is not as mature and has a rough wet-mass estimated mass of 900 kg. For the current estimate, and to place an upper limit on flyout speed, we consider a separated spacecraft mass for all three

options of 860.0 kg. n.b. For the SOM case (Option 3), the thermal system and associated masses, such as a balance mass to keep the center of mass aligned with the kick-stage symmetry axis during the SOM “burn,” are bookkept as additions to the separated, wet-spacecraft mass, as is the mass of the SOM kick stage.

For comparison purposes with the previous—and early—examples just discussed, we first characterize “best performance” as being defined by the largest asymptotic escape speed within the scope of the model. But we will come back and revisit this with what has been found to be a better metric, namely the heliocentric distance reached 50 years after launch.

So, first, using the mass of 860.0 kg, we proceed as before and obtain:

Option 1 best performance is again with the SLS plus Centaur-3 plus Star 48BV.

$C_3 = 304.07 \text{ km}^2/\text{s}^2$, asymptotic speed with no JGA is 4.50 au/year, asymptotic speed with gravity assist at the cloud tops is 7.48 au/year, and corresponding flight times to 500 au are 108.9 years and 67.1 years, respectively.

Option 2 best performance is again with the SLS plus Centaur-3 plus Star 48GXV.

For Option 2, $C_3 = 178.8 \text{ km}^2/\text{s}^2$ and $\Delta V = 3.35 \text{ km/s}$. For these parameters, the alignment of the outgoing asymptotic velocity vector with Jupiter’s orbital velocity vector implies a closest approach of less than one Jupiter radius. So, fixing the closest approach at $1 R_J$ (i.e., $r_p/r_0 = 1$) yields an asymptotic speed with gravity assist at the cloud tops of 7.85 au/year and a corresponding flight time to 500 au of 64.3 years. The asymptotic speed is faster than that for Option 1 by 0.37 au/year with a shorter arrival time of 2.6 years to 500 au.

Option 3 best performance is with Centaur-3 plus Oberth maneuver at $2 R_s$ with an Orion 50XL.

Using a metal carbide on carbon (MC/C) shield for the 860-kg “basic mass” plus 40 kg for Option 3 plus 300 kg for the “smart interstage” plus contingency and margin yields a final-stage “payload” mass of 7929 kg. Escape speed from the Sun = 8.05 au/year, reaching 500 au (total flight time) in 65.1 years (C_3 controlled to $108.29 \text{ km}^2/\text{s}^2$ and $\Delta V = 2.05 \text{ km/s}$).

Note that while the Option 3 case provides the highest asymptotic speed, Option 2 actually provides the shortest flight time to 500 au. There are two reasons for this: (1) the flyout speed from Earth to Jupiter is slowest for Option 3; from a global maximization perspective, Option 3 works best with the largest kick stage allowable (here the Orion 50XL, which is more massive than either the Star 48BV or the Star 48GXV), and (2) Option 3 also requires the additional time to “fall into the Sun” and also get back out to Jupiter’s orbit, during which time both the Option 2 and Option 1 vehicles have been gaining more distance from the Sun.

In addition to these considerations, we note that all of these “best cases” are ~15 years over the nominal 50-year lifetime requirement. This suggests that a better evaluation of “best” options is to drop back the “test distance” from 500 au to 400 au and ask what option and configuration provides the shortest flight time to a heliocentric distance commensurate with a 50-year design lifetime for the spacecraft.

So, if we search on shortest flight time to 400 au, we obtain the following:

Option 1 best performance is again with the SLS plus Centaur-3 plus Star 48BV.

This is the same as the best performance Option 1 configuration immediately above. The flyout time from Earth to 400 au is 53.79 years.

Option 2 best performance is again with the SLS plus Centaur-3 plus Star 48GXV.

This is the same as the best performance Option 2 configuration immediately above. The flyout time from Earth to 400 au is 51.59 years.

Option 3 best performance is with the Centaur-3 plus an Oberth maneuver at $2 R_s$ with an Orion 50XL.

This is the same as the best performance Option 3 configuration immediately above. The flyout time from Earth to 400 au is 52.73 years.

In this case, Option 2 is “best,” Option 3 is “second best,” and Option 1 is in “third place.” That said, the flight times are all within 2.2 years of each other. It is also clear that the implementation of Option 1 involves the least risk, Option 2 is the second most risky (including a need to flight qualify a Star 48GXV stage and deep-space thermal control of that stage), and Option 3 has the most risk, involving the development and qualification of the thermal shield assembly, the “smart” interstage to control the spacecraft attitude during the burn, the mechanical interfaces between the rocket stage and the rest of the stack, and the development of a Ka-downlink and its associated pointing control. Both Options 2 and 3 of course also require remote mission-critical burns at significant light-times from Earth. At most, these issues would trade against an ~4% decrease in a flight to ~400 au in 50 years.

These considerations of the cost-risk and advantages of a SOM mitigate against its implementation for this mission. The thermal requirements—even with new materials just now investigated—tend to negate all the previously perceived advantages.

D.4.2 Point Design Case Study

To evaluate the performance of the SOM architecture, a case study is examined for comparison with non-SOM concepts. The parameters of the study are outlined in Table D-6. First, a grid search is performed across the range of launch years from 2030 to 2042 to compute the set of Lambert arcs that provide transfer from Earth to Jupiter. Launch C_3 values over the ranges provided in Table D-6 are considered, where the upper bound corresponds to the maximum lift capability of the SLS Block 2 with a Centaur-3 upper stage. Upon arrival at Jupiter, the gravity assist is simulated by varying the direction of the outgoing relative velocity (“v-infinity,” v_∞) over a range of “pump” and “crank” angles. The sampled outgoing velocities for which the perijove radius is $\geq 1.05 R_J$ are then

Table D-6. Point design studied for SOM architecture.

Perihelion Bounds (R_s)	Lift Mass (kg)	Observatory Mass (kg)	SRM Engine	SOM ΔV (km/s)	Launch C_3 (km^2/s^2)
2.95–3.05	7000	900	Star 48BV	0.971	100–144

propagated from Jupiter to perihelion, and those that fall within the perihelion bounds listed in Table D-6 are retained.

D.4.2.1 Optimal Solutions

For each solution that satisfies the perihelion constraints, the SOM ΔV is applied and the post-SOM energy is computed, where speed at 100 au ($v_{100 \text{ au}}$) is used to represent energy. The result is a set of feasible mission trajectories, from which optimal solutions can be identified. Optimality is defined in terms of a combination of metrics: (1) launch C_3 , (2) time of flight (TOF) to perihelion, and (3) speed at 100 au. The subset of optimal solutions is then identified; each solution in the optimal set minimizes launch C_3 and/or TOF required to maximize post-SOM energy. An example of the full solution space appears in Figure D-3, with the optimal subset indicated using black circles. As expected, $v_{100 \text{ au}}$ is maximized as launch C_3 increases (i.e., lift mass decreases). Launch date ranges associated with the optimal solutions across the full range of launch years are provided in Table D-7, as well as the highest value of $v_{100 \text{ au}}$ for that year.

D.4.2.2 Comparison with Non-SOM Performance

To maximize $v_{100 \text{ au}}$, launch in the early 2030s/early 2040s is optimal. A “maximum speed performance sky map” (Schlei et al., 2021) representing the optimal SOM scenarios for each launch year is provided in Figure D-4. Here, maximum speed at 100 au is captured, and solutions are displayed

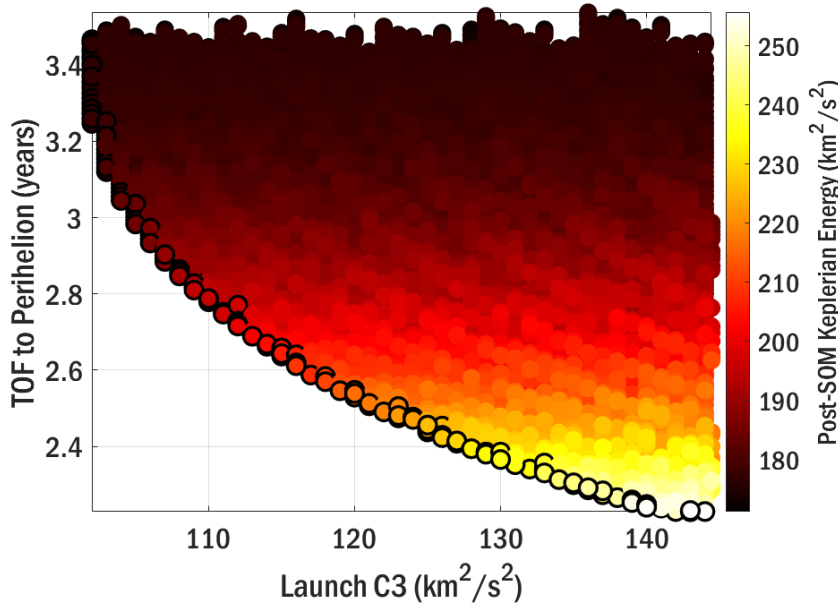
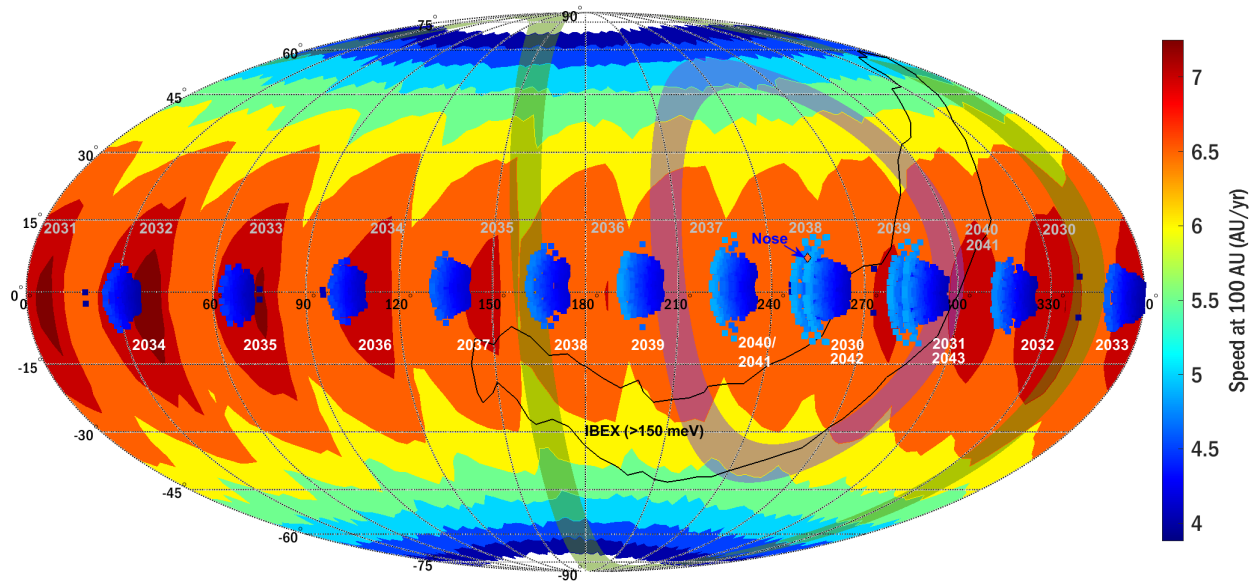


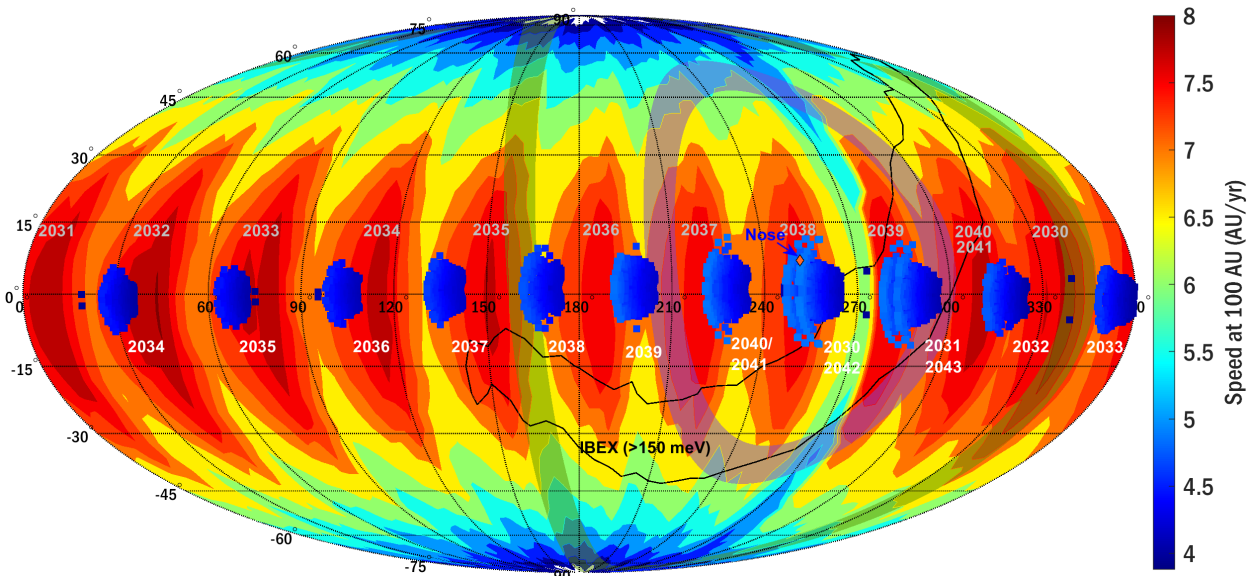
Figure D-3. The full space of solutions computed via a broad search is plotted in terms of optimality metrics launch C_3 , TOF, and post-SOM energy (here translated into $v_{100 \text{ au}}$). The optimal subset of solutions is identified via black circles. As expected, the best-performing solutions in terms of TOF and energy are found at the highest C_3 values (2030 launch). (Image credit: Johns Hopkins Applied Physics Laboratory.)

Table D-7. Launch date ranges for optimal solutions, with $\max(v_{100 \text{ au}})$ given (launch years highlighted in yellow correspond to departure toward the nose of the heliopause).

Launch Range	2030	2031	2032	2033	2034	2035	2036	2037	2038	2039	2040/2041	2042	2043
	Jan–Feb	Feb–Mar	Mar–Apr	Apr–May	May–Jun	Jul–Aug	Aug–Sep	Sep–Oct	Oct–Nov	Nov–Dec	Dec–Jan	Jan–Feb	Feb–Mar
Max $v_{100 \text{ au}}$	4.87	4.85	4.76	4.62	4.51	4.47	4.53	4.63	4.73	4.83	4.87	4.88	4.83



(a) Background map: ballistic JGA, observatory mass 900 kg, C_3 272 km²/s²



(b) Background map: powered JGA (Star 48BV), observatory mass 930 kg, C_3 204 km²/s²

Figure D-4. Optimal SOM solution subsets across all launch years are plotted as the dark blue regions near the ecliptic plane, with launch year labeled beneath in white. Background surface sky maps depicting the analogous non-SOM ballistic JGA (a) and powered JGA (b) solutions are included for comparison, with launch years labeled in gray. Clearly, the non-SOM cases significantly outcompete the SOM case study. (Image credit: Johns Hopkins Applied Physics Laboratory.)

according to their outbound right ascension and declination in the ecliptic J2000 frame. SOM trajectory data appear in both panels of Figure D-4 as the groups of blue points near the ecliptic plane, with each group labeled in white according to launch year. For comparison, the background of the maps in each panel is colored to represent ballistic JGA performance (panel a) and powered

JGA performance (panel b), with launch years labeled in gray (Schlei et al., 2021). Clearly the fastest SOM cases are on par with the slowest (highest declination) non-SOM solutions.

D.4.2.3 Determining “Break-Even” Mass for SOM versus Non-SOM Architectures

While the design summarized in Table D-1 is clearly not competitive, questions about shield mass targets to enable a competitive mission are addressed by considering a range of lift masses. Assuming launch in 2030, masses are sampled over [2500, 7000] kg, and the process described previously is repeated for each case. The resulting values of $\max(v_{100 \text{ au}})$ for each scenario are plotted as a function of lift mass in Figure D-5, where points are colored according to the ΔV delivered by the SRM and labeled by associated launch C_3 . For comparison, the range of $\max(v_{100 \text{ au}})$ possible across all launch years for the two non-SOM architectures from Figure 3-1 and Figure C-1 are included as the purple and orange bands. For the SOM architecture to simply *break even* with the ballistic JGA design, lift mass (i.e., shield mass and associated structure) must be reduced by ~30–40%; for the powered JGA design, a reduction of ~50–60% is required. Considering the mass of the observatory plus SRM alone is ~3 tons, in addition to the added cost and complexity of the SOM architecture, a competitive SOM scenario is not likely to exist under the assumptions of this case study.

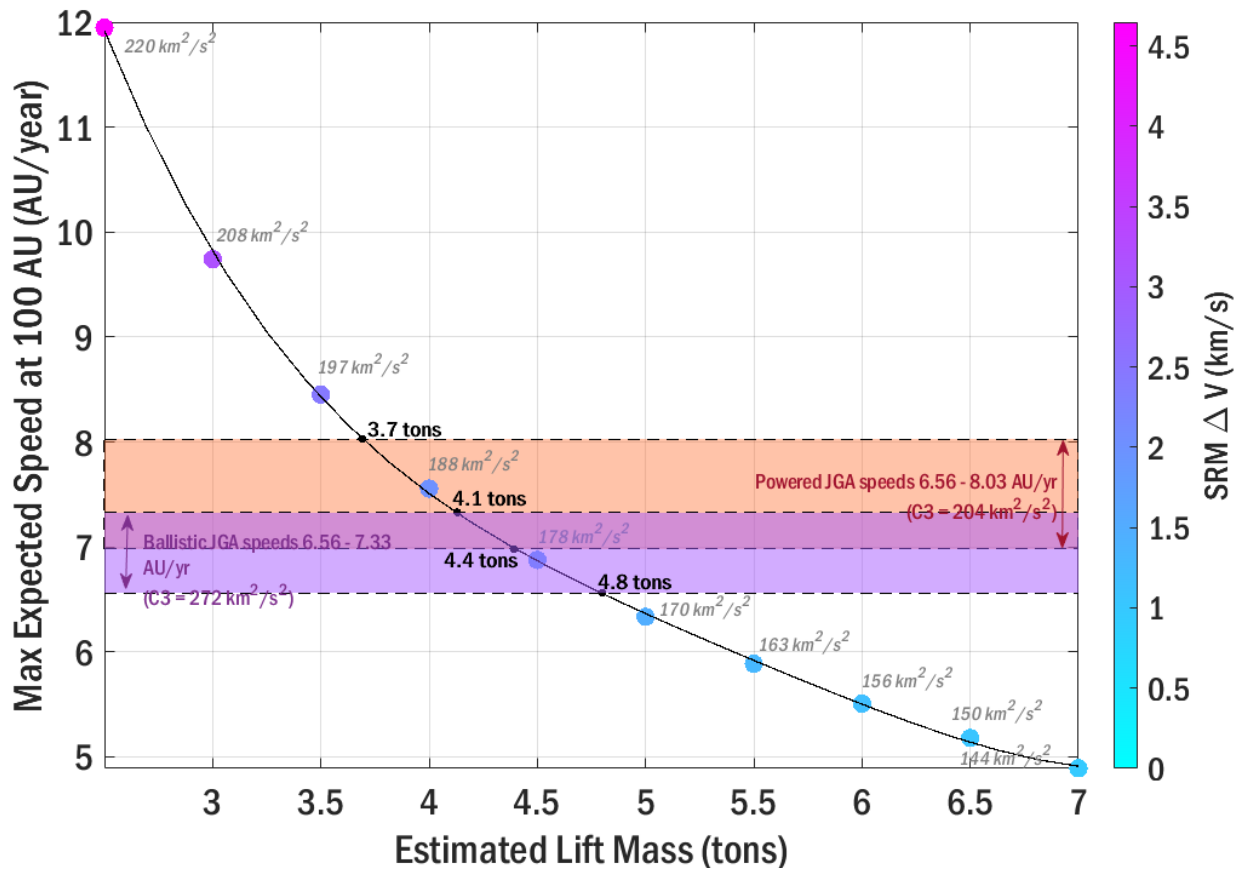


Figure D-5. Fastest single trajectory is shown for a range of lift mass values (case study appears as a 7-ton point solution; launch in 2030 is assumed for all cases). Each point is colored by associated SRM ΔV and labeled with corresponding maximum launch C_3 . The best ballistic and powered JGA performance ranges across 2030–2042 are included as the purple and orange bands, respectively. (Image credit: Johns Hopkins Applied Physics Laboratory.)

D.5 Constraints and Risks

The SOM trajectory imposes significant constraints on the mission and flight system design and results in significant technical risks that are not present in other options. These risks and additional burdens on the flight system also result in increased cost and risks associated with development of new technology and with flight components not needed in other options. The most challenging of these are detailed below.

D.5.1 System Constraints

The SOM mission requires an SRM to be fired at perihelion, with distance from the Sun significantly closer than performed by Parker Solar Probe. While Parker Solar Probe was able to achieve a perihelion of $\sim 10 R_{\odot}$ over a 7-year mission that included seven Venus flybys, a similar trajectory for Interstellar Probe cannot lower the perihelion to the $2\text{--}5 R_{\odot}$ needed to achieve speeds similar to the JGA options. Therefore, the SOM mission must consist of a JGA used to target the perihelion followed by the SOM itself, then a coast away from the Sun to a safe distance before separating the observatory from the remaining flight system components. This trajectory drives the design and operation of the mission.

- The SRM temperature must be controlled through all segments of the trajectory before firing. During the transit to Jupiter and back inside 1 au, a thermal control system will be required to keep the motor warm, most likely by redistributing waste heat from the RTGs on the spacecraft through a pumped-loop or heat-pipe system.
- The observatory and SRM must be protected from solar illumination beginning at ~ 0.7 au from the Sun, through perihelion, and back to ~ 0.7 au. Based on experience from Parker Solar Probe, 0.7 au represents the closest distance to the Sun where solar illumination becomes high enough to drive flight system temperatures and the system must be kept in the TPS's umbra. The flight system must maintain attitude control continuously during that time to prevent umbra exceedances, including from faults. Parker Solar Probe is designed to recover attitude control within tens of seconds to prevent damage from unintended solar illumination; given that the flight system is about 10 times bigger for Interstellar Probe and the perihelion distance is 4–5 times closer, this constraint is likely to be much tighter for Interstellar Probe.
- Thermal gradients across the SRM must be tightly controlled. During the close approach to the Sun, the TPS will form an umbra to shade the SRM from direct illumination. However, the back side of the shield will reach high temperatures as well, and will radiate onto the SRM over a significant area. Thermal gradients across the motor must be kept within motor specifications.
- All flight system components must be kept within the umbra formed by the TPS. To minimize the TPS mass, the observatory diameter is constrained to be about the same size as the SRM diameter. This limits the size of the HGA and requires the RTGs to be deployed to final configuration after the observatory is separated from the remainder of the flight system.

D.5.2 Additional Technical Risks

The constraints imposed by the SOM and the technological solutions needed to meet them involve risks not associated with the baseline mission. These risks show that the SOM is significantly more complicated than the baseline mission, even though this option does not offer a reduction in the time required to achieve the interstellar medium.

- The need to travel from Jupiter to perihelion and then back to regions near Earth before separating the observatory from the rest of the flight system increases the difficulty of controlling the trajectory during this extended period. Given the greatly increased mass of the flight system, a much larger propulsion system, including >100 kg of propellant, will be needed to ensure that the system will perform the JGA to target perihelion and reach perihelion to execute the firing of the SRM itself. It is likely that this extra propulsion system will reside on the interstage ring; however, control will be through the observatory avionics and power systems, complicating observatory separation. An additional challenge is in the layout of thrusters for the extra propulsion system so that hardware remains in the shield umbra while still providing full control in all directions.
- Inside ~ 0.7 au, the flight system must maintain tight control of the stack attitude to prevent unintended exposure of flight hardware to solar illumination. Given the mass of the flight system, control will have to be accomplished using thrusters, which must provide the range of control needed while remaining in the shield umbra. Failing to maintain control or not restoring control quickly enough (tens of seconds) in this region is likely to be mission ending.
- During the SOM, the thrust vector of the SRM must remain in alignment with the center of mass of the system. Although the thrust vector control system of the SRM allows for some control over the direction of thrust as well as some course correction, this ability is limited and is used to correct issues within the motor, such as uneven propellant use. We have added a ballast mass to the flight system to correct for the center of mass offset due to the TPS, but a risk remains that the system alignment will not be sufficiently precise to allow control of the motor burn.
- The ability of the flight system to perform as needed is accomplished through system testing and analysis. For the flight system, there is no test facility that can be used to perform an end-to-end system test of the guidance and control system, including issues such as control through the SRM burn. Depending on analysis and component level, testing adds risk to the mission.
- After a successful SOM, and once the flight system has reached a safe distance from the Sun, the observatory is separated from the remainder of the flight system to continue on to complete the science mission. Mechanically, the interface of the observatory to the flight system is at the interstage ring. This ring and the observatory are behind the TPS, and separation must be performed in such a way as to avoid contact between the observatory and the TPS; this is complicated by the increased number of interfaces needed across the

separation plane to allow the spacecraft to control the flight system stack before and during the SOM. A two-stage separation could be designed, in which the TPS is ejected first, followed by observatory separation; however, this doubles the number of devices that must fire to successfully separate the observatory.

- Late in the mission, accuracy of pointing the HGA to Earth is critical to maintaining the downlink rates needed to get the required science data back to the ground. The baseline mission uses a 5-m HGA with X-band, and it is still a challenge to point the dish accurately enough. The flight system in the SOM case cannot use the large fixed HGA so as to minimize the TPS size and mass. Instead, either a smaller HGA at Ka band or a larger deployable X-band HGA must be used. In either case, the pointing accuracy requirements become more challenging to meet, and if not met, the observatory may not be able to downlink data during the most interesting part of the mission.
- The SOM requires a deep dive into the Sun’s corona—as much as five times closer to the Sun than Parker Solar Probe. The TPS needed to protect the observatory during this maneuver is new technology and must be qualified before flight to show that it will indeed perform as required. No facility exists that can test the TPS to demonstrate performance or support the flight shield design effort. Depending on analysis and component level, testing adds risk to the mission.
- The flight system design shown in Figure D-1 includes two RTGs; however, no thermal design for the flight system has been completed. If the power provided by the two RTGs is insufficient to run the observatory systems and also maintain the SRM temperature gradient to a level within specification, a third RTG may be needed.

D.6 Programmatic Issues

As noted, there are a variety of different developments that would be required to implement the SOM option, regardless of the advantage it might, or might not, offer technically:

1. The spacecraft would require a dual-mode guidance and control system. Spinner concepts were explored long ago for near-Sun solar probe concepts and found to be problematic in any case (JPL, 1981). Such an approach would require a thermal shield to surround the spacecraft, adding more mass. It would also preclude a clear view of space by the radiators of the RTG.
2. As a result, deployment of the Plasma Wave Subsystem (PWS) booms would not be possible until the spacecraft was outbound from the maneuver.
3. Deployment of a long magnetometer boom before the maneuver would be problematic.
4. The thermal shield size would limit the HGA size (due to the fairing size), driving the system to use either a deployable X-band HGA or a small-diameter Ka-band HGA with active fine-precision guidance control.

5. The RTGs would need to remain folded up against the spacecraft, limiting the power output until after the maneuver, as well as running the risk of this critical deployment being unsuccessful ~3 years postlaunch (earlier concepts based on a New Horizons-like configuration might be implemented to avoid this issue, but with the trade-off being a smaller and far less capable spacecraft for the baseline mission (McNutt et al., 2019).
6. The TPS itself would require extensive development work, modeling, and spot testing. While the ultra-high-temperature (UHT) MC/C materials explored in this study suggest that a possible solution to approaching the Sun to within 2–3 R_s of its center may be possible, the current investigation of coupon-sized samples (approximately square centimeters) is very far from an operational system of approximately tens of square meters. As with other spacecraft that have closely approached the Sun for extended periods of time (Mercury Surface, Space Environment, Geochemistry, and Ranging [MESSENGER] and Parker Solar Probe), the thermal extremes preclude “test as you fly” at the full system level. It must be borne in mind that approaching the Sun to within “only” 3 R_s of its center is already a factor of $(9.86/3)^2 \sim 11$ greater than what Parker Solar Probe will experience after its final Venus gravity assist. This is about the same increase in thermal flux experienced by MESSENGER in traveling from Earth to Mercury.

The risk mitigation study for what became Parker Solar Probe was performed by the Johns Hopkins Applied Physics Laboratory (APL) from 3 May 2005 through 31 March 2008 in concert with other risk mitigation studies and support of the NASA-established Science and Technology Definition Team (STDT). While the initial study examined issues for a perihelion as close as 4 R_s of the Sun’s center (Potocki et al., 2006), work continued on refining the TPS even after the perihelion had been relaxed to 9.86 R_s , eliminating the need for the primary shield (McComas et al., 2005, 2008).¹

This nearly \$10M effort (carried out under NASA’s Living With a Star [LWS] program at NASA Headquarters) had as its purpose technology development to lower risk:

The purpose of this task is to identify Solar Probe Mission technology development approach, and to exercise the appropriate risk reduction plans that will enable the mission's implementation from a technical and cost perspective. In order to achieve this goal, these technologies will need to be advanced to higher TRL levels (TRL 7-9) in order to make them flight worthy. The following list includes (but is not limited to) candidate technologies that shall investigate:

I Thermal Protection System Risk Reduction Plan...

II Solar Probe Telecommunications ... (power amplifiers and HGA to operate at Ka band)

III Effects of Solar Dust on Solar Probe

¹ The change was made when the use of RTGs for power was ruled out, effectively eliminating a mission using a JGA. The alternative trajectory using multiple Venus gravity assists is limited by the launch energy available.

Similar efforts would be required here to take the spacecraft at least a factor of 3 closer to the Sun. While a cost-loaded research plan has not been developed as part of this effort, an order of magnitude more work to deal with an order of magnitude more thermal loading with currently experimental materials not (yet) made in bulk would not be surprising. Nor would a significant increase in development time over that of the corresponding study for what became Parker Solar Probe (it should be borne in mind that the APL-led effort benefited from ~20 years of prior thought and development of thermal mitigation strategies carried out by the Jet Propulsion Laboratory [JPL] from ~1980 to 2000).

In the face of these uncertainties, and working with Advanced Ceramic Fibers, LLC, in Idaho Falls on novel UHT materials, we did go ahead and assemble a concept for the SOM approach as indicated above. At this time we can conclude the following:

1. Approach to the Sun—even on a fast trajectory—to within $2 R_s$ of the Sun’s center is at the very limit of any known or hypothesized materials. Oberth’s “example” of an approach to $1.5 R_s$ of the Sun’s center (Oberth, 1970) is simply not doable with any known or hypothesized material. Any active cooling system would also remain problematic as well as heavier, driving power requirements to new, higher levels (fiction is fun to read, but it is still fiction; Bradbury, 1967).
2. The mass of any shield is not going to be any less than a shield mass assuming carbon’s density.
3. A better (light and stronger with low thermal conductivity) material than titanium, as used on Parker Solar Probe, is not available for ensuring the structural integrity of the TPS during the rocket engine burn required for the SOM.
4. The lifting power of current and envisioned SHLLVs limits the total lift mass to the Sun to ~8 mt at most.
5. High propellant fraction (>90%) rocket engines in this mass category are limited to solid propellant with specific impulses of ~300 seconds as an upper limit.
6. Subject to these constraints and NASA-mandated rules on mass margins and reserves, along with the extra time accumulated in traversing to Jupiter, into the Sun, and back out past Jupiter’s orbit, the performance of the SOM for time distance reached in a 50-year flight time is, at best, projected to be on par with the Option 1 or 2 trajectories.
7. Compared with even Option 2 trajectories, the use of a SOM after proving the TPS technology as assumed with optimistic characteristics carries exceptionally large execution risks for the mission for all the reasons noted above.

While one could suggest a much higher specific impulse based on (a nonexistent) NTP rocket engine, the requirements for fitting within the mass constraints of the envisioned class of SHLLVs preclude an engineering design from closing, even for a New Horizons (or smaller) spacecraft (Ralph L. McNutt Jr. et al., 2021).

Even if further study gave rise to some hope of “engineering optimism,” these execution complexities, coupled with the multiple required engineering developments, would also run the additional risk of unexpected costs and schedule slips during spacecraft development. On large strategic missions (such as Parker Solar Probe and as this would be), the encountering of issues not foreseen until actual implementation can literally add hundreds of millions of dollars and multiple years of additional development to optimistic—and initial—cost projections (National Academies of Sciences & Medicine, 2017). Given the low technology readiness levels (TRLs) of the UHT materials and the increased need for mechanisms (RTG deployment and active HGA fine-pointing control), coupled with the mission-critical SOM burn itself, which cannot be tested in the real environment under which it will operate, and other issues yet to be identified, exercising a great deal of caution would be prudent.

While Oberth’s original *gedanken* experiment gave rise to a great deal of optimism about an “easy” means of very rapidly departing the solar system, it remains a truism that one cannot fly close to the Sun “at night.” That has been, and remains, an underestimated but vastly significant engineering problem.

D.7 Appendix D References

- Bradbury, R.D. (1967) The Golden Apples of the Sun. In *The Golden Apples of the Sun* (pp. 164-169). New York, New York: Bantam Books, Inc. (Reprinted from: 3rd).
- Cedillos-Barraza, O., Manara, D., Boboridis, K., Watkins, T., Grasso, S., Jayaseelan, D.D., Konings, R.J.M., Reece, M.J., Lee, W.E. (2016) Investigating the highest melting temperature materials: A laser melting study of the TaC-HfC system. *Scientific Reports* 6, 37962. doi: 10.1038/srep37962
- Fox, N.J., Velli, M.C., Bale, S.D., et al. (2016) The Solar Probe Plus Mission: Humanity’s First Visit to Our Star. *Space Science Reviews* 204(1), 7-48. doi: 10.1007/s11214-015-0211-6
- Greenwood, S.W. (1975) Definition of specific impulse. *Journal of Spacecraft and Rockets* 12(1), 62-62. doi: 10.2514/3.27809
- JPL (1981) *Starprobe Science Options - Appendixes* (JPL 715-127). Pasadena, California: Laboratory, J.P.
- McComas, D.J., Acton, L.W., Balat-Pichelin, M., et al. (2005) *Solar Probe: Report of the Science and Technology Definition Team*. Greenbelt, MD: NASA.
- McComas, D.J., Acton, L.W., Balat-Pichelin, M., et al. (2008) *Solar Probe Plus: Report of the Science and Technology Definition Team*. Greenbelt, MD: NASA.
- McNutt Jr, R.L., Elsperman, M.S., Gruntman, M., Klaus, K.K., Krimigis, S.M., Roelof, E.C., Smith, D.B., Vernon, S.R., Wimmer-Schweingruber, R.F. (2014) *Enabling Interstellar Probe with the Space Launch System (SLS)*. Paper presented at the 65th International Astronautical Congress, Toronto, Ontario, Canada.

- McNutt Jr., R.L. (2021) *Optimized Jupiter Gravity Assists – Analytic Approximations*. Paper presented at the 31st AAS/AIAA Space Flight Mechanics Meeting, Virtual.
https://www.space-flight.org/docs/2021_winter/31stSFM_Program_FINAL.pdf.
- McNutt Jr., R.L., Wimmer-Schweingruber, R.F., Gruntman, M., et al. (2021) *Interstellar Probe – Destination: Universe!* Paper presented at the 72nd International Astronautical Congress (IAC), Dubai, United Arab Emirates.
- McNutt, R.L., Wimmer-Schweingruber, R.F., Gruntman, M., et al. (2019) Near-Term Interstellar Probe: First Step. *Acta Astronautica* 162, 284-299. doi:
<https://doi.org/10.1016/j.actaastro.2019.06.013>
- National Academies of Sciences, E., Medicine (2017) *Powering Science: NASA's Large Strategic Science Missions*. Washington, DC: The National Academies Press. doi:10.17226/24857
- Oberth, H. (1970) *Ways to Spaceflight* (Agence Tunisienne de Public-Relations, T., Tunisia, 1970, Trans.): National Aeronautics and Space Administration. Retrieved from
https://ia600503.us.archive.org/21/items/nasa_techdoc_19720008133/19720008133.pdf
- Potocki, K.A., Dantzler, A., Mehoke, D., Drewry, D. (2006) *Solar probe thermal protection system risk mitigation study: FY 2006 final report*. Laurel, Maryland:
- Schlei, W., Atchison, J., Gomez-Cano, B., Lathrop, B., Villac, B. (2021) *Pragmatic Trajectory Options Applicable to an Interstellar Probe Mission*. In 2021 IEEE Aerospace Conference. doi: 10.1109/AERO50100.2021.9438398
- Schnitzler, B., Borowski, S. (2007) Neutronics Models and Analysis of the Small Nuclear Rocket Engine (SNRE). In *43rd AIAA/ASME/SAE/ASEE Joint Propulsion Conference & Exhibit*: American Institute of Aeronautics and Astronautics.
- Schnitzler, B., Borowski, S. (2008) Small Nuclear Rocket Engine and Stage Benchmark Model. In *44th AIAA/ASME/SAE/ASEE Joint Propulsion Conference & Exhibit*: American Institute of Aeronautics and Astronautics.
- Schnitzler, B., Borowski, S., Fittje, J. (2009) A 25,000-lbf Thrust Engine Options Based on the Small Nuclear Rocket Engine Design. In *45th AIAA/ASME/SAE/ASEE Joint Propulsion Conference & Exhibit*: American Institute of Aeronautics and Astronautics.
- Shabalin, I.L. (2014) *Ultra-high temperature materials I: Carbon (graphene/graphite) and refractory metals*: Springer Netherlands. 10.1007/978-94-007-7587-9
- Williams, D.R. (2018) Sun fact sheet. *Planetary Fact Sheets*. Retrieved from
<https://nssdc.gsfc.nasa.gov/planetary/factsheet/sunfact.html>.

Appendix E. Radiation Work

E.1 Environments Overview

Initial (concept study–level) environments and derived requirements have been developed for total ionizing dose (TID), total nonionizing dose (TNID), single-event effects (SEEs), and spacecraft charging (both surface charging and internal charging).

Space radiation–related environments vary significantly over the candidate Interstellar Probe mission trajectory. TID, TNID, and spacecraft charging effects are dominated by the proposed Jovian flyby, while omnipresent galactic cosmic ray (GCR)–induced SEE fluxes will vary with astronomical units (distance) and the heliosphere crossing.

Figure E-1 illustrates the predicted accumulation of TID over the mission lifetime. Included, and visible, in this figure are the following:

1. ~0.2-year launch and checkout;
2. ~0.6-year cruise to Jupiter;
3. Jupiter gravity assist (JGA);
4. ~12-year (inner) heliosphere phase;
5. ~5-year heliosheath phase;

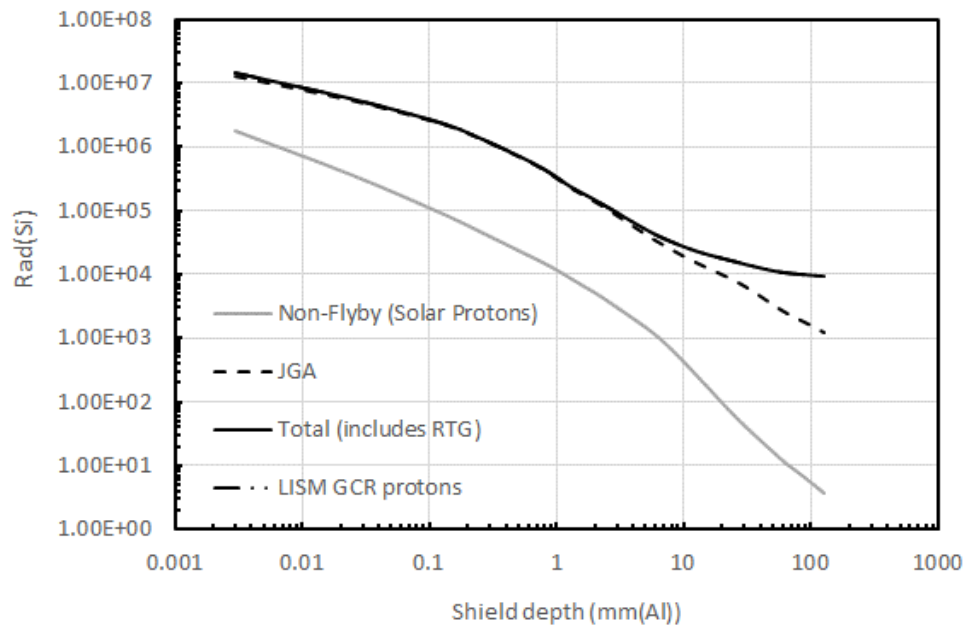


Figure E-1. Spherical shell cumulative dose [rad(Si)] versus depth (millimeter equivalent aluminum) illustrating contributions from the inner heliosphere mission phase, JGA, LISM, and background RTG. (Image credit: Johns Hopkins Applied Physics Laboratory.)

6. ~35-year interstellar phase (very local/local interstellar medium [VLISM/LISM]); and
7. background radioisotope thermoelectric generator (RTG) gammas.

Dose accumulations from the launch/checkout and cruise to Jupiter mission phases occur, chronologically, first; therefore, these contributions are clearly visible in the figure (gray line). The dominant contributor to mission TID is the JGA (dashed black line), discussed in the next section. Remaining contributors to mission doses are comparatively small—barely visible within the line widths. The exception is the “background” gamma contributions from the next-generation RTG (NextGen RTG). Doses and dose rates were approximated using modeling results of the Selenide RTG performed for the International Solar Polar Mission (ISPM; the copper elenide converters were dropped during development in favor of the SiGe converters used in the Galileo RTG; cf. e.g., Shirbacheh (1984)). We considered only a source-to-hardware distance of 0.5 m on a stepwise decay (constant dose rate in the inner heliosphere and a decayed constant dose rate in the LISM). As plainly visible in Figure E-1, RTG gammas offer a meaningful contribution to mission dose at well-shielded depths (nearly 10× increase at 100 mm). Neutron fluxes, doses, and dose rates are more than two orders of magnitude less than gammas and therefore offer insignificant contributions to predicted mission dose rates at any depth.

NOVICE (Jordan, 1991) was utilized to produce all TID-versus-depth and TNID-versus-depth results for multiple kernels.

E.2 Description of Ballistic Jupiter Gravity Assist Jovian Flyby Environments

The baseline ballistic (passive) JGA will place the probe within the Jovian magnetosphere ($R_J < 50$) for multiple (~3.8) days, during which time the spacecraft will be subjected to high fluxes of relativistic electrons and protons and therefore the space environment hazards thereby induced. The fluxes and corresponding hazards present during the JGA are substantially higher than during all remaining mission phases; in some cases, these conditions will drive the probe design to ensure mitigation throughout.

In preparing initial JGA environment descriptions, derived environments, and design guidance, APL leveraged the recent verification and flight activities relating to the Europa Clipper and Juno missions.

The Jovian system causes TID, TNID, dose rate, and SEEs in microelectronics and detectors. All such threats are considered for the probe and instruments.

The Galileo Interim Radiation Environment Model Ver. 3 (GIRE3; Divine & Garrett, 1983; Garrett et al., 2003; Garrett et al., 2012), as implemented in GRID3, a lookup-table-based publicly available version of GIRE3 (Evans & Brinza, 2014), was used to predict trapped proton and trapped electron fluences for updated mission trajectories. We continue to evaluate the utility of the JOSE (Jovian Specification Environment) models for locations inside the orbit of Europa (Nénon et al., 2017, 2018; Sicard-Piet et al., 2011) but, given that GRID results are enveloping at present, consider the GRID-

based results the initial baseline. NOVICE (Jordan, 1991) was used to produce TID versus depth and TNID versus depth for the JGA flyby (Figure E-2).

Trapped protons in the Jovian system possess energy ranges comparable to those found in solar particle events (SPEs). Contributions to proton-induced SEEs should consider the time, albeit brief, spent in passage of the Jupiter trapped proton environment as the rapid intensification in proton fluxes will, for a short time, increase risk of proton SEEs in sensitive electronics.

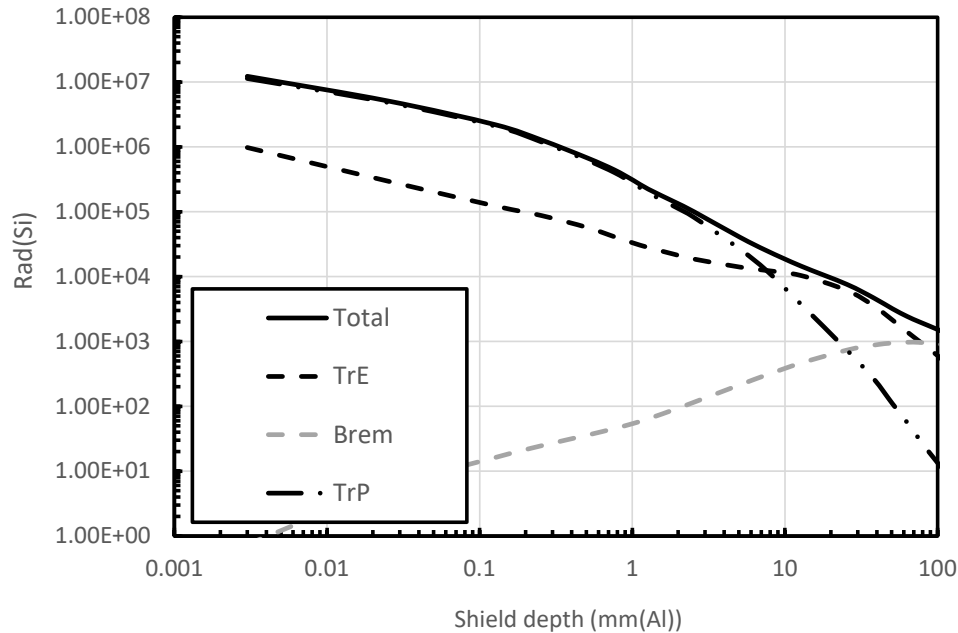


Figure E-2. Spherical shell dose [rad(Si)] versus depth (millimeter equivalent aluminum for Interstellar Probe’s JGA; no margins are reflected). Dose at 100 mil (2.54 mm) aluminum is at least 10× less than predicted Europa Clipper mission doses. (Image credit: Johns Hopkins Applied Physics Laboratory.)

E.3 Heliosphere, Heliosheath, and Interstellar Radiation Environments

Interstellar Probe’s mission design includes (times notional/approximate) ~12 years in the inner portion of the heliosphere (1–60 au), ~5 years in the heliosheath (90–120 au), and ~35 years in interstellar space (>120 au) for total mission duration of ~50 years. Although the JGA offers a short-duration, comparatively extreme space radiation/plasma environment, the probe will be subjected to space environmental effect hazards (TID, TNID, SEEs, and spacecraft charging) in all mission phases.

TID during heliosphere phases is dominated by solar protons. Solar proton fluxes were modeled using SAPPHIRE (Solar Accumulated and Peak Proton and Heavy Ion Radiation Environment) (Jiggins et al., 2018) with a confidence level (CL) of 95%.

SEE represents the predominant space radiation hazard for the majority of Interstellar Probe’s mission lifetime. It is caused by the passage of single ions through an electrical and electronic equipment (EEE) device active volume. The particle loses energy and deposits charge as it traverses the target device. The response of the target device to this charge generation may take

several forms. Specific SEE threats include destructive SEEs (or DSEEs) such as single-event latchup (SEL), single-event burnout (SEB), or single-event gate rupture (SEGR), as well as nondestructive SEEs (NDSEEs) such as single-event functional interrupt (SEFI), single-event transient (SET), single-bit errors (SBEs), multiple-bit errors (MBEs), or single-event upset (SEU). DSEEs may instantaneously and catastrophically impact a specific EEE device, circuit, and/or function, whereas NDSEEs may cause momentary interruptions in a device, circuit, and/or function where nominal system operations are affected.

The Interstellar Probe spacecraft will be subjected to a background of modulated GCR ions, solar protons, and periodic extreme SPEs.

E.4 Interstellar and Local Interstellar Medium Environments

The Interstellar Probe mission design projects >35 years of operation in interstellar space (>120 au) and now assumed to be beyond the influence of the Sun and solar particles. Consequently, solar protons were excluded from dose predictions, and TID contributions were exclusively from LISM GCR fluxes. GCR protons, whose abundance far exceeds heavier ions, were considered (Cummings et al., 2016). Although predicted doses were determined, their contributions, which are comparatively insignificant, are not obviously visible in Figure E-1.

GCR differential spectra for elements from hydrogen through nickel ($Z = 1-28$) were calculated from Voyager I data (Cummings et al., 2016). Comparison to the spectra at 1 au makes evident the heliospheric modulation of GCRs for all elements, most strongly for low- Z elements and in the 10- to 1000-MeV/nucleon range. Vanderbilt's CRÈME96 tool (Tylka et al., 1997) was used to transport these spectra through 2.54-mm (100-mils) idealized aluminum shielding and to convert to a single flux versus linear energy transfer (LET) spectrum for the LISM. The LISM and 1-au GCR LET spectra are plotted in Figure E-3 and display the effects of modulation by the heliosphere.

No attempt is made here to account for any radial gradient in GCR fluxes that may occur if some degree of GCR modulation occurs beyond the heliopause; the existence and magnitude of any such gradient is not conclusive (Cummings et al., 2016; Kóta & Jokipii, 2014; Scherer et al., 2011) but would be potentially significant on the scale of Interstellar Probe's trajectory.

A notional SEU rate calculation (Allen et al., 2010) was performed to be representative of a moderately sensitive memory device. SEU rates for GCRs in the LISM were calculated to be approximately four times those for the 1-au environment. The LISM GCR environment is therefore the driving case for SEEs for the bulk of the mission and defines the "operate through" SEE environment.

E.5 Spacecraft Charging

Spacecraft charging results from the accumulation of electric charge on, or within, spacecraft surfaces. The undesirable impacts resulting from spacecraft charging include the following:

1. Electrostatic discharge (ESD) resulting from the sudden, rapid release of stored electrical charge or due to differential surface potentials

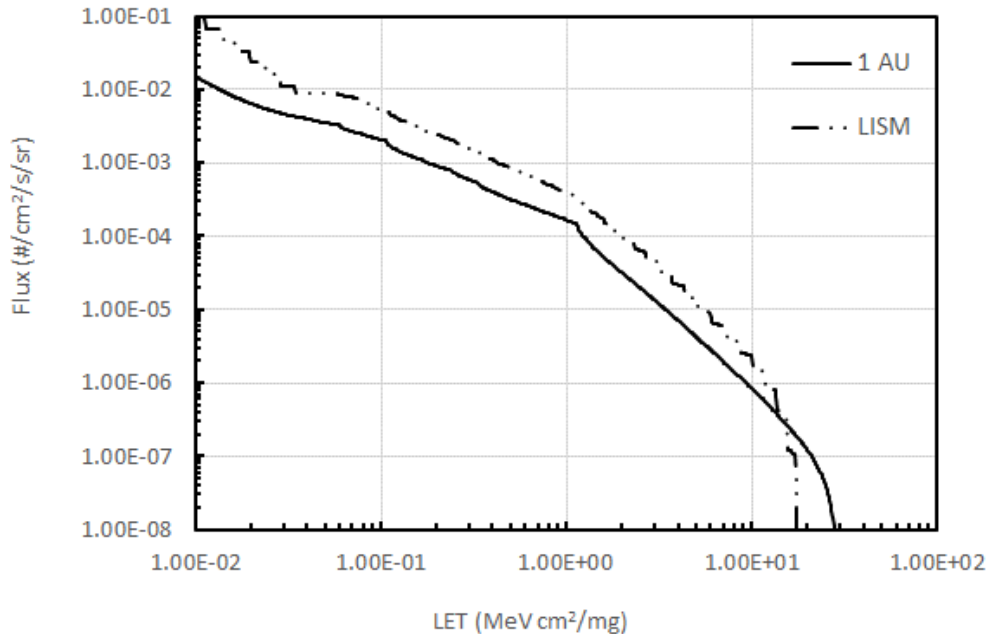


Figure E-3. LET spectrum for GCR ions of $Z = 1$ to $Z = 28$ at a shielding depth of 2.54 mm. GCR fluxes at most LETs are two to four times higher in the LISM. (Image credit: Johns Hopkins Applied Physics Laboratory.)

2. Electromagnetic interference (EMI) or electromagnetic pulses (EMPs) associated with the frequency components of ESD
3. Rapid fluctuations in, or extreme amplitudes of, spacecraft frame potential

In-flight anomalies resulting from spacecraft charging are well published (see, for example, proceedings of the Spacecraft Charging Technology Conference). Voyager 1, specifically, experienced noteworthy anomalous events, eventually attributed to spacecraft charging, during the March 1979 Jovian flyby (Leung et al., 1986).

The ~ 3.8 -day JGA represents the most severe, transient relativistic spacecraft charging environment predicted for Interstellar Probe. Although the flyby is quite rapid, the peak high-energy electrons encountered while the spacecraft traverses the Jovian system are comparable to those considered when assessing spacecraft charging risks for recent missions, specifically Juno and Europa Clipper (Figure E-4).

The top panel of Figure E-4 presents the integral trapped electron (TrE) flux for >1 -MeV and >10 -MeV energy bands, illustrating the spacecraft approach and retreat from its $\sim 1.05 R_J$ closest approach. This plot illustrates the ~ 4.5 -hour period of highest predicted fluxes, which enables determination of the fluences shown in the bottom panel of Figure E-4. It should be evident that the total electron fluences (no margins) predicted for the Interstellar Probe JGA are quite similar to those considered for recent projects and, in fact, exceed fluences at highly penetrating >25 -MeV electrons. Interstellar Probe should consider both the peak flux and total encounter fluence with statistical margin applied as per Juno and Europa Clipper (Kim et al., 2017). All internal charging environments

were derived via high-fidelity (30-second time step) GIRE3 (GRID) simulations for all closest approaches and application of statistics based on Galileo EPD observations (Kim et al., 2017).

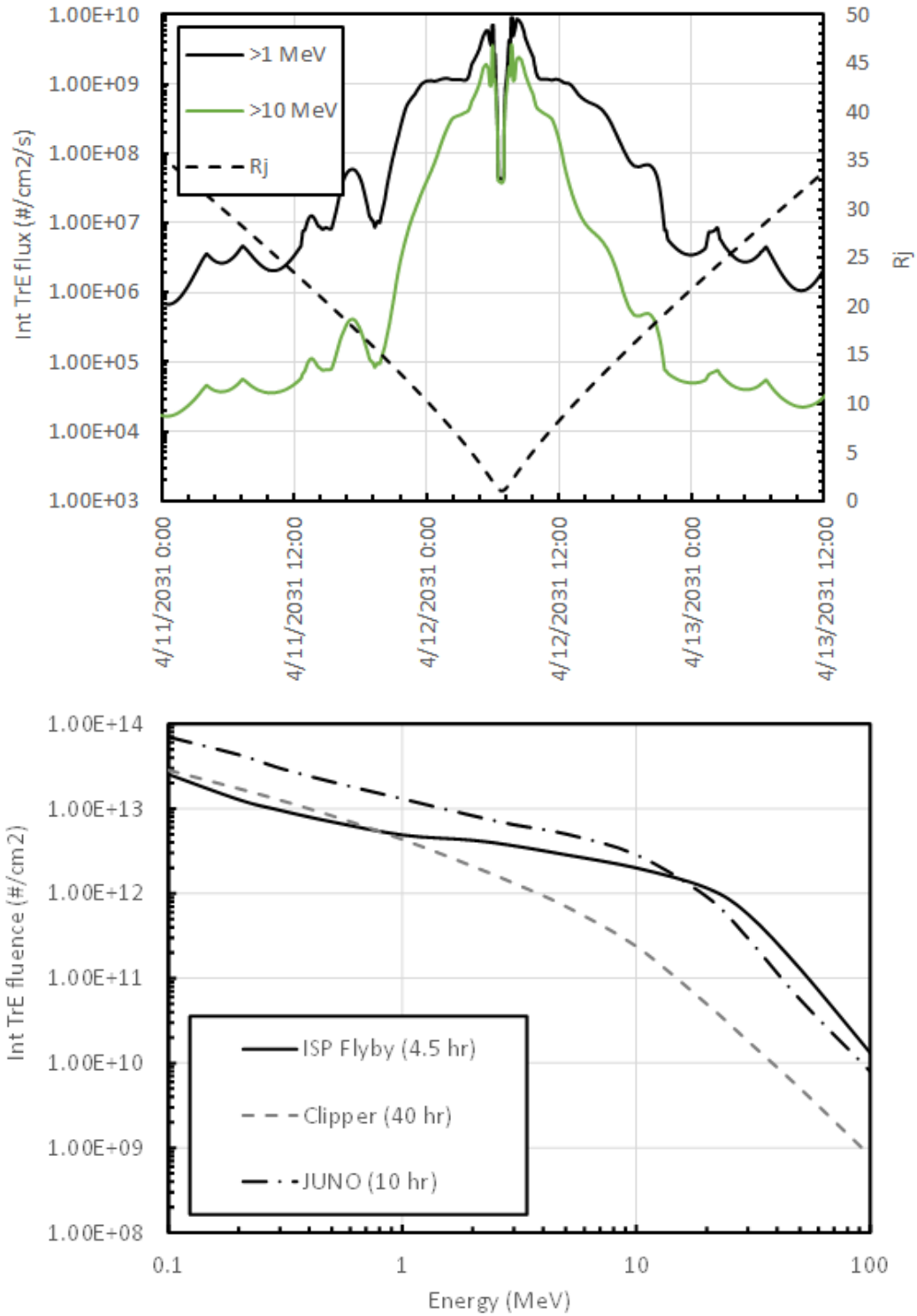


Figure E-4. Interstellar Probe's JGA results in short-duration internal charging fluxes (top panel) and fluences (bottom panel) comparable with recent Jovian missions. (Image credit: Johns Hopkins Applied Physics Laboratory.)

Effects of the Jovian trapped electrons may be exacerbated by the “pre-charging” of highly (electrically) resistive materials ($>10^{19}$ ohm-cm), which will be experiencing low-level, near-constant solar wind conditions for ~ 6 months before arrival at the Jovian system and an additional ~ 12 years in the heliosphere after departure of the Jovian system. This long-duration charging of highly resistive insulators leads to development large electric fields and, potentially, ESD (Dennison et al., 2007; Paulmier et al., 2015). In addition to the transient passage through the Jovian trapped electrons, Interstellar Probe should consider low-level, long-duration charging while in the heliosphere.

E.6 Appendix E References

- Allen, G.R., Edmonds, L., Tseng, C.W., Swift, G., Carmichael, C. (2010) Single-event upset (SEU) results of embedded error detect and correct enabled block random access memory (Block RAM) within the Xilinx XQR5VFX130. *IEEE Transactions on Nuclear Science* 57(6), 3426-3431. doi: 10.1109/TNS.2010.2085447
- Cummings, A.C., Stone, E.C., Heikkila, B.C., Lal, N., Webber, W.R., Jóhannesson, G., Moskalenko, I.V., Orlando, E., Porter, T.A. (2016) Galactic cosmic rays in the local interstellar medium: Voyager 1 observations and model results. *The Astrophysical Journal* 831(1), 18. doi: 10.3847/0004-637x/831/1/18
- Dennison, J.R., Gillespe, J., Hodges, J., Hoffmann, R., Abbott, J., Hunt, A. (2007) *Radiation Induced Conductivity of Highly-Insulating Spacecraft Materials*. In Proceedings of the 10th Spacecraft Charging Technology Conference, Biarritz, France.
- Divine, N., Garrett, H.B. (1983) Charged particle distributions in Jupiter’s magnetosphere. *Journal of Geophysical Research: Space Physics* 88(A9), 6889-6903. doi: <https://doi.org/10.1029/JA088iA09p06889>
- Evans, R. W., Brinza, D. E. (2014) *Grid2: A Program for Rapid Estimation of the Jovian Radiation Environment: A Numeric Implementation of the GIRE2 Jovian Radiation Model for Estimating Trapped Radiation for Mission Concept Studies*. Pasadena, California: Jet Propulsion Laboratory.
- Garrett, H., Jun, I., Ratliff, J., Evans, R., Clough, G., McEntire, R. (2003) *Status of the Galileo Interim Radiation Electron Model (JPL 03-006)*. Pasadena, California: Jet Propulsion Laboratory.
- Garrett, H., Kokorowsk, M., Jun, I., Evans, R.W. (2012) *Galileo Interim Radiation Electron Model Update—2012 (JPL 12-9)*. Pasadena, California: Jet Propulsion Laboratory.
- Jiggins, P., Heynderickx, D., Sandberg, I., Truscott, P., Raukunen, O., Vainio, R. (2018) Updated model of the solar energetic proton environment in space. *J. Space Weather Space Clim.* 8, A31. Retrieved from <https://doi.org/10.1051/swsc/2018010>
- Jordan, T.M. (1991, Sept.) *Space System Analysis Using The NOVICE Code System*. In RADECS 91 First European Conference on Radiation and its Effects on Devices and Systems. doi: 10.1109/RADECS.1991.213584

- Kim, W., Chinn, J., Jun, I., Garrett, H. (2017) *Internal Electrostatic Discharge (iESD) Design Environments for Jovian Missions*. In Applied Space Environments Conference.
- Kóta, J., Jokipii, J.R. (2014) Are cosmic rays modulated beyond the heliopause? *The Astrophysical Journal* 782(1), 24. doi: 10.1088/0004-637x/782/1/24
- Leung, P., Whittlesey, A.C., Garrett, H.B., Robinson, P.A., Jr. (1986) Environment-induced electrostatic discharges as the cause of Voyager 1 power-on resets. *Journal of Spacecraft and Rockets* 23(3), 323-330. doi: 10.2514/3.25805
- Néron, Q., Sicard, A., Bourdarie, S. (2017) A new physical model of the electron radiation belts of Jupiter inside Europa's orbit. *Journal of Geophysical Research: Space Physics* 122(5), 5148-5167. doi: <https://doi.org/10.1002/2017JA023893>
- Néron, Q., Sicard, A., Kollmann, P., Garrett, H.B., Sauer, S.P.A., Paranicas, C. (2018) A physical model of the proton radiation belts of Jupiter inside Europa's orbit. *Journal of Geophysical Research: Space Physics* 123(5), 3512-3532. doi: <https://doi.org/10.1029/2018JA025216>
- Paulmier, T., Dirassen, B., Belhaj, M., Rodgers, D. (2015) Charging properties of space used dielectric materials. *IEEE Transactions on Plasma Science* 43(9), 2894-2900. doi: 10.1109/TPS.2015.2453012
- Scherer, K., Fichtner, H., Strauss, R.D., Ferreira, S.E.S., Potgieter, M.S., Fahr, H.J. (2011) On cosmic ray modulation beyond the heliopause: Where is the modulation boundary? *The Astrophysical Journal* 735(2), 128. doi: 10.1088/0004-637x/735/2/128
- Shirbacheh, M. (1984) *International Solar Polar Mission GPHS-RTG Radiation Summary Report* (JPL D-896), Document No. 1628-43. Pasadena, California: Jet Propulsion Laboratory.
- Sicard-Piet, A., Bourdarie, S., Krupp, N. (2011) JOSE: A new Jovian specification environment model. *IEEE Transactions on Nuclear Science* 58(3), 923-931. doi: 10.1109/TNS.2010.2097276
- Tylka, A.J., Adams, J.H., Boberg, P.R., Brownstein, B., Dietrich, W.F., Flueckiger, E.O., Petersen, E.L., Shea, M.A., Smart, D.F., Smith, E.C. (1997) CREME96: A revision of the cosmic ray effects on micro-electronics code. *IEEE Transactions on Nuclear Science* 44(6), 2150-2160. doi: 10.1109/23.659030

Appendix F. Longevity Analysis for Interstellar Probe

F.1 Introduction

Reaching the local interstellar medium to complete the science objectives for a mission like Interstellar Probe is going to require a spacecraft, a ground system, and an organizational structure that can not only last but perform well for at least 50 years. These topics collectively are referred to as “longevity” in the context of the Interstellar Probe study. To this end, the longevity portion of the study has two principal goals:

- Identify the processes for the flight system, the supporting ground infrastructure, and mission staffing to ensure a successful outcome when mission success requires 50-plus years, by design, of successful operation
- Provide information about current and past missions with supporting analysis that will provide stakeholders with the confidence necessary to support such a mission

The longevity task of the Interstellar Probe study was formally initiated in 2019. The following paragraphs (adapted slightly) are taken from the 2019 report that stated the intent of the longevity study (as above) and provided the initial background. In 2019 these were the goals; this appendix provides the results of the effort. This appendix also details challenges and solutions to the longevity requirement identified in Section 3 regarding longevity issues for Interstellar Probe.

A review of the literature indicated that Voyager was the most well-known long-term mission with regard to lifetime but not the only one (Fox et al., 2013). The literature noted that if spacecraft continue to operate for a few years (no infant mortality), they tend to function for a very long time. The often-assumed constant failure rate models are not appropriate for such long-term missions, and a Weibull distribution of failure rates (i.e., failure rate decrease over time) is a better model (Saleh & Castet, 2011). As the details of mission requirements and the spacecraft architecture progressed, a statistical analysis of Interstellar Probe reliability was developed and mitigations were recommended where that analysis indicates additional work will be required to ensure the reliability risk is acceptable.

The ground segment for an Interstellar Probe mission study is based on a concept of operations (CONOPS) whose initial outlines are described in Section 3. Experience from past and current missions such as Voyager and New Horizons has provided guideposts to help and forms the basis for the challenges for the ground segment described below. A number of these challenges have been defined, and solutions are recommended in Section F.3 of this appendix. These recommendations can be used as guidelines for future Interstellar Probe mission development.

As stated above, prior missions such as Voyager, Cassini, and New Horizons have operated for long periods of time. Other missions are currently planning for eventual workforce transitions, such as NASA's Europa Clipper (Weber, 1968) and the European Space Agency's (ESA's) Jupiter Icy Moons Explorer (JUICE). The timeline of an interstellar mission, however, is so extreme as to largely eclipse any and all prior activities. Arrival at the target destination will not take place for 50 years, a period longer than Voyager's operational timeline, now expected to terminate 45 years after launch. Several of Voyager's initial principal investigators (PIs) have already passed away (Bradford A. Smith, 2018; Rudolf A. Hanel, 2015; Herbert S. Bridge, 1995; Von R. Eshleman, 2017; James Warwick, 2013; Frederick L. Scarf, 1988), with deputies taking on leadership roles only once the PI has died, akin to a form of kingship or inheritance (Weber, 1968). Voyager data management and updating efforts began over 20 years after launch. On Cassini, those who joined after selection and became the lifeblood of mission planning and operations had to wait until several years into the mission before they were offered an official mission role; while PIs could add newcomers to their teams, facility instrument leaders on Cassini could not do so without NASA Headquarters' approval. A late addition of a participating scientist's program enabled some mobility of these juniors into official roles. New Horizons is still under the command of its PI, with deputies in charge of encounter planning experiencing role turnover in extended-mission phases. As such, many of the innovations that enable such mission longevity have been implemented on an ad hoc basis, according to the timeline of mission extension or need, and were not part of the initial mission plan, personnel assignments, or proposal, as driven by budgetary limits.

This ad hoc approach to temporality and change will simply not work on the Interstellar Probe mission. Most of the original team will be dead by the time the spacecraft reaches its targeted end of mission of 50 years past launch. Even if the spacecraft arrives fully operational at the interstellar medium, without appropriate operational plans in place, the initial team that operated it will have dissolved into postmortem factions, with potentially archaic data standards that are no longer supported and little to no resources to support the upkeep of essential equipment or the successful promotion of juniors to leadership roles, and the mission will be a failure. Just as extreme distance drives technical parameters associated with speed and trajectory, which, in turn, impact instrumentation and design, ***the extreme temporality associated with the mission lifetime must drive the mission's teaming and data architectures because they are essential to enable full mission success.*** These issues are discussed more fully in Sections F.3 and F.4 of this report.

The majority of this appendix (Section F.2) is devoted to discussing the reliability engineering tasks performed for the study. We define success with an examination of robustness in science requirements; establish degraded cases and functional redundancies; model spacecraft configurations; mine the historical record of long-lived missions to better quantify time-dependent failure rates (missions with actual or design life of >15 years) to discover what failed

and why and, more importantly, what did not fail; and, lastly, examine physics-of-failure (PoF) methods for key technologies. We relied on expertise from the University of Maryland Center for Advanced Life Cycle Engineering (CALCE).

Sections F.3 and F.4 are dedicated to the understanding of the ground segment issues and long-term organizational issues. These three major challenges of reliability, ground segments, and organization as well as the solutions discussed in this appendix are summarized in the concluding Section F.5, which also discusses work recommended to be carried forward after this concept study concludes.

F.2 Long-Duration Mission Reliability

F.2.1 Introduction

The Interstellar Probe study documents mission concepts that can be practically implemented by the early 2030s. Several potential trajectories, spacecraft architectures, and science payloads were explored, the results of which are discussed in the body of this document. A significant portion of the work revolved around creating confidence that such a mission could have longevity of at least 50 years. The purpose of this section is to present the work substantiating the claim that a mission lasting 50 years is currently achievable.

The Interstellar Probe study team is not the only one thinking about long-duration missions. Several white papers supporting the National Academies 2023–2032 Planetary Decadal Survey¹ have emphasized science in the outer solar system. The Outer Planets Assessment Group (OPAG) for example states “For the decade 2023–2032, OPAG endorses a new start for two directed missions: first, a mission to Neptune or Uranus [the ice giants] with atmospheric probe(s), and second, a life detection Ocean World mission” (Moore et al., 2020). Several PIs mention long mission times as part of their concept descriptions. Rymer describes a mission to Neptune and Triton needing a “12–16 year cruise phase to Neptune.” Although not stated, the science collection portion of the mission could be 2–5 years (Rymer et al., 2020). Robbins discusses missions to revisit and orbit Pluto and, as such, notes that there are “significant time requirements to reach the system with a low enough capture velocity, and the power and related age issues that result.” This would be a mission longer than New Horizons (Robbins et al., 2020). Cohen notes the constraint that radioisotope power source (RPS) lifetimes have in his discussion of a proposed Uranus mission: “With current technology (i.e., 14-year multi-mission radioisotope thermoelectric generator [MMRTG] flight design life), a typical baseline would be a <12-year cruise (potentially with a Centaur flyby) and a 2-year mission at Uranus with a system tour that enables surface mapping of the large satellites as well as spatial coverage of the planet & rings/small moons; this baseline could be significantly lengthened if the lifetime of future RPS were improved” (Cohen et al., 2020). Neveu advocates for sample returns from Enceladus with various options, with a Sun orbiter taking up to 34 years, a Saturn orbiter taking 13–15 years, or landers taking >26 years (Neveu et al., 2020).

¹ All Planetary Decadal white papers referenced were accessed at: Planetary Science and Astrobiology Decadal Survey 2023-2032, The National Academies of Sciences, Engineering, Medicine, <https://www.nationalacademies.org/our-work/planetary-science-and-astrobiology-decadal-survey-2023-2032>.

F.2.1.1 Scope

Longevity of space missions can cover a vast array of topics. This study has focused the efforts on estimating the mission reliability of the baseline mission concept. The data analysis has emphasized interplanetary missions as the analog for Interstellar Probe. Launch vehicle reliability is not discussed because it is expected to be consistent with the launch risk of all missions.

F.2.1.2 Interstellar Probe Mission Lifetime Goal

The stated goal for Interstellar Probe is to continuously return meaningful science data for at least 50 years. While very early concepts showed reaching 1000 au by 50 years, engineering limitations have made this impractical. Yet the 50-year goal stayed as a marker pointing to a significant entry into the local interstellar medium or 350 au. With this time goal, Interstellar Probe will pass through each of the phases outlined in Table F-1.

Table F-1. Constituent mission phases create the mission lifetime goal of 50 years.

Mission Phase	Time Period	Duration (years)
Launch to Jupiter	Commissioning and Cruise	1
Inner Heliosphere Phase	Jupiter – 90 au	12
Heliosheath Phase	90–120 au	4
Interstellar Phase to 50 Years*	120–352.4 au	33

*To provide some context about 50 years from a reliability perspective, no spacecraft have yet operated for 50 years, although the Voyager spacecraft are approaching this milestone. The longest mission design life requirement has only been 15 years (Piquette et al., 2019).

F.2.1.3 Interstellar Probe Reliability Design Philosophy

Resilience to potential failures has been a major focus for the spacecraft design team. For the most part, the spacecraft bus features a fully redundant architecture. There are places where this could not be achieved within the constraints of mass and power. For example, flying two or more of each instrument is impractical, so the instrument suite’s resilience comes in the form of functional redundancy with respect to the mission science objectives. The remaining single-point failures are discussed later in the appendix.

F.2.2 Literature Survey

Of interest to (and with bearing on) the study is the literature pertaining to how reliability engineering has developed for space missions, particularly those interplanetary missions with longer durations. In addition, we have examined the literature for information about component- and system-failure mechanisms that come into play many years after system deployment. This section summarizes the literature in these areas.

F.2.2.1 Space System Reliability

Reliability is defined by NASA as the “probability that an item will perform its intended function for a specified interval under stated conditions” (*Safety and Mission Assurance Acronyms, Abbreviations, and Definitions*, 2018). This definition is unchanged since its inception as an

engineering term in 1957 in the U.S. military's Advisory Group on the Reliability of Electronic Equipment report (U.S. Advisory Group of Reliability of Electronic Equipment, 1957). The literature describing reliability engineering spans the history of spaceflight, with the earliest reliability studies on spacecraft being performed since the early 1960s. General understanding of spacecraft reliability has evolved, as has the scope of these assessments. For example, Stanbery (1964) wrote about reliability for *long mission* spacecraft, by which he meant “flight from three months to two years.” Two main threads are examined: (1) the evolution and understanding of how spacecraft fail and (2) the change in spacecraft models.

As the industry was learning how to make machines work in space, failure rates were high, leading programs to adopt a philosophy of flying more than one spacecraft to meet mission objectives (e.g., Mariner 6 and 7, Pioneer 10 and 11, Viking 1 and 2, and Voyager 1 and 2). In the 1980s, confidence had grown. Paired spacecraft missions had been replaced with large fully redundant spacecraft like Galileo and Cassini. By the mid-2000s, New Horizons launched with a mass of <500 kg and near full redundancy to meet its 15-year mission. The majority of early failures (1960s through mid-1990s) were attributed to design errors and the space environment (Sarsfield, 1998), although as Harland and Lorenz (Harland & Lorenz, 2005) point out, this distinction is somewhat arbitrary based on context and expected knowledge of the environment. At the same time, the failures attributed to parts and quality continued to decrease.

Parts have traditionally been viewed as the primary source of failure in spacecraft systems. In the early years of the space program, this was indeed the case, mainly because of quality and reliability problems with evolving microelectronics (Hamiter, 1990). However, data show that parts and quality factors have become a minor constituent of spacecraft failures. These data are corroborated by other studies, including one conducted by Pecht & Ramappan (1992) that found part failures to be negligible. The decline in the percentage of parts-related failures can be attributed to the increasing reliability of electronic parts plus the implementation of disciplined parts programs by NASA and the Department of Defense.

A NASA EEE Parts Assurance Group (NEPAG; Zambotti, 2007) indicates that parts failures can be more accurately associated with inadequacies in design or improper handling of components or workmanship. A NASA Jet Propulsion Laboratory (JPL) study (as cited by Sarsfield) reviewed electronic parts-related failures in the Viking, Voyager, Magellan, and Galileo spacecraft. Only 27 failure reports for these missions could be traced to problems with parts, and all but 8 were later attributed to design or test deficiencies. None of the parts-related problems was considered serious, although redundant systems prevented an escalation of the problem in seven of the cases.

In the 1970s, reliability for missions of 10 years (instead of the 1- to 2-year missions) was being contemplated (Draper & Gavin, 1970; Jet Propulsion Laboratory, 1973). In their review, Castet & Saleh (2010) find many early reliability studies assumed a constant failure rate model, which was standard for the time. By the early 1970s, this assumption was being challenged because the data from several studies (Baker & Baker, 1980; Bloomquist, 1984; H. Hecht & Hecht, 1985; Timmins & Heuser, 1971) showed that using this assumption underpredicted the actual reliability of spacecraft in the long run but overpredicted the reliability in the short term. These analyses found decreasing failure rates in the spacecraft data, pointing out the discrepancy with the constant

failure rate models proposed in the military reliability handbook, MIL-HDBK-217, as unrealistic for system reliability predictions. Conrad (1976) attempted to solve this problem with a “two-rate reliability model” that uses one failure rate for shortly after launch and a different, and much lower, failure rate for the rest of the mission.

To better represent this nonconstant failure rate, reliability engineers turned to using the fairly new Weibull distribution as the most suitable model for assessing spacecraft and spacecraft system reliability (Baker & Baker, 1980; H. Hecht & Hecht, 1985; M. Hecht & Fiorentino, 1988; Krasich, 1995). The Weibull distribution is simply a power transformation of the exponential distribution, and it possesses considerable flexibility because it has increasing failure rate when the shape parameter β is more than 1, constant failure rate (exponential) when β equals 1, and decreasing failure rate when β is less than 1. For this reason, the Weibull distribution has become increasingly important as a reliability model in the past five decades.

In addition to lasting longer, spacecraft also outlive their design lives. Several studies (Brown et al., 2010; Castet & Saleh, 2010; Edwards et al., 2021; Fox et al., 2013; Smith et al., 2021) have noted this behavior across various data sets for low Earth orbit, geostationary Earth orbit (GEO), and interplanetary missions. For interplanetary missions, the stated design lives tend to be 5–10 years, with the outlier being New Horizons, which was designed around a 15-year requirement. The Voyager spacecraft, with 40+ years of continuous operations, were only designed for a 4.5-year mission. While this study focuses on interplanetary missions, it is worth noting that many other spacecraft have exhibited long lives. For example, NASA is currently flying spacecraft that have been operating since the late 1990s: Geotail, Solar & Heliospheric Observatory (SOHO), Wind, Advanced Composition Explorer (ACE), Landsat-7, and Hubble. IMP-8 and International Sun-Earth Explorer-3 (ISEE-3) each lasted over 30 years before their missions ended. Communication satellites in GEO are another category of spacecraft that routinely last 15 years. In Section F.2.4, the design life versus actual life plot of interplanetary missions is provided.

F.2.2.2 Failure Mechanisms for Long Durations

Historical information exists regarding missions that have lasted several decades. Although we can certainly learn from the design decisions made, caution needs to be taken because the data are for technology that is also several decades old. Many of the technologies launched in the 1970s and 1980s have been replaced or updated. Key to using these data is the understanding of relevance between current and past technologies and materials. In particular, we need to understand how current technology would fail 50 years from now.

Long-term space travel may result in exposure to various aspects of space weather. It is vital to document and account for the different wearout failure mechanisms that may propagate. To complete device qualification, the Automotive Electronics Council (AEC) requires manufacturers to provide testing data, methods, calculations, and internal criteria for the following die-level wearout failure mechanisms: electromigration (EM), time-dependent dielectric breakdown, negative-bias temperature instability, hot carrier injection, and stress migration (Haifley, 2014). Other wearout failure mechanisms that will be considered are package-level failure mechanisms: solder joint fatigue and creep (Dasgupta & Pecht, 1991).

F.2.2.2.1 Die-Level Wearout Mechanisms

EM is when the formation of a high current density, caused by local heating, parasitic currents, and other sources, results in the flow of metallic atoms in the direction of current flow. This flow of metallic atoms impacts electronic function over time. The flow of metallic atoms essentially causes the formation of voids in some areas of the overall lattice (potentially leading to open circuits) as well as the nucleation of denser metallic layers and the formation of hillocks (Rudra & Jennings, 1994), potentially leading to short circuits (Young & Christou, 1994). Figure F-1 demonstrates the EM process.

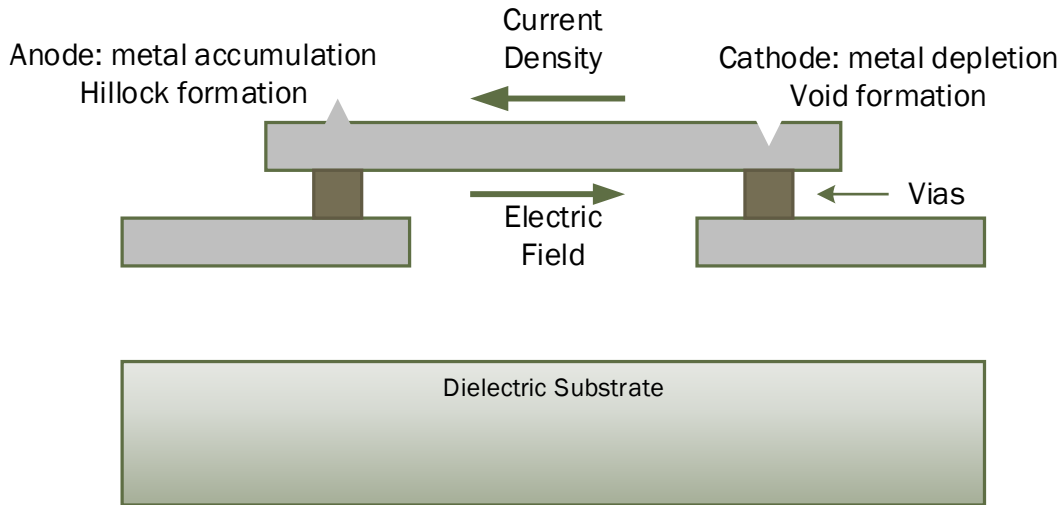


Figure F-1. Electromigration process in a given electronic package (Khan, 2012). (Image credit: Johns Hopkins Applied Physics Laboratory.)

Stress migration is the phenomenon where internal tensile stress gradients within the material lattice of the device ultimately lead to the formation of voids within the device. Eventually, the voids will grow to the point that open circuits begin to form within the device structure, leading to reduced device operation. These stress gradients may be exacerbated by additional sources, including during thermal processing (J. Li & Dasgupta, 1994; T. Wang et al., 2004). Figure F-2 demonstrates this process along with EM.

Time-dependent dielectric breakdown is the failure mechanism that occurs when a constant electronic field application less than the breakdown strength of the dielectric material eventually wears down the gate oxide of a metal–oxide–semiconductor field-effect transistor (MOSFET). The gate oxide is composed of silicon dioxide. Given that a device may maintain a load state or dormant state for extended periods in long-term space travel, the effects of time-dependent dielectric breakdown become even more significant. Time-dependent dielectric breakdown is caused by creating conductive paths (such as the formation of hillocks) or other leakage current sources. Figure F-3 is a snapshot of time-dependent dielectric breakdown.

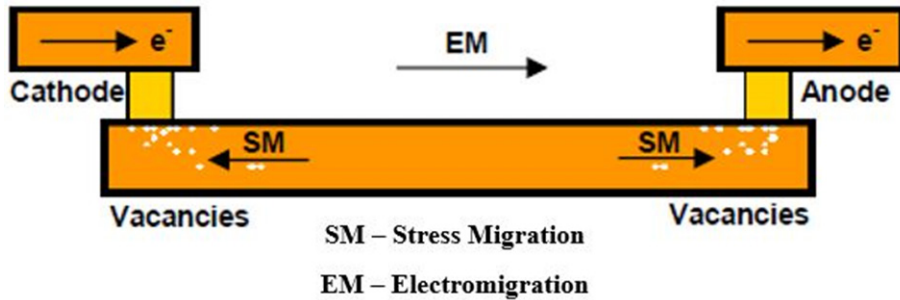


Figure F-2. Stress migration on a device. (Reprinted from Heryanto et al. (2010) with permission; © 2010 IEEE.)

Negative-bias temperature instability is the process by which p-channel-type metal–oxide semiconductor (pMOS) transistors, in particular those with elevated negative gate voltages, lead to trapped positively charged holes. These trapped holes increase the threshold voltage, which is the voltage required for transistor operation. The higher the threshold voltage, the higher the power necessary to turn on the transistor, leading to delayed circuit operation or even open circuits.

The last die-level wearout failure mechanism is hot carrier injection, a phenomenon where energized carriers (due to high-energy photons, for example) from MOSFET silicon channels end up injected into the MOSFET gate oxide. These “hot” carriers create a leakage current out of the silicon channel region and damage the dielectric material (Radamson & Thylén, 2014). Figure F-5 displays the hot carrier injection process.

F.2.2.2.2 Package-Level Failure Mechanisms

The first package-level wearout failure mechanism is solder joint fatigue. Solder joint fatigue is caused by cycles of stresses due to thermomechanical considerations (such as fluctuations in temperature) exacerbated by mismatches in the coefficient of thermal expansion at the interface between the die and the solder, and likewise between the solder and the substrate. The solder joints perform critical tasks: to act as a thermal dissipater for heat generated during operation, to act as an electrical connection between the die and substrate, and also to act as a mechanical interface for bonding the die and substrate to provide structural rigidity (Lee et al., 2000).

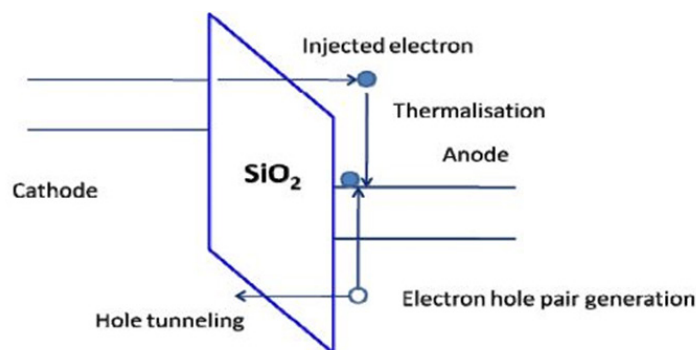


Figure F-3. A snapshot of the electron motion that leads to time-dependent dielectric breakdown (Wong, 2012).

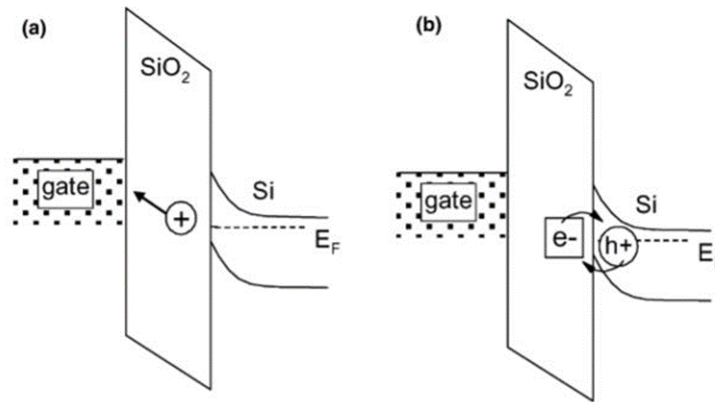


Figure F-4. The processes by which negative-bias temperature instability may occur. (a) The net charge at the dielectric interface may have positive ion drift occurring, leading to a decrease in the net charge. (b) If there is a charge imbalance on either side of the dielectric interface, then there may be an exchange of an electron for a proton (or hydrogen ion), causing a net-positive increase in the charge in the dielectric interface. (Reprinted from Stathis & Zafar (2006), with permission from Elsevier.)

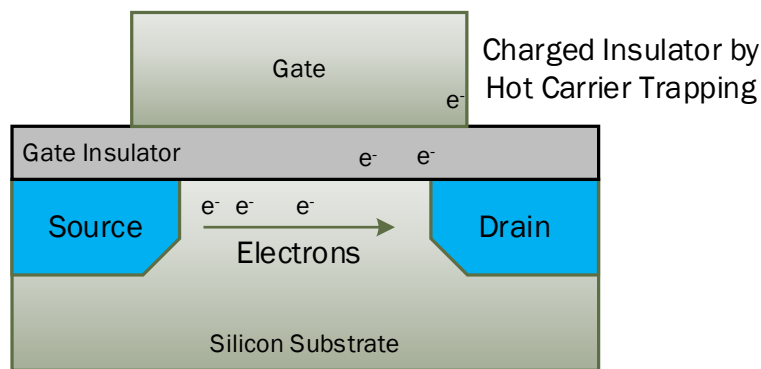


Figure F-5. The hot carrier injection process (Noda, 2008). (Image credit: Johns Hopkins Applied Physics Laboratory.)

Another source of wearout failure in package assemblies is creep deformation, where creep is the highly time-dependent material deformation due to a constant loading application at elevated temperatures (J. Li & Dasgupta, 1993). This is in direct contrast to fatiguing, which is cycle-dependent material deformation involving a variable loading at any temperature. One example of creep deformation in electronic packaging is the creep deformation of the epoxy molding compound in the package assembly (Kiasat et al., 2001).

F.2.3 Industry Communications and Panel Discussions

As this study was being conducted, the longevity team reached out to the systems engineering and reliability engineering communities for their thoughts on building a spacecraft that needed to last at least 50 years. We would like to express our gratitude to Tony Diventi (NASA Reliability & Maintainability Technical Fellow) and Nancy Lindsey (NASA Deputy Reliability & Maintainability Technical Fellow) for their contributions and assistance in making introductions, setting up meetings, and providing technical expertise.

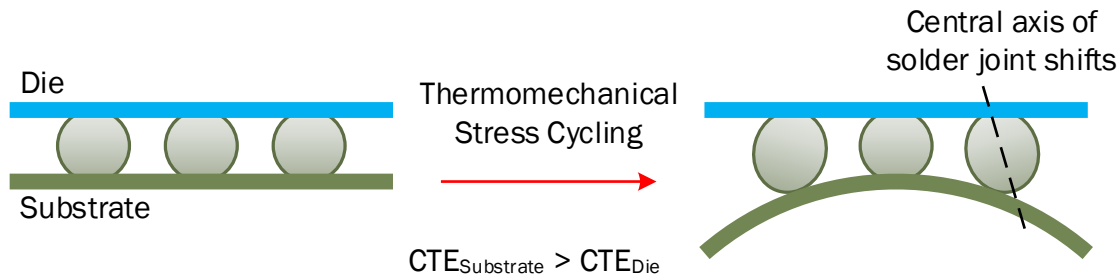


Figure F-6. Demonstration of the effects of solder fatigue on the package assembly (Serebreni, 2021). (Image credit: Johns Hopkins Applied Physics Laboratory.)

F.2.3.1 Panels for Reliability of Long-Duration Missions

Two panel sessions were held at AIAA’s ASCEND 2020 Conference (virtual event) and AIAA’s SciTech Forum (virtual event). NASA tech seminars invited the panel members to also present as part of their ongoing webinar series. Panel members were as follows:

- Nancy Lindsey, Deputy Reliability & Maintainability Technical Fellow at NASA Headquarters and Reliability, Maintainability, and Availability subject-matter expert at the NASA Goddard Space Flight Center (GSFC).
- Dr. Michael Pecht, Director of CALCE at the University of Maryland, where he is also a professor in applied mathematics. He has served as editor in chief of *IEEE Transactions on Reliability* for 9 years and as the editor in chief of *Microelectronics Reliability*. He has 11 patents and has written over 30 books and 500 papers on electronics design, testing, quality, and reliability.
- Dr. Diganta Das, Associate Research Scientist for CALCE and a member of the graduate faculty. He chairs the Reliability Prediction working group of the IEEE Standards Association.
- Steven Battel, President of Battel Engineering and a professor of electrical engineering and climate and space at the University of Michigan.
- David Kusnierkiewicz (retired), Chief Engineer in the Johns Hopkins Applied Physics Laboratory’s (APL) Space Exploration Sector and Mission Systems Engineer for the New Horizons mission.

The panel discussions focused on a few areas of interest:

- Historical perspective of NASA long-duration missions and impacts to the assurance process
- Transitioning away from traditional reliability methods toward prognostics and the use of artificial intelligence (AI)
- Enhancements to systems engineering design philosophy
- Expanding role of testing and validation

Ms. Lindsey started the discussions with an overview of NASA spacecraft lifetime performance, pointing to many examples of spacecraft lasting a long time, although not all were interplanetary missions. The discussion accompanying these data was about the assurance process, but no correlation was developed between this process and long lifetime. As Mr. Battel stated, “even with useful guidance from Voyager, however, there is no relevant statistical evidence indicating that existing 2021 space technology, design approaches, manufacturing standards, and test methods can be confidently extrapolated to a 50+-year lifetime.”

Many of the speakers’ comments revolved around recognizing that something is likely to go wrong during a 50-year mission. In response, the design teams need to “logically construct a system approach that maximizes the value of what you know and minimizes the potential impact of what you do not know or cannot know.” This translates to how requirements are developed and how the testing program is systematically defined. The resulting architectures need to take advantage of redundancy and onboard recovery responses. Dr. Pecht and Dr. Das suggested that a 50-year mission “initiate the use of AI-based data analytics and physics of failure for design trade-offs, test planning, digital twin development, and in situ health monitoring and management.”

All the panel members emphasized the need to understand uncertainties, known and unknown. Mr. Kusnierkiewicz discussed the role of a coherent testing campaign to give the various decision boards confidence in the reliability of a spacecraft design. He reiterated the belief from other panelists that testing be strongly coupled to the PoF models for parts.

F.2.3.2 Other Discussions with NASA

As part of the study, the team engaged with members of the NASA reliability community at Headquarters, the NASA Engineering and Safety Center, GSFC, and JPL. Discussions ranged from specific redundancy concepts on Interstellar Probe to fundamental failure mechanisms. The GSFC engineers emphasized the types of failure mechanisms observed with equipment returned from Hubble Space Telescope after being on orbit for 20 years. Of particular interest was the EM occurring in some of the integrated circuits.

The JPL reliability engineers (with special thanks to Angel Garnica, JPL Deputy Manager for Reliability Engineering and Mission Environmental Assurance Office) participated in several events and had direct interaction with the APL team. Their comments mirror many of the concerns the team has, and many of their comments are addressed herein. Emphasis should be placed on the uncertainty involved with such an endeavor, which is reflected in the wide distributions shown for the statistical analyses and predictions.

Discussions were held with the NASA Statistical Engineering Team (Finseth, 1991). This team is composed of statisticians, about half of whom wholly or partly specialize in reliability analysis. This organization is charged with supporting the NASA Engineering and Safety Center. During the discussions, several resources were identified for the longevity team to investigate.

F.2.4 Data Analysis of Interplanetary Missions

Many interplanetary missions have flown to explore the solar system. This section is a statistical treatment of the reliability and duration data in order make inferences about a mission that must

last at least 50 years. This analysis was originally published by Edwards et al. (2021), and the analyses have been updated with new information since the initial publication. The initial list of interplanetary spacecraft was sourced from SpaceTrak (Fuller, 2020), an analytical system documenting event histories and technical specifications for all unclassified satellites since the launch of Sputnik in 1957. A total of 179 spacecraft were identified as having interplanetary orbits. Specific SpaceTrak data of interest included spacecraft launch date, mission status or end date, orbit category, and design life, as well as any information on spacecraft failures or reason for retirement. Additional data on this group from the NASA Space Science Data Coordinated Archive (NSSDCA) Master Catalog (<https://nssdc.gsfc.nasa.gov/nmc/>) and NASA’s Solar System Exploration website (<https://solarsystem.nasa.gov/missions/>) provided more information on each spacecraft’s technical profile and mission objectives. This resulted in further refinement of the original interplanetary spacecraft list with the removal of spacecraft classified as:

- Technology test or demonstration missions (13 removed)
- Small hoppers, landers/impactors, or balloons (41 removed)
- Majority “passive” satellites (e.g., Elon Musk’s Tesla Roadster or ARTSAT2, a deep-space art sculpture) (5 removed)

These types of missions do not reflect the systems or design limitations consistent with an interstellar probe mission. Technology demonstration missions often lack robust architectures across the system because it is not their focus. Hoppers, impactors, and landers are designed for use in very different environments. Although it is true that the cruise portions of these missions could count as right-censored data—data for which an exact failure time is not known—for convenience they were removed. “Passive” satellites do not adhere to the same standards for their probability of success. The insufficient quantity and lack of clarity of information surrounding satellites fabricated by the Soviet Union also resulted in the removal of USSR spacecraft (22) from the list. In the absence of a clear science-based reason to exclude them, an ANOVA (analysis of variance) confirmed that Soviet-era spacecraft have a different statistical distribution than non-Soviet spacecraft. Lastly, failures due to a launch vehicle or separation failures (36) were dropped from consideration. This extensive culling process resulted in a significantly shorter list of 60 interplanetary-orbit spacecraft, which are shown in Table F-2.

Table F-2. Interplanetary spacecraft listing for longevity analysis.

Spacecraft	Launch Date	Duration* (years)	Design Life (years)	End of Mission
PIONEER 05 (P-2)	3/11/1960	0.29		Decommissioned
MARINER 02 (VENUS)	8/27/1962	0.35		Decommissioned
MARINER 04 (MARS)	11/28/1964	3.09	1	Unknown
PIONEER 6 (PIONEER A)	12/16/1965	34.98	0.51	Decommissioned
EXPLORER 33 (IMP D)	7/1/1966	5.21	1	Unknown
PIONEER 7 (PIONEER B)	8/17/1966	28.62	0.51	Decommissioned
MARINER 05 (VENUS)	6/14/1967	0.47	0.51	Telemetry, tracking, and command failure
PIONEER 8 (PIONEER C)	12/13/1967	28.69	1	Unknown

Spacecraft	Launch Date	Duration* (years)	Design Life (years)	End of Mission
PIONEER 9 (PIONEER D)	11/8/1968	14.52	1	Unknown failure
MARINER 06 (MARS)	2/25/1969	2.31	1	Unknown
MARINER 07 (MARS)	3/27/1969	2.22	1	Unknown
MARINER 09 (MARS)	5/30/1971	1.41	1	Depletion of fuel
PIONEER 10 (JUPITER)	3/3/1972	30.89	7	Depletion of power
EXPLORER 47 (IMP H)	9/23/1972	6.11	1	Decommissioned
PIONEER 11 (JUPITER/SATURN)	4/6/1973	22.48	7	Depletion of power
EXPLORER 50 (IMP J)	10/26/1973	32.95	6	Unknown
MARINER 10 (MERCURY)	11/3/1973	1.39	1	Depletion of fuel
HELIOS 1 (NASA)	12/10/1974	7.85	2	Unknown
VIKING 1 MARS ORBITER	8/20/1975	4.96	4	Depletion of fuel
VOYAGER 2	8/20/1977	44.06	5	Active
VOYAGER 1	9/5/1977	44.02	5	Active
PIONEER 12 (VENUS)	5/20/1978	14.43	3	Depletion of fuel
GIOTTO	7/2/1985	7.06	1	Depletion of fuel
SUISEI	8/18/1985	5.51	3	Depletion of fuel
MAGELLAN	5/4/1989	5.44	2	Intentional impact/burn-up
GALILEO	10/18/1989	13.93	8	Intentional impact/burn-up
ULYSSES	10/6/1990	18.73	5	Depletion of power
MARS OBSERVER	9/25/1992	0.91	5	Propulsion failure
NEAR SHOEMAKER	2/17/1996	5.03	5	Intentionally subjected to extreme temperatures
MARS GLOBAL SURVEYOR	11/7/1996	9.99	4.25	Software failure
CASSINI	10/15/1997	19.92	11	Depletion of fuel
NOZOMI (PLANET B)	7/3/1998	5.44	2.51	Propulsion failure
MARS CLIMATE ORBITER	12/11/1998	0.78	3	Software failure
STARDUST-NEXT	2/7/1999	12.13	6	Depletion of fuel
MARS ODYSSEY ORBITER	4/7/2001	20.42	3.51	Active
MARS EXPRESS	6/2/2003	18.26	2	Active
SPITZER SPACE TELESCOPE	8/25/2003	16.43	2.51	Decommissioned
ROSETTA	3/2/2004	12.58	10.59	Depletion of power
MESSENGER	8/3/2004	10.74	6	Depletion of fuel
EPOXI (DEEP IMPACT)	1/12/2005	8.69	2	Software failure
MARS RECONNAISSANCE ORBITER	8/12/2005	16.07	5.51	Active
VENUS EXPRESS	11/9/2005	9.1	2	Depletion of fuel
NEW HORIZONS	1/19/2006	15.63	15	Active
STEREO AHEAD	10/26/2006	14.86	2	Active
STEREO BEHIND	10/26/2006	9.91	2	Guidance and control failure
PHOENIX MARS LANDER/CRUISE STAGE	8/4/2007	1.27	1	Environment-induced failure
DAWN	9/27/2007	11.09	10	Depletion of fuel
KEPLER	3/7/2009	9.65	3.51	Depletion of fuel
AKATSUKI (VENUS)	5/20/2010	11.29	4.5	Active
JUNO	8/5/2011	10.08	6	Active
MARS ORBITER MISSION (MOM)	11/5/2013	7.83	1.51	Active

Spacecraft	Launch Date	Duration* (years)	Design Life (years)	End of Mission
MAVEN	11/18/2013	7.79	3	Active
HAYABUSA 2	12/3/2014	6.75	6	Active
EXOMARS 1 - TRACE GAS ORBITER	3/14/2016	5.47	6	Active
OSIRIS-REX/SAMPLE RETURN	9/8/2016	4.98	7	Active
MARS INSIGHT	5/5/2018	3.33	1.99	Active
PARKER SOLAR PROBE	8/12/2018	3.06	7	Active
BEPICOLOMBO - MMO (MIO - JAXA)	10/20/2018	2.87	8	Active
BEPICOLOMBO - MPO (ESA)	10/20/2018	2.87	8	Active
BEPICOLOMBO - MTM (ESA)	10/20/2018	2.87	8	Active

*Duration for active spacecraft is calculated on 1 September 2021

F.2.4.1 Probability of Success of Interplanetary Missions

There are several metrics by which to show estimated reliability. One of the most straightforward is the ratio of the number of successful missions to the number of total missions. Mission success can also be visualized by using a cumulative probability plot (Figure F-7), which shows this ratio over time for the list of interplanetary spacecraft. In this case, mission success was defined as a spacecraft meeting or exceeding its design life.

Excluding launch vehicle failures, the historical record for successful missions is 0.94, where failures of several specific spacecraft launched during the 1990s and early 2000s account for decreases in overall probability of success for interplanetary missions. Loss of contact with Mars Observer likely resulted from a fuel line rupture before a planned entry into Mars orbit, while the

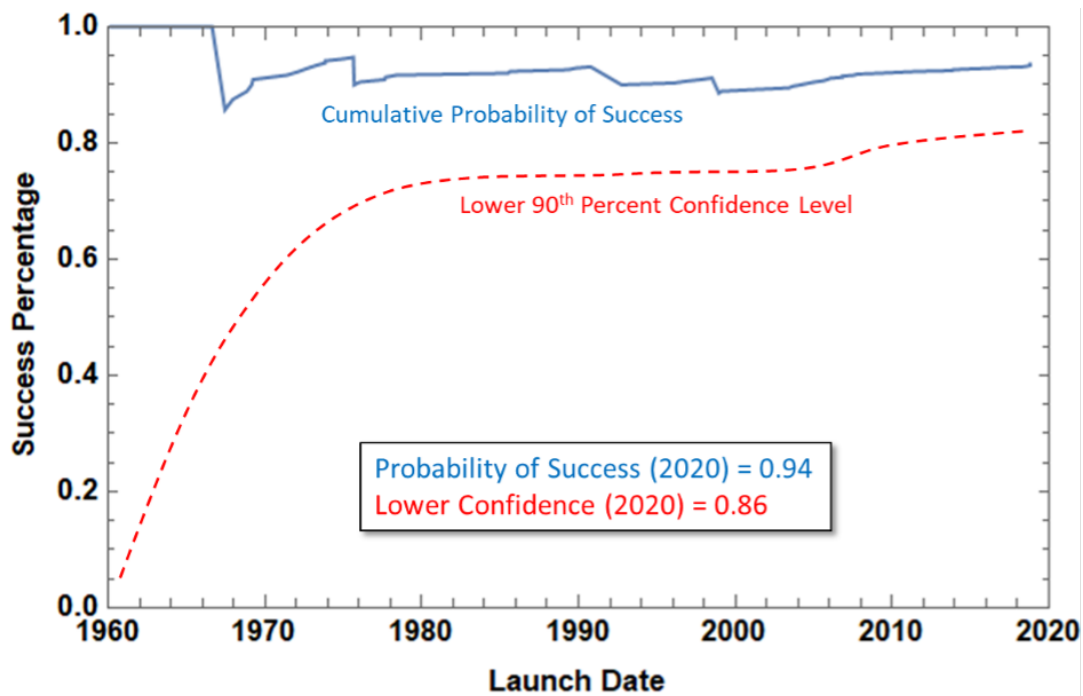


Figure F-7. Probability of success for interplanetary missions as measured against design life is high (Edwards et al., 2021). (Image credit: Johns Hopkins Applied Physics Laboratory.)

Mars Climate Orbiter failed because of a unit discrepancy in commands sent to the spacecraft. Nozomi, Japan’s first Mars explorer, suffered a series of failures, with a failure in the main thruster finally ending the mission.

The fact that the probability of success metric is so high is a testament to the organizations that built these (usually) flagship missions. The attention to detail in analysis, part selection, testing, and operations is typically far higher than for other missions.

F.2.4.2 *Reasons Long Missions End*

Analysis of interplanetary missions included an examination of spacecraft retirement, a process that started with the compilation of readily available launch and inactive dates and soon led to a deeper literature review to unearth the root causes behind the eventual retirements. Although certainly time-consuming, the process contributed to better understanding and accurately recording the nature and causes of these retirements and served as an important prerequisite for the failure analyses presented in the following sections. The insight gained from the process is also an interesting area of study in and of itself.

Retired spacecraft data fell into the four different groups listed here, with percentages of each occurrence shown in the pie chart in Figure F-8.

1. Retired because of failure: A failure of the spacecraft or its software—or an error in commands sent from the ground—led to the end of the mission.
2. Retired without failure: Operations ceased before the spacecraft exhibited a mission-terminating failure (i.e., because of lack of funding, exhausting fuel supplies, or intentionally burning up in the atmosphere of a planet).
3. Unknown reason for retirement: A specific reason for retirement could not be determined (provided in the sources used).
4. Active: At the time of data collection, the spacecraft was still operating.

A further breakdown of the data reveals additional details for each spacecraft that were used to break down the first two groups into subcategories (see the bar chart in Figure F-8). Note that the colors in the bar chart match the category of retirements from the pie chart. For retirement resulting from spacecraft failure, the culprit subsystem was noted. Non-failure retirements were described as a result of the following:

1. Depletion of fuel
2. Depletion of power
3. Intentional termination of operations
4. Intentional impact/burn-up

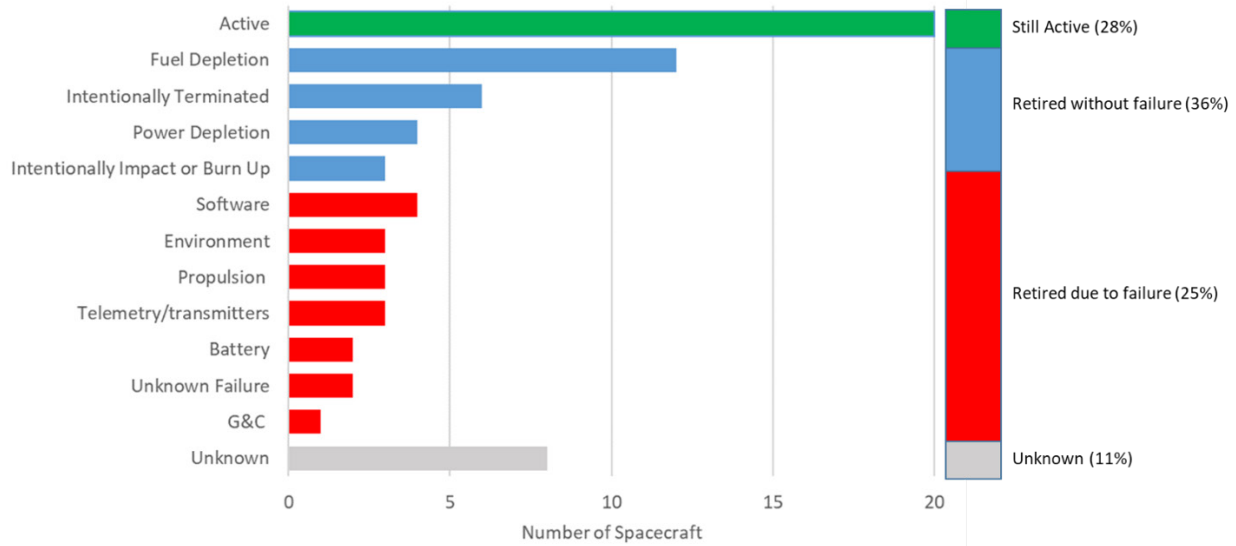


Figure F-8. Majority of interplanetary spacecraft retire without failure (Edwards et al., 2021). (Image credit: Johns Hopkins Applied Physics Laboratory.)

The data do not point conclusively to any one particular subsystem driving the technical failures of interplanetary spacecraft; however, it is interesting to note the appearance of failures related to the propulsion; telemetry, tracking, and command (Rodríguez-Pacheco et al., 2020); battery; and guidance and control (G&C) subsystems. In his research analyzing failures of Earth-orbiting satellites successfully launched between 1990 and 2008, Saleh found the top three subsystems responsible for mission-ending failures to be the TTC, G&C, and thruster subsystems, quickly followed by battery failures (Saleh, 2011). A deeper analysis of the historical reliability of these subsystems and others remains necessary to gain a better understanding of how individual subsystems drive the overall reliability of long-lived interplanetary spacecraft.

The causes of spacecraft retirement listed also demonstrate that technical failures are often not the reason for a spacecraft’s retirement; rather, many spacecraft operate nominally until either a resource is depleted or institutional support for the mission wanes. This suggests that historical spacecraft operational lifetimes frequently reflect intentional mission design decisions rather than poor reliability or limits in engineering capability.

F.2.4.3 Mission time versus Design Life

Another tool used to examine reliability is a visual comparison of operational lifetimes for interplanetary spacecraft in relation to their design lives, and it draws inspiration from a similar satellite design life study carried out by Fox et al. (2013). Figure F-9 plots design life versus actual operational life for each spacecraft, where operational life begins on the date of launch. Different markers indicate whether a spacecraft retired because of failure, retired without failure, or remains active. Markers above the dashed line in the green area represent spacecraft that have achieved their intended design life, while those below have yet do so or failed before doing so. Table F-3 gives an additional numerical summary of these data.

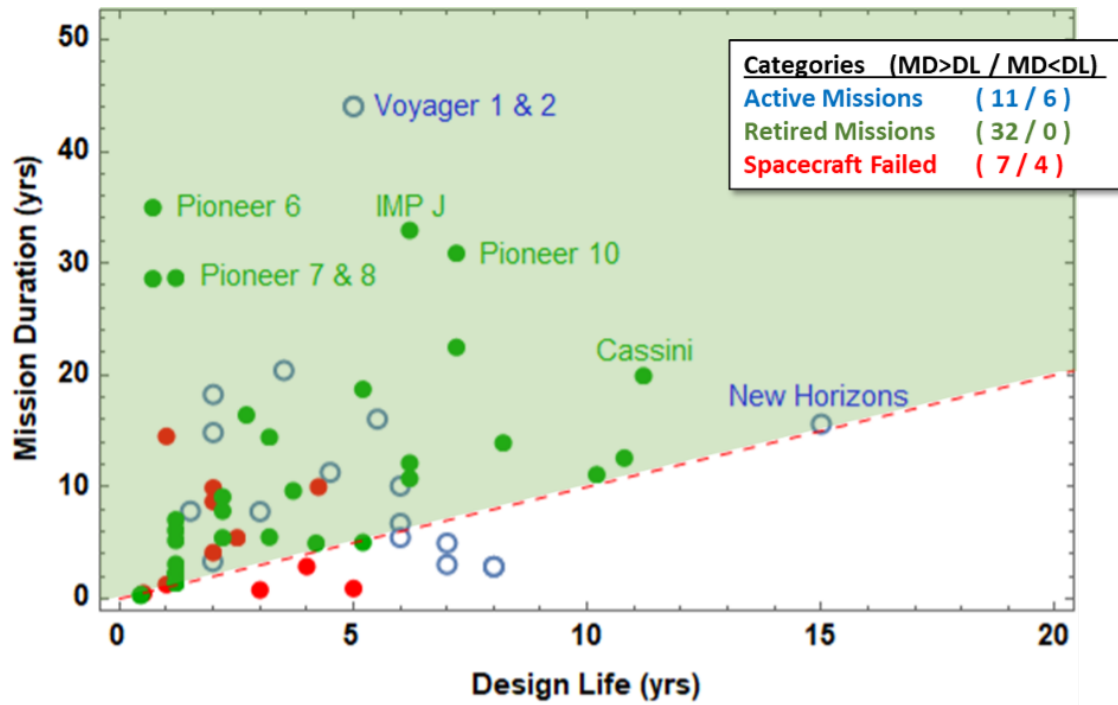


Figure F-9. Design life versus actual life illustrates the margin that an interplanetary spacecraft possesses (Edwards et al., 2021). DL, design life; MD, mission duration. (Image credit: Johns Hopkins Applied Physics Laboratory.)

Regression analysis of design life versus actual life suggests that design life is not a predictor of actual life for this group of spacecraft.

This design life versus actual life analysis depicts a group of spacecraft that have largely succeeded in outliving their design lives. In fact, the average spacecraft in this group lived to seven times its design life, indicating that the maximum achievable lifetime of a spacecraft is not typically reflected in its stated life expectation. This leads to questions about what factors beyond technical capability historically drive or limit the definition of a spacecraft’s design life. Per Saleh et al., considerations of mass and cost are some of the major factors limiting design life, even though much longer actual lifetimes are technologically achievable (Saleh et al., 2006).

Table F-3. Weibull parameters using Bayesian updating.

	Mean	Lower 5th	Upper 95th
Shape (β)	0.8049	0.5768	1.066
Scale (η)	64.11	32.12	126.1

F.2.4.4 Lifetime Assessment

The reliability analysis used a combination of parametric and nonparametric methods, the results of which serve to determine failure trends for historical interplanetary spacecraft and enable the calculation of a mean time to failure (MTTF) and its associated uncertainty.

The data input into the reliability analysis are similar to those used to construct the design life versus actual life graph. Operational lifetime was considered to begin at the time of launch and end at the time of retirement—or, in the case of active spacecraft, the time of data collected. Knowledge of the reason for spacecraft retirement was used to censor the data; lifetimes

associated with spacecraft that retired before experiencing a failure or that are still active were considered right-censored data points.

F.2.4.4.1 Nonparametric Analysis

A nonparametric analysis was performed using the Kaplan–Meier estimator, a method well suited for handling right-censored data (Saleh, 2011). It should be noted that the increased dispersion of the 95% pointwise confidence regions with increasing time is a result of the large number of right-censored data points. The trends of this analysis are analyzed jointly with the following parametric analysis.

F.2.4.4.2 Parametric Analysis

To more conclusively see failure trends, a maximum likelihood estimation (Bennett et al., 2006) method with right censoring was used to fit a Weibull distribution to the data. The shape and scale parameters describing this distribution were found to be $\beta = 0.84$ and $\eta = 48.6$. A shape parameter β less than 1 indicates a slight infant mortality trend in the data and, therefore, a failure rate that decreases over time, which agrees with trends found by Saleh & Castet (2011) and Fox et al. (2013). Using this Weibull distribution, the MTTF was calculated to be 53 years. The resultant lifetime distribution is shown in Figure F-10.

Bayesian methods accounting for the right censoring of non-failed spacecraft were also used to capture uncertainty in the Weibull parameters. Prior distributions for both the shape and scale parameters were non-informative and were updated using failure data from the culled interplanetary spacecraft list. The mean of the resulting distributions for β and η as well as a 90% confidence interval are summarized in Table F-4.

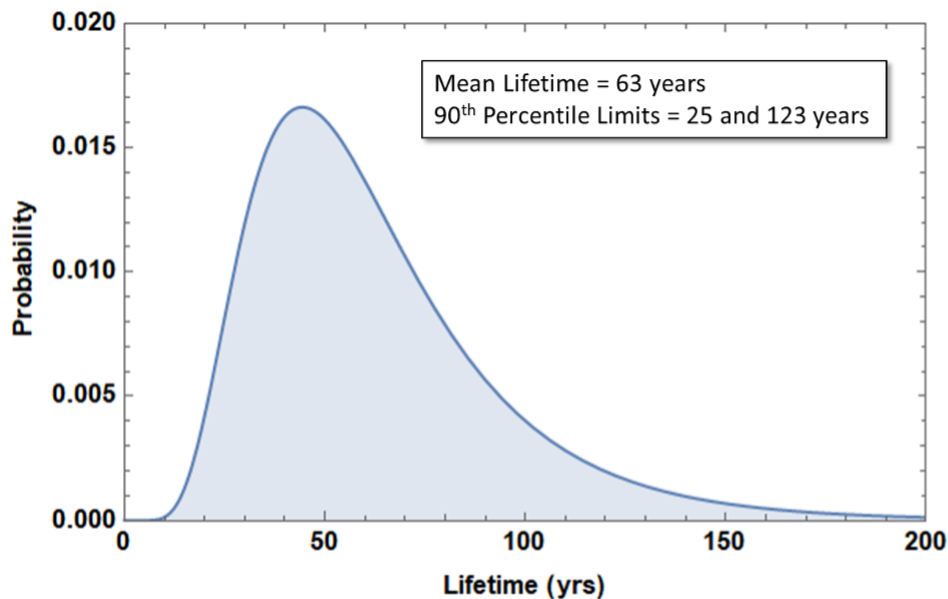


Figure F-10. Lifetime distribution indicates a high confidence of an interplanetary spacecraft lasting for longer than 50 years.

Table F-4. Studies showing that the hazard rate of electronics is dominated only by wearout mechanisms.

Authors	Electronic Components Studied	Value of Weibull Shape Parameter
Romero et al. (2020)	Tantalum electrolytic capacitors	>1.6
Meng et al. (2016)	Microelectromechanical systems	1.9
Srinivas et al. (2010)	Solder joints of package on package assemblies	>2.8
Valentin et al. (2003)	Solder joints between package leads and printed wiring boards	4.4
Yizhou Lu & Christou (2017)	Transistor modules	5.6
Osterman & Pecht (2007)	Printed circuit boards	>4
Qi et al. (2009)	Solder joints of printed circuit board assemblies	2.6
Hwang et al. (2011)	Capacitors	2.9–17.4
Jóźwiak (1992)	Microcomputer system	4.9
Chan et al. (2011)	White-light-emitting diode	>12
Muñoz-Gorritz et al. (2020)	Metal-insulator-semiconductor capacitor	>4
Bossuyt et al. (2011)	Stretchable electronic substrates	>2.8
Choi et al. (2020)	Insulated-gate bipolar transistor (IGBT) power module	6.6
F. Liu et al. (2015)	Ball grid array packages	>1.9
Nogueira et al. (2016)	Blue-light-emitting diode	>4.8
Putala et al. (2011)	Ceramic antenna assemblies	>5.5
Ferrara et al. (2012)	Power amplifier module	>2
Le Coq et al. (2010)	Wafer-level chip scale packages	>3.4
Schilling et al. (2016)	Power diodes	>1.2
Rajaguru et al. (2015)	Power electronic module	>38
X. Li et al. (2008)	n-MOSFETs	10.6
Xu et al. (2019)	Gold-plated electrical interconnects	>20

The parameter results found using Bayesian updating differ slightly from those determined using the MLE method; however, the MLE-derived values fall well within the 90% confidence interval given for the Bayesian model. This wide confidence interval is largely a result of the number of right-censored data points input into the model, as most spacecraft either are still active or retired before failure.

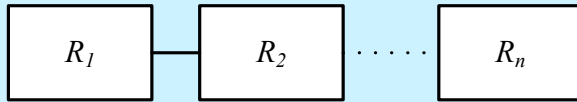
F.2.5 Reliability Engineering

Reliability is a broad term that focuses on the ability of a system to perform its intended function. NASA defines reliability as “the probability that an item will perform its intended function for a specified interval under stated conditions” [NASA-STD-8729.1]. This section will give a brief introduction to the reliability engineering methods used in the Interstellar Probe analyses.

What is often found in reliability assessments of systems are qualitative analysis (e.g., failure mode and effects analysis [FMEA]) and quantitative analyses (e.g., fault trees or reliability block diagrams [RBDs]). An FMEA has not been performed as part of the Interstellar Probe study and will not be covered. An RBD was used to generate the predictions for the baseline Interstellar Probe mission. An RBD is an inductive model wherein a system is divided into blocks that represent distinct

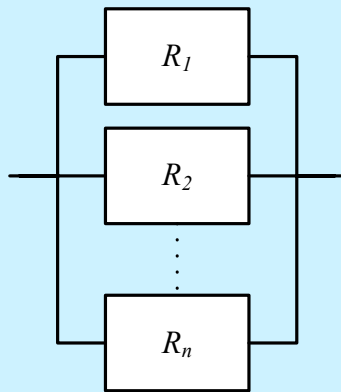
Reliability Block Diagram

Series



$$R_{sys} = \prod_{i=1}^n R_i$$

Parallel



Identical Components

$$R_{sys} = \prod_{i=1}^n R_i = 1 - \prod_{i=1}^n (1 - R_i)$$

Nonidentical Components

$$R_{sys} = \sum_{i=0}^{n-1} \binom{n}{i} R^i (1 - R)^{n-i}$$

elements such as components or subsystems. These elemental blocks are then combined according to system-success pathways. RBDs are generally used to represent active elements in a system, in a manner that allows an exhaustive search for and identification of all pathways for success. Dependencies among elements can be explicitly addressed. The mission-level RBD was successively decomposed down to boards and commercial off-the-shelf (COTS) items. Each block is quantified as probability of success or reliability. The RBD logic structure is used with the following equations to determine the reliability of the system.

Reliability for components is traditionally expressed as an exponential distribution. This assumes a constant failure rate (λ) over the life of the mission and is expressed as:

$$R(t) = e^{-\lambda t}.$$

As discussed in Section F.2.2, this is not a valid assumption for spacecraft systems. The following section details more explicitly why the constant failure rate model should not be used.

F.2.5.1 Invalidity of Constant Failure Rate Models

Reliability prediction had its start in the 1950s with the development of a handbook to estimate in-service failure rates of electronic equipment. MIL-HDBK-217A was published in 1965, and subsequent revisions led to MIL-HDBK-217F in 1991.

In the mid-1990s, CALCE at the University of Maryland conducted a research project to develop alternatives to reliability prediction handbooks. Today, CALCE serves the electronics industry as a

resource and knowledge base for the development of reliable, safe, and cost-effective products. Supported by over 300 of the world’s leading companies, CALCE conducts fundamental reliability science research in the areas of failure mechanism identification and modeling, accelerated test methods, prognostics and health management approaches, and supply-chain management techniques, as well as the application of AI for remaining life and fault prediction of electronic devices and assemblies. In addition to its active research, CALCE provides test and failure analysis services. CALCE also provides continuing education opportunities to practicing engineers through their open website, monthly webinars, industry symposia, and professional development courses.

The bathtub model (Figure F-11) predicts that electronics will have a period in which the hazard rate is constant, and this will occur after an infant mortality period and before a wearout period. This prediction of the hazard rate (referred to as failure rate in the figure) is based on the assumption that the only failures during this period are random and that there is no wearout, two assumptions that are rarely true for electronics.

When discussing the hazard rate, it will often be described using the shape parameter of a Weibull distribution.

F.2.5.1.1 *Invalidity of the Constant Failure Rate in the Useful (Normal) Life Period*

Wong (1991) gave a historical perspective to the hazard rate for electronics, noting that “in the 1950s many people, after observing available data, which as we know now was erroneous, concluded that the failure rates of electronics are constant during the equipments’ useful life times. Now we know that the data was tainted by equipment accidents, repair blunders, inadequate failure reporting, reporting of mixed age equipment, defective records of equipment operating times, mixed operational environmental conditions, complete neglect of thermal cycling data and many additional undesirable factors.” He also stated that the influence of so many incidental factors led the data to appear random and effectively led to the erroneous observation

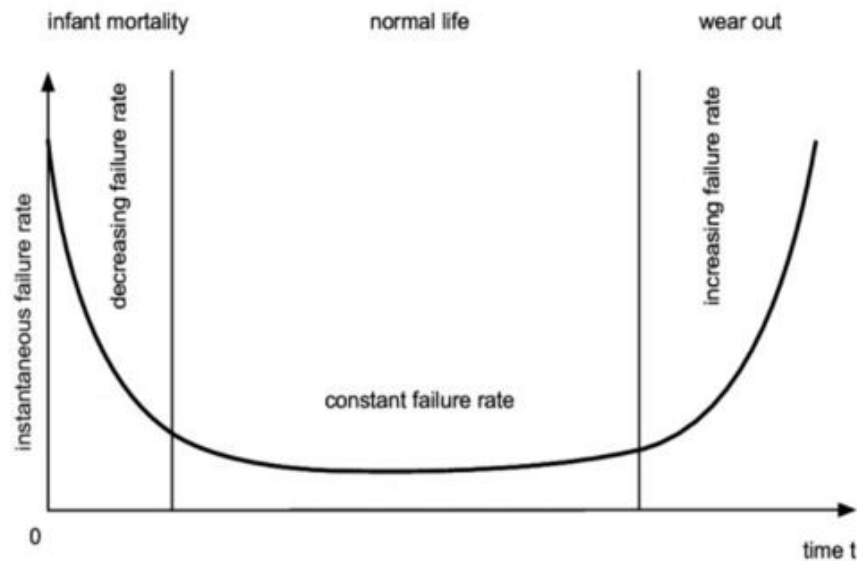


Figure F-11. An example of a failure rate bathtub curve for a given product. (Reprinted from Lu et al. (2016) with permission; © 2016 Springer Nature Limited.)

Weibull Distribution

Life-data analysis (also called “Weibull analysis”) is used to make predictions about life by fitting a statistical distribution to life data from a representative sample of units. “Life data” refers to measurements of product life. The parameterized distribution for the data set can then be used to estimate reliability or probability of failure at a specific time, the mean life, and the failure rate.

The Weibull distribution is a continuous function used by reliability engineers to model time to failure data. It is a versatile and powerful tool that can model time-dependent failure rates. The probability density function (PDF) is a mathematical function that describes the distribution of the number of cycles to failure, while the cumulative density function (CDF) provides the probability of reaching a specified time to failure. For the Weibull distribution, the PDF, $f(t)$, and the CDF, $F(t)$, are:

$$f(t) = \frac{\beta}{\eta} \left(\frac{t}{\eta}\right)^{\beta-1} e^{-(t/\eta)^\beta} \quad \text{Equation 1}$$

$$F(t) = 1 - e^{-(t/\eta)^\beta} \quad \text{Equation 2}$$

where: t is the time to failure
 β is the Weibull shape parameter
 η is the Weibull scale parameter

Parameters (η and β) control the scale and shape of the *pdf* function. The scale parameter (η) defines where the bulk of the distribution lies, while the shape parameter (β) defines the shape of the distribution. Furthermore, β defines the behavior of the failure model by indicating whether the failure rate changes with time:

- $\beta = 1$, indicates constant failure rate (exponential model)
- $\beta > 1$, indicates an increasing failure rate over time
- $\beta < 1$, indicates a decreasing failure rate over time

Typically, to fit a statistical model to a life data set, the analyst estimates the parameters of the distribution that will make the function most closely fit the data using a process known as the maximum likelihood estimation (Bennett et al.) method. The limitation of MLE is that it will not produce an estimate of the uncertainty around the probability of failure. For this, Bayesian analysis techniques are combined with the Weibull data analysis.

of a constant failure rate. Further, McLeish (2010) states that overstress failures are rare and random, and if these occur frequently, it means that the device is not suitable for the application.

Yang et al. (2013), using field data of machining centers, showed the shape parameter to be 1.17 for the electrical system, 1.77 for the computer numerical control machine system, and 2 for the servo system (implying that their hazard rates were increasing throughout the life). The studies by Waghmode & Patil (2016), Patil et al. (2018), Keller et al. (1982), and Dai et al. (2003) on computerized numerical control machine tools show that the hazard rates of their electronic components are not constant.

The literature shows that some proponents ("FIDES Guide 2009 Edition A (English)," 2010; Morris, 2011; Shah & Elerath, 2005) of the constant hazard rate assumption believe that although most individual mechanisms may not be represented by a constant hazard rate, their superposition leads to an apparent constant hazard rate for the system. However, the resultant of the superposition of hazard rates is dependent on the distribution of dominant failure mechanisms over time. For example, Shah & Elerath (2005), based on their study of disk drives, concluded that the resultant hazard rate is dependent on which failure mechanism is dominant at what time.

The distribution of failure mechanisms is dependent on the distribution of the usage and environmental stresses acting on a system. This distribution causes the hazard rate to vary over time. For example, the National Research Council's report, *Reliability Growth: Enhancing Defense System Reliability* (NRC, 2020), states that a device degrades in multiple ways, and its lifetime is thus a function of different failure mechanisms and modes. The report infers that the failure rate of a product varies throughout its life and cannot be represented by a constant failure rate model.

For a system composed of electronic components, the bathtub model is often inappropriate. Mortin et al. (1995) modeled the hazard rate for a system having three identical electronic devices using the constant hazard rate assumption and a distribution representing the actual failure mechanism. Their study demonstrated that as the number of components increases, the difference between the instantaneous hazard rate calculated using the constant failure rate distribution and actual hazard rate distribution also increases. Yuan et al. (2018) observed that the fault data of an aero-engine, a complex electromechanical system, has a Weibull shape parameter greater than 1 (showing that the system's failure rate is increasing, not constant). Pascale et al. (2018) showed that electronic railway signaling systems do not have a constant hazard rate. Verma et al. (2018) observed failures in the electromechanical system of an automated hematology analyzer (used in medical laboratories) and found the system to have an increasing failure rate throughout its lifetime. Similarly, Rastayesh et al. (2019) predicted the reliability of a power stage of wind-fuel cell hybrid energy systems assuming Weibull and exponential distributions. They found that the Weibull distribution (with increasing hazard rate) predicted the reliability more accurately.

Similarly, Chiodo & Lauria (2015) stated that the hazard rate of a redundant system is a function of time and can never be constant. They proved that even for a system consisting of components with constant hazard rates, the resultant hazard rate of the system varies with time. That is, for a parallel system with two independent components, the reliability $R(t)$ is given by:

$$R(t) = R_1(t) + R_2(t) - R_1(t)R_2(t). \quad (3)$$

For two components, both having a constant failure rate λ ,

$$R(t) = 2R_1(t) - R_1^2(t) = 2e^{-\lambda t} - e^{-2\lambda t}. \quad (4)$$

It is observed that the two exponential functions of Equation 4 cannot be combined to express as a single exponential function. Thus, the hazard rate of the system will not be constant over time, as opposed to the useful life period of the bathtub model.

F.2.5.1.1 *Invalidity of the Constant Failure Rate during Wearout*

The mechanisms causing failures in electronics are predominantly of a wearout nature (Ebeling, 2004; Sangwine, 2018). These failure mechanisms start as soon as the product is put into operation (Harms, 2010) and not after a period of random failures, as implied by the bathtub model. Dasgupta et al. (1990) state that most failures in electronics are caused by mechanical failure mechanisms such as fatigue, corrosion, and fracture. Because these mechanisms are primarily wearout mechanisms, they cannot be represented by constant failure rates.

Modern electronics are observed to undergo wearout failures earlier in life as opposed to the belief that the wearout takes place only after the end of use. Harms (2010) stated, “the commercial industry has been driven largely by consumer electronics to produce parts that no longer compare to the parts produced prior to 1995. The parts being used currently have a shorter service life, often in the three to five year time frame. This essentially pulls in the right hand of the bathtub curve to the point where it is now necessary to pay attention to wearout as part of the reliability prediction process.”

One of the reasons for the early wearout of the electronics is the reduction in the feature size of components. Customer expectations are continuously forcing electronics manufacturers to reduce the size of the components and products with enhanced processing capacity. Blome et al. (2006) explained, “as CMOS [complementary metal–oxide semiconductor] feature size scales to smaller dimensions, voltage is expected to scale at a much slower rate, increasing on-chip power densities. Areas of high power density increase local temperatures leading to ‘hot spots’ on the die.” They further stated that because temperature and power density are the stress factors for many wearout mechanisms in electronics, such as time-dependent dielectric breakdown, hot carrier injection, EM, and negative-bias temperature instability, future technologies will encounter wearout mechanisms more commonly.

The literature and the studies conducted at the University of Maryland provide numerous examples of reliability studies on electronics where the population exhibited “only” wearout failures. In 1990, Michel Pecht (1990) showed that microelectronic packages under corrosive environments followed a Weibull distribution, with a shape factor close to 2, which corresponds to a wearout failure mechanism. Pecht and Nash (Pecht & Nash, 1994), in their case study conducted on light-emitting diode (LED) lasers, observed that the devices exhibited a gradually occurring wearout failure mechanism. Similarly, Wang et al. (J.-S. Wang et al., 2012) evaluated LED packages and found only wearout failures for packages with various encapsulation materials. Mattila et al. (Mattila et al., 2012), in their study on the reliability of electronic component boards, observed only wearout failures at all testing temperatures. Mei et al. (Mei et al., 2018) showed that solder joints, when exposed to self-heating, led to wearout failures with a shape factor above 1, indicating wearout.

Similarly, Al Athamneh et al. (2020) performed reliability modeling of aged SAC305 solder joints and found the hazard rate to have shape parameters of >2 . Liu et al. (Y. Liu et al., 2014) showed that the interconnects undergo wearout when subjected to vibrations, at both fixed and random frequencies. Virkki & Tuukkanen (2010) studied tantalum capacitors under various temperature ranges and observed only increasing failure rates. Hoffmann et al. (2020) showed that insulated-gate bipolar transistors (IGBTs) failed by wearout when exposed to combined thermomechanical

and electrochemical stresses. White et al. (2011) found that the main failure distribution in dynamic random access memory has an increasing hazard rate. Quintero et al. (2008) conducted reliability and life studies on semiconductor die-substrate assemblies of different sizes under different temperatures. They observed that the Weibull shape parameter was always >1 , showing an increasing hazard rate existed rather than a constant hazard rate. Table F-4 provides additional case studies of electronics where the Weibull distribution was used to fit the data and the observed shape parameter values were >1 , indicating that only wearout was observed.

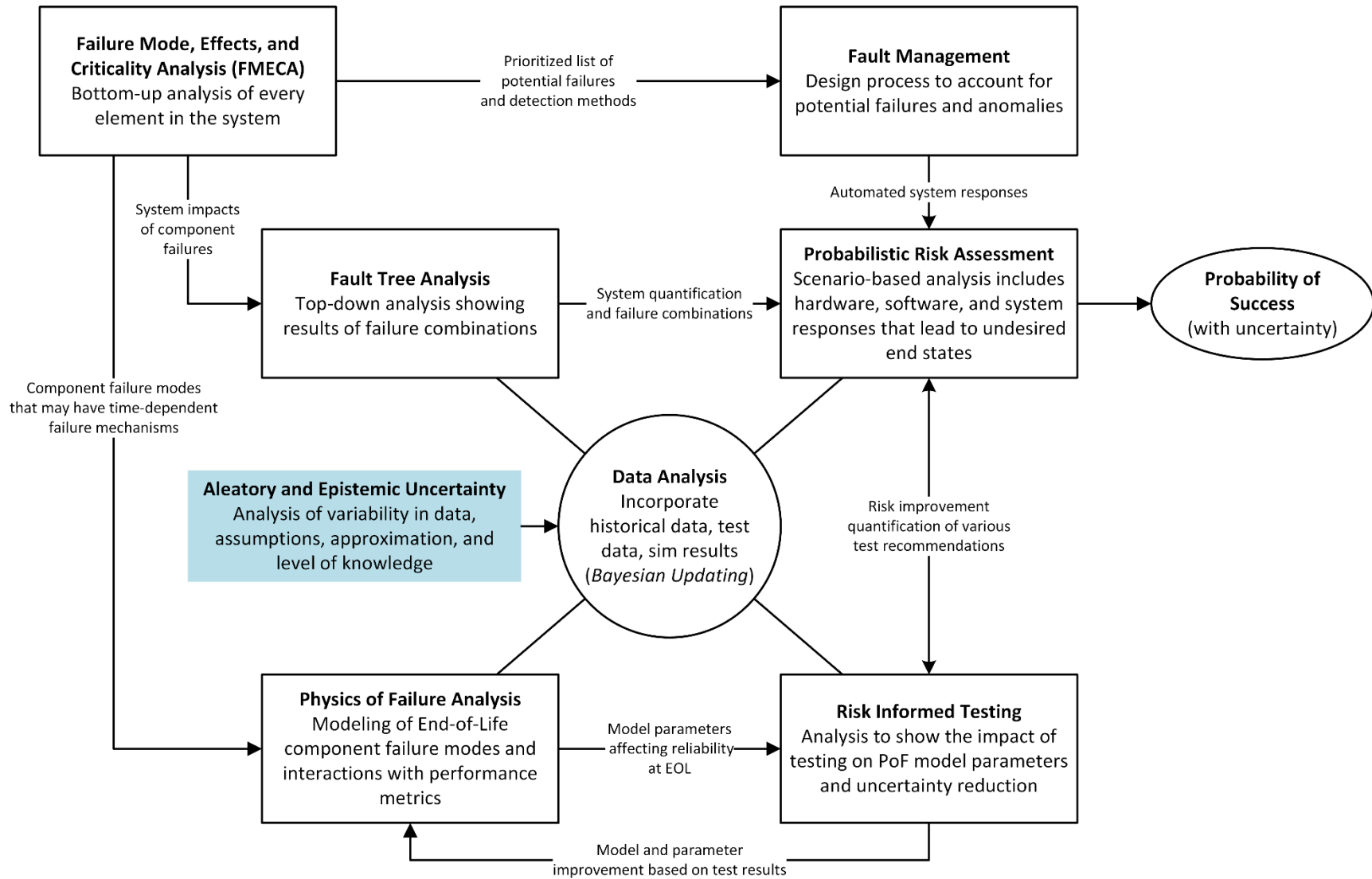
F.2.5.2 Reliability Framework for Interstellar Probe

A reliability program for a 50-year mission must augment the typical reliability engineering products. Special attention must be given to failure mechanisms in order to develop an understanding of how devices and materials can fail in the presence of various radiation and thermal environments and characterize the physics of degradation processes out to 50 years. This likely means adding design tests to discover behavior of systems, subsystems, components, and materials at end of life (EOL), including tests to characterize lifetime uncertainties and employ various acceleration methods to test at 50 years.

Because no interplanetary mission has yet survived for 50 years, the uncertainties will be large. In this context, the testing paradigm will need to change from a system collecting many hours showing confidence in the lifetime to a system that provides confidence in the understanding of how the system can fail at EOL. More specifically, we cannot rely on a constant failure rate model assuming homogenous populations where we divine failure rates by collecting number of hours and failures. Time to failure (TTF) will be evaluated as a function of physics model parameter distributions. Data derived from testing will update the distributions and reliability be computed as the probability of reaching the intended goal of 50 years.

PoF models must be integrated into all the typical reliability analysis as shown in Figure F-12. In this framework, the probability of mission success will be developed using a probabilistic risk assessment (Reuter et al., 2018) that will have scenarios for potential failures, inherent resilience of the system, and mitigations of autonomy and fault management systems. These scenarios will also explore overlapping instrument measurements and science requirements. The PRA, in conjunction with the PoF models, informs the testing regime for the program. Not all components can have accelerated testing applied or applied to extend 50 years. Decomposition to material parameters may force testing at that level and aggregated back up to system level by analysis.

The survival analysis accounting for the right-censored data provides an indication that a 50-year mission is in the realm of the possible. Indeed, the data, failures, and right-censored missions show that the mean of interplanetary history is the 50-year goal. Much work is needed to take this compendium of missions and create engineering solutions and associated test campaigns for systems and components to derive survival estimates with a confidence level sufficient for an interstellar mission.



With this initial assessment, an overall reliability goal is created. Using the spacecraft baseline design, reliability allocations can be derived for the various systems, instruments, and components. This allocation takes the form of Weibull parameters. With two parameters, the trade space needs to be explored for reasonableness and relation to current technology. Here the PoF approaches, with an understanding of failure modes and mechanisms, are used to model and simulate potential futures. Both aleatory and epistemic uncertainties are captured and rolled into the models. The testing to be done needs to collect data consistent with these models in order to build confidence in the spacecraft.

Feeding this framework will be an enhanced parts selection process covered in Section F.2.8.2.

F.2.6 Defining Mission Success

For space mission design teams, reliability translates into using the best parts available, testing the spacecraft and its instruments, adding redundant components, and implementing a fault management system to make the mission the most reliable within mass and power constraints. An often-overlooked piece in the reliability engineering process under the control of the teams is the “intended function.” This section examines how the Interstellar Probe team used the science requirements to define mission success criteria while allowing for functional redundancy and not overly constraining the design solution space.

As part of the science definition activities, the team mapped the Interstellar Probe’s top-level requirements to mission success criteria to ensure that a failure of any one science instrument would not translate to a failure of the entire mission. This section details this analytical process and shows how the results were folded into the reliability assessments. APL has used this process to great effect with the Parker Solar Probe mission (Smith & Kinnison, 2021).

NASA defines several criteria to evaluate missions: baseline mission requirements, threshold mission requirements, and mission success criteria. Baseline mission requirements are simply the set of objectives that the mission is designed to accomplish, and they are established early in the design cycle. It is not unusual for the baseline requirements to change as mission development progresses—as a result of risk reduction, cost overruns, or difficulties in development, for example. The threshold mission requirements are the minimum set of objectives for a mission that must be accomplished for the mission to be worth launching. Note that both baseline and threshold mission requirements are established before launch, and a mission is evaluated against these requirements as part of the launch approval process. Mission success criteria are different in that this is the set of objectives that must be completed for the mission to be declared a success, a determination that is made after launch, usually at the end of a mission. One of the goals of reliability analysis during the development process is to maximize the likelihood that a mission can meet the threshold requirements and mission success criteria, often by analyzing robustness to failure and making recommendations with regard to redundancy and the minimization of single-point failures.

F.2.6.1 Science Traceability Matrix

Here we will show highlights of the science traceability matrix (STM) to illustrate the process. For more information about the development of the STM, see Section 2. Interactions between the

science team and reliability team were an interactive process that involved creating the logical models and then testing for understanding. Ultimately, both teams arrived at the structure presented here. The process consisted of the following steps:

- Define the success criteria
- Map science requirements to instruments and functional backups
- Construct a logic model
- Evaluate the model looking for single-point failures

F.2.6.2 Fault Tree Analysis

Before proceeding further with science requirement decomposition, we introduce the logic modeling method known as fault tree analysis. The logic structure created by the requirements document is translated to a fault tree that maps science objectives and questions to the required measurements and instruments to make those measurements. The fault tree explicitly shows all the different relationships that are necessary to result in an undesirable event, loss of science. In constructing the fault tree, a thorough understanding is obtained of the logic and basic causes leading to this top event.

A fault tree is a top-down logical diagram that displays the interrelationship between an undesirable event and its causes. The approach systematically deduces and identifies the possible ways for this event to occur. The diagram is a graphical representation of Boolean expression of failure in terms of basic events. This logical (binary) model thus represents the qualitative characterization of the system logic. In this case, that logic is the definition of success for the various measurements that must be obtained. These results allow for the identification of single-point failures and potential nominations for redundancy.

Briefly, the fault tree consists of a top event (the undesirable event), basic events, and logic gates. Basic events are the lowest level of identified causes. Logic gates, such as OR or AND gates, give the logical relationship between the top event and the basic events. From a qualitative perspective, the fault tree is analyzed to identify the *minimal* cut sets. Cut sets are the set of basic events whose simultaneous occurrence ensures that the top event occurs. The modifier minimal describes the smallest set of events needed after Boolean reduction takes place on the logic. For more details, consult a reference such as *Fault Tree Handbook with Aerospace Applications* (Stamatelatos et al., 2002). Figure F-13 provides the symbology of the logic trees included in this report. Keep in mind that the fault trees show logic defined in failure space. Therefore an OR gate means any failure of an event under the gate fails the gate. Conversely, an AND gate means that failure of all events under the gate would be required to fail the gate. Also included is a *k/m* gate, which signifies that if *k* events fail, the gate fails.

F.2.6.3 Science Requirement Assessments

The *top* event of interest is loss of science as defined by the success criteria. For Interstellar Probe, the success criteria are defined as answering at least two science questions under each science

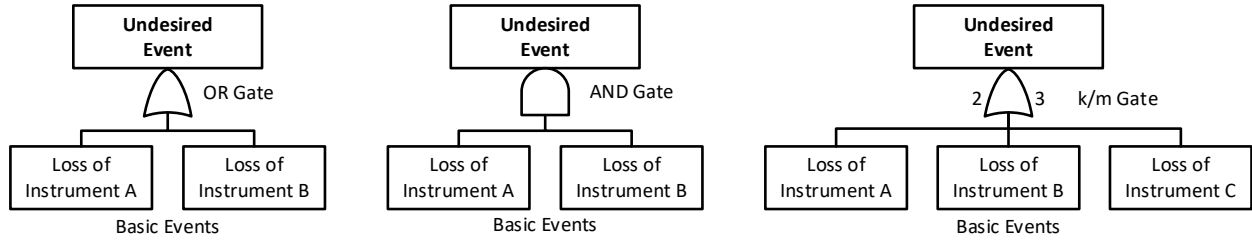
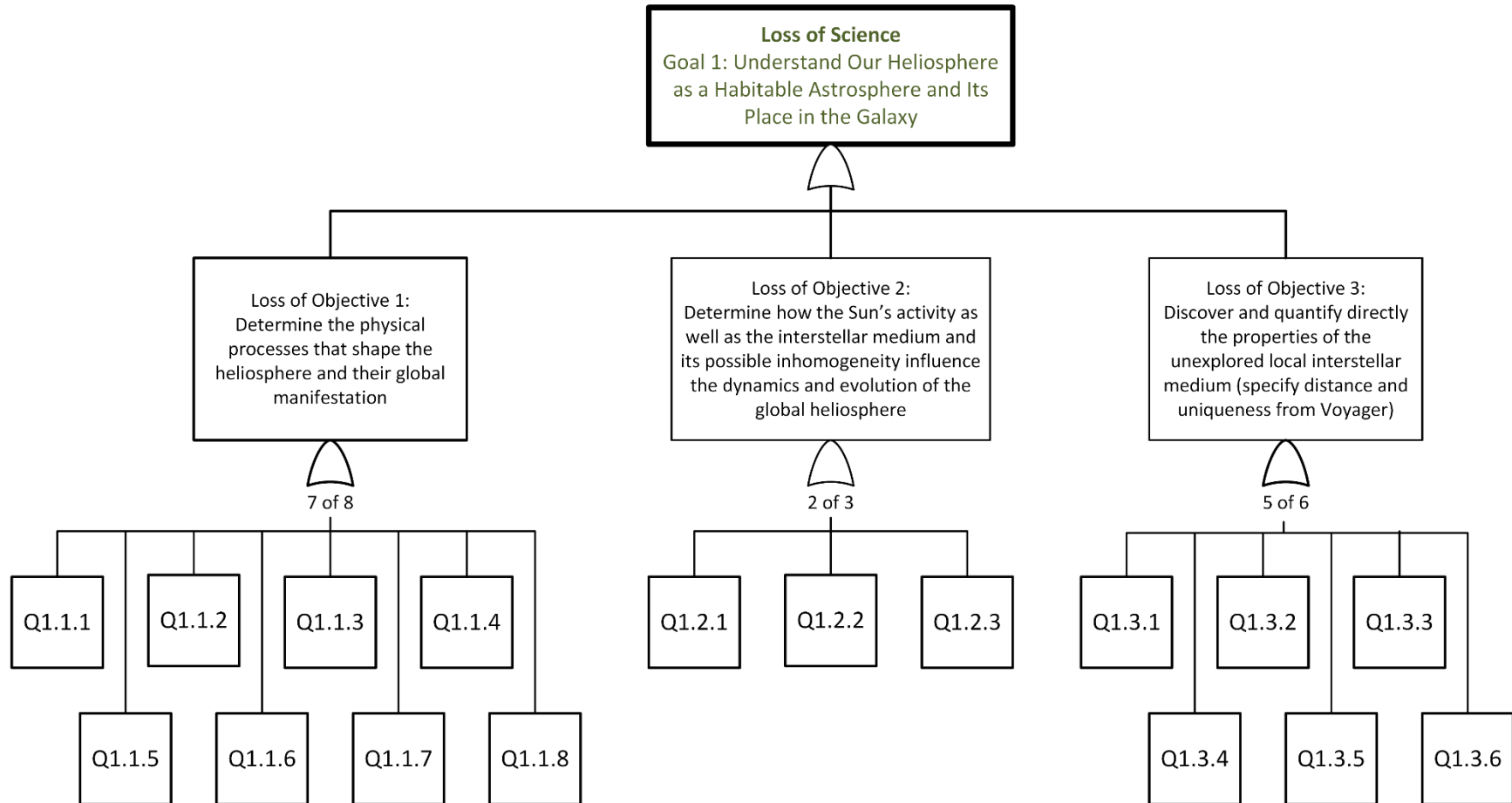


Figure F-13. Fault tree symbols.

objective and, under each chosen science question, meeting at least one Priority 1 measurement objective. This definition translates to the top of the fault tree shown in Figure F-14 where loss of science is logically decomposed to three objectives and then to questions (Q1.x.x).

7



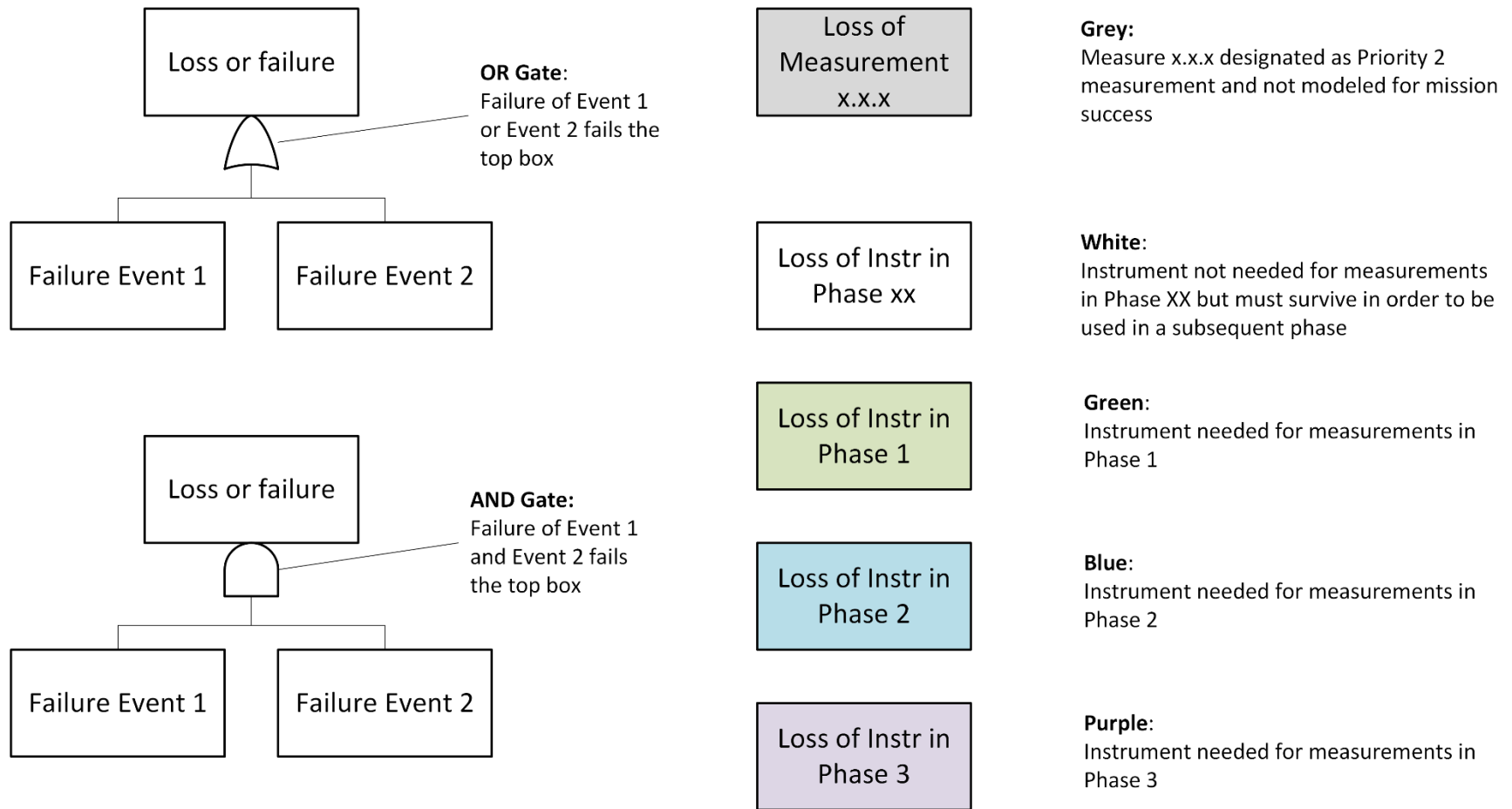


Figure F-16. Legend for fault trees. (Image credit: Johns Hopkins Applied Physics Laboratory.)

What is the size, shape, and structure of the heliosphere?

Determine the thickness and plasma flows of the heliosheath by detecting the termination shock and heliopause with in situ measurements of magnetic fields, plasma moments, energetic particles, pickup ions, and galactic cosmic rays. Image the heliosheath structure in energetic neutral atoms from an external vantage point beyond the heliopause. Estimate the heliosheath shape on outward trajectory throughout the heliosphere and heliosheath crossing by remotely detecting the 2.5-kHz radio emissions from shocks reflecting at density gradients near the heliopause. Constrain the heliosheath topology (open versus close) by measuring globally spectra of H Lyman- α emission with high resolution.

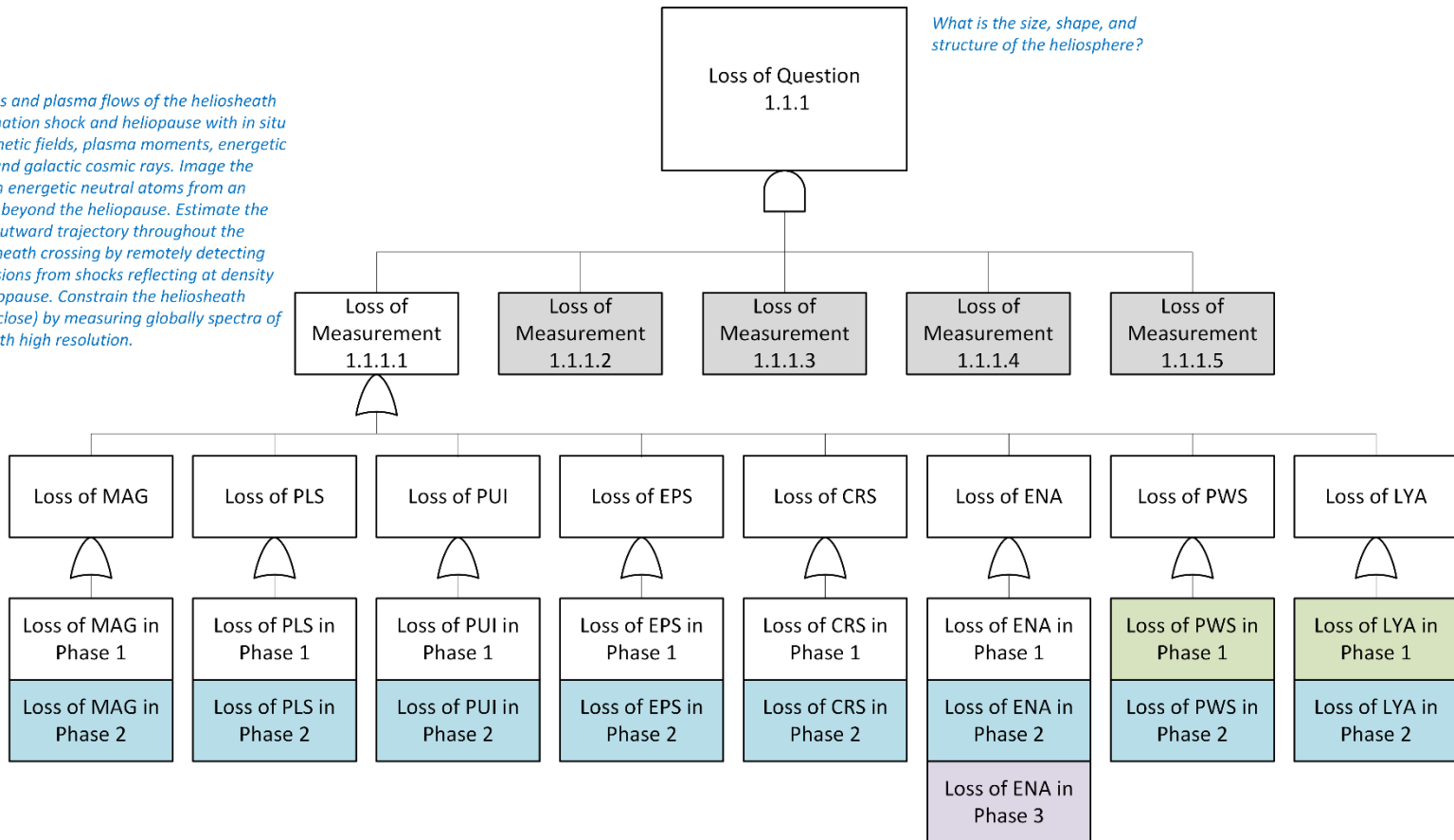


Figure F-17. STM fault tree for Question 1.1.1. (Image credit: Johns Hopkins Applied Physics Laboratory.)

Determine the energy partitioning and pressures across the termination shock, heliosheath to the heliopause by measuring the in situ particle distribution functions of thermal to suprathermal plasma, and the magnetic field. Measure in situ pickup ions to follow the evolution of major species of pickup ions from Earth to the interstellar medium. Measure the magnetic field beyond the heliopause.

What processes and particle distributions uphold the force balance of heliosheath against the local interstellar medium?

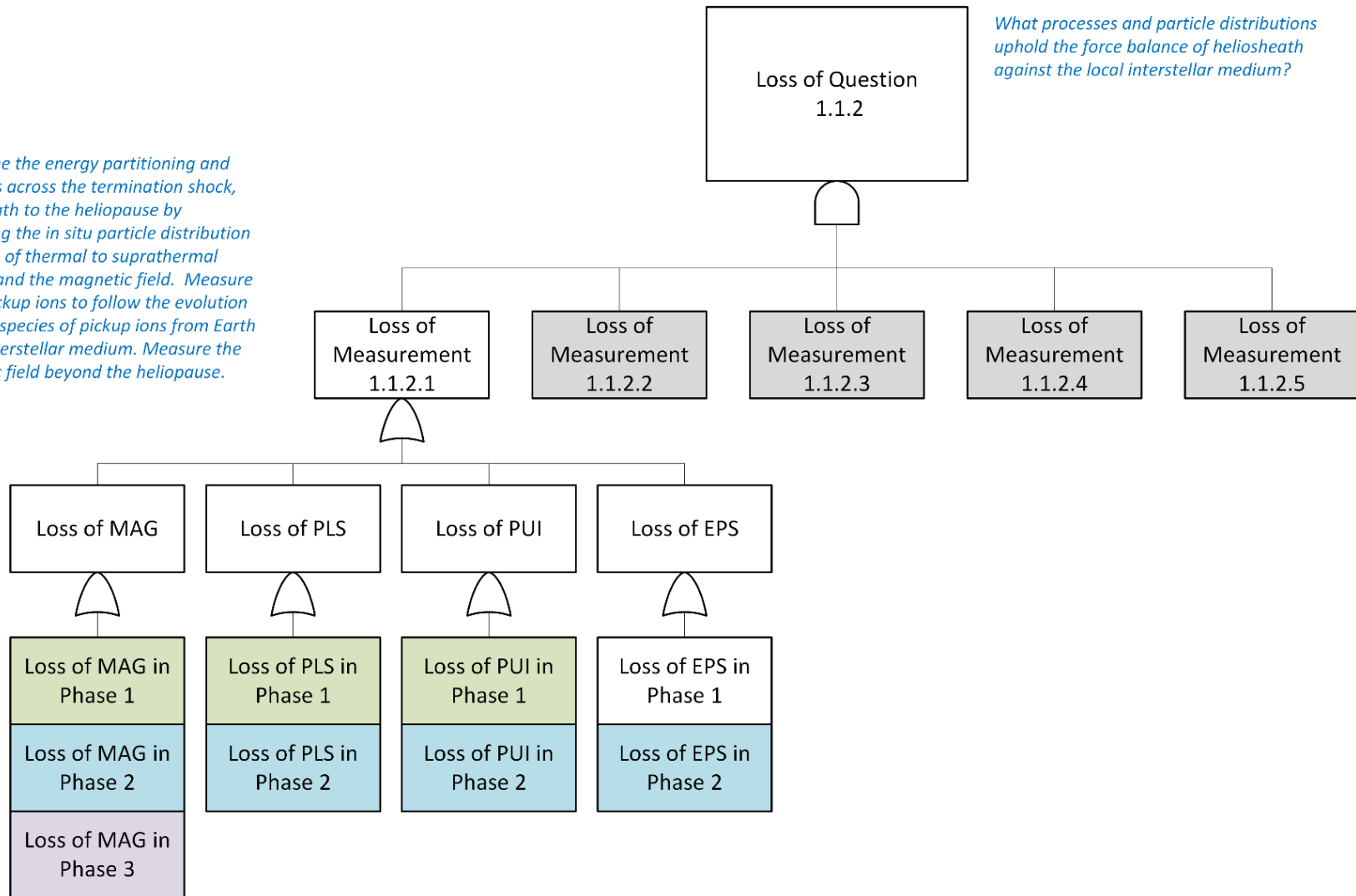


Figure F-18. STM fault tree for Question 1.1.2. (Image credit: Johns Hopkins Applied Physics Laboratory.)

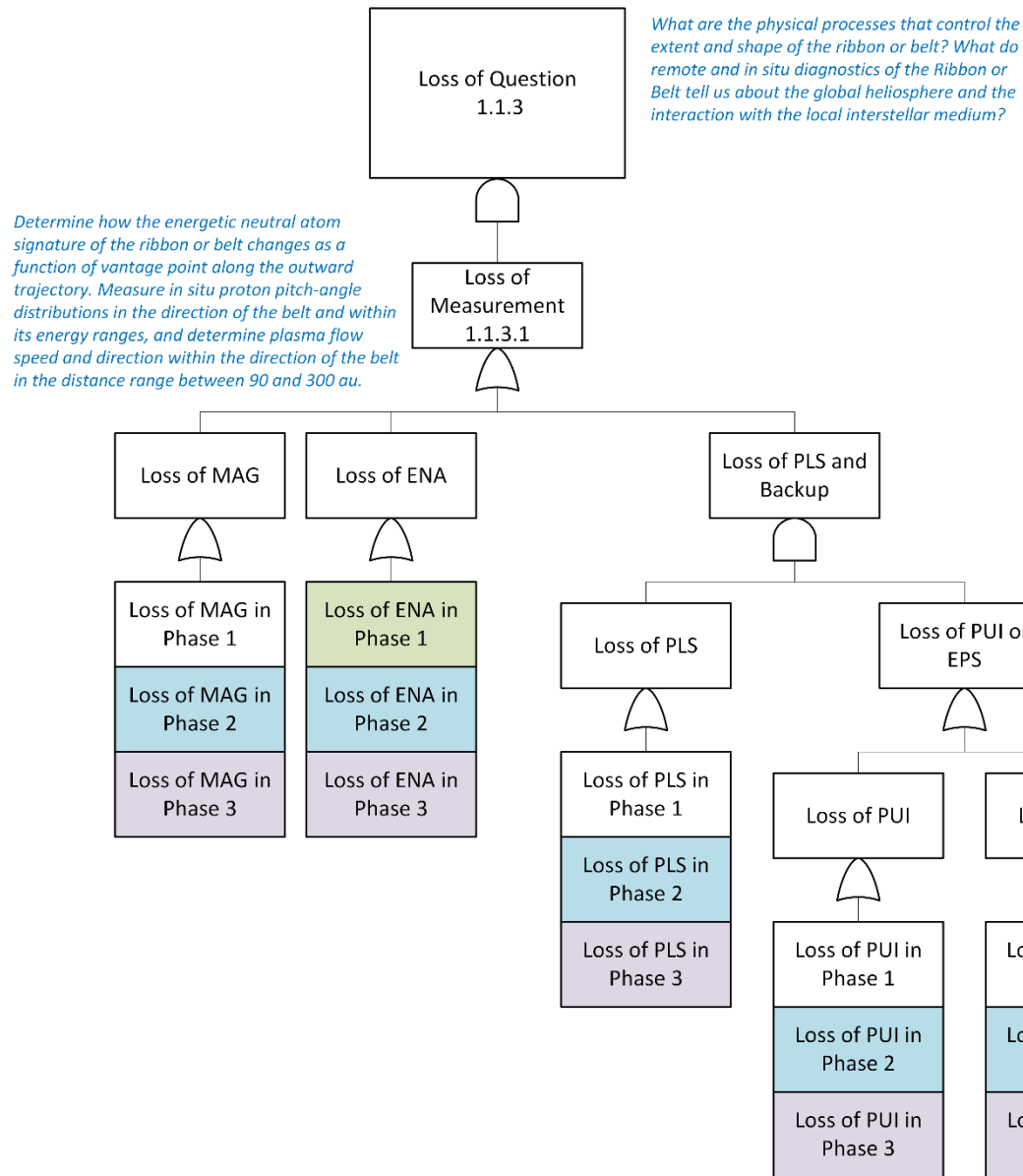


Figure F-19. STM fault tree for Question 1.1.3. (Image credit: Johns Hopkins Applied Physics Laboratory.)

Measure the 1–100 MeV/nuc ACR and 10s to 100s of keV/nuc suprathermal spectra for several ion species (including interstellar medium abundant species/isotopes) plus electrons and magnetic field (B0 plus turbulence and waves and transient structures) environments on either side of the termination shock, throughout the heliosheath, and on either side of the heliopause to determine the source distributions and test which acceleration mechanism(s) [e.g., McComas and Schwadron, GRL, 2006; Fisk and Gloeckler, ASR, 2008] may be active/dominant to generate the observed anomalous cosmic ray spectra and spatial distribution throughout the heliosheath: is anomalous cosmic ray acceleration predominantly occurring locally or remotely (e.g., near the nose, at higher heliocentric latitudes, or along the heliospheric flanks)?

What are the source(s) and dominant acceleration mechanism(s) of anomalous cosmic rays in the heliosheath?

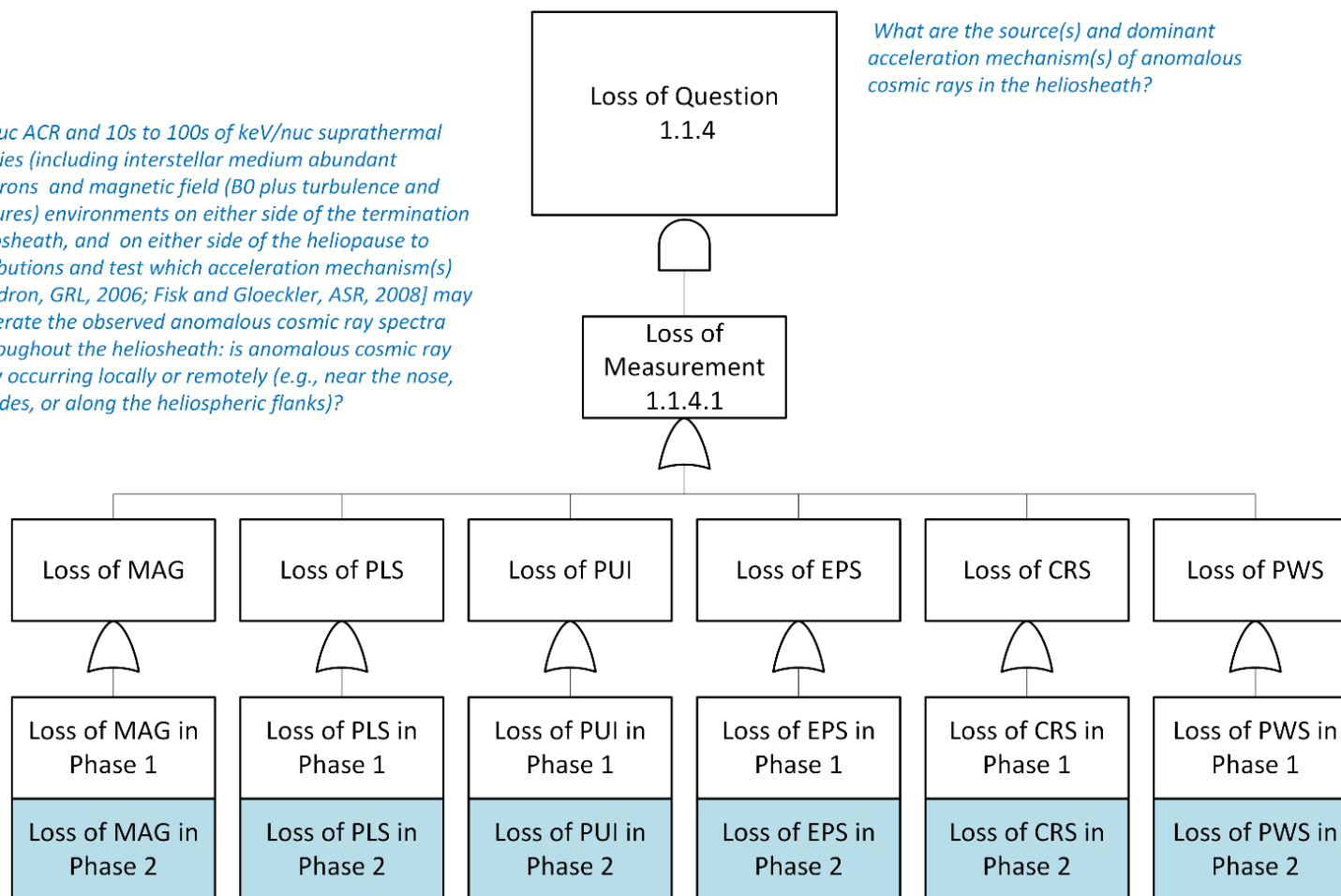


Figure F-20. STM fault tree for Question 1.1.4. (Image credit: Johns Hopkins Applied Physics Laboratory.)

Loss of Question 1.1.5

What is the energy balance at the termination shock, and how does particle acceleration occur at the termination shock, at other heliospheric or interstellar shocks, and via interactions between them?

Measure the composition, [ion charge-states?], and energy and angular spectra of thermal, suprathermal, pickup ion, and anomalous cosmic ray up to ≥ 100 MeV/nuc ions plus thermal and suprathermal electrons, and magnetic and electric fields and waves within ± 2 au of the termination shock to determine the energy balance at that boundary.

Loss of Measurement 1.1.5.1

Loss of Measurement 1.1.5.2

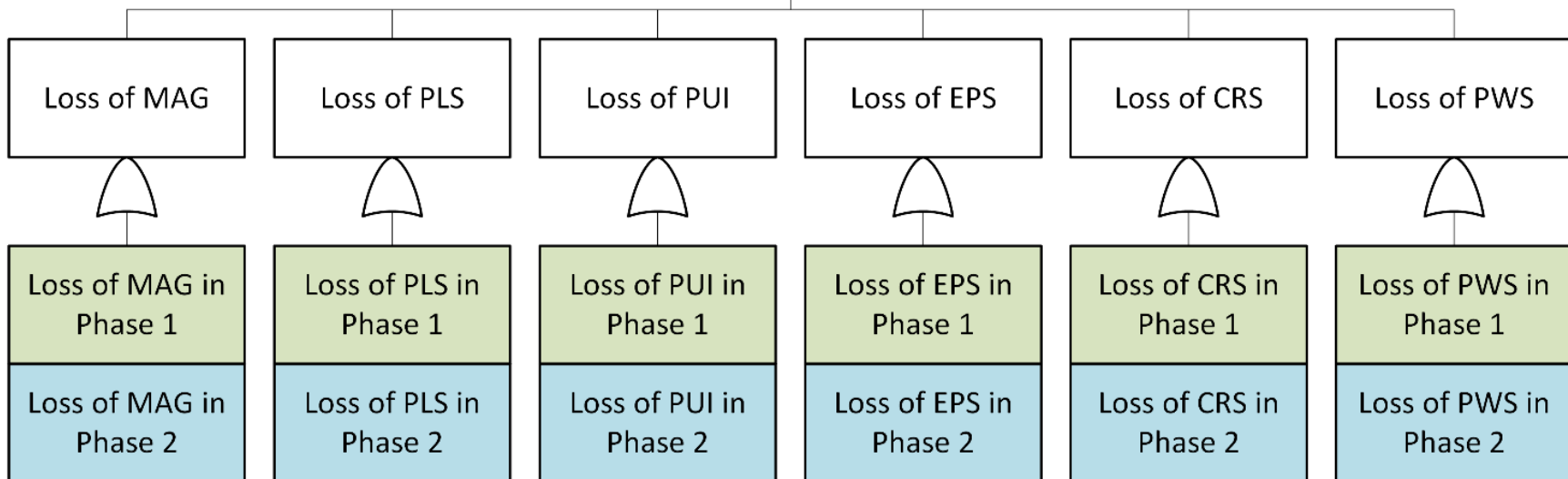


Figure F-21. STM fault tree for Question 1.1.5. (Image credit: Johns Hopkins Applied Physics Laboratory.)

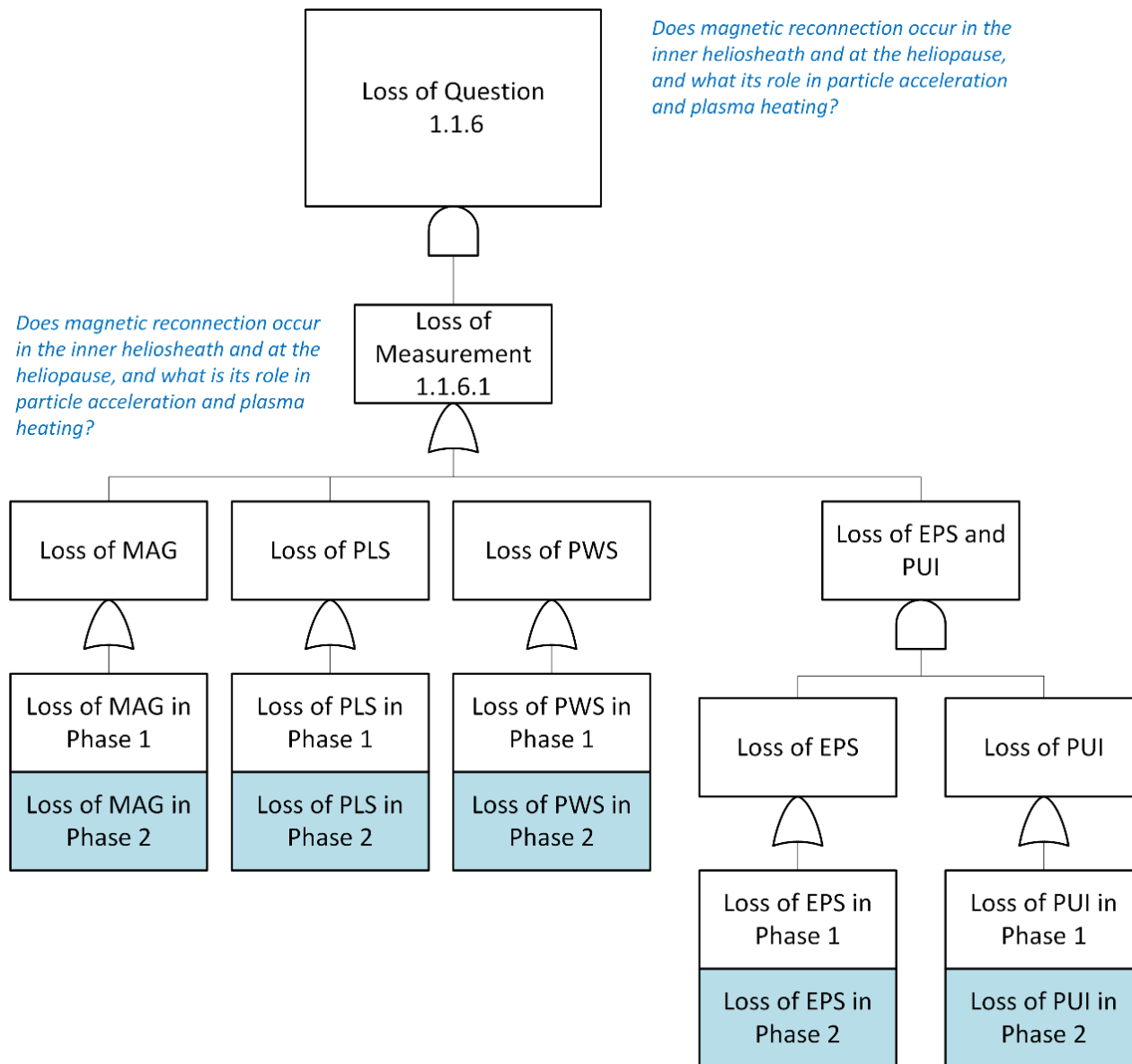


Figure F-22. STM fault tree for Question 1.1.6. (Image credit: Johns Hopkins Applied Physics Laboratory.)

What is the structure and nature of the heliopause?

Measure in situ magnetic fields, plasma, and pickup ion distributions as well as energetic particle intensities up to cosmic ray energies to determine the structure of, and interaction with, the heliopause and the magnetic field topology out into the very local interstellar medium.

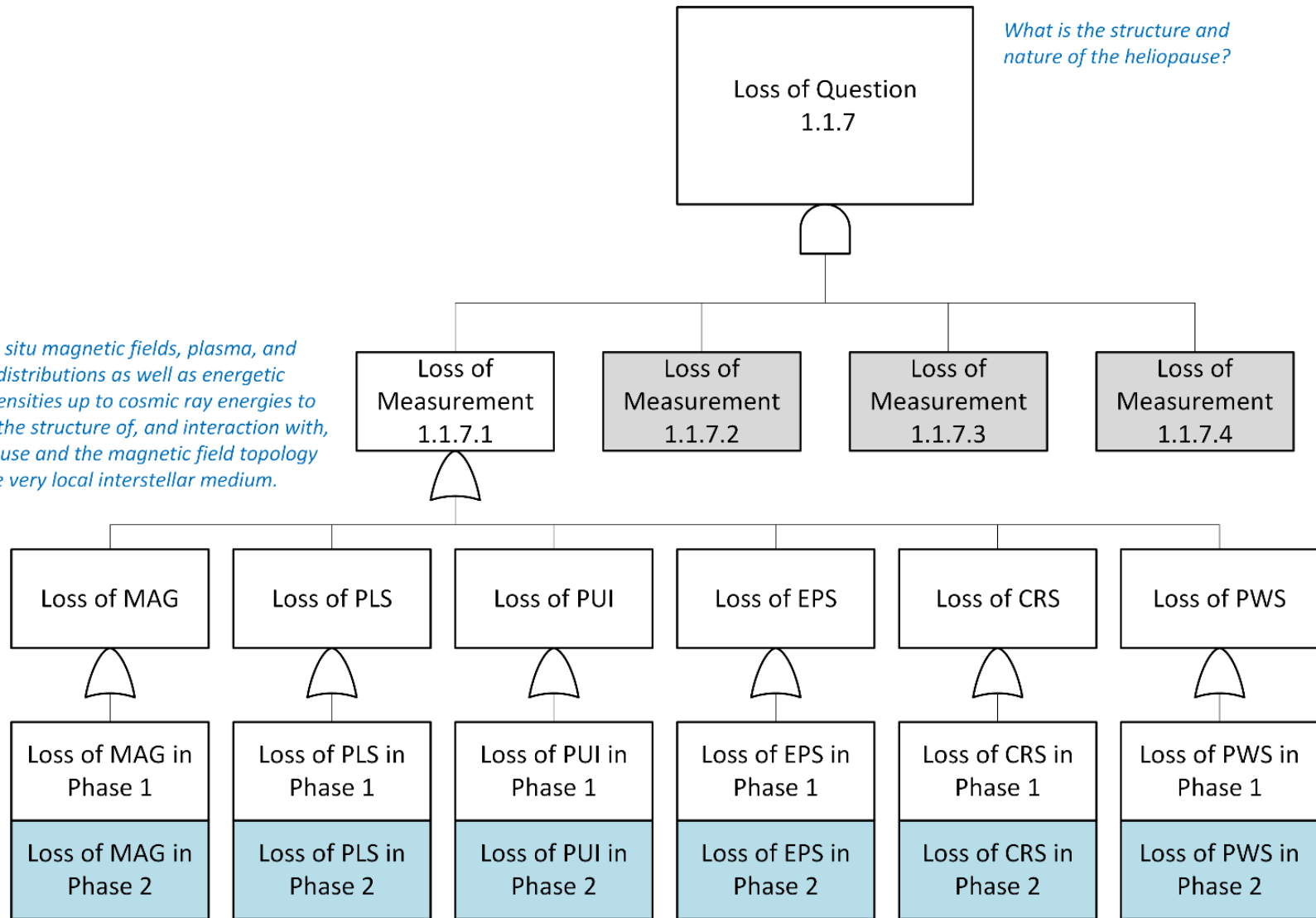


Figure F-23. STM fault tree for Question 1.1.7. (Image credit: Johns Hopkins Applied Physics Laboratory.)

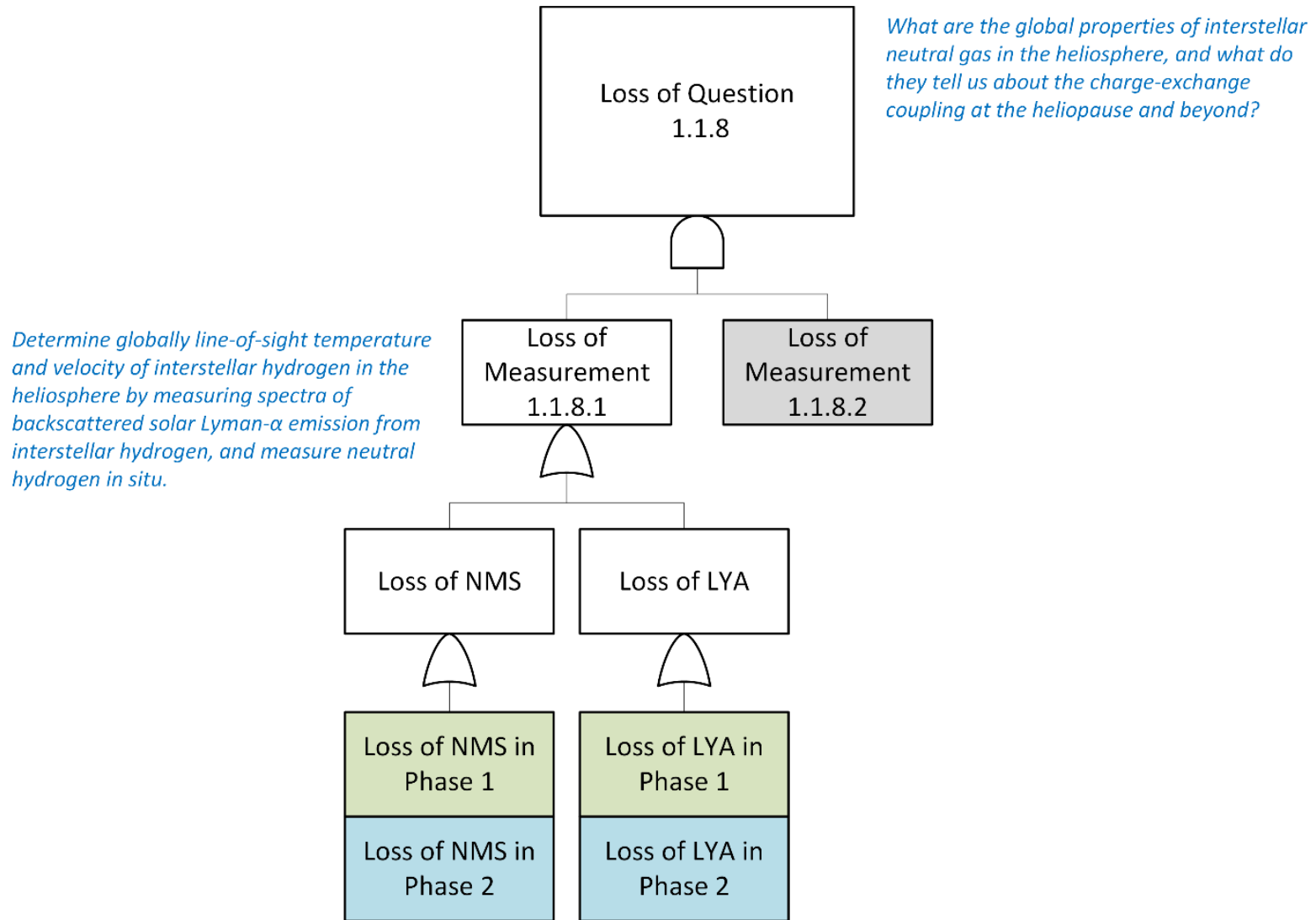


Figure F-24. STM fault tree for Question 1.1.8. (Image credit: Johns Hopkins Applied Physics Laboratory.)

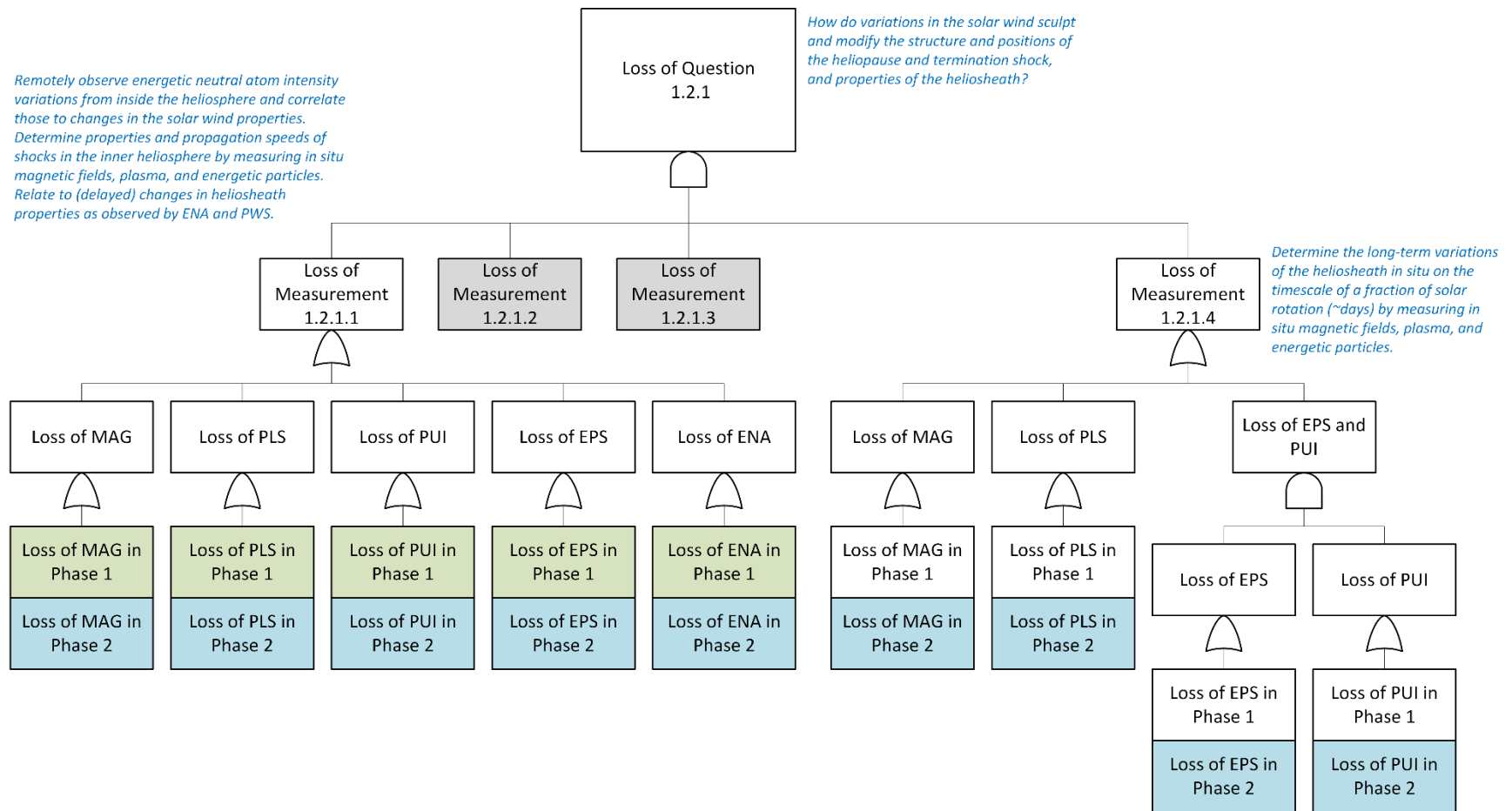


Figure F-25. STM fault tree for Question 1.2.1. (Image credit: Johns Hopkins Applied Physics Laboratory.)

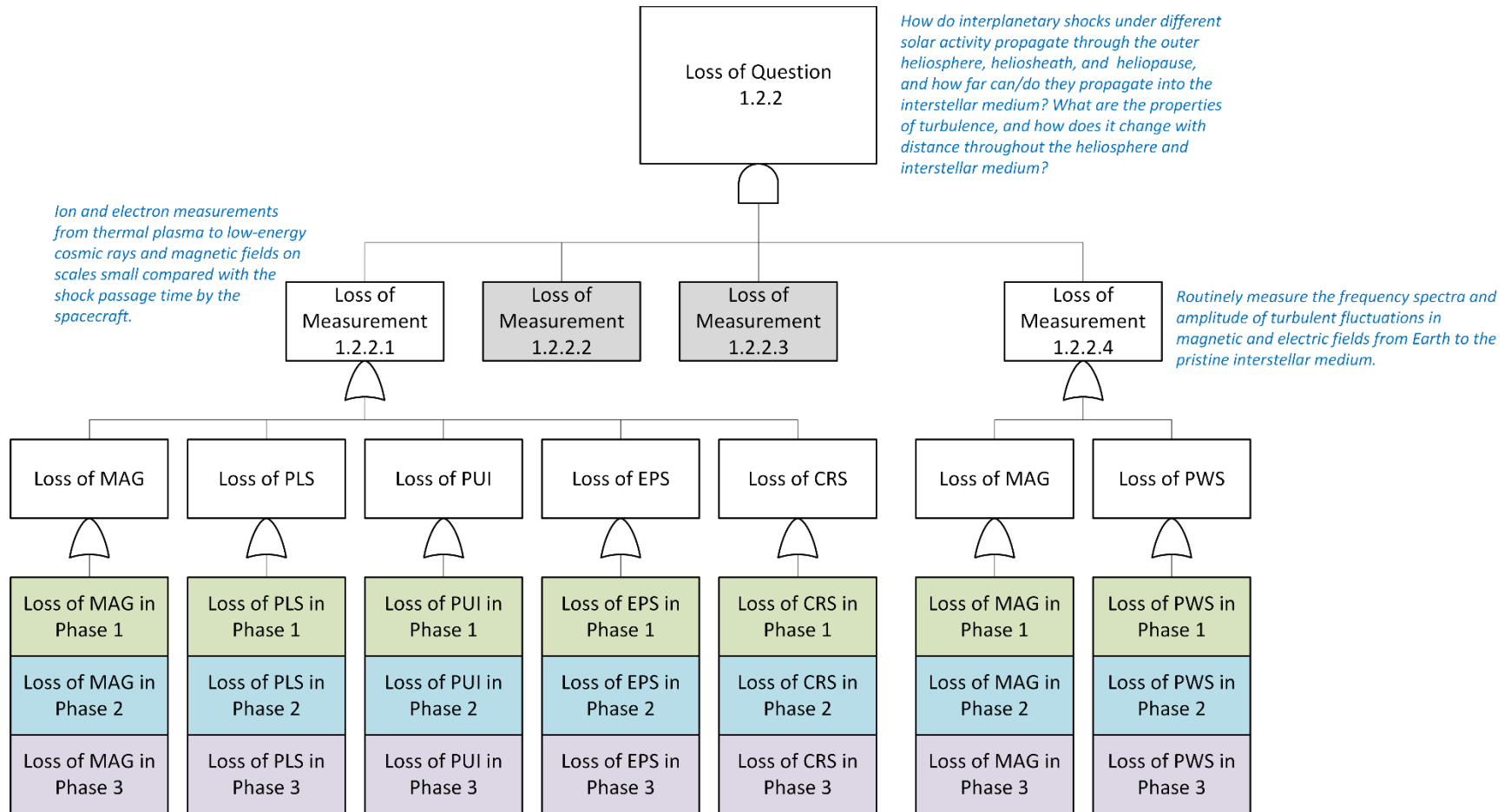


Figure F-26. STM fault tree for Question 1.2.2. (Image credit: Johns Hopkins Applied Physics Laboratory.)

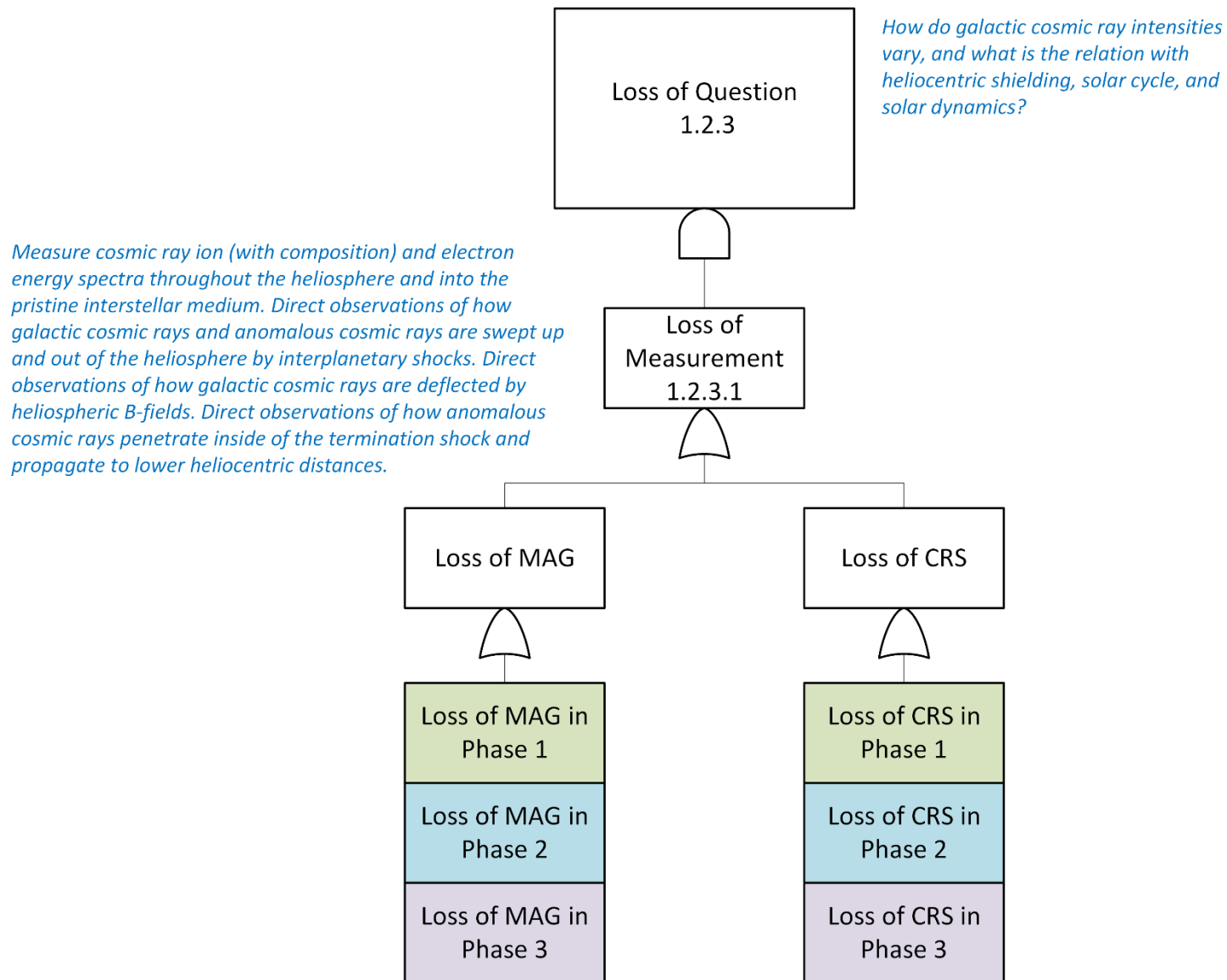


Figure F-27. STM fault tree for Question 1.2.3. (Image credit: Johns Hopkins Applied Physics Laboratory.)

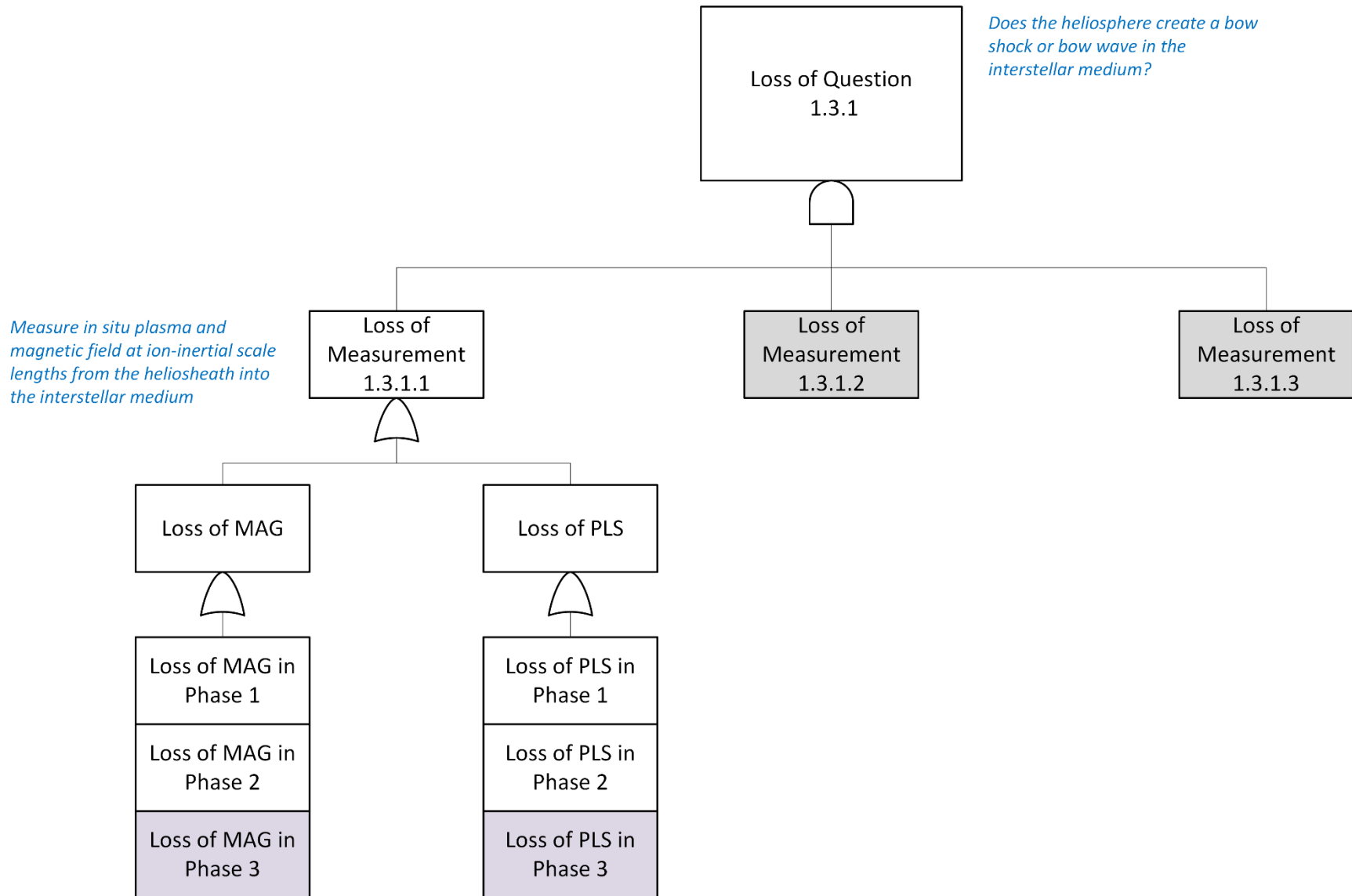


Figure F-28. STM fault tree for Question 1.3.1. (Image credit: Johns Hopkins Applied Physics Laboratory.)

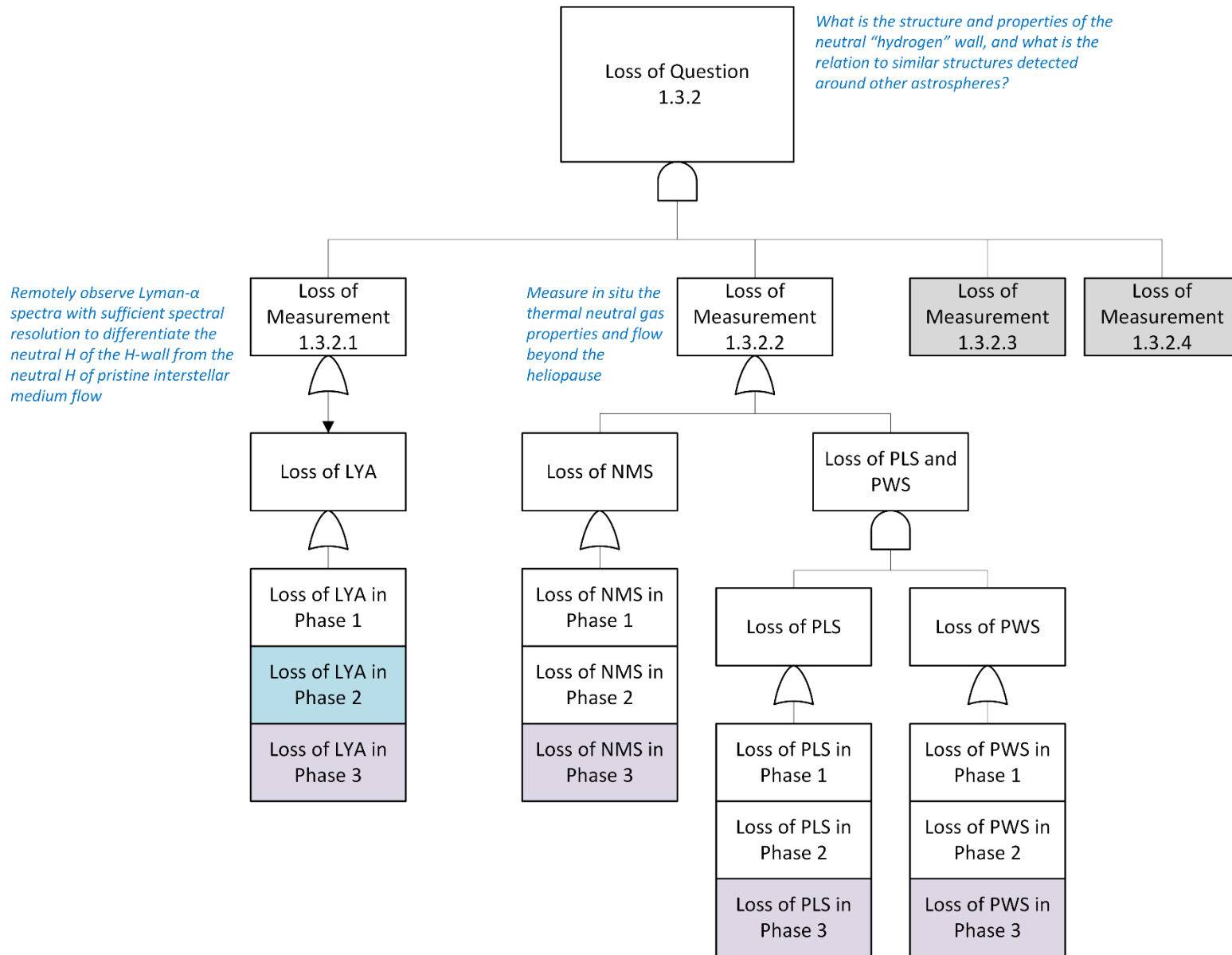


Figure F-29. STM fault tree for Question 1.3.2. (Image credit: Johns Hopkins Applied Physics Laboratory.)

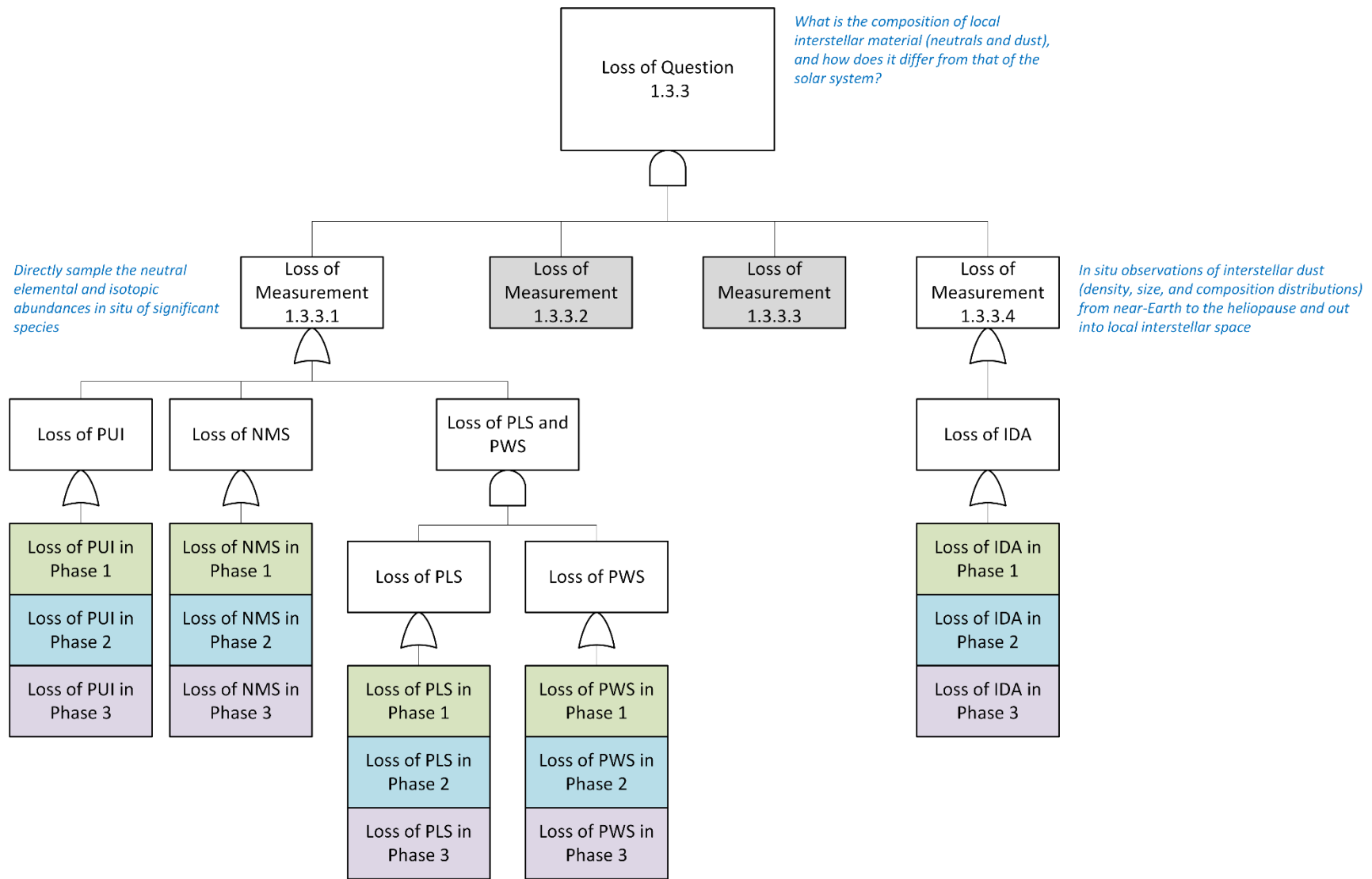


Figure F-30. STM fault tree for Question 1.3.3. (Image credit: Johns Hopkins Applied Physics Laboratory.)

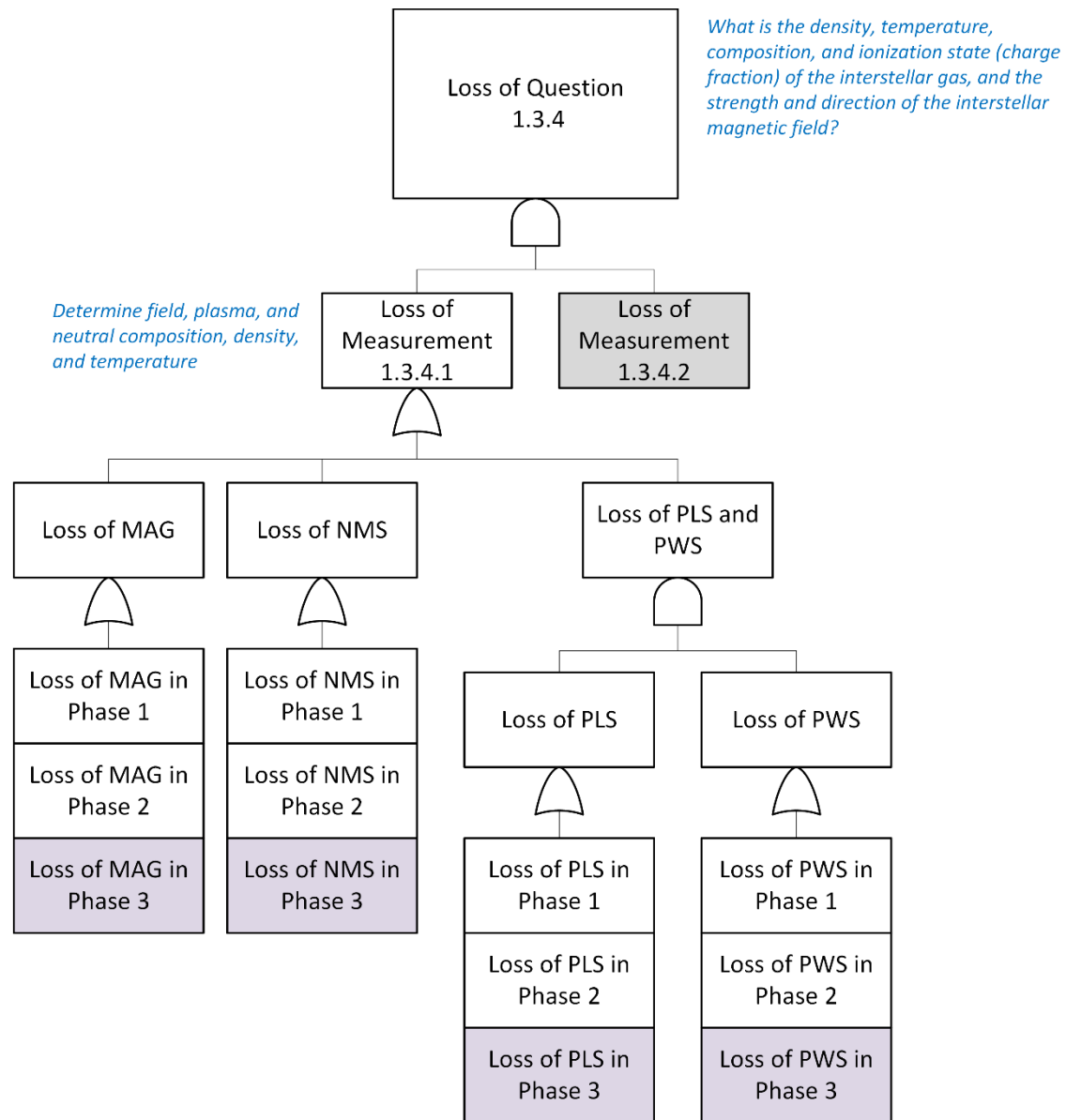


Figure F-31. STM fault tree for Question 1.3.4. (Image credit: Johns Hopkins Applied Physics Laboratory.)

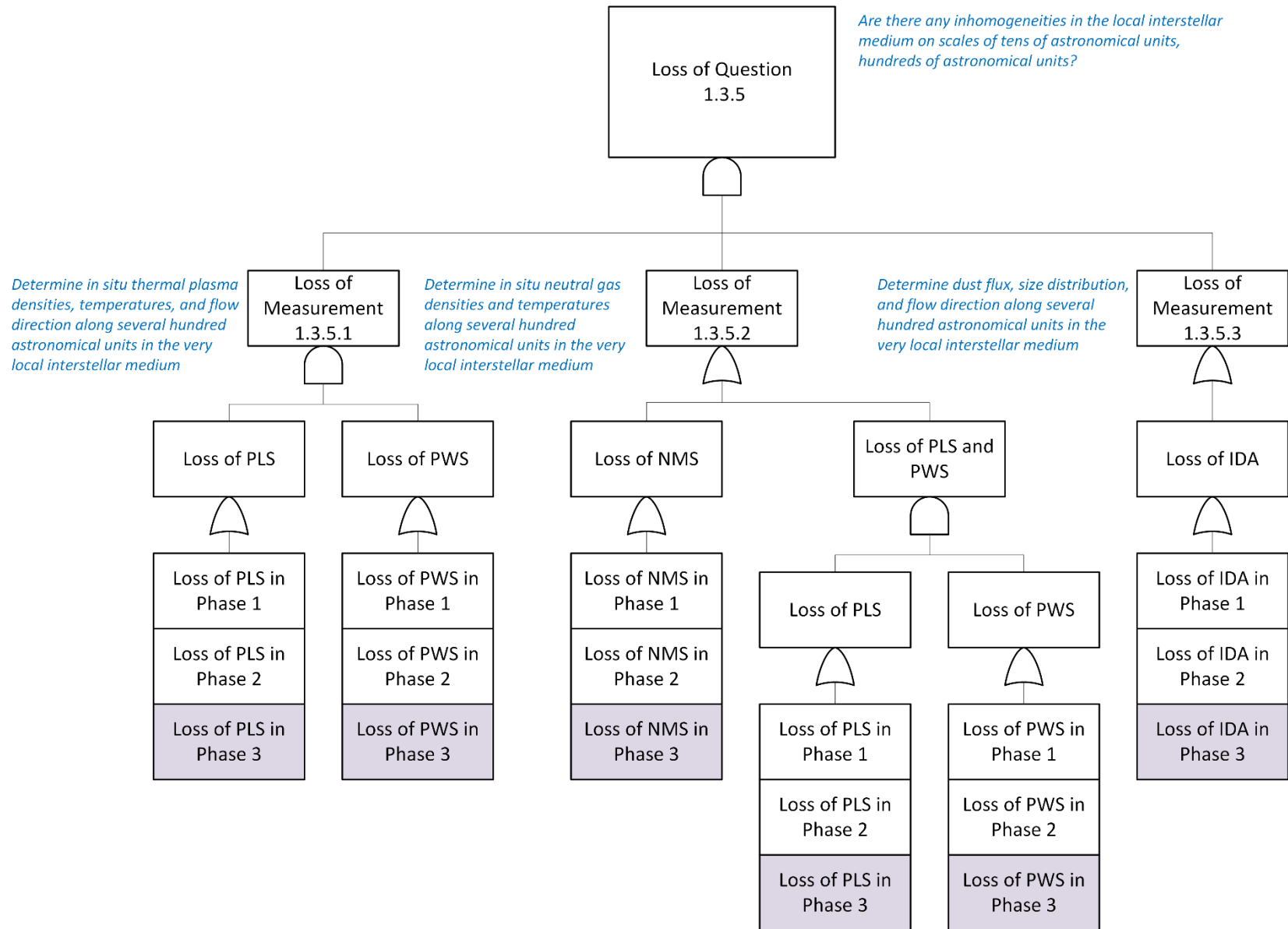


Figure F-32. STM fault tree for Question 1.3.5. (Image credit: Johns Hopkins Applied Physics Laboratory.)

What are the origins of galactic cosmic rays?

Determine the composition and spectra of galactic cosmic rays beyond the heliopause, and compare their relationship to galactic gamma-ray and radio emissions observed from ground; from relative abundances of different elemental and isotopic abundance ratios and radioactive “cosmic ray clocks” (both with relatively short and long half-lives, used in identifying time since nucleosynthesis; e.g., ^{14}C , ^7Be , ^{10}Be , ^{22}Ne , ^{26}Al , ^{36}Cl , ^{54}Mn , ^{55}Fe , ^{59}Ni versus ^{59}Co), distinguish galactic cosmic ray sources from various stellar and other astrophysical objects (e.g., supernova remnant shocks), elemental fractionation, and spallation in the interstellar medium; test our current parameterization of the “leaky box” model for galactic cosmic rays.

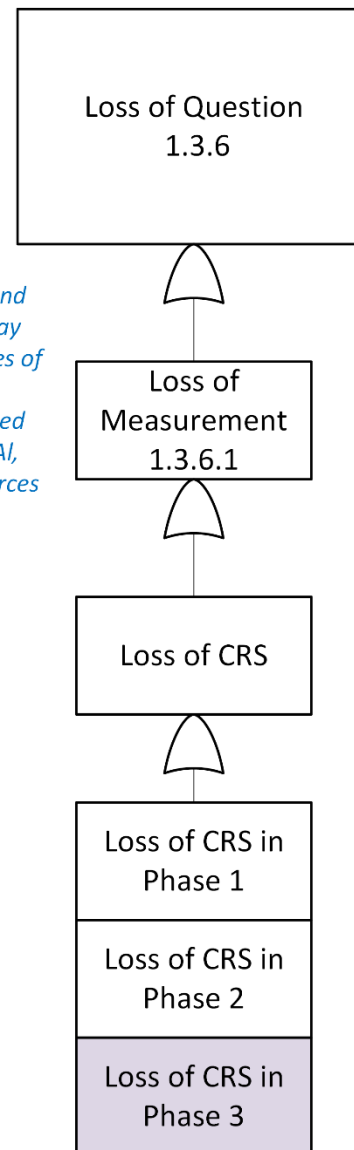


Figure F-33. STM fault tree for Question 1.3.6. (Image credit: Johns Hopkins Applied Physics Laboratory.)

When analyzing the entire science objective fault tree, we get the Boolean reduction of combinations of instrument failures that lead to loss of science objectives. Table F-5 provides the list of these combinations, called cut sets. There are 469 cut sets in total, with three being singles. These are the magnetometer in each phase, meaning that the failure of the magnetometer in any phase would fail the mission. The magnetometer shows up as a vital instrument in several measurements. To alleviate this reliance on the magnetometer, it should be designed to be internally redundant.

Table F-5. Instrument cut sets.

Singles	Doubles		Other
MAG-1	PLS-1, PWS-1	CRS-3, PLS-2	208 triples
MAG-2	CRS-2, PWS-1	ENA-2, PLS-2	
MAG-3	CRS-1, PWS-1	ENA-3, PLS-2	
	CRS-3, PWS-1	EPS-2, PLS-2	211 quadruples
	PLS-2, PWS-1	EPS-3, PLS-2	
	CRS-2, PLS-1	LYA-2, PLS-2	
	ENA-1, PLS-1	NMS-2, PLS-2	
	NMS-1, PLS-1	PLS-1, PWS-3	
	LYA-1, PLS-1	CRS-2, PWS-3	
	EPS-1, PLS-1	CRS-1, PWS-3	
	CRS-1, PLS-1	CRS-3, PWS-3	
	CRS-3, PLS-1	PLS-2, PWS-3	
	ENA-2, PLS-1	PLS-1, PWS-2	
	ENA-3, PLS-1	CRS-2, PWS-2	
	EPS-2, PLS-1	CRS-1, PWS-2	
	EPS-3, PLS-1	CRS-3, PWS-2	
	LYA-2, PLS-1	PLS-2, PWS-2	
	NMS-2, PLS-1	PLS-1, PUI-3	
	CRS-2, PLS-2	PLS-2, PUI-3	
	ENA-1, PLS-2	PLS-1, PUI-1	
	NMS-1, PLS-2	PLS-2, PUI-1	
	LYA-1, PLS-2	PLS-1, PUI-2	
	EPS-1, PLS-2	PLS-2, PUI-2	
	CRS-1, PLS-2		

The analysis also shows 47 doubles, combinations of two instrument failures leading to loss of science. For example, the last item the first doubles column (CRS-1, PLS-2) means the mission would fail its science objectives should the Cosmic Ray System fail in the first mission phase and the Plasma System fail in the second mission phase. In addition, the logic yields 208 combinations with three failures and 211 combinations with four failures.

This is not the full picture. By only evaluating to the instrument level, the functional and measurement robustness is not accounted for. The next step (during the design phase) is to develop a fault tree with higher resolution down to the sensor and circuit-board level. At this point, we would show any internal and functional redundancies within the instruments.

This section shows the analyses the team performed, which concluded that the magnetometer needs to be redundant and that no other instrument is a single-point failure.

F.2.7 Reliability Prediction

F.2.7.1 Interstellar Probe Reliability Model

As part of the exploration of longevity for the Interstellar Probe study, a reliability model was developed and used to estimate the probability of success (reliability) for such a mission. Developing the model required two main components: logic for mission success and quantification of the system reliability and its associated elements. Figure F-34 is the RBD for the mission consisting of the spacecraft bus and separately the instrument payload suite. RBDs show items necessary for the mission as blocks in series and redundancy as blocks in parallel. For each item in the RBD, more detailed RBDs represent the component and their internal redundant structure.



Figure F-34. Top-level Interstellar Probe mission RBD. Each box is further decomposed with the bus and payload RBDs. (Image credit: Johns Hopkins Applied Physics Laboratory.)

The reliability models have been constructed with some assumptions that would not be made for models developed during a mission development phase. These are:

- Launch vehicle perfectly delivers the spacecraft to orbit.
- Software is perfect.
- There are no common-cause failures (failures that act to defeat both sides of redundancy simultaneously).
- No dependencies are modeled.
- Failure rate data are from vendors’ marketing material.
- Failure rates are assumed to be time dependent according to historical spacecraft analyses.
- Performance degradation is not modeled.

This section describes the data sources and analysis for quantifying the constituent elements in the RBDs and logic diagrams for all the systems quantified. The results of the modeling estimates are also shown.

F.2.7.2 Spacecraft Bus Model

The spacecraft bus requires all seven systems to operate for the duration of the mission. This is represented in the RBD as series of blocks, as shown in Figure F-35. For each system block, another more detailed RBD is created to model the configurations and redundancy that exist. The system RBDs (Figure F-36 through Figure F-41) show detail down to the major component or “box” level. The quantification of reliability is performed at this level. During the development phase of a program, the level of detail for this analysis would go down to the board and even the piece-parts

on the board. However, because that level of design is not within the scope of this study, the models are created at the level of current design maturity (see Sections 3 and 5)

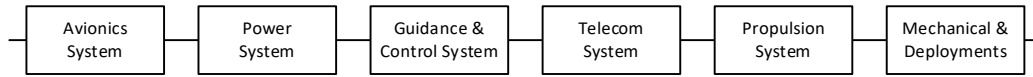


Figure F-35. Spacecraft bus RBD. Each system box is decomposed into its own RBD. (Image credit: Johns Hopkins Applied Physics Laboratory.)

The avionics system has been designed to be fully redundant in such a way that the loss of any one major component does not fail the system. As shown in the functional block diagram (see Section 5), all these items have two connections to two different routers, making for a robust design.

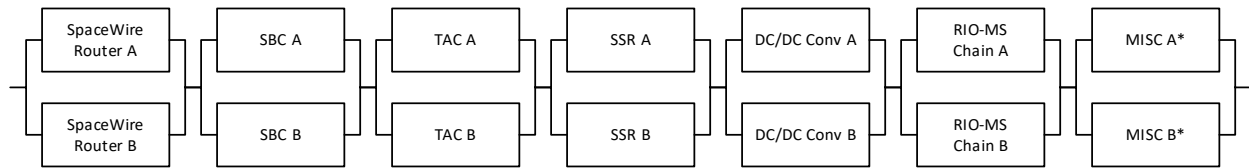


Figure F-36. Avionics system RBD. (Image credit: Johns Hopkins Applied Physics Laboratory.)

The power system features two radioisotope thermoelectric generators (RTGs) that must provide power through the entirety of the mission. Although these are modeled as single-point failures, an analysis has been conducted to show that science requirements can be met with one operating RTG at EOL, albeit at a much reduced bandwidth. The other single-point failure is the shunt regulator unit (SRU). The internal structure of this unit will have some redundancy, but that detail has yet to be determined.

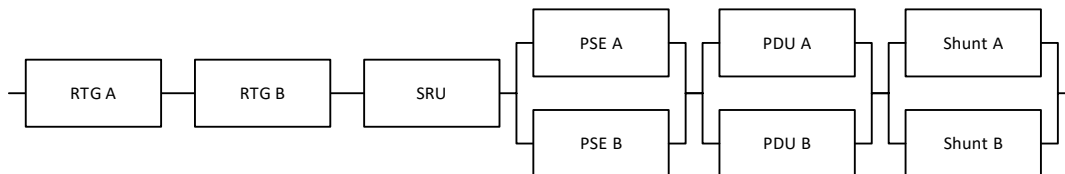


Figure F-37. Power system RBD. (Image credit: Johns Hopkins Applied Physics Laboratory.)

The model for the guidance, navigation, and control (GNC) system only shows the sensors and the computing hardware that is already modeled in the avionics system.

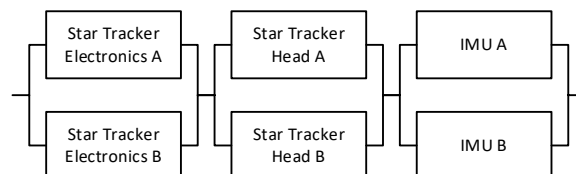


Figure F-38. Guidance, navigation, and control sensors RBD. (Image credit: Johns Hopkins Applied Physics Laboratory.)

The telecom system RBD is a simplified representation of the reliability model. The system modeled does not account for degraded states of the system that can overcome several failures. For example, a failure in a switch is likely to result in the inability to switch but still allow signals to be passed

through the path it is currently stuck on. Internally, fault management and ground intervention will be able to work around such issues. As such, this model is likely to be conservative in nature.

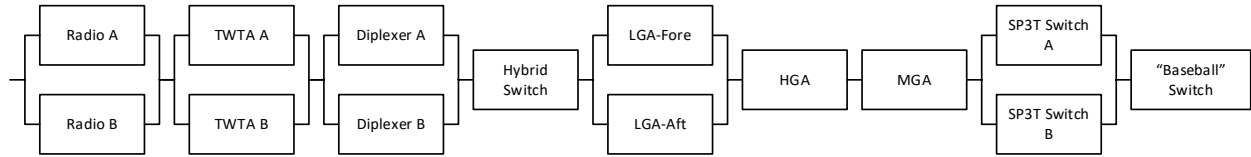


Figure F-39. Telecom RBD. (Image credit: Johns Hopkins Applied Physics Laboratory.)

The RBD for the propulsion system captures the major components. Because the specific concept of operations and orientation have not fully been designed, the model includes the assumptions that all 12 small thrusters and their latch valves are required and that all 4 large thrusters and one of two latch valves are required. As with most spacecraft propulsion designs, the thruster orientation will allow for several failures to occur without compromising the mission.

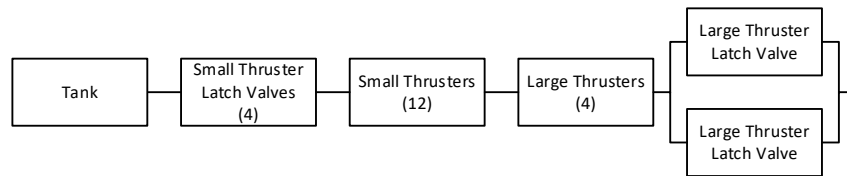


Figure F-40. Propulsion system RBD. (Image credit: Johns Hopkins Applied Physics Laboratory.)

The mechanism RBD models the separation system as three of four ordnance devices. Six assumed release mechanisms (also modeled as ordnance devices) are included.

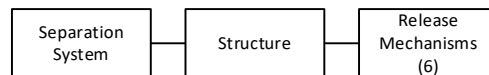


Figure F-41. Structure and mechanisms RBD. (Image credit: Johns Hopkins Applied Physics Laboratory.)

F.2.7.3 Instrument Suite Model

The reliability model for the payload is based on the breakdown of science requirements and mapping to the instruments. The resulting cut sets (Table F-5) are the combinations of failure that would result in loss of mission as defined by the science requirements.

To quantify the suite of instruments, failure probabilities of each instrument are propagated using the Boolean logic of the fault tree. Each combination line in the table, or minimal cut set, is the product of the instrument failure probabilities in that combination:

$$Pr(\text{Minimum Cut Set}_i) = \prod Pr(\text{Instrument}_j).$$

To get the probability of loss of science, the probabilities for all of the minimum cut sets are added together (known as the rare event approximation).

$$Pr(\text{Loss of Science}) = \sum Pr(\text{Minimum Cut Set}_i).$$

The probability values for the instruments are described below.

F.2.7.4 Data Sources and Analysis

This section describes the methods for estimating the reliability of the various components that are contained in the reliability model. The data and methods are presented to allow traceability into the computations made with the RBDs.

Components

As discussed earlier, spacecraft failures follow the behavior of a Weibull model (i.e., a time-dependent failure rate and not an exponential model or constant failure rate). The Weibull distribution is a continuous function used by reliability engineers for modeling TTF data.

Typically, to fit a statistical model to a life data set, the analyst estimates the parameters of the distribution that will make the function most closely fit the data using a process known as the MLE method. The limitation of MLE is that it will not produce an estimate of the uncertainty around the probability of failure. For this, Bayesian analysis techniques are combined with the Weibull data analysis.

For convenience within the scope of this study, the β parameter is assumed to be that of interplanetary spacecraft, $\beta = 1.3$, and the η parameter is assumed to be equal to the value of a constant failure rate.

COTS Devices

For the COTS devices, an aggregation of vendor reliability estimates gathered from past APL missions has been used. These data are shown in Table F-6. The uncertainty is shown in the table as the 5th and 95th percentiles of lognormal distributions describing the values η could take.

Table F-6. COTS device reliability data.

Component	η Mean	η 5th	η 95th
Solid-State Recorder (SSR)	2.01E-9	1.42E-8	6.95E-7
Star Tracker	3.61E-7	6.45E-8	1.01E-6
Inertial Measurement Unit (Altobelli et al., 2016)	4.51E-8	8.04E-9	1.25E-7
Radio	7.89E-7	1.12E-7	2.36E-6
Traveling-Wave Tube Amplifier (TWTA)	1.50E-7	1.06E-8	5.24E-7
Radio Frequency (RF) Switch	4.49E-9	8.04E-10	1.25E-8
Antenna	9.97E-10	7.09E-11	3.47E-9
Propulsion Tank	1.50E-8	1.39E-9	4.96E-8
Latch Valve	4.99E-7	3.53E-8	1.74E-6
Thruster	5.00E-9	4.62E-10	1.65E-8

Integrator Build Devices

For unique builds, a reliability estimate is built up with a variety of electronic boards as a basis of modeling. Reliability values developed for “boards” are based on previous reliability analysis of APL-built boards for several missions and updated with flight experience.

Table F-7. Electronic board reliability data.

Component	η Mean	η 5th	η 95th
Generic Electronics Board	3.6E-08	6.9E-9	9.8E-8
Complex Electronics Board	4.25E-8	5.0E-9	1.3E-7
Power Electronics Board	2.75E-7	3.7E-8	8.3E-7

Instruments

The reliabilities for the instruments are a combination of the electronics board numbers. Each instrument was assumed to have five “General Electronics Boards” and one “Power Board.” The magnetometer was also assumed to be internally redundant based on the analysis.

F.2.7.5 Dust Impact Probabilities

Consequences of dust particle impacts will also be folded into the reliability estimation when the development program is initiated. Impacts to “wire” booms and other instruments will be the main concern. The paper “Estimate of the risk of damage to the THEMIS wire boom fine wires due to micrometeoroid and orbital debris impacts” by Scott Tucker provides some methodology and estimates on wire breakage (Tucker, 2010). This analysis was done in support of the Magnetospheric Multiscale (MMS) mission and also looked at damage to thicker elements supporting the axial helical booms. It is not only the loss of the science-gathering capability but also the possible spin-axis misalignment with the loss of any boom that would not allow the communication link to close.

In assessing the breakage risk to wire booms on an interstellar probe, McNutt et al. (2021) points out that significant changes exist in dust environment between 1 au (where the breaks have been recorded) and much farther out (where the Interstellar Probe will go). Changes in particle size, flux, and velocity are relevant.

F.2.7.6 Mission Reliability Results

This section shows the results of the Interstellar Probe baseline mission reliability estimation model. The model logic is shown as RBDs, and the components are modeled using a Weibull distribution.

F.2.7.6.1 Reliability Prediction

The reliability estimate for the mission is 0.74. Figure F-42 shows the mean value (white line) and that the uncertainty in the estimate spans the range of 0.25 at the 5th percentile to 0.93 at the 95th percentile (each end of the bars). This is the aggregated uncertainty from all the components.

Contributing to the overall mission uncertainty are the payload, power system, and telecom systems. The payload shows up as the driver because there are several combinations of instrument failure that could end the mission. Figure F-43 shows the contribution from the systems. Neither avionics nor mechanisms seem to appear, and this is because the values are very close to 1.0 and do not show on this linear scale. Also, the lower numbers for power and telecom come from the single-point failures and the conservative modeling assumptions.

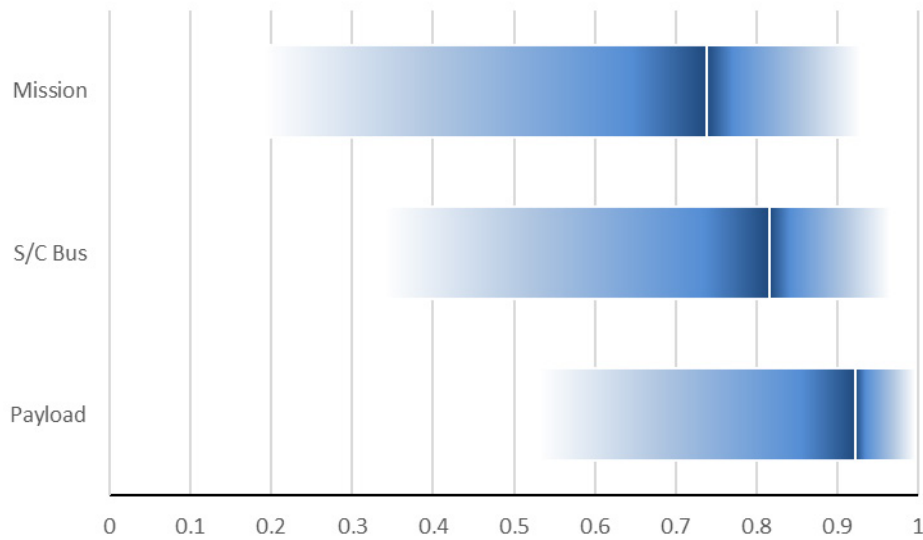


Figure F-42. Top-level reliability estimates with uncertainty. (Image credit: Johns Hopkins Applied Physics Laboratory.)

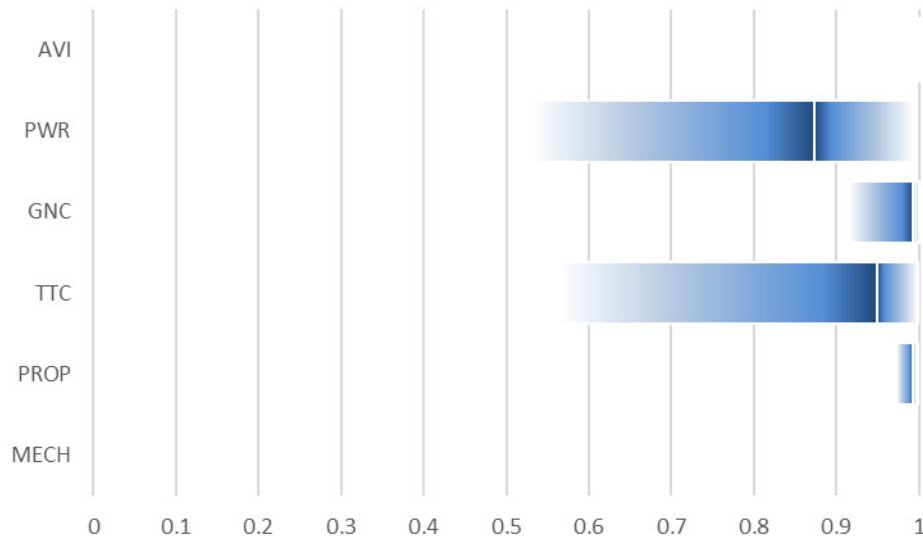


Figure F-43. System-level reliability estimates with uncertainty. (Image credit: Johns Hopkins Applied Physics Laboratory.)

F.2.7.6.2 Single-Point Failures

An inspection of the RBDs shows the boxes in series with the rest of the systems. These are the single-point failures. Several of these will not be single-point failures once the overly conservative assumptions are revised during the development phase of the program.

- RTG × 2 – Functional workarounds with lower bandwidth may overcome degradation.
- SRU – Internal redundant structures exist.

- Radio-frequency (RF) hybrid switch and RF “baseball” switch – Typically fails to switch, leaving the system in a specific configuration. If that configuration is sufficient, no loss of mission is encountered.
- High-gain antenna (HGA)
- Medium-gain antenna (MGA)
- Propulsion tanks
- Latch valves and thrusters (result of conservative assumption that all thrusters are needed)
- Release mechanisms – Current assumption is that all release mechanisms must work. Actual design will account for failure cases.

F.2.7.6.3 Limited-Life Items

As part of the longevity picture, limited-life items are also addressed. Table F-9 is an initial list of limited-life items and items with aging effects. The distinction of this list is that failures are likely dependent on use or on number of cycles within the control of the operations team. This list was created from those typically developed for interplanetary missions, with some items appearing because of the long mission durations.

Table F-8. Limited-life items.

Electronics	Electronic aging effects (electromigration, solder fatigue, ...) Nonvolatile memory writes High-voltage insulators High-voltage on/off cycles
Power	Relays (failure due to cycles, failure due to non-use [cold weld]) Shunt capacitors RTG (various items to consider)
Radio Frequency	Traveling-wave tube amplifier Oscillator drift (ultra-stable oscillator stability) Baseball switches Steerable antenna mechanism (if any)
Propulsion	Thruster cycles Propellant breakdown Accumulation of impurities Pressurant leakage (nominal rate or other mechanisms, creep)
Thermal	Solder/connector fatigue for heaters
Other	Scan mirrors Surface effects of dust Adhesive aging

F.2.7.7 *Augmented Mission Architecture*

From a reliability perspective, the augmented mission architecture is the same. The driving factor is time, and the same equipment is exposed to 50 years in both cases.

F.2.8 *Probabilistic Physics of Failure*

F.2.8.1 *Physics of Failure Modeling*

The probabilistic PoF approach to reliability must be used in conjunction with established reliability, testing, and part-selection techniques. According to Pecht and Dasgupta, “The application of the PoF approach to electronic products is founded on the conviction that the failure of electronics is governed by fundamental mechanical, electrical, thermal, and chemical processes. For this reason, potential problems in new and existing technologies can be identified and solved before they occur, by understanding the possible failure mechanisms” (Pecht & Dasgupta, 1995). The probabilistic portion comes from the uncertainty in the equations, their constants, the variability of data, and the extrapolation from the current data sets out beyond 50 years. This section describes several of the physics models governing electronics failures. To our knowledge, the existing pedagogy covers the failure mechanisms for electronics within the scope of Interstellar Probe.

F.2.8.1.1 *Electromigration (Black’s Equation)*

This section will provide a summary of failure models relevant to EM-related failure. Equations for modeling EM are included where practical; for models based on complex series of physical equations, a summary is provided along with a tabulation of the requisite inputs, parameters, and physical assumptions.

Black’s equation provides an estimate of MTTF based on the interconnect dimensions, absolute temperature, physical material properties, electron current density, and activation energy for EM to occur and an experimentally determined exponent that varies depending on the EM failure mode. This model assumes that empirical values attained during accelerated testing can be applied to normal use conditions to provide a model of MTTF (Wolff et al., 2021).

Blech Effect

The Blech effect describes a phenomenon wherein interconnects demonstrating a sufficiently low product of conductor length and current density do not exhibit EM failure. This effect arises from the assumption that the substrate provides enough support to the interconnect material to generate a hydrostatic force in opposition to the electron wind force, which causes EM voids and hillocks to form. Input values used to calculate the critical parameter below which EM does not occur are the current density, conductor length, atomic volume of the conductor material, effective charge of the conducting atoms, interconnect resistivity, and intra-conductor stress gradient. Empirical data are available, which experimentally validates the Blech effect at 65- and 45-nm feature sizes (Cheng et al., 2008).

Electron Wind Model

This model can determine the electron wind force due to direct current (DC) flow, which plays the primary role in creating voids in interconnects. The physical parameters from which this calculation comes are the concentration of atoms in the conducting material, the diffusivity of those atoms, the conductor temperature, the charge of the migrating atoms, the resistivity of the conductor, and the current density (Cheng et al., 2008).

Interconnect Diffusion Path Model

This models the diffusivity of the conductor material through the dominant diffusion paths by representing the diffusivity for aluminum interconnects with polygranular and bamboo-type microstructures in addition to the diffusivity of copper interconnects using Si_3N_4 as the dielectric diffusion barrier, forming the primary diffusion path for EM. The model requires the following as physical input parameters: diffusivity at the grain boundaries and conductor/boundary coating interface, metallic grain dimensions, diffusion interface width, absolute temperature, and activation energy for diffusion. This model can be used to estimate conductor diffusion rates of different interconnect geometries to determine the lifetime to EM failure (Alam et al., 2005).

Electromigration in Alternating Current Signal Wires

This model incorporates the effect of Joule heating on Black's equation to evaluate EM failure in interconnects carrying alternating current (typically signal wires or memory read/write modules). This model modifies the temperature value used in Black's equation, adding a Joule heating term to the absolute temperature of the interconnect. In addition to the inputs required by Black's equation, this model also uses the root mean square current in the conductor, interconnect resistance, the dielectric insulator thickness, the thermal conductivity of the dielectric, and the length and width of the interconnect. Experimental corroboration of this model exists to 22-nm feature size (Posser et al., 2014).

Thermal Gradient Effect on Black's Equation

This computational model incorporates the effect of nonuniform temperature gradients through interconnects on EM. Parameters are equivalent to those used in Black's equation and for calculating the critical parameter for the Blech effect, with the addition of a thermal gradient and thermal flux terms used to solve for a steady-state solution iteratively. COMSOL modeling integrated with this model can also determine temperature gradients and thermal stresses for model input parameters (Abbasinasab & Market-Sadowska, 2019).

Void Growth Model

This model predicts the nucleation time for a void due to EM stress and the subsequent TTF defined by an arbitrary increase in conductor resistivity. The inputs used in this model are as follows: the effective charge of the migrating atoms, the resistivity of the conductor, the atomic volume of the conductor material, the elastic modulus of the boundary surrounding the conductor, the absolute temperature at the nucleation site, the hydrostatic stress required for void nucleation, and the atomic diffusivity and current density in the interconnect. The calculation of TTF assumes that the EM void spans the entire width and height of the conductor channel. In

addition to the above inputs, the calculation of TTF also requires the length of the interconnect, the ratio of the change in resistance that characterizes a failure, and the cross-sectional areas and resistivity of the interconnect and boundary materials (Haga & Saleh, 2011; Korhonen et al., 1992).

Layout Sensitivity Model

This model may be used to predict the sensitivity of a given circuit layout to EM failure due to narrow interconnects caused by defects incorporated during manufacturing. The model formulation uses a probabilistic approach to calculate the frequency of occurrence of life-shortening defects based on the following inputs: interconnect trace width and spacing, the density of interconnect channels, the size of a potential defect, the number of interconnect channels impacted by a defect of the chosen size, and a critical width below which the narrowed interconnect is considered a failure. This model predicts circuit sensitivity to defects of varying sizes for feature sizes ranging from 90 to 32 nm, along with an estimated reduction in MTTF from that predicted using Black's equation for each feature size (Ghaida & Zarkesh-Ha, 2007).

Small Feature Scaling Limits Model

This model considers the effects of changing physical input parameters on Black's equation and calculating the Blech effect critical value. The change in diffusivity, hydrostatic stress, bulk conductor modulus, void nucleation stress, and interconnect resistivity as a function of feature size from 135 to 10 nm is considered and incorporated into determining the impact of EM on life. In addition, this model considers nonideal insulator behavior at the ends of interconnects, allowing ion flux from adjoining interconnects to change the EM failure life (Zahedmanesh et al., 2019).

Granularity Effects on Electromigration

This model considers the effect of granularity in copper interconnects on the parameters that drive void diffusion and eventual EM failure. It uses inputs similar to those of the electron wind and void growth models, except that the resistivity and void diffusion parameters are modified to account for granularity in the copper conductor at small feature sizes. The model calculates the change in conductor resistance due to granularity. Calculating the ratio of interconnect resistance to bulk material resistance requires the electron mean free path, trace width, probability of electron scattering from material interfaces, average grain diameter, and probability of electron scattering from grain boundaries. The modification to the void diffusion term accounts for the different diffusion rates in the grain boundaries, grain bulk, and material interfaces (Filipovic & Selberher, 2020; Oates, 2014).

Stochastic Effective Current Model

This model considers the effect on EM failure life of long-term variability in interconnect current flow. It modifies Black's equation to include time-variant terms for current flux and covariant terms. This modification of Black's equation results in a model capable of estimating the mean value of the interconnect stress and the variance about the mean to present a statistically meaningful evaluation of EM stress (Issa et al., 2020).

F.2.8.1.2 Time-Dependent Dielectric Breakdown (TDDB)

TDDB refers to a physical process in which a dielectric body stored under a constant electric field less than the breakdown strength of the material breaks down over time. Because long-term spaceflight may cause electronic equipment to stay in a dormant state or load state for a long time, the risk of failure caused by dielectric breakdown greatly increases. In the presence of TDDB, it will be difficult to control the on-current of the MOSFET device. At the same time, nanoscale CMOS circuits also suffer from increased gate leakage current and power consumption. TDDB mainly appears on silicon dioxide (SiO_2) in electronic components, the main material for low-k copper interconnects and integrated circuits. Therefore, most failure mechanisms and related models will be developed around these two aspects (Wong, 2012).

The formation of conductive paths causes TDDB through low-k dielectrics between metals. This can result in a significant increase in leakage current between interconnects, thereby reducing circuit performance and causing chip operation to fail. The TDDB in the on-chip interconnect stack is one of the most critical failure mechanisms in microelectronics. At the same time, the TDDB in SiO_2 -based dielectrics is one of the more important failure mechanisms of integrated circuits (ICs) because ICs use a large number of MOSFETs. For these reasons, TDDB is one of the most-studied IC failure mechanisms, and many models have been proposed so far. Even so, there is still no consensus between the proposed TDDB model and the basic physical principles of dielectric breakdown, especially in back-end-of-line (BEOL) interconnects (McPherson, 2012; Wong, 2012).

The most commonly used TDDB model is based on the degradation caused by the magnetic field, the degradation caused by the current, or the combination of the degradation caused by the magnetic field and the degradation caused by the current (McPherson, 2012).

Thermomechanical E Model

McPherson (2012) originally developed the thermochemical model to predict the breakdown time of thin gate oxides. The key concept in the thermochemical model is that the generation of TDDB breaks weak chemical bonds in the dielectric network caused by an electric field, leading to new defects called traps. The current flowing through the oxide plays a secondary role at best. The interaction of the applied electric field and the dipole moment related to oxygen vacancies in SiO_2 reduces the activation energy required for hot bond rupture and accelerates the dielectric degradation process.

In thermochemical theory, the bond/coordination failure rate constant κ of a strained molecule depends on the number of interactions between the strained molecule and the surrounding lattice ν_0 ($\nu_0 = \text{vibration frequency} \approx 10^{13}/\text{s}$) multiplied by the Boltzmann probability (i.e., given the interaction with the lattice, the bond will gain enough energy to break the bond/coordination). Eventually, the charge is trapped at the fractured binding site, and its wave functions overlap and lead to the formation of a conductive sub-band. Therefore, severe Joule heating occurs during the oxide breakdown stage.

Although the thermochemical E model has been widely recognized, this alone is not enough to prove the validity. For very thin oxides, the breakdown time is no longer just a function of the electric field, and under the same oxide electric field, the breakdown time greatly reduces as the

thickness increases. Further experiments found that TDDB is inversely proportional to the current density, which indicates that the breakdown is mainly affected by high-energy electrons rather than the electric field in the oxide.

1/E Model

The 1/E model was first proposed by Chen et al. (2006) to explain TDDB in the thin gate oxide. In the 1/E model of TDDB, it is assumed that the damage is due to Fowler–Nordheim (F-N) conduction, which causes the current flowing through the dielectric to accelerate from the cathode to the F-N electrons injected into the conduction band of SiO₂ to the anode. Because of impact ionization, as electrons accelerate through the dielectric, the dielectric may be damaged. When these accelerated electrons finally reach the anode, holes are generated, tunneling back into the dielectric, causing damage (McPherson & Mogul, 2004). This is also known as the anode hole injection (AHI) model.

Because one electrode in the 1/E model must be a semiconductor, it is questionable whether the 1/E model can be applied to the embedded Cu low-k interconnect structure. In addition, for gate oxides, it has been proven that the 1/E model cannot correctly predict TTF in very low fields.

Lloyd Model

Lloyd et al. (2005) proposed this conceptually simple low-k TDDB model in 2005. The key idea in Lloyd’s model is that high-energy electrons cause damage in low-k dielectrics. There are several assumptions in the Lloyd model. First, electrons are injected into the low-k dielectric through the Poole–Frenkel mechanism. Second, the electron path length to the scattering point in the dielectric follows an exponential distribution. The third assumption is that there is threshold energy for defect generation in the dielectric, and the threshold energy is constant with respect to space and time. Finally, the model assumes that the breakdown time depends on the rate at which defects are created in the low-k dielectric.

Haase Model

The uniqueness of the Haase model is that it does not aim to establish a TTF relationship because some of the micro-mechanisms used in the previous model lack an empirical basis. Instead, it attempts to numerically simulate the low-k leakage current as a function of time and uses the time to minimum current (TTMC) as the criterion for dielectric failure. The assumptions made in the Haase model are similar to those made in the Lloyd model. In addition, the model also believes that electrons can interact with photons in a network of low-k dielectric atoms (Wong, 2012).

Before discussing various low-k TDDB models, it is necessary to focus on these materials’ main dielectric leakage mechanisms. This is because, in some of these models, the current leakage is an integral part of the model. There are seven known conduction mechanisms in insulating materials. These include F-N tunneling, direct (Giaever) tunneling, Schottky emission, Poole–Frenkel emission, ohmic conduction, space charge limited conduction, and ion conduction. For low-k dielectrics, the conduction mechanisms that have been observed experimentally are ohmic conduction, Schottky emission, and Poole–Frenkel emission. In the Schottky mechanism, electrons are injected from the rectifier contact. The work function of the metal should be greater than the electron affinity of the

dielectric. The difference between the two is that the electronic barrier of Schottky contact is high from the metal's point of view. Those electrons with sufficient energy in the metal can surpass the energy barrier and enter the dielectric. The Poole–Frenkel conduction mechanism occurs in dielectrics with inherent defects (traps), such as silicon nitride (SiN) and silicon oxynitride (SiON). These traps are formed during the deposition process, and their Coulomb potential can trap electrons. Conduction occurs through the field-assisted thermal excitation of electrons between the traps. For Poole–Frenkel emission, the barrier height B of the trapped electron is given by the trapped energy relative to the edge of the conduction band. Like Schottky emission, the barrier height can be reduced by applying an electric field (Chen et al., 2006; Mishra et al., 2018).

$E^{1/2}$ Models

Allers (2004) first proposed an $E^{1/2}$ dielectric reliability model for metal–SiN–metal capacitors. Subsequently, two models that predict the dependence of TTF on the square root of the electric field in low-k dielectrics are reported. Unlike Lloyd's model and the thermochemical model, which involve inherent failure mechanisms, the $E^{1/2}$ model for low-k dielectrics involves Cu migration into the low-k dielectric before breakdown.

Two research teams put forward different views on this model. According to the research of Suzumura et al. (2006), they believe that a dielectric cap layer is deposited on the copper interconnect and the internal low-k dielectric. The cover layer provides a leakage path from one Cu conductor to an adjacent conductor. It causes electrons at the cathode to undergo thermally assisted tunneling until they reach the (positive) anode. Then the leakage mechanism changes from a Poole–Frenkel to an F-N mechanism, and the leakage current will further increase over time (McPherson & Mogul, 2004).

(Chen et al., 2006) believe that electrons are injected from the cathode into the low-k dielectric through Schottky emission. They also propose two mechanisms by which the eventual failure may occur. In the first case, Cu^+ ions combine with electrons and become neutral Cu atoms. However, this assumption is inconsistent with the results of Lloyd et al. (2005). In the second case, the Cu atoms, by virtue of their size, can increase the local strain dielectric in low-k values and promote bond rupture.

E^2 Model

The E^2 model was proposed by Achanta et al. (2007). Like the $E^{1/2}$ model, it assumes that the diffusion and drift of Cu^+ ions play a major role in the TDDB of low-k dielectrics. Instead of adding F-N tunneling, it can be assumed that the enhanced electric field at the cathode will eventually lead to bond rupture at the defect in the dielectric, as in the thermochemical model (Wong, 2012).

However, it is found that if the exponential function in the thermochemical model is used without modification, the measured TTF cannot be fitted by a set of fitting parameters only through experimental data collected from test structures of different structures.

The advantage of this model is that when this equation is applied to experimental data collected at different temperatures, all data can be satisfactorily fitted with only one set of fitting parameters (McPherson & Mogul, 2004).

F.2.8.1.3 Negative-Bias Temperature Instability (NBTI)

Although there are still many controversies about the physical mechanism behind the degradation and the exact cause of bias temperature instability, it is believed that two effects are at play: trapping positively charged holes and generating interface states. It has been found that a broad consensus is that when a MOSFET is stressed with a constant gate voltage at an elevated temperature, positive charges will accumulate in the SiO₂/Si interface or gate oxide layer. This charge leads to the deterioration of transistor parameters (Enter, 2007).

The current mainstream view is that the mechanism of NBTI is the degradation of Si-H bonds destroyed by chemical reactions with high-energy holes on the SiO₂/Si surface. The preexisting traps located in the dielectric body are filled with holes from the pMOS channel. When the stress voltage is removed, these wells can be emptied. When interface traps are generated, and when the pMOS device is biased to the “on” state when biased with a negative gate voltage, these interface states become positively charged. After the stress is removed, some interface states may fail (De et al., 2019).

Several models have been developed to characterize the effects of NBTI. These are listed and explained in subsequent subsections.

Degradation Model

In this model, the generation of interface traps is based on the reactive diffusion model (i.e., the rupture of the Si-H bond at the Si/SiON interface caused by the inversion hole and the subsequent hydrogen diffusion). Afterward, the preexisting bulk oxide traps are charged and reach saturation after a long time. This generates a large number of oxide traps and can cause TDDB failure (De et al., 2019). Ultimately, the overall degradation is equal to the sum of these three components.

The time dependence of the threshold voltage shift is found to follow a power-law model. NBTI degradation is thermally activated and sensitive to temperature. An Arrhenius relationship models the temperature dependence of NBTI. The activation energy appears to be highly sensitive to the type of potentially reactive species and the type of oxidation method used. An improved model is proposed after the simple power-law model (Bernstein, 2014).

Reaction–Diffusion (R-D) Model

The R-D model is the forerunner of the NBTI description. Jeppson & Svensson (1977) first proposed it, and it can reproduce the time evolution of device degradation due to negative-bias temperature stress, allowing a wide range of measurements. The model describes equipment degradation as a combination of two effects. First, a field-related electrochemical reaction occurs at the SiO₂/Si interface. The electrically inert passivated silicon dangling bond Si-H is destroyed. Second, the model describes the migration of hydrogen species from the interface to the dielectric. Likewise, the reverse process is also possible: transport the diffused hydrogen species back to the interface and passivate the Si dangling bonds again. For each generated interface trap, a hydrogen atom is released.

For the stress stage, the solution of the R-D model can be divided into five different states. Their difference lies in the different time indexes n of degradation. In the modeling approach, the species N_x is separated into two distinct contributions: the conducting, N_c , and trapped, N_t , particles. The trapped particles are distributed in energy where the density at a trap energy-level E_t is given as $\rho(x, E_t, t)$. The trapped particles do not contribute to the transport. When the stress is relieved, the generation of new hydrogen from the interface state will also stop. As a result, the device can restore a certain degree of performance because the hydrogen located near the interface state will return to the removed dangling bonds. According to this model, the generation rate of interface traps initially depends on the dissociation rate of the Si-H bond and the local self-annealing process (Enter, 2007; Schuster, 2006).

Using solution variables of the semiconductor equations, the NBTI model can be applied to arbitrary device geometries.

Tsetseris' Model

Tsetseris et al. (2005) used the Vienna ab initio simulation package (VASP) to study the subject of bias temperature instability (BTI) at the atomic level. They proposed a proton-based dissociation model to describe the rupture of Si-H bonds at the silicon-dielectric interface induced by BTI. This model can explain the different susceptibility of n-channel and p-channel MOSFETs to positive- and negative-bias stress.

pMOS negative bias: The dissociation energy of P-H in the depletion region is significantly reduced, and the positively charged protons accelerate toward the interface.

pMOS positive bias: Because no depletion layer is formed, the dissociation energy of P-H is very high. Therefore, degradation is significantly suppressed.

n-channel-type metal-oxide semiconductor (nMOS): In p-type substrates, there are B-H bonds instead of P-H bonds. However, even in the depletion layer, the dissociation activation energy of these complexes is much greater than that of the P-H complex, resulting in less hydrogen available to degrade the interface.

Lifetime Model

NBTI failure is defined as reaching the threshold. Based on the degraded model such as the previous model, the NBTI life can be expressed as a combination of equations for the field and voltage (Bernstein, 2014).

F.2.8.2 Ensuring Confidence in Parts

The objective of this section is to provide a workflow for identifying part reliability information in order to evaluate each part's ability to withstand ≥ 50 years of interstellar space travel. This section is an approach for ultimately identifying the parts for application that maximize part reliability with minimized costs of implementation and testing. Figure F-44 shows the overall workflow for identifying the best parts for application.

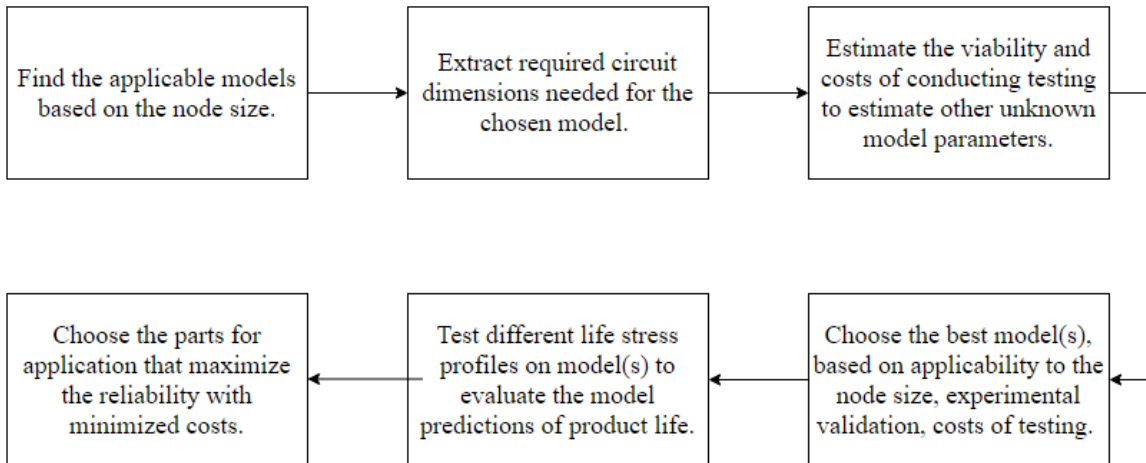


Figure F-44. Workflow for identifying the most reliable part for application. (Image credit: Johns Hopkins Applied Physics Laboratory.)

The workflow in Figure F-44 is an application of IEEE Standard 1413, section 5.4.1, which states the process for completing stress and damage modeling for reliability prediction. This process states that for a given system, the first step is to identify the geometry, the material properties, and the variability of these properties intrinsic to the system. With this in mind, the next step is to estimate and identify a life-cycle profile or a series of profiles to which the system will be subjected. After this, the next objective is to use failure modes, mechanisms, and effects analysis to identify potential failure sites and critical failure mechanisms based on the system properties and application conditions. Using the results of failure modes, mechanisms, and effects analysis (FMMEA), the next step is to identify the specific failure models needed and then ultimately calculate different reliability metrics, such as TTF and other metrics (Figure F-45).

F.2.8.2.1 Description of Required Information

Deconstructing the workflow in Figure F-44, without accounting for the costs of experimentation to identify unknown model parameters, Figure F-45 details the inputs and analysis process needed for garnering reliability information (e.g., TTF distributions, uncertainty distributions).

In terms of inputs, the workflow will need all information on the estimated application use conditions, part specifications for each tested part, and model constants for each part corresponding to the different failure models. All of this information will then be used to first evaluate different failure mechanisms to identify the most critical of them. The decision of criticality will come using information garnered from a survey of previous research in industry and academia or by using FMMEA tables. Next, the input application conditions, part specifications, and modeling information will be input into the failure models that correspond to the most critical failure mechanisms. Using these failure models, the next step is to calculate and evaluate the desired reliability information such as TTF and time-dependent failure rates with associated uncertainty distributions.

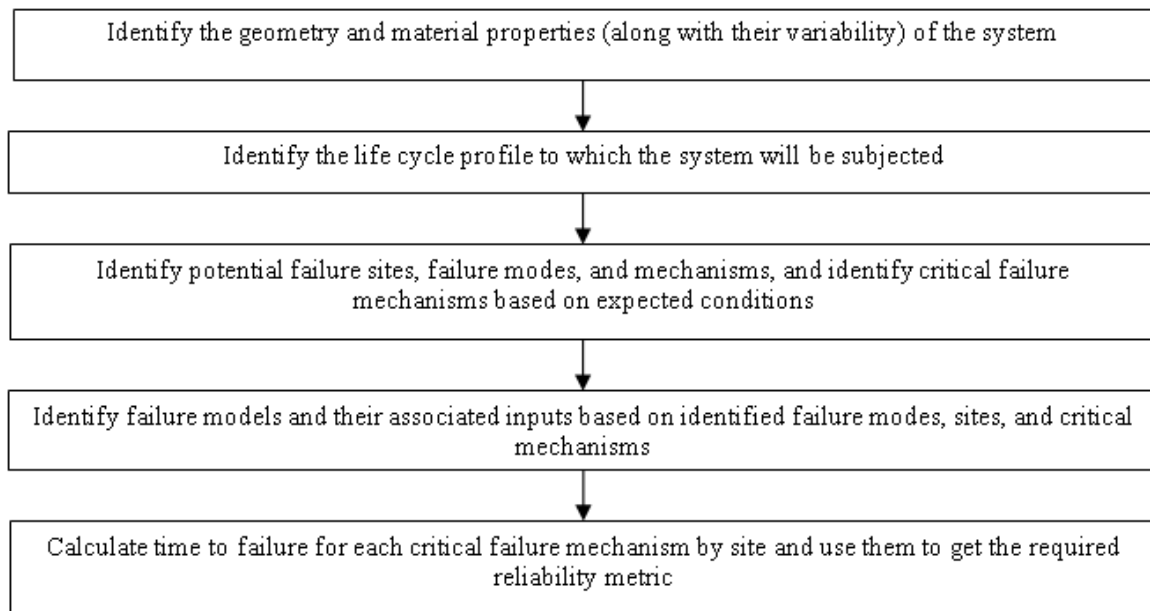


Figure F-45. Process for completing stress and damage modeling for reliability prediction. (From Smith et al. (2021); reprinted with permission from AIAA.)

F.2.8.2.2 Methods for Obtaining Reliability Information

To obtain estimations of TTF for different application conditions and to analyze the uncertainty of product survival, several types of information are required, including information about the parts to be used, different failure models, and application conditions.

Gathering Information about Different Parts

To gather information about each part that is intended for application, the researchers will investigate two main sources of information. These two sources are the information directly supplied by the manufacturer and estimations of characteristics using related parts from a survey of literature. The Automotive Electronics Council (AEC) requires several wearout failure mechanisms to be amply studied and documented before product qualification occurs, and this documentation is a significant source of information. Additionally, IPC Standard 1752/1752A requires companies within a supply chain to provide information on all the materials that make up a given product. This information may broadly include information on the supplier and the manufacturing process, the material declaration required by the Restriction of Hazardous Substances (RoHS) Directive, and a homogenous material composition declaration for electronic products. Manufacturer-provided documentation that can supply important part characteristics includes datasheets, qualification reports, product change notifications, application notes, part webpages, and reliability reports.

From the datasheets, one can glean information about different part ratings (e.g., threshold voltage, maximum substrate current) and environmental ratings (e.g., temperature bounds, humidity). Qualification reports may contain data about different part dimensions (e.g., dielectric oxide thickness, node size) and a report on product testing and levels of testing. Product change

notifications may include the material composition and information about the part structure/package. Application notes may have recommendations for application conditions and information about the most common failure mechanisms. Part webpages may include relevant information such as the node size and part classification if no other sources of information are available. Finally, any available reliability reports would provide failure data for the product (e.g., mean time between failures, the failure in time).

For additional information, or for information in the absence of manufacturer-provided data, the next step is to survey existing literature. The literature that may be examined might include a survey of industry standards by different entities that regulate the product manufacturing and characteristics. These organizations may include IEEE, IPC, AEC, and other groups. The different standards may provide the researchers with estimations of the material type and characteristics, qualification testing levels, and information on the required application conditions and limits the type of part in question must be able to endure. An alternative source of information may be a survey of research documents by different entities within industry or academia. These research documents may contain information about different model parameter/constants for failure modeling and information about the activation energy or conditions needed for failure mechanisms to propagate.

If no part-specific information can be found for a given part, the next step is to work backward from the year of part introduction to industry. Following Moore's Law node size scaling, which states that a transistor node size halves every 2 years, using the year of introduction (adjusted by 2 years for design and development time), one can estimate the transistor node size. By surveying similar products from the same year of introduction, one can estimate the product characteristics and use them in further failure analysis. Figure F-46 shows an example of this method. Additionally, by looking at research papers from the year of introduction, one can extract information on the state of the art of product modeling at that time.

Gathering Information about Failure Models

To identify relevant failure models, there are a few sources of information to look in. One of the main sources is different standards and handbooks published by many different organizations. These may include IEEE 1413, the MIL-HDBK-217 handbook, and other sources. Another source of information is journal articles or review papers published in *Microelectronics Reliability* (a journal published by Elsevier), *IEEE Transactions on Reliability*, and others. The journal articles will look at individual state-of-the-art research and studies, while the review papers will give an overarching timeline for the evolution of different research and studies.

F.2.8.2.3 Example of Modeling Failure with Researched Part Parameters

Using the information gathered from analyzing manufacturer-provided documentation, standards, research papers, and other sources, different model parameters can be implemented into a model to solve for TTF. An example of this is estimating the TTF of a failure mechanism model of TDDB. The equation for TTF is as follows:

$$TTF = A_0 \exp\left(-\gamma \frac{V_g}{t_{ox}}\right) \exp\left(\frac{E_{aa}}{kT_j}\right) \quad (5)$$

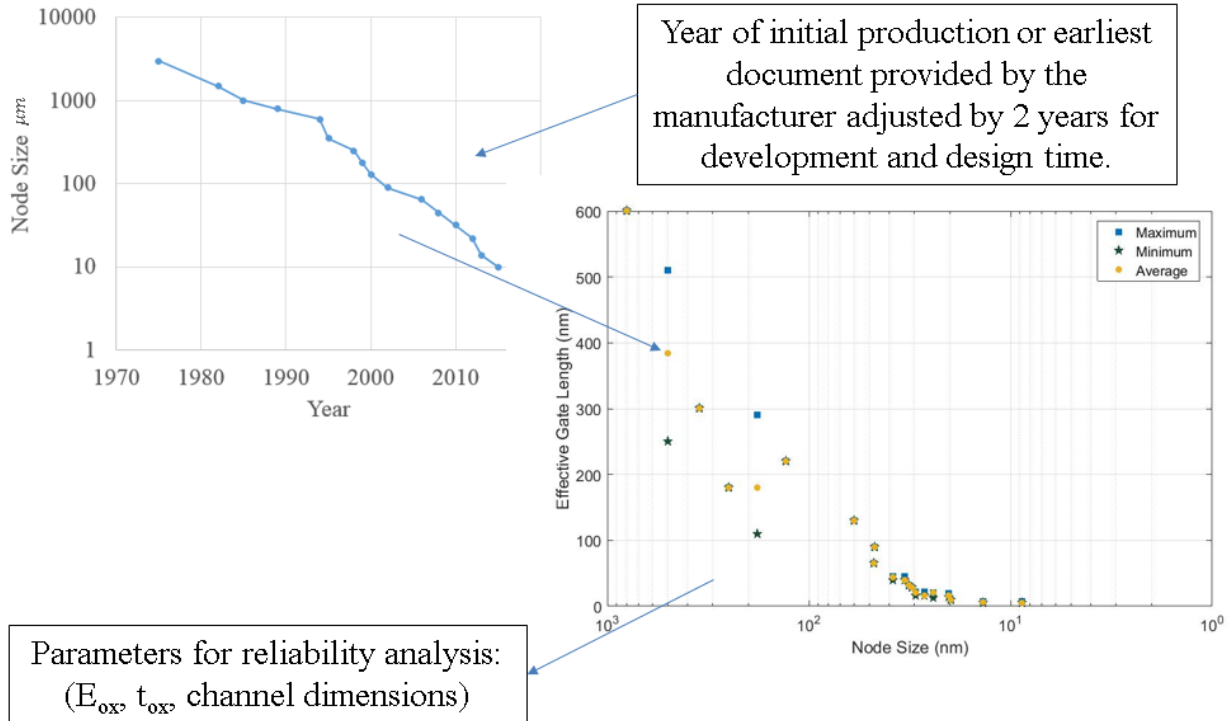


Figure F-46. Using Moore's Law scaling to estimate node size and, in due course, estimate the effective gate length for the transistor. (Image credit: Johns Hopkins Applied Physics Laboratory.)

Table F-10 lists all the parameters, their function or purpose, and the dependency/range for each parameter.

Table F-9. List of parameters needed to solve for time to failure in Equation 1, with the source information and estimated range of values of the parameter.

Parameter	Function or Purpose	Dependency/Range
A_0	Scaling factor constant	Part-specific
γ	Electric field constant	$0 < \gamma < 2^*$
V_g	Gate threshold voltage	Application conditions
t_{ox}	Oxide thickness layer	Part parameter
E_{aa}	Apparent activation energy for TDDDB mechanism	$0.3 < E_{aa} < .6^*$
T_j	Junction temperature	Application conditions

*Model constant value ranges come from JEP122H standard on wearout failure mechanism models.

F.2.8.2.4 Method for Evaluating Parts for 50-Year Life Cycles

After identification of failure models for different parts in different application conditions, the next step is to evaluate the part's ability to withstand 50 years of required operation and life cycling without failure. Because the different failure models may not cover up to 50 years of operation in their predictions, certain safeguards may be required to attempt to account for different effects or modes of operation or application conditions that have thus far not been able to be accounted for.

One example is implementing redundant systems in the integrated circuit that begin to work once the previous steps in the circuit fail. Using the reliability information for systems in operation during exposure to application conditions, the required number of redundant systems can be included. Further minimization of the required number of redundant systems comes from analyzing a single system that undergoes application conditions but not operation. It may also become necessary to investigate any potential unaccounted for integrated circuit failure sites and mechanisms that may arise from making the integrated circuit more complex.

Another example is to derate different products so that products that are rated to withstand much tougher application conditions get implemented into the system. “Tougher” products may be able to withstand variabilities in operation and application and be able to fully complete the 50-year interstellar journey with a greater certainty. However, the use of derated products may require additional FMMEA and failure-model identification to ensure that other potentially critical failure mechanisms would not induce early failure.

A final example is to conduct accelerated life testing on the chosen parts to fully estimate the reliability metrics over the desired 50 years of operation. This accelerated life testing may be conducted on the parts themselves, on the redundant systems, or on the derated parts. By taking the estimated failure models, extrapolating them out to 50 years of operation, and comparing them to accelerated life tests on the different products, the discrepancies between the extrapolated data and accelerated test data can be addressed and accounted for in the failure models.

Each of the above approaches for evaluating parts for 50 years of operation comes with its own intrinsic costs for redesign, experimentation, and implementation. Based on the part or parts in question, how viable the reliability metrics predictions may be for extrapolating 50 years of operation, and how complex or compulsory different experiments are, the parts will therefore be chosen for further testing and potential implementation.

F.2.9 Material Longevity

Much of the reliability discussion focused on the failure of parts. In tandem is the need to focus on materials usage and their potential degradation over time and ultimate longevity.

F.2.9.1 Interstellar Environment

Despite the long transit time, one mitigating factor for an interstellar mission is the relatively benign conditions during most of its operation. The majority of the Interstellar Probe mission does not involve the extreme temperatures of the Sun or Venus. The spacecraft will not orbit a planet, where it might regularly encounter magnetospheric plasmas, atomic oxygen, or orbital debris. The vast majority of its time will be spent far from planetary bodies, where conditions do not become extreme by definition. However, the launch trajectory necessarily involves a gravity assist around Jupiter. The spacecraft will therefore experience high radiation conditions for at least part of its life cycle, but the duration is small relative to the overall length of the mission.

F.2.9.1.1 Radiation

Some of the most intense radiation in our solar system occurs near the Sun and at various locations around the planets. Jupiter and Saturn have particularly intense magnetospheric plasmas. Far from the Sun and its orbiting planets, an interstellar probe will experience a relatively benign radiation environment for the majority of its trajectory.

The largest source of radiation is solar photons. These range in wavelength roughly from 0.1 to 3 μm . In terms of material interactions, the largest effect is simple absorption and conversion into heat. However, the more energetic photons in the ultraviolet band (>4 eV) excite chemical changes in organic molecules, as will be described later.

Solar wind is the second largest contribution. It consists of ions with a composition consistent with the Sun. The positively charged ions are accompanied by a corresponding flux of electrons with similar thermal energies. Like solar photons, they spread outward from the Sun, decaying in flux with the inverse square of distance.

F.2.9.1.2 Thermal Environment

Far from the Sun, the thermal management of an interstellar probe is mostly focused on internal heat sources. It does not develop large thermal gradients, nor does it need to contend with a heat source that varies in strength and location with time. Despite the lack of sunlight, the waste heat from the RTGs and electronics is sufficient to maintain the spacecraft between 10°C and 30°C. The spacecraft would be covered in multiple layers of aluminized Kapton, which insulate like a solar blanket. They minimize the loss of heat through passive radiation to space. New Horizons, for example, has an automated heating system that monitors power levels to ensure that the electronics are dissipating enough power to maintain safe temperatures. Small heaters placed strategically around the spacecraft compensate if the heat emitted by the electronics is insufficient. An interstellar probe would likely take a similar approach.

F.2.9.2 Material Degradation Mechanisms

Many degradation mechanisms exist, because of the environments discussed above. The mechanisms also differ based on the material and its use. Benkoski & Gerger (2021) discuss these mechanisms in detail.

F.2.9.3 Implications of Materials for System Failure

Table F-11 provides a summary of the consequences of the various material failures.

F.2.9.4 System Test Requirements

F.2.9.4.1 Thermal Acceleration

Materials reliability at long times is typically predicted through a combination of modeling and experimental validation with accelerated testing. Unfortunately, thermal acceleration is one of the few accepted methods for experimentally simulating long times (Blanks, 1973). In addition, the level of thermal acceleration has limits. Properties unrelated to physical aging, such as melting or thermally induced changes in failure mechanism, constrain the maximum aging temperature.

Table F-10. Materials reliability factors for materials on an interstellar probe.

Property	Long-Duration Consequence	Risk	Mitigation
Fatigue crack propagation	Additional order of magnitude of cycles	The number of thermal cycles is primarily associated with operation of electronics	Likely not needed
Fracture toughness	Additional order of magnitude of radiation dose	Loss of ductility may exacerbate fatigue crack growth	Choose materials with lower initial degrees of hardening
Stiction	Long time near room temperature	Room-temperature diffusion could cause cold welds in vacuum at long times	Avoid actuating mechanisms and metal-metal contact under compression
Single-event upset	Low flux of cosmic radiation for much longer times	Greater number of soft errors	Standard mitigations sufficient; long data transfers must not be interrupted
Single-event latch-up	Low flux of cosmic radiation for much longer times	Greater likelihood of latch-up	Higher stringency on part selection
Radiation-induced cracking	High total ionizing dose by end of mission	Polymers will shrink in volume, become brittle, and crack	Rely more heavily on epoxies, polyimides, and silicones

Another limitation of thermally accelerated lifetime testing is that different mechanisms are not accelerated equally. Because of differences in activation energy, a given rise in temperature can produce an effectively large acceleration for one mechanism and a minor acceleration for another (Stewart, 1969). Thermal acceleration is therefore biased toward failure mechanisms with higher activation energies.

To simulate material degradation during a 50-year mission, it is probably necessary to abstract the testing away from the primary failure mechanism toward more fundamental processes, such as solid-state diffusion. Diffusion is well understood, and it can be predicted to a high degree of accuracy at long times, such as 50 years. Diffusion also has a well understood relationship with grain growth, dislocation removal, precipitation, sintering, and other forms of microstructural evolution. Because these changes in microstructure also have a well-understood relationship with material properties and failure mechanisms, one can then overcome the limits of thermal acceleration and extrapolate to longer times by modeling from first principles.

F.2.9.4.2 Mechanical Acceleration

To accelerate fatigue failure, one must increase the amplitude of the stress and/or the frequency. For a 50-year mission such as the Interstellar Probe, cyclic stresses are expected to be relatively small. Their magnitude provides an opportunity to increase the amplitude without entering a low-cycle fatigue regime where plastic deformation controls the crack growth rate. Metallic and ceramic materials are not especially rate sensitive, so large cycling rates (10^2 – 10^4 Hz) can be applied without necessarily affecting the measured fatigue life. Testing to long fatigue lives ($>10^8$ cycles) can therefore be accomplished in days or weeks (Boyer, 1985). For polymeric materials, the strain rate must be chosen more carefully. Because of the aforementioned time-temperature superposition, a higher test frequency is equivalent to a lower test temperature from the perspective of the polymer's mechanical properties. In particular, polymers become more brittle at lower temperatures, and a higher strain rate may artificially decrease the measured fatigue life.

Fortunately, polymers are generally not used as primary mechanical structures on a spacecraft. The main areas of concern on the Interstellar Probe are interfacial failure and delamination.

Fatigue testing of interfaces is typically accomplished through thermal cycling. Here, interfacial stresses arise from mismatch between the coefficients of thermal expansion. The main issue here is that thermal cycling rates are limited by several factors: thermal mass, thermal conduction, and the maximum ramp rate of the oven. Thermal cycling is two to three orders of magnitude slower than mechanical testing, and only if the change in temperature is relatively small. One factor working in favor of the Interstellar Probe is that these conditions are generally true. A realistic thermal cycle of the Interstellar Probe would not involve cryogenic temperatures. Such a requirement would have quickly become impractical because of the large quantities of liquid nitrogen involved. Instead, thermal cycling occurring on the Interstellar Probe is caused by ohmic heating that occurs through natural variations in electric load.

The mitigation for the low cycle frequency is parallelization. Many interfaces can be tested in parallel by, for example, applying a large set of adhesives to a large aluminum panel. However, many mechanical adhesives will not be subject to thermal or mechanical cycling on the Interstellar Probe. More relevant would be the testing of materials used in close proximity to electrical components. Here it may be advantageous to use ohmic heating of resistors to more rapidly test the fatigue resistance of solder joints, metallic plating, epoxy underfills, wire insulation, encapsulants, and so forth. To speed up the process, one may consider performing the test under forced convection in an inert atmosphere, such as argon. Thus, the elevated temperatures caused by ohmic heating can more quickly return to baseline levels.

F.2.9.4.3 Radiation Acceleration

Because of the relatively modest rates of exposure to ionizing radiation, the total ionizing dose (TID) on the Interstellar Probe is manageable, even after 50 years. Testing regimens would be similar to past probes that have operated in the Jovian magnetosphere or Van Allen Belt. More problematic is the exposure to cosmic rays. The issue is not so much the energy dose but the fact that the probability of single-event effects (SEEs) increases linearly with time. The increased probability increases the need for single-event transient (SET) and single-event latch-up (SEL) screening across a wider range of electronic components.

Heavy ion test facilities routinely struggle to keep pace with demand. Even under normal conditions, heavy ion tests are scheduled many months in advance, and the full request for time is rarely met. This chronic undersupply poses a high risk for program delays. Coupled with these scheduling issues is the greater probability of a test failure by virtue of the greater number of parts requiring testing. Consider how a part yielding unacceptable heavy ion test results needs to be removed from the current circuit design, which results in circuit board redesign and potentially retesting of the new parts and boards.

F.2.9.5 Conclusions

The relatively benign operating conditions of the Interstellar Probe offset some of the greatest material reliability challenges of a 50-year mission. In essence, the length of time is an order of

magnitude larger than for most standard planetary missions. For many material degradation mechanisms, this longer duration manifests itself as a tenfold increase in the probability or a tenfold progression of degradation. The linear relationship is particularly true of radiation, where the dose is equal to the product of flux and time. The radiation environment is not as extreme as one might find in magnetospheric plasmas, so the overall radiation dose after 50 years is still lower than that for the upcoming Europa Clipper mission.

Mechanical processes such as fatigue are analogous to radiation in the sense that the number of cycles is more-or-less tenfold greater than for a typical planetary mission. Here again, the amplitude of mechanical stresses due to thermal cycling or actuation is small relative to that experienced by many heritage designs. The smaller stresses somewhat offset the larger number of cycles.

The mechanisms having the greatest number of unknowns are thermal processes. These are also the most difficult processes to test through accelerated experiments.

F.2.10 Radioisotope Thermoelectric Generator Longevity

This section explores the need for RPS designs that are intended to last much longer than the current requirement of 14 years (17 years after fueling) and explores the historical record for actual versus design lifetimes to show the feasibility of building a long-lasting RPS. In addition to examining the historical record, a power analysis was performed using a current RTG performance model of the General Purpose Heat Source RTG (GPHS-RTG) using the JPL Lifetime Performance Prediction (LPP) tool to make top-level inferences about power output at end of mission; it discusses how reliability engineering and testing methods can be brought to bear to increase confidence in delivering sufficient power at end of mission.

With growing demand to pursue longer-lasting missions, we examined all U.S. missions that flew RPSs to determine how long they lasted. We also investigated the power output at EOL through current performance models and historical power curves, extending them to 50 years.

F.2.10.1 Historical Lifetime Data Analysis

This section examines the historical record of RPSs and provides a statistical analysis for probability of success and lifetime. Table F-12 is a listing of all RPS missions used in the data set. The list is based on a NASA compilation (Abelson et al., 2005), with the mission information provided from the SpaceTrak database (Fuller, 2020). For each table entry, mission name, type of RPS, and quantity are provided. The dates listed are the mission launch date and the date of last contact showing the RPS as operational. For missions that are still active, no end date is given. Mission design and RPS design life are provided separately. The “RPS Failure” column indicates an RPS failing before the end of the RPS design life. Note: No nuclear heater units are included.

Table F-11. Listing of radioisotope system that have flown.

Mission Name (No. of Units)	Power Source	Launch Date	RPS End Date	Mission Design Life (years)	RPS Design Life* (years)	RPS Anomaly	RPS Failure
Transit 4A	SNAP-3B	06/29/1961	07/01/1962	0.05	5.00		
Transit 4B	SNAP-3B	11/15/1961	08/02/1962	0.05	5.00	X	RTG failure in June
Transit 5BN-1	SNAP-9A	09/28/1963	12/22/1963	0.05	5.00		
Transit 5BN-2	SNAP-9A	12/05/1963	11/01/1964	0.05	5.00		
Transit 5BN-3	SNAP-9A	04/21/1964	04/21/1964	0.05	5.00	n/a	Launch failure
SNAPSHOT	SNAP-10A	04/03/1965	05/16/1965	1.00	1.00		SNAP lasted 43 days
Nimbus B-1 (2)	SNAP-19	05/18/1968				n/a	Launch failure
Nimbus III (2)	SNAP-19	04/14/1969	01/22/1972	2.00	1.00		SNAP salvaged from NIMBUS B
Apollo 12 Apollo Lunar Surface Experiments Package (ALSEP)	SNAP-27	11/14/1969	07/01/1977	2.00	2.00		
Apollo 13 ALSEP	SNAP-27	04/11/1970				n/a	Device did not reach the moon
Apollo 14 ALSEP	SNAP-27	01/31/1971	07/01/1977	2.00	2.00		
Apollo 15 ALSEP	SNAP-27	07/26/1971	07/01/1977	2.00	2.00		
Pioneer 10 (4)	SNAP-19	03/03/1972	01/23/2003	7.00	3.00		
Apollo 16 ALSEP	SNAP-27	04/16/1972	07/01/1977	2.00	2.00		
Triad 1	TRANSIT-RTG	09/02/1972	07/01/2006	1.00	5.00		Nuclear Regulatory Commission indicates RTG still operational as of 2006
Apollo 17 ALSEP	SNAP-27	12/07/1972	07/01/1977	2.00	2.00		
Pioneer 11 (4)	SNAP-19	04/06/1973	11/24/1995	7.00	3.00		
Viking 1 lander (2)	SNAP-19	08/20/1975	11/13/1982	1.25	1.25		RPS design for 1 year of travel + 90 days of operations
Viking 2 lander (2)	SNAP-19	09/09/1975	04/12/1980	1.25	1.25		RPS design for 1 year of travel + 90 days of operations
Lincoln Experimental Satellite (LES) 8 (2)	MHW-RTG	03/15/1976	07/01/2004	3.00	5.00		
LES 9 (2)	MHW-RTG	03/15/1976	05/20/2020	3.00	5.00		
Voyager 2	MHW-RTG	08/20/1977		4.50	5.00		
Voyager 1	MHW-RTG	09/05/1977		4.50	5.00		
Galileo (2)	GPHS-RTG	10/18/1989	09/21/2003	8.00	5.00		

Mission Name (No. of Units)	Power Source	Launch Date	RPS End Date	Mission Design Life (years)	RPS Design Life* (years)	RPS Anomaly	RPS Failure
Ulysses	GPHS-RTG	10/06/1990	06/30/2009	5.00	5.00		
Cassini (3)	GPHS-RTG	10/15/1997	09/15/2017	11.00	5.00		
New Horizons	GPHS-RTG	01/19/2006		15.00	5.00		
Mars Science Laboratory (MSL)/ Curiosity Rover	MMRTG	11/26/2011	12/08/2014	2.50	14.00	X	Battle short first used on sol 816
Perseverance Rover	MMRTG	07/30/2020		2.50	14.00		

*RPS design life information found in G. L. Bennett (1995).

GPHS-RTG, General Purpose Heat Source Radioisotope Thermoelectric Generator; MHW-RTG, Multihundred-Watt Radioisotope Thermoelectric Generator.

Of the 29 missions listed, 3 failed to become operational (Transit 5BN-3 and Nimbus B-1 failed to reach orbit, while Apollo 13 ALSEP failed to reach the moon) and are removed from the analysis. This represents a total of 40 RPS units.

Some entries appear as mission data, but because we are interested in how long the RPS equipment lasted, some of the end dates are dates of last contact and not mission end. For example, routine contact with Pioneer 10 ended in March 1997, but last documented contact was January 2007. Also, the Triad mission ended in 1972, but signals from the spacecraft indicate that the RTG was still operational as of 2006.

Owing to the small sample sizes, a traditional statistical analysis is augmented with a Bayesian analysis to show the uncertainty distributions in the results.

F.2.10.1.1 Probability of Success

RPSs have an outstanding record for producing power for space missions. Of the 40 missions listed, all fulfilled their mission duration as designed. All but two units were working at the time the mission ended. The reasons for missions ending are attributed to other systems or the spacecraft being retired after successful extended missions. Two units had significant anomalies and are considered to have failed for this paper; however, both anomalies presented after the initial mission objectives were met but before the end of the RPS design life. Although some ambiguity as to the nature of the failures exists, we consider them as failed to provide a worst-case view of the data. The two anomalies are Transit 4B and Mars Science Laboratory (MSL)/Curiosity.

After meeting all its mission objectives, the SNAP-3B system power intermittently dropped to zero for several days and then failed completely in June 1962, 7 months after launch. It is believed that either the RPS DC/DC converter failed or the thermoelectric converters in the power unit failed (Hoffman, 2010).

On mission sol 456, MSL engineering operations staff observed an unexpected shift in bus balance voltage telemetry; the balance voltage shifted from its nominal ~11 V to ~4 V. The team has deduced

that an internal low impedance short on the MMRTG is the only credible root cause of the anomaly. This short spontaneously cleared on sol 461 when the rover was asleep. The MSL team has learned to identify an internal MMRTG short and explicitly clear a persistent soft short, “invoking a battle short” (Wood et al., 2016). The first time this procedure was used (sol 816) is considered the time of the anomaly for this paper. Again, this is a worst-case assumption but is considered because the method to clear it was discovered by happenstance elsewhere in the instrument suite and was not part of the power design. Over time, the frequency of shifts has increased.

With no mission-ending failures, it would be tempting to declare 100% reliability of the systems. This is inaccurate as a predictor for these missions and especially for a mission of 50 years. We now incorporate the two RPS failures to present as a bounding case. Using Bayesian updating, probability of success metrics are computed (see Table F-13).

Table F-12. Probability of success metrics.

	Units	Fails before End of System Design Life	Mean	5th	95th
All	44	2	0.939	0.879	0.981
SNAP	28	1	0.944	0.877	0.988
RTG	16	1	0.922	0.829	0.982

*Prior: Beta distribution with 5th = 0.75 and 95th = 0.99.

F.2.10.1.2 Mission Design Life versus Actual Mission Duration

Computing how long the systems last is more difficult because all but two units were working at the time the missions ended. Figure F-47 shows the RPS design life versus actual life. The dashed line is where design life equals mission duration. The markers represent the missions, with green being active missions and red being the two anomalies. Note that the majority of missions are above the dashed line, indicating that the RPSs are lasting longer than their design lives.

F.2.10.1.3 Lifetime Assessment

If one were to take the average mission duration (16.9 years) as the metric for how long these systems can last, that would not tell the correct story because all but two systems were operational at the end of the mission. A statistical analysis technique called a survival analysis is often used when some of the data are right censored (operation halted before a failure), but this technique struggles to determine the mean life. When the analysis is applied to the subpopulations of SNAP and RTG systems, the difficulty is magnified with only one failure for each. A Bayesian analysis is used to update a prior belief with the observations available to provide a distribution of lifetime.

The life model used is a Weibull distribution. It has two defining parameters: β , which defines the shape indicating infant mortality or wearout, and η , which is the “characteristic life.” Both parameters are unknown and are what the Bayesian analysis will solve for. Our prior for each is defined as lognormal distributions with 5th and 95th percentiles of:

β : between 0.5 and 5

η : between 10 and 75 years

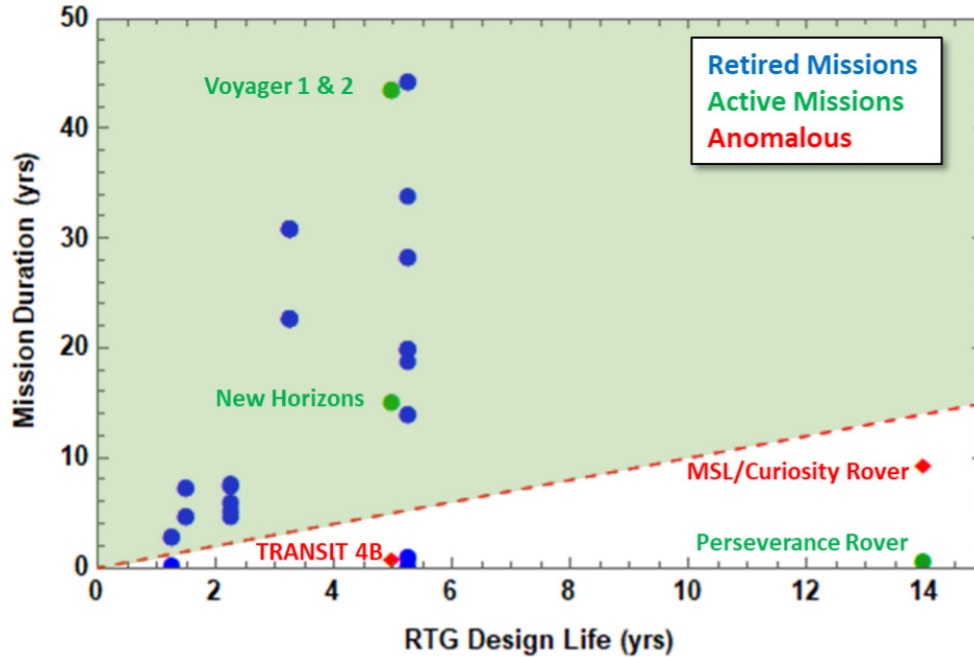


Figure F-47. RPS systems last longer than their intended design lives. (Image credit: Johns Hopkins Applied Physics Laboratory.)

Updating with all the data produces a distribution of TTF (see Figure F-48). The resulting mean lifetime is just over 100 years and a lower 5th percentile around 50 years.

F.2.10.2 Radioisotope Thermoelectric Generator Reliability

While statistical assessments of past systems show a long life is possible, much work needs to be done to understand how the system degrades over time and how various time-dependent failure mechanisms behave. A PoF and probabilistic approach are needed. Two activities are currently ongoing supporting reliability analysis. Risk-informed life testing (RILT) is a physics-based assessment to model time-dependent failure mechanisms (Ndu & Smith, 2018). The RPS office is currently constructing a reliability framework to apply to all RPS technologies to inform the probability of delivering advertised power at EOL.

F.2.10.3 Time-Dependent Performance Analysis

LPP is a capability developed at JPL that is used to model thermoelectric conversion physics in RTGs for a variety of missions and storage environments over long durations. Having the ability to accurately model and predict performance is critical in mission and operations planning in order to optimize the science return during mission activities. LPP accepts several types of inputs to perform predictions in order to achieve the level of accuracy these missions require. Features unique to each RTG such as thermoelectric and insulation material properties as a function of time and temperature coupled with mission characteristics such as fin root temperature and load voltage allow LPP to output results of interest such as power, internal resistance, and interface temperatures. Experimentally collected data that are of importance to the long-term performance predictions for RTGs include degradation effects of key interfaces and insulation (i.e., electrical and

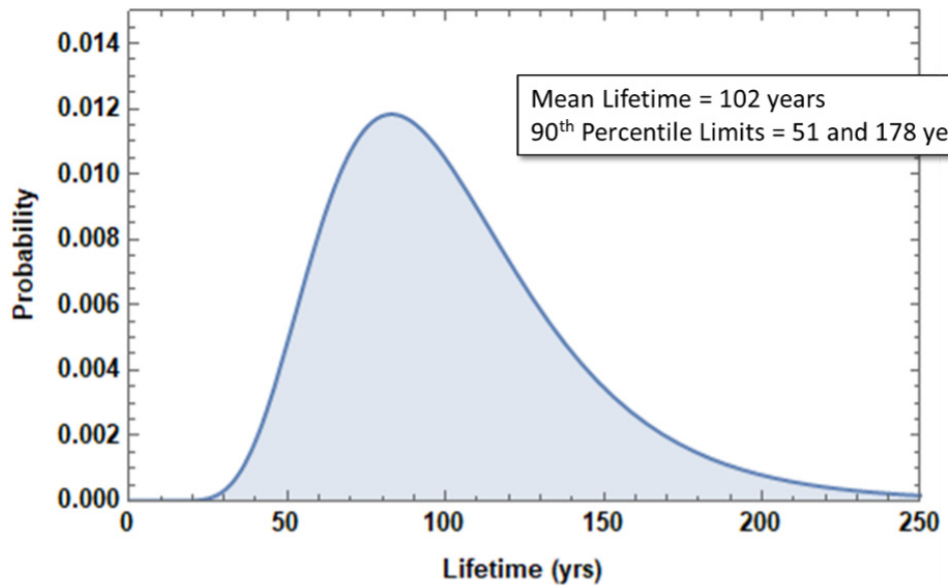


Figure F-48. Bayesian assessment shows uncertainty of both Weibull distribution parameters. (Image credit: Johns Hopkins Applied Physics Laboratory.)

thermal contact resistance of hot side interfaces and changes to insulation thermal conductivity). By relying on large amounts of relevant test data, LPP can accurately match measured results gathered from flagship missions such as the MMRTG on Curiosity and Perseverance.

LPP was used to examine the power output over time and estimate the point at which the unit would no longer produce power. Figure F-49 shows a 16-GPHS unit operating for 73 years until no power is produced with the following inputs: 224-W beginning-of-mission power, hot and cold junction temperatures of 830°C and 296°C, respectively, and a constant 30-V bus.

A similar analysis with 18 GPHS units shows power being produced out to 85 years. Note, these are not the specifications for the RTGs that would be used on an interstellar probe mission; instead, they represent typical 1990s generations of RTGs.

F.2.10.4 Conclusion

RPS designs have progressed to keep pace with the demands of space missions. These systems continue to outperform their stated design life regardless of era. While the statistical analyses of life and power performance show that multi-decadal missions are possible, caution must be used with these results. The old adage about extrapolating beyond the data set applies. Further, limitations on the material degradation and potential chemical reactions have not been fully examined here. However, the results do show promise of extended life lasting several decades.

F.3 Ground Longevity

F.3.1 Introduction

The multi-organizational effort associated with operating highly complex space missions over multiple decades requires significant planning, coordination, and consensus building within a

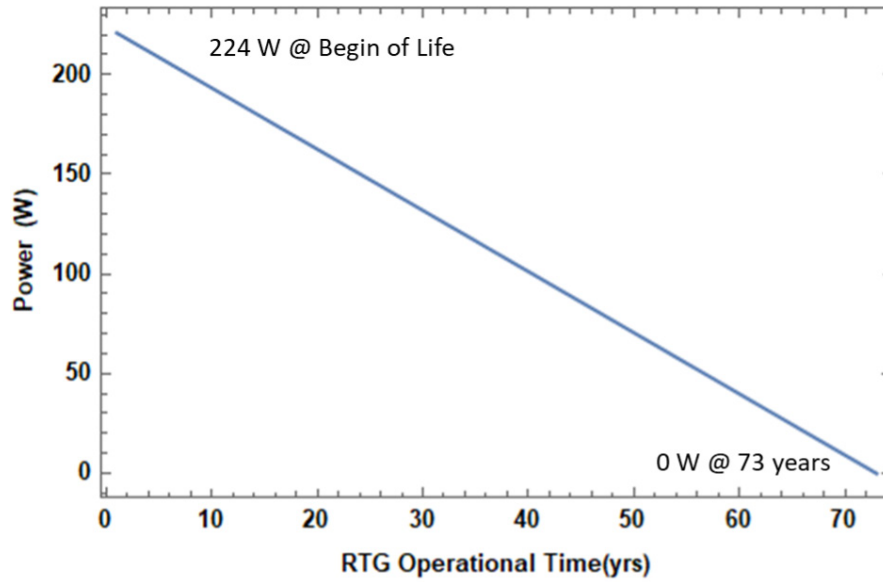


Figure F-49. GPHS-RTG power prediction for Interstellar Probe through 100 years with 16 GPHS units. (Image credit: Johns Hopkins Applied Physics Laboratory.)

highly distributed community of stakeholders long before launch. Resources must be dedicated to building a system for handling hardware and software updates, sparing approach, as well as infrastructure to allow spacecraft communications over 50+ years, and for handling archiving, data storage, and record retention. Resources must also be dedicated to developing a distributed, diverse, international consortium of organizations pursuing the common scientific goal of learning more about our solar system, galaxy, and universe.

Further, each of these considerations affects multiple systems within the mission, with many areas of intersection among them all. Spacecraft and instrument engineering teams, software developers, mission operators, science teams, communications infrastructure providers, data storage providers, sponsoring organizations, and each individual stakeholder organization must all agree on a system to solve these problems.

Historically, several planetary science missions have been able to use their ground segments over multiple decades. However, most of these were not deliberately planned for the long term. Nevertheless, these missions' experiences should be explored to discover serendipitous design decisions and circumstances that have enabled their long operational lives, and what lessons we can learn from aspects of their ground segments that have made operations decades later more difficult.

The New Horizons mission to explore Pluto has a design life of 15 years. Because of its long cruise and the expectation that the spacecraft could potentially support exciting extended mission opportunities, the mission was planned with a very long operations period in mind. New Horizons' longevity plan should be used as a case study for long-term mission planning. Further, lessons learned in New Horizons', Voyager's, and Cassini's experience of implementing longevity plans are an important source of guidance.

F.3.2 Mission Operations Center (Srama et al.), Science Operations Center (SOC), and Ground Data System (GDS) Infrastructure

F.3.2.1 Upgrades

It is both an advantage and a disadvantage of ground systems that they can be maintained. While the space segment, postlaunch, is forever out of the reach of technology trends and updates and will be encapsulated within a relatively benign environment, the ground segment ages, decays, and can/should be readily fixed when it breaks. Interstellar Probe should plan and budget for a regular schedule of ground system upgrades and maintenance. A hardware/software refresh should be planned for a cadence of roughly every 5 years, to correspond with warranty expiration. To minimize risk to the mission, the upgrade schedule will need to avoid major mission events, such as flybys, which will occur more frequently in the first 10 years of the mission and disappear entirely once the spacecraft exits the solar system. Budgeting and executing the full number of ground system upgrades over the course of the mission will mitigate the risk that equipment degradation, outdated software, and technological incompatibility will cause mission failures as the system ages. Although the requirement to change out the ground system 10 times over the course of the mission may seem expensive, there are steps the mission can take to make this process quicker and easier, based on lessons learned from New Horizons and other long-lived missions.

F.3.2.2 Platforms

Several successful long-duration missions can be cited as pathfinders for developing a GDS infrastructure that can withstand the test of time. GDS hardware planning must take into account the possibility that platforms chosen early in the mission can become obsolete before the mission has accomplished all its goals. Upgrades or change-outs to ground hardware, as recommended above, must be understood. If the mission chooses to move to cloud-based computing platforms, great care must be taken in choosing the provider because this would be a major point of dependency for the mission. Cloud computing presents an alternative to owning, storing, and maintaining decades-old hardware, but it comes with its own set of challenges. Although hardware no longer runs the risk of becoming obsolete, the organizations providing the cloud service do. However, cloud computing offers the advantage of outsourcing platform migration for some parts of the GDS hardware to an organization that specializes in solving these problems. Interstellar Probe will still have on-premises systems (e.g., command and control) that require longevity plans to take platform independence into account, but large parts of the GDS can be hosted off-site, in a commercial or government cloud.

F.3.2.3 Simulators and Ground Support Equipment

For equipment kept and maintained by mission executors, hardware storage and maintenance must also be carefully planned out. It will be imperative that these items have appropriate space for decades, and organizations must commit to housing them *safely*. This will involve defining and committing to appropriate climate conditions and security for the entirety of the 50-year mission life.

Simulators for a 50-year mission need backups, and backups for their backups. As New Horizons experienced, when one simulator requires maintenance or repair, having a second simulator that

is fully functional is advantageous. Interstellar Probe should plan to maintain two complete, functional, interchangeable simulators at all times, plus a kit of spare parts for a third. That way, if one simulator requires maintenance or repair, the second one can be at the ready. Spare equipment will need to be stored in a library under conditions conducive for long life. The storage space and environmental control requirements for all sparing hardware need to be planned, agreed to, and budgeted for through the life of the mission.

Similarly, instrument ground support equipment requires a longevity plan. For each spacecraft instrument, at least two functional, flight-like engineering models should be kept in mission test beds, and a third functional, flight-like engineering model should be kept with the instrument team. Spare parts should also be kept in the mission's hardware archive. Because this arrangement will affect many organizations, explicit agreements need to be in place regarding storage space and climate requirements.

Under the best of conditions, there is still no guarantee that Interstellar Probe's ground support equipment or its spares will still be operational at the 50-year mark. One solution to this problem is the creation of high-fidelity, software-only simulators. Unlike hardware, these simulators can be duplicated without limit or increase in cost, and they do not decay over time (although all the longevity requirements for ground software apply). A software simulator can theoretically be engineered postlaunch as long as the mission has at least one working hardware simulator on which to model it. Interstellar Probe's mission developer will need to study the cost effectiveness of a high-fidelity, software-only simulator during early mission design phases.

F.3.2.4 *Data Storage Systems*

For data storage and backup, the Interstellar Probe mission needs a longevity plan as well. The mission's Technology Maven can provide significant insight here, anticipating different types of data storage changes, shifts in supported file formats, hardware obsolescence, etc. While short-term problems might be solved with adapters, regular upgrades to the ground hardware will prevent whole systems from becoming unusable. Even risk-mitigated systems, such as random arrays of independent disks (RAIDs), can fail in unanticipated ways. New Horizons discovered that because hard drives had a tendency to be roughly the same age, and aging at roughly the same rate, there were correlated failures of multiple disks within the array. Compounding the problem, when one or more disks failed, strain on the rest of the RAID would precipitate further failures. Thorough reliability and risk analysis will be required to ensure that Interstellar Probe's data storage system withstands the test of time.

F.3.2.5 *Ground Software*

One of the most striking lessons learned from New Horizons is the importance of having platform independence. Wherever possible, source code must be open source (or provided to the managing organization via contractual agreements), and the mission developer should own the software. To this end, software engineers must settle on an open-source software development language that supports platform independence. The ground system should be developed using Advanced Multi-Mission Operations System (AMMOS) software, which is also open source. Open-

source software can be “frozen” at the appropriate point in the mission, and the mission operator can then control it to maintain backward compatibility.

However, it will be impossible to ensure that the full compendium of Interstellar Probe software is open source and platform independent. For software that relies on external providers, Interstellar Probe needs a backup plan to mitigate the risk that its software is eventually unsupported. New Horizons, which relies on some proprietary software in its operations, made agreements with the providers to keep the source code in escrow so that it can be accessed if the developer goes out of business. It is also possible to plan for proprietary software going obsolete and being replaced with new proprietary software. For example, the mission can generate a graceful set of regression tests to validate new software before the old software is retired. Interstellar Probe can mitigate the expense of rebuilding capabilities as they are lost to obsolescence by planning for different scenarios. Writing its own wrapper code, creating its own tools, or generating a transition tool are all options to achieve a balance between relying on proprietary solutions and maintaining control over the system.

Like other space missions, Interstellar Probe can benefit from adherence to data standards that enhance interoperability and cross-support. However, while other missions can focus on international and organizational interoperability, Interstellar Probe will need to consider its data standards from a very long term perspective. It needs to be *generationally* interoperable and to have cross-support handed down across successions of engineers over decades. This will be essential to ensuring the long-term success of an interstellar probe. The mission should implement its software systems in compliance with Consultative Committee for Space Data Systems (CCSDS) standards, taking the entirety of the ground segment into account.

For mission-developed software solutions, automated testing can be implemented to ensure that the software is robust to updates and changes over the life of the mission. This represents a significant effort early in the development cycle, which will need to be planned and budgeted for.

The Role of the Technology Maven

Interstellar Probe will need to define the role of Mission Technology Maven as an integral part of the full duration of the mission. This function will have a complete, up-to-date understanding of all technologies on which Interstellar Probe’s success depends. They will keep abreast of technological trends and changes that could adversely affect Interstellar Probe and create and maintain plans for migrations, upgrades, plugs, and repairs that become necessary to ensure that the mission can continue as planned. The role is not confined to hardware and software upgrades! The Technology Maven will also need to keep abreast of file-format trends and requirements to ensure that Interstellar Probe’s compendium of documentation and records will remain accessible and readable for many generations to come. One aspect of the Technology Maven’s value to the mission is their ability to structure and guide ground system updates to maximize utility and longevity. Budgeting for these upgrades at the outset is essential, but equally important is leaving sufficient flexibility in the plan to respond to technology trends *as they develop*. No mission can anticipate 50 years of technology evolution, but a well-planned mission will mitigate the risks associated with it. The Technology Maven will need to develop and maintain a broad technology road map for the mission. Interstellar Probe can mitigate these risks by employing a Technology Maven to manage the trends as they occur over the years, recognize how these changes will affect Interstellar Probe, and make recommendations that keep the mission’s ground segment running strong.

However, automated testing presents a reduction in effort and cost during validation and later on in the software upgrade cycle, because it generates the specifications to which to write the code. Over the course of a 50-year life cycle, the savings will be significant. However, it is important to note that implementation of automated testing should be understood in a narrow sense, to mitigate against system failure caused by patches, upgrades, etc. Users of the GDS should have the opportunity to develop regression tests as a means of training successive generations of Interstellar Probe engineers.

Another New Horizons lesson, learned the hard way, was that code must be endian neutral, or bi-endian. This will prevent sweeping rewrites to accommodate future shifts in hardware endianness trends. Furthermore, reaching back to the space segment, all the early design decisions associated with spacecraft and instrumentation must be made not only with the reliability of the system but also with the longevity of the ground segment in mind. Engineering discipline to opt for simple, high-heritage designs and to rely only on commonly used and supported software tools and languages is essential.

F.3.3 Navigation, Mission Design, and Ground Communications Infrastructure

F.3.3.1 Communications and Navigation Longevity Challenges

One of the greatest challenges for the concept study, and likely for the mission itself, is understanding the communications network infrastructure that will be available to transmit and receive data over the many decades of Interstellar Probe's operational phase. The concept study is currently baselining access to the 70-m antennas of the Deep Space Network (DSN) for the early part of the mission. However, that infrastructure is not guaranteed to be available in 50 years. Furthermore, use and maintenance of the DSN requires multinational planning and accord, and this need will carry forward to any following generation of deep-space communications assets. One of the most foundational findings of the concept study is that this requirement must be addressed early.

The Interstellar Probe mission has conducted radio-frequency communications (RF) subsystem trades to determine the baseline design and requirements, including which frequency band the mission expects to use. Section 3 provides detailed information about the considerations, analysis, and results of the trade, which concluded that X-band should be baselined for RF. This means that sponsoring organizations need to commit to retaining X-band communications capabilities for the duration of the mission.

Navigating the spacecraft at large distances presents the problem of taking longer and longer delta differential one-way ranging (delta DOR) observations. While the DSN continues to operate, the triangulation process is understood, but the mission does not expect to use the DSN alone for its full life cycle. As noted in Section 5, the Interstellar Probe study team is baselining the use of the next-generation Very Large Array (ngVLA) for downlink after many of the 70-m DSN stations are no longer in use. This significantly increases gain, but it effectively prevents the conventional approach to triangulating the spacecraft because a large array of receivers acts as a single receiver.

Another consideration is that, as the spacecraft travels farther and farther from Earth, beamwidth pointing becomes more and more difficult. Even aside from pointing challenges related to distance, the ngVLA beamwidth is expected to be much tighter than that of a 70-m DSN antenna. The RF subsystem development effort will need to baseline the tightest possible beamwidth on Earth and the tightest possible beam that the spacecraft can point. More about these design considerations can be found in Section 5. Still another challenge for navigation is maintaining a radiometric capability. As the concept of the mission matures, the navigation team will need to understand how radiometric requirements change as the spacecraft moves through various phases of the mission, getting farther and farther away. This is an area of development for the Interstellar Probe mission that will involve multiple cooperating organizations. Developing the radiometric capabilities will be an undertaking to which NASA and other sponsoring organizations will need to commit in order to ensure Interstellar Probe's success.

Indeed, it will be extremely important for the mission and sponsoring organizations to collaborate closely with the National Radio Astronomy Observatory (NRAO) to ensure that the mission can use the ngVLA for its downlink as effectively as possible. Interstellar Probe navigation engineers will need to know the impact on the ground system and teaming between DSN and NRAO as non-DSN stations are brought online for downlink. The mission will need to baseline the use of both the DSN and ngVLA during a transition period that allows scientists and engineers to compare the data coming from the ngVLA against the data from the DSN. It is essential to note that Interstellar Probe is baselining the use of the DSN for uplink during the entirety of the mission, as explained in Section 5. Sponsoring organizations and the international DSN community will need to commit to maintaining this capability in order to successfully execute the Interstellar Probe mission.

F.3.3.2 Network Security

The Interstellar Probe mission will be required to address network vulnerabilities that cannot be anticipated. The mission will need to have a team responsible for meeting this need and adapting to the change. Threats to network security have evolved quickly over the last several decades and will likely continue to shift and create challenges. NASA's Risk Information Security Compliance System (RISCS) database for archiving network security documentation is assumed to be the continuing repository. It will need to have a longevity plan in place to preserve archived information in a readable format, as discussed below.

Interstellar Probe will need all stakeholder organizations to participate in regular scans of any networked systems and to patch, update, and rebuild systems as required by the findings. This is one of the areas where automated testing becomes so important, because handling software patches on a monthly cadence could otherwise be prohibitively labor intensive and expensive. Assuming the mission uses AMMOS software, AMMOS's developing organization will also need to participate in regular scans, closely monitoring third-party dependencies in particular, such as libraries.

Interstellar Probe resources that rely on encryption technology will also need special attention to withstand the test of time. Obsolescence in encryption technology could render important documentation and resources irretrievable unless the mission closely follows the technology

changes and addresses them immediately. This is another area for the Technology Maven to focus on.

F.3.4 Archiving and Records Retention

Development and maintenance of appropriate documentation for long-duration missions is a deceptively complex problem. The mission will need to address in what format data will be stored and reach a consensus among all participating organizations. For electronic data formats, it will be essential to ensure that the chosen formats can be supported and read over multiple decades, a feature that cannot be guaranteed for any electronic file format option. Electronic file format approaches will need guaranteed support and maintenance across the life of the project. One approach to mitigating the risk that mission documentation becomes unreadable because of obsolescence of the file format is to migrate the library of electronic records on a regular basis. Here again, the role of the Technology Maven will come into play. This person will stay abreast of file format evolution, anticipate the impending doom of any file format technology on which the mission depends, and initiate a migration process in time to prevent the loss of any data. They will also recommend the successor technology, with an eye toward minimizing the frequency with which a migration has to take place.

Even paper documentation requires the commitment of multiple organizations for storage and maintenance. Ominous anecdotes should give us pause, such as remodeling projects that created climate conditions that destroyed records, or leadership changes that resulted in the loss of precious artifacts because their value was no longer known.

Beyond ensuring storage over 50+ years, distribution then also becomes problematic. How many copies should be stored? How can they be retrieved, and when, and by whom? In any event, if Interstellar Probe decides to rely on a paper library, it seems prudent for multiple organizations to keep identical libraries of documents in order to distribute the risk of destruction. The organizational agreements for storage and climate conditions will have to be treated as contracts, with consideration; storage space costs money, and Interstellar Probe will need to budget for it.

No matter whether electronic or paper, archiving the great record of what makes Interstellar Probe tick will be an essential part of ground segment planning. With the Technology Maven's recommendations, an electronic library can be kept alive and well for the duration of the mission. If paper records are kept, formal contracts for storage and maintenance can be a reliable way to ensure that readable copies of the records persist. However, in either event, the mission needs a librarian to manage the archive.

F.3.5 Science

Much like the ground communications infrastructure, science teams working on Interstellar Probe have the challenge that they are likely to be extremely distributed. Even this concept study for Interstellar Probe boasts an international science team, with nine countries (and counting) currently represented! One of the more pedestrian aspects of building a ground segment that can withstand the test of time will be getting all the organizations involved to agree and adhere to the set of rules and expectations governing how Interstellar Probe should conduct its science segment.

The Interstellar Probe concept study is baselining the use of the Planetary Data System (PDS) for its science data storage and archiving. This started out as a trade, because the mission falls more cleanly into the Heliophysics Division of the Science Mission Directorate. However, with a focus on longevity, it quickly became clear that the question is more complicated than simply which scientific community benefits the most from an interstellar probe.

APL has experience using various data archives for its space mission science return, including the PDS, where several of our missions' data reside (e.g., MESSENGER [Mercury Surface, Space Environment, Geochemistry, and Ranging]), and the Space Physics Data Facility (SPDF), which houses Parker Solar Probe's data. The primary advantage of the SPDF is in its user friendliness. It uses Common Data Format (CDF) software that makes formatting and uploading science data efficient and easy to learn.

On this front, the PDS cannot compete. The PDS requires significant up-front data manipulation, along with the generation of copious metadata to accompany each science data set. The PDS is subject to regular updates to comply with its charter, and missions using it have to change their process and update their data to keep up with PDS evolution. This aspect of the SOC is frequently poorly understood during mission development, and missions relying on the

PDS for data storage discover during Phase E that the task of formatting, calibrating, and uploading data to the PDS is much more onerous than they had originally planned for.

However, the PDS has one major advantage over the SPDF: it is congressionally required to store NASA's data in the National Archives, in an accessible format, in perpetuity. It is ISO (International Organization for Standardization) compliant, and in addition to the metadata requirements that ensure that the data make sense for generations to come, the PDS goes through its archive and verifies that all of the data can be read once every 6 months. Interstellar Probe can certainly

The Role of the Librarian

The Voyager spacecraft, originally intended to fly for 12 years, have been a case study in serendipitous space mission longevity. Because the mission was never intended to last as long as it has, many of the recommendations Interstellar Probe is making with regard to longevity are the direct result of lessons that Voyager has learned. When problems arise, documentation is scarcely available, and the mission is known to call long-retired engineers for help. Interstellar Probe will reach a point where this is no longer possible. Maintaining the record of the mission's intricacies is one thing. Ensuring that it is useable is quite another. Interstellar Probe will need a librarian.

The Interstellar Probe mission librarian will be in charge of the library of records associated with the mission. This person will understand the scope of the documents and the various classes of documents that make up the full record of the foundation of the mission. They will be responsible for ensuring accessibility, searchability, and usability. Note that here, we are not talking about science return data. These are the record of the mission's *inputs*, rather than its outputs, which must be carefully maintained for future generations of scientists, engineers, and operators working on this mission. The library is not for posterity; rather, it is an active, living toolbox that *must be accessible* to mission personnel decades into the future.

Information technology comprises a significant part of the modern discipline of library science, and the mission could have overlap between the Librarian's role and that of the Technology Maven, particularly when it comes to records retention. Interstellar Probe can take advantage of efficiencies here.

overcome the burdensome process associated with preparing data for the PDS; many missions have. Overwhelmingly, the PDS is the only science data storage system that makes sense, given the longevity of Interstellar Probe. In the time it will take for Interstellar Probe to get halfway to its destination, many data storage systems will have come into existence, engulfed large swathes of valuable data, and died away, taking the science with them. Beyond even the duration of the threshold mission, which is already ~50 years, planners must consider that the data returning from Interstellar Probe should be available to scientists for many generations *after* that. It is not hyperbole to state that this mission's development team will have a duty to future generations to ensure the preservation of its science return.

The Science Data Archivist

Learning from other missions' experiences with meeting PDS requirements, Interstellar Probe should have a science data archivist in charge of calibrating, formatting, bundling with metadata, and submitting data to the PDS. This role needs to be housed within the Science Operations Center, as a dedicated individual, *not* a member of the science teams. Experience with MESSENGER indicates that the best approach is to have a single person in charge of getting all of the science data, from all of the instruments, ingested into the PDS, rather than having bits and pieces attended to by science personnel on each of the instrument teams. This ensures that the work is budgeted for and planned for and that other science work cannot supersede it.

F.3.6 Long-Term Ground Segment Planning

In addition to the considerations addressed above, the concept study recommends that Interstellar Probe stakeholders address multi-organizational and international commitments and agreements early, according to the nature of each organization's contributions, including everything from science teams to the communications infrastructure (DSN and beyond). All interfaces and dependencies between organizations should be identified. Potential backup plans associated with each organization's contributions must be explored and formalized. Sponsoring organizations will need to know what happens if an infrastructure provider, for example, becomes incapable of honoring its commitment to the mission. These backup plans must take into account the significance and urgency of each organization's contributions, how rare the capability is, and what resources would be required to restart or replace them.

Format and storage of documentation and any ground-based hardware should be formally addressed in an Interstellar Probe longevity plan, with the commitment and consensus of the full range of contributing organizations, as appropriate.

Multiple organizations will have responsibility for various interoperating pieces of a long-term mission like Interstellar Probe. In no area is that more clear than during the operations phase, when the mission will rely on spacecraft engineers, ground software developers, mission operators, instrument scientists, instrument software developers, navigation engineers, and mission designers, along with an international communications network infrastructure. This could encompass dozens of organizations and multiple countries. Longevity planning is essential to ensure that mission-critical stakeholders have the endurance to support the mission over the

years. Section F.5 will discuss more thoroughly the recommended approach to attracting, training, and retaining a multigenerational team.

F.4 Organizing for the Long Term

An early element of the longevity study was the mission demands placed on the implementing organization(s) and the mission team members. The results of that work were documented in the 2019 Interstellar Report. That initial work is provided here along with subsequent work as referenced.

Many scientists in the planetary science, astrophysics, and heliophysics communities are used to a model of PI ownership in which individuals become charismatically associated with their instruments and the success of those instruments. Transition from one leader to another can prove difficult or even destructive to the instrument because the loss of knowledge and perceived leadership is devastating for the instrument and for the team. *This model will not work for a mission that must, by definition, outlive all of its original leadership team before it becomes fully operational.* The team must therefore meet this challenge head-on, with considerable forethought. Fortunately, examples from organizational sociology and the sociology of science offer opportunities to innovate in order to ensure scientific success.

F.4.1 A Bureaucratic Structure

Over a hundred years ago, Max Weber explained that the charismatic form of leadership does not endure beyond the lifetime of the charismatic individual—unless the organization successfully transitions to a bureaucratic hierarchy (Weber, 1968). While the former social form is characterized by leadership through forceful “personality” and individual participants’ adherence to the leader, bureaucracies are seen as more legitimate and efficient social forms, characterized by strong centralized authority and a clear chain of command and communication such as that seen in military operations or among a fleet of ships. Such systems rely on individual expertise but also provide clear roles for participants, opportunities for advancement should this be desired, and clear mechanisms for training and evaluating candidates. They also provide meaningful employment and connection to the cause. Individuals move in and out of roles (or “bureaus”) with clearly defined tasks, and their evaluation is based on their performance of the role’s tasks, not their personality. Newcomers have the opportunity to enter and to move up the chain, criteria for advancement are clear, and decision-making is comparatively transparent.

This model has already been used to great effect in voyages of exploration and discovery, which took place under social structures that endure for generations, such as national navies or private companies. This includes the voyages initiated by the Hudson’s Bay Company (e.g., the voyage of the *Nonsuch* in 1668) or the Dutch East India Company (Vereenigde Oostindische Compagnie; VOC; e.g., the voyages of Henry Hudson); the three Pacific voyages of James Cook, while he was an officer in the Royal Navy (Great Britain); the circumnavigation of the globe by the Imperial Russian Navy under Admiral Fabian Gottlieb von Bellingshausen; or the voyages of the Chinese Treasure Fleet under the command of Zheng He (鄭和). While now remembered for certain charismatic discoverers and captains, these expeditions were actually organized under the rubric of large, national-level institutions, and not undertaken by isolated entrepreneurs.

There are advantages to this model of group operations. Ship operations led cognitive scientist Ed Hutchins to develop the notion of “distributed cognition,” which relies on clear roles and communication pathways between members of such a well-oiled machine. There is even evidence that bureaucratic hierarchies may be better for women and minorities because of these criteria, unlike other models of hiring and promotion that operate based on perceived “fit” and that persistently conflate this standard with merit (Castilla & Benard, 2010; Freeman, 1972; Rivera, 2012). Most importantly for the Interstellar Probe mission, however, such social systems endure much longer than corporations, militias, or religions that are predicated on following single, charismatic individuals and that are likely to fizzle out once that leader is gone.

Most NASA teams in the directed or Flagship class provide strong structures in the form of individual instrument teams. However, leadership on these instrument teams is often charismatic in form and does not change hands. There is no single role at the top of the chain, equivalent to a CEO or an admiral. The “project scientist” (PS) role is more subservient, transmitting the concerns of the PI to those constructing instrumentation, with no functional hierarchical authority—a form of “structural powerlessness” (Kanter, 1993). Although some PSs have managed a form of control because of charisma (i.e., Ed Stone of the Voyager project), others have stayed within the traditional confines of the role. To follow the ship analogy, what is necessary is for each instrument to be managed by a captain and the overall fleet by an admiral. While individuals in these roles can be replaced through formal procedures, the roles and their authority remain.

To convert the common NASA Flagship team structure into one with staying power to last multiple generations of scientists, we recommend the following modifications:

- Organize the mission around a “plank” institution that is capable of maintaining the bureaucratic structure throughout the mission duration.
- Write contracts to allow the PI-ship to exchange hands over the lifetime of the instrument. Instrument leadership should be promoted from within the instrument team and/or competed participating scientist programs, not necessarily within the institution; contracts and instrument development plans must be written accordingly.
- Formalize deputy roles for all PI-ships, and formalize mechanisms for their replacement.
- Formalize procedures for PI and PS replacement through the ranks.
- Create and classify clear roles on the mission team (beyond simply co-investigator [Co-I] or instrument engineer) that allow the responsibilities to remain with the roles.
- Assign formal deputies, apprenticeships, or assistantships to all roles for junior scientists to build mentorship and continuity into the architecture of the mission.
- Formalize mechanisms and procedures for advancement (i.e., selection of the next PI or PS, rotation of deputies through the ranks, mobility of juniors among roles and up the chain of command). The mission must not be allowed to grow stale in its leadership or among its membership ranks.

F.4.2 Instrumentation and Leadership

An essential property of such bureaucratic organizations is the ability to draw a clear distinction between instrument development, leadership, and management on the one hand and individual scientific investigations on the other. This model is already in place in related research infrastructures that support particle physics and astronomy. Observatories, for instance, are founded on the premise that they will produce a shared resource that is managed by a scientific community, that is kept reasonably up to date in terms of operational capacity and instrumentation, and that enables community participation and observation (e.g., the Space Telescope Science Institute [STScI], established for the Hubble Space Telescope in 1981). While groups of technicians manage the physical upkeep of the equipment, groups of scientific experts decide which investigators may use the instrumentation (McCray, 2000; Traweek, 1988). Meanwhile, particle accelerators, synchrotrons, and neutrino detectors (Doing, 2004; Knorr Cetina, 1999; Pinch, 1986; Traweek, 1988) are also built to support the long-term goals of physicists working in a collaborative environment over a long duration. This includes particle accelerator facilities, such as the Stanford Linear Accelerator (SLAC)—now the SLAC National Accelerator Laboratory—begun in 1962 at Stanford University; the High Energy Accelerator Research Organization (高エネルギー加速器研究機構 *Kō Enerugī Kasokuki Kenkyū Kikō*), known as KEK, established in 1997; and CERN (derived from *Conseil européen pour la recherche nucléaire*), established in 1954. At these facilities, which have been studied by social scientists (Knorr Cetina, 1999; Traweek, 1988), the goal is to provide an infrastructure for long-term scientific work that supports multiple scientists’ investigative goals and that cares for and provides regular upkeep and upgrades for equipment.

Thus far, this has not been the model on NASA spacecraft teams. On such teams, individuals naturalize the notion that PIs expect the data from their instruments in return for their hard work and investment. They assume that the kind of detailed knowledge of the instrument necessary for design, construction, maintenance, and use can *only* be held by the PI. Given the proclivity of other scientific fields to structure themselves differently, this assumption is false; it is instead the outcome of an organization in which individuals are permitted to possess charismatic leadership roles with the “special powers” that presumes. Should instruments be built instead with the express assumption that they are to outlive their progenitors and that the role of the PI is one of an instrument steward amid generations of leadership, these assumptions will change.

We therefore recommend something that will sound outrageous to many NASA scientists and PIs: that instruments may begin under the purview of a charismatic individual, but within 10 years of their construction, they must transition to more of a “facility”-style instrument: one managed over the long term by an institution and series of technicians. These technicians may initially be selected and trained by the PI, but the contract must go to an institution and laboratory with the capability to host and manage instrumentation over generations of instrumental stewards. To that end, we recommend the following:

- Clear instructions should be provided to proposers stipulating that even if the instruments are at first built by individual PIs, they must transition to facility support in the early stages of the mission, such that an institution can robustly manage the instrument’s continued

operations. *The goal is to produce instruments that will outlive their creators, and for the creators to imbue them with qualities that will enable that transition.*

- Successive generations of PIs may be responsible for guarding and safeguarding the institutional instrumentation and making decisions as to its management.
- Scientists in charge of facility instrumentation must not be subject to structural powerlessness (i.e., saddled with the responsibility for instrumentation but having limited true authority over its construction or management). Akin to new captains put in charge of existing vessels in a fleet, they must be allowed to make decisions regarding the operation, care, and maintenance of the instrument entrusted to their care.
- Future rounds of PI selection may disentangle instrumentation management entirely from investigation management, as is the case with research infrastructures at locations such as CERN or at large telescope centers. This would enable cross-collaboration among instrument groups within the project science group through cross-functional teams.

F.4.3 Ritualized Role Turnover

Most missions do not plan for promotions or shifting roles. PI-ships are rarely transferred, and contracts are established with institutions with the understanding that the named individuals and organizations will endure. In reality, many missions must confront this problem should a team member retire or pass away, and must work at cross-purposes with contracts and institutions to resolve the problem. An interstellar mission that goes beyond the life expectancy of any of its founders can and indeed must plan for such a reality in advance by building this expectation into its socio-technical structure.

Far from a disadvantage, role turnover can be advantageous if considered well enough in advance to establish appropriate organizational structures and practices. However, this turnover cannot simply happen once, or when a PI dies or retires. This would cause too much of an exogenous shock to the team system, with uncontrollable effects (Haveman et al., 2001). The team must instead ritualize role and leadership turnover, such that it becomes part of the team's temporal rhythm (Jackson et al., 2011). Research in the Carnegie School of organizational sociology indicates that routines can be a source of both stability and change (Feldman, 2000; Feldman & Pentland, 2003). As such, routinized and ritualized handover of instrumental authority can be a source of stability for the Interstellar Probe team even as it allows for some administrative fresh air. Further, if elements at the core of the organization—its social structure and its technical resources—do not change, then social theory suggests that the organization will develop a strong degree of structural inertia that enables flexibility and adaptability without compromising the durability and success of the organization as a whole (Hannan & Freeman, 1984).

Taking these considerations into account, we suggest a novel approach to the problem of team turnover on the Interstellar Probe mission team. Instead of treating turnover as an ad hoc or exogenous event, we propose its routine ritualization as part of the core of the mission structure. Ideally such leadership transitions should take place with a regular cadence and a regular set of predictable activities. They should enable a leader to have enough charge over an instrument to

come to know it intimately, but without developing such a close relationship that the instrument cannot effectively be handed over (indeed, the instrument *must* be developed with handover in mind). Such transitions must allow a leader to make an impact in their position but not be in power for so long that the instrument's operation is unimaginable without them. Much like how mission teams require an operational readiness test to practice and perfect their operational constraints and concerns, role transitions must occur more than once over the lifetime of the mission, and certainly more than once before arrival at the interstellar medium.

We recommend a *decadal cadence* to satisfy these requirements. By the time of the mission's arrival, leadership will have changed hands four times, allowing for much room for the transition's improvement. This also offers the opportunity to align leadership periodicity with naturally occurring changes on the mission, for instance:

- Years 1–10: PIs selected; spacecraft and instruments built and launched; initial databases established for data collection.
- Years 11–20: Deputy PI promoted to PI (former PI remains on the team as PI Emeritus); new deputies and internal leads promoted. Appoint 10 participating scientists to use instrumentation; conduct planetary science exploration phase throughout solar system cruise. User testing in situ of databases, software, and hardware required for data collection and circulation.
- Years 21–30: Deputy PI promoted to PI; new deputies and internal leads promoted. Deploy lessons learned from initial solar system cruise.
- Years 31–40. Review to ensure continuity by initiating a new wave of participating scientists. Produce and promote cross-functional teams for physical sciences that deploy multiple instruments.
- Years 41–50. New wave of participating scientists. New PI-level leaders for cross-functional teams. Implement lessons learned and system upgrades based on operations to date.

The team must spell out the rules for instrument delivery and transition in advance so that PIs, team members, and community members know what to expect in terms of the legacy of their instrumentation.

All phases of transition require robust transfer of knowledge, skills, and institutional memory—what is typically called “knowledge management.” Work by anthropologists and sociolinguists at NASA Ames Research Center to support the former Constellation program considered these same concerns with respect to human spaceflight, many of which apply here:

- Rotate mission roles among a roster of apprenticed teammates, with members appointed and transitioning from roles on a regular basis on multiyear terms. This reinforces that knowledge is localized to the role, not to the individual, and also spreads embodied knowledge of the mission and its particulars among more team members, especially those who may move up into positions of decision-making authority.

- Develop an onboarding process for all newly appointed team members that introduces them to the customs, culture, and instrumentation of the mission team.
- Ensure a robust online-and-offline document and information repository for knowledge capture.
- Encourage blogging, oral histories, and memoir writing by members of the team to encourage the relay of stories and information across generations (Linde, 2001). The “spirit” of the team has to transition to the next generation, along with specific technical knowledge.
- Use simulators, regression testing, and operations readiness tests to support the transmission of tacit knowledge from one generation of team members to the next (see Section 3).

F.4.4 Funding Management

By their nature, “large strategic missions” (aka “Flagship” missions) provide significant funding challenges to go with their significant scientific opportunities (National Academies of Sciences & Medicine, 2017). Precisely because they are large, cost overruns and/or schedule slips can have a significant negative impact on all stakeholders in a variety of ways outside of just monetary impact (Zelizer, 2017). An example of what to avoid is that of the James Webb Space Telescope [JWST]). Originally proposed as the Next Generation Space Telescope (NGST) by the Astrophysics Decadal Survey in 2001 for a cost of \$1 billion (NRC, 2001), JWST is now planned to be launched in December 2021 with a mission cost of \$9.7 billion. There are two challenges. The first is that NASA “bookkeeps” the mission cost as that established as the baseline at mission confirmation, which follows the Preliminary Design Review. However, costs at that point can already be in excess of the estimates put forth in initial planning documents such as the Decadal Surveys, and that in itself can be problematic for keeping large missions sold. Up-front cost estimates are difficult to make for cutting-edge large missions, but they can be mitigated to some extent by advanced engineering studies of critical technologies, such as that begun here. A quantitative predictor remains problematic, although NASA’s establishment of the CADRe (Cost Analysis Data Requirement) system and the use of the CATE (cost and technical evaluation) process are given a measure of credit in eliminating cost surprises (National Academies of Sciences & Medicine, 2015). The previous methodology that NASA investigated as embodied by “Gruhl’s Rule” (Honour, 2004) makes qualitative sense (the more money spent on initial concept engineering, the less the final overrun), but its quantitative validity has been called into question by some.

Funding management is a multisided issue with any large mission, and this one will be no exception. In any event, no mission can ever be considered solidly sold until it is successfully launched. Research is underway to characterize the effects of shifting budgetary conditions on spacecraft development and operations (Vertesi, 2016). With considerable mismatch between congressional cycles of funding allocation and the life expectancy of an interstellar mission as well as an inability to predict long-term fiscal and political realities, there will be significant challenges both in the development phase and in the cruise phase for the project and its management. Such

periods of uncertainty are not new, but the long timescale of this project by design will exacerbate difficulties experienced by previous long-term projects.

Mission success criteria must also be carefully crafted to maintain NASA and the public's support. To that end, the success criteria should reflect success at various stages of the mission. For the Interstellar Probe, each of the phases identified in Section 2 (inner heliosphere phase, outer heliosphere phase, and interstellar phase), as well as the planetary and astrophysics phases if the augmented mission is selected, would each be stand-alone achievements. Such a mission construction would enable important milestones as the mission proceeds and provide the mission sponsors with tangible measures of success.

F.5 Summary and Work Going Forward

The analysis of long-duration missions such as that proposed for the Interstellar Probe indicates that they are very viable based on the past history of missions (especially planetary missions where the environment is stable). Success will come by carefully shaping the spacecraft design to match the science requirements and by a careful choice of system elements and appropriate testing; it will also require a managing organization that will set cultural norms for the mission team and carefully manage the knowledge base and ground infrastructure for the long term. The longevity study documented in this appendix has defined the methodology and identified the major elements needed for success. It has also identified additional work needed before the mission concept documented in this report can transition from concept to implementation. These major elements and work to be accomplished are summarized in the following sections.

F.5.1 Summary of Spacecraft Reliability

Reliability analyses will be vitally important in developing an Interstellar Probe mission. History points to a very good chance of success.

- Spacecraft last a very long time once they get past the initial commissioning phase.
- RTGs show a much longer life potential compared to the current design life of 17 years used by the RPS program office.
- Success criteria have been tuned to minimize the chance of mission failure due to the loss of any one instrument.
- Physics models currently exist for all known failure modes of electronic parts and materials.
- Testing being performed by component manufacturers is correct for long-duration space applications but currently should not be extrapolated out to 50 years (see Section F.5.4).
- Reliability estimates show a reasonable probability of success, but uncertainties in the data result in a wide distribution.

F.5.2 Summary of Ground System

The study identified several specific actions that Interstellar Probe can take to maximize the longevity of the ground segment. These are summarized in the list below.

- Plan and budget for regular, scheduled upgrades to the GDS.
- Design software for platform independence to the extent possible.
- Plan for at least two fully functional simulators, plus spare parts.
- For each instrument, plan for two functional, flight-like engineering models for the test beds and one functional, flight-like engineering model for the instrument teams.
- Define space and climate control requirements for all hardware simulators and ground support equipment. Use formal agreements to ensure that these requirements can be met.
- Wherever possible, developer organizations should own or have access to the source code for Interstellar Probe's software.
- Implement software using automated testing best practices.
- Write endian-neutral software.
- Maximize the use of simple, high-heritage designs that rely on commonly used, well-supported software. Minimize reliance on newer technologies.
- Establish the role of the Technology Maven, and budget for this role for the duration of the mission.
- Ensure that ground stations can support X-band for the life of the mission.
- Collaborate closely with NRAO and NASA early in development.
- Commit to development of new radiometric capabilities to transition communications from the DSN to follow-on ground station technology.
- Commit to preservation of a 70-m DSN station for the life of the mission, which will require one for uplink.
- Plan and budget for frequent network vulnerability scans.
- Ensure that file formats used to store electronic records are stable and supported; budget to migrate to new file formats as older ones become obsolete.
- Establish the role of the Mission Librarian, and budget for this role for the duration of the mission.
- Ensure that all stakeholder organizations agree to adhere to longevity requirements.

- Use the PDS for science return data storage.
- Establish the role of the Science Archivist, and budget for this role for the duration of the mission.

F.5.3 Summary of Teams and Organization

Spacecraft are socio-technical systems. That is, their success comes from both strong technical capabilities, including redundancies, and a strong human component. The infrastructure of a long-duration mission must account for the human element of the technical apparatus and preferably anticipate its projection into the future. Major recommendations for long-term mission planning include the following:

- Succession planning must be built into the organizational structure during formulation and followed throughout the mission.
- Make diversity a cornerstone of the team structure.
- Mentorship opportunities are essential to bringing in new scientists and engineers to work in a meaningful, sustainable way with the “community of practice.”
- Deploy and maintain mission simulators and flight-spare instruments with their associated ground test equipment not only to support flight operations but also to transfer tacit knowledge from one generation of team members to the next.
- Phase E will require sufficient funds to support upgrades, maintenance, and repair of the ground system as an ongoing activity.
- Ground the mission in “plank” institutions that can sustain the effort over very long time spans.
- Support cross-institutional partnerships with long-term agreements.
- Finally, to combat funding asynchrony, create a mission plan that will continue to transmit stages of mission success to the stakeholders.

F.5.4 Work Going Forward

Going forward, the longevity team recommends the following:

- Although new longer-duration missions will be planned, the electronics industry is increasingly focused on small feature sizes lasting 2–5 years for consumer applications. Part data does not exist for the duration of interest. We recommend that NASA initiate a systematic PoF approach with accelerated testing to anchor future reliability efforts.
- Devices with mechanical moving parts, such as thrusters, pose challenges for longer missions. This requires working with thruster manufacturers to understand long-term effects on failure behavior and develop testing to anchor this understanding.

- With the large uncertainties uncovered herein, we recommend the refinement of this methodology so that it is a recognized toolset by the sponsoring agencies to provide confidence that systems and components will last the designed lifetime of a mission.
- Coordinate with NASA’s RPS office and the Department of Energy to understand how to approach certifying an RPS for a long-lifetime mission.
- Perform a formal trade analysis to determine whether to develop a high-fidelity software simulator for the mission to mitigate the risk that hardware is unusable before the end of the mission.

F.6 Appendix F References

- Abbasinasab, A., Market-Sadowska, M. (2019) Non-uniform temperature distribution in interconnects and its impact on electromigration. *Proceedings of the 2019 Great Lakes Symposium on VLSI (GLSVLSI '19)*, 117-122.
- Abelson, R.D., Balint, T., Evans, M., Schriener, T., Shirley, J.H., Spilker, T.R. (2005) Extending exploration with advanced radioisotope power systems. *JPL D-28903, PP-266*.
- Achanta, R.S., Plawsky, J.L., Gill, W.N. (2007) A time dependent dielectric breakdown model for field accelerated low-k breakdown due to copper ions. *Applied Physics Letters* 91(23), 234106.
- AEC (1965) Press Kit - SNAP-10A (Space Nuclear Power Reactor) [Press release]. Retrieved from <https://indigitalibrary.inl.gov/PRR/91009.pdf>.
- Al Athamneh, R., Hani, D.B., Ali, H. (2020) Reliability modeling for aged SAC305 solder joints cycled in accelerated shear fatigue test. *Microelectronics Reliability* 104, 113507.
- Alam, S.M., Wei, S.Y., Gan, C.L., Thompson, C.V., Troxel, D.E. (2005) Electromigration reliability comparison of Cu and Al interconnects. *Sixth International Symposium on Quality Electronic Design*, 303-308.
- Allers, K.-H. (2004) Prediction of dielectric reliability from I–V characteristics: Poole–Frenkel conduction mechanism leading to νE model for silicon nitride MIM capacitor. *Microelectronics Reliability* 44(3), 411-423.
- Altobelli, N., Postberg, F., Fiege, K., et al. (2016) Flux and composition of interstellar dust at Saturn from Cassini’s Cosmic Dust Analyzer. *Science* 352(6283), 312-318. doi:10.1126/science.aac6397
- Baker, J., Baker, G.S. (1980) Impact of the space environment on spacecraft lifetimes. *Journal of Spacecraft and Rockets* 17(5), 479-480.
- Benkoski, J., Gerger, A. (2021) *Meeting materials reliability challenges for a 50-year interstellar mission* (to be presented). Paper presented at the AGU Fall Meeting 2021. New Orleans, LA.
- Bennett, G.L. (1995) Space applications. In Rowe, D.M. (Ed.), *CRC Handbook of Thermoelectrics* (pp. 520-534). Boca Raton, Florida: CRC Press.

- Bennett, G.L., Lombardo, J.J., Hemler, R.J., et al. (2006) *Mission of daring: The General-Purpose Heat Source Radioisotope Thermoelectric Generator, AIAA 2006-4096*. Paper presented at the 4th International Energy Conversion Engineering Conference and Exhibit (IECEC). San Diego, CA.
- Bernstein, J. (2014) Chapter 3 - Failure Mechanisms. *Reliability Prediction from Burn-In Data Fit to Reliability Models*, 31-48.
- Blanks, H. (1973) A review of new methods and attitudes in reliability engineering. *Microelectronics Reliability* 12(4), 301-IN302.
- Blome, J.A., Feng, S., Gupta, S., Mahlke, S. (2006) *Online timing analysis for wearout detection*. In Workshop on architectural reliability.
- Bloomquist, C.E. (1984) *Spacecraft Anomalies and Lifetimes*. In Annual Reliability and Maintainability Symposium, 1984. Proceedings., IEEE.
- Bossuyt, F., Günther, J., Löher, T., Seckel, M., Sterken, T., De Vries, J. (2011) Cyclic endurance reliability of stretchable electronic substrates. *Microelectronics Reliability* 51(3), 628-635.
- Boyer, H.E. (1985) *Atlas of fatigue curves*. ASM International.
- Brown, N., Cohen, N., Cavanaugh, M., Richardson, G. (2010) *Spacecraft Lifetime Study (TOR-2010(8582)-3)*.
- Castet, J.-F., Saleh, J.H. (2010) Beyond reliability, multi-state failure analysis of satellite subsystems: A statistical approach. *Reliability Engineering & System Safety* 95(4), 311-322.
- Castilla, E.J., Benard, S. (2010) The paradox of meritocracy in organizations. *Administrative Science Quarterly* 55(4), 543-576. doi: 10.2189/asqu.2010.55.4.543
- Chan, S.I., Hong, W.S., Kim, K., Yoon, Y.G., Han, J., Jang, J.S. (2011) Accelerated life test of high power white light emitting diodes based on package failure mechanisms. *Microelectronics Reliability* 51(9-11), 1806-1809.
- Chen, F., Bravo, O., Chanda, K., McLaughlin, P., Sullivan, T., Gill, J., Lloyd, J., Kontra, R., Aitken, J. (2006) *A comprehensive study of low-k SiCOH TDDDB phenomena and its reliability lifetime model development*. In 2006 IEEE International Reliability Physics Symposium Proceedings.
- Cheng, Y.-L., Lee, S.Y., Chiu, C.C., Wu, K. (2008) Back stress model on electromigration lifetime prediction in short length copper interconnects. *IEEE International Reliability Physics Symposium*, 685-686.
- Chiodo, E., Lauria, D. (2015) Some basic properties of the failure rate of redundant reliability systems in industrial electronics applications. *IEEE Trans. Ind. Electron.* 62(8), 5055-5062.
- Choi, U., Vernica, I., Zhou, D., Blaabjerg, F. (2020) Comparative evaluation of reliability assessment methods of power modules in motor drive inverter. *Microelectronics Reliability* 114, 113730.

- Cohen, I., Beddingfield, C., Chancia, R., et al. (2020) *New Frontiers-class Uranus Orbiter: Exploring the feasibility of achieving multidisciplinary science with a mid-scale mission*. Johns Hopkins University Applied Physics Laboratory. Retrieved from <https://www.nationalacademies.org/our-work/planetary-science-and-astrobiology-decadal-survey-2023-2032>.
- Conrad, D. (1976) Estimation of satellite lifetime from orbital failure experience. *Journal of Spacecraft and Rockets* 13(2), 75-81.
- Dai, Y., Zhou, Y.F., Jia, Y.Z. (2003) Distribution of time between failures of machining center based on type i censored data. *Rel. Eng. Syst. Saf.* 79(3), 377-379.
- Dasgupta, A., Barker, D., Pecht, M. (1990) Reliability prediction of electronic packages. *Journal of the IES* 33(3), 36-45.
- Dasgupta, A., Pecht, M. (1991) Material failure mechanisms and damage models. *IEEE Transactions on Reliability* 40(5), 531-536.
- De, S., Tewari, S., Biswas, A. (2019) negative bias temperature instability (NBTI) effects on p-Si/n-InGaAs hybrid CMOSFETs for digital applications. *Microsystem Technologies* 26(4), 1173-1178.
- Doing, P. (2004) 'Lab Hands' and the 'Scarlet O': Epistemic politics and (scientific) labor. *Social Studies of Science* 34(3), 299-323.
- Draper, R., Gavin, T. (1970) *Reliability in long-life missions*. In 7th Annual Meeting and Technical Display.
- Ebeling, C.E. (2004) *An introduction to reliability and maintainability engineering*: Tata McGraw-Hill Education.
- Edwards, R., Smith, C., Whitley, S. (2021) *Reliability for a 50+ Year Mission – Interstellar Probe*. Paper presented at the Reliability, Availability, and Maintainability Symposium. Orlando, FL.
- Enter, R. (2007) Negative Bias Temperature Instability. In *Modeling and Simulation of Negative Bias Temperature Instability: Dissertation* (Vol. 2021). Vienna, Austria: Technische Universität Wien.
- Feldman, M.S. (2000) Organizational Routines as a Source of Continuous Change. *Organization Science* 11(6), 611-629. Retrieved from <http://www.jstor.org/stable/2640373>
- Feldman, M.S., Pentland, B.T. (2003) Reconceptualizing organizational routines as a source of flexibility and change. *Administrative Science Quarterly* 48(1), 94. doi: 10.2307/3556620
- Ferrara, M., Stephens, M., Marchut, L., Yang, C., Fryar, V., Scott, P. (2012) Analysis of in situ monitored thermal cycling benefits for wireless packaging early reliability evaluation. *Microelectronics Reliability* 52(1), 9-15.
- FIDES Guide 2009 Edition A (English) (2010). FIDES Group.
- Filipovic, L., Selberher, S. (2020) Granularity effects in electromigration. *IEEE Latin America Electronic Devices Conference (LAEDC)*, 1-4.

- Finseth, J.L. (1991) *Overview of Rover engine tests: Final report*, Document No. NASA CR-184270. Huntsville, Alabama: NASA.
- Fox, G., Salazar, R., Habib-Agahi, H., Dubos, G.F. (2013, 2-9 March 2013) *A satellite mortality study to support space systems lifetime prediction*. In 2013 IEEE Aerospace Conference. doi: 10.1109/AERO.2013.6497352
- Fox, G., Salazar, R., Habib-Agahi, H., Dubos, G.F. (2013) *A satellite mortality study to support space systems lifetime prediction*. In Aerospace Conference, 2013 IEEE.
- Freeman, J. (1972) The tyranny of structurelessness. *Berkeley Journal of Sociology* 17, 151-164. Retrieved from <http://www.jstor.org/stable/41035187>
- Fuller, T. (2020) Space Trak Database. Retrieved from <https://www.seradata.com/products/spacetrak/>.
- Ghaida, R.S., Zarkesh-Ha, P. (2007) Estimation of electromigration-aggravating narrow interconnects using a layout sensitivity model. *22nd IEEE International Symposium on Defect and Fault-Tolerance in VLSI Systems (DFT 2007)*, 59-67.
- Haga, R.A., Saleh, J.H. (2011) Epidemiology of satellite anomalies and failures: A subsystem-centric approach. *Acta Astronautica* 69(7-8), 676-690.
- Haifley, T. (2014) *Failure mechanism based stress test qualification for integrated circuits*. In Automotive Electronics Council.
- Hamiter, L. (1990) *The history of space quality EEE parts in the United States*. In ESA Electronic Components Conference, ESTEC, Noordwijk, The Netherlands.
- Hannan, M., Freeman, J. (1984) Structural inertia and organizational change. *American Sociological Review* 49(2), 149-164.
- Harland, D.M., Lorenz, R. (2005) *Space Systems Failures: Disasters and Rescues of Satellites, Rockets and Space Probes*. Chichester, UK: Springer.
- Harms, J.W. (2010) *Revision of MIL-HDBK-217, reliability prediction of electronic equipment*. In 2010 Proceedings-Annual Reliability and Maintainability Symposium (RAMS), IEEE.
- Haveman, H.A., Russo, M.V., Meyer, A.D. (2001) Organizational environments in flux: The impact of regulatory punctuations on organizational domains, CEO succession, and performance. *Organization Science* 12(3), 253-273. doi: 10.1287/orsc.12.3.253.10104
- Hecht, H., Hecht, M. (1985) *Reliability Prediction for Spacecraft*. (RAD-TR-85-229). Griffiss AFB.
- Hecht, M., Fiorentino, E. (1988) Causes and effects of spacecraft failures. *Quality and Reliability Engineering International* 4(1), 11-20.
- Heryanto, A., Pey, K., Lim, Y., Liu, W., Wei, J., Raghavan, N., Tan, J., Sohn, D. (2010) *Study of stress migration and electromigration interaction in copper/low-k interconnects*. In 2010 IEEE International Reliability Physics Symposium, IEEE.

- Hoffman, E. (2010) *Satellites and Spacecraft Designed and Built by the Johns Hopkins University Applied Physics Laboratory (SDO-1600)*. Laurel, MD: Johns Hopkins University Applied Physics Laboratory.
- Hoffmann, F., Schmitt, S., Kaminski, N. (2020) *Impact of combined thermo-mechanical and electro-chemical stress on the lifetime of power electronic devices*. In 2020 22nd European Conference on Power Electronics and Applications (EPE'20 ECCE Europe), IEEE.
- Honour, E.C. (2004) 6.2.3 Understanding the Value of Systems Engineering. *INCOSE International Symposium* 14(1), 1207-1222. doi: 10.1002/j.2334-5837.2004.tb00567.x
- Hwang, D.-H., Park, J.-W., Jung, J.-H. (2011) *A study on the lifetime comparison for electric double layer capacitors using accelerated degradation test*. In 2011 International Conference on Quality, Reliability, Risk, Maintenance, and Safety Engineering, IEEE.
- Issa, A., Sukharev, V., Najm, F.N. (2020) Electromigration checking using a stochastic effective current model. *IEEE/ACM International Conference on Computer Aided Design (ICCAD)*, 1-8.
- Jackson, S.J., Ribes, D., Buyuktur, A., Bowker, G.C. (2011, 2011) *Collaborative rhythm: Temporal dissonance and alignment in collaborative scientific work*, ACM Press. doi: 10.1145/1958824.1958861
- Jeppson, K.O., Svensson, C.M. (1977) Negative bias stress of MOS devices at high electric fields and degradation of MNOS devices. *Journal of Applied Physics* 48(5), 2004-2014.
- Jet Propulsion Laboratory (1973) *Thermoelectric Outer Planets Spacecraft (TOPS)*, Document No. NASA-CR-131451. Pasadena, CA.
- Jóźwiak, I.J. (1992) Reliability exploration of microcomputer systems using the Weibull distribution. *Microelectronics Reliability* 32(3), 337-340.
- Kanter, R.M. (1993) *Men and women of the corporation*. New York, NY: Basic Books.
- Keller, A.Z., Kamath, A.R., Perera, U.D. (1982) Reliability analysis of CNC machine tools. *Rel. Eng.* 3(6), 449-473.
- Khan, S.A. (2012) *Electromigration analysis of high current carrying adhesive-based copper-to-copper interconnections*. Georgia Institute of Technology.
- Kiasat, M., Zhang, G., Ernst, L., Wisse, G. (2001) *Creep behavior of a molding compound and its effect on packaging process stresses*. In 2001 Proceedings. 51st Electronic Components and Technology Conference (Cat. No. 01CH37220), IEEE.
- Knorr Cetina, K. (1999) *Epistemic cultures: How the sciences make knowledge*. Cambridge, Mass: Harvard University Press.
- Korhonen, M., Børgesen, P., Li, C.-Y. (1992) Mechanisms of stress-induced and electromigration-induced damage in passivated narrow metallizations on rigid substrates. *MRS Bulletin* 17(7), 61-69.
- Krasich, M. (1995) Reliability Prediction Using Flight Experience-Weibull Adjusted Probability of Survival, WAPS.

- Le Coq, C., Tougui, A., Stempin, M.-P., Barreau, L. (2010) Experimental study of WL-CSP reliability subjected to a four-point bend-test. *Microelectronics Reliability* 50(7), 1007-1013.
- Lee, W., Nguyen, L., Selvaduray, G.S. (2000) Solder joint fatigue models: Review and applicability to chip scale packages. *Microelectronics Reliability* 40(2), 231-244.
- Li, J., Dasgupta, A. (1993) Failure-mechanism models for creep and creep rupture. *IEEE Transactions on Reliability* 42(3), 339-353.
- Li, J., Dasgupta, A. (1994) Failure mechanism models for material aging due to interdiffusion. *IEEE Transactions on Reliability* 43(1), 2-10.
- Li, X., Qin, J., Bernstein, J.B. (2008) Compact modeling of MOSFET wearout mechanisms for circuit-reliability simulation. *IEEE Transactions on Device and Materials Reliability* 8(1), 98-121.
- Linde, C. (2001) Narrative and social tacit knowledge. *Journal of Knowledge Management* 5(2), 160-170. Retrieved from <http://www.emerald-library.com/ft>
- Liu, F., Lu, Y., Wang, Z., Zhang, Z. (2015) Numerical simulation and fatigue life estimation of BGA packages under random vibration loading. *Microelectronics Reliability* 55(12), 2777-2785.
- Liu, Y., Sun, F., Zhang, H., Wang, J., Zhou, Z. (2014) Evaluating board level solder interconnects reliability using vibration test methods. *Microelectronics Reliability* 54(9-10), 2053-2057.
- Lloyd, J., Liniger, E., Shaw, T. (2005) Simple model for time-dependent dielectric breakdown in inter- and intralevel low-k dielectrics. *Journal of Applied Physics* 98(8), 084109.
- Lu, Y., Miller, A.A., Hoffmann, R., Johnson, C.W. (2016) Towards the automated verification of Weibull distributions for system failure rates. In *Critical Systems: Formal Methods and Automated Verification* (pp. 81-96): Springer.
- Lu, Y., Christou, A. (2017) Lifetime estimation of insulated gate bipolar transistor modules using two-step Bayesian estimation. *IEEE Transactions on Device and Materials Reliability* 17(2), 414-421.
- Mattila, T.T., Li, J., Kivilahti, J.K. (2012) On the effects of temperature on the drop reliability of electronic component boards. *Microelectronics Reliability* 52(1), 165-179.
- McCray, W.P. (2000) Large telescopes and the moral economy of recent astronomy. *Social Studies of Science*. Retrieved from <http://www.jstor.org/stable/285761>
- McLeish, J.G. (2010) *Transitioning to Physics of Failure Reliability Assessments for Electronics*. In ISSAT Int. Conf. Rel. and Qual. Des, Washington D.C.
- McNutt, R.L., Jr., Malapina, D., Lisse, C., et al. (2021) *Opportunities, Instrumentation, and Hazards for an Interstellar Probe*. Johns Hopkins University Applied Physics Laboratory.
- McPherson, J. (2012) time dependent dielectric breakdown physics - Models revisited. *Microelectronics Reliability* 52(9-10), 1753-1760.

- McPherson, J.W., Mogul, H.C. (2004) Underlying physics of the Thermochemical E Model in describing low-field time-dependent dielectric breakdown data. *Journal of Applied Physics* 95, 8101-8109.
- Mei, J., Haug, R., Lanier, O., Grözinger, T., Zimmermann, A. (2018) Effect of Joule heating on the reliability of solder joints under power cycling conditions. *Microelectronics Reliability* 88, 684-690.
- Meng, J., Douglas, S.T., Dasgupta, A. (2016) MEMS packaging reliability in board-level drop tests under severe shock and impact loading conditions—Part I: Experiment. *IEEE Transactions on components, packaging and manufacturing technology* 6(11), 1595-1603.
- Mishra, S., Parihar, N., Dabhi, C., Chauhan, Y., Mahapatra, S. (2018) NBTI-related variability impact on 14-nm node FinFET STRAM performance and static power: Correlation to time zero fluctuations. *IEEE Transactions on Electronic Devices* 65(11), 4846-4853.
- Moore, J., Spilker, L., Cable, M., et al. (2020) *Exploration for the Outer Planets 2023-2032: Goals and Priorities* NASA Ames Research Center. Retrieved from <https://www.nationalacademies.org/our-work/planetary-science-and-astrobiology-decadal-survey-2023-2032>.
- Morris, S. (2011) Bathtub curve. *Reliability Analytics Blog*. Retrieved from <https://www.reliabilityanalytics.com/blog/2011/08/31/bathtub-curve/>.
- Mortin, D.E., Krolewski, J.G., Cushing, M.J. (1995) *Consideration of component failure mechanisms in the reliability assessment of electronic equipment-addressing the constant failure rate assumption*. In Annual Reliability and Maintainability Symposium 1995 Proceedings, IEEE.
- Muñoz-Gorritz, J., Gonzalez, M., Campabadal, F., Suñé, J., Miranda, E. (2020) Analysis of the successive breakdown statistics of multilayer Al₂O₃/HfO₂ gate stacks using the time-dependent clustering model. *Microelectronics Reliability* 114, 113748.
- NASA (2018) *Safety and Mission Assurance Acronyms, Abbreviations, and Definitions* (NASA-HDBK-8709.22). Washington, D.C.: NASA.
- National Academies of Sciences, Engineering, and Medicine (2015) *The Space Science Decadal Surveys: Lessons Learned and Best Practices*. Washington, D.C.: The National Academies Press. doi:10.17226/21788
- National Academies of Sciences, Engineering, and Medicine (2017) *Powering Science: NASA's Large Strategic Science Missions*. Washington, D.C.: The National Academies Press. doi:10.17226/24857
- Ndu, O.K., Smith, C. (2018) *A risk-informed life test modeling framework for uncertainty characterization and life estimation*. In 2018 Annual Reliability and Maintainability Symposium (RAMS), IEEE.
- Neveu, M., Anbar, A., Davila, A., Glavin, D., MacKenzie, S., Phillips, C., Sherwood, B., Takano, Y., Williams, P., Yano, H. (2020) *Returning samples from Enceladus for life detection*.

- University of Maryland. Retrieved from New Frontiers-class Uranus Orbiter: Exploring the feasibility of achieving multidisciplinary science with a mid-scale mission.
- Noda, K. (2008) *Using hot carrier injection for embedded non-volatile memory*. NSCore, Inc., Fukuoka, Japan, White Paper WhitePaper_081002.
- Nogueira, E., Orlando, V., Ochoa, J., Fernandez, A., Vázquez, M. (2016) Accelerated Life Test of high luminosity blue LEDs. *Microelectronics Reliability* 64, 631-634.
- NRC (2020) *Reliability Growth: Enhancing Defense System Reliability*. Washington, D.C.: The National Academies Press.
- NRC (2001) *Astronomy and Astrophysics in the New Millennium*. Washington, D.C.: The National Academies Press. doi:10.17226/9839
- Oates, A. (2014) Strategies to ensure electromigration reliability of CU/Low-K interconnects at 10 nm. *ECS Journal of Solid State Science and Technology* 4(1).
- Osterman, M., Pecht, M. (2007) Strain range fatigue life assessment of lead-free solder interconnects subject to temperature cycle loading. *Soldering & Surface Mount Technology*.
- Pascale, E., Bouillaut, L., Freneaux, T., Sista, R., Sannino, P., Marmo, P. (2018) A weibull approach for enabling safety-oriented decision-making for electronic railway signaling systems. *Safety* 4(2), 17.
- Patil, R.B., Kothavale, B.S., Waghmode, L.Y. (2018) Selection of time-to-failure model for computerized numerical control turning center based on the assessment of trends in maintenance data. *Proc. Inst. Mech. Engineers Part O: J. Risk Rel.* 233(2), 105-117.
- Pecht, M. (1990) A model for moisture induced corrosion failures in microelectronic packages. *IEEE transactions on components, hybrids, and manufacturing technology* 13(2), 383-389.
- Pecht, M., Ramappan, V. (1992) Are components still the major problem: A review of electronic system and device field failure returns. *IEEE transactions on components, hybrids, and manufacturing technology* 15(6), 1160-1164.
- Pecht, M., Dasgupta, A. (1995) *Physics-of-failure: An approach to reliable product development*. In IEEE 1995 International Integrated Reliability Workshop. Final Report, IEEE.
- Pecht, M.G., Nash, F.R. (1994) Predicting the reliability of electronic equipment. *Proceedings of the IEEE* 82(7), 992-1004.
- Pinch, T. (1986) *Confronting Nature: The Sociology of Solar-Neutrino Detection*. Dordrecht: D. Reidal.
- Piquette, M., Poppe, A.R., Bernardoni, E., et al. (2019) Student dust counter: Status report at 38 AU. *Icarus* 321, 116. doi: 10.1016/j.icarus.2018.11.012
- Posser, G., Mishra, V., Reis, R., Sapatnekar, S. (2014) Analyzing the electromigration effects on different metal layers and different wire lengths. *21st IEEE International Conference on Electronics, Circuits, and Systems (ICECS)*, 682-685.

- Putala, J., Nousiainen, O., Komulainen, M., Kangasvieri, T., Jantunen, H., Moilanen, M. (2011) Influence of thermal-cycling-induced failures on the RF performance of ceramic antenna assemblies. *IEEE Transactions on Components, Packaging and Manufacturing Technology* 1(9), 1465-1472.
- Qi, H., Osterman, M., Pecht, M. (2009) A rapid life-prediction approach for PBGA solder joints under combined thermal cycling and vibration loading conditions. *IEEE Transactions on Components and Packaging Technologies* 32(2), 283-292.
- Quintero, P., Oberc, T., McCluskey, P. (2008) *Reliability assessment of high temperature lead-free device attach technologies*. In 2008 58th Electronic Components and Technology Conference, IEEE.
- Radamson, H., Thylén, L. (2014) Moore's Law for photonics and electronics. In *Monolithic Nanoscale Photonics-Electronics Integration in Silicon and Other Group IV Elements*: Academic Press.
- Rajaguru, P., Lu, H., Bailey, C. (2015) Sintered silver finite element modelling and reliability based design optimisation in power electronic module. *Microelectronics Reliability* 55(6), 919-930.
- Rastayesh, S., Bahrebar, S., Bahman, A.S., Sørensen, J.D., Blaabjerg, F. (2019) Lifetime estimation and failure risk analysis in a power stage used in wind-fuel cell hybrid energy systems. *Electronics* 8(12), 1412.
- Reuter, D.C., Simon, A.A., Hair, J., et al. (2018) The OSIRIS-REx Visible and InfraRed Spectrometer (OVIRS): Spectral maps of the asteroid Bennu. *Space Science Reviews* 214(2), 54. doi: 10.1007/s11214-018-0482-9
- Rivera, L.A. (2012) Hiring as cultural matching: The case of elite professional service firms. *American Sociological Review* 77(6), 999-1022. Retrieved from <http://www.jstor.org/stable/41723081>
- Robbins, S., Stern, A., Binzel, R., Grundy, W., Hamilton, D., Lopes, R., McKinnon, B., Olkin, C. (2020) *Pluto System Follow On Missions: Background, Rationale, and New Mission Recommendations*. Southwest Research Institute. Retrieved from <https://www.nationalacademies.org/our-work/planetary-science-and-astrobiology-decadal-survey-2023-2032>.
- Rodríguez-Pacheco, J., Wimmer-Schweingruber, R.F., Mason, G.M., et al. (2020) The Energetic Particle Detector. *A&A* 642, A7. Retrieved from <https://doi.org/10.1051/0004-6361/201935287>
- Romero, J.A., Azarian, M.H., Pecht, M. (2020) Life model for tantalum electrolytic capacitors with conductive polymers. *Microelectronics Reliability* 104, 113550.
- Rudra, B., Jennings, D. (1994) Failure-mechanism models for conductive-filament formation. *IEEE Transactions on Reliability* 43(3), 354-360.
- Rymer, A., Runyon, K., Smith, T., et al. (2020) *Neptune and Triton: A Flagship for Everyone*. Johns Hopkins University Applied Physics Laboratory. Retrieved from

<https://www.nationalacademies.org/our-work/planetary-science-and-astrobiology-decadal-survey-2023-2032>.

- Saleh, J.H., Torres-Padilla, J.-P., Hastings, D.E., Newman, D.J. (2006) To reduce or to extend a spacecraft design lifetime? *Journal of Spacecraft and Rockets* 43(1), 207-217.
- Saleh, J.H. (2011) *Spacecraft reliability and multi-state failures: A statistical approach*: Wiley.
- Saleh, J.H., Castet, J.-F. (2011) *Spacecraft Reliability and Multi-State Failures*: John Wiley & Sons, Ltd. 10.1002/9781119994077
- Sangwine, S. (2018) *Electronic Components and Technology*. CRC Press.
- Sarsfield, L.P. (1998) *The Cosmos on a Shoestring: Small Spacecraft for Space and Earth Science*. Santa Monica, CA: RAND Corporation.
- Schilling, O., Leitner, K., Schulze, K.-D., Umbach, F. (2016) End of life and acceleration modelling for power diodes under high temperature reverse bias stress. *Microelectronics Reliability* 64, 458-463.
- Schuster, C.M. (2006) *Negative bias temperature instability (NBTI) experiment*.
- Serebreni, M. (2021) *System Level Effects on Solder Joint Reliability*. Retrieved from https://www.dfrsolutions.com/hubfs/Resources/System_Level_Effects_on_Solder_Joint_Reliability.pdf.
- Shah, S., Elerath, J.G. (2005) *Reliability analysis of disk drive failure mechanisms*. In Annual Reliability and Maintainability Symposium, 2005. Proceedings., IEEE.
- Smith, C., Edwards, R., Whitley, S. (2021) *APL's Spacecraft Reliability Performance*. Paper presented at the Reliability, Availability, and Maintainability Symposium. Orlando, FL.
- Smith, C., Kinnison, J. (2021) *Mission Robustness Starts with Science Requirements Definition*. Paper presented at the AIAA SciTech Forum and Exposition. Virtual.
- Srama, R., Ahrens, T.J., Altobelli, N., et al. (2004) The Cassini Cosmic Dust Analyzer. *Space Science Reviews* 114(1), 465-518. doi: 10.1007/s11214-004-1435-z
- Srinivas, V., Osterman, M., Farrell, R. (2010) Reliability evaluation of one-pass and two-pass techniques of assembly for package on packages under torsion loads. *APEX EXPO, IPC*.
- Stamatelatos, M., Vesely, W., Dugan, J., Fragola, J., Minarick, J., Railsback, J. (2002) *Fault tree handbook with aerospace applications*.
- Stanbery, R. (1964) *Development of Reliability Prediction Techniques for Long Mission Spacecraft*. (MS). University of Arizona.
- Stathis, J.H., Zafar, S. (2006) The negative bias temperature instability in MOS devices: A review. *Microelectronics Reliability* 46(2-4), 270-286.
- Stewart, R. (1969) Effect of failure kinetics on time-to-failure distributions. *IEEE Transactions on Electron Devices* 16(4), 401-402.

- Suzumura, N., Yamamoto, S., Kodama, D., Makabe, K., Komori, J., Murakami, E., Maegawa, S., Kubota, K. (2006) *A new TDDDB degradation model based on Cu ion drift in Cu interconnect dielectrics*. In 2006 IEEE International Reliability Physics Symposium Proceedings, IEEE.
- Timmins, A., Heuser, R. (1971) *A study of first-day space malfunctions*. National Aeronautics and Space Administration.
- Traweek, S. (1988) *Beamtimes and Lifetimes: The World of High Energy Physicists*. Cambridge, MA: Harvard University Press.
- Tsetseris, L., Schrimpf, R.D., Fleetwood, D.M., Pease, R.L., Pantelides, S.T. (2005) Common origin for enhanced low-dose-rate sensitivity and bias temperature instability under negative bias. *IEEE Transactions on Nuclear Science* 52(6), 2265-2271.
- Tucker, S. (2010) *Estimate of the risk of damage to the THEMIS wire boom fine wires due to micrometeoroid and orbital debris impacts*. Boulder, CO.
- U.S. Advisory Group of Reliability of Electronic Equipment (1957) *Reliability of military electronic equipment*. Washington, D.C.: U.S. Government Printing Office.
- Valentin, R., Osterman, M., Newman, B. (2003) *Remaining life assessment of aging electronics in avionic applications*. In Annual Reliability and Maintainability Symposium, IEEE.
- Verma, A., Narula, A., Katyal, A., Yadav, S.K., Anand, P., Jahan, A., Pruthi, S.K., Sarin, N., Gupta, R., Singh, S. (2018) Failure rate prediction of equipment: Can Weibull distribution be applied to automated hematology analyzers? *Clinical Chemistry and Laboratory Medicine (CCLM)* 56(12), 2067-2071.
- Vertesi, J. (2016) Pricing the priceless spacecraft: The social life of money in robotic planetary exploration. Retrieved from https://www.nsf.gov/awardsearch/showAward?AWD_ID=1633314.
- Virkki, J., Tuukkanen, S. (2010) Testing the effects of temperature cycling on tantalum capacitors. *Microelectronics Reliability* 50(8), 1121-1124.
- Waghmode, L.Y., Patil, R.B. (2016) Reliability Analysis and Life Cycle Cost Optimization: A Case Study from Indian Industry. *Int. J. Qual. Rel. Manage.* 33(3), 414-429.
- Wang, J.-S., Tsai, C.-C., Liou, J.-S., Cheng, W.-C., Huang, S.-Y., Chang, G.-H., Cheng, W.-H. (2012) Mean-time-to-failure evaluations of encapsulation materials for LED package in accelerated thermal tests. *Microelectronics Reliability* 52(5), 813-817.
- Wang, T., Hsieh, T., Wang, M.-T., Su, D.-S., Chang, C.-H., Wang, Y., Lee, J.Y.-m. (2004) Stress migration and electromigration improvement for copper dual damascene interconnection. *Journal of The Electrochemical Society* 152(1), G45.
- Weber, M. (1968) *Economy and Society: An Outline of Interpretive Sociology*. Edited by Guenther Roth and Claus Wittich. Translators: Ephraim Fischhoff [and others]. New York: Bedminster Press.
- White, M., Qin, J., Bernstein, J.B. (2011) *A study of scaling effects on DRAM reliability*. In 2011 Proceedings-Annual Reliability and Maintainability Symposium, IEEE.

- Wolff, F., Weyer, D., Papachristou, C., Clay, S. (2021) Design for reliability: Tradeoffs between lifetime and performance due to electromigration. *Microelectronics Reliability* 117.
- Wong, K.L. (1991) The Physical Basis for the Roller-Coaster Hazard Rate Curve for Electronics. *Qual. and Rel. Eng. Inc* 7(6).
- Wong, T. (2012) Time dependent dielectric breakdown in copper low-K interconnects: Mechanisms and reliability models. *Materials* 5(9), 1602-1625.
- Wood, E.G., Herman, J.A., Hall, R.A., Mitchell, A.W., Stella, P.M., Valdez, T.I. (2016) *Multi-mission radioisotope thermoelectric generator experience on Mars*. In Nuclear and Emerging Technologies for Space 2016, Huntsville, AL.
- Xu, L., Ling, S., Lin, Y., Li, D., Wu, S., Zhai, G. (2019) Fretting wear and reliability assessment of gold-plated electrical connectors. *Microelectronics Reliability* 100, 113348.
- Yang, Z.J., Chen, C.H., Xu, B.B. (2013) Reliability analysis of machining center based on the field data. *Maintenance Rel.* 15(2).
- Young, D., Christou, A. (1994) Failure mechanism models for electromigration. *IEEE Transactions on Reliability* 43(2), 186-192.
- Yuan, Z., Deng, J., Wang, D. (2018) *Reliability estimation of aero-engine based on mixed Weibull distribution model*. In IOP Conference Series: Earth and Environmental Science, IOP Publishing.
- Zahedmanesh, H., Pedreira, O., Wilson, C., Tokei, Z., Croes, K. (2019) Copper electromigration: Prediction of scaling limits. *IEEE IITC*.
- Zambotti (2007) *Zambotti Summary of Satellite Failures and Initial Correlation to Parts Programs and Space Anomalies*.
- Zelizer, V.A. (2017) *The Social Meaning of Money: Pin Money, Paychecks, Poor Relief, and Other Currencies*. Princeton, New Jersey: Princeton University Press. Retrieved from <https://press.princeton.edu/titles/11007.html>

Appendix G. Cost Trades

The cost estimate prepared for Interstellar Probe is commensurate with a concept maturity level (CML)-4 mission concept. Section 6 details the methodology used to arrive at the baseline cost estimate. The same methodologies are applied to arrive at the augmented mission and solar Oberth maneuver (SOM) cost trades. The augmented payload and SOM spacecraft estimates capture resources required for a preferred point design for the mission concept trades and take into account the technical and performance characteristics of components. Phase E estimates for both the augmented mission and SOM trade have been updated based on revised timelines for those options.

The result are estimates that are comprehensive and representative of expenditures that might be expected if the Interstellar Probe mission is executed as described by the two options. The estimates are presented in fiscal year 2025 (FY25) dollars, similar to the baseline estimate. The estimates are shown with the same reserve posture as the baseline mission, which carries 50% unencumbered reserves in Phases A–D and 25% unencumbered reserves in Phase E. The development cycle is still assumed to be 8 years with ~50 years of mission operations.

G.1 Augmented Mission

Interstellar Probe		
WBS		FY25\$M
1	Project Management (PM)	
2	Systems Engineering (SE)	\$184
3	Mission Assurance (MA)	
4	Science	\$50
5	Payload	\$429
6	Spacecraft (S/C)	\$388
7/9	Mission Operations and Ground Data Systems (MOps/GDS)	\$37
8	Nuclear Launch Approval	\$26
10	Integration and Test (I&T)	\$104
	Subtotal	\$1217
	Phase A–D Unencumbered Reserves (50%)	\$608
	<i>Phase A–D Total</i>	<i>\$1825</i>
	Phase E Subtotal	\$1270
	Phase E Unencumbered Reserves (25%)	\$317
	<i>Phase E Total</i>	<i>\$1587</i>
	Total Project Cost	\$3413

The cost estimating trades that were analyzed for the augmented mission option included an augmented payload and slight changes to mission activities during Phase E. The augmented mission cost estimate is \$3413M FY25. For Phases A–D, the cost estimate is \$1825M FY25. The Phase E estimate for the augmented option is \$1587M FY25.

G.1.1 Augmented Payload

The Interstellar Probe augmented payload includes many of the same instruments as the notional baseline payload, with the replacement of the Lyman- α Spectrograph with the VisNIR Imager and VisIR Spectral Mapper. In both cases, the payload is notional and assumed to be competed, so this cost element still holds a high degree of uncertainty. As such, it is the cost element with the cost risk. The costing methodology is the same approach that was used for the notional baseline payload, and the technology readiness level (TRL) assumption is the same as well.

Instrument	Cost (FY25\$M)
Payload PMSEMA (project management, systems engineering, and mission assurance)	\$32
Fluxgate Magnetometer (2) + Boom	\$15
Plasma Wave Instrument + Boom	\$51
Solar Wind	\$22
PUI	\$17
Suprathermals and Energetic Ions	\$23
Cosmic Ray Spectrometer	\$35
Interstellar Dust Analyzer	\$20
Neutral Ion Mass Spectrometer	\$74
ENA	\$31
VisNIR Imager	\$98
VisIR Spectral Mapper	\$11
Total	\$429

The estimated cost for the augmented payload is \$429M FY25 compared to the \$361M FY25 of the likely baseline payload estimate.

G.1.2 Augmented Phase E

Mission Operations Cost Model (MOCET) output for Augmented Phase E

Description	Duration (months)	Cost/Mo (FY25 \$M)	Total Cost (FY25 \$M)
Launch & Checkout	2	3.36	6.52
Cruise to Jupiter	7	2.95	20.72
Jupiter Flyby	2	5.23	10.50
Jupiter Flyby Science Data Downlink	1	3.01	3.07
Planetary Flyby Prep	24	5.01	120.35
Planetary Flyby Execution	6	5.23	31.15
Planetary Flyby Data Downlink	3	3.01	9.11
Prep of Flyby Data for PDS	6	3.01	18.03
Inner Heliosphere Phase	142	1.83	260.01
Switch to ngVLA	12	3.01	36.16
Heliosheath Prep/Commanding	2	2.34	4.60
Heliosheath Phase	49	1.83	89.61
Interstellar Prep/Commanding	2	2.34	4.67
Interstellar Phase to 50 Years	358	1.83	655.38
End of Mission		Total	\$ 1,269.89

Similar to the baseline Phase E cost estimate, the NASA Missions Operations Cost Estimating Tool (MOCET) was used to generate the estimate. The augmented mission includes updates to Phase E activities over the baseline. Changes from the baseline Phase E activities include additional activity phases as part of the dwarf planet flyby (preparation, execution, data downlink, prepare data for the Planetary Data System [PDS]). The baseline Phase E cost estimate is \$1.164B FY25 for ~50 years, while the augmented Phase E cost estimate is \$1.270B FY25 for the same time frame.

The costs for the first decade of the augmented mission option are detailed below.

FY	2036	2037	2038	2039	2040	2041	2042	2043	2044	2045	2046
Cost (FY25\$M)	\$3.4	\$42.5	\$60.1	\$60.3	\$47.2	\$24.3	\$22.0	\$22.0	\$22.0	\$22.0	\$22.0

G.2 Solar Oberth Maneuver (SOM)

Interstellar Probe		FY25\$M
WBS		
1	Project Management (PM)	\$264
2	Systems Engineering (SE)	
3	Mission Assurance (MA)	
4	Science	\$50
5	Payload	\$361
6	Spacecraft (S/C)	\$808
7/9	Mission Operations and Ground Data Systems (MOps/GDS)	\$37
8	Nuclear Launch Approval	\$26
10	Integration and Testing (I&T)	\$149
	Subtotal	\$1695
	Phase A–D Unencumbered Reserves (50%)	\$848
	<i>Phase A–D Total</i>	<i>\$2543</i>
	Phase E Subtotal	\$1204
	Phase E Unencumbered Reserves (25%)	\$301
	<i>Phase E Total</i>	<i>\$1505</i>
	Total Project Cost	\$4048

The cost estimating trades that were analyzed for the SOM mission option included an updated spacecraft design that makes the SOM possible and slight changes to mission activities during Phase E. The SOM option mission cost estimate is \$4048M FY25. For Phases A–D, the cost estimate is \$2543M FY25. The Phase E estimate for the SOM option is \$1505M FY25.

G.2.1 SOM Spacecraft

The SOM spacecraft option cost estimate includes the baseline spacecraft cost estimate plus additional efforts for the SOM-specific elements. The SOM elements include: additional SOM hardware for the baseline spacecraft (interface [I/F] cards, propulsion diode box, radioisotope thermoelectric generator [RTG] deployment hinges, additional harness), an interstage, a Star 48BV, shield and support structure, and a ballast. The estimate also includes minor cost savings for the reduction of the high-gain antenna (HGA) from 5 m to 2 m.

Subsystem	SOM Estimate	Notes
Spacecraft PMSEMA (project management, systems engineering, and mission assurance)	\$73	
Baseline Spacecraft Hardware	\$335	
Flight Software	\$28	
SOM-Specific Hardware	\$372	

Subsystem	SOM Estimate	Notes
Interstage	\$61	Includes structure, separation hardware, bipropellant subsystem
Star 48BV	\$48	
Shield	\$177	Includes support structure
Ballast	\$72	Includes support structure
Miscellaneous Hardware	\$13	I/F cards, propulsion diode box, RTG deployment hinges, additional harness; savings on HGA diameter reduction
Total (FY25\$M)	\$808	

The TruePlanning parametric estimate was also updated to show cost realism and validate the primarily SOM spacecraft cost estimate. The TruePlanning estimate is shown by subsystem and overall is within 3% of the primary SOM spacecraft estimate. In general, most subsystems are validated within 30%, which is expected for this level of maturity.

Subsystem	SOM Estimate	Price TruePlanning	Delta (%)
Spacecraft PMSEMA (project management, systems engineering, and mission assurance)	\$73	\$71	-3%
Mechanical and Structures	\$41	\$21	-50%
Electrical Power (EPS)	\$148	\$171	15%
Thermal Control	\$5	\$6	23%
Avionics	\$57	\$51	-11%
Telecommunications	\$52	\$44	-16%
Guidance, Navigation, and Control	\$16	\$17	4%
Propulsion	\$15	\$17	19%
Flight Software	\$28	\$28	0%
SOM-Specific Hardware	\$372	\$355	-5%
Total (FY25\$M)	\$808	\$780	-3%

G.2.2 SOM Phase E

Similar to the baseline Phase E cost estimate, the MOCET tool was used to generate the SOM Phase E estimate. The SOM option includes changes to Phase E activities over the baseline. In particular, updates from the baseline Phase E activities include: a longer cruise to Jupiter, solar-encounter-related phases (transit, encounter), and spacecraft separation. The baseline Phase E cost estimate is \$1.164B FY25 for ~50 years, while the augmented Phase E cost estimate is \$1.204B FY25 for the same time frame.

Mission Operations Cost Model (MOCET) output for SOM Phase E

Description	Duration (months)	Cost/Mo (FY25 \$M)	Total Cost (FY25 \$M)
Launch & Checkout	2	3.36	6.52
Cruise to Jupiter	15	2.95	44.29
Jupiter Flyby	2	5.23	10.47
Jupiter Flyby Science Data Downlink	1	3.01	3.06
Transit to Solar Encounter	24	2.95	70.63
Solar Encounter to Spacecraft Separation	4	3.01	12.08
Wire Antenna Deployment	1	3.01	3.07
Inner Heliosphere Phase	142	1.83	259.81
Switch to ngVLA	12	3.01	36.16
Heliosheath Prep/Commanding	2	2.34	4.76
Heliosheath Phase	49	1.83	89.55
Interstellar Prep/Commanding	2	2.34	4.67
Interstellar Phase to 50 Years	360	1.83	659.05
End of Mission		Total	\$ 1,204.14

The costs for the first decade of the SOM mission option are detailed below.

FY	2036	2037	2038	2039	2040	2041	2042	2043	2044	2045	2046
Cost (FY25\$M)	\$3.4	\$35.8	\$40.0	\$35.4	\$35.7	\$22.0	\$22.0	\$22.0	\$22.0	\$22.0	\$22.0

G.3 Comparisons to Baseline

The cost estimate for the baseline Interstellar Probe mission is detailed in Section 6. The baseline Interstellar Probe cost estimate, including 50% reserves on Phases A–D and 25% reserves on Phase E, is \$3144M FY25. The table below compares this estimate to the Phases A–D, Phase E, and total mission cost for the augmented and SOM options.

	Cost in FY25\$M		
	Baseline	Augmented	SOM
Phases A–D	\$1689	\$1825	\$2543
Phase E	\$1455	\$1587	\$1505
Total Mission	\$3144	\$3413	\$4048

The first decade of Phase E operations also differs between the three options. A comparison of the first decade of operations, by fiscal year, is presented below. It should be noted that all three options launch in September 2036, so FY36 includes only a month of costs.

FY	2036	2037	2038	2039	2040	2041	2042	2043	2044	2045	2046
Baseline	\$3.4	\$40.7	\$22.0	\$22.0	\$22.0	\$22.0	\$22.0	\$22.0	\$22.0	\$22.0	\$22.0
Augmented	\$3.4	\$42.5	\$60.1	\$60.3	\$47.2	\$24.3	\$22.0	\$22.0	\$22.0	\$22.0	\$22.0
SOM	\$3.4	\$35.8	\$40.0	\$35.4	\$35.7	\$22.0	\$22.0	\$22.0	\$22.0	\$22.0	\$22.0

The baseline Phase E plan has a quick Jupiter flyby in 2037 before transitioning to nominal operations. The augmented option includes both a Jupiter flyby and another planetary flyby. The SOM option includes a Jupiter flyby and a solar encounter.

Appendix H. Mission Architecture

H.1 Background

As noted elsewhere, consideration of the use of super heavy-lift launch vehicles (SHLLVs; Wikipedia, 2021), and, in particular, those with a payload capability to low Earth orbit (LEO) of greater than 90 mt, began with a National Academies study (NRC, 2008) based on the Ares V concept (Wikipedia, 2021c). To date, the only operational vehicle in this class that was also successful was the Saturn V of the Apollo lunar program.¹

After a chance encounter with a member of Boeing’s Mission Concept Formulation group at the fall 2012 meeting of the Division for Planetary Sciences (DPS) of the American Astronomical Society (AAS), Boeing provided a variety of initial analyses of upper stages on NASA’s Space Launch System (SLS). These analyses were performed while the SLS design and characteristics continued to evolve (R. L. McNutt, Jr. et al., 2014; R. L. McNutt, Jr., Benson, et al., 2015). The analyses also led to a set of (mostly) currently operational stages² for consideration in analyses undertaken with the aid of personnel at Marshall Space Flight Center (MSFC) several years later. Members of the Interstellar Probe study team began working with members of the SLS team after an informal, chance meeting at the 68th International Astronautical Congress (IAC) in Adelaide, Australia, in late September 2017. Multiple technical exchanges led to a comprehensive set of staging curves (injected mass versus C_3) in December 2019, which have been used in the Interstellar Probe trade-space study (Stough et al., 2019).

While the performance of the vehicle configuration used in the analysis, namely the SLS Block 2 Cargo, will continue to evolve, this performance prediction “snapshot” provides for a consistent, quantitative basis in looking at the overall SHLLV trade space that could be available in the time frame of the 2030s. The text and figures that follow are excerpted from R. L. McNutt, Jr. et al. (2021) (©2021 by The Johns Hopkins University; published by the International Astronautical Federation [IAF], with permission, and released to the IAF to publish in all forms).

H.2 Trade-Space Methodology

H.2.1 Staging Selections

Informed by the previous work in the 2012–2017 time period, MSFC began looking at staging configurations, as suggested by the pre-Interstellar Probe Study group at the Johns Hopkins Applied Physics Laboratory (APL) in 2018. The initial “data drop” was in August 2018. The initial eight cases studied were all based on the SLS Block 1B+ (cargo)—now referred to as the SLS Block 2 Cargo.

¹ The Soviet N-1 moon rocket had four unmanned test flights, all of which failed with catastrophic failure of the first stage in flight.

² For comparison purposes, the Star 48GXV stage, originally in development for potential use on NASA’s Parker Solar Probe mission, and the Centaur D, now retired, were used for some comparison with other stages.

These cases (and the notation) all assume that the SLS second stage is the Exploration Upper Stage (EUS) and that the solid boosters are from the Booster Obsolescence Life Extension (BOLE) program. MSFC has also applied what they consider to be appropriate Manager's Reserves; those have been used as "pass throughs" in the following analyses applied here.

To accommodate calculations of option 2 and option 3 performance with a three-stage vehicle (i.e., with the SLS core [first stage] plus EUS [second stage] plus an additional kick stage [third stage] combination), data in the form of injected mass versus C_3 (as a table of points), were provided by MSFC for the following:

1. (Two stages) The SLS Block 1B+ (alone)
2. (Three stages) SLS Block 1B+ with
 - a. Castor 30B
 - b. Castor 30XL
 - c. iCPS
 - d. Centaur III (upper stage of the Atlas V series)
3. (Four stages) SLS Block 1B+ with
 - a. Castor 30B + Star 48BV
 - b. Castor 30XL + Star 48BV
 - c. Centaur III + Star 48BV

On 18 November 2019, additional cases calculated included the following:

1. (Three stages) SLS Block 1B+ with
 - a. Star 48BV
 - b. Star 48GXV
 - c. Orion 50XL
 - d. Centaur D
2. (Four stages) SLS Block 1B+ with
 - a. Castor 30B + Star 48GXV
 - b. Castor 30XL + Star 48GXV
 - c. Centaur III + Star 48GXV
 - d. Orion 50XL + Star 48BV

- e. Orion 50XL + Star 48GXV

One day later (19 November 2019), these were augmented with two final cases:

1. (Four stages) SLS Block 1B+ with
 - a. Centaur D + Star 48BV
 - b. Centaur D + Star 48GXV

H.2.2 Parametric Injected Mass Inversion

To determine the launch configuration performance as a function of the stack mass, parametric fits of the C_3 as a function of the injected mass m were derived. A logarithmic fit was used when adequate (13 cases), and power laws were used otherwise ($O(m^4)$ for one case and $O(m^6)$ for the other four). The algorithms are in Table H-1, where $y \equiv C_3$ and $x \equiv m$.

H.2.3 Additional SLS and Non-SLS Cases

Extensive analyses are not, in general, available for other existing (less capable) launch vehicles or for other cases. Exceptions include a lunar L-1 (Gateway departure) using a three-stage combination of Advanced Cryogenic Evolved Stage (ACES) (“first” stage) plus Centaur III (second stage) plus Star 48BV (third stage), the use of a Fregat upper stage, and a Delta IV Heavy plus Star 48GXV stage. The latter used a mass performance curve from preliminary Parker Solar Probe studies. The parametric representation corresponding to those with the SLS in Table H-1 is (m in kg; C_3 in km^2/s^2):

$$C_3 = 8.4742 \times 10^{11} m^3 + 2.0862 \times 10^{-6} m^2 - 0.024103 m + 115.8.$$

A third case (point design) considered the use of two SLS B1B+ launch vehicles. Launch dates were restricted to calendar year 2030 and using a solar Oberth maneuver (SOM) at a $5 R_S$ perihelion. Both orbital units are docked in Earth orbit (similar to the Earth orbital rendezvous [EOR] scenario initially considered using two Saturn V launches for Apollo missions to the Moon) (Von Braun, 1962). The SOM offered better performance for an 850-kg spacecraft; however, there was no mass included for a thermal shield, likely invalidating the approach. As with the EOR approach for Apollo, the need for two expensive launch vehicles to both launch in a limited window puts the second launch into an operational critical path.³

An additional point design discusses a SOM with a dual Jupiter flyby (Gath, 2019). Fairly large propulsive maneuvers are required, and there is no discussion of thermal shield requirements for the SOM. Other more exotic configurations also using a SOM have also been considered (Alkalai et al., 2020), but the key question of the required solar thermal shield has not been studied in a system-consistent fashion.

³ The dual Gemini/Agena launches finally worked on Gemini VIII (failure on Gemini side), Gemini X, Gemini XI, and Gemini XII. The Agena failed to orbit on Gemini VI, leading to the Gemini VIa/VII rendezvous, and the Agena on Gemini IX suffered a launch failure. The subsequent Gemini IX-A using the backup Augmented Target Docking Adapter (ATDA) precluded docking because of the failure of the fairing ejection on the latter.

Table H-1. Parametric C_3 versus injected mass.

Case	Configuration	Formula	R^2
1	B1B+	$y = 8.5586E-06x^4 - 1.7760E-03x^3 + 1.4092E-01x^2 - 6.3957E+00x + 1.2989E+02$	0.997800
2	B1B+ w Castor 30B	$y = 1.709493E-06x^6 - 2.420856E-04x^5 + 1.346626E-02x^4 - 3.749635E-01x^3 + 5.583832E+00x^2 - 4.725456E+01x + 2.680922E+02$	0.999026
3	B1B+ w Castor 30XL	$y = 1.410757E-06x^6 - 1.923049E-04x^5 + 1.037400E-02x^4 - 2.838831E-01x^3 + 4.267825E+00x^2 - 3.885251E+01x + 2.508873E+02$	0.999685
4	B1B+ w Castor 30B + Star 48BV	$y = -69.455841\ln(x) + 255.566072$	0.998520
5	B1B+ w Castor 30XL + Star 48BV	$y = -70.330884\ln(x) + 256.023114$	0.999131
6	B1B+ w Star 48BV	$y = -50.88571\ln(x) + 194.71810$	0.998140
7	B1B+ w Star 48GXV	$y = -54.628104\ln(x) + 206.371212$	0.999245
8	B1B+ w Centaur III	$y = 7.936102E-07x^6 - 1.226799E-04x^5 + 7.517819E-03x^4 - 2.345327E-01x^3 + 4.047305E+00x^2 - 4.242123E+01x + 3.057394E+02$	0.999723
9	B1B+ w Centaur III + Star 48BV	$y = -77.68341\ln(x) + 292.35354$	0.999590
10	B1B+ w Centaur III + Star 48GXV	$y = -77.13453\ln(x) + 290.41551$	0.999310
11	B1B+ w Castor 30B + Star 48GXV	$y = -69.21686\ln(x) + 255.46901$	0.999040
12	B1B+ w Castor 30XL + Star 48GXV	$y = -70.53395\ln(x) + 257.31655$	0.999310
13	B1B+ w Orion 50XL	$y = -55.01960\ln(x) + 208.06835$	0.999050
14	B1B+ w Orion 50XL + Star 48BV	$y = -65.06501\ln(x) + 237.84223$	0.997030
15	B1B+ w Orion 50XL + Star 48GXV	$y = -63.63289\ln(x) + 236.89191$	0.998940
16	B1B+ w Centaur D	$y = 4.02373E-06x^6 - 4.65738E-04x^5 + 2.13711E-02x^4 - 5.00513E-01x^3 + 6.53171E+00x^2 - 5.25347E+01x + 3.13606E+02$	0.999812
17	B1B+ w Centaur D + Star 48BV	$y = -76.55688\ln(x) + 287.40936$	0.999280
18	B1B+ w Centaur D + Star 48GXV	$y = -75.64832\ln(x) + 284.50096$	0.999160

Notes:

Mass entries are all in metric tons (mt); C_3 units are km^2/s^2 .

All cases, except for 1, 2, and 3 are valid for $200 \text{ kg} \leq m \leq 3,000 \text{ kg}$.

Case 1 valid range: $300 \text{ kg} \leq m \leq 30,000 \text{ kg}$.

Cases 2 and 3 valid range: $1,500 \text{ kg} \leq m \leq 30,000 \text{ kg}$.

Finally, in an attempt to compare a space-storable bipropellant system, we have included options 2 and 3 for the use of a Fregat stage (Wikipedia, 2021a; mostly for the purpose of looking at option 3). This is the least massive bipropellant stage identified but is not really internally consistent, because there is a limited lifetime driven by the use of an onboard battery rather than the use of a longer-term power supply.

H.2.4 Implementation of the SOM Cases

The SOM cases of option 3 add an additional, and nontrivial, amount of complexity to globally scoping the full extent of the trade space. Locating the optimal trajectory for a given observatory

mass and configuration using a given kick stage is a design-dependent, nonlinear iterative process (repeated from Appendix D):

1. Select (separated) spacecraft mass.
2. For all launch vehicle stacks with “valid” solutions (e.g., sufficient launch C_3 to reach Jupiter), locate the “best” cases by examining the asymptotic flyout speeds and corresponding flight times to some “target” distance (we have been using 500 au).
3. For each “selected case,” check that the design perihelion is less than the actual perihelion achieved.
4. For the cases in item (3), choose the one for which the two numbers are closest; this will be the “optimal” solution for that vehicle stack.
5. Compare across stacks and pick the best.
6. Compare with best-performing option 1 and best-performing option 2 cases for the given, separated spacecraft mass.
7. Use this “best” solution as the starting point for more detailed trajectory analyses, including actual planetary orbits, finite launch windows, and backup launch windows.

H.2.4.1 *Input Conditions*

The initial inputs consist of (1) the separated spacecraft mass, here referred to as the “observatory mass.” This is the wet mass of the separated spacecraft after the final kick-stage burn, including all propellant (with residuals and pressurant, as required), margins, and contingencies. From this, we can determine the component of maximum launch C_3 , which determines minimum achievable perihelion distance R_s ($1 R_s$ is defined as the solar radius; distances are measured from the *center* of the Sun). In addition, we can determine the component of achievable ΔV at the Sun from the kick-stage burn.

We also require (2) the observatory configuration (i.e., the component of the thermal shield constraint that, in turn, drives the thermal shield mass).

Finally, there is (3) the selected kick stage. Its mass drives the maximum launch C_3 achievable. Also, its configuration drives the thermal shield mass (from the required umbra from the thermal shield), and finally, the propellant load also drives maximum achievable ΔV .

Additional mass liens fall on both options 2 and 3 because of the need for heat distribution to the kick stage to keep both the temperature of and thermal gradients across the propellant within specifications to allow a successful burn. In principle, this can be accomplished with electrical heaters drawing electrical power from the radioisotope thermoelectric generators (RTGs) directly or by tubing and a pumped working fluid to move the rejection heat directly. A full-up system trade study has not been undertaken, but a study of the typical mass required for the working fluid approach for the various stages under consideration has been made, including an allowance for a thermal shroud for the kick stage (Table H-2).

Other mass liens for the use of a kick stage in deep space include the adaptor to the kick stage from the Earth-ignition stages and the adaptor to the observatory from the kick stage.

In addition to these items, there are further liens for option 3. Even with a “balance mass,” a not-designed “interstage” is still required as part of the observatory-to-kick-stage adaptor to support the thermal system and provide guidance and control (G&C) and an attitude articulation and control system (AACS) to control the kick stage/thermal shield system during the kick-stage burn.

The current thermal system concept comprises four parts: (1) thermal protection system (TPS) – carbon shield, (2) thermal shield assembly (TSA) – carbon shield support, (3) up to three additional shields and their supports, and (4) a balance mass and its structural support (to maintain the system center of gravity along the centerline of the kick stage during the kick-stage burn). Even with this, the interstage control system is still required to “fine-tune” the pointing to ~1° during the burn, based on experience with the pointing and control system implemented on Parker Solar Probe.

The master equipment list (MEL) is based on a more detailed one for the option 1 observatory. Figure H-1 shows MEL “ground rules” for the option 3 configuration. Figure H-2 shows the option 3 thermal system masses for the Star 48BV, Star 48GXV, and Orion 50XL using the ultra-high-temperature (UHT) shield material. Detailed designs were not made for the Castor 30B and Castor 30XL because it was already clear that those stacks with the corresponding thermal shields would be too heavy to use.

H.2.4.2 Option 3 Study Approach

The overall study approach was resource limited and can be described as follows:

1. Initiate thermal shield configuration study with known materials from Parker Solar Probe study augmented by (known) refractory metals to go to closer perihelion than Parker Solar Probe (Parker Solar Probe specifications all available).

Table H-2. Thermal control kick-stage mass.

Motor	Thermal Shroud (kg)	Total (kg)
Star 48BV	7.60	28.36
Star 48GXV	11.63	32.39
Orion 50XL	11.58	32.35
Castor 30B	9.35	29.95
Castor 30XL	41.20	62.30

Basis of SOM MEL Estimate			
Item	CBE	Contingency	Total
Spacecraft	900	0%	900
Interstage	200	50%	300

Figure H-1. MEL basis for option 3. The spacecraft adds 40 kg to the 860-kg option 1 observatory to accommodate the twin RTG booms that must be deployed after the SOM (in practice after passing Venus’ orbit outbound). This provides a better view of deep space and, hence, a lower cold-side temperature to allow the RTGs to come up to full power. Given all of the uncertainties, an unallocated margin of 30% is added to the spacecraft, interstage, and thermal shield assembly and all of those masses. CBE, current best estimate. (Image credit: Johns Hopkins Applied Phys-

Star 48BV	2Rs	3Rs	4Rs	5Rs	6Rs
	kgs	kgs	kgs	kgs	kgs
Main TPS	253.8757	176.9827	149.3453	130.4849	124.1845
Refractory shield 1	33.9786	23.2557	19.9762	N/A	N/A
Refractory shield 2	35.3167	24.2128	20.4525	N/A	N/A
Refractory shield 3	36.7364	25.2061	20.7700	N/A	N/A
Ref shield support 1	17.2138	13.0771	11.0314	N/A	N/A
Ref shield support 2	18.5111	13.2268	10.6458	N/A	N/A
Ref shield support 3	18.3523	13.6168	10.4916	N/A	N/A
Main shield support	239.4287	234.4166	200.9732	195.2488	190.5723
Balance mass	457.5477	370.9705	315.1152	215.0708	207.8905
Balance mass support	21.0331	21.0331	21.0331	21.0331	21.0331

Star 48GXV	2Rs	3Rs	4Rs	5Rs	6Rs
	kgs	kgs	kgs	kgs	kgs
Main TPS	275.9384	194.5276	163.6471	143.2717	136.2183
Refractory shield 1	36.8907	25.7051	21.8586	N/A	N/A
Refractory shield 2	38.3558	26.7665	22.3893	N/A	N/A
Refractory shield 3	39.9071	27.8188	22.7703	N/A	N/A
Ref shield support 1	18.1618	13.8346	12.1381	N/A	N/A
Ref shield support 2	20.2665	13.6803	11.4759	N/A	N/A
Ref shield support 3	20.4207	14.1385	11.3716	N/A	N/A
Main shield support	275.4213	263.4691	226.3109	220.2917	214.7896
Balance mass	509.1847	411.6532	350.5453	241.5017	233.3506
Balance mass support	21.4277	21.4232	21.4186	21.4141	21.4141

Orion 50XL	2Rs	3Rs	4Rs	5Rs	6Rs
	kgs	kgs	kgs	kgs	kgs
Main TPS	273.9335	192.9265	162.3498	142.1241	135.1252
Refractory shield 1	36.6276	25.4919	21.6863	N/A	N/A
Refractory shield 2	38.0791	26.5488	22.2124	N/A	N/A
Refractory shield 3	39.6168	27.5966	22.5889	N/A	N/A
Ref shield support 1	18.1618	13.8346	12.1381	N/A	N/A
Ref shield support 2	20.2665	13.6803	11.4759	N/A	N/A
Ref shield support 3	20.4207	14.1385	11.3716	N/A	N/A
Main shield support	275.1491	262.9294	225.7711	219.7474	214.2362
Balance mass	506.1093	409.5985	348.6629	240.4720	232.3391
Balance mass support	21.4595	21.4957	21.4912	21.4867	21.4867

Figure H-2. Thermal shield assembly component masses for a Star 48BV, Star 48GXV, and Orion 50XL motor as a function of perihelion distance (2–6 solar radii from the center of the Sun). (Image credit: Johns Hopkins Applied Physics Laboratory.)

2. Initiate thermal shield size and shape study by assuming use of New Horizons spacecraft with RTG opposite thermal shield to provide (1) some mass balance and (2) maximum power from maximum radiator view into deep space.
3. No attempt to “balance” the configuration during kick-stage burn (would provide unacceptably large torques about the assembled center of gravity during the burn without significant attitude control system thrusters and propellant – not included).

4. Initiate trade study with assumed perihelia of $3R_s$, $4R_s$, and $5R_s$. n.b. At distances closer than $3R_s$, all Parker Solar Probe-era refractory materials melt and/or lose all structural integrity (Ralph L. McNutt, Jr. et al., 2019).
5. Initiate study of post-Parker Solar Probe UHT materials to identify shield materials lighter than refractory metals but with their strength and higher melting points.
6. Focus on new metal carbide-on-carbon (MC/C).
7. Begin systematic laboratory tests (thermal and strength).
8. Complete initial thermal shield configuration and mass studies for $3R_s$, $4R_s$, and $5R_s$ for the following kick stages: Star 48BV, Castor 30B, Castor 30XL, Centaur D (size study only; cryogenic long-term storage not credible), and Orion 50XL. Star 48GXV added subsequently. All told, yielded 18 thermal shield point designs.
9. To further explore the trade space, point designs at $6R_s$, and $12R_s$ were subsequently added for the Orion 50XL case and at $6R_s$ for both the Star 48BV and Star 48GXV cases (four more cases for 22 point designs).
10. An initial cut eliminated configurations for option 3 in which the designated kick stage could not be lifted to Jupiter on a direct trajectory.
11. Eliminated kick stages include Castor 30XL, Castor 30B, Centaur D (cryogenic anyway), and Centaur III (cryogenic anyway).
12. Heavier stages would similarly not reach Jupiter, and these were dropped without any study: ACES (Vulcan Centaur stage) and iCPS.
13. Although some other configurations could reach Jupiter, those showing promise included only the Star 48BV, Star 48GXV, and Orion 50XL as the kick stage for the maneuver.
14. After the completion of the MC/C material study, an initial concept design of a baseline spacecraft almost twice the mass of New Horizons (860 kg versus 478.3 kg) was completed. That was repackaged with a nominal observatory mass of 900 kg and used (with the MC/C material) as the basis for point designs of thermal shields to go with the Star 48BV, Star 48GXV, and Orion 50XL kick stages at perihelia of $2R_s$, $3R_s$, $4R_s$, $5R_s$, and $6R_s$. This yielded 15 new thermal shield point designs (Figure H-3). To evaluate a space-storable, liquid, higher-specific-impulse case, the lowest-mass Fregat motor was included in the trade space. For this “Fregat” case, the Orion 50XL model was adopted to approximate the likely mass of a shield for the much heavier Fregat.

H.2.4.3 Option 3 Solution Methodology

Problem: For a given spacecraft (mass and configuration), determine the optimal kick stage (from available set) and minimum time to a set distance.

Interrelationships: For a given kick stage, the combined configuration and mass of the kick stage plus spacecraft assembly dictate the required thermal shield mass for a set perihelion distance. However, the actual perihelion is set by the total mass of the spacecraft plus kick stage plus thermal shield.

Issues:

1. If the actual perihelion is less than the design perihelion, the trajectory would lead to the destruction of the spacecraft.
2. If the actual perihelion is larger than the design perihelion, the trajectory will provide less than optimal performance.

Approach:

1. If the actual perihelion is greater than the design perihelion, accept the solution as is.
2. If the actual perihelion is less than the design perihelion, decrease the launch C_3 until the actual perihelion increases to the design perihelion (this is accomplished by under-burning the last liquid stage during trans-Jupiter injection from Earth; see Table H-3).
3. For the given observatory mass plus kick stage plus kick-stage mass, select the thermal shield/perihelion combination that provides the minimal travel time to a set distance.
4. Increment or decrement the observatory mass and repeat to build up the appropriate trade-space curve for that particular kick stage.
5. Repeat for all kick stages, but reject all kick stages too heavy to reach Jupiter with a minimum-mass observatory (< 10 kg).

Complications Inherent in the Approach:

1. Appropriate thermal shield designs are not elements of a continuum (i.e., they are all inherently point designs for the given observatory configuration and mass).

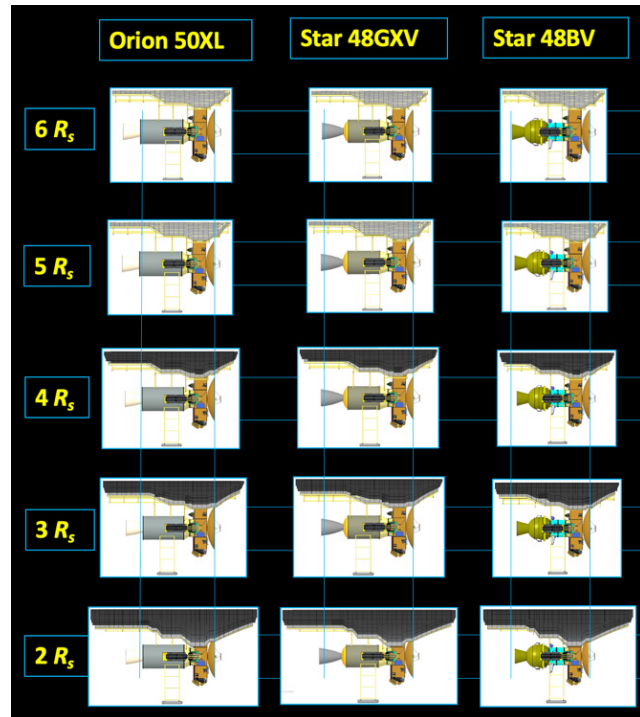


Figure H-3. Point-design matrix for option 3 baseline spacecraft. Decreasing kick-stage engine size is to the right, and decreasing perihelion design distance is toward the bottom. The number of shields required to “step down” the external temperatures on the shield exposed directly to sunlight increases with decreasing distance, as does the length and width of the shield because of the increasing solid angle filled by the solar disk. The Orion 50XL and Star 48GXV have comparable lengths, with the latter having a smaller diameter (and less propellant load). (Image credit: Johns Hopkins Applied Physics Laboratory.)

2. If the observatory configuration and mass change, a re-optimized thermal shield will affect the trajectory performance.
3. For a given observatory configuration and mass, it is not a priori evident how coarse or fine a grid of perihelion “target designs” suffices to locate the optimal performance point.
4. The optimization is inherently non-linear.
5. Provision of point designs for a given perihelion distance is an inherently time-consuming process.
6. The thermal shield mass affects the ΔV from a given kick stage; the ΔV and perihelion together define the trajectory performance.

Table H-3. Nominal minimum C_3 s for indicated perihelia (ideal circular planetary orbits; R. L. McNutt, Jr. (2021)).

Perihelion (R_s)	C_3 (km^2/s^2)
12.0000	101.1122
6.0000	104.5441
5.0000	105.2960
4.0000	106.1398
3.0000	107.1130
2.0000	108.2887
1.0000	109.8555
0.0000	113.7982

One can then finally make some 0th-order estimates of the upper limit of performance by using an analytic, simplified, patched-conic model for the calculations (R. L. McNutt, Jr., 2021).

The “correct” C_3 s vary, of course, over Jupiter’s ~ 11.86 -year solar orbit because of the inclination of Jupiter’s orbit with respect to the ecliptic and the non-zero eccentricities of the orbits of Earth and Jupiter. Nonetheless, the numbers provided in Table H-3 give good estimates of the minimal C_3 required to reach the stated perihelion (assuming the Jupiter-to-Sun transfer orbit remains in the assumed common orbital plane).

H.2.5 “Best” Trajectories

H.2.5.1 Guidelines

As noted previously, the observatory mass is agnostic with respect to payload, for convenience by design. The Heliophysics Baseline payload or Augmented (Planetary Science and Astrophysics) payload are sufficiently close in mass that they can be taken as interchangeable at this level of analysis.

Across the three options, in addition to the thermal control for the kick stage in options 2 and 3 and the TSA for option 3, the assumed “nominal mass” also varies:

- Option 1: 860 kg
- Option 2: 930 kg
- Option 3: 900 kg + 200 kg “interstage”
- Reserves and margins

The kick-stage-to-spacecraft adaptor mass also includes ~ 75 kg for the “smart-stage” avionics used on Parker Solar Probe in that upper stage. As noted previously, option 1 carries a mass of 860 kg,

and option 2 adds an additional 70 kg of propellant to the nominal mass for G&C during the kick-stage burn at Jupiter.

The constraints of the thermal shield required a significant rethinking of the spacecraft layout for option 3 (see Figure H-6). In particular, the 5-m-diameter high-gain antenna (HGA) baselined for options 1 and 2 cannot be accommodated for option 3 because the corresponding thermal shield would no longer fit in the SLS Block 2 Cargo payload fairing. To provide communications before the SOM, a 3-m-diameter HGA was baselined along with a switch from X-band to Ka-band. This renews all of the pointing requirements and threats that now require a new technical solution without the use of reaction wheels, none of which can currently last for the required 50 years (Ashtari et al., 2021).

Similarly, the two RTGs must now be on deployable booms, similar to the case for the Voyagers (Heacock, 1980), but remaining folded behind the thermal shield for several years until the SOM. An additional 40 kg is allocated for these, bringing the nominal option 3 spacecraft mass up to 900 kg (from 860 kg for option 1). This also adds an additional mission risk that the power for almost the entire mission will be lower than nominal if the RTG booms fail to deploy to provide a better cold sink to deep space for the radiator fins on them. In addition, any asymmetry in the deployment will complicate further the spin stabilization of the spacecraft, precession of the HGA for downlink, and pointing accuracy of the Ka-band HGA for downlink. These are additional risks to the mission for this architecture. Also, in this case, the G&C, AACS, and associated propellant are carried in an additional 200-kg “interstage” to which a 50% contingency (100 kg) has been assigned.

In addition, unallocated margins of 30% have been assigned to the thermal system, observatory, and other mass liens on option 3. Given the current maturity level, risks as noted, and uncertainties of the design at the moment, such mass margins are appropriate and in line with current NASA practice at this stage of such a study.

H.2.5.2 Trajectory Results

In adapting and expanding the initial thermal shield system (Ralph L. McNutt, Jr. et al., 2019), the steps outlined in Sections H.2.4.2 and H.2.4.3 (above) yielded a total of 181 configurations under investigation over the course of this study. Of those, 18 configurations were too heavy to reach Jupiter with no payload (<100-kg spacecraft), performance data were not available for 24, and 4 were duplicate entries. Results are tabulated for the baseline spacecraft for each option (see Section H.2.5.1) in Table H-4.

Given this analysis, the “best case” characteristics for each option are shown in Table H-5. Here V_{esc} is the asymptotic escape speed from the Sun (Voyager 1 is currently fastest at ~ 3.6 au/year), C_3 is the launch C_3 , ΔV_J is the kick-stage boost at Jupiter for option 2, ΔV_S is the kick-stage boost for the SOM at the Sun for option 3, and $\tau_{400 au}$ is the time it takes for the observatory to get to 400 au after launch.

Table H-4. Option results for 860-kg observatory.

Option	Total	Valid	Rejected
1	28	19	9
2	28	18	10
3	125	75	50
All	181	112	69

Several observations are in order. First, all of these are four-stage launch stacks; in each case, the third stage is a Centaur III (the same stage as used for the second stage of the Atlas V launch vehicle). Second, the fourth stages are abbreviated because of spacing constraints: “48BV” = Star 48BV, “48GXV” = Star 48GXV, and “50XL(2)” = Orion 50XL at 2 R_s perihelion using the advanced MC/C thermal shield material. Third, although the option 3 escape speed is highest, it reaches 400 au per year later than option 2 because of the additional time spent in the inner solar system and getting near the Sun. Fourth, option 2 has a flyout time ~ 0.5 au/year faster than option 1; option 1 reaches 400 au ~ 1 year later than option 3 and 2 years later than option 2. Note that 400 au was chosen as the reference distance because it is reached just over the nominal lifetime requirement of 50 years.

Table H-5. “Best” trajectories for 860-kg observatory.

Quantity
Stack
V_{esc} [au/yr]
C_3 [km ² /s ²]
ΔV_J [km/s]
ΔV_S [km/s]
τ_{400} [yr]

We also note that the injected mass increases in going from option 1 to option 2 to option 3. For option 2, the final injected mass from Earth (including all contingencies, reserves, and margins) is 4470.84 kg, and for option 3, the injected mass is 7928.87 kg. The corresponding fourth-stage mass—if separated—for option 1 would be 3302.02 kg (in practice, this is an intermediate step occurring as part of the Earth launch sequence). These numbers go with the entries by option in Table H-5.

It should be noted that the Star 48GXV, while test fired during the Parker Solar Probe development program, was never fully qualified for flight. If one “drops back” to comparing option 1 against other option 2 stacks, then the option 2 version using the Centaur III and an Orion 50XL takes only 0.11 years longer to reach 400 au and that with the Star 48BV takes ~ 0.6 years longer.

In general, the option 2 trajectories are slightly faster than with the same hardware for option 1, but the hardware masses for option 2 are subject to more uncertainty, and thermally maintaining the working kick stage to Jupiter also incurs more risk. Also, the large acceleration at Jupiter when the kick stage fires will preclude the deployment of the magnetometer or plasma wave electric field antenna booms until after the Jupiter flyby. The same, of course, holds true for option 3: those deployments will have to wait until the spacecraft is at about Venus’ orbit outbound from the Sun, about 3 years into the mission. This later deployment is a science risk to the mission, which must be taken into consideration.

H.2.5.3 Trajectory Overview

An overview of all valid trajectories, which include those highlighted in Table H-5, are shown in Figure H-4 and Figure H-5. Figure H-5 shows all 112 valid trajectory results of Table H-4 plotted to 1000 au with flight times of up to 200 years. In this representation (time versus distance traveled), steeper slopes correspond to slower trajectories. Several patterns emerge, with some overlaps and crossovers with increasing distance.

Figure H-5 expands the view from 0 (the Sun) to 50 au traveled, showing the travel time from 0 to 10 years; that is the first 1/20th of Figure H-4. Both figures plot time from Earth launch versus

heliocentric distance reached from the Jupiter gravity assist for options 1 and 2 and from the SOM for option 3.

In Figure H-5, the trajectories can be seen to group in three distinct classes. Option 1 and 2 trajectories begin at the average heliocentric Jupiter orbital distance at a variety of “start times” there. Those at larger times also exhibit steeper slopes (longer flyout times) for option 1 and shallower slopes for option 2 (slower transits to Jupiter but injected into faster trajectories with the kick-stage burn there). The option 3 trajectories exhibit a “stairstep” appearance: Trajectories starting closer to the Sun are also shallower (i.e., faster, as one might expect).

Of note are the two option 3 trajectories in Figure H-5 that start at the largest times and are the steepest (i.e., the slowest). These correspond to the lowest-mass Fregat stage. For this example, the added specific impulse provides no advantage over the solids.

Interstellar Probe - Flyout Times to Given Distance for All Launch Configurations for Baseline (860 kg) Spacecraft

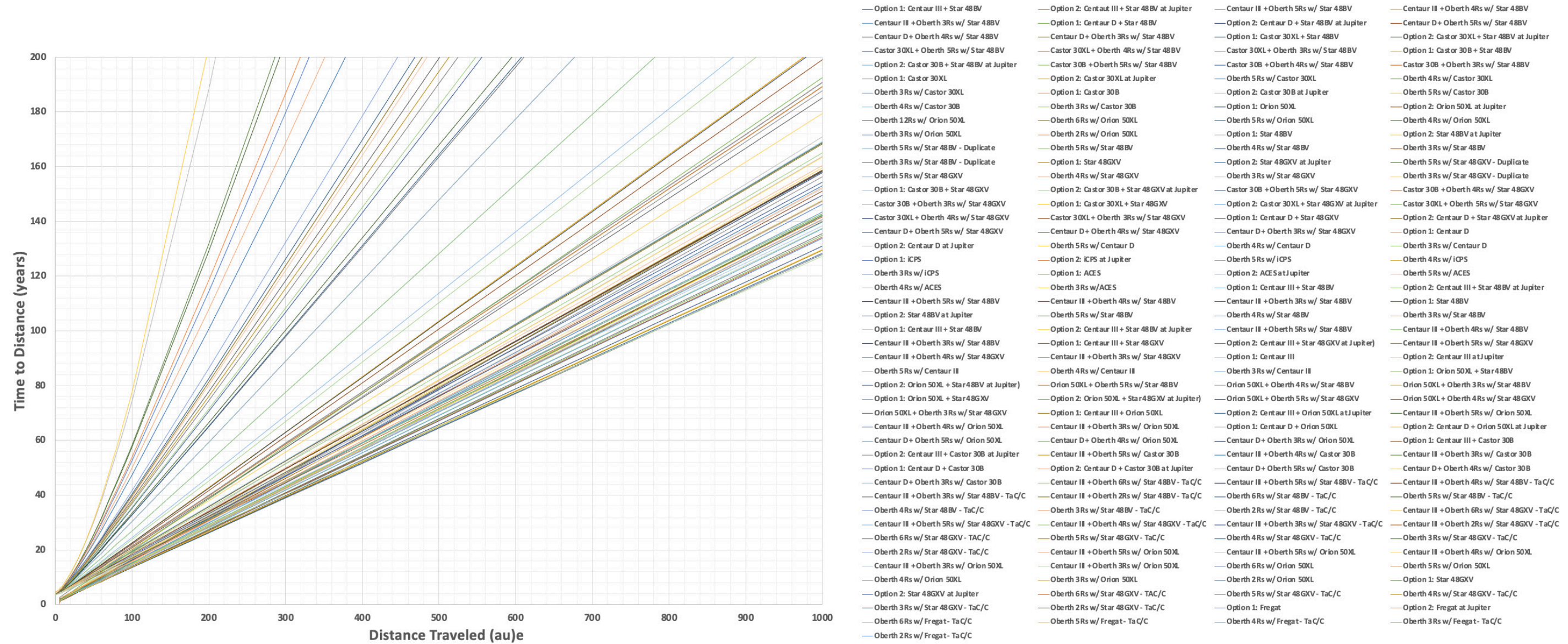


Figure H-4. Time versus distance for the 860-kg observatory case across all three options. Flyout times to 200 years versus heliocentric flyout distances to 1000 au are plotted for 112 valid trajectories (another 69 trial trajectories did not work). (Image credit: Johns Hopkins Applied Physics Laboratory.)

Interstellar Probe - Flyout Times to Given Distance for All Launch Configurations for Baseline (860 kg) Spacecraft

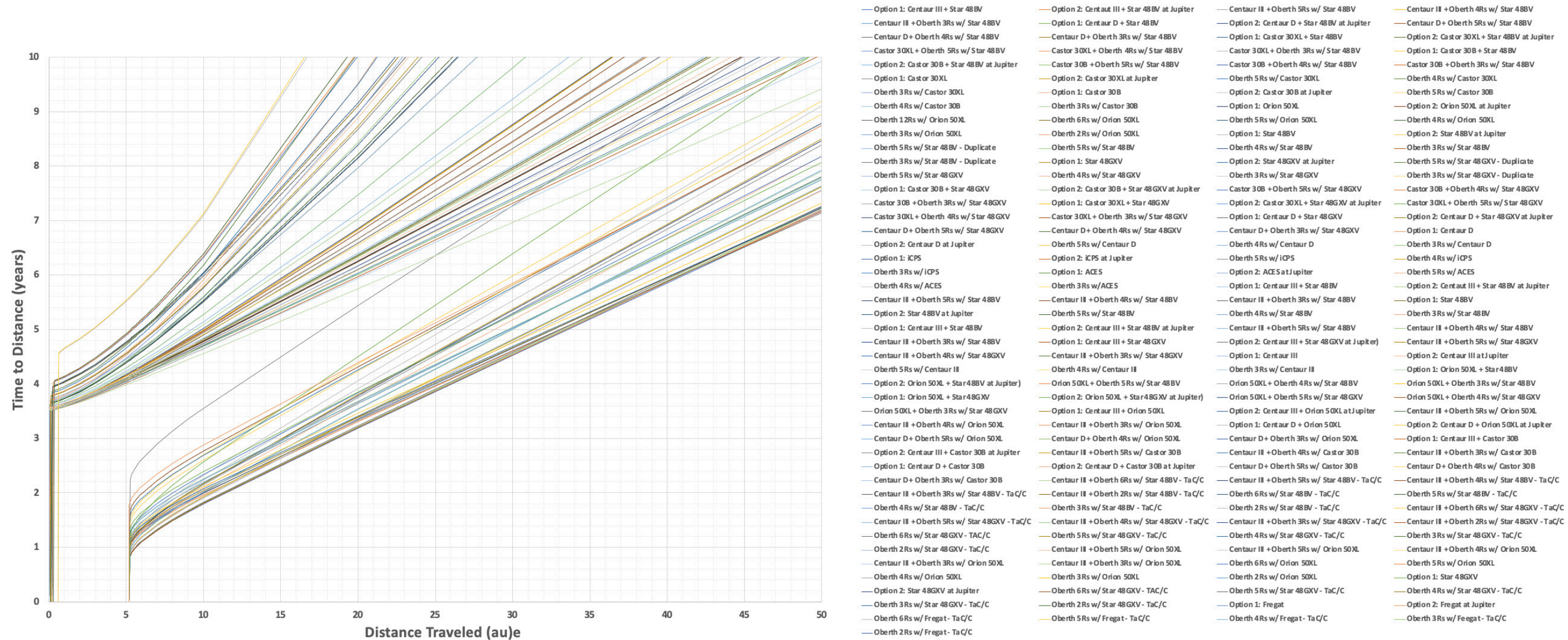


Figure H-5. Expansion of the lower left-hand corner of Figure H-4 by a factor of 5. Options 1 and 2 are clearly separated from option 3 trajectories. Option 3 trajectories also show different performances for Parker Solar Probe versus new UHT material thermal shields. Only a few option 3 trajectories overtake option 1 and 2 trajectories within 50 au. (Image credit: Johns Hopkins Applied Physics Laboratory.)

H.3 Available Performance versus Implementation “Requirements”

H.3.1 Past Studies

All write-ups and studies have stated that an interstellar probe mission must be capable of making a “significant” penetration into the nearby (aka “very local”) interstellar medium (VLISM⁴; Holzer (1989)) in a “reasonable” amount of time. The terms “significant” and “reasonable” have varied over the past 60 years, usually reflecting the perceived “near-term technology horizon” of the time. Implied speeds have ranged from 5 au/year to ~120 au/year to distances of 150 au to 0.1 ly (6,320 au) with travel times of ~20–50 years (reproduced from McNutt Jr. et al. (2021), Table 6). Asymptotic escape speeds from the Sun in excess of ~10 au/year have been—and continue to be—problematic.

H.3.1.1 High-Speed “Solutions”

A review of the entries in Table H-6 points to three different “solutions” that have been invoked in numerous studies. However, each of these has—and continues to have—shortcomings that make their application to Interstellar Probe in the near term problematic.

Solar Oberth Maneuver (SOM)

As discussed in more detail above, the SOM occupied a place in an extended study as part of this effort. Its “promise” has been well documented, beginning with Oberth’s first discussion of it in 1929 (Team, 2021). The issue has been that, until now, there has never been a detailed engineering look at the thermal problems intrinsic to its use. As part of this effort, and drawing on the driving science and payload concerns (Brandt et al., 2021), a spacecraft design that “closes” with the science trades has been developed. Advanced thermal shield material can (on paper) lower accessible perihelia to ~2 solar radii (from the center of the Sun), with better thermal and mass performance than previously thought available from using heavy refractory materials such as tungsten (Ralph L. McNutt, Jr. et al., 2019).

In this study example, the ~900 kg plus the “interstage”/adaptor to an Orion 50XL kick stage are also mated to an ~1600-kg TSA (Figure H-6).

The characteristics of the trajectory are shown in the rightmost column of Table H-5. Decreasing the observatory mass to 251.8 kg (that of Pioneer 10) increases the escape speed to 8.9032 au/year and the ΔV at the Sun to 2.4242 km/s, while decreasing the flight time to 400 au from 52.73 years to 48.08 years. The flyout speed is higher, but the science case no longer closes (limited power, limited HGA and data rates, and limited payload).

Most of the thermal shield mass is associated with protecting the kick stage (Orion 50XL). Lowering the perihelion to 1 solar radius (“touching” the photosphere – not possible to deal with the temperature of 5772 K) would only increase the speed by a factor of $\sim 2^{1/4} = 1.19$ (~20%).

⁴ The VLISM was defined by Holzer in 1989 as the distance out to 0.01 parsecs (pc) from the Sun (i.e., 2062.6 au ~ 11.9 light days).

Table H-6. Interstellar Probe mission requirements and concepts, 1960–2019.

Year	Study	Speed (au/yr)	Means	Distance (au)	Wet Mass (kg)
1960	Simpson Committee	5 or 6	Not specified	Not specified	Not specified
1968	Galactic Jupiter Probe – GSFC	10 au in 3 yr	Passive JGA	10 au (comms limit)	500 lbs (~230 kg)
1971	Ultrplanetary Probe – Ehricke	126	Close solar flyby; 1.06 R_S at $\Delta V = 300$ km/s; NPP	6320 au (0.1 ly); 50 yr	Not specified
1977	Interstellar Precursor – JPL	20	500 kWe NEP at 17 kg/kWe with Hg propellant	400 au (20 yr); 1000 au extended (50 yr)	32,000
1987	TAU – JPL	22.4	1 MWe NEP at 12.5 kg/kWe with LXe at I_{sp} of 12,500 s	1000 au	61,500
1988	(NRC, 1988)	11.7	SOM at 4 R_S at $\Delta V = 5$ km/s	>100 au; less than 20 yr	500–1000
1990	Interstellar Probe/ Frontier Probe	14.7	Two-stage SOM with $I_{sp} = 290$ s	200 au	200
1995	Small interstellar probe	14	SOM with chemical stage after ΔV -VEEGA) to Jupiter	200 au in 25 yr or less	~200
1999	IPSTDT – NASA/JPL	~15	400-m-diameter solar sail from 0.25 au	>200 au in 15 yr	150
2000	Realistic Interstellar Explorer, NIAC Phase I – APL	20.2	SOM at 4 R_S at $\Delta V = 15.4$ km/s; nuclear pulse/NTP/STP	1000 au toward ϵ Eri	50
2002	Realistic Interstellar Explorer, NIAC Phase II – APL	~12	SOM at 4 R_S using STP	1000 au toward ϵ Eri	147
2005	Interstellar Probe Vision Mission using NEP – University of Michigan	Not specified	NEP with LXe and $I_{sp} = 5000$ s; 17,050 kg; Prometheus spacecraft with JGA	150 au in 20.5 yr	36,000
2005	Interstellar Probe Vision Mission (IIE) – APL	8.3	Outbound JGA + 1.0 kWe REP with LXe at I_{sp} of 3734 s	200 au in 28.8 yr	1135
2009	IIE extension to Ares V at large C_3 – APL	9.7	Multistage ballistic with REP + JGA	200 au in 23.2 yr	1230
2014	SLS – APL	>7.4	Ballistic with unpowered JGA	200 au in 25–30 yr	~500
2015	KISS Workshops – JPL	>13	SLS Block 1B + ΔV -EGA and SOM with STP	200 au in 20.5 yr	544; 16,766 kg at launch
2017	Updated JPL	19.1	SLS Block 1B + ΔV -VVEEGA and SOM with STP ($I_{sp} \sim 1350$ s) at 3 R_S at $\Delta V = 11.2$ km/s	200 au within 20 yr	~550; 15,720 kg LH ₂ ; ~28,000 kg total
2019	SLS Block 1B; Part 1 of this study – APL	Varies	Ballistic: Passive JGA, Powered JGA, SOM	≤1000 au	478.3 (Piquette et al., 2019)

Notes: EGA, Earth gravity assist; GSFC, Goddard Space Flight Center; IIE, Innovative Interstellar Explorer; IPSTDT (NASA), Interstellar Probe Science and Technology Definition Team; I_{sp} , specific impulse; JGA, Jupiter gravity assist; JPL, Jet Propulsion Laboratory; KISS, Keck Institute for Space Studies; LH₂, liquid hydrogen; LXe, liquid xenon; NEP, nuclear electric propulsion; NIAC, NASA Institute for Advanced Concepts; NPP, nuclear pulse propulsion; NTP, nuclear thermal propulsion; REP, radioisotope electric propulsion; SLS, Space Launch System; SOM, Solar Oberth maneuver; STP, solar thermal propulsion; VEEGA, Venus–Earth–Earth gravity assist; VEGA, Venus–Earth gravity assist; VVEEGA, Venus–Venus–Earth–Earth gravity assist

If one could replace the solid fuel with zero-boil-off (ZBO) liquid hydrogen (LH₂) and replace the Orion 50XL mass with a nuclear thermal rocket (Boelter et al., 1959) engine with a specific impulse of 900 s (PEWEE-1 test (Finseth, 1991)), only then could the flyout speed be increased significantly: to 16.7 au/year.

Even with ZBO LH₂, this does not close; the Small Nuclear Rocket Engine (SNRE) design engine (Durham, 1972a, 1972b, 1972c) is approximately seven times the mass of the *empty* Orion 50XL motor (which includes the propellant “tank”).

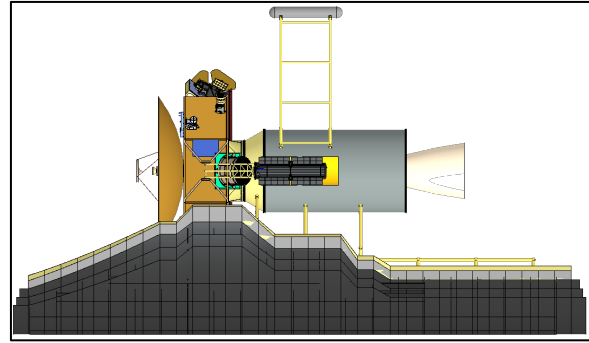


Figure H-6. Baseline spacecraft for option 3 with “interstage” (yellow), ballast (top), Orion 50XL kick stage, undeployed RTGs (one visible at center), and TSA designed for 2R_s perihelion. (Image credit: Johns Hopkins Applied Physics Laboratory.)

Nuclear Electric Propulsion (NEP)

The first (and only to date) planned NEP spacecraft in the United States was the SNAPSHOT spacecraft using the SNAP-10A reactor and a small cesium ion engine. The latter was battery powered, with the battery being charged by the reactor. Total program cost was estimated at the time (1965) as \$111.8M (AEC, 1965). The NASA inflation rate table gives an inflation factor of 11.014 to the current year or ~\$1.23B in current-year dollars. The small unit (500 We) was designed for 1 year of operations (Marshall et al., 2008), but there was a nonnuclear failure 43 days into the mission that scrambled the reactor, jettisoning the beryllium control shields as planned. The parts remain in a nuclear-safe orbit (R. L. McNutt, Jr., Aleman, et al., 2015).

The projected price for the Jupiter Icy Moons Orbiter (JIMO) as the first use of the Prometheus system (Taylor, 2005) apparently precluded that development. Projected development costs and schedules for space nuclear reactors have been an ongoing issue from SNAPSHOT to JIMO (Dix & Voss, 1984; *The SP-100 nuclear reactor program: Should It Be Continued?*, 1992) despite continued calls (Mason & Poston, 2014) for their development (NRC, 2006).

Common elements include: (1) need unattended/autonomous reactor operation for ~10 years, (2) major mass driver is waste heat rejection radiator system, and (3) cost. The Prometheus reactor module development cost was estimated as \$4.165B. The “Project Prometheus Final Report” noted “Analysis of the critical path to launch shows the Reactor Module (and associated Power Conversion) development and testing activities as the most critical path.” (Taylor, 2005) The power systems are also projected to be massive. The 200-kWe Prometheus reactor module had an estimated mass of 6100 kg plus an additional 3336 kg for the waste heat rejection segment.

The technology horizon (2030) plus programmatics led us to conclude that the NEP cost and development risk makes its use problematic (at best) for the purposes of this study.

Solar Sail

Solar sails are an old concept. Spacecraft propulsion with “light pressure” was discussed by Tsiolkovskii and Tsander in the Soviet Union (Tsander, 1967), “rediscovered” in the U.S. by Garwin (Garwin, 1958), popularized by Clarke (Clarke, 1964), and extended to propulsion by laser by Marx

(Marx, 1966). Their use was invoked for an interstellar probe from a challenge by then-NASA-administrator Daniel Goldin and adopted as primary propulsion by the (NASA) Interstellar Probe Science and Technology Definition Team (IPSTDT) (Liewer et al., 2000; Liewer et al., 2001; Team, 2021; Wallace, 1999). Kinematic possibilities have been studied extensively (e.g., (Dachwald et al., 2008); McInnes (2003)), but less has been examined on structural limits (Greschik & Mikulas, 2002).

To enable rapid solar system escape, one needs the “lightness number”

$$\lambda \equiv \frac{\text{(ideal)solar radiation pressure force}}{\text{gravitational force}} = \frac{1.540 \text{ gm}^{-2}}{\sigma_{eff}} \geq 1. \quad (2)$$

Here, σ_{eff} is an effective surface area of the sail craft defined by dividing the total mass (observatory, sail, deployment mechanisms, and sail structure) by the sail area facing the Sun. The “release point” for a solar sail craft needs to be from a location with a sufficiently high speed; typically heliocentric radii of $20 R_s$ to $25 R_s$ have been discussed. To do this, an additional heat shield (= mass) is required. The sail craft to date have been too small to provide science closure to the mission here. Similarly, there has yet to be any engineering closure except for $\lambda \ll 1$ (cf. (R. L. McNutt, Jr. et al., 2011)). For example, for the Solar Cruiser mission (Johnson et al., 2019), the sail area is 1650 m^2 for a 90-kg spacecraft. Hence,

$$\lambda \sim 1.54 \frac{1,650}{90,000} = 0.03 \ll 1. \quad (3)$$

Parker Solar Probe provides a model of a spacecraft that could come close to having the capability to carry sufficient instruments for science closure for Interstellar Probe: it includes a thermal shield capable of solar approach to $\sim 10 R_s$. With its 685-kg mass, obtaining $\lambda = 1$ would require a sail area of greater than 0.44 km^2 or 667 m on a side (this is a lower limit because the sail and support mass are not included).

For this example, each of four 472-m-long spars would have to carry its share of increased radiation pressure near the Sun at the release point. The required materials strength and stiffness per unit mass exceed the current state of the art.

Again, this effort’s technology horizon of 2030 precludes solar sails from being viable. Even with significant additional development, it is not at all obvious whether there is any clear path to what would be the required advances for the science scope of the mission as discussed in this report.

H.3.2 State-of-the-Art Ballistic Opportunities

While the modern history of ballistic rockets is extensive, the technical state of the art was pushed forward largely by World War II. Development of space launch vehicles has proven to be an expensive, dangerous, and time-consuming undertaking. Theoretical underpinnings were advanced by Tsiolkovskii in the (then) Russian Empire (Tsiolkovskiy, 1967) with similar work undertaken by Goddard (United States) (Goddard, 1919, 1920), Oberth (Germany) (Oberth, 1970), and Esnault-Pelterie (France) (Esnault-Pelterie, 1913; Mike Gruntman, 2007). Goddard demonstrated the first liquid-fueled rocket on 16 March 1926, but the direct application of the technology did not occur until the development of the Vergeltungswaffe 2, or V-2, by the Germans during World War II

(M. Gruntman, 2004). All told, the German V-2 ballistic rocket program has been estimated to have cost ~\$40B (FY2015 dollars), with 6048 rockets built and 3225 launched at civilian and military targets. Of importance here is the fact that this effort directly seeded the ballistic missile programs in both the United States and the Soviet Union and also enabled the “Space Race” and the “Moon Race,” all with additional billions of dollars of investment by all parties. For example, the F-1 rocket engine, which was essential to the American Saturn V, was begun as a U.S. Air Force project in 1955 but later picked up by NASA. Its 8-year development cost for use on the Saturn V was estimated as \$1.77B in 1991 (FY1991 dollars) (Day, 2019).

The largest rocket systems ever built were for human landings on the Moon. The Soviet N-1 had four uncrewed flights, all of which ended in failure of the first stage during launches. There were 15 builds of the Saturn V: 13 successful launches including six human lunar landings and 2 canceled flights that became museum exhibits because of the cost of the program (Wikipedia, 2021b).

In the early 1960s, a Saturn V with a Centaur upper stage was considered for use in robotic space exploration (Schulte, 1965). It was baselined for use in the original “Voyager” program of Mars landers, which envisioned one Saturn V delivering two orbiters with two landers to Mars with one launch (Cortright, 1967). As Saturn V launch costs increased, this original “Voyager” was first de-scoped to a Saturn IB launcher and then canceled altogether. The program was resurrected with separate launches and rechristened as Viking 1 and Viking 2.

The idea of using SHLLVs for robotic exploration lay dormant 40 years. It was reviewed by NASA during the Constellation Program and posed in terms of what science missions could be enabled with the then-contemplated Ares V launch vehicle. This was a Saturn V-class launch vehicle, which was key to Constellation. Its use for an interstellar probe mission was advanced both in consideration by the National Academies (NRC, 2008) and in a follow-up NASA Workshop (Langhoff et al., 2008).

Follow-up (unfunded) study results were reported out at IAC meetings in 2009 (R. L. McNutt, Jr. & Wimmer-Schweingruber, 2011), 2010 (R. L. McNutt, Jr. et al., 2011), 2014 (R. L. McNutt, Jr. et al., 2014), 2015 (R. L. McNutt, Jr., Benson, et al., 2015), 2016 (R. L. McNutt, Jr. et al., 2016), and 2017 (R. L. McNutt, Jr. et al., 2017). Initial and evolving results from this (funded) effort were reported out at the subsequent IAC meetings in 2018 (Ralph L. McNutt, Jr. et al., 2019), 2019 (Ralph L. McNutt, Jr. et al., 2019), 2020 (virtual) (R. L. McNutt, Jr. et al., 2020), and 2021 (R. L. McNutt, Jr. et al., 2021). The evolution of thought about staging and vehicle performance can be traced through these publications.

The analyses have concentrated on the 18 SLS cases provided by MSFC (Stough et al., 2019) because similar high- C_3 performance curves for SHLLVs from other potential vendors have not been made available in the public literature (to date). To provide some insight into performance for the 18 MSFC option 1 stacks (refer to Section H.2.3 above), we have replotted the injected mass curves in semi-log format in Figure H-7. Within the caveats of regions of validity of the curves, this allows one both to appreciate the relative locations of the various case curves as well as to see the (positive) effect on adding a fourth stage on performance for lower mass payloads.

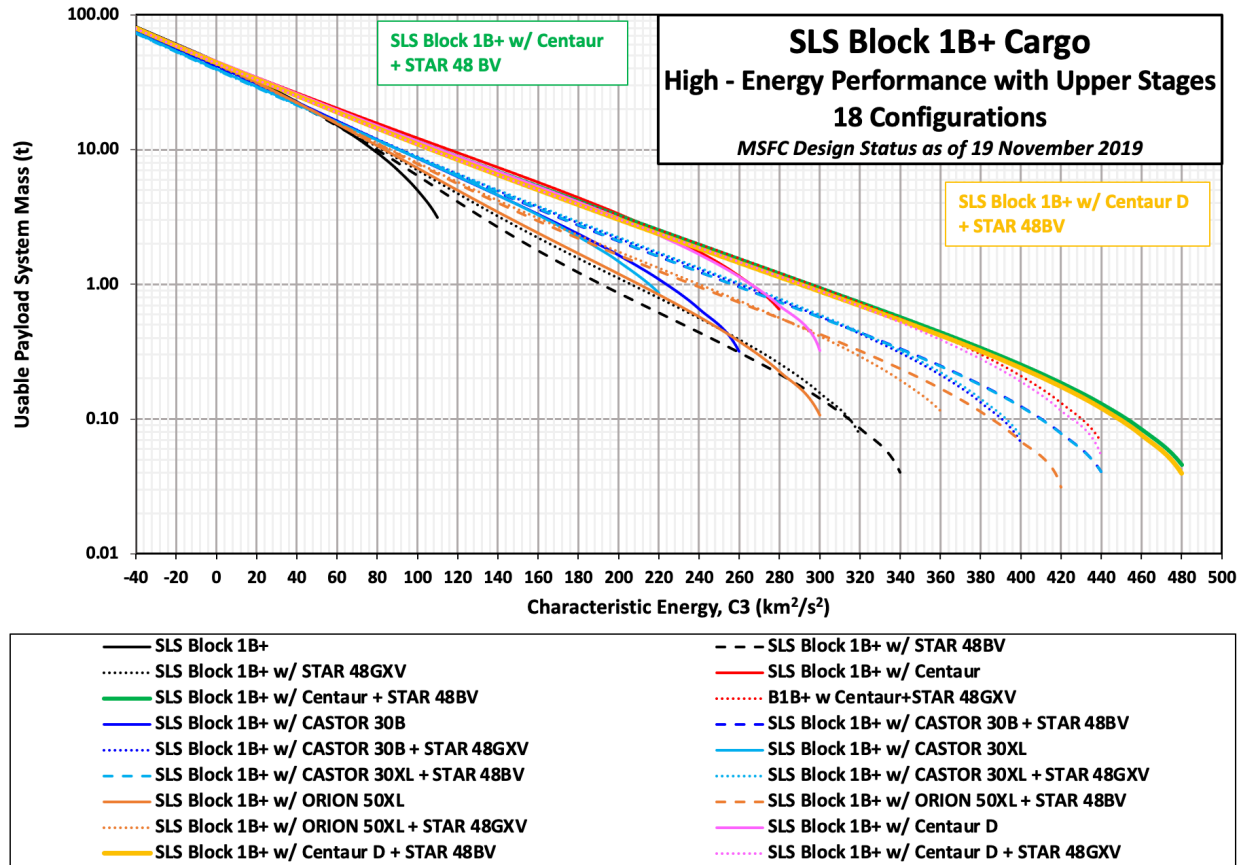


Figure H-7. SLS Block 1B+ Cargo, now referred to as SLS Block 2 Cargo, high-energy performance with upper stages for 18 of the configurations used in this study. (Image credit: Johns Hopkins Applied Physics Laboratory.)

H.4 Appendix H References

AEC (1965) Press Kit - SNAP-10A (Space Nuclear Power Reactor) [Press release]. Retrieved from <https://inldigitallibrary.inl.gov/PRR/91009.pdf>.

Alkalai, L., Karimi, R., Sauder, J., Preudhomme, M., Mueller, J., Cheikh, D., Sunada, E., Couto, A., Arora, N., Rapinchuk, J. (2020) *Rapid access to the interstellar medium and solar-gravity lens focus: A feasibility study*. Paper presented at the 71st International Astronautical Congress (IAC) – The CyberSpace Edition. Virtual.

Ashtari, R., Copeland, D.J., Kinnison, J.D., Rogers, G.D., McNutt Jr, R.L. (2021) *Interstellar communications*. In 2021 IEEE Aerospace Conference, IEEE, Virtual.

Boelter, L.M.K., Stever, H.G., Summerfield, M., et al. (1959) *Space Technology* (Seifert, H.S. Ed.). New York: John Wiley and Sons, Inc.

Brandt, P.C., Provornikova, E.A., Turner, D., et al. (2021) *Interstellar Probe: Humanity's exploration of the galaxy begins*. Paper presented at the 72nd International Astronautical Congress (IAC). Dubai, United Arab Emirates.

Clarke, A.C. (1964) The Sumjammer. *Boy's Life*, 8.

- Cortright, E.M. (1967, 14-15 March) *The Voyager Program*. In American Astronautical Society Annual Goddard Memorial Symposium, AAS Publications Office, Tarzana, California, Sheraton-Park Hotel, Washington, D.C.
- Dachwald, B., Seboldt, W., Lämmerzahl, C. (2008) Solar sail propulsion: An enabling technology for fundamental physics missions. In Dittus, Lämmerzahl, Turyshev, S.G. (Eds.), *Lasers, Clocks, and Drag-Free Control - Exploration of Relativistic Gravity in Space* (pp. 365-381): Springer.
- Day, D.A. (2019) A mighty thunderous silence: The Saturn F-1 engine after Apollo. Retrieved from <https://www.thespacereview.com/article/3724/1>.
- Dix, G.P., Voss, S.S. (1984) *The Pied Piper - A Historical Overview of the Space Power Reactor Program*.
- Durham, F.P. (1972a) *Nuclear engine definition study preliminary report*, Document No. LA-5044-MS. Los Alamos, New Mexico:
- Durham, F.P. (1972b) *Nuclear engine definition study preliminary report*, Document No. LA-5044-MS.
- Durham, F.P. (1972c) *Nuclear engine definition study preliminary report*, Document No. LA-5044-MS. Los Alamos, New Mexico:
- Esnault-Pelterie, M. (1913) Considérations sur les résultats d'un allégement indéfini des moteurs. [A consideration of the effect of indefinitely reducing the weight of motors.]. *Journal de Physique Théorique et Appliquée* 3(1), 218-230. doi: 10.1051/jphys:019130030021800
- Finseth, J.L. (1991) *Overview of Rover engine tests: Final report*, Document No. NASA CR-184270. Huntsville, Alabama:
- Garwin, R.L. (1958) Solar sailing - A practical method of propulsion within the solar system. *Jet Propulsion* 28(3), 188-189. Retrieved from <https://www.fas.org/rlg/030058-SS.pdf>
- Gath, P.F. (2019) *Dual Jupiter swing-by trajectory for Interstellar Probe*. Paper presented at the 70th International Astronautical Congress (IAC). Washington D.C., United States.
- Goddard, R.H. (1919) A method of reaching extreme altitudes. *Smithsonian miscellaneous collections* 71(2), 82. Retrieved from <https://library.si.edu/digital-library/book/smithsonianmisc711921smit>
- Goddard, R.H. (1920) A Method of Reaching Extreme Altitudes. *Nature* 105(2652), 809-811. doi: 10.1038/105809a0
- Greschik, G., Mikulas, M.M. (2002) Design Study of a Square Solar Sail Architecture. *Journal of Spacecraft and Rockets* 39(5), 653-661. doi: 10.2514/2.3886
- Gruntman, M. (2004) *Blazing the Trail: The Early History of Spacecraft and Rocketry*. Reston, VA: AIAA.
- Gruntman, M. (2007) *From Astronautics to Cosmonautics - Space Pioneers Robert Esnault-Pelterie and Ary Sternfeld*. North Charleston, South Carolina: Booksurge. Retrieved from <http://www.astronauticsnow.com/astrocosmo/index.html>

- Heacock, R.L. (1980) The Voyager spacecraft. *Proceedings of the Institution of Mechanical Engineers* 194, 211-224. Retrieved from <http://stickings90.webspace.virginmedia.com/voyager.pdf>
- Holzer, T.E. (1989) Interaction Between the Solar Wind and the Interstellar Medium. *Annual Review of Astronomy and Astrophysics* 27(1), 199-234. doi: 10.1146/annurev.aa.27.090189.001215
- Johnson, L., Curran, F.M., Disssly, R.W., Heaton, A.F. (2019) The Solar Cruiser Mission: Demonstrating Large Solar Sails for Deep Space Missions. Retrieved from <https://ntrs.nasa.gov/api/citations/20190032304/downloads/20190032304.pdf>.
- Langhoff, S., Spilker, T., Martin, G., Sullivan, G. (2008) *Workshop Report On Ares V Solar System Science* (NASA/CP-2008-214592), Document No. 20110012889 Moffett Field, California 94035-1000: NASA Ames Research Center; Moffett Field, C., United States.
- Liewer, P.C., Mewaldt, R.A., Ayon, J.A., Wallace, R.A. (2000) *NASA's interstellar probe mission*. In Space Technology and Applications International Forum (STAIF)-2000, Albuquerque, NM.
- Liewer, P.C., Mewaldt, R.A., Ayon, J.A., Gamer, C., Gavit, S., Wallace, R.A. (2001) Interstellar probe using a solar sail: Conceptual design and technological challenges. In Scherer, K., Fichtner, H., Fahr, H.-J., et al. (Eds.), *COSPAR Colloquium on The Outer Heliosphere: The Next Frontiers COSPAR Colloquia Series* (Vol. 11, pp. 411-420). New York: Pergamon Press.
- Marshall, A.C., Haskin, E.F., Usov, V., A. (Eds.) (2008) *Space Nuclear Safety*. Malabar, Florida: Krieger Publishing Company.
- Marx, G. (1966) Interstellar Vehicle Propelled By Terrestrial Laser Beam. *Nature* 211(5044), 22-23. Retrieved from <http://dx.doi.org/10.1038/211022a0>
- Mason, L.S., Poston, D.I. (2014) 9.1. Surface Power Systems. In Drake, B.G., Watts, K.D. (Eds.), *Mars Design Reference Architecture 5.0 – Addendum #2* (pp. 12). Washington, D.C.: NASA.
- McInnes, C.R. (2003) Solar sailing: mission applications and engineering challenges. *Philosophical Transactions of the Royal Society of London. Series A: Mathematical, Physical and Engineering Sciences* 361(1813), 2989-3008. doi: doi:10.1098/rsta.2003.1280
- McNutt Jr., R.L., Wimmer-Schweingruber, R.F., Gruntman, M., Krimigis, S., Roelof, E., Brandt, P., Vernon, S., Paul, M., Stough, R., Kinnison, J. (2021) *Interstellar Probe – Destination: Universe!* Paper presented at the 72nd International Astronautical Congress (IAC). Dubai, United Arab Emirates.
- McNutt, R.L., Jr., Gruntman, M., Krimigis, S.M., Roelof, E.C., Wimmer-Schweingruber, R.F. (2011) Interstellar Probe: Impact of the Voyager and IBEX results on science and strategy. *Acta Astronautica* 69(9-10), 767-776. Retrieved from <http://www.sciencedirect.com/science/article/pii/S0094576511001639>
- McNutt, R.L., Jr., Wimmer-Schweingruber, R.F. (2011) Enabling interstellar probe. *Acta Astronautica* 68(7-8), 790-801. Retrieved from

<http://www.sciencedirect.com/science/article/B6V1N-50T9475-1/2/fa0fc0accdbcee487278c47c06797bec>

- McNutt, R.L., Jr., Elsperman, M.S., Gruntman, M., Klaus, K.K., Krimigis, S.M., Roelof, E.C., Smith, D.B., Vernon, S.R., Wimmer-Schweingruber, R.F. (2014) *Enabling Interstellar Probe with the Space Launch System (SLS)*. Paper presented at the 65th International Astronautical Congress. Toronto, Ontario, Canada.
- McNutt, R.L., Jr., Aleman, S.M., Amato, M.J., et al. (2015) *Nuclear Power Assessment Study - Final Report*, Document No. TSSD-23122. Laurel, MD: Center, N.G.R.
- McNutt, R.L., Jr., Benson, W.W., Gruntman, M., Krimigis, S.M., Roelof, E.C., Vernon, S.R., Wimmer-Schweingruber, R.F. (2015) *Enabling Interstellar Probe: Space Launch System (SLS) trades*. Paper presented at the 66th International Astronautical Congress. Jerusalem, Israel.
- McNutt, R.L., Jr., Wimmer-Schweingruber, R.F., Gruntman, M., Krimigis, S.M., Roelof, E.C., Zank, G.P., Stone, E.C., Brandt, P.C., Vernon, S.R. (2017) *Near-Term Exploration of the Interstellar Medium*. Paper presented at the 68th International Astronautical Congress. Adelaide, Australia.
- McNutt, R.L., Jr., Wimmer-Schweingruber, R.F., Gruntman, M., Krimigis, S.M., Roelof, E.C., Brandt, P.C., Mandt, K.E., Vernon, S.R., Paul, M.V., Stough, R.W. (2019) *An Interstellar Probe for the Next Heliophysics Decadal Survey*. Paper presented at the 70th International Astronautical Congress. Washington, D.C.
- McNutt, R.L., Jr., Wimmer-Schweingruber, R.F., Gruntman, M., et al. (2019) Near-Term Interstellar Probe: First Step. *Acta Astronautica* 162, 284-299. doi: <https://doi.org/10.1016/j.actaastro.2019.06.013>
- McNutt, R.L., Jr., Wimmer-Schweingruber, R.F., Gruntman, M., et al. (2020, 12 - 14 October 2020) *A Pragmatic Interstellar Probe Mission: Progress and Status*. In 71st International Astronautical Congress (IAC) — IAC CyberSpace Edition, Virtual. Retrieved from <https://dl.iafastro.directory/event/IAC-2020/paper/56295/>
- McNutt, R.L., Jr. (2021) *Optimized Jupiter Gravity Assists – Analytic Approximations*. Paper presented at the 31st AAS/AIAA Space Flight Mechanics Meeting. Virtual. https://www.space-flight.org/docs/2021_winter/31stSFM_Program_FINAL.pdf.
- McNutt, R.L., Jr., Wimmer-Schweingruber, R.F., Gruntman, M., Krimigis, S., Roelof, E., Brandt, P., Vernon, S., Paul, M., Stough, R., Kinnison, J. (2021) *Interstellar Probe – Destination: Universe!* Paper presented at the 72nd International Astronautical Congress (IAC). Dubai, United Arab Emirates.
- McNutt, R.L., Jr., Zurbuchen, T.H., Gruntman, M., Krimigis, S.M., Roelof, E.C., Vernon, S.R., Wimmer-Schweingruber, R.F. (2016) *Interstellar probe: Requirements*. Paper presented at the 67th International Astronautical Congress. Guadalajara, Mexico. <https://iafastro.directory/iac/paper/id/35475/ext/appendix/IAC-16,D4,1,9,x35475.pdf>.

- NRC (1988) *Solar and Space Physics: Space Science in the Twenty-First Century -- Imperatives for the Decades 1995 to 2015*. Washington, D.C.: National Academies Press. doi:10.17226/755
- NRC (2006) *Priorities in Space Science Enabled by Nuclear Power and Propulsion*. Washington, D.C.:
- NRC (2008) *Launching Science: Science Opportunities Provided by NASA's Constellation System*. Washington, D. C.: The National Academies Press. Retrieved from <http://www.nap.edu/catalog/12554.html>
- Oberth, H. (1970) *Ways to Spaceflight* (Agence Tunisienne de Public-Relations, T., Tunisia, 1970, Trans.): National Aeronautics and Space Administration. Retrieved from https://ia600503.us.archive.org/21/items/nasa_techdoc_19720008133/19720008133.pdf
- Piquette, M., Poppe, A.R., Bernardoni, E., et al. (2019) Student Dust Counter: Status report at 38 AU. *Icarus* 321, 116. doi: 10.1016/j.icarus.2018.11.012
- Schulte, L.O. (1965) *Saturn V payload planner's guide* (Douglas Report SM-47274). Santa Monica, California:
- The SP-100 nuclear reactor program: Should It Be Continued?*, U.S. House of Representatives. 15 (1992).
- Stough, R.W., Hitt, D., Holt, B., Philips, A., Patrick, M. (2019) *Supporting Material for APL's Interstellar Probe Final Report* (M20-7868), Document No. 20200000989. NASA Technical Reports Server:
- Taylor, R. (2005) *Prometheus Project: Final Report* (982-R120461). Pasadena, CA:
- Team, I.P.S. (2021) *Interstellar Probe Study 2019 Report*. Web:
- Tsander, F.A. (1967) *From a Scientific Heritage* (NASA TT F-541). Moscow:
- Tsiolkovskiy, K.E. (1967) *Study of outer space by reaction devices*, Document No. NASA TT F-15571. Washington, D.C.:
- Von Braun, W. (1962) *Appendix B, Manned Lunar Landing Program Mode Comparison* (NASA TM-74929), Document No. NASA TM 74929. Washington, D. C.:
- Wallace, R.A. (1999, 03/06/1999 - 03/13/1999) *Precursor missions to interstellar exploration*. In Aerospace Conference 1999, Snowmass at Aspen, CO. doi: 10.1109/AERO.1999.794348
- Wikipedia (2021a) Fregat. Retrieved from <https://en.wikipedia.org/wiki/Fregat>.
- Wikipedia (2021b) Saturn V. Retrieved from https://en.wikipedia.org/wiki/Saturn_V.
- Wikipedia (2021c) Ares V. Retrieved from https://en.wikipedia.org/wiki/Ares_V.
- Wikipedia (2021) Super heavy-lift launch vehicle. Retrieved from https://en.wikipedia.org/wiki/Super_heavy-lift_launch_vehicle.

Appendix I. Acronyms and Abbreviations

AA	Associate Administrator (NASA)
AACS	Attitude Articulation and Control System
AAS	(1) American Astronautical Society
AAS	(2) American Astronomical Society
AC	Alternating Current
ACE	Advanced Composition Explorer
ACE Lab	APL Concurrent Engineering Laboratory
ACES	Advanced Cryogenic Evolved Stage
ACF	Advanced Ceramic Fibers (LLC)
ACO	Advanced Concepts Office
ACR	Anomalous Cosmic Ray
AEC	Automotive Electronics Council
AGU	American Geophysical Union
AHI	Anode Hole Injection
AI	Artificial Intelligence
AIAA	American Institute of Aeronautics and Astronautics
AIM	Aeronomy of Ice in the Mesosphere (Satellite)
ALMA	Atacama Large Millimeter/submillimeter Array
ALSEP	Apollo Lunar Surface Experiments Package
AMMOS	Advanced Multi-Mission Operations System
AMR	Atlantic Missile Range
AMPTE	Active Magnetospheric Particle Tracer Explorers
ANOVA	Analysis of Variance
AoA	Analysis of Alternatives

AOGS	Asia Oceania Geosciences Society
APL	Johns Hopkins Applied Physics Laboratory
ASEE	American Society for Engineering Education
ASME	The American Society of Mechanical Engineers
ASRG	Advanced Stirling Radioisotope Generator
au	Astronomical Unit, defined as exactly 149,597,870,700 meters
B2	Block 2 (of the Space Launch System)
BCE	Before Common Era
BEOL	Back End of Line
BOE	Basis of Estimate
BOLE	Booster Obsolescence Life Extension
BPPP	Breakthrough Propulsion Physics Program
BTI	Bias Temperature Instability
C_3	Square of the Excess Hyperbolic Escape Speed from the Earth
CADRe	Cost Analysis Data Requirement
CALCE	(The) Center for Advanced Life Cycle Engineering (at the University of Maryland)
CAPS	Committee on Astrobiology and Planetary Sciences, committee of the SSB
CATE	Cost and Technical Evaluation
CCE	Charge Composition Explorer
CCD	Charge-Coupled Device
CCKBO	Cold Classical Kuiper Belt Object
CCSDS	Consultative Committee for Space Data Systems
C&DH	Command and Data Handling
CDA	Cosmic Dust Analyzer
CDE	Cosmic Dust Experiment
CDF	(1) Common Data Format

CDF	(2) Cumulative Distribution Function
CDR	Critical Design Review
CDS	Correlated Double Sampling
CENA	Chandrayaan-1 Energetic Neutrals Analyzer
CER	Cost-Estimating Relationship
CETI	Communication with Extraterrestrial Intelligence
CFC	Chlorofluorocarbon
CFDP	CCSDS File Delivery Protocol
CIB	Cosmic Infrared Background
CIBER	Cosmic Infrared Background Experiment
CIBR	Cosmic Infrared Background Radiation
CICG	Centre International de Conférences de Genève
CIR	Corotating Interaction Region
CIVA	Comet Infrared and Visible Analyser
CL	Confidence Level
CMBR	Cosmic Microwave Background Radiation
CME	Coronal Mass Ejection
CMIR	Corotating Merged Interaction Regions
CML	Concept Maturity Level
CMOS	Complementary Metal–Oxide Semiconductor
COB	Cosmic Optical Background
CoDICE	Compact Dual Ion Composition Experiment
COBE	Cosmic Background Explorer
Co-I	Co-investigator
CONOPS	Concept of Operations
COSPAR	Committee on Space Research

COTS	Commercial Off-the-Shelf
CRIS	Cosmic Ray Isotope Spectrometer
CRS	Cosmic Ray Subsystem
CSF	Close Solar Flyby (per Ehricke)
CSSP	Committee on Solar and Space Physics, committee of the SSB
CTR	Controlled Thermonuclear Reactor (controlled fusion with net energy gain)
CU	University of Colorado
CY	Calendar Year
DART	Double Asteroid Redirection Test
DC	(1) Direct Current
DC	(2) Dust Counter
D-DOR	Delta Differential One-Way Ranging
DFMS	Double Focusing Mass Spectrometer
DFVLR	Deutsche Forschungs- und Versuchsanstalt fuer Luft- und Raumfahrt e. V.
DGL	Diffuse Galactic Light
DIRBE	Diffuse InfraRed Background Experiment
DMSP	Defense Meteorological Satellite Program
DOD	Department of Defense (U.S.)
DOE	Department of Energy (U.S.)
DOI	Digital Object Identifier
DOR	Differential One-Way Ranging
DPS	Division for Planetary Sciences (of the American Astronautical Society)
DRACO	Didymos Reconnaissance and Asteroid Camera for OpNav
DS1	Deep Space One, science and electric propulsion technology test mission
DSA	Deep Space Avionics
DSEE	Destructive Single-Event Effect

DSIF	Deep Space Information Facility
DSM	Deep-Space Maneuver
DSN	Deep Space Network
EAC	Estimate at Completion
EBL	Extragalactic Background Light
EEE	Electrical and Electronic Equipment
EGA	Earth Gravity Assist
Δ V-EGA	Delta-V, Earth Gravity Assist
EGU	European Geosciences Union
EIS	(1) Energetic Ion Spectrometer
EIS	(2) Europa Imaging System
EKB	Edgeworth-Kuiper Belt
EM	Electromigration
EMFISIS	Electric and Magnetic Field Instrument Suite and Integrated Science
EMI	Electromagnetic Interference
eMMRTG	Enhanced Multi-Mission Radioisotope Thermoelectric Generator
EMP	Electromagnetic Pulse
ENA	Energetic Neutral Atom
EOL	End of Life
EOR	Earth Orbital Rendezvous
EPD	Energetic Particle Detector
EPS	(1) Energetic Particle Spectrometer
EPS	(2) Energetic Particle Subsystem
EPSC	European Planetary Science Congress
ERBS	Earth Radiation Budget Satellite
ESA	(1) Electrostatic Analyzer

ESA	(2) European Space Agency
ESAS	Exploration System Architecture Study
ESD	Electrostatic Discharge
EUS	Exploration Upper Stage
EUV	Extreme Ultraviolet
FC	Faraday Cup
FGM	Fluxgate Magnetometer
FIR	Far Infrared
FISO	Future In-Space Operations
FMEA	Failure Mode and Effects Analysis
FMMEA	Failure Modes, Mechanisms, and Effects Analysis
F-N	Fowler–Nordheim
FOV	Field of View
FPA	Focal Plane Array
FPGA	Field-Programmable Gate Array
FRG	Federal Republic of Germany, aka “West Germany” (1949–1990)
FUV	Far Ultraviolet
FWHM	Full Width at Half Maximum
FY	Fiscal Year
GA	Gravity Assist
G&C	Guidance and Control
GCR	Galactic Cosmic Ray
GDF	Globally Distributed Flux
GDS	Ground Data System
GEO	Geostationary Earth Orbit
GFE	Government-Furnished Equipment

GHR	Goddard High Resolution Spectrograph
GIRE3	Galileo Interim Radiation Environment Model Version 3
GMIR	Global Merged Interaction Region
GNC	Guidance, Navigation, and Control
GPHS	General-Purpose Heat Source
GTO	Geosynchronous Transfer Orbit
GUVI	Global Ultraviolet Imager
HabEx	Habitable Exoplanet Observatory
HAE	High-Amplification Event, continuum emission from quasars
HENA	High-Energy Neutral Atom
HETS	High-Energy Telescope System
HfC	Hafnium Carbide
HGA	High-Gain Antenna
HIS	Heavy Ion Sensor
HOPE	Helium Oxygen Proton Electron (instrument)
HP	Heliopause
HRI	High-Resolution Instrument
HSO	Heliophysics System Observatory
HST	Hubble Space Telescope
HTC	Halley-Type Comet
HUT	Hopkins Ultraviolet Telescope
HV	High Voltage
H-wall	Hydrogen Wall
IAA	International Academy of Astronautics
IAC	International Astronautical Congress
IAF	International Astronautical Federation

IAU	International Astronomical Union
IBEX	Interstellar Boundary Explorer, Heliophysics Small Explorer
IC	Integrated Circuit
ICME	Interplanetary Coronal Mass Ejection
ICPS	Interim Cryogenic Propulsion Stage
IDA	Interstellar Dust Analyzer
IDEX	Interstellar Dust Explorer
IDP	Interplanetary Dust Particle
IEEE	Institute of Electrical and Electronics Engineers
I/F	Interface
IFOV	Instantaneous Field of View
IGBT	Insulated-Gate Bipolar Transistor
IHP	Interstellar Heliopause Probe
IIE	Innovative Interstellar Explorer, APL Interstellar precursor “Vision Mission” study
IKAROS	Interplanetary Kite-craft Accelerated by Radiation of the Sun
IM	Interstage Module
IMAGE	Imager for Magnetopause-to-Aurora Global Exploration
IMAP	Interstellar Mapping and Acceleration Probe
IMF	Interplanetary Magnetic Field
IMU	Inertial Measurement Unit
INCA	Ion and Neutral Camera
INMS	Ion and Neutral Mass Spectrometer
IOC	Initial Operational Capability
IPD	Interplanetary Dust
IPSTDT	Interstellar Probe Science and Technology Definition Team (three meetings at JPL in 1999)
IR	Infrared

IRAS	Infrared Astronomy Satellite
IRIS	Infrared Interferometer Spectrometer and Radiometer
IRM	Infrared Spectral Mapper
ISD	Interstellar Dust
ISEE-3	International Sun-Earth Explorer-3
ISM	Interstellar Medium
ISMF	Interstellar Magnetic Field
ISN	Interstellar Neutral
ISO	(1) Infrared Space Observatory
ISO	(2) International Organization for Standardization
I_{sp}	Specific Impulse
ISPM	International Solar Polar Mission
IT	Information Technology
I&T	Integration and Testing
IUS	Inertial Upper Stage
IUVS	Imaging Ultraviolet Spectrograph
IW	Interstellar Wind
JAXA	Japan Aerospace Exploration Agency
JEDI	Jupiter Energetic-particle Detector Instrument
JENI	Jupiter Energetic Neutrals and Ions
JFC	Jupiter-Family Comet
JGA	Jupiter Gravity Assist
JIMO	Jupiter Icy Moons Orbiter
JoEE	Jovian Energetic Electrons
JOI	Jupiter Orbit Insertion
JOSE	Jovian Specification Environment

JPL	Jet Propulsion Laboratory
JUICE	JUpiter ICy Moons Explorer
JWST	James Webb Space Telescope
KB	Kuiper Belt
KBO	Kuiper Belt Object
keV	Kiloelectronvolt
KISS	Keck Institute for Space Studies
KSC	Kennedy Space Center
λ	“Lightness Number,” Photon Sails
LADEE	Lunar Atmosphere and Dust Environment Explorer
LANL	Los Alamos National Laboratory, designation since 1981
LASL	Los Alamos Scientific Laboratory, designation from 1945 to 1980 (1943–1945 “Project Y”)
LASP	Laboratory for Atmospheric and Space Physics (at the University of Colorado)
LATMOS	Laboratoire atmosphères, milieux, observations spatiales (Laboratory for Atmospheres, Environments, Space Observations)
LBTI	Large Binocular Telescope Interferometer
LCC	Life-Cycle Cost
LCCE	Life-Cycle Cost Estimate
LCPMC	Low-Cost Planetary Missions Conference
LDEX	Lunar Dust Experiment
LDPC	Low-Density Parity Check
LECP	Low-Energy Charged Particle
LED	Light-Emitting Diode
LEISA	Lisa Hardaway Infrared Mapping Spectrometer (formerly Linear Etalon Imaging Spectral Array)
LENA	Low-Energy Neutral Atom Imager
LEO	Low Earth Orbit

LES	Lincoln Experimental Satellite
LET	Linear Energy Transfer
LF ₂	Liquid Fluorine, energetic cryogenic rocket oxidizer, notional
LGA	Low-Gain Antenna
LHB	Late Heavy Bombardment
LH ₂	Liquid Hydrogen, cryogenic rocket fuel
LIC	Local Interstellar Cloud
LISM	Local Interstellar Medium
LLC	Limited Liability Company (or Corporation)
LORRI	Long Range Reconnaissance Imager
LOS	Line of Sight
LOX	Liquid Oxygen, cryogenic rocket oxidizer
LPP	Lifetime Performance Prediction
LPSC	Lunar and Planetary Science Conference
LRD	Launch Readiness Date
LSST	Legacy Survey of Space and Time
LST	Lifetime Study Team
LUVOIR	Large Ultraviolet Optical Infrared Surveyor
LV&S	Launch Vehicle and Services
LWS	Living With a Star, program within NASA's Heliophysics Division
LXe	Liquid Xenon, space-storable rocket propellant for low-thrust, electric engines
ly	Light Year, = 9,460,730,472,580,800 meters (exactly) \approx 63,241.077 au (per IAU)
LYA	Lyman-Alpha
MA	Mission Assurance
MAG	Magnetometer
mas	Milliarc Second

MAVEN	Mars Atmosphere and Volatile Evolution
MBB	Messerschmitt-Boelkow-Blohm GmRH
MBE	Multiple-Bit Error
MC/C	Metal Carbide on Carbon
MCP	Microchannel Plate
MCR	Mission Concept Review
MDR	Mission Design Review
MEL	Master Equipment List
MENA	Medium-Energy Neutral Atom
MEOP	Maximum Expected Operating Pressure
MEPA	Medium-Energy Particle Analyzer
MESSENGER	Mercury Surface, Space Environment, Geochemistry, and Ranging
MEV	Maximum Expected Value
MGA	(1) Mass Growth Allowance
MGA	(2) Medium-Gain Antenna
MHD	Magnetohydrodynamic
MHW	Multi-Hundred Watt
MLE	Maximum Likelihood Estimation
MLI	Multilayer Insulation
MMH	Monomethyl Hydrazine, space-storable rocket fuel
MMRTG	Multi-Mission Radioisotope Thermoelectric Generator
MMS	Magnetospheric Multiscale (Mission)
MOC	Mission Operations Center
MOCET	Missions Operations Cost Estimating Tool
MON	Mixed Oxides of Nitrogen, space-storable rocket oxidizer
MOps	Mission Operations

MOSFET	Metal–Oxide–Semiconductor Field-Effect Transistor
MPD	Magnetoplasma Dynamic, notional, in-space, high-power electric rocket engine
MRR	Mission Readiness Review
MSFC	Marshall Space Flight Center
MSL	Mars Science Laboratory, aka Curiosity
mt	Metric Ton, defined as 1000 kg
MTOF	Mass Time of Flight
MTTF	Mean Time to Failure
MTF	Modulation Transfer Function
MVIC	Multispectral Visible Imaging Camera
Myr	Million Years
NARA	National Archives and Records Administration
NASA	National Aeronautics and Space Administration
NBTI	Negative-Bias Temperature Instability
NDSEE	Nondestructive Single-Event Effect
NE	Nuclear Electric
NEOCAM	Near-Earth Object Camera
NEP	Nuclear Electric Propulsion
NEPAG	NASA EEE Parts Assurance Group
NERVA	Nuclear Engine for Rocket Vehicle Application
NETS	Nuclear and Emerging Technologies for Space
NEXT	NASA Evolutionary Xenon Thruster
NGMS	Neutral Gas Mass Spectrometer
NGRPS	Next Generation Radioisotope Power Source
NGST	Next Generation Space Telescope
ngVLA	Next Generation Very Large Array

NIAC	NASA Institute for Advanced Concepts
NICM	NASA Instrument Cost Model
NIM	Neutral gas and Ion Mass Spectrometer
NIRSpec	Near Infrared Spectrograph
NLS – II	NASA Launch Service – II
NMIS	Near Infrared Mapping Spectrometer
nMOS	N-Channel-Type Metal–Oxide Semiconductor
NMS	Neutral Mass Spectrometer
NPP	Nuclear Pulse Propulsion
NPR	NASA Procedural Requirement
NRA	NASA Research Announcement
NRAO	National Radio Astronomy Observatory
NRC	National Research Council
NRE	Nonrecurring Engineering
NSET	NASA Statistical Engineering Team
NSSDC	National Space Science Data Center
NSSDCA	NASA Space Science Data Coordinated Archive
NTE	Not-to-Exceed
NTO	Nitrogen Tetroxide, space-storable rocket oxidizer
NTP	Nuclear Thermal Propulsion
NTR	Nuclear Thermal Rocket
NYC	New York City
O-wall	Oxygen Wall
OCC	Oort Cloud Comet
OPAG	Outer Planets Assessment Group
OpNav	Optical Navigation

ORR	Operational Readiness Review
OSIRIS-REx	Origins, Spectral Interpretation, Resource Identification, Security, Regolith Explorer
OSS	Office of Space Science
OVIRS	OSIRIS-REx Visible and Infrared Spectrometer
PACS	Photodetector Array Camera and Spectrometer
PAM	Payload Assist Module, kick stage designator
PAM – S	Payload Assist Module – Special, unique build for Ulysses (ESA) mission
pc	Parsec, distance at which a star exhibits an Earth-based parallax of 1" (of arc)
PDR	Preliminary Design Review
PDS	Planetary Data System
PDU	Power Distribution Unit
PEP	Particle Environment Package
PEPSSI	Pluto Energetic Particle Spectrometer Science Investigation
PER	Pre-Environmental Review
PI	Principal Investigator
PIR	Panel on Interstellar Research
PLS	(1) Plasma Science
PLS	(2) Plasma Subsystem
PM	Project Management
pMOS	P-Channel-Type Metal–Oxide Semiconductor
PMS	Propulsion Module Subsystem
PMSEMA	Project Management, Systems Engineering, and Mission Assurance
PMSR	Project Management and System Review
PoF	Physics of Failure
PPD	Protoplanetary Disk
PRA	Probabilistic Risk Assessment

PS	Project Scientist
PSE	Power Supply Electronics
PSR	Pre-Ship Review
PSW	Payload System Weight
PUI	Pickup Ion
PVDF	Polyvinylidene Fluoride
PWS	(1) Plasma Wave Spectrometer
PWS	(2) Plasma Wave Subsystem
px	Pixel
QOZ	Quasi-Optical Zone (per Ehricke)
QTN	Quasi-Thermal Noise
RAID	Random Array of Independent Disks
RBD	Reliability Block Diagram
RBSPICE	Radiation Belt Storm Probes Ion Composition Experiment
R-D	Reaction–Diffusion
REP	Radioisotope Electric Propulsion
RF	Radio Frequency
RILT	Risk-Informed Life Testing
RISCS	Risk Information Security Compliance System
R_J	Jovian Radius, using 1 $R_J = 71,492$ km
RMAP	Remote Memory Access Protocol
RoHS	Restriction of Hazardous Substances
ROM	Rough Order of Magnitude
ROSINA	Rosetta Orbiter Spectrometer for Ion and Neutral Analysis
RPM	Retropropulsion Model
RPS	(1) Radioisotope Power Source

RPS	(2) Radioisotope Power System
RPWS	Radio and Plasma Wave Science
R_S	Solar Radius, with 1 R_S taken herein as 695,700 km
RTG	Radioisotope Thermoelectric Generator
RTLTL	Round-Trip Light Time
RTOF	Reflectron Time of Flight
SAE	(formerly) Society of Automotive Engineers; now “SAE International”
SAPPHIRE	Solar Accumulated and Peak Proton and Heavy Ion Radiation Environment
SARA	Sub-keV Atom Reflecting Analyzer
SBE	Single-Bit Error
S/C	Spacecraft
SDC	Student Dust Counter
SDI	Strategic Defense Initiative
SDT	Science Definition Team
SE	Systems Engineering
SEB	Single-Event Burnout
SEC	Sun–Earth Connection
SEE	Single-Event Effect
SEFI	Single-Event Functional Interrupt
SEGR	Single-Event Gate Rupture
SEL	Single-Event Latch-up
SEP	Solar Electric Propulsion
SEPICA	Solar Energetic Particle Ionic Charge Analyzer
SERT I	Space Electric Rocket Test I
SET	Single-Event Transient
SETI	Search for Extraterrestrial Intelligence

SEU	Single-Event Upset
SHINE	Solar, Heliospheric, and INterplanetary Environment
SHLLV	Super Heavy-Lift Launch Vehicle
SHS	Spatial Heterodyne Spectrometer
SIR	(1) Stream Interaction Region
SIR	(2) System Integration Review
SIS	(1) Solar Isotope Spectrometer
SIS	(2) Suprathermal Ion Spectrograph
SIT	Suprathermal Ion Telescope
SLAC	Stanford Linear Accelerator
SLS	Space Launch System
SMD	Science Mission Directorate
SNR	Signal-to-Noise Ratio
SNRE	Small Nuclear Rocket Engine
SOC	Science Operations Center
SOHO	Solar and Heliospheric Observatory
SOM	Solar Oberth Maneuver
SOZ	Suboptical Zone (per Ehricke)
SPDF	Space Physics Data Facility
SPE	Solar Particle Event
SPICE	Spectral Imaging of the Coronal Environment
SPIE	SLS Spacecraft/Payload Integration and Evolution (Office)
SRB	Standing Review Board
SRM	Solid Rocket Motor
SRR	(1) System Readiness Review
SRR	(2) System Requirements Review

SRU	Shunt Regulator Unit
SSB	Space Studies Board, derived from Space Science Board in 1989
SSD	Solid-State Detector
SSG	Science Steering Group (Voyager Project)
SSMM	Solid-State Mass Memory
ssr	Solar System Radius, using 40 au (per Ehricke)
SSR	Solid-State Recorder
SSUSI	Special Sensor Ultraviolet Spectrographic Imager
STDT	Science and Technology Definition Team
STEREO	Solar Terrestrial Relations Observatory
STIS	Space Telescope Imaging Spectrograph
STM	Science Traceability Matrix
STP	Solar Thermal Propulsion
STS	Space Transportation System, aka <i>Space Shuttle</i>
STSci	Space Telescope Science Institute
SUDA	SURface Dust Analyzer
SW	Solar Wind
SWA	Solar Wind Analyser
SWAN	Solar Wind Anisotropies
SWAP	Solar Wind Around Pluto
SWEAP	Solar Wind Electrons Alphas and Protons
SWEPAM	Solar Wind Electron Proton Alpha Monitor
SWICS	Solar Wind Ion Composition Spectrometer
SWIR	Short-Wave Infrared
TAU	Thousand Astronomical Units, interstellar precursor mission concept at JPL, late 1980s
TCM	Trajectory-Correction Maneuver

TCS	Thermal Control Subsystem
TDDDB	Time-Dependent Dielectric Breakdown
TDI	Time-Delay Integration
TESS	Transiting Exoplanet Survey Satellite
3D	Three-Dimensional
TID	Total Ionizing Dose
TIMED	Thermosphere Ionosphere Mesosphere Energetics and Dynamics
TNID	Total Nonionizing Dose
TNO	Trans-Neptunian Object
TOF	Time of Flight
TPS	(1) The Planetary Society
TPS	(2) Thermal Protection System
TRL	Technology Readiness Level
TS	Termination Shock
TSA	Thermal Structure Assembly
TTC	Telemetry, Tracking, and Command
TTF	Time to Failure
TTMC	Time to Minimum Current
TV	Thermal Vacuum
TWTA	Traveling-Wave Tube Amplifier
UDMH	Unsymmetrical Dimethylhydrazine, space-storable rocket fuel
UHT	Ultrahigh Temperature
ULA	United Launch Alliance
ULEIS	Ultra Low Energy Isotope Spectrometer
UMDH	Unsymmetrical Dimethyl Hydrazine
UV	Ultraviolet

UVS	Ultraviolet Spectrometer
UVV	Ultraviolet/Visible
UZ	Ultraplanetary Zone (per Ehrlicke)
VAFB	Vandenberg Air Force Base
VASIMR	Variable Specific Impulse Magnetoplasma Rocket, developmental rocket engine
VASP	Vienna Ab Initio Simulation Package
vdf	Velocity Distribution Function
VEEGA	Venus–Earth–Earth Gravity Assist
VGA	Venus Gravity Assist
VIM	Voyager Interstellar Mission
VIMS	Visible and Infrared Mapping Spectrometer
VIR	Visible-Infrared Mapper
VIRTIS	Visible and Infrared Thermal Imaging Spectrometer
VISIR	Visible Through Infrared
VISNIR	Visible and Near Infrared
VLBI	Very-Long Baseline Interferometry
VLF	Very Low Frequency
VLISM	Very Local Interstellar Medium, original definition of within 0.01 pc of the Sun
VVEEGA	Venus–Venus–Earth–Earth Gravity Assist
W	Watt
WBS	Work Breakdown Structure
WISE	Wide-field Infrared Survey Explorer
WMAP	Wilkinson Microwave Anisotropy Probe
ZBO	Zero Boil Off
ZI	Zone of Isolation (per Ehrlicke)
ZL	Zodiacal Light

